INVESTIGATING BACTERIAL LIPOPOLYSACCHARIDES AND INTERACTIONS WITH ANTIMICROBIAL PEPTIDES

by

Joshua Strauss

A Thesis

Submitted to the Faculty

of the

WORCESTER POLYTECHNIC INSTITUTE

in partial fulfillment of the requirements for the

Degree of Master of Science

in Chemical Engineering

_____

Jan. 2009

APPROVED:

_____

Terri A. Camesano, Ph.D., Research Advisor
Associate Professor of Chemical Engineering
Worcester Polytechnic Institute

_____

David DiBiasio, Ph.D., Department Head
Associate Professor of Chemical Engineering
Worcester Polytechnic Institute

Table of Contents

List of Tables

List of Figures

Acknowledgements

The past 3½ years that I spent in Professor Camesano's research laboratory have been a wonderful experience. My degree would not be possible without Professor Camesano for making this experience possible. She has guided me to become a better scientist and presenter of our work to the public and scientific community. I treasure her encouragement after shredding the many publication drafts that I have submitted and her comments and corrections have made me a better writer. The trips to Orlando, Palo Alto, Toronto, and New Orleans were some of the best experiences in the lab and I would like to thank her for making these experiences possible.

Next I would like to thank Paula Restrepo for encouraging me to join the lab following my IQP in Costa Rica, Eric Wong for being a great friend and roommate all these years, and Russ Grossman for the many Star Trek and MacGyver discussions. I am still amazed you let us duct tape you to a chair just to be more like MacGyver.

Professor Rawson and Mr. Gagnon for words of encouragement, Professor Prusty Rao for help drawing the LPS structures, and Professor McGimpsey for allowing us to use his lab's instruments. Dr. Charlene Mello and Josh Uzarski for useful discussions with the cecropin work.

People in my lab and research group including Christine Cronin, Andrea Kadilak, Ray Emerson, Arzu Atabek, Laila Abu-lail, Lauren Blake, Sena Ada, Kathleen Wang, and Yuanyuan Tao. Eftim Milkani was great playing tennis with. Ma. Crisela Santos Toto was helpful with the SAS program. Yatao Liu and Paola Pinzón-Arango have been in the lab since I first joined and have made the experience enjoyable and have given me wonderful advice to strengthen myself as a researcher.

My family has been totally supportive during these years. My parents Liz and David Strauss have always kept their house open for whenever I wanted to get out of Worcester and the car is awesome to have. My aunts Trudy and Margie have been wonderful for opening their homes in Hillsdale and Sturbridge. My brothers Ben and Jacob, as well as my grandparents Carol and Bernie Strauss have been inspiring all these years.

For all of those who not mentioned for understanding it's almost impossible to acknowledge everyone who has inspired and helped me through these years.

Finally, last but certainly not least my girlfriend Elissa Wolf has been a wonderful inspiration all of these years and I'm looking forward to the lifetime together we have ahead of us.

1: Research Motivation

There are currently >900 antimicrobial peptides (AMPs) isolated from multi- and single cellular species that are active against bacteria[4], fungi[5], cancer cells[6], and viruses[7]. The original purpose of isolating antimicrobial peptides from specimens was to replace the aging supply of antibiotics that have been plagued by bacterial resistance[8]. Antibiotics work best against actively-reproducing planktonic bacteria[9-11]. DNA and cell wall formation will be disrupted by antibiotics, and therefore enabling the body's immune system to overcome an infection. In the past few decades, scientists have learned of growing bacterial resistance to once easily-treatable diseases such as tuberculosis, meningitis, and gonorrhea[12-14]. Now it is common for a first-line prescription antibiotic to be ineffective, requiring more powerful antibiotic prescriptions and, at times, leaving doctors without an effective treatment[15-19].

Beginning in the 1980's, research began in earnest to better understand peptides' role in the immune system of multicellular organisms[20, 21]. From the cecropia moth in 1981[22], and later pig intestine[23], scientists isolated what became known as cecropin peptides, which are cationic and alpha helical in structure[24, 25]. AMPs are typically chains of 19-82 amino acids and were subsequently discovered in single cellular organisms, such as bacteria, and multicellular organisms[26].

AMPs have maintained effectiveness over millions of years of evolution against bacteria, viruses, and fungi, which makes them attractive as antibiotics[2, 26]. General commercialization is years or decades away, but nisin, for example, is a peptide that was approved in 1988 for use as a food preservation[27-29]. Some characteristics that hamper

product development of AMPs are that they can lead to hemolytic activity[30], and data suggests that they are most effective against insurgent microbes when a variety of AMPs are present[31-33].

While research is ongoing with respect to antibiotic substitutions, we have recognized a different potential for AMPs; development of a novel biosensor. Biosensors, for the most part, use antibodies or nucleic acid detectors that bind to specific locations on the host cell[34, 35]. Although still under development, nucleic acid detectors lack batch-to-batch consistency and are extremely expensive to implement. Our approach differs in that we are employing AMPs, specifically cecropin P1, as the cellular marker.

The need for reliable biosensors has been illustrated by the numerous *Escherichia coli* outbreaks associated with meats and fresh produce. *E. coli* O157:H7, identified as the culprit in the 1982 outbreak of dysentery in the United States[36, 37], has been associated with recent food recalls such as the fall 2006 recall of spinach[38] and numerous other ground beef recalls in the United States such as a 1997 recall of beef patties from Colorado[39], 2000 outbreak of *E. coli* O157:H7 in Minnesota[40], and continues to be found in ground beef samples[38, 41, 42].

The effectiveness of AMPs has been well documented against pathogens; however, relatively little is understood regarding their underlying mechanisms of action against bacteria. Although creating an AMP biosensor to detect *E. coli* O157:H7 would be a breakthrough, we seek to take a step further and discover how AMPs interact with bacterial lipopolysaccharides (LPS) that have been well characterized in terms of core polysaccharide groups and O-antigen structures.

By immobilizing cecropin P1 (CP1) to silicon nitride and gold (CP1-cys), we measured the binding forces between bacteria and peptides, and explored important bacterial features such as LPS composition and length that influence binding affinity with CP1. The structure of the LPS is comprised of 3 sections: lipid A, core group, and O-antigen. We are mostly interested in the initial binding between AMP and LPS since our goal is to develop a novel biosensor that can detect pathogenic bacteria within seconds of exposure. Considering the short exposure period, the AMP would only be exposed to the O-antigen and outer core groups, which are repeating sugar chains that are essential for bacterial pathogenicity and adhesion to substrates. Although geared for use as a novel biosensor, results of this study can also be applied to the using AMPs for replacing or enhancing the activity of antibiotics. Our work suggests that CP1 may not be serotype specific, but targets the O-antigen before interfering with phospholipid groups of the bacterial membrane. Other factors that assist in pathogenicity, such as LPS length, may also be important for consideration of CP1 potency.

2: Literature Review

2.1: The Biofilm

Bacteria may be found in two separate forms; planktonic (i.e. free in suspension), and as part of biofilm. In nature, 99.9% of bacteria are found within biofilms[43]. Biofilms are commonly thought of as 3-dimensional matrices consisting of 75% to 95% 'slime' with the remainder being the cells[44]. The slime is most important for the survival of the bacteria, and in certain cases, toxic for the host. The slime acts as a shield against antibiotics, environmental stresses, and bodily defenses, making it the pristine environment for bacteria to thrive[44].

The 'slime' is different for each type of bacterium, consisting largely of negatively charged and neutral polysaccharide groups[44]. The polysaccharides give the 'slime' its sticky characteristics that attach cells to substrates and each other. Indwelling charges are important for ion exchange between cells in the biofilm. This is important for trapping and distributing food, such as iron, within the biofilm so that the cells do not starve. In some environments, such as water distribution systems, cells have demonstrated an amazing ability to survive given a limited nutrient environment of only trace amounts of iron and other organic compounds[45].

Two main molecular groups, polymeric carbohydrates and polymeric proteins, have been shown to promote bacterial retention to substrates. In the case of *S. epidermidis*, two prominent polysaccharides have been identified including capsular polysaccharide (PSA) and polysaccharide intercellular adhesion (PIA)[45]. The accessory gene regulator (*agr*) system influences both biofilm dispersal and attachment of cells to

surfaces, but does not regulate PIA expression[46]. Studies have shown that disrupting the *agr* locus of *S. epidermidis* results in superior adhesion to polystyrene, increased biofilm formation, and increased expression of the AtlE gene that enhances attachment to abiotic surfaces[45].

Once attachment occurs, phenotypic changes alter protein expression within the cell in a matter of seconds; thus initiating the biofilm[45, 47]. The proteins irreversibly anchor the bacteria to the surface. Within 12 minutes, cells begin accumulating proteins and polysaccharide slime that further bond the cells to the substrate and to other cells within the matrix[45]. The biofilm grows in an upwards motion as daughter cells are created through further division.

Eventually, the biofilm may grow as high as 60 μm before shear stresses in the bloodstream break off sections of the biofilm[48]. It is also suspected that cell-to-cell signaling may provoke this detachment in order to keep cells at the bottom of the biofilm from starving. Alginate lyase is one such component that has been shown to cause early detachment of bacteria from a biofilm[49]. Other factors including pH, rate of oxygen uptake, electron transport, and heat production may also be useful for signaling to bacteria that a biofilm is overly mature[50].

2.2: LPS and Serotpying *E. coli*

2.2.1 Importance of E. coli *Lipopolysaccharide*

Recent *E. coli* outbreaks in spinach and meat products have demonstrated the continuing threats posed by pathogenic *E. coli*[38, 41, 42]. However, *E. coli* are ubiquitous in nature and most *E. coli* are harmless and are necessary for human digestion[51]. *E. coli* harbor in the gut tract and consume nutrients supplied during the digestive process. *E.*

coli O157:H7 differ from most *E. coli* by causing severe diarrhea and dysentery in humans. Farm and wild animals are believed to be the sources of most *E. coli* O157:H7 outbreaks. For instance, when fresh produce is contaminated with *E. coli* O157:H7, the bacteria can usually be traced from fecal matter of nearby animals[52-54]. Cows test positive for *E. coli* O157:H7 the most among farm animals[55], but sheep, poultry, and pork can also be carriers of *E. coli* O157:H7[56].

Testing for pathogenic *E. coli* includes serotyping of the O-antigen, which for *E. coli* O157 and O113 usual indicates severe symptoms of dysentery for the infected[57-60]. O-antigen is an important indicator for determining if an isolated *E. coli* strain is pathogenic, however, the role that the O-antigen has for initiating infection remains unclear. For instance, *E. coli* O157 is synonymous with widespread foodbourne outbreaks[61-63] and uropathogenic *E. coli* tend to be of the serotpyes O4, O6, O14, O22, O75, and O83[64]. However, there are no universal relationships between serotype and pathogenicity.

LPS is comprised of the lipid A that extends from the bacterial membrane, followed by a conserved inner and outer core, and a repeating O-antigen chain[65-67] (Figure 2.1). The lipid A is a known toxin to epithelial cells[68, 69]. Through a 3-deoxy-d-manno-octulsonic Acid (kdo) bond, the lipid attaches to the sugar groups of the core polysaccharide, but there is a lack of understanding regarding how the lipid binds to the bacterial membrane[70]. Saturated fats comprise nearly all of lipid A, along with phospholipids that give the bacteria a negative charge[67]. The fatty acids $C_{12}OH$ and $C_{14}OH$ have been reported as being the most toxic components in lipid A[68, 69]. Antibiotic treatments against *E. coli* O157:H7 can hasten bloody diarrhea by disrupting bacteria

A

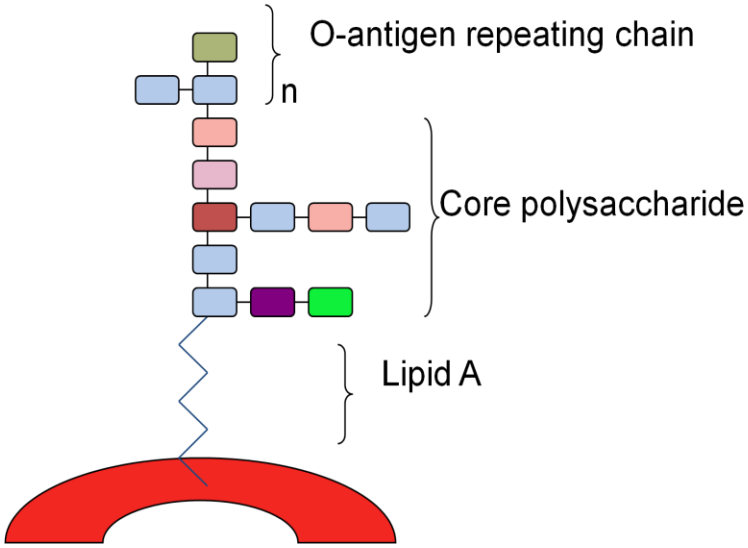

B

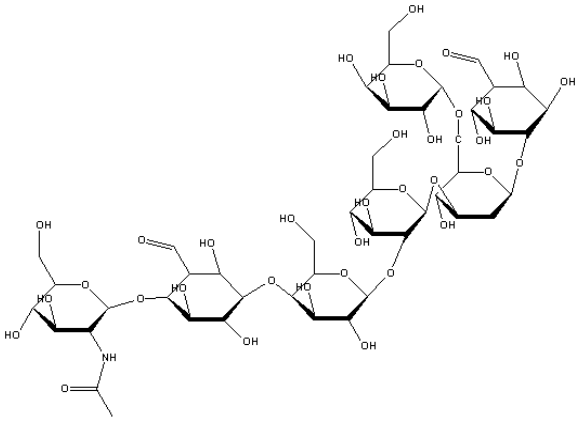

Figure 2.1 Schematic of the bacterial LPS for *E. coli* strains. A. The bacterial membrane is attached to Lipid A, followed by the inner core, and outer core. Rough bacteria will have no O-antigen. Semi-rough bacteria have an O-antigen, but it is not a repeating unit. Smooth bacteria, which comprise the overwhelming majority of bacteria, have a repeating O-antigen. B. Shematic of the K12 core group. Neutrally charged and comprised of sugars, the O-antigen may attach to the core group for smooth and semi-rough strains.

membranes and releasing deadly levels of lipid A into the body[71, 72]. Antibiotic regimens that target lipid A synthesis, followed with common treatments such as penicillin, have be shown to be more effective[73].

The O-antigen of >180 *E. coli* strains have been well characterized[74]. O-antigen is used for serotpying *E. coli* and is important for adhesion to host cells. The O-antigen is a polysaccharide with repeating units of 1 to >100[75, 76]. Rough bacteria are common laboratory strains lacking the O-antigen. Semi-rough bacteria are less commonly found, having one unit of the O-antigen, and smooth bacteria are the most commonly found, which express repeating O-antigen units[77]. The LPS core and O-antigen are key components that mediate bacterial binding with substrates and enable aggregation with other cells[78]. The O-antigen assists *E. coli* binding through hydrogen binding[79] and can self-aggregate[67, 80]. While the O-antigen is known to be important for *E. coli* pathology, the evolutionary advantages of the numerous O-antigens remains unclear.

Analysis of bacterial O-angtien is used for serotyping different bacterial strains. For example, *E. coli* species have >180 designated O-antigens, from O1A to O178[81]. The LPS core and O-antigen are key components that mediate bacterial binding with substrates and enable aggregation with other cells[78]. Beyond lipid A, the LPS is comprised of sugar molecules that, through hydrogen bonding, firmly bind the bacteria to substrates[79, 82] and can self-aggregate[67, 80].

For *E. coli*, there are five outer core groups known as K12, R1, R2, R2, and R4. Figure 2.1 A illustrates the differing sections of the LPS, while Figure 2.1 B shows the sugars of the K12 core. These sugar chains are constrained to the outer potion of the core LPS and connect to the O-antigen, although the exact point where this connection occurs

is not understood for all strains[1, 68, 69]. Bacteria lacking the O-antigen are non-pathogens and cannot survive outside a laboratory setting[83], which raises the question concerning the role the O-antigen plays in bacterial virulence. Considering the sources of toxicity and negative charge among *E. coli* strains are derived from the lipid A, it is likely that the O-antigen is used for initial adhesion to host cells and substrates[78].

2.2.2 Expression of Shiga-like Toxins

Pathogenic *E. coli* exert toxins identified as shiga-like toxins, which have been linked to symptoms of dysentery[72, 84-86]. Cattle are resistant to shiga toxins, possibly due to lack of binding spots on enterocytes and blood vessels[87]. Rabbits are 1,000-10,000 more susceptible to shiga toxins than species such as cattle, rats, and guinea pigs[85, 88]. Also, intimins on the bacterial membrane have been identified in enteropathogenic *E. coli* (EPEC) and enterotoxigenic *E. coli* (EHEC) and these proteins may also be toxic for humans[89-91].

True shiga toxins are derived from the bacterium *Shigella dysenteriae* and are very similar to toxins produced by *E. coli*[84-86]. Testing for shiga toxins is a common method for identifying pathogenic bacteria. Shiga-like toxins are produced through the *stx* gene pathway[87, 92-94], whereas the gene *eae* is essential for attaching the bacterium to the gut tract[95-97]. The *stx* and *eae* genes are present in most pathogenic *E. coli* and are usually expressed by *E. coli* of select serotypes such as O157[98, 99]. One of the most commonly employed methods for identifying a bacterium is by characterizing the O-antigen. Serotpying identifies *E. coli* in terms of the O-antigen, flagella antigen, and capsular antigen[65]. Bacterial lipopolysaccharide (LPS) is one of the most important components that determine bacterial pathology. For instance, *E. coli* O157 is

synonymous with widespread foodbourne outbreaks[61-63] and uropathogenic *E. coli* tend to be of the serotpyes O4, O6, O14, O22, O75, and O83[64].

Stx I was first identified by Konowalchk *et al*. in 1978,[100] and is estimated to have a molecular weight of 70,000[85]. Subunits of *Stx* I and a related toxin *Stx* II (VT1-A, VT2-A, and 5 subsequent B polypeptides) have revealed some of the mechanisms for pathology. For instance, rabbits were discovered to be amongst the most vulnerable species to *stx* I & II, whereas monkeys, hamsters, mice, rats, and guinea pigs were 5, 40, 700, 5,000, and 10,000 times more resistant to the toxics effects[85, 88]. Researchers have therefore focused efforts on why rabbit cells are especially susceptible to *stx* and how guinea pig cells resist the toxic effects.

Rabbit cells, being among the most sensitive to shiga toxins, have been subjected to numerous studies with the goal of determing whether toxins disrupt host cellular functions or promote adhesion for the invading *E. coli*. Robinson *et al*. found that an *E. coli* O157:H7 *stx1*-/*stx2*+ strain had marked improvement to binding to rabbit cells over the isogenic *E. coli* O157:H7 *stxI*-/*stxII*- (TUV86-2). When *stxII* was inoculated onto the host cell prior to treatment with TUV86-2, comparable adhesion was observed[101]. These results compare well with prior studies of *stx*, and may provide a target for treating *E. coli* infections[38].

2.2.3 E. coli *Diseases*

Each *E. coli* O157:H7 isolate can produce different toxins or none at all. For instance, when testing for *E. coli* O157:H7, it is common to include an analysis of the toxins that the isolate produces[102, 103]. In addition to serotyping in terms of O, K, and H, *E. coli* can be classified on basis of symptoms that they cause. Detecting *E. coli*

producing shiga toxins is a superior method for determining the threat posed by an isolated strains[103]. The classes of *E. coli* pathogens include enteropathogenic *E. coli* (EPEC), enterotoxigenic *E. coli* (ETEC), enteroinvasive *E. coli* (EIEC), enterohaemorrhagic *E. coli* (EHEC), enteroaggregative *E. coli* (EAEC), diffusely adherent *E. coli* (DAEC), and uropathogenic *E. coli* (UPEC)[104]. Table 2.1 lists some of the *E. coli* strains that lead to these infections.

EPEC: *E. coli* were first described as potentially virulent in 1945 by Dr. Bray when an *E. coli* outbreak of among children under 5 who had symptoms of watery diarrhea, vomiting, and low-grade fever. Since the time of this outbreak, improved food safety protocols and sanitation have made similar outbreaks significantly less common among developed countries, however, outbreaks remain common among inhabitants of poorer nations[105-107].

ETEC: Symptoms of ETEC are normally mild and brief when compared to most other *E. coli* infections. Infection usually occurs through contaminated water, but can spread through contaminated fresh produce. ETEC is often called the "traveler's diarrhea" since the local population in a less developed nation may be immune from the bacteria causing disease[108].

EIEC: More severe than EPEC and ETEC, EIEC often leads to dysentery, or watery diarrhea. EIEC during diagnosis is often mistaken with *Shigella* spp. and often occurs in random outbreaks. Bacillary dysentery can occur if EIEC occurs in concert with a *Shigella* spp. infection, which is described as a combination of mucus and blood in the stool[104].

EHEC: Is the most severe *E. coli* infection that readily renders the elderly and neonates with kidney failure, dysentery, and can lead to death within days or weeks of infection. EHEC is associated with either *stxI*, *stxII*, or a combination of toxins. Through the *eae* gene, bacteria mitigate adhesion to the colon and small intestine where internal lesions develop. Unfortunately, antibiotics have been found to worsen symptoms by summarily releasing potently toxic levels of *stx*. Treatments against EHEC are thereby limited to hydrating the patient until the bacteria are purged from the body. EHEC have caused large outbreaks in both industrialized nations, such as the United States, and poorer nations where bacteria associated with ETEC commonly occur. All EHEC bacteria are pathogenic to humans regardless of repeated infection[104].

EAEC: A significant emerging disease in pediatric medicine, bacteria involved in EAEC are persistent pathogens, which often infect children <5 years of age. EAEC do not secrete enterotoxins, but instead adhere to HEp-2 cells[104, 109]. Although not associated with dysentery, mucosal damage does occur and symptoms can last for weeks at a time.

DAEC: Diffusively attached bacteria to animal cells occur through surface pili, but little is known about which serotypes cause DAEC. Patients with DAEC often have symptoms of watery diarrhea but do not have bloody diarrhea[110]. Similar to most other *E. coli*, children <5 years of age are most susceptible to infections with DAEC.

UPEC: The most common *E. coli* infection occurs in the urinary tract, which is called a urinary tract infection (UTI). Type 1, type P, and other pili significantly aid in the adhesion of *E. coli* to uroepithelial cells[64]. UPEC are readily treatable with antibiotics and the disease is rarely fatal unless bacterema develops. Severe infection can lead to

kidney failure and disease is commonly associated among neonates, the elderly, and women.

Table 2.1 *E. coli* Pathotypes Associated with Verified O-antigens[104, 111]

Pathotype	EPEC	ETEC	EIEC	EHEC	EAEC	DAEC	UPEC
O-antigen	O18ac, O20, O25, O26, O44, O55, O86, O91, O111, O114, O119, O125ac, O126, O127, O128, O142, O158	O6, O8, O11, O15, O20, O25, O27, O78, O128, O148, O149, O159, O173	O28ac, O29, O112ac, O124, O136, O143, O144, O152, O159, O164, O167	O4, O5, O16, O26, O46, O48, O55, O91, O98, O111ab, O113, O117, O118, O119, O125, O126, O128, O145, O157, O172	O3, O7, O15, O44, O77, O86, O111, O126, O127	O8, O17, O26, O55, O86, O95, O119, O128	O4, O6, O14, O22, O75, O83

2.3: Antimicrobial Peptides

The concept of using AMPs for medicinal purposes is >30 years old, and has caused significant excitement as over 900 isolates have been identified[2]. Antimicrobial peptides are found in every investigated single-cellular organism, to more complex species including plants and animals[112]. Numerous peptide isolates are commonly derived from multicellular species such as toads, moths, pigs, and more[113]. Every species offers unique peptides, which is an indication that the discovered AMPs represent less than 1% of the total in nature.

AMPs generally have a cationic charge ranging from +2 to +9, and charge is an underlying mechanism that enables binding with bacteria[26, 112, 114-121]. The bacterial LPS structure contains anionic phospholipids that have made bacteria evolutionarily vulnerable to AMPs[114, 121]. Hence, antibacterial peptides are positively charged with few exceptions[114, 121].

Eukaryotic cells have membranes comprised of zwitterionic and neutral lipids. Phosphatidylglycerol is the main component for such cells[122], while prokaryotes have acidic phospholipids that include phosphatidylglycerol, Phosphatidylserine, and cardiolipin[121]. Surface charges of eukaryotes are generally lower than those of bacteria, which assists AMPs in targeting pathogens.

AMPs come in various shapes but mostly fall into one of two structural categories (Figure 2.2)

a. α-helical/linear
b. β-sheet/disulfide stabilized

Rarer structures include extended helices and cyclized loops. Whether the AMP is of these two forms does not appear to determine the mechanism of cellular action[123], although continuing research may eventually prove otherwise. In addition, charge, hydrophobicity, and length were nonfactors for AMP activity against *P. aeruginosa* and *Escherichia coli*[124]. Indeed, studies hereto forth have failed to identify ligand-receptors between AMPs and bacteria[123].

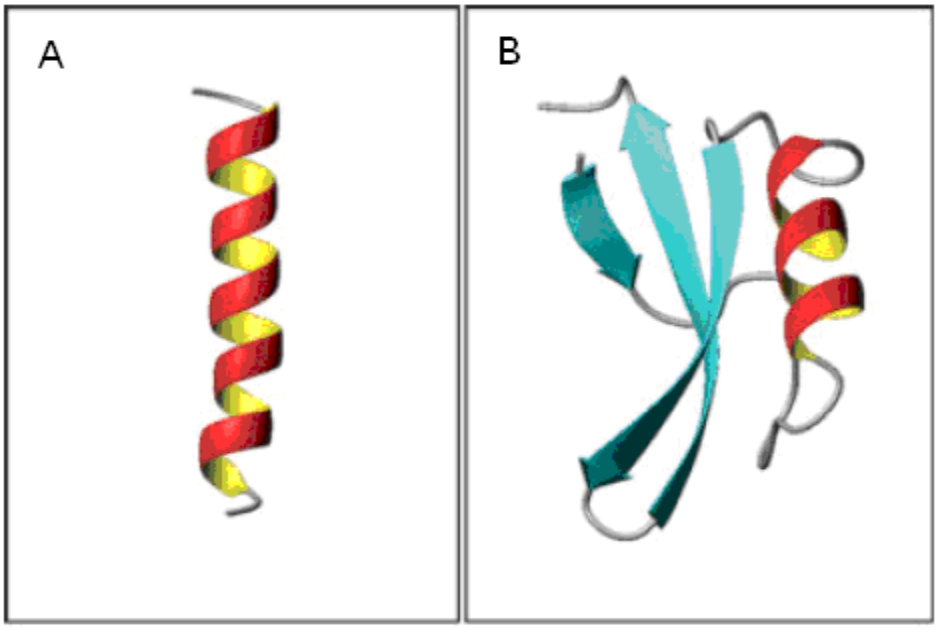

Figure 2.2 A. α-helical/linear B. Cysteine stabilized α- β-sheet
(Adapted from Yount, *et al.*[2])

A study conducted by Matsuzaki *et al.* measured zeta potential changes that occur when the cationic AMP Tachyplesin I acetamidomethyl and L-α-phosphatidylglycerol are present on membranes[125]. For every 20 mV decrease in the zeta potential of the membranes, the AMP was 200 times more favorable to attach[2, 125]. Considering the near-neutral charge of mammalian cells and zeta potentials of bacteria of -30 mV, there is

strong data eluding the preferential binding of AMPs to bacteria versus host mammalian cells.

One of the most traditional methods for discovering antimicrobial agents is to use zones of inhibition on agar plates. For example, Chen *et al.* inoculated Brucella broth plates with the AMP odorranain-HP to test against *H. pylori*, *S. aureus*, *E. coli*, *B. dysenteriae*, and *C. albicans*[116]. Minimal inhibitory concentrations were determined against each strain, which were 20, 5, 30, 30, and 25 μg/mL for the aforementioned bacteria, respectively[116].

2.3.1 Bacterial Resistance to AMPs

While rare, bacterial resistance to AMPs has been discovered in both Gram-positive and Gram-negative strains. Studies have demonstrated that alterations in charge of the lipid A region of the LPS have significant effect of whether the AMP kills the bacteria. Peschel *et al.* has found that expression of the mprF gene in *S. aureus* and *E. coli* led to the positively charged L-lysine to be suppressed in the lipid A region[126]. Bacteria expressing this gene were more susceptible to AMPs than those without the gene[127]. The PagP gene that causes acylation of the lipid A was found to have a significant affect for AMP permeability in *Legionella pneumophila*[128]. The degradation, efflux, and external trapping are some other proposed mechanisms that may assist bacteria to resist AMPs[127].

Among *S. aureus* strains, an exoprotein called staphlyokinase is expressed and released; activating host plasminogen[127]. In addition to this process, Jin *et al.* found that staphlyokinase also binds to the α-definsins produced by mammalian cells[129]. When the *dlt* and *mprF* genes, which are responsible for generating the α-definsins, were not

expressed, the cells became susceptible. *Enterococcus faecalis* and *P. aeruginosa* trap and degrade AMPs by forcibly releasing dermatan sulfate from epithelial cells[129]. By exploiting deocorin and other protoeoplycans from the surfaces of host cells, dermatan is released, which binds to many AMPs and renders AMPs inactive[127].

A prominent method by which cells have developed resistance to antibiotic treatments is by effectively pumping out the toxic compounds. Using an ATP driven pump, toxic compounds are released from the host cell[130]. An example of this system is the *mex*CD-*opr*J pump that is expressed in *P. aeruginosa*[131]. Although known to work against antibiotics[131], it may also be used against host definsins[127].

Finally, bacterial resistance may be mitigated by suppressing pathways by which AMPs are expressed altogether. For example, cathelicidin is found in high concentrations in both mice and humans when infiltrated with Group A *Streptococcus*[132]. β-definsin is another mechanism produced by cells to fight off infection that is induced by contact with lipteichoic acid, which is derived from the cell wall[133, 134].

In order to stay healthy, the host needs cells that can freely express these components, however, in the case of cystic fibrosis; *P. aeruginosa* inhibits β-definsin and cathelicidin. Using a matrix-assisted laser desorption ionization time-of-flight spectrometer, it was found that human β-defensins 2 and 3 were broken down by cysteine proteases cathepsins B, L, and S[135]. The results of Taggert *et al.* suggest *P. aeruginosa* manages to persist in the lungs by expressing the inhibitor cathepsin.

2.3.2 AMPs Mode of Action against Bacteria

Certain AMPs, such as LL37, may not actively seek and destroy infectious agents, but rather act as an alarm when the epidermis is punctured. LL37 expression by

epithelial cells causes plasmacytoid dendritic cells to accumulate in a location of injury[136]. LL37 is only found in areas of injury, but accumulations of LL37 are also linked to causing skin lesions and rheumatoid arthritis[137]. Paulsen *et al.* acknowledges that LL37 works synonymously with plasmacytoid dendritic cells, but no evidence exists that LL37 lyses the cells[137].

Even though peptides are naturally produced with seemingly endless numbers yet to be discovered, a significant step towards wide scale commercialization is to increase potency and ensure that they will not interfere with mammalian cells. Tew *et al*. have taken the approach of synthesizing polymeric phenylene ethynylene that mimics many of the features found in AMPs including being cationic and amphiphilic[138]. A CellTiter 96 well plate measured the reduction of tetrazolium dyes to formazan by dehydrogenase enzymes found in metabolically active cells and was read at 490 nm in a microplate reader. It was found that even *S. aureus* was resistant to ciprofloxacin, but was susceptible to norloxacin[138]. These results are very encouraging, but Tew *et al.* also went further by testing for cytotoxicity against mammalian 3T3 and HepG2 cells. The researchers were able to conclude that there was a significantly greater amount of prokaryotic cells killed compared to mammalian cells, which is important if the goal is to use these chemicals as a replacement for antibiotics.

Scientists have been unable to determine the exact mechanism that AMPs use to kill bacteria, and are debating whether each peptide uses a different mechanism. Since there is evidence that bacteria interact with peptides very differently, it is plausible to consider multiple models that can explain how bacteria are killed by host peptides.

Regardless of the proposed model, the peptide must find a binding spot to the bacterium. This can be accomplished by peptides in monomer or polymer-form either attaching to the polysaccharide core or lipid A. Once a certain concentration threshold is reached, the peptide is then able to penetrate the cell membrane[139].

Two models have been proposed that explain how AMPs kill bacteria. One is called the barrel-stave model and the other is called the carpet model[26]. Both models are yet to be verified since the mechanisms leading to cellular death have yet to be unraveled (Figures 2.3 and 2.4).

Peptides will operate differently depending if the bacterium is Gram-positive or Gram-negative[140]. Gram-positive bacteria have a thicker peptidoglycan layer than do Gram-negative bacteria. However, Gram-negative bacteria possess an inner cytoplasmic membrane. Therefore, in order to disrupt the bacterial membrane of a Gram-negative bacterium the peptide requires the specifically-targeting barrel stave approach by the AMP, while the Gram-positive bacterium can be compromised by a non-specific approach employed by the carpet model[140, 141].

While the literature has focused largely on how AMPs lyse bacteria, ongoing research has demonstrated that CP1 can be used to replace antibodies in biosensors against pathogenic *E. coli*. For example, CP1 binds 10-fold better to *E. coli* O157:H7 relative to a Cy5 labeled anti-*E. coli* O157:H7 antibody[4]. Gregory and Mello suggested that the O-antigen or the flagella antigen may be targets for AMPs since HB101 does not bind as well to CP1 when compared to O157:H7[142]. CP1 is an excellent candidate for biosensor material, and performs better than other available AMPs such as pleurocidin, cecropin A, and cera totoxin A[143].

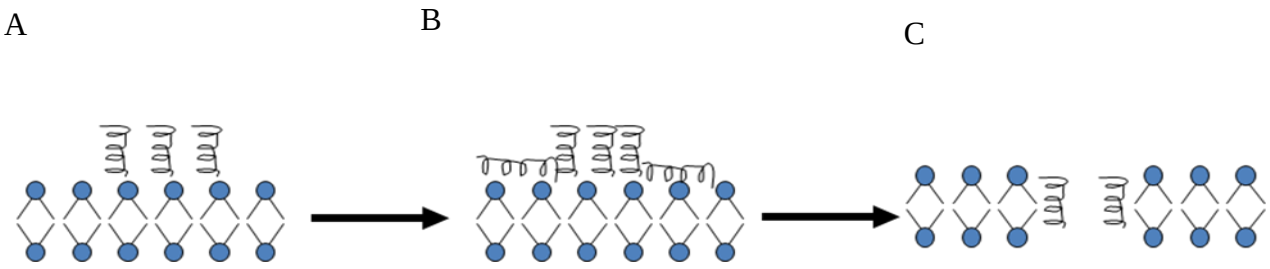

Figure 2.3 Barrel Stave model. A. Peptides approach the cell surface in the alpha-helical formation. B. Peptide monomers undergo reorientation as the cellular phospholipids of Lipid A face the peptide hydrophobic groups. C. The bacterial membrane is then ruptured and the pore size may increase depending on the quantity of AMPs. The AMPs will specifically disrupt inner cellular functions that will lead to cell death.

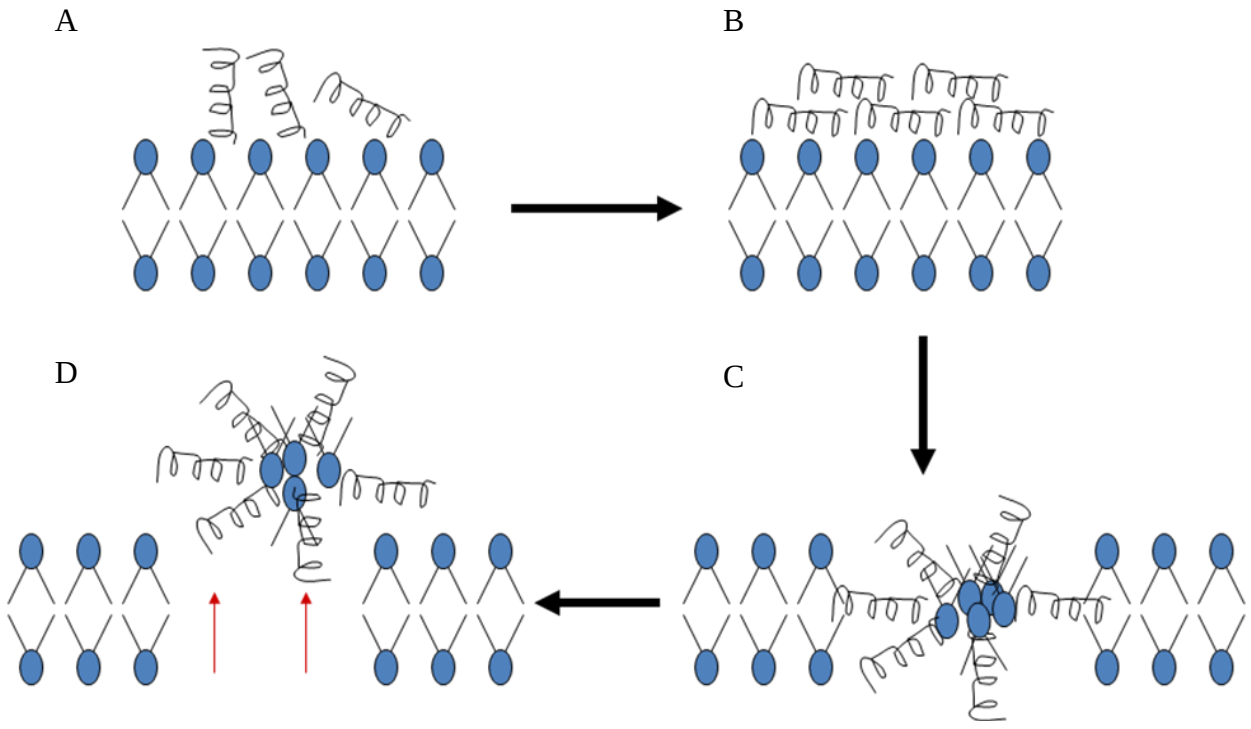

Figure 2.4 Carpet Model. A. Peptides covalently attach to phospholipid groups onto the cell surface. B. Peptides reorientate so that the hydrophilic groups face the Lipid A region. C. Hydrophobic domains of the peptide then face the lipid, causing membrane distributions once a certain peptide threshold is reached. D. The peptides carve out sections of the bacterial membrane, which leads to cytoplasmic leakage and death.

2.4: The Atomic Force Microscope

2.4.1 Principles of AFM

The 1986 Nobel Prize in Physics was awarded to three scientists; Dr. Gerd Binnig and Dr. Heinrich Rohrer. Binnig and Rohrer were awarded the prize for their work on the scanning tunneling microscope (STM)[144]. The STM relies on a very sharp, conductive tip that scans along a sample that is, likewise, highly conductive. The Scanning Electron Microscope (SEM), which depends on the same principle of conductivity, coats a sample with gold nano-particles to make it conductive and the current is interpreted into topographical data instead of scanning a sample like a record player[145, 146].

The STM belongs to a class of microscope known as the Scanning Probe Microscope (SPM). The STM differs from Scanning Near-field Optical Microscopes (SNOMs) by 'feeling' instead of 'seeing'. Unfortunately, researchers had to be very selective regarding the samples that were studied using SPMs in the 1980's. Samples needed to be resistant to alterations that could occur during a scan, and that limited the SPMs' uses to metallic surfaces. Further applications of the SPM would have been extremely limited without innovation. In 1986, Binnig and Rohrer reported the invention of the atomic force microscope[144], which would prove far more versatile than prior SPMs.

The AFM operates by scanning a sharp probe that is typically less than 50 nanometers in diameter over a surface to obtain 2-dimensional data. The probe is capable of moving nanometers by adjusting the voltage through a piezo. A laser reflects off the

AFM probe and hits photodiode, where voltage is converted to cantilever deflection and converted to force[147]. A change in a laser's deflection due to alterations on the sample's surface enables height data to be recorded. By shifting the probe's position by nanometers along the 'y-x' axes with a sensitive piezo, a combination of the line profiles yields 3-dimensional data. The AFM tip is at least 100 times smaller than a bacterium, making it possible to obtain detailed information of microbial surfaces and their biomolecules. In imaging, the AFM is capable of capturing magnifications between 100-100,000,000 times[148]. Some ultra-sharp probes are even capable of imaging DNA[149-151]. The 'x-y'range by which the AFM can scan is typically 100 micrometers to 0.3 nm. The versatility of the AFM provides superior options for scanning that appeal to researchers in numerous disciplines.

For decades microbiology has been completely reliant upon tools such as electron microscopy, contact angles, epifluorescent microscopy, and X-ray photoelectron spectroscopy[152]. These methods are, for the most part, destructive to bacteria, and cannot be used on living cells. In addition, many of these methods look at cells in a macroscopic fashion, often blending hundreds or thousands without garnering data of individual cellular variations. The electron microscope is capable of viewing individual cells following gold sputtering of the sample, which kills the cell[153, 154]. The AFM offers a unique perspective at the micro-scale by focusing in on single cells as part of a study.

The AFM has two primary functions that include image mode and force mode. Image mode can operate via a tapping mode, which oscillates a probe on top of a surface or in contact mode that bends the probe as it is dragged along a surface[144, 155]. Tapping mode works by the AFM's piezoelectric motor generating vibrations at the resonance

frequency of the tip to induce maximum oscillation. Tapping mode is the most popular among biological researchers since it deforms samples the least[156]. The imaging of a sample can be accomplished under liquid or air depending on the sample.

Force mode operates by fluctuating the AFM probe in the Z direction. The AFM measures force between the probe and sample in a force-versus-distance plot to generate force curves[157]. Figure 2.5 is a representation of a typical force curve.

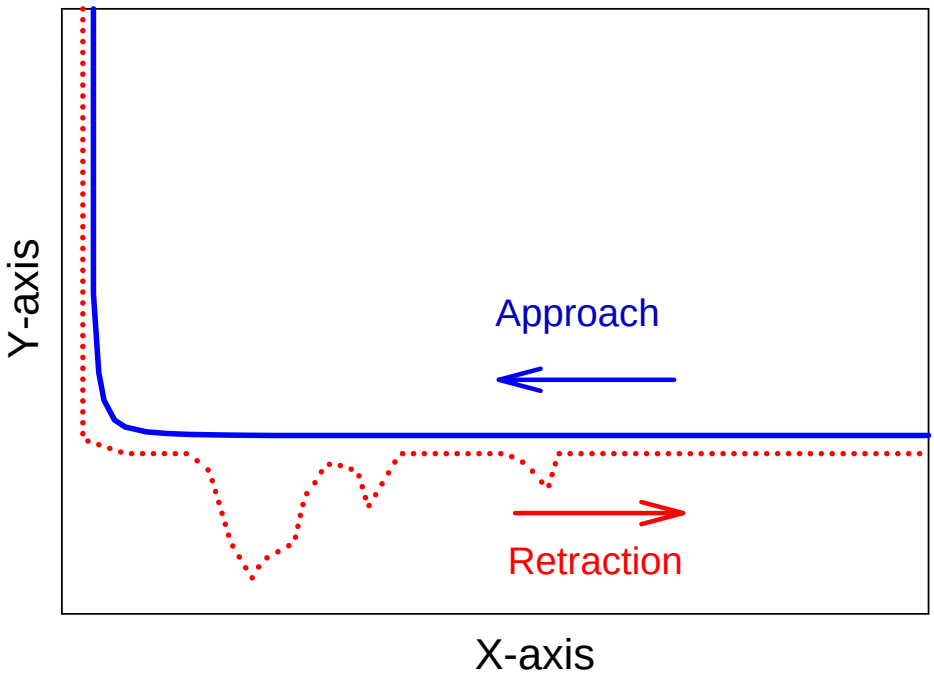

Figure 2.5 Representation of a Force Curve While Probing Bacterial LPS

The force cycle is composed of two curves; one being the approach curve in blue, and the retraction curve depicted in red. For much of the approach curve, the forces acting on the probe are negligible, which is called the zero interaction region, followed by the probe encountering repulsive forces. These repulsive forces are a combination of van der Waals electrostatic forces, solvation, hydration, and steric/bridging forces[157]. When

retracting from touching an object, there tends to be an adhesive pull-off force required to break the linkage between two objects. This demonstrates the binding strength between tip-sample, since we can measure the pull-off force.

The correlation of force data should be conducted under aqueous conditions due to inherent capillary forces. In air, a layer of water will cover both the sample and the probe, which forms a meniscus causing an attractive force of 10-100 nN[152]. This makes operating under water much more common for microbiologists and is required for meaningful force curves[152].

In force mode, when the cantilever contacts the sample of interest, the cantilever compresses, and elongates when being held to the surface during retraction[144]. The motion of the cantilever is comparable to the motion of a spring, which makes force measurements significantly more precise. The spring constant, k_z, is a measurement of the force required to deflect the cantilever a given distance[158]

$$k_z = \frac{N}{m} \quad . \tag{1}$$

Here, N is force in Newtons, m is distance in meters, and k_z is the spring constant.

Using Hooke's law, Equation 2, the forces encountered during the force cycle can be determined with[158]

$$F = -k_z \quad . \tag{2}$$

While manufacturers often provide an estimate of the cantilever spring constants, multiple researchers have noted that the spring constants of their cantilevers do not fall within the manufacturer's specifications[159]. Hence, each researcher should determine the spring constant using one of the available methods. Advantages of using the thermal

method are ease of use, independence of material, and geometry comprising the cantilever.

2.4.2 AFM Method for Studying Bacterial Interactions

The AFM is an innovative tool compared to existing microscopy methods in that samples require minimal preparation and high resolution images can be achieved with little sample deformation. Force mode is a tool unique to the AFM and enables measurement of molecular-molecular interactions between the AFM probe and LPS. AFM force profiles have been used extensively in numerous microbiological studies such as analyzing effects of cranberries on *E. coli* pili and *Pseudomonas aeruginosa* LPS binding to silicon.

Liu *et al*. used both approach and retraction data to analyze cranberry effects on pathogenic *E. coli* and *E. coli* HB101 that would not be considered capable of causing urinary tract infections[160]. Using steric modeling software, pili lengths were found to decrease significantly under cranberry treatment from 150 nm to 50 nm. Additionally, pull-off forces definitively showed that for the pDC1 strain, 80% of the attractive forces were >0.5 nN, whereas higher concentrates of cranberry juice resulted in only 40% of the retraction forces being >0.5 nN[160].

The AFM is capable of interacting with structures nanometers in length, which makes it ideal for studying bacterial O-antigens. Mechanically probing the O-antigens elucidates unique properties that would otherwise for unnoticed with other microscopy or chemical analyses. Atabek *et al*. also carried out novel research primarily with the AFM by comparing *P. aeruginosa* PAO1, which expresses the A-band and B-band O-antigen, with AK1401 that expresses only the A-band antigen[161]. By analyzing the retraction

forces and pull-off distances, PAO1 was found to have longer O-antigens and was the only strain to have attractive forces of >1.2 nN[161].

2.5: Quartz Crystal Microbalance with Dissipation Monitoring

The QCM was an innovative tool that measures small deposits of mass onto a quartz crystal. The QCM is sensitive enough to measure 10^{-11} g-cm^{-2}, which is significantly more sensitive than conventional scales. The QCM takes advantage of minute changes in resonant frequency due to adsorbed mass. Other advantages of the QCM are realtime monitoring of adsorption and custom coatings of quartz crystals. Although the QCM was capable of tasks unique to this instrument, the limitation of the 'missing mass effect' due to viscoelastic properties of some samples was problematic[162]. The Sauerbrey equation, which was the primary method for data evaluation, correlated frequency changes to changes in mass. Consequently by neglecting viscoelastic effects that dampen quartz crystal oscillations, the Sauerbrey equation would underestimate adsorbed mass. Quartz crystal usage was therefore limited to systems with rigid deposits until dissipative effects could be accounted for.

2.5.1 Principles of QCM-D

In the past decade the quartz crystal microbalance has evolved with the addition of dissipation-monitoring, which has made this technique more useful in life sciences research. Similar to how the AFM made it possible for SPMs to study biological samples, the QCM-D has made it possible for highly viscous samples such as whole cells, viruses, peptides, etc. to be studied. Being a recent innovation, researchers are still developing modeling components to calculate thickness, shear stress, and viscosity.

Nevertheless, the QCM-D is significantly more powerful than its predecessor, the QCM, because it accounts for dissipative affects that make thickness and adsorbed mass calculations significantly more accurate.

In 1959, Sauerbrey derived an equation relating the frequency shift, Δf, of an AT-cut oscillating piezoelectric crystal induced by added mass. Now known as the Sauerbrey equation, QCM makes use of[163]

$$\Delta f_N = -\frac{f_N^2}{N}\frac{2\Delta m}{A\sqrt{\rho_q \mu_q}} \quad , \tag{3}$$

where A is the quartz crystal active area, μ_q is the shear modulus for an AT-cut quartz crystal ($2.947\times10^{11}\ \frac{g}{cm^2 s}$), ρ_q is the quartz crystal density ($2.648\ \frac{g}{cm^3}$), Δm is the change in mass per unit area, and f_N is the fundamental resonant frequency of the crystal at N overtone. The crystal will resonate when the quartz thickness is at odd integers of half wavelengths of the induced waves[164]. Hence, the user will operate the crystal at the 1st, 3rd, 5th, etc. overtone numbers, which affects the resonant frequency as

$$f = n\frac{v_q}{2t_q} = nf_0 \quad , \tag{4}$$

where n is the overtone number, v_q is the velocity of found through the quartz, and t_q is the thickness of the quartz.

In order to validate the results of the Sauerbrey equation, the areal mass must be assumed to be evenly distributed throughout the crystal. Equation 5 can then be used to express either a thickness or density on the crystal

$$\frac{M}{A} = m_q = t_q \rho_q \left(\frac{m\cdot kg}{m^3}\right) \Rightarrow \left(\frac{kg}{m^2}\right) \quad , \tag{5}$$

where *M* is the added mass, and A is the active area. In addition to being evenly dispersed, the added mass must also be small relative to the crystal and be rigid so that there is no deformation induced by the oscillations.

Traditional QCM is only valid in gaseous conditions. This was the case until 1995 when an innovation accounted for dissipation effects[165], giving rise to the QCM-D. Rigid deposits will resonate with the crystal and the energy lost per oscillation will be significantly less than if the deposit is highly viscoelastic. Viscoelastic films, for example, will absorb more energy per oscillation. This loss of energy is not accounted for in the Sauerbrey Equation[163, 165, 166]. Briefly, dissipation (D) is defined as

$$D = \frac{E_{lost}}{2\pi \cdot E_{stored}} \quad , \tag{6}$$

where E_{lost} is the energy lost per oscillation and E_{stored} is the energy that remains following an oscillation.

Life science research is often conducted in a liquid environment to retain cells in their natural state and conserve viability. Cellular adhesion to quartz crystals can be monitored, along with viscoelastic properties with a dissipative factor that accounts for liquid environments

$$\Delta d_N = 2\frac{f_N^{0.5}}{N}\left(\frac{\Delta\rho\Delta\eta}{\pi\rho_0\mu_0}\right)^{0.5} \quad . \tag{7}$$

Here $\Delta\rho$ is the density change of the bulk liquid and $\Delta\eta$ is the viscosity change of the bulk liquid. Equation 8 corrects for bulk liquid viscosity and density changes that are also monitored with crystal frequency changes[167, 168],

$$\Delta f_N = -\frac{f_N^{1.5}}{N}\left(\frac{\Delta\rho\Delta\eta}{\pi\rho_0\mu_0}\right)^{0.5} \quad . \tag{8}$$

Indeed, incorporating dissipative effects is important for correcting "loss of mass" that acoustic sensors encounter under non-idealistic conditions[162]. The Sauerbrey relation clearly is an over simplification, which can be used in Equation 8 for calculating a mass, but significantly deviates from the true mass[162]

$$M_s = M\left(1 - \frac{\eta_2 \rho_2 \omega}{\rho_1} \frac{G''}{G'^2 + G''^2}\right) \quad . \tag{9}$$

Here M_s is the Sauerbrey mass, M is the true mass, 1 refers to the thin soft overlayer, 2 refers to the liquid bulk phase, ρ is the density, η is the shear viscosity coefficient, G' is the storage modulus, and G'' is the loss modulus.

Undergoing further simplification, Equation 9 may be reduced to[162]

$$M_s = M\,(1-\alpha) \quad , \tag{10}$$

where α is a modification neglected by the Sauerbrey relation due to mechanical properties of the overlayer material and aqueous solution, M is the true mass, and M_s is the Sauerbrey mass. By making dissipation monitoring possible, QCM-D becomes much more useful to life science research.

Voigt Viscoelastic modeling includes terms such as bulk liquid viscosity and density that allows for precise film thickness and areal mass calculations. From QCM-D raw data, the deposited layer thickness can be calculated using Voigt viscoelastic modeling for a film in liquid[169, 170]

$$\Delta f = \frac{\mathrm{IM}(\alpha)}{2\pi d_q \rho_q} \tag{11}$$

$$\Delta D = -\frac{\mathrm{Re}(\alpha)}{\pi n f_0 d_q \rho_q} \tag{12}$$

$$\alpha = \frac{\left(2\pi n f_0 \eta \xi_1 - i\mu_q \xi_1\right)\left(1 - \beta \exp\left(2\xi_1 d\right)\right)}{2\pi n f_0 \left(1 + \beta \exp(2\xi_1 d)\right)} \tag{13}$$

$$\beta = \frac{(2\pi n f_0 \eta \xi_1 - i\mu_q \xi_1 + 2\pi n f_0 \eta_1 \xi_2)}{(2\pi n f_0 \eta \xi_1 - i\mu_q \xi_1 - 2\pi n f_0 \eta_1 \xi_2)} \quad (14)$$

$$\xi_1 = \sqrt{-\frac{(2\pi n f_0)^2 \rho_q}{\mu_q + i2\pi n f_0 \eta}} \quad (15)$$

$$\xi_2 = \sqrt{\frac{i2\pi n f_0 \rho_1}{\eta_1}}. \quad (16)$$

Here d_q is the quartz thickness, ρ_1 is bulk liquid density, η_1 is bulk liquid viscosity, η is shear viscosity of adsorbed layer, μ is shear modulus, and d is film thickness.

2.5.2 Applications of QCM-D

The realm of research involving quartz crystal technology has expanded to development of self-assembled monolayers (SAMs), deposition and orientation of cells and proteins, and polymer construction. While useful for fundamental research, the QCM-D is also being used as a novel biosensor for detection of biological agents such as bacteria, fungi, and viruses.

2.5.2.1 QCM-D and Polymer Development

A novel use for the QCM-D is to create 'smart' surfaces that have undergone dramatic changes that alter their wettability[171] or respond to temperature, light, and pressure[172, 173]. Such desire for new material has led several groups to study thin films on gold surfaces. Using the QCM-D in association with X-ray photoelectron spectroscopy and contact angles, Park *et al.* demonstrated the thermoresponsive properties of polymers in temperature ranges from 25°C to 60°C[171]. By monitoring dissipation at the seventh harmonic, the polymer absorbed 3 times of the amount of energy per oscillation per 3°C increase.

Dissipative effects of adsorbed samples are amplified by what is termed the swelling effect[174-177]. Swelling of a sample occurs in a liquid environment where

polymers accumulate water. Such effects can be monitored with dissipation monitoring. A study following up on swelling effects explored this phenomena by comparing the adsorption of ethyl(hydroxyethyl) cellulose (EHEC) and a modified EHEC on hydrophobic gold domains[175]. Surprisingly, the hydrophically modified EHEC retained significantly more water, as was determined through the dissipation monitoring. The viscoelastic modeling indicated a thickness of 2.6 nm and 10.0 nm for the hydrophilic and hydrophobic adsorbents, respectively, indicating the hydrophilic polymers were densely packed. A large degree of contact between polymers on the hydrophilic surface likely did not favor the trapping of water, while the hydrophobic EHEC was more distributed and entrapped water molecules[175].

2.5.2.2 QCM-D and Protein Development

The QCM-D can be vital for understanding protein behavior, such as for preventing bacterial aggregation on protein-coated implanted catheters. Bovine submaxillary gland mucin (BSM) and bovine serum albumin (BSA) are model proteins commonly used to mimic *in vivo* conditions[178]. The QCM-D used to show that BSA adsorbs in a rigid layer and can prevent the adsorption of BSM[178].

Protein swelling leads to conformational changes that expose different functional groups for cell-cell interactions. Fibrinogen was found to absorb more water when adhered to titanium oxide when compared to gold and tantalum substrates. This conclusion was reached by monitoring the dissipation of fibrinogen films adsorbed to metallic substrates. The authors were unable to explain the mechanisms for differences in protein uptake of water, but the study demonstrated that different surface materials can lead to significant changes in protein orientation during adsorbtion[179].

2.5.2.3 DNA Biosensor Development

One of the newest proposed applications of the QCM-D is to use the device as a biosensor. Biosensors can use any single or combination of methods that include optics, microbalances, electrochemistry, and temperature[180]. For instance, the QCM-D real-time monitor assembly of DNA[181]. In a recent study, two 45-case DNA monomers consisting of two 20-base sequences, which were separated by a 5-base DNA sequence, were reintroduced to the quartz crystal in 10 successive steps[182]. Between steps, HEPES was used to remove non-specifically adhered DNA monomers. Lazeerges *et al.* demonstrated that with each successive step, the frequency change monitored decreased from Δf_1=-166 *Hz* to Δf_{10}=-52 *Hz*. This pattern can be attributed to steric hindrance between DNA strands and to increased thickness of the DNA layer that induced energy losses, which is due to increasing viscosity[182].

The DNA biosensors took advantage of di-sulfide bonding to construct repeating polymer chains. Carmon *et al.* used the same principle to immobilize estrogen onto gold-quartz crystals and test for the adherence of xenoestrogens[183]. The C-terminal hormone-binding domain was considered the control, which has demonstrated a strong affinity to estrogen[184]. The study demonstrated that testosterone and progesterone had no binding ability to estrogen, but estroil binds well to estrogen. Therefore, chemicals such as estriol are important for treating atrophic vaginitis[185].

2.5.2.4 Mammalian Cell Studies

QCM-D has been used to help design substrates that resist cellular adhesion. Applications for such a biosensor vary from preventing catheter related bloodstream infections to improving wound healing. Andersson *et al.* proposed using a supported

phospholipid bilayer (SPB) with QCM-D and fluorescent microscopy techniques and found a nearly total reduction of rat pancreatoma cellular adhesion[186]. The observed reduction was attributed to phosphorylcholine groups that have been found to also reduce protein[187-189] and platelet adsorption[190] to polymers and metals.

In one study, epithelial cells were grown on quartz crystals and monitored by measuring frequency (*Hz)* and resistance (*Ω*)[191]. Once an established extracellular matrix was constructed, as was verified using fluorescence light microscopy, cells were treated with nocodazole. Nocodazole, a microtubule binding drug, is important for understanding signaling pathways for cancerous cells[192-194]. Marx *et al.* monitored the deposition of nocodazole onto the epithelial cells and found frequency signaling drops of 360 *Hz* and a small increase in resistance of 14 *Ω*[191]. They associated the changes to both nocodazole adhesion to the cells, as well as cellular rounding and spreading on the surface that was induced by the nocodazole.

Marx *et al.* further studied epithelial cell responses to ethylene glycol bis(2-aminoethyl ether)-*N*,*N* -tetraacetic acid (EGTA)[195]. After 2 hours of exposure on the quartz crystal, fluoresce ence microscopy confirmed that the epithelial cells were entirely removed. A surprising finding was that the resistance after shifting to 0 (indicating no cells were present), rose by 50 *Ω* before subsequent EDTA treatments. This is indicative of the remaining cells becoming more rigid and attempting to further anchor to the substrate[195].

2.5.2.5 Bacterial Biosensor

The QCM-D has been well documented for its potential as a biosensor, but recently the intention of using it for detecting pathogenic bacteria has been suggested[34].

The piezoelectric biosensor has been commonly proposed to operate by depositing an underlying layer of antibodies that would selectively bind to pathogenic bacteria[196-199]. Other methods that used antibodies first masked the gold layer with SAMs that immobilize *E. coli* O157:H7 with hydrazide linkers. Once the bacteria were firmly attached to the SAMs, antibodies were introduced to specifically target *E. coli* O157:H7and a change in mass resulting from antibody adhesion to bacteria yielded that the antibodies targeted *E. coli* O157:H7[200].

2.5.2.6 Preventing Bacterial Adhesion

The QCM-D has also been used to monitor the effectiveness of materials and conditions that can prevent bacterial adhesion. For example, ionic strength and hydrophobicity were found to effect adhesion of the fimbriated (MS7fim+) to gold quartz crystal, whereas the nonfimbriated (MS7fim-) *E. coli* was not impacted[201]. Otto *et al.* found both sets of bacteria to preferentially adhere to the hydrophobic substrate (methyl-terminated gold) compared to the hydrophilic gold. In addition, the nonfimbriated strain adhered better in every ionic strength solution and surface condition. Although unexpected, the authors attributed these results to shielding effects of the cellular surface charges and dipole interactions at higher ionic strengths. The fimbriae may also be affected due to the presence of ionic groups leading to additional surface charge[201].

2.5.2.7 Disrupting Biofilms

For applications with medical devices, prevention of bacterial adhesion is widely deemed as the most viable option for combating bacterial infection, Reipa *et al.* used the QCM-D in order to monitor biofilm disruption[202]. *Pseudomonas aeruginosa* were grown on a gold quartz crystal and a bleach solution was applied. The depletion of the biofilm

was monitored in real time. Bleach is a popular sterilizing agent, but is not safe for *in vivo*. The search for chemical agents that specifically target biofilms is ongoing, and it is important to have a basis for understanding how potent chemicals such as bleach disrupt the biofilm.

2.5.3 *Effects of Acoustic Waves on Biological Samples*

The QCM has also been used extensively to study cellular adhesion and growth on quartz crystals; however, the calculated changes in mass are controversial due to the viscoelastic nature of cells. Only in the past decade have researchers begun to explore whole cell binding with acoustic wave sensors. Several groups have raised doubts on whether the oscillating crystal can break non-specific bonds, receptor-ligand bonds, and covalent bonds[203, 204]. In these studies, virus removal was detected as the drive amplitude increased from the nominal value of 1 V to 10 V. However, Evardsson *et al.* discovered contradicting results when attempting to remove 1-Palmitoyl-2-oleoyl-*sn*glycero-3-phosphocholine and 1,2-dipalmitoyl-*sn*-glycero-3-phosphoethanol amine-*N* from the quartz crystal[205]. Regardless of the voltage used, mass was not removed from the substrate. Frequency and dissipation results were identical for when experiments were repeated at drive amplitudes of 0 (50 mV), 5, and 10 V, meaning biological samples remain unperturbed by the QCM-D[205]. Descrepancies between the studies were attributed to the use of plano-convex crystals that increase the maximum oscillation amplitude, irregular shape of the viruses that increase torque, and antibody-antigen bonds were weaker for the case of viral adhesion[205].

2.5.4 AFM/QCM-D Studies

To date, many studies have combined QCM techniques with fluorescence microscopy and SPR for studying cellular adhesion, but few have incorporated AFM imaging and none have compared binding forces with the AFM to QCM-D. Another significant area of study is monitoring adsorption of self-assembled monolayers that have also demonstrated an ability to significantly alter surface characteristics such as wettability and surface free energy[178, 206, 207]. Briand *et al.* immobilized thiolate SAMs onto gold substrates and explored the binding of rabbit immunoglobulin G (rIgG)[208]. AFM tapping mode™ was used for topographical imaging for roughness analysis. The AFM was employed in part to validate QCM-D for the system of interest since a homogenous substrate is necessary for viscoelastic modeling. Since the AFM is unable to analyze beyond the topography, the rigidity of the immunoglobulin on the SAMs was also investigated. In another AFM-QCM study, the deposition of platinum on gold electrodes was monitored in real time with the QCM, while roughness was observed with the AFM[209].

While rare, a few studies have made efforts to combine the techniques of AFM and QCM for studying whole cells. Using a polyurethane-coated quartz crystal, attached *S. bayanus, L. oenus, and E. coli* following *S. cerevisiae* imprinting (residues of yeast left behind following rinsing) were imaged[210, 211]. Tapping mode AFM was capable of capturing images of *S. cerevisiae* imprinting to verify residuals remained. The dual-AFM/QCM technique was capable of determining the adhesion strengths of yeast cells and proved the combination could be used as an effective biosensor.

In a study by de Kerchove and Elimelech, adsorbtion of alginate to silica quartz crystals were monitored with the QCM-D and further analyzed under AFM force mode[212]. *P. aeruginosa* produces alginates in the extracellular polymeric substances (EPS) to form biofilm matrices[213, 214]. Alginates are produced by the mucoid strain *P. aeruginosa* SG81, which concentrates calcium ions in the biofilm[213]. The goal of de Kerchove and Elimelech was to evaluate over a range of ionic strength solution (0- 300 mM) how dissolved calcium alters the alginate layer. Using the QCM-D, areal mass, thickness, and viscoelastic properties of the adsorbed alginate were determined from real time adsorption data, while the AFM was useful for determining adhesion forces and pull-off distance of the adsorbed alginate. The pull-off distance increased as ionic strength of the alginate layer also increased from 0-100 mM, while F_{adh} decreased over the same range of ionic strength. The QCM-D results demonstrate the adsorbed alginates form more rigid layers as the dissipation decreased with correlation to increased ionic strength. Decreases in adsorbed water in alginates has been found to be due to reduction of hydrogen bonds[215]. The larger distances obtained with AFM at higher ionic strength in the presence of calcium suggest that the presence of higher concentrations of monovalent ions induces the alginate complexes to be less efficiently bound together. The study demonstrated electrostatic interactions resulting from ionic strength solution changes impact the alginate layer and may lead to treatments against *P. aeruginosa* infection.

2.6: Interfacial Free Energy

Thermodynamics may be employed to understand the microscopic forces that promote bacterial attachment to substrates. To understand the thermodynamics of bacterial adhesion, some assumptions need to be made. Bacterial adhesion is considered

favorable if the change is negative upon creation of the bacteria-surface interface[216]. Likewise, adhesion is not considered favorable if surface free energy increases. Neglecting electric and biochemical interactions, the change in surface free energy for a given bacterium may be expressed as[216]

$$\Delta F^{adh} = \gamma_{BS} - \gamma_{BW} - \gamma_{SW} \quad , \tag{17}$$

where F^{adh} is the free energy of adhesion, γ_{BS} is the bacterium-substratum interfacial tension, γ_{BW} is the bacterium-liquid interfacial tension, and γ_{SW} is the substratum-liquid interfacial tension. Young's Equation expands on the above free energy balance and can be used to obtain data on interfacial tensions of solid surfaces with the relation[217]

$$\gamma_{SB} - \gamma_{SW} = \gamma_{WB} \cos(\theta) \quad , \tag{18}$$

where γ_{SB} is the interfacial tension between a solid substratum and bacterium, γ_{SW} between the solid substratum and liquid, γ_{WB} between the liquid and bacterium, and θ is the contact angle of the liquid resting on the solid. Since γ_{SW} is a function of both γ_{SB} and γ_{WB}, using experimentally derived contact angle data and surface free energy data and combining with Young's Equation, the relationship yields[216]

$$\cos(\theta) = \frac{(0.015\gamma_{SB} - 2.00)\cdot\sqrt{\gamma_{SB}\cdot\gamma_{WB}} + \gamma_{WB}}{\gamma_{WV}\cdot(0.015\sqrt{\gamma_{SB}\cdot\gamma_{WB}} - 1)} \quad . \tag{19}$$

The purpose of thermodynamic studies is to determine how bacterial adhesion varies when different types of substrates are each considered. γ_{BV} relates to the tension of the liquid medium (γ_{lv}) in three ways[218]

$$\gamma_{WS} < \gamma_{BS} \quad , \tag{20}$$

$$\gamma_{WS} > \gamma_{BS} \quad , \tag{21}$$

$$\gamma_{WS} = \gamma_{BS} \quad . \tag{22}$$

In the case of Equation 20, ΔF^{adh} decreases, and we would expect an increase in the number of bacteria adhering to a substrate. In Equation 21, the opposite would be true. This scenario would represent a decrease in the number of adhering bacteria. In the case of Equation 22, bacterial adhesion is independent of surface tension[216].

One method for calculating a substrate's surface free energy is to measure contact angles with water, water n-propanol mixtures, or α-bromonaphthalene, which vary in terms of polarity. A more common set of liquids that can be used to measure contact angles to calculate the surface free energy includes water, formamide, and diiodomethane. Surface free energy can be calculated with the following[219]

$$\cos(\theta) = -1 + 2 \cdot (\gamma_S^d \cdot \gamma_W^d)^{0.5} \cdot \gamma_W^{-1} + 2 \cdot (\gamma_S^p \cdot \gamma_W^p)^{0.5} \cdot \gamma_W^{-1} - \pi_e \cdot \gamma_W^{-1} \quad , \tag{23}$$

where *d* is the dispersion component, *p* is the polar component, γ_S is the surface free energy of the solid, γ_W is the surface free energy of the liquid, and π_e represents the spreading pressure. Equation 23 generates a least squares regression analysis useful for multiple measured angles to obtain the surface free energy[219].

Surface tensions can be calculated via the Young-Dupré Equation[178, 220]

$$\gamma_W(\cos(\theta_W) + 1) = 2\sqrt{\gamma_B^{LW} \cdot \gamma_W^{LW}} + 2\sqrt{\gamma_B^+ \cdot \gamma_L^-} + 2\sqrt{\gamma_B^- \cdot \gamma_W^+} \quad , \tag{24}$$

where γ^- and γ^+ are the electron donor and electron acceptor parameters, *B* is bacterium, *L* is liquid and

$$\gamma_W^{LW} + \gamma_W^{AB} \gamma_W^{LW} + \gamma_W^{AB} \tag{25}$$

is the surface tension of the probe in the liquid[220].

To calculate the total interaction energy between the bacterium and substrata in water (ΔG_{adh}^{Total}), the forces between dipole-dipole, dipole-induced dipole, and induced

dipole LW long-range interactions are expressed in a single term, and the acid-base short range force characteristics are presented as a separate term yielding[220]

$$\Delta G_{adh}^{Total} = \Delta G_{adh}^{LW} + \Delta G_{adh}^{AB} \quad , \tag{26}$$

where

$$\Delta G_{adh}^{LW} = (\sqrt{\gamma_B^{LW}} - \sqrt{\gamma_S^{LW}})^2 - (\sqrt{\gamma_B^{LW}} - \sqrt{\gamma_W^{LW}})^2 - (\sqrt{\gamma_S^{LW}} - \sqrt{\gamma_W^{LW}})^2 \quad , \tag{27}$$

and

$$\Delta G_{adh}^{AB} = 2(\sqrt{\gamma_W^+}(\sqrt{\gamma_B^-} + \sqrt{\gamma_S^-} + \sqrt{\gamma_W^-}) + \sqrt{\gamma_W^-}(\sqrt{\gamma_B^+} + \sqrt{\gamma_S^+} + \sqrt{\gamma_W^+}) - \sqrt{\gamma_B^-\gamma_S^+} - \sqrt{\gamma_B^+\gamma_S^-}) \quad . \tag{28}$$

Another method for determining (ΔG_{adh}^{Total}) can be to measure the free energy between bacteria [1], substratum [2], and the medium in with which the substratum is immersed in [3], and γ_3, which is the surface tension of the water that is expressed as $\Delta G_{1,2,3}$. The sum of the interactions is[221]

$$\Delta G_{1,2,3} = \Delta G_{1,2} - \Delta G_{1,3} - \Delta G_{2,3} - 2\gamma_3 \quad . \tag{29}$$

To calculate the free energy between bacterium, substratum, and immersion liquid, ΔG_{ij}, where *i* and *j* represent [1], [2], or [3], the following equation can be used[221]

$$\Delta G_{ij} = \gamma_{ij} - \gamma_i - \gamma_j = -2(\sqrt{\gamma_i^{LW} \times \gamma_j^{LW}} + \sqrt{\gamma_i^- \times \gamma_j^+} + \sqrt{\gamma_i^+ \times \gamma_j^-}) \quad . \tag{30}$$

In a study comparing 5 strains of bacteria, a thermodynamic model predicted the attachment of bacteria to substrates including sulfonated polystyrene, acetal resin, polyethylene, polystyrene, and fluorinated ethylene-propylene copolymer during the initial stages of experimentation[216]. An unexpected result occurred during the experiment when bacteria were retained to the substrates, despite $\Delta F^{adh} > 0$. Absolom *et al.* suggested that this phenomenon may have been due to electrostatic interactions between the

substrate and bacteria. When the ionic strength of the liquid was very low, bacterial adhesion was virtually non-existent due to increased electrostatic repulsion[216, 222].

Postollec *et al*. explored the coaggregation of *Streptococcus sanguis* and *Actinomyces naeslundii*, which are found in the human oral cavity. By collecting thermodynamic data on the bacteria using contact angles, they found that the bacteria have a high affinity towards each other since heat is released during binding. Hence, bacterial coaggregation was found to be enthalpy driven[223].

While the thermodynamic model is preferable for some researchers of bacterial surface retention, DLVO theory is an alternative method, which will be developed in the next two sections.

2.7: Guoy-Chapman Model of Electrostatic Interactions

The Gouy-Chapman theory suggests a correlation between the charge density and electrical potential of a substrate to the concentration of ions in a surrounding solution[224]. This is especially important in measuring ions in solution that may impact the viability or adhesion of bacteria. According to the Nernst Equation, activity of a solution may be measured in equilibrium partitioning between two phases (0 and ∞)[225, 226]

$$\alpha_{10} = \alpha_{\infty} \exp(-ZFE_{0\to\infty}/RT) = C_{\infty}\Gamma_{\infty} \exp(-Z_i FE_{0\to\infty}/RT) \quad , \qquad (31)$$

where α is the chemical activity of the ion, C is the ion concentration, E is the electric potential, Γ is the activity coefficient of the ion, Z is the charge on the ion, E is the electrical potential difference between phases *0* and *∞*, R is the gas constant, T is temperature, and F is the Faraday constant[225, 226].

If the concentration of ions can be computed in phase 0, then the activity coefficient may also be determined[226]

$$C_{i0} = (C_{i\infty}\Gamma_{\infty}/\Gamma_{i0})\exp(-Z_i F E_{0\to\infty}/RT) \quad , \qquad (32)$$

where the variables correspond to phase ∞.

The Gouy-Chapman theory was established to form a relationship between solutions and charged surfaces and is expressed in the Grahame Equation[226]

$$\sigma^2 = (0.00345)\sum_i C_{i\infty}(\exp(-Z_i E_0/25.7) - 1) \quad , \qquad (33)$$

where σ is the density of charged particles, E_o is the electrical potential, and $C_{i\infty}$ is the ion concentration at infinite distance from the substrate[226].

The Poisson-Boltzmann Equation yields the potential, electric field, and counterion density at any point between two substrates. The Poisson-Boltzmann Equation is expressed as[226]

$$d^2\Psi/dx^2 = -ze\rho/\varepsilon\varepsilon_0 = -(ze\rho_0/\varepsilon\varepsilon_0)e^{-xe\Psi/kT} \quad , \qquad (34)$$

where Ψ is the potential, ρ is the number density of ions of valency *z*, *k* is the Boltzmann's constant, *T* is temperature, ε_0 is the permittivity of free space, and *e* is electronic charge.

Substituting the Grahame Equation into the Poisson-Boltzmann Equation yields[226]

$$d^3E_x/(dx^2) = -1/(\varepsilon_1\varepsilon_0)\sum_i Z_i F C_{i\infty}\exp(-Z_i F E_0/RT) \quad . \qquad (35)$$

This equation is useful for calculating the electric potential of a solution and the external concentrations when α is a low value[224].

Stern made a modification to the Gouy-Chapman theory by taking into account changes in α due to ion binding onto the substrate surface. This relationship between surface ligand *Q"* and an ion *S'* is expressed in the following form[225]

$$[QS^{X+Y}] = K_{QS}[Q'][S']_0 \quad , \qquad (36)$$

where *Q''* and $[QS^{x+y}]$ are ion concentrations, S'_0 is the ion concentration at the surface, K_{QS} is an association constant, and *x* and *y* are charges[225].

Gouy and Chapman combined both the Poisson Equation, which describes the attraction of counterions to a surface, and the Boltzmann relation, which describes the repulsion of counterions in an area of high concentration. In the case with low surface potential, $\Psi(0)$, the following statement can be made[225]

$$\Psi(0) = \sigma/(\varepsilon_a \varepsilon_0 \kappa) \quad , \tag{37}$$

where ε_a is the dielectric constant, ε_0 is the permittivity of free space, σ is the surface charge density, and κ is the inverse Debye length ($[(\varepsilon_0 \varepsilon_a kT)/(2z^2e^2c)]^{0.5}$). Across a distance, *x*, the potential varies as[225]

$$\Psi(x) = \Psi(0)\exp(-\kappa x) \quad . \tag{38}$$

The surface potential, $\Psi(0)$, is predicted by the Gouy Equation and is directly related to the concentration of ions in solution, *c*, and the surface charge density, σ, by[225]

$$\sinh[ze\Psi(0)/2kT] = A\sigma/(c)^{0/5} = (8\varepsilon_a \varepsilon_0 kT)^{-0.5}\sigma/(c)^{0.5} \quad . \tag{39}$$

When the potential is larger than 25 mV, Gouy-Chapman theory predicts the rate at which the potential drops increases near the substrate as[225]

$$\Psi(x) = \frac{(2kT)}{e}\ln\left(\frac{\exp[\frac{e\Psi(0)}{2kT}]-1}{\exp[\frac{e\Psi(0)}{2kT}]+1}\right)\ln\frac{[1+\alpha\exp(-\kappa x)]}{[1-\alpha\exp(-\kappa x)]} \quad . \tag{40}$$

By having an understanding of the mechanisms that lead to colloidal interactions, it is possible to predict what certain substrate modifications will have on bacterial retention.

2.8: DLVO Theory

DLVO theory, developed by Derjaguin, Landau, Verwey, and Overbeek, provides a quantitative framework to calculate molecular interaction profiles, by summing electrostatic and van der Waals interactions[227]. Electrostatic forces arise from double-layer theory. When an object is placed into an electrolyte solution, its surface becomes charged. If the object, for example, contacts oxygen molecules on the surface, then hydrogen atoms in the water will be attracted to the charged molecules[228]. Usually a small amount of the oxygen molecules will interact with the hydrogen molecules, leaving a net negative charge on the substrate. The net negative charge attracts positively-charged ions in the solution that would normally have been dissociated. Double-layer theory can be applied to bacterial adhesion by correlating electrostatic potential produced by charges to the ion density in a bacterium's cytoplasm[228].

London dispersion forces undergo polarization of molecules into dipoles[228]. Originally, van der Waals forces were considered the only intermolecular forces, but this definition neglected specific interactions forces, solvation forces and depletion forces. Between two spheres, the van der Waals interactions may be expressed as[228]

$$F_v = -\frac{A_{123} a_m a_p}{6h^2 (a_m + a_p)} \quad , \tag{41}$$

where h is the separation distance, evaluated as H_0, the theoretical closest distance 1.57 Å, A_{123} is the Hamaker constant, a_m is the radius of the bacteria, and a_p is the radius of the tip.

The Hamaker constant, A, is equal to

$$\pi^2 q^2 C' \quad , \tag{42}$$

where q is the number of molecules per unit volume interaction between two bodies, $C'=251e^2\alpha^2$, e is the energy, and α is energy of interaction between two atoms with static polarisability.

The Hamaker constant is valid for vacuum between particles, but for a liquid medium, an effective Hamaker constant is used[229],

$$A_{123} = A_{12} + A_{33} - A_{13} - A_{23} \quad (43)$$

Taking the geometric means of each phase,

$$A_{132} = (A_{11}^{0.5} - A_{33}^{0.5})(A_{22}^{0.5} - A_{33}^{0.5}) \quad (44)$$

and for interaction of identical particles,

$$A_{131} = (A_{11}^{0.5} - A_{33}^{0.5})^2 \quad (45)$$

Figure 2.6 displays the forces as a function of particle separation.

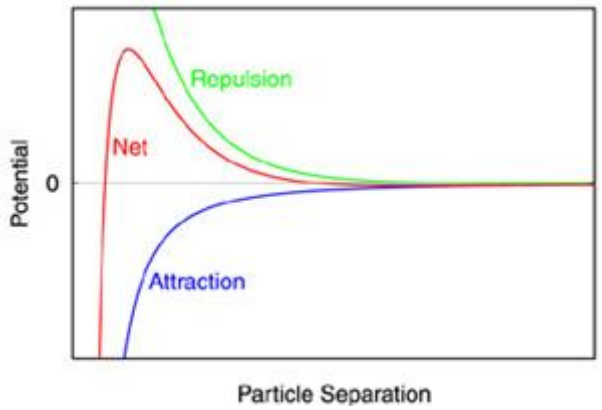

Figure 2.6 DLVO interactions between two spheres. The blue curve represents van der Waals potential (attraction), the green curve represents electrostatic potential (repulsion), and the red curve is the net potential. The energy barrier is when the net potential reaches a maximum. As the distance between objects increases, DLVO potential approaches zero. Adapted from[3].

A modification to the DLVO theory incorporates hydrophobic effects, also known as acid-base interactions or electron donor/electron acceptor. XDLVO and DLVO-AB are exactly the same since hydrophilic substrates tend to be more acidic, and hydrophobic

substrates have a tendency towards being basic[230]. In some cases, bacterial retention to a substrate is better modeled using the modified XDLVO theory as opposed to the DLVO model, but both ignore important factors such as surface roughness and nanoscale molecular forces on the substrates[230].

Another modification that has been made is called soft-particle DLVO theory. Soft particles are assumed to be polyelectrolyte brushes. Soft-particle DLVO is pertinent to AFM probing of LPS since bacteria have soft membranes. The expression of soft-particle theory is[231-233]

$$\mu = \frac{\varepsilon_0 \varepsilon_r}{\eta} \frac{\frac{\psi_0}{\kappa_m} + \frac{\psi_{DON}}{\lambda}}{\frac{1}{\kappa_m} + \frac{1}{\lambda}} + \frac{eZN}{\eta \lambda^2} \quad . \tag{46}$$

Here, μ is electrophoretic mobility, ε_0 is permittivity of vacuum, ε_r is relative permittivity of the medium, η is medium viscosity, and e is elementary charge. κ_m is Debye-Hueckel parameter of the surface region, ψ_{DON} is Donnan potential, and ψ_0 is potential at boundary between surface regions, which are expressed as,

$$\psi_{DON} = \frac{kT}{ze} ln \left[\frac{ZN}{2zn} + \left(\left(\frac{ZN}{2zn} \right)^2 + 1 \right)^{0.5} \right] \quad , \tag{47}$$

$$\psi_0 = \frac{kT}{ze} \cdot \left\{ ln \left[\frac{ZN}{2zn} + \left(\left(\frac{ZN}{2zn} \right)^2 + 1 \right)^{0.5} \right] + \frac{2zn}{ZN} \cdot \left(1 - \left(\left(\frac{ZN}{2zn} \right)^2 + 1 \right)^{0.5} \right) \right\} \quad , \tag{48}$$

$$\kappa_m = \kappa \left[1 + \left(\frac{ZN}{2zn} \right)^2 \right]^{0.25} , \tag{49}$$

where k is the Boltzmann constant, T is temperature, z is valency of bulk ions, and n is concentration of bulk ions.

Sharma and Rao found that *Paenibacillus polymyxa* adhesion to pyrite and chalcopyrite minerals was better predicted with DLVO theory over the thermodynamic method[229]. Indeed, the thermodynamic method predicted no bacterial adhesion to the

minerals would occur, which was experimentally disproven. The DLVO theory accounts for repulsive forces between bacteria and flocculation of minerals, which better predicted the experimentally observations of bacterial adhesion.

While there has been some success in predicting bacterial adhesion using DLVO theory[229, 234-240], usually bacterial adhesion is governed by forces other than those included in the DLVO theory[241-244]. Treating bacteria as if they are inert particles is the limiting factor in this model, and in words of Henri Theil, "models are to be used, not to be believed"[245].

2.9: Zeta Potential

In order to quantify electrostatic interactions for colloids, we typically measure the zeta potential. A general definition of the zeta potential is the potential at the solid-liquid interface for any colloid[246]. The zeta potential measures the colloidal charge at the point of the slipping plane. DLVO theory predicts whether a colloidal system is stable with respect to van der Waals attractive and double layer repulsive forces. For a system to be considered stable, the double layer repulsive forces must be greater than the van der Waals attractive forces[246].

Charges are induced when colloids are immersed in aqueous solution, which creates a double layer around each particle or surface. The charge density is namely caused by protonation, deprotonation, and adsorption, and leads to an electric field that attracts oppositely charged ions while repulsing co-ions. The charges are dispersed in several distinct barriers (Figure 2.7):

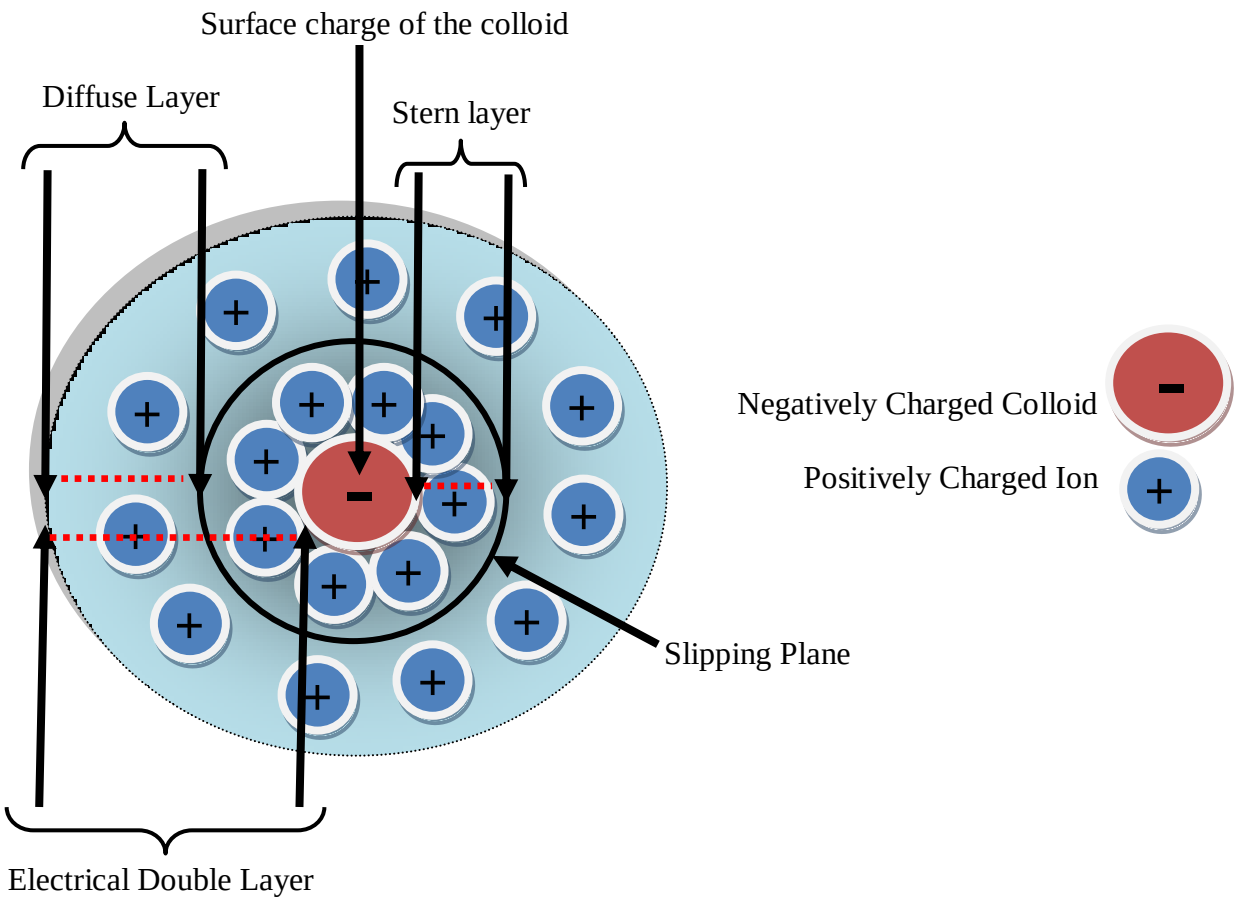

Figure 2.7 Representation of solvent layers surrounding a colloid.

For an *E. coli* colloid, since the bacterial surface charge is negatively charged, oppositely charged ions will be drawn in; hence the Stern and diffuse layers will be net positively charged.

Zeta potential analyzers do not directly measure the zeta potentials, but are derived through the Smoluchowski approximation[247]

$$U_E = \frac{2\varepsilon \cdot z \cdot f(ka)}{2\eta} \quad , \qquad (50)$$

where U_E is the electrophoretic mobility (charge on ion/frictional coefficient), ε is the dielectric constant, z is the zeta potential (mV), $f(ka)$ is Henry's function (assigned the

value of 1 for particle sizes <0.2 μm and 1.5 for colloids > 0.2 μm), and η is the viscosity (Pa·s).

The objective of measuring the bacterial zeta potential is to predict how a bacterium, through electrostatic interactions, will behave in a particular environment and what agents can alter the bacterial zeta potential. Atabek and Camesano used zeta potentials to verify that chemicals used to bind bacteria to glass did not have adverse side effects on a Pseudomonas strain[161]. They were able to definitely argue that the 1-ethyl-3-(3-dimethylaminopropyl) carbodiimide hydrochloride (EDC) / *N*-hydroxysuccinimide (NHS) treatment was not altering the bacterial LPS when compared to poly-L-lysine (PLL).

Emerson and Camesano reported how differing ionic strength solutions altered zeta potentials of *C. parapsilosis* and *P. aeruginosa*[241]. In general, higher ionic strength MES buffer resulted in the bacteria having a reduced zeta potential. Changes in zeta potentials in lower ionic strength solutions were attributed to soft-particle DLVO theory being invalid under these conditions[241].

3: Methods and Materials

3.1: Cell Culturing

In order to probe the role of LPS properties, a total of 13 *E. coli* strains were used; 3 being control strains that lacked the O-antigen with the K12 core-group, and the remaining having well defined core types and O-antigens (Table 3.1).

Table 3.1 Strains Used in Present Study
Green font denotes control strains (No O-antigen).

Strain	Source
E. coli HB101 (ATCC 33694)	ATCC[1]
E. coli K12 (ATCC 29425)	Natick Labs[2]
E. coli ML35 (ATCC 43827)	Natick Labs
E. coli O26:K60:H11	CCUG[3]
E. coli O35:H10 (ATCC 23525)	ATCC
E. coli O55:H7	ECOR[4]
E. coli O117:K98:H4	CCUG
E. coli O113:H4	Health Canada
E. coli O113:H21	ECOR
E. coli O157:H7 (ATCC 43895)	ATCC
E. coli O157:H12	Health Canada
E. coli O157:H16	Health Canada
E. coli O172:H-	CCUG

[1]American Type Culture; [2]US Army Natick Soldier Research, Development and Engineering Center; [3]Culture Collection, University of Göteborg, Sweden. [4]*Escherichia coli* Reference Collection.

Cells were stored long term in 50/50 vol% glycerol-water at -80°C and short term stored (<2 weeks) on Luria Broth Agar (LBA) (Sigma-Aldrich, USA) plates. Bacterial colonies were streaked from individual colonies and pre-cultured in a 10 ml flask of Luria Broth media (LB) (Amresco, USA) for ~14 hours at 37°C. A 0.5 ml sample of pre-cultured bacteria was used to inoculate 50 ml of LB media and cells were cultured at mid-exponential phase to an absorbance of 0.50, which was determined with a spectrophotometer at 600 nm (Thermo Spectronic, USA). Cells were washed 3 times by centrifugation for 10 mins with sterile pH 7.4 0.01 M phosphate buffer saline + 0.138 M NaCl + 0.0027 KCl (Sigma-Aldrich, USA).

3.2: Cecropin P1 (CP1) and Cecropin P1 with Cysteine Residue at the C-terminus (CP1-cys)

CP1 (≥95% purity, Sigma-Aldrich) was short-term stored (<3 months) at 4°C as a lyophilized powder. CP1 was reconstituted in ultrapure water (18.2 MΩ cm resistivity and <10ppb total organic carbon, Millipore Milli-Q plus, Billerica, MA, USA) that was adjusted to pH 5.0 to protonate residues and maximize charge. The same procedure was used for CP1-cys, which was modified with a cysteine at the C-terminus (≥85% purity, New England Peptides). CP1 and CP1-cys solutions were diluted to 10 µM in PBS for all experiments.

3.3: Motility Test

Testing for bacterial flagella was conducted using a motility test (Acumedia Manufacturers, Inc., Lansing, Michigan). Briefly, 22 grams of motility test agar were stirred with 1 L ultra pure water and autoclaved. Media was poured into small vials and set for 24 hours. Bacteria were grown to an absorbance of 0.9 on the spectrophotometer

and 2 µl of bacterial solution was injected down the center of each vial. When the motility test agar became cloudy to the edge of the tube, the bacteria expressed flagella.

3.4: Live/Dead Kit Technique

The viability of bacteria attached to gold, gold CP1-cys, silicon nitride crystals, and silicon nitride CP1 were quantified. Following peptide adsorption, bacterial solution was pumped through the QCM-D and crystals were rinsed with PBS until frequency and dissipation equilibration. Quartz crystals were submerged in 4 ml PBS to avoid cellular dehydration. A BacLight™ live/dead kit (Molecular Probes, Faraday, CA) was used to quantify bacterial retention and viability on the substrate containing adsorbed peptide. Syto 9 and propidium iodide, diluted in dimethyl sulfoxide (DMSO) (Sigma, St. Louis, MO, USA), were added to the 4 ml PBS + quartz crystal to yield final concentrations of 0.835 µM and 0.5 µM, respectively. A 60x objective equipped with FITC and Texas Red filters were used to capture bacterial images and the accompanying software Spot Advanced was used to capture and merge the pictures. (Nikon Eclipse E400; Mercury-100W lamp, Chiu, Technical Corp). Experiments were carried out in triplicate for reproducibility.

3.5: Atomic Force Microscopy

Glass slides were cleaned measuring ~1 cm x 1 cm. Slides were rinsed with copious amounts of ultra pure water (18.2 MΩ cm resistivity and <10ppb total organic carbon; Millipore Milli-Q plus, Billerica, MA, USA), followed by sonication for 15 mins. Slides were immersed in 3:1 (vol/vol) HCl / HNO_3 solution for 30 mins, followed by rinsing with ultra pure water. Slides were soaked in piranha solution (7:3 (vol/vol) H_2SO_4/H_2O_2 solution) for 30 mins followed by rinsing with ultra pure water. Glass slides

were then immersed in 30/70% 3-aminopropyltrimethoxysilane/methanol (Sigma-Aldrich) and rinsed with methanol and ultrapure water.

A 10 ml vial of bacterial solution was combined with 300 µl of 100 mM 1-ethyl-3-(3-dimethylaminopropyl) carbodimide hydrochloride (pH 5.5, EDC, Pierce). The vial was set on a rotator for 10 mins to equilibrate. Following EDC treatment, 300 µl of 40 mM N-hydroxysulfosuccinimide (pH 7.5, Sulfo-NHS, Pierce) was combined with the bacterial solution for another 10 mins. Bacterial solution was poured over glass slides and agitated at 40 rpm for 10-12 hours to promote a well spread bacterial lawn.

Silicon nitride probes were cleaned by immersion in 100% ethanol for 1 hour followed by UV treatment (365 nm) to remove organic films. Spring constants of the silicon nitride cantilevers were measured using a thermal calibration method, and were found to be 0.07 ± 0.01 N/m[248]. The AFM was a Digital Instruments Dimension 3100 with a Nanoscope III Controller (Santa Barbara, CA). Images were captured in intermittent contact mode in PBS to mimic physiological conditions. The scan rate was 1 Hz and images were captured with 512 x 512 resolution. For each strain, 10 cells probed and 5 force profiles were captured for each one; hence 50 force curves were analyzed per condition. Each force profile contained 512 data points. F_{adh} was measured from the retraction portions of the force cycles. Prior to and following a force cycle on a bacterium, force measurements were made on a clean glass slide. If a single sharp peak was observed at ~0-5 nm, then the probe was considered clean and could be used for subsequent experiments. Loading rate, which is the product of spring constant and retraction velocity[249], was measured as 864 nN/s.

AFM was used for conducting force profiles between bacterial LPS and silicon nitride probes or modified probes with cecropin P1 (CP1) (≥ 85% purity, New England Peptides, Gardner, USA). Probes were modified by immerging silicon nitride tips (DNPS, Veeco Instruments, Inc, CA) in 10 μM CP1/PBS solution. Adhesion was monitored with the QCM-D under similar conditions to characterize deposition (discussed in depth in the QCM-D section).

Force profiles were analyzed by exporting the ASCII files to a Matlab to make the constant compliance region aligned with the 'Y' axis and the zero interaction region to align with the 'X' axis. Such calibration was carried out for both the approach and retraction curves. The forces required to overcome attraction forces between the silicon nitride probe and sample were recorded, as is illustrated in Figure 3.1.

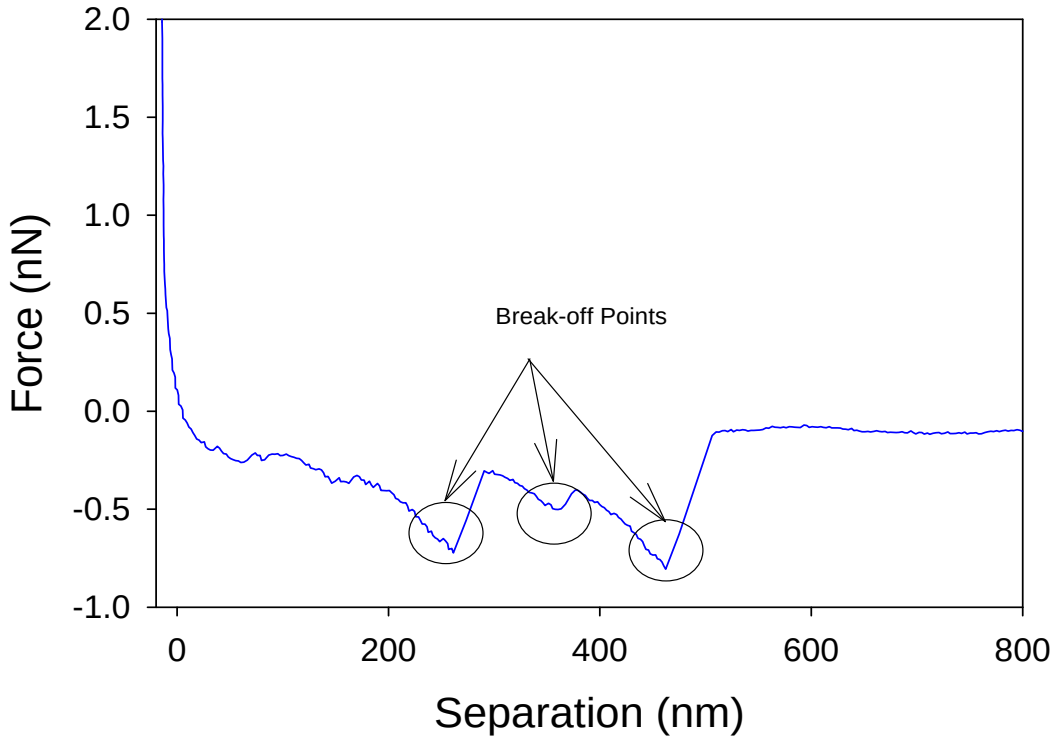

Figure 3.1 Bare Tip with *E. coli* O157:H12

While the AFM has become the instrument of choice for studying in-depth studies of biological samples, external noise can be registered in both the approach and retraction profiles. Since the noise level can vary due to mechanical vibrations and other external sources, AFM force profiles were captured either before 9 am or after 6 pm. The measured noise level was found to be 0.05 nN, which meant peaks occurring at or below that level were random events and not included in the final analysis.

Approach curves were modeled to account for steric interactions. During approach of the tip to the bacterial membrane, the AFM tip must overcome steric hindrance due to the overlapping of electron clouds[250] of the LPS on the bacterial membrane. Approach curves were fit with the models of Alexander[251] and de Gennes[252], as modified by Butt *et al* for AFM analysis[253].

$$\ln\left(\frac{F}{F_0}\right) = \frac{-2\pi}{L}\delta \qquad (51)$$

where, F is the steric force, F_0 is the force at zero separation, L is a fitting parameter for representing equilibrium polymer brush length, and δ is the tip-sample separation (Figure 3.2 A & B).

Statistical software from SigmaStat (vs. 2.03) and SAS® were employed for statistical analysis of the AFM data. One way ANOVA tests were used to compare retraction force profiles with bare silicon nitride probes to CP1 coated tips. In addition, SAS software was used to conduct normality tests for the steric modeling and to grasp a better understanding of the variability of the *E. coli* LPS.

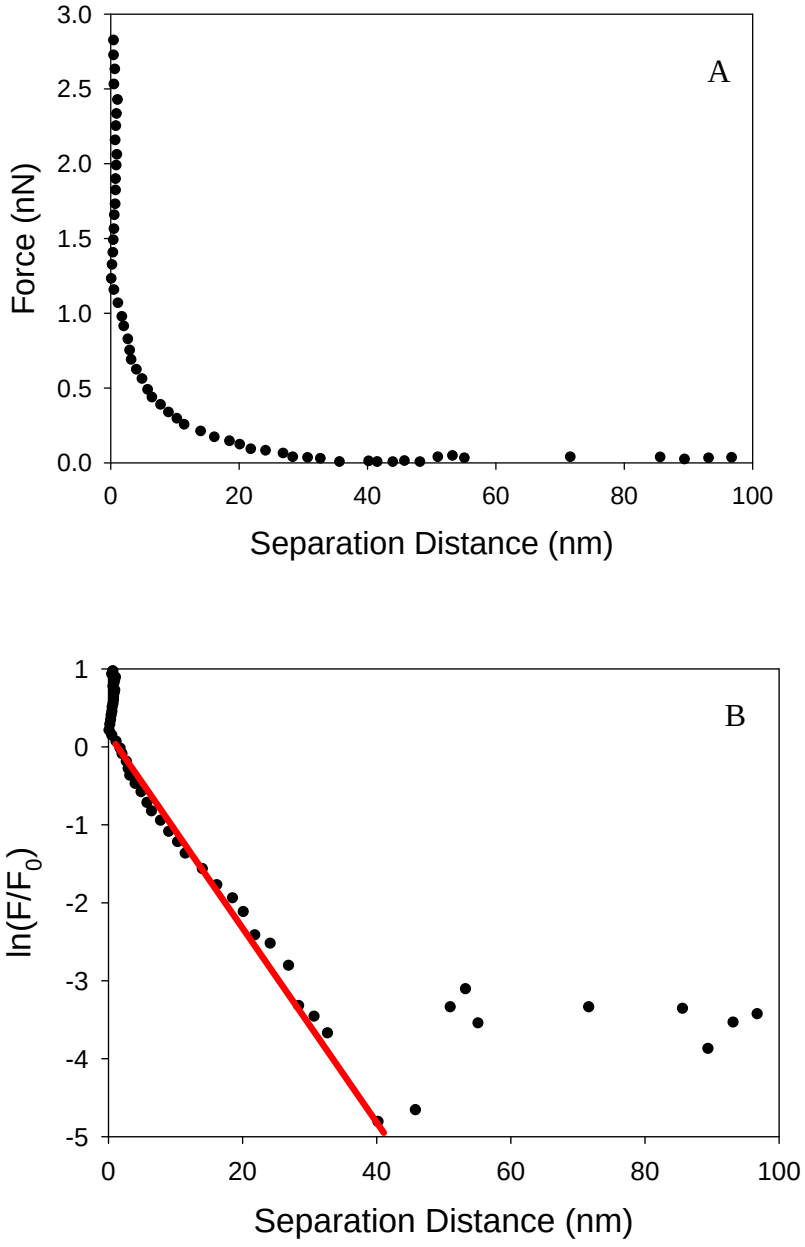

Figure 3.2. Representative approach curves for *E. coli* O157:H7. A. Representative approach curve on a single bacterium. B. Steric modeling of approach curve, with slope of fitting line equal to $-2\pi/L$. Zero separation and zero interaction regions of the approach curves are not incorporated into the steric model. $R^2>0.90$ for all steric modeling. Based on equilibrium fit, LPS length is 49 nm.

3.6: Zeta Potentials

The zeta potential for each of the 13 strains was measured using a zeta potential analyzer (Zetasizer Nano ZS; Malvern Instruments, Worcestershire, UK). *E. coli* were washed 3 times in PBS to remove growth media.. Cells were diluted to a concentration of 1 x 10^8 cells/ml and injected in a folded capillary cell (DTS1060; Malvern Instruments). Three rounds of at least 10 measurements (100 max) were conducted to ensure reproducibility. Between each round the solution equilibrated for 2 mins. Using the Smoluchowski Equation[247] the electrophoretic motilities and surface potentials were converted to Zeta potentials to better understand the extent of the negative charge of the bacteria.

Ten μM CP1-cys and CP1 solutions were measured in PBS. Peptide solutions were injected into folded capillary cells and three replicates of at least 10 measurements were made.

3.7: Contact Angles

Bacteria were grown to the late exponential phase of 0.9 absorbance and 20 ml of bacterial suspension was centrifuged at 190 x g and washed 3 times in PBS. By the final rinse, the bacterial solution was concentrated to below 2 ml. The solution was pumped through a 0.45 μm filter (Membrane Filters, Millipore, MA) to trap bacteria on the surface. Three filters per bacterial strain were prepared and resulting contact angles were averaged to conduct surface free energy calculations. Three probe liquids of varying polarities were used including ultrapure water, diiodomethane (Alfa Aesar, MA), and formamide (J. T. Baker, NJ). Each droplet was 2 μl in volume and a video monitored when the droplet contacted the filter paper, before the liquid could be absorbed by the

filter paper. Contact angles were performed using a Ramé-Hart model 100-00 (Ramé-Hart, NJ) and analyzed with the DROPimage software (Ramé-Hart, NJ).

3.8: QCM-D

Silicon nitride (Cr, 5 nm, Au, 100 nm, Si_3N_4, Q-sense, Sweden) and gold (Cr, 5 nm, Au, 100 nm, Q-Sense, Sweden) AT-cut quartz crystals were used for QCM-D experiments. Silicon nitride crystals were used to simulate CP1 adsorption to the AFM probes, while the gold-coated quartz crystals were used to better control adsorption of CP1-cys. CP1-cys binds at the c-terminal where the cysteine residue is located. This method has been widely used to form self assembled monolayers (SAMs)[206, 254, 255] and has also been used to immobilize peptides[256].

Silicon nitride quartz crystals were cleaned in 2% sodium dodecyl sulfate (SDS) (Sigma-Aldrich) solution for 30 min, followed by copious rinsing with ultrapure water and UV treatment (365 nm) for 30 min. Nitrogen was used to remove water droplets. Gold-coated quartz crystals were cleaned in 5:1:1 ultrapure water, hydrogen peroxide (Alfa Aesar), and ammonia hydroxide (Sigma-Aldrich) at 75°C for 30 min. The gold-coated crystals were cleaned in the same way. The E4 (Q-Sense, Sweden) was cleaned by mounting cleaning crystals in the chambers prior to and following an experiment. Ultrapure water was pumped through each chamber for 20 min at 200 µl/min, followed by Hellmanex®II (Sigma-Aldrich) for 20 mins at 100 µl/min, and ultrapure water for 30 min at 200 µl/min. Chambers were nitrogen-dried following the rinse cycle.

The chamber temperature was set to 23°C prior to each experiment and ultrapure water was pumped over the experimental crystals for at least 20 min at 150 µl/min before monitoring began. Once frequency and dissipation monitoring initiated, a baseline with

ultrapure water was established before switching to PBS where a new baseline would be established. The pump flow-rate was reduced to 50 µl/min whenever peptide or bacteria at a concentration of 1 x 10^8 cells/ml were introduced to the quartz crystal to promote adhesion. A follow-up rinse at 50 µl/min removed loosely deposited material until stabilization in terms of frequency and dissipation.

Typically, experiments were conducted by monitoring the 3rd, 5th, 7th, and 9th harmonics, although the fundamental harmonic was monitored when it was necessary to compare data with QCM models than only operated at the fundamental harmonic. Resonances were found for each crystal at all specified harmonics. Table 3.2 displays typical values at the differing harmonics.

Table 3.2 Typical Dissipation Values for Operable Crystals

Harmonic	In Air (D 10^{-6})	In Liquid (D 10^{-6})
1	10-50	200-400
3	10-30	150-250
5	5-20	100-200
7	0-20	100-150
9	0-20	50-150

The chamber temperature was set to 23°C prior to each experiment and ultrawater pumped over the experimental crystals for at least 20 mins at 150 µl/min before monitoring began. Once frequency and dissipation monitoring initiated, a baseline with ultrawater was established before switching to PBS or 0.01 M phosphate buffer (PB) where a new baseline was established. The pump flow-rate would be reduced to 50 µl/min whenever CP1 or bacteria was introduced to the quartz crystal to promote

adhesion. A follow-up rinse with PBS at 50 µl/min removed loosely deposited material until stabilization in term of frequency and dissipation.

CP1 was stored in 1.5 ml vials of 100 µM concentrated CP1 at pH 5.5 in ultrapure water. Prior to experiments with trifluoroethanol (TFE) or Tris(2-carboxyethyl)phosphine hydrochloride (TCEP), CP1 would be thawed and combined with phosphate buffer at the desired concentration (Table 3.3). The concentration of TFE was 25% vol/vol and TCEP was dissolved into solution to yield a 50 mM solution.

Table 3.3 QCM-D Trials to Enhance CP1-cys adsorption to Gold Quartz Crystals

Trial	CP1 Concentration	Buffer	pH	Additive
1	10 µM	0.01 M PB	pH 7.4	None
2	10 µM	0.01 M PB	pH 9.2	None
3	10 µM	0.01 M PB	pH 7.4	25% TFE
4	10 µM	0.01 M PB	pH 9.2	25% TFE
5	10 µM	0.01 M PB	pH 7.4	50 mM TCEP
6	10 µM	0.01 M PB	pH 9.2	50 mM TCEP
7	29.1 µM	0.01 M PB	pH 7.4	None
8	29.1 µM	0.01 M PB	pH 9.2	None
9	29.1 µM	0.01 M PB	pH 7.4	25% TFE
10	29.1 µM	0.01 M PB	pH 9.2	25% TFE
11	29.1 µM	0.01 M PB	pH 7.4	50 mM TCEP
12	29.1 µM	0.01 M PB	pH 9.2	50 mM TCEP
13	0 µM	0.01 M PB	pH 7.4	25% TFE
14	0 µM	0.01 M PB	pH 7.4	50 mM TCEP

Modeling of the data was conducted using both the Sauerbrey relation and the viscoelastic modeling software accompanying the E4 (Qsoft401 & QTools 2.1.6.134). The Sauerbrey relation is useful for determining the areal mass (given fundamental frequency), thickness (given density), or density (given film thickness). The simple relation can only take into account a single frequency harmonic in its calculation and is valid for only rigid films. A viscoelastic Voigt Modeling method was used to incorporate viscoelastic properties of the film such as dissipation, as well as frequency shifts at

multiple harmonics to enhance modeling capability. The film thickness is calculated with Voigt viscoelastic modeling and areal mass be calculated by multiplying by the film density (thickness (t_{voigt}) x density ($\rho_{effective}$)).

3.9: AFM Section Analysis vs. QCM-D Voigt Viscoelastic Modeling

Gold quartz crystals were mounted in the QCM-D and the frequency and dissipation responses were monitored at ~15, 25, 35, 45, and 55 Mhz, which correlate to the 3rd, 5th, 7th, 9th, 11th harmonics, respectively. The temperature was held at 23°C and liquid flowrate was constant at 50 µl/min.

We employed a model protein, fetal bovine serum (FBS) in 0.01 M phosphate buffer saline (PBS), which was adsorbed to gold QCM-D sensors (E4, Q-Sense). Gold sensors were mounted in the QCM-D at 23°C and liquid flowrate was 50 µl/min. FBS was studied at concentrations of 0%, 0.1%, 1%, 10%, and 100% in PBS. From QCM-D raw data, the deposited layer thickness was calculated using Voigt viscoelastic modeling for a film in liquid[169, 170] (See Equations 11-16).

Parameters for the Voigt model were set to have the viscosity (kg/ms) between 0.01 and 100, the shear (Pa) forced between 1000 and 1 x 10^9, and the film thickness (m) forced between 1 x 10^{-11} and 1 x 10^{-6}. The fluid density has a minor impact on the modeling and was assumed to be 1000 kg/m^3 since PBS and water have no appreciable difference. Frequency and dissipative data were input into the Voigt model at the 3rd, 5th, 7th, and 9th harmonic. Generally, we tried to achieve Chi squared values of 5 x 10^7 or less when fitting our data to the model.

Crystals were withdrawn from the QCM-D and imaged with AFM (Dimension 3100, Veeco Metrology) via tapping mode (TM) in PBS, at a scan rate of 1 Hz. AFM probes were silicon nitride with spring constants of 0.06 N/m (Veeco). At least three height and amplitude (10 μm x 10 μm) images were scanned per condition. Crystals were dried for 2 hours and rescanned using TM AFM in air. Five thickness calculations were performed per image using the section analysis software. One Way Analysis of Variance was used to compare QCM-D thickness calculations with the AFM section analysis. A statistically significant difference was defined by $P<0.05$.

4: Results

4.1: Using QCM-D and AFM to Study Protein Adsorption

4.1.1 QCM-D Calibration with Ethanol

The mixing process that occurs inside the QCM-D chambers was observed by switching between water/ethanol. The level of displacement could be calculated by monitoring the overall frequency shift from 0% ethanol to 100%, according to[167]. Several flow rates were selected, which were measured at the fundamental frequency for comparison (Figure 4.1).

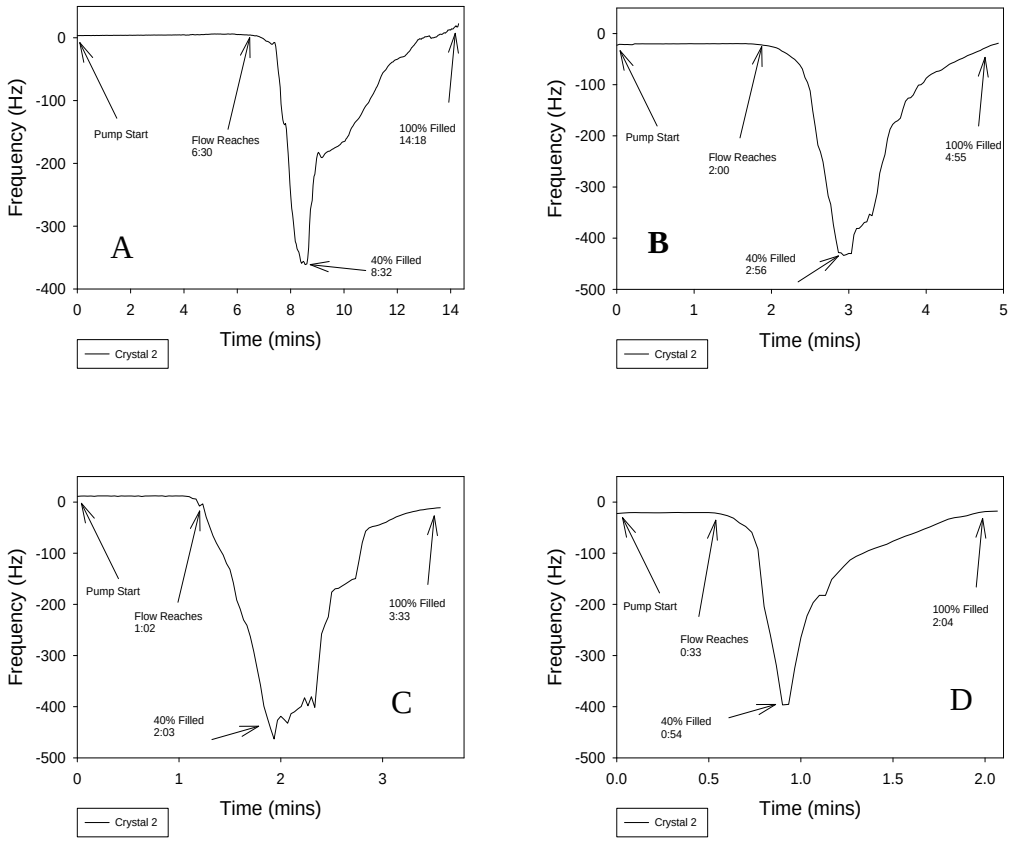

Figure 4.1 Frequency Shifts from Water to Ethanol as Measured with the Fundamental Frequency A. 50 µl/min, B. 150 µl/min, C. 200 µl/min, and D. 400 µl/min.

According to[167], the minimum frequency shift occurs when 40% of the mixture in the chamber is ethanol. When the frequency reaches a plateau, the ethanol has then completely displaced the water. Since the tubing leading to the 4 crystals is of different lengths, each crystal was calibrated (Table 4.1).

Table 4.1 Calibration of Ethanol Reaching and Rate of Mixing Inside the QCM-D Chambers

	Flow Rate	**Ethanol Reaches Chamber**	**Chamber 40% Ethanol Filled**	**Chamber 100% Ethanol Filled**
Chamber 1	50 µl/min	6 mins 36 secs	7 mins 48 secs	14 mins 32 secs
	100 µl/min	2 mins 42 secs	3 mins 24 secs	4 mins 18 secs
	150 µl/min	1 min 48 secs	2 mins 35 secs	2 mins 58 secs
	200 µl/min	1 min 15 secs	1 min 33 secs	2 mins 36 secs
	400 µl/min	42 secs	49 secs	1 min 54 secs
Chamber 2	50 µl/min	6 mins 30 secs	8 mins 32 secs	14 mins 18 secs
	100 µl/min	4 mins 10 secs	5 mins 15 secs	6 mins 15 secs
	150 µl/min	2 mins 0 secs	2 mins 56 secs	4 mins 55 secs
	200 µl/min	1 min 2 secs	2 mins 3 secs	3 mins 33 secs
	400 µl/min	33 secs	54 secs	2 mins 4 secs
Chamber 3	50 µl/min	4 mins 18 secs	5 mins 51 secs	9 mins 15 secs
	100 µl/min	1 min 20 secs	2 min 25 secs	3 min 16 secs
	150 µl/min	1 min 10 secs	1 min 58 secs	2 min 42 secs
	200 µl/min	42 secs	1 min 18 secs	2 mins 3 secs
	400 µl/min	21 secs	40 secs	1 min 6 secs
Chamber 4	50 µl/min	4 mins 18 secs	5 mins 51 secs	9 mins 15 secs
	100 µl/min	1 min 33 secs	2 mins 33 secs	3 mins 25 secs
	150 µl/min	1 min 6 secs	1 min 49 secs	4 mins 8 secs
	200 µl/min	48 secs	1 min 12 secs	1 min 53 secs
	400 µl/min	15 secs	30 secs	57 secs

The profiles from Figure 4.1 largely agree with the experimental and theoretical calculations of[167]. As ethanol begins filling the chamber, there is a steep drop in frequency, followed by a more gradual return to the baseline until steadying out as the ethanol concentration in the chamber approaches 100% (App A).

4.1.2 Adhesion of FBS to Gold: Comparing AFM Section Analysis to Voigt Viscoelastic Modeling

FBS was deposited onto gold crystals at subsequently increasing concentrations to ascertain the saturation concentration of FBS. According to Figure 4.2, at 10% FBS concentration a maximum layer of ~15 nm of FBS could be deposited. Indeed, film thickness increased marginally from 0.1% FBS to 10.0% FBS as monitored with crystals 1 and 2. According to crystals 3 and 4, saturation was achieved when 1% FBS flowed into the chamber. The discrepancy between saturation points may be due to sensitivity differentials of the mounted crystals[257].

The 100% FBS solution had noticeable viscosity effects on the frequency and dissipation, which is observable when the final rinse reduced the calculated film thickness back to the level observed with 10% FBS. Besides viscosity changes, it is also probable that much of the accumulating FBS was loosely attached and washed off during the rinse.

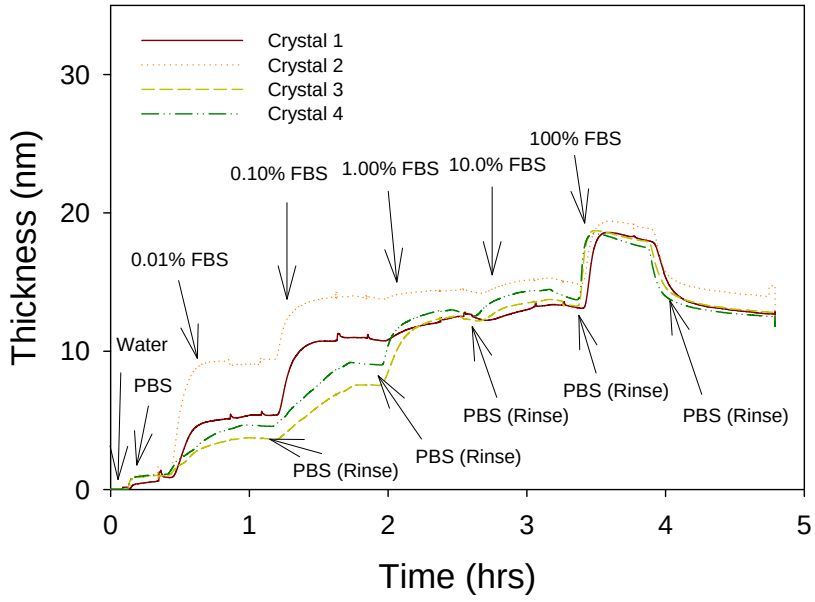

Figure 4.2 Viscoelastic modeling of the FBS deposition

The literature contains numerous comparative studies with the AFM and QCM-D[258-260]; however, none have compared the Voigt viscoelastic modeling results with the AFM's section analysis. Since the two methods can be used under similar environments but each has specific advantages, it is important to ascertain how the thickness of a well-dispersed film compares depending on the utilized method. Knowing how the two correlate, a user of the AFM's section analysis would find the QCM-D's real time analysis tool advantageous.

By comparing thickness calculations with the AFM section analysis versus the QCM-D, we found insignificant differences when comparing systems with similar quantities of FBS deposition (Figure 4.3). The QCM-D monitoring found that regardless of 1% FBS, 10% FBS, or 100%, surfaces became saturated with FBS in 5-10 mins (Figure 4.4). Although more FBS adhered in the cases of 10% and 100% FBS, the final rinse with PBS washed off loosely bound protein such that the final thicknesses were the same.

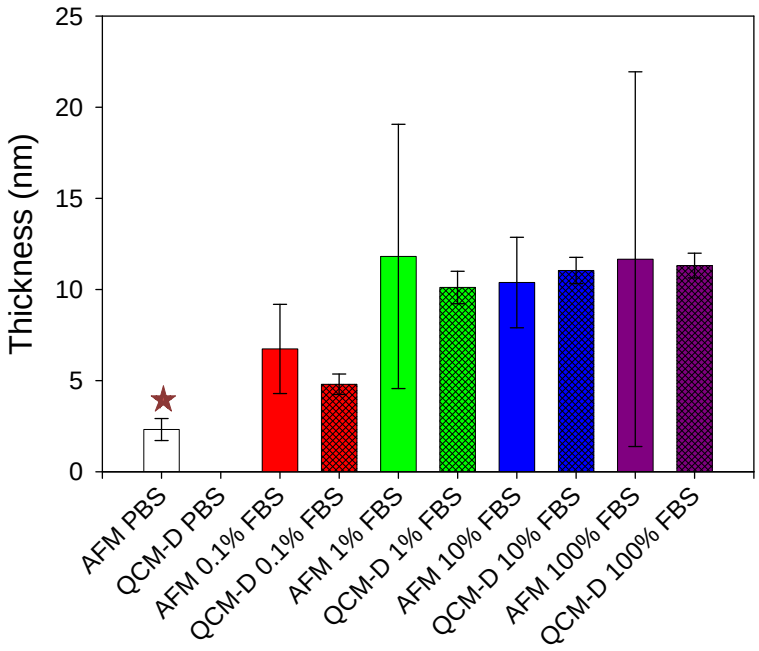

Figure 4.3 AFM in Intermittent Contact Mode Liquid Compared to QCM-D Voigt Viscoelastic Modeling. Star represents statistical difference ($P<0.05$).

The only circumstance when there was a discrepancy between QCM-D and AFM was the control case when only PBS was introduced to the system. The disagreement under the control case is attributable to the quartz crystal not being perfectly smooth, which yielded the height information under the AFM section analysis.

Additionally, when changing the liquid media from water to PBS, viscosity changes caused a shift in the frequency and dissipation, which the modeling registered as film thickness. Indeed, viscosity differences between liquids is an important parameter to consider and can have a major impact on frequency and dissipation data (App A)[167]. The FBS solutions will have different viscosities depending on concentration, which impacts frequency and dissipation data. For the case when only PBS flowed over the gold quartz

crystal the calculated film thickness was neglected by subtracting the final calculated thickness when being rinsed with PBS.

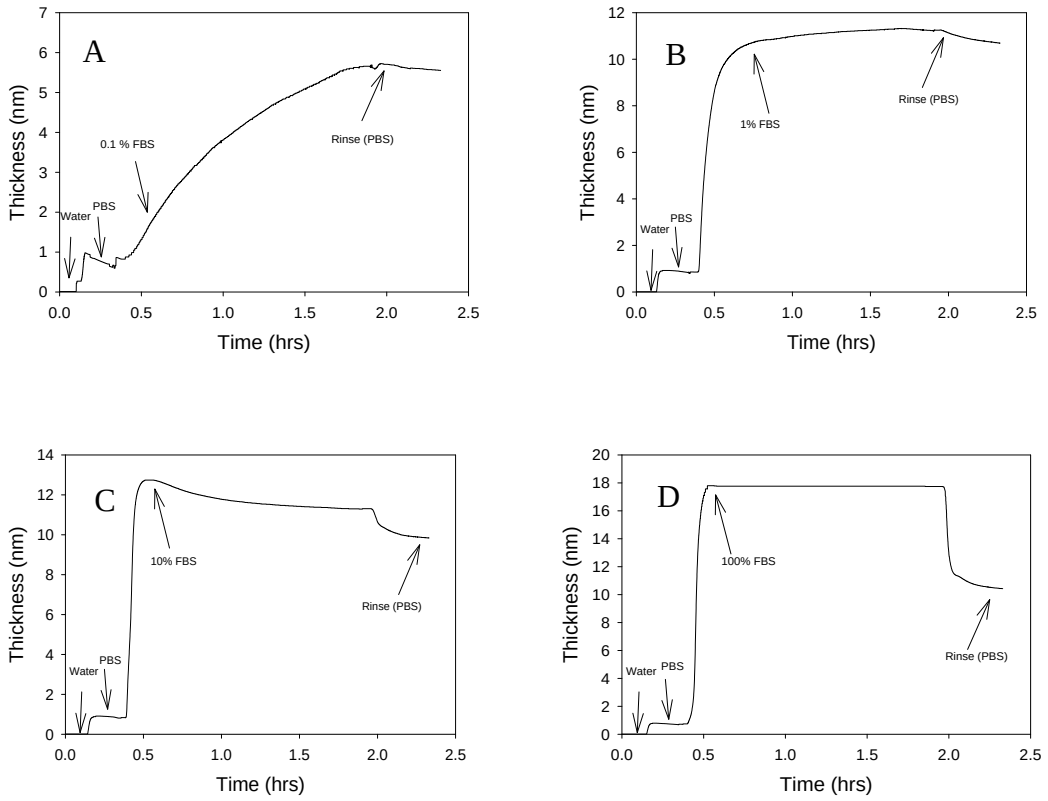

Figure 4.4 Voigt Viscoelastic Modeling of FBS Adsorption. A. 0.1 % FBS / 99.9 % PBS, B. 1.0 % FBS / 99.0 % FBS, C. 10 % FBS / 90.0 % PBS, D. 100% FBS. Each deposition process was followed by a rinse with 100% PBS to remove loosely bound proteins.

A final rinsing procedure of PBS is therefore necessary to both remove loosely deposited FBS, and to change the viscosity of the surrounding liquid back to that of PBS (App B & C). The QCM-D thicknesses reported herein are the final calculated thicknesses minus the thickness calculated when switching from water to PBS.

Although the average thicknesses between the QCM-D and AFM under similar circumstance were the same, the level of variability in the AFM data is largely due to

relatively small sample data compared to the overall quartz crystal. The QCM-D results constitute a combination of 3 separate FBS deposition experiments and we attribute the smaller error bars to a more systematic and reproducible method of calculating film thickness.

We also considered the circumstance of AFM quartz crystal analysis in air versus QCM-D results that were taken in liquid. Figure 4.5 compares AFM section analysis in air versus the QCM-D results, while Figure 4.6 confirms the significant differences between operating in air versus liquid by comparing AFM in liquid to air. We found the topography to be significantly different, which we contribute to crystallization of the PBS and aggregation of the protein following drying. The crystalline features that were pronounced on the 0% FBS crystal were not found in the cases with FBS deposition and were clearly FBS deposits. Hence, when comparing AFM and QCM-D data, it is essential to do so in identical environments.

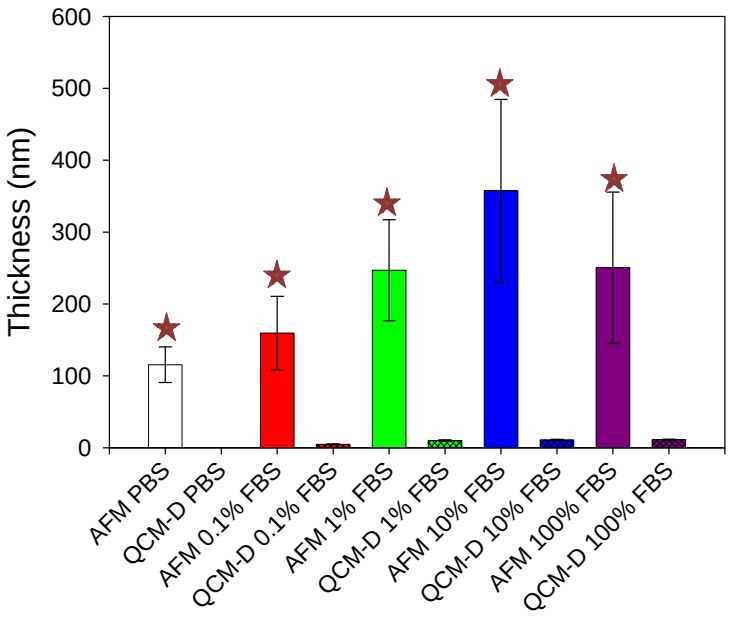

Figure 4.5 AFM in Contact Mode Air Compared to QCM-D Voigt Viscoelastic Modeling. Stars represent statistical difference between AFM and QCM-D analysis on the same crystal ($P<0.05$).

The roughness analysis results correlated well to the respective section analysis trend. Figure 4.7 shows that under each circumstance the RMS roughness was significantly greater for environments in air compared to liquid. This was due to crystallation of the PBS and FBS (Figure 4.8). Indeed, comparing Figure 4.8 A & C, the features are completely different. The FBS deposited more rounded deposits onto the gold surface, while the salt created flakes on the surface, which is expected for dried salt. In liquid, few discernable features are present for protein deposition when compared to a non-protein deposition scenario (Figure 4.8 B & C).

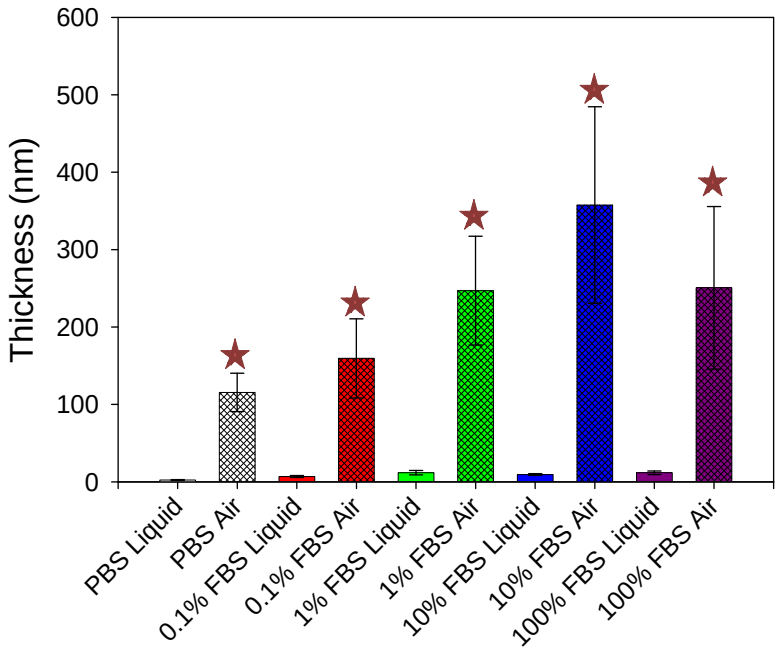

Figure 4.6 AFM in Intermittent Contact Mode Liquid Compared to AFM Contact Mode Air. Stars represent statistical difference between AFM and QCM-D analysis on the same crystal ($P<0.05$).

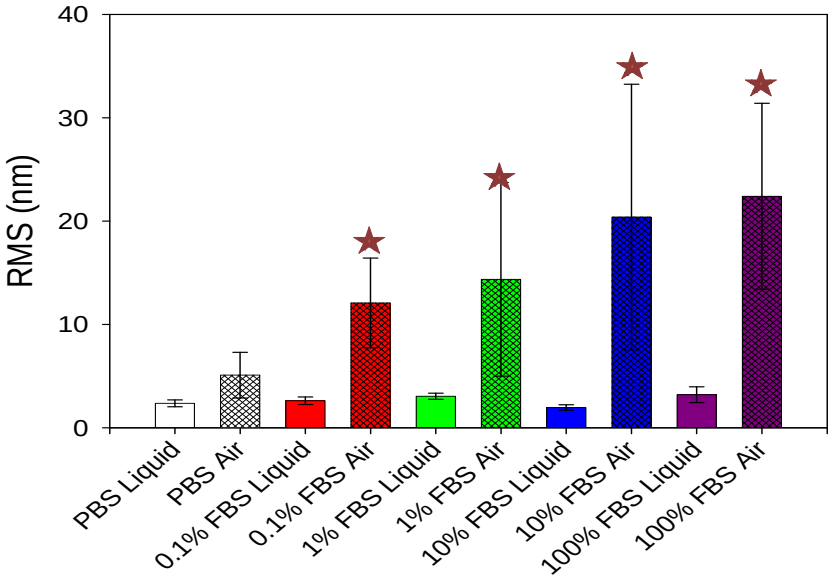

Figure 4.7 AFM Roughness Analyses of Images Captured in Intermediate Contact Mode Liquid and Contact Mode Air

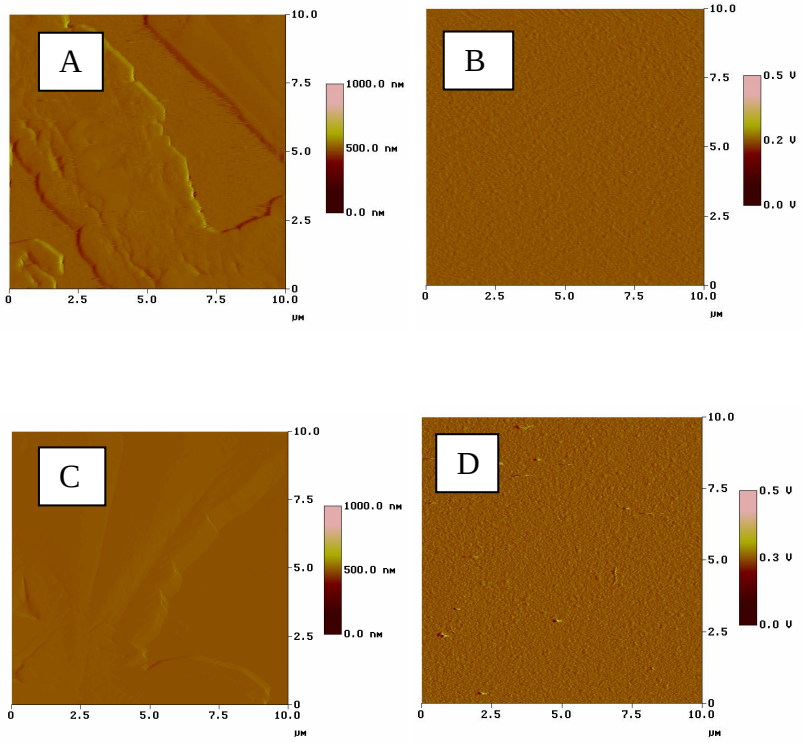

Figure 4.8 A. 100% FBS AFM Contact Mode in Air. B. 100% FBS AFM intermittent contact mode in liquid. C. 0% FBS AFM intermittent contact mode in air. D. 0% FBS AFM intermittent contact mode in liquid. (Bars indicate z scale)

As would be expected, higher roughness readings corresponded well to greater thicknesses as measured from the section analysis[261]. In air, the R^2 value between section and roughness was 0.70, which indicates a strong linear trend (Figure 4.9). In liquid, an outlier at 10% FBS concentration resulted in a weak linear correlation of just R^2=0.28 (Figure 4.10). Removing the outlier of 10% FBS yields a linear regression of R^2=0.95. The roughness results were not unusual for protein deposition experiments and further confirmed nothing unusual occurred during the FBS deposition[262, 263].

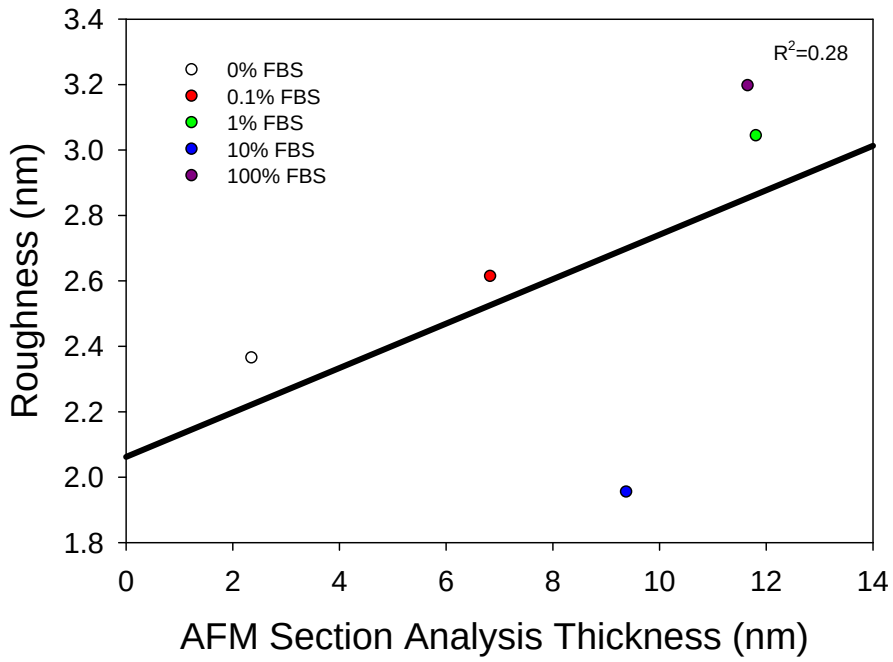

Figure 4.9 AFM Intermittent Contact Mode Liquid; Section Analysis Compared to Roughness Analysis

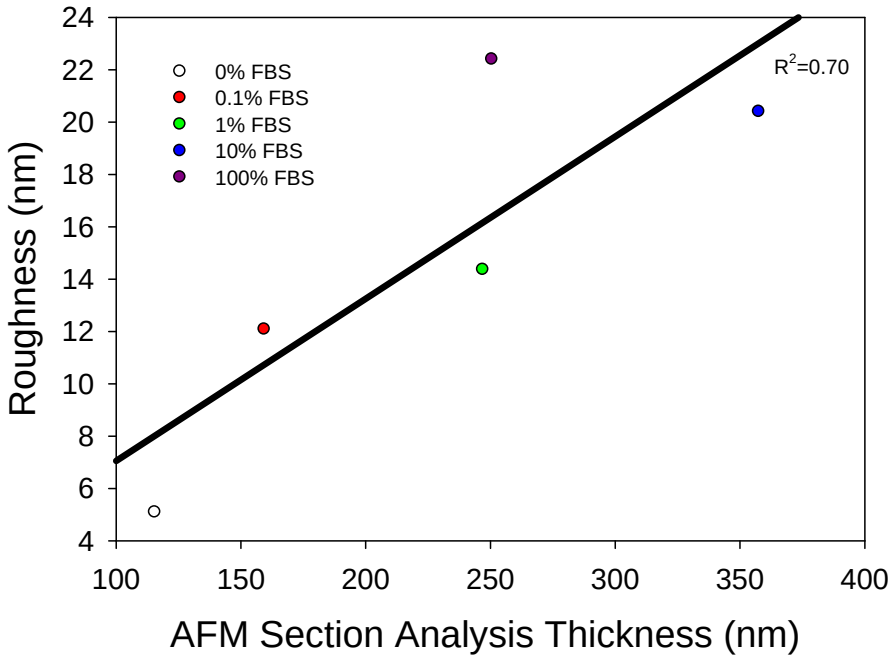

Figure 4.10 AFM Contact Mode Air; Section Analysis Compared to Roughness Analysis

4.2: Enhancing Adsorption of CP1-cys to Gold

The influence of pH on CP1-cys adsorption in terms of areal mass and film thickness were investigated (Figures 4.11 and 4.12). The pH appears to have some influence on CP1-cys adhesion. For the cases of 10 μM concentrated CP1-cys in TFE and 29.1 μM CP1-cys without chemical additives, there was no observed difference in peptide adsorption. Areal adsorption was significantly higher for the remaining experimental conditions at neutral pH. Significant differences in areal mass calculations were not observed for conditions with similar additives but differing peptide concentrations. Therefore, neutralizing the cationic regions of the peptide via pH alterations had a minor impact on whether CP1-cys could adhere to gold.

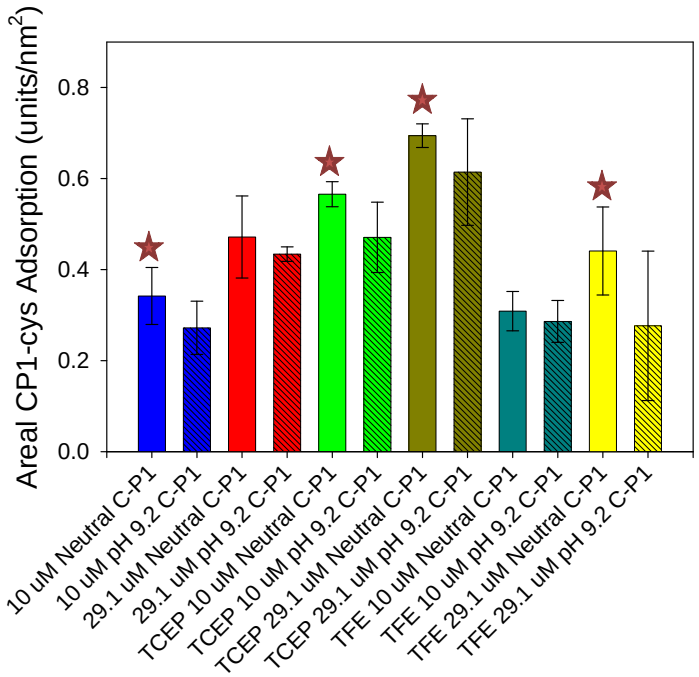

Figure 4.11 Areal Units of CP1-cys Adsorption to Gold Quartz Crystals. Stars represent statistical differences when comparing solutions of identical additive and CP1-cys concentration but differing pH ($P<0.05$).

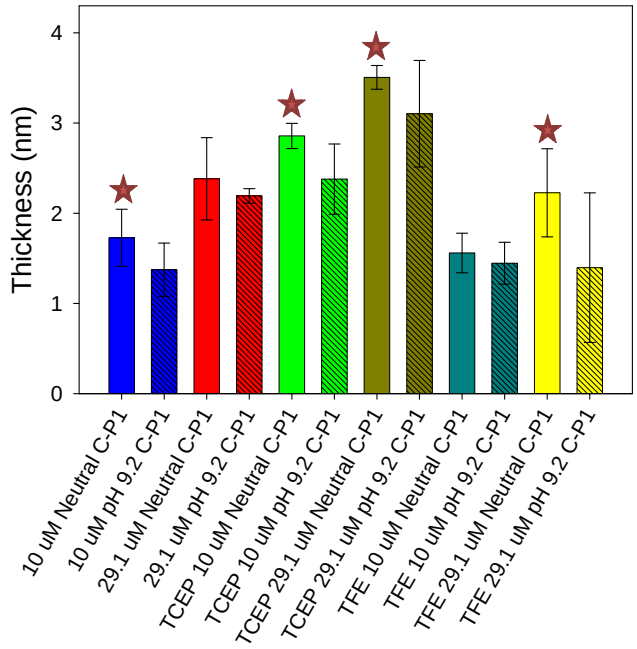

Figure 4.12 Film Thickness of Adsorbed CP1-cys to Gold Quartz Crystals. Stars represent statistical differences when comparing solutions of identical additive and CP1-cys concentration but differing pH ($P<0.05$).

Figures 4.13 and 4.14 compare solution CP1-cys concentrations while holding pH and additive constant. In the cases when no additives were involved, the 29.1 μM CP1-cys solution yielded significantly more areal mass and film thickness. Similar trends were found with the additives TCEP and TFE (Figures 4.13 & 4.14; $P<0.05$). For cases of no additives, we observed approximately double the CP1-cys density on the gold quartz crystals at 29.1 μM versus 10 μM. The differences were not as significant for differing pHs or when additives were present. The QCM-D analysis showed that the substrata were saturated at the differing concentrations used, which is indicated via frequency and dissipation stability following peptide passivation and a final rinse (App C).

CP1-cys concentration was important for saturating the gold crystals. Under most circumstances, 29.1 μM CP1 solution yielded greater peptide deposits. Only in the cases of TFE solution at pH 9.2 did saturation not depend on CP1-cys concentration. For neutral PB without additives, the amount of adsorbed CP1-cys increased by 91%, while at pH 9.2, the amount of adsorbed CP1-cys increased by 60%. However, in the case with TCEP, adsorbed mass increased by only ~33%, but the net increase of areal mass was >100 ng/cm^2, which is greater than all other circumstances (Figure 4.13).

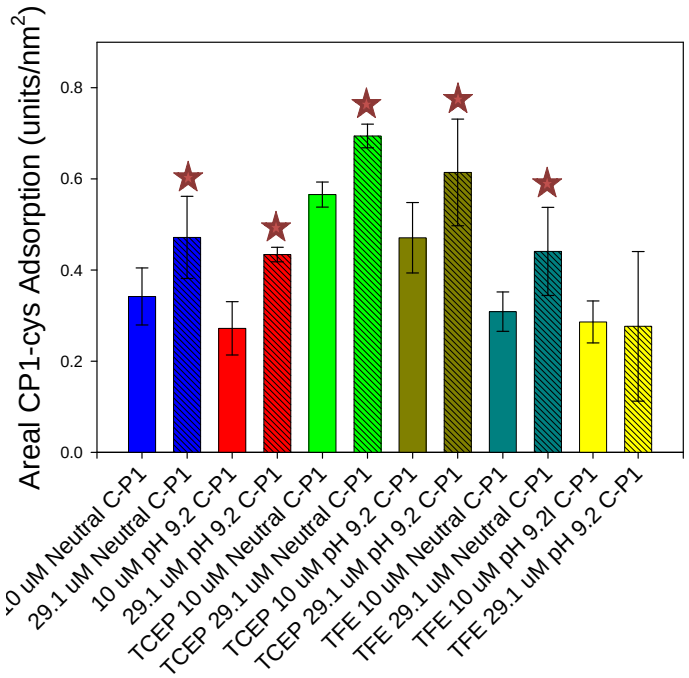

Figure 4.13 Areal Units of CP1-cys Adsorption to Gold Quartz Crystals. Stars represent statistical differences when comparing solutions of identical additive and pH but differing CP1-cys concentration (P<0.05).

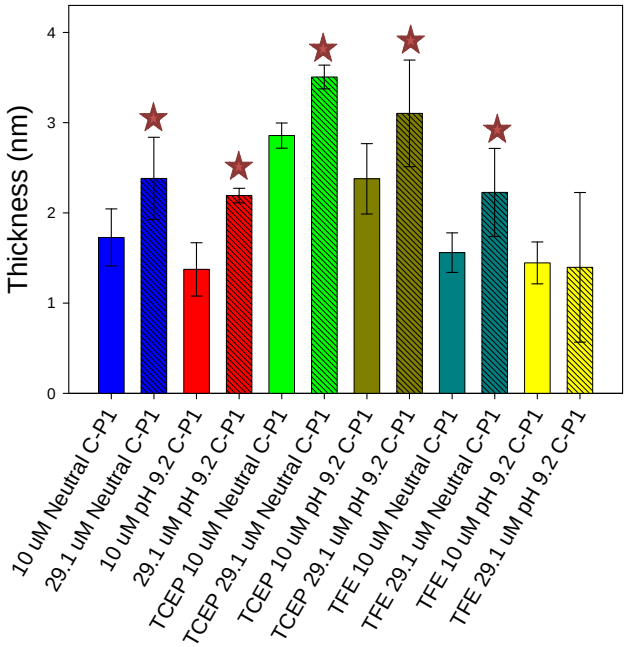

Figure 4.14 Film Thickness of CP1-cys Adsorption to Gold Quartz Crystals. Stars represent statistical differences when comparing solutions of identical additive and pH but differing CP1-cys concentration (P<0.05).

The trifluorethanol runs yielded unexpected degrees of viscosity changes and mixing inside the QCM-D chambers (Figure 4.15). According to the Voigt Modeling, the film thickness was greater at the 10 µM CP1-cys concentration than at the 29.1 µM. We attribute these erroneous results to difficulties operating with TFE since the viscosity effects appear to be outside the design of the modeling software. Using more dilute concentrations of TFE may enhance modeling for further study.

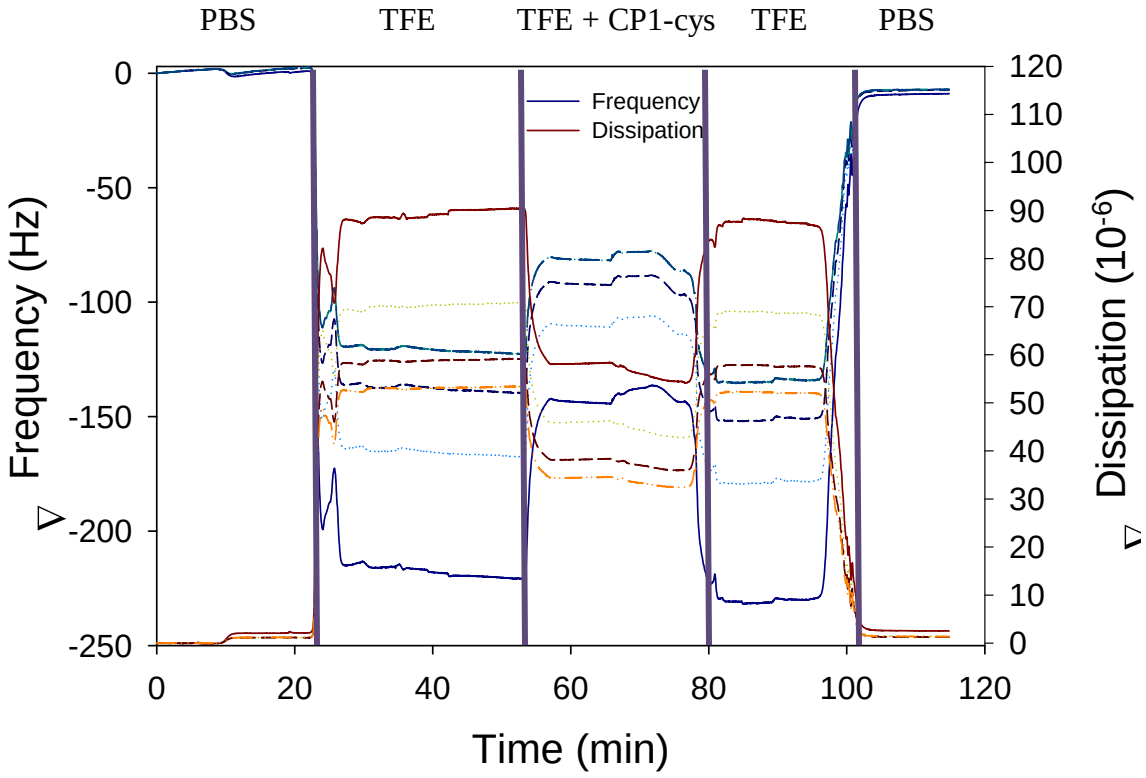

Figure 4.15 QCM-D measurement of TFE and 10 µM CP1-cys to gold quartz crystals. From t=0-21 mins, PB flowed over the gold quartz crystal followed with TFE. From t=55-78 mins, CP1-cys + TFE flowed over the gold quartz crystal. A rinse of TFE followed peptide adsorption and at t=95 mins the crystal was rinsed with PB to remove loosely deposited peptide.

Comparisons between the effects of additives show significant increases for when TCEP was present (Figure 4.16 and 4.17). TCEP was found to adhere to the gold substrates, therefore areal mass calculations of peptide adsorption accounted for the adsorption of TCEP (Figure 4.18 & 4.19). In terms of the areal mass, TCEP enhanced the adhesion of CP1-cys regardless of pH. TCEP in concert with neutralized cationic regions may have the desired effect of enhancing CP1-cys orientation to gold, but did not significantly affect adhesion and retention.

Thickness calculations were more inconclusive since TFE was difficult to model, however the additive TCEP was easier to model. When TCEP passivated the gold quartz crystal, we observed increased CP1-cys film thickness and more vertically oriented peptide on the gold than without the additive. This is due to dissipation increasing and frequency decreasing significantly more than compared to without additive. TCEP improved binding between peptide and gold even at the higher pH, which indicates the lysines had a lesser role in peptide adhesion. TFE resulted in no increased CP1-cys adsorption and dissipation results are difficult to quantify due to bulk shifts in viscosity and density.

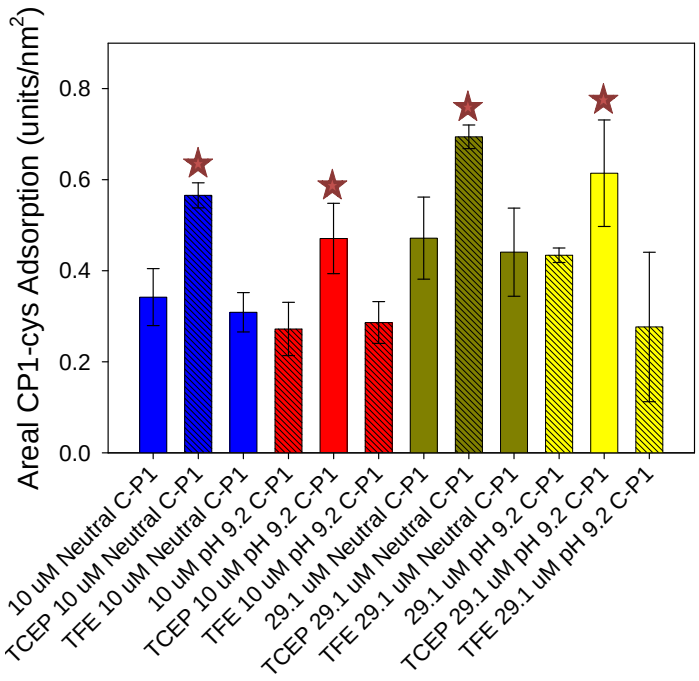

Figure 4.16 Areal Mass of CP1-cys Adsorption to Gold Quartz Crystals. Stars represent statistical differences when comparing solutions of identical CP1-cys concentration and pH but differing additive ($P<0.05$).

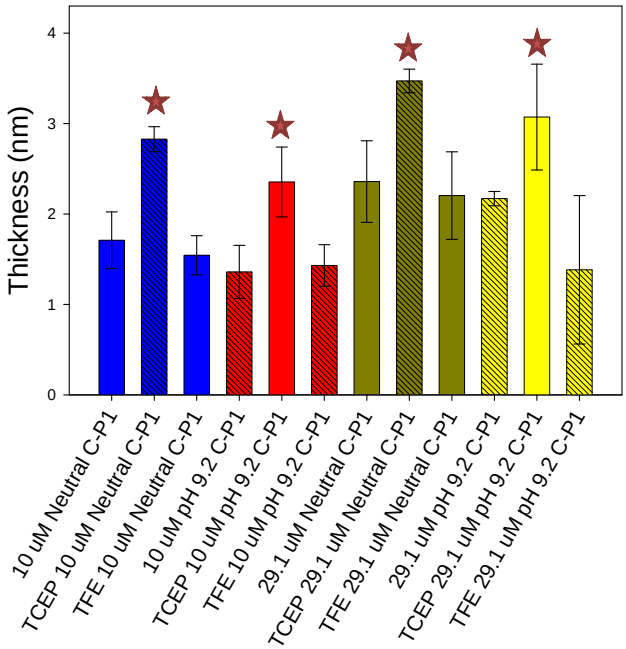

Figure 4.17 Film Thickness of CP1-cys Adsorption to Gold Quartz Crystals. Stars represent statistical differences when comparing solutions of identical CP1-cys concentration and pH but differing additive ($P<0.05$).

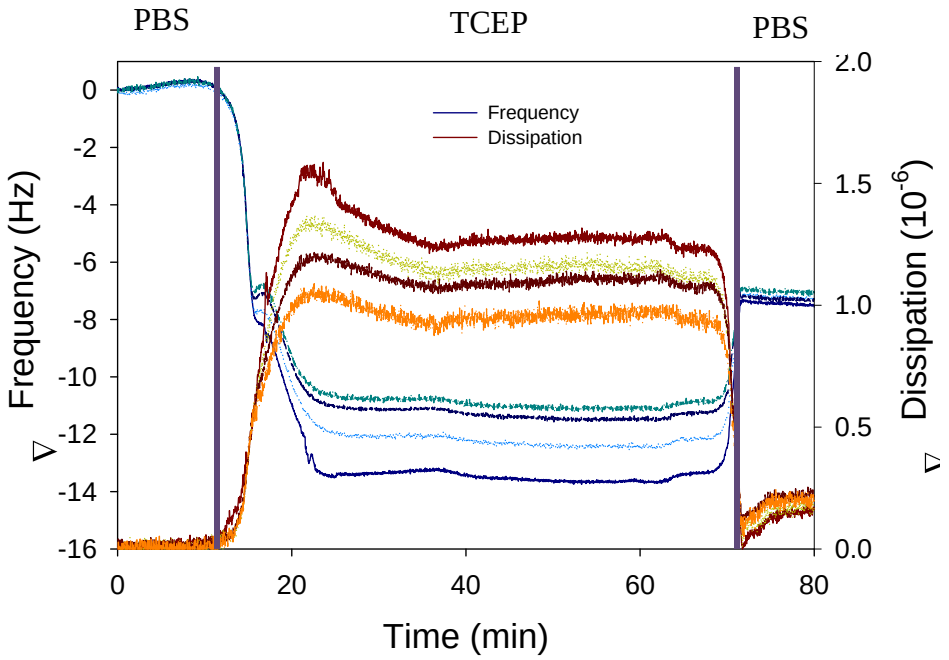

Figure 4.18 Frequency and Dissipation response to TCEP adsorption to gold quartz crystal in PB. From t=0-13 min, PB flowed over crystals. From 13 min to 70 min TCEP solution was introduced, which was followed by rinsing with PBS.

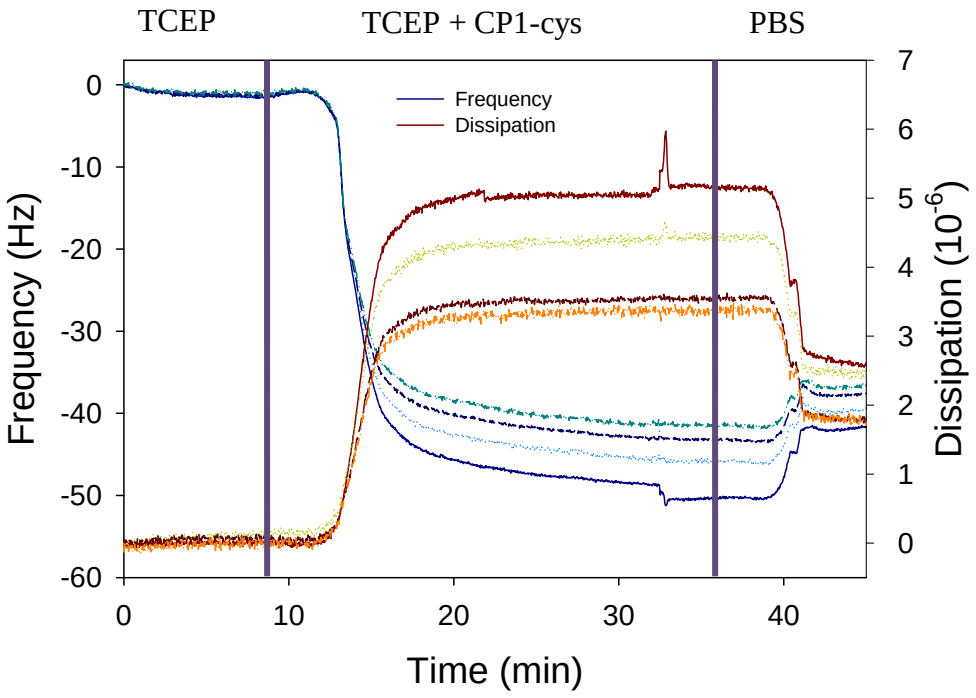

Figure 4.19 Frequency and Dissipation response to TCEP + CP1-cys adsorption to gold quartz crystal in PB. From t=0-13 min, TCEP solution flowed over crystals. From 13 min to 38 min TCEP + CP1-cys was introduced, which was followed by rinsing with PBS. Frequency and dissipation data from Figure 4.18 was subtracted from analysis so that the effects of adsorbed TCEP were not included in quantifying adsorbed peptide.

4.3: Bacterial Adhesion + Properties of LPS

4.3.1 Motility Test

The 13 *E. coli* strains expressed flagella when the serotype specified flagella production (Table 4.2). These results are expected, and demonstrate that the storage and growth of the *E. coli* had no adverse side effects on the bacteria.

The motility test is a simple indication of whether the *E. coli* strains express flagella. After 24 hr since inoculation, bacteria possessing flagella will be able to colonize agar within several millimeters. There are some important parameters to consider. The agar needs to be fresh and be solid enough to hold form, but be easily pierced by an inoculation loop. Additionally, temperature is important to consider or else the bacteria may not be in condition to use the flagella. For example, *Yersinia enterocolitica* is motile between 20-25°C but not outside this range[264]. Since the results comply with the bacterial serotypes, these results demonstrate the rinsing procedure, which includes vortexing, did not cause significant damage to the bacteria.

Table 4.2 Motility Test Results for 13 *E. coli* Strains

Strain	Motility
***E. coli* HB101**	**NO**
***E. coli* K12**	**NO**
***E. coli* ML35**	**NO**
***E. coli* O26:K60:H11**	**YES**
***E. coli* O35:H10**	**YES**
***E. coli* O55:H7**	**YES**
***E. coli* O113:H4**	**YES**
***E. coli* O113:H21**	**YES**
***E. coli* O117:K98:H4**	**YES**
***E. coli* O157:H7**	**YES**
***E. coli* O157:H12**	**YES**
***E. coli* O157:H16**	**YES**
***E. coli* O172:H-**	**NO**

4.3.2 Steric Model on E. coli *to Determine LPS Length*

Steric repulsion was observed in all approach curves. The distance from the bacterium to the AFM probe at which repulsive forces were encountered varied for each strain. The variations in approach curves are reflected in differences of LPS length (Table 4.3) and distribution of these data (Table 4.4). The steric model was applied to the approach curves (Fig 3.2 A) and an R^2 >0.90 was achieved for all data (Fig 3.2 B). Data from the zero interaction and 0 seperation regions of the approach curves were not considered for steric modeling.

Table 4.3 Bacterial LPS properties

Strain	Equilibrium Length (nm)	Core Type	Absolute Adhesion Force (nN)
HB101	**5± 3**	**K12**	0.4 ± 0.1
K12	**3 ± 2**	**K12**	0.5 ± 0.2
ML35	**3 ± 2**	**K12**	0.7 ± 0.4
O26:K60:H11	15 ± 5	R3	0.2 ± 0.1
O35:H10	39 ± 14	NA	1.0 ± 0.5
O55:H7	38 ± 10	R3	0.9 ± 0.4
O113:H4	17 ± 10	R3	0.6 ± 0.6
O113:H21	37 ± 9	R1	1.0 ± 0.4
O117:K98:H4	40 ± 12	NA	1.3 ± 0.6
O157:H7	30 ± 13	R3	0.7 ± 0.4
O157:H12	25 ± 9	R2	0.6 ± 0.2
O157:H16	19 ± 6	R2	0.5 ± 0.2
O172:H-	41 ± 12	R3	1.5 ± 0.7

Core types from Amor *et al* [1]. Bold text represents control K-12 strains that do not express the O-antigen. Force cycles with bare silicon nitride probe.

The LPS lengths were the shortest for the three strains that lacked the O-antigen: HB101, K12, and ML35. Average LPS lengths of control strains, which are composed of the lipid A and core polysaccharide, was 3.5 nm. Averaged equilibrium polymer lengths

for control strains were statistically similar based on the ANOVA test (P=0.92). By applying steric modeling to the approach curves of the 5 O-antigen expressing strains, we could make quantitative comparisons based on LPS characteristics. LPS lengths varied from 17 to 37 nm for strains with O-antigens (Table 4.3). *E. coli* with the same O-antigen sugar composition had significantly different LPS lengths. For example, the lengths for O157:H7 when compared to O157:H12 and O157:H16 were significantly different ($P<0.05$). The two O113 serotypes had LPS lengths of 17 ± 10 nm (for O113:H4) and 37 ± 9 nm (for O113:H21). This difference of 20 nm was statistically different ($P<0.05$). Further, LPS lengths of the control strains were significantly shorter compared to all O-antigen expressing strains ($P<0.05$).

4.3.3 Shapiro-Wilk Test for LPS Length Distribution

Another method for exploring the differences of the bacterial LPS is by conducting a Shapiro-Wilk Test for normal distribution (Table 4.4)[265-267]. The test assumes that a large sample relative to the overall population has been taken and the results serve as an indication of whether the bacterial surface is homogenous. Approach curves corresponding to retraction force curves that were found to be outliers in terms of retraction distance were removed (App D).

The normality test was conducted for the 13 *E. coli* strains and is based on data obtained for length. Nearly all bacteria were normally distributed in terms of their polymer lengths. Even strains that possessed the highly variable O-antigen distribution of the LPS length was normal. These results indicate suffificent sample size was achieved to grasp an overall understanding of the *E. coli* LPS. Only *E. coli* O26:K60:H11 and O113:H4 had abnormally distributed LPS. These two strains also had

the shortest averaged LPS length, but it remains unclear if increasing the sample size would have resulted in a more normal distribution of data. Instead of 50 force curves that probe 10 bacteria selected from a population of billions, it may be advantageous to take significantly more data by conducting 'force mapping' of hundreds or thousands of bacteria within a sample to more accurately ascertain the distribution of LPS length[268-270].

Table 4.4 Shapiro Wilk Test for Normality of the Polymer Length for the 13 *E. coli* Strains

	Length	
Serotype	W[a]	Normal Distribution
E. coli HB101	0.89	Yes
E. coli ATCC 29425	0.92	Yes
E. coli ML35	0.96	Yes
E. coli O26:K60:H11	0.80	No
E. coli O35:H10	0.97	Yes
E. coli O55:H7	0.98	Yes
E. coli O113:H4	0.80	No
E. coli O113:H21	0.90	Yes
E. coli O117:K98:H4	0.95	Yes
E. coli O157:H7	0.91	Yes
E. coli O157:H12	0.96	Yes
E. coli O157:H16	0.96	Yes
E. coli O172:H-	0.96	Yes

[a]Normal Distribution Defined by W≥0.89

4.3.4 E. coli *Adhesive Forces with Silicon Nitride*

The adhesion force analysis provides the forces required to overcome adhesive forces between LPS molecules and silicon nitride probe. Once the probe contacts the LPS, polymers attach to the silicon nitride tip causing multiple polymer breakages. The detachment of the polymers occurs at differing points due to Brownian motion of the AFM probe[160]; hence there are commonly multiple pull-off events of varying F_{adh}.

Each *E. coli* strain had a different F_{adh} with the silicon nitride. Even for the control strains, there were some differences in the adhesion to the AFM tip. Absolute adhesion forces for HB101, K12, and ML35 were 0.4 ± 0.1 nN, 0.7 ± 0.4 nN, and 0.5 ± 0.2 nN, respectively (Table 2). *E. coli* ML35 adhered significantly greater to silicon nitride than HB101 and K12 ($P<0.05$).

Of the 10 O-antigen expressing strains, only *E. coli* O35:H10, O113:H21, O117:K98:H4, and O172:H- adhered significantly greater to silicon nitride than the control strains (Figure 4.20). Bacteria among the same serotype were expected to have similar adhesion forces due to identical chemical O-antigen compositions. Our hypothesis held true for O157:H7 and O157:H12, however, retraction forces were significantly less for O157:H16 ($P<0.05$). Absolute adhesion forces for the 3 strains were 0.7 ± 0.4 nN, 0.6 ± 0.2 nN, and 0.5 ± 0.2 nN, respectively. However, the O113 serotype differed with O113:H21, having significantly greater retraction forces than O113:H4 ($P<0.05$).

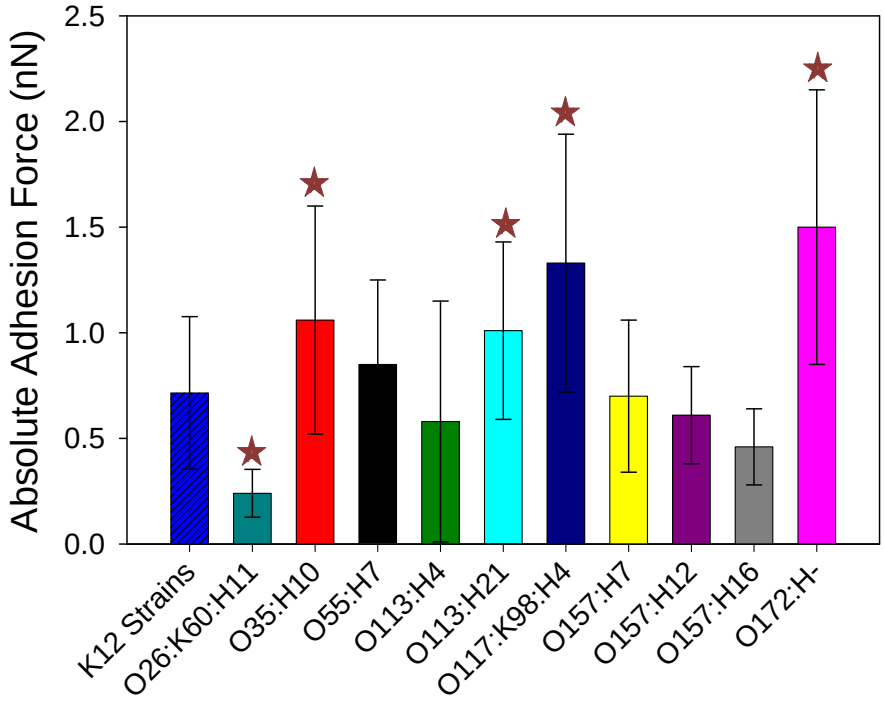

Figure 4.20 AFM Retraction Force Analyses on Bare Silicon Nitride Probes. Stars represent statistical difference between K12 strains and O-antigen containing strains ($P<0.05$).

4.3.5 Effect of Core Types

The core type had little effect on F_{adh}, with F_{adh} values being statistically similar for K12, R2, and R3 cores (Figure 4.20). F_{adh} seemed larger for the R1 core strain (O113:H21), but we could not make a comparison since no other strain had an R1 core (Table 4.3). The control strains that express the K12 core had conserved equilibrium polymer lengths significantly shorter than bacteria of the R1, R2, and R3 core types ($P<0.05$). However, R1, R2, and R3 strains also expressed the O-antigen that we associated with the longer LPS.

4.3.6 Correlating LPS Length to F_{adh} *with Silicon Nitride*

There was no correlation between fitted LPS length and F_{adh} with silicon nitride for any of the control strains. For strains O113 and O157, F_{adh} values correlated positively with LPS length (Table 4.5). The strongest correlations were observed for O157:H7 and O157:H12 (R^2>0.90). Strain O157:H16, which expressed the shortest LPS, had a weak correlation (R^2=0.54).

When we grouped strains according to whether they expressed the O-antigen, average LPS lengths correlated well with average F_{adh} for O-antigen expressing strains (R^2=0.84) (Table 4.5). However, when no O-antigen was present, the correlation was poor (R^2=0.30). By correlating mean F_{adh} for all strains with LPS length yielded a positive correlation with R^2=0.53. The weaker overall trend was due to the control strains that appeared to bind to the AFM probe independently of LPS length.

Table 4.5. Bacterial LPS properties measured from steric modeling.

Strain	Equilibrium Length (nm)	Core Type[1]	F_{adh} (nN)	Linear Trend (F_{adh} versus LPS Length)	
HB101[2]	**5 ± 3**	**K12**	**0.4 ± 0.1**	**Control Strains**	**y=0.79-0.08x**
K12	**3 ± 2**	**K12**	**0.5 ± 0.2**		**R^2=0.30**
ML35	**3 ± 2**	**K12**	**0.7 ± 0.4**		
O113:H4	17 ± 10	R3	0.6 ± 0.6	O-antigen Strains	y=0.07+0.02x
O113:H21	37 ± 9	R1	1.0 ± 0.4		R^2=0.84
O157:H7	30 ± 13	R3	0.7 ± 0.4	All Strains[3]	y=0.42+0.01x
O157:H12	25 ± 9	R2	0.6 ± 0.2		R^2=0.54
O157:H16	19 ± 6	R2	0.5 ± 0.2		

[1]Core types from Amor *et al* [1].
[2]Bold text represents control K12 strains that do not express the O-antigen.
[3]Only *E. coli* with strains that have O-antigens identical to at least one other strain was included.

4.4: Bacterial Interactions with Peptide

4.4.1 Non-specific Binding of CP1 to Silicon Nitride

QCM-D was used to monitor the adsorption of CP1 to silicon nitride and gold. It is expected that CP1 will bind non-specifically to either substrate. On silicon nitride, CP1 adsorbed to the substrate rapidly, as indicated by a drop in frequency and an increase in dissipation as soon as CP1 was added (Figure 4.21 A). Saturation was usually reached 5-10 min following introduction of CP1 solution. While frequency dropped by 20 Hz, dissipation increased by only ~7.0 x 10^{-7}. Using the Voigt viscoelastic model, the maximum film thickness of 1.7 nm was calculated at 12 min, but this number includes changes of the bulk solution's viscosity and density, as well as effects of adsorbed mass on the crystal (Figure 4.21 B). During the rinse phase, loosely deposited peptide was removed and the film thickness of CP1 was 1.15 nm at the end of the experiment (Figure 4.21 B). Frequency increased by10 Hz during the rinse, but dissipation changed little.

Based on a film thickness of 1.15, the areal mass was calculated (ρ_{CP1} =1100 kg $\cdot m^{-3}$=1.26 x 10^{-12} ng x 1.15 nm^{-3}=1.26 x 10^{-12} ng nm^{-2} [areal density]. MW_{CP1} ~3338 g $\cdot mol^{-1}$=1.8 x 10^{11} $CP1_{unit}$ $\cdot ng^{-1}$. 1.26 x 10^{-12} ng $\cdot nm^{-2}$ x 1.8 x 10^{11} $CP1_{unit}$ $\cdot ng^{-1}$= 2.3 x 10^{-1} $CP1_{unit}$ $\cdot nm^{-2}$). This corresponds to 0.23 units of CP1 nm^{-2} adhering to the silicon nitride. Unmodified peptide should also bind non-specifically to gold, as was monitored by QCM-D (4.22 A & B). The areal mass and thicknesses of adsorbed peptide were almost identical to that on silicon nitride, at 0.22 units of CP1 nm^{-2} and 1.11 nm, respectively.

4.4.2 Binding of CP1-cys to Gold Quartz Crystals

By using cysteine-terminated cecropin P1 (CP1-cys), we determined how the peptide adsorbed to gold when covalent bonds were forming (Figure 4.23 A). From zero

to 18 min, PBS was pumped through the chamber, followed by a 14 min addition of CP1-cys solution (until we visually observed that equilibration was reached). Frequency dropped by ~23 Hz and dissipation increased by 3.4×10^{-6}. Following the rinse, the areal mass of adsorbed peptide was calculated as 1.9 ng nm^{-2} or 0.34 units of CP1-cys per nm^2, while film thickness was calculated to be 1.70 nm (Figure 4.23 B). Qualitatively, the shape of the frequency and dissipation curves continued to mirror each other. By the conclusion of the rinse, frequency had increased by 3 Hz for a net change of 20 Hz, and dissipation had a net decrease of 2.8×10^{-6}. When covalent bonds could form, CP1-cys bonded ~55% more and packed more tightly on the gold crystals than for CP1 physisorbed to silicon nitride.

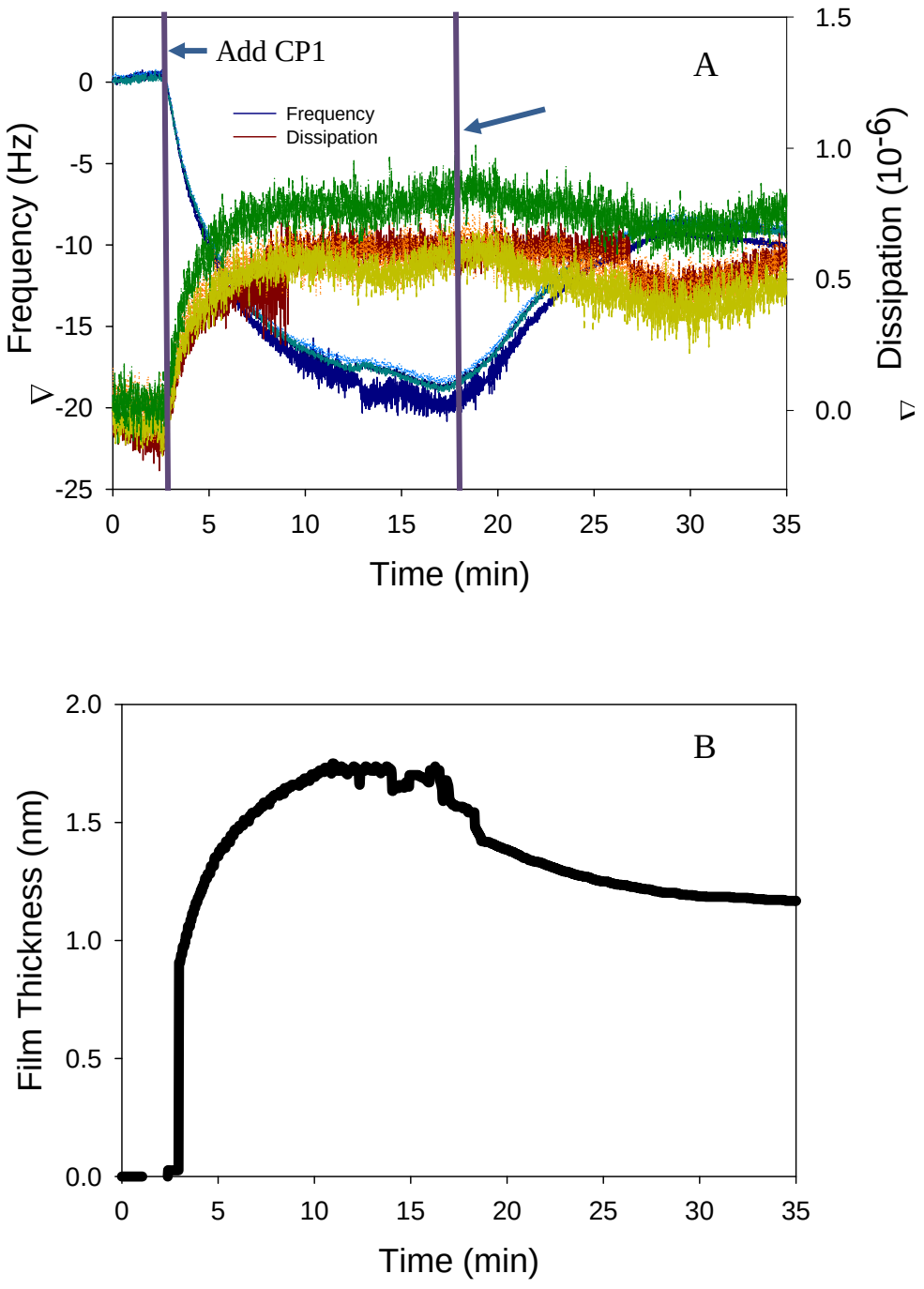

Figure 4.21 Monitoring attachment of CP1 to silicon nitride. A) Monitoring frequency and dissipation for PBS, followed by addition of 10 μM solution of CP1, and rinse with PBS. Frequency and dissipation changes were monitored with the 3rd, 5th, 7th, and 9th harmonics. B) Voigt viscoelastic monitoring of the frequency and dissipation data was used to calculate the peptide layer thickness on silicon nitride. Areal adhesion for CP1 on silicon nitride is 0.23 units of CP1 nm^{-2}.

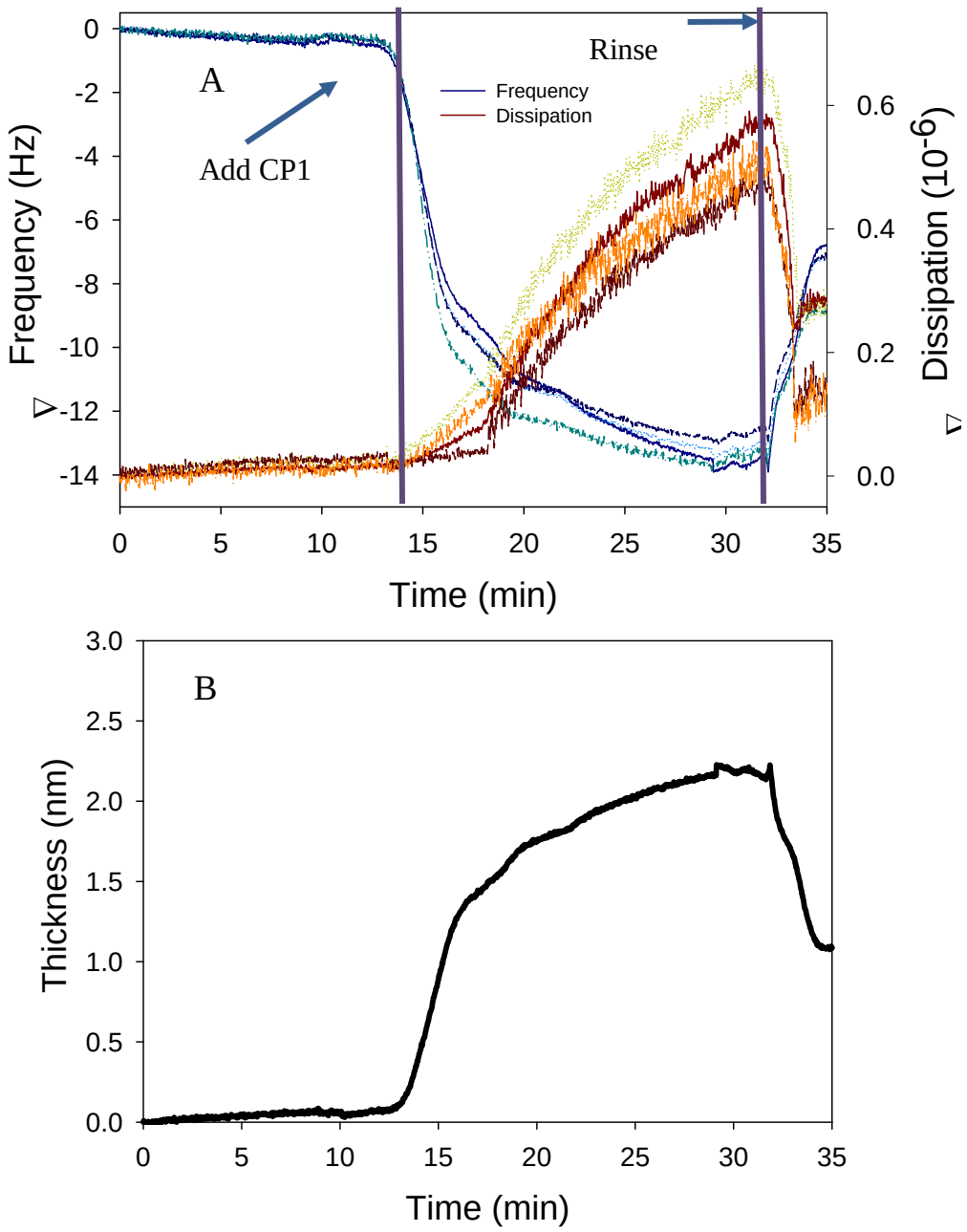

Figure 4.22 Monitoring attachment of CP1 to gold. A) Monitoring frequency and dissipation for PBS, followed by addition of 10 μM solution of CP1, and rinse with PBS. Frequency and dissipation changes were monitored with the 3rd, 5th, 7th, and 9th harmonics. B) Voigt viscoelastic monitoring of the frequency and dissipation data was used to calculate the peptide layer thickness on silicon nitride. Areal adhesion for CP1 on gold is 0.22 units of CP1 nm^{-2}.

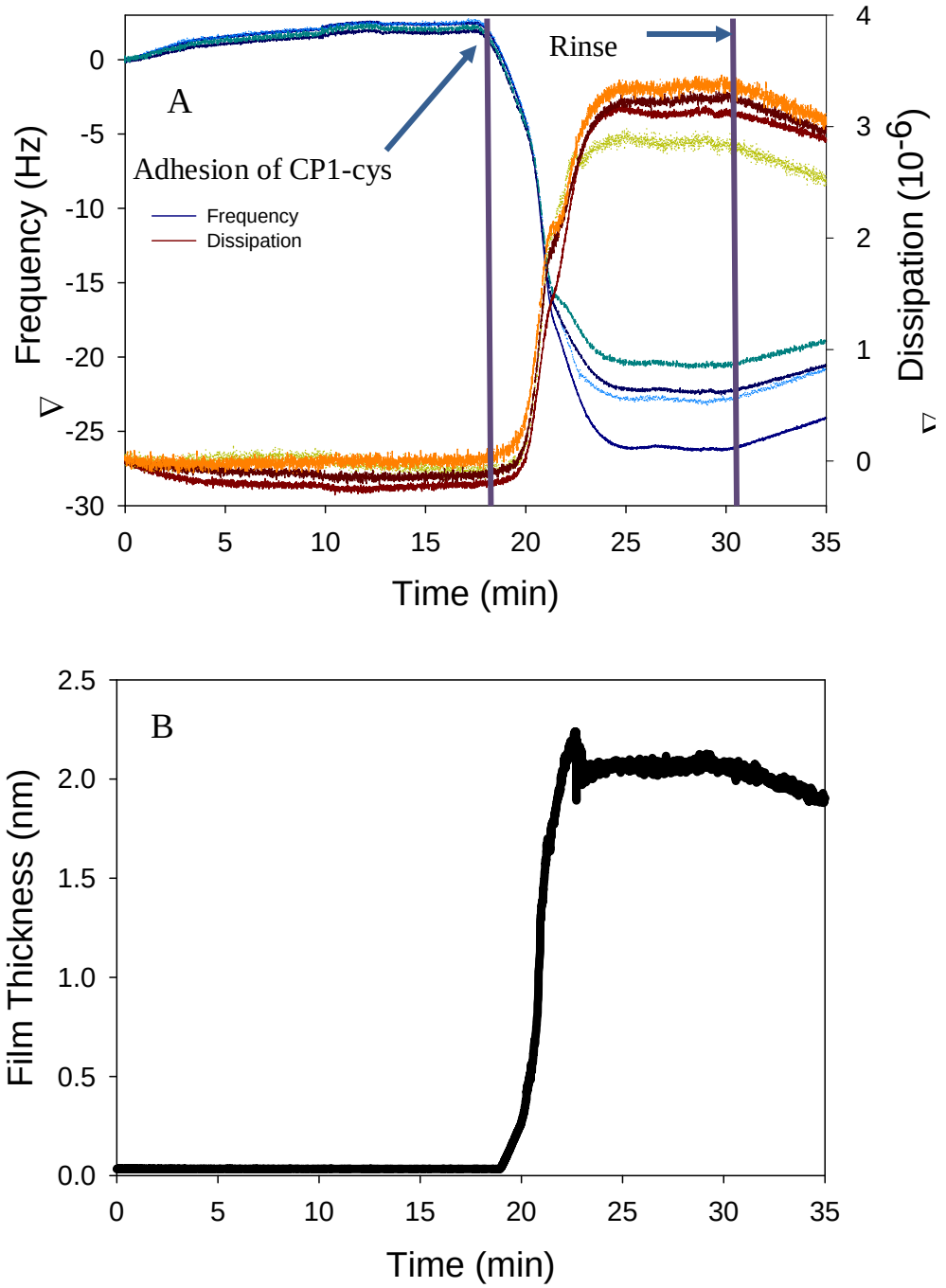

Figure 4.23 Monitoring attachment of CP1-cys to gold. A) Monitoring frequency and dissipation for PBS, followed by addition of 10 μM solution of CP1, and rinse with PBS. Frequency and dissipation changes were monitored with the 3rd, 5th, 7th, and 9th harmonics. B) Voigt viscoelastic monitoring of the frequency and dissipation data was used to calculate the peptide layer thickness on silicon nitride. Areal adhesion for CP1-cys on gold is 0.34 units of CP1-cys nm^{-2}.

4.4.2 CP1 and Silicon Nitride Interaction with Glass

Retraction force curves conducted with bare silicon nitride and modified tips with CP1 led to significantly greater pull-off forces for 10 of the 13 *E. coli* strains ($P<0.05$). These results were based on 50 force curves per condition and were conducted in liquid to avoid capillary forces from affecting the pull-off force[271]. In addition, the pull-off force with bare glass was significantly greater between bare glass and silicon nitride than with the modified AFM probe (Figure 4.24). Considering all had a single sharp peak in the range of 0-5 nm, the curves demonstrate no specific adhesion occurs between glass and AFM probes and that the glass slides were properly cleaned Figure (4.25 A & B).

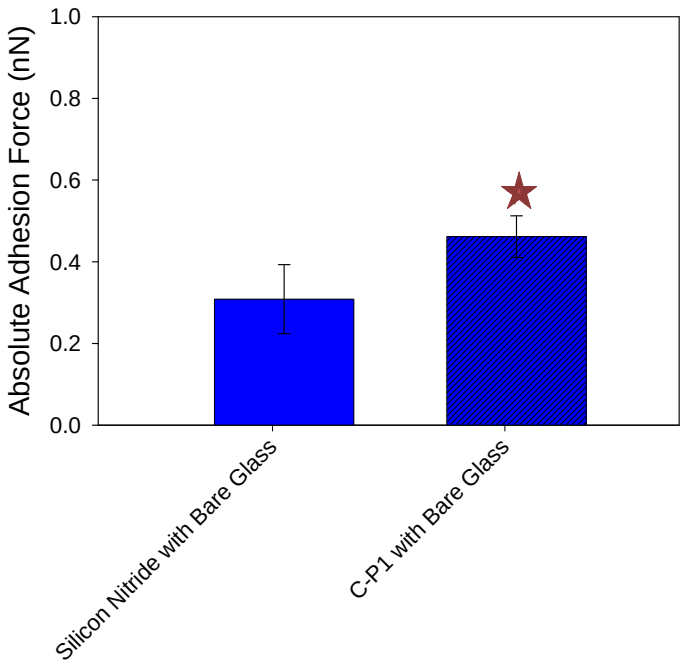

Figure 4.24 AFM Retraction Force Analyses on Bare Glass. Stars represent statistical difference between bare and CP1 modified probe ($P<0.05$).

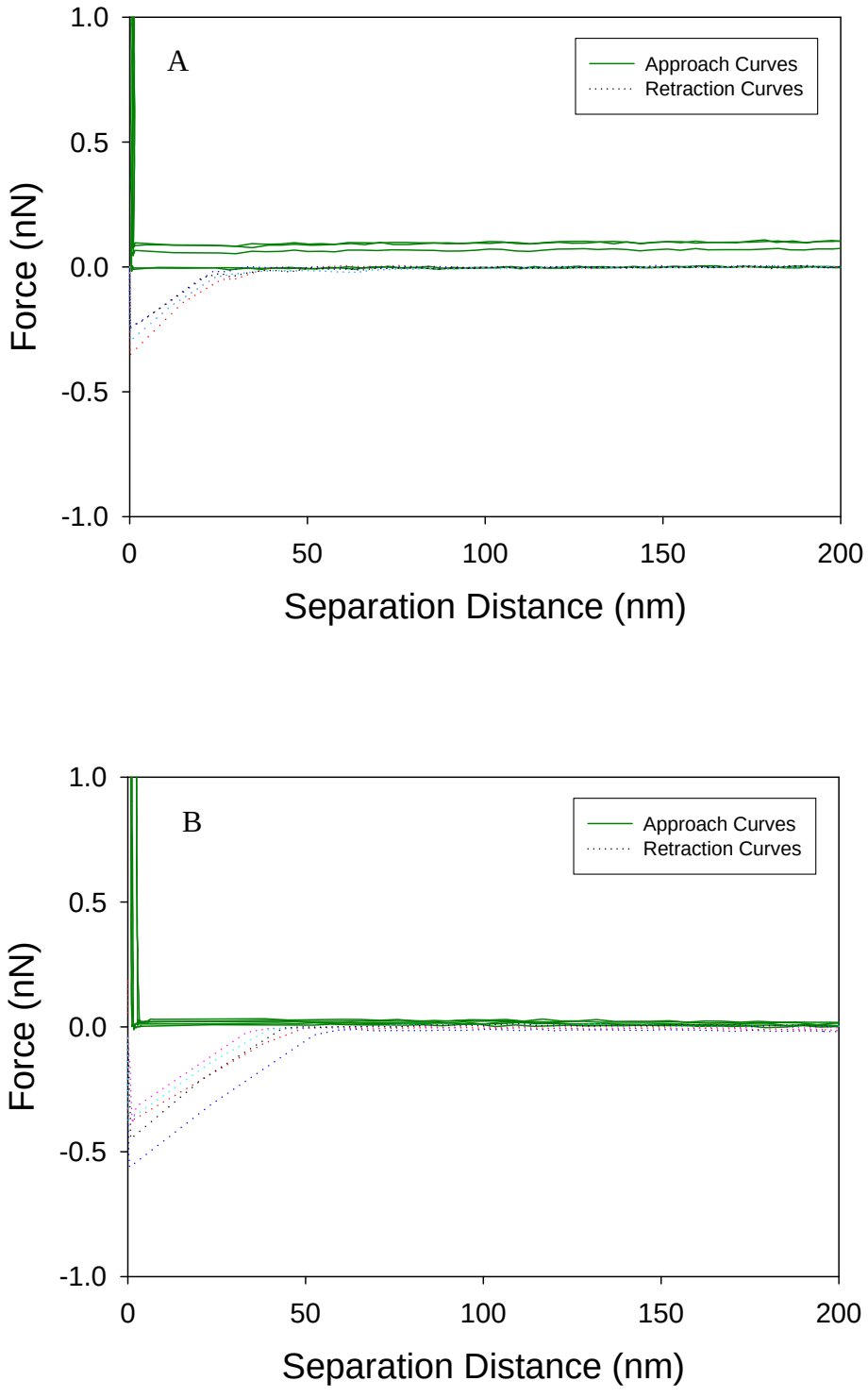

Figure 4.25 Five Approach and Retraction Force Curve Interactions of Bare Glass with A. Silicon nitride and B. CP1.

Since CP1 has a net +5 charge, we expect the modified tip to have an enhanced ability to adhere to glass through electrostatic interactions. The fact that the retraction force profile is of a single sharp peak indicates the CP1 layer is very thin and rigid film, which correlates well with the QCM-D data. Steric repulsion forces based on the decay lengths were negligible under both conditions, which we expect for a stiff surface without polymers extending from a surface[232, 272].

4.4.3 Molecular Investigation of Bacterial Adhesion to the Peptide CP1

This study comprised of three control strains; HB101, K12, and ML35. None have flagella or an O-antigen and all possess the same core type (App E). The force profiles (App F & G) show that the retraction forces extend upward to 400 nm. The pull-off events were commonly comprised of multiple peaks, which are caused by multiple polymers on the bacterial membrane temporarily binding to the AFM probe. The retraction force profiles are random events caused by numerous factors: contact points, polymer density and length of the bacterium at the point of contact, proteins, LPS, or pili that may be probed on the surface, preparation for the binding of bacteria to glass, etc. The AFM was used to measure adhesion forces between each bacterial strain and a probe that was either uncoated silicon nitride, or silicon nitride with physisorbed CP1. The average force of adhesion (F_{adh}) between *E. coli* and the CP1 probe was significantly greater than adhesion to bare silicon nitride for 9 of the 13 strains (Figure 5; $P<0.05$).

E. coli HB101 and K12 retraction forces occurred at roughly the same pull-off distances of below 200 nm for both silicon nitride and CP1 modified probes (App G). The strongest absolute adhesion forces occurred with the modified CP1 probe 0.5 nN and 1.0 nN, respectively, compared to silicon nitride of 0.4 nN and 0.7 nN (Figure 4.26).

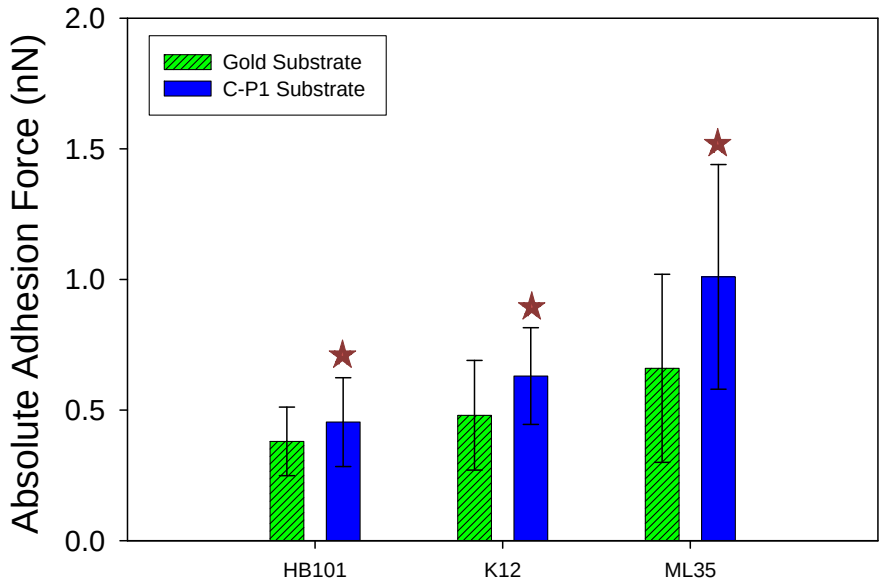

Figure 4.26 AFM Retraction Force Analyses on Control Strains. Stars represent statistical difference between bare and CP1 modified probe ($P<0.05$).

Of the 10 O-antigen containing strains, 7 displayed greater adhesion forces with the CP1 modified probe than with the bare silicon nitride probe. The strains showing statistically significant preference to CP1 included O26:K60:H11, O113;H21, O117:K98:H4, O157:H7, O157:H12, O157:H16, and O172:H- ($P<0.05$). *E. coli* O35:H10, O55:H5, and O113:H4 were not statistically different when comparing bare silicon nitride to CP1 probes ($P<0.05$).

A steric model was used to calculate LPS lengths of the bacterial strains, based on modeling the approach profiles of the interactions between a bare silicon nitride tip and a bacterium on a glass slide. We have previously applied this method to estimate LPS lengths for *E. coli* and other bacteria[273]. When all the strains were grouped together, it was difficult to observe any trend between LPS length and the adhesion force with the peptide-covered AFM tip (Figure 27 A). However, for certain subgroupings, we

observed weak positive correlations between LPS length and F_{adh} between the bacterium and CP1 (Figure 27 B & C). When either the O113 or O157 strains were compared against the control strains, longer LPS length was associated with increased adhesion forces with the peptide CP1.

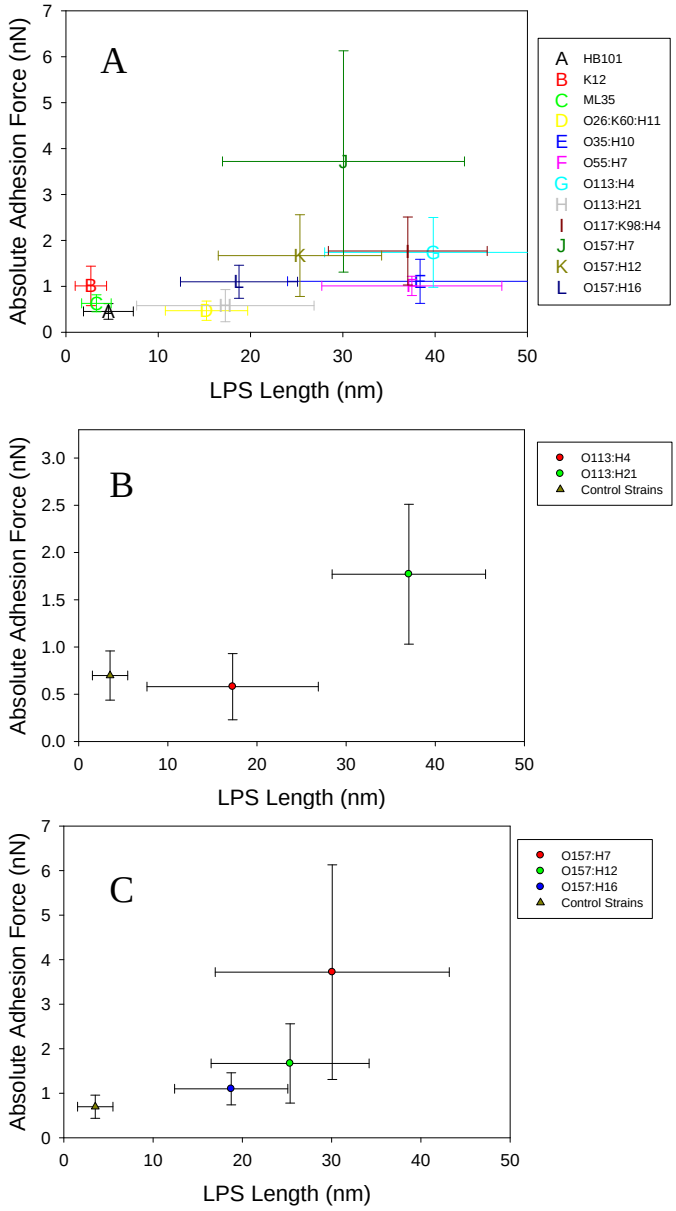

Figure 4.27 Correlating absolute adhesion force with equilibrium LPS length for all *E. coli* strains. Silicon nitride AFM probes were functionalized with CP1 to measure F_{adh}, however, steric modeling was conducted using a bare probe and analyzed with Equation 1. A) Comparison of all strains F_{adh} versus calculated LPS length. B) Comparison of O113 strains F_{adh} versus LPS length. C) Comparison of O157 strains F_{adh} versus LPS length.

4.4.4 Force Profiles with Strains Lacking Comparable O-antigens

The 5 strains; O26:K60:H11, O35:H10, O55:H7, O117:K98:H4, and O172:H- varied in terms of significance in the case of CP1 adhesion when compared to the bare silicon nitride probe. Strain O172:H- had the furthest pull-off forces, extending upward to ~700 nm. On average, O172:H- had pull-off distances of 272 ± 139 nm and 274 ± 187 nm for silicon nitride and CP1. Such distances are quite significant, when considering the LPS for O172:H- is only 41 nm, which means the LPS was being extended upwards to 13 times the nominal length. Although pull-off distances were comparable, the absolute adhesion forces were more muted with the silicon nitride (1.5 ± 0.7 nN versus 2.0 ± 1.1 nN). The LPS length was 41 ± 12 nm with an estimated O-antigen length of 37 nm. This finding is within the same range found with the O157 strains and correlates well within the expected range for the O-antigen length having an impact on adhesion force. Indeed, strain O26:K60:H11 has the shortest LPS length of 15 ± 4 nm and also had comparably small absolute adhesion forces (0.5 ± 0.2 nN and 0.2 ± 0.1 nN).

Strains O35:H10 and O55:H7 had LPS lengths of 23 nm longer than O26:K60:H11 and both strains encountered no significant difference in adhesion to silicon nitride and CP1 ($P<0.05$). Whether the LPS length, sugars comprising the O-antigen, or some other mechanism were responsible for the resulting adhesion is unclear without other strains of the same O-antigen.

That strain O117:K98:H4 had a longer slightly longer LPS (40 nm) than O35:H10 and O55:H7, which may have enhanced the adhesion of CP1 versus bare silicon nitride

(0.6 ± 0.2 nN vs. 1.7 ± 0.9 nN). The binding results of O117:K98:H4 differ significantly with those of O55:H7 under both scenarios, however, under neither case did O117:K98:H4 differ significantly from O35:H10 ($P<0.05$).

4.4.5 O-antigen Probing with Silicon Nitride versus CP1

The AFM was used to measure F_{adh} between silicon nitride probes and probes that have been modified with the addition of CP1. F_{adh} was significantly greater for 10 of 13 strains ($P<0.05$). We observed greater F_{adh} for all control strains, O113:H21, all O157 strains, O26:K60:H11, O117:K98:H4, and O172:H-. Although F_{adh} was ≥ for when CP1 was present, the differences for strains O113:H4, O35:H10, and O55:H7 were not great enough to be considered statistically significant (Figure 4.28).

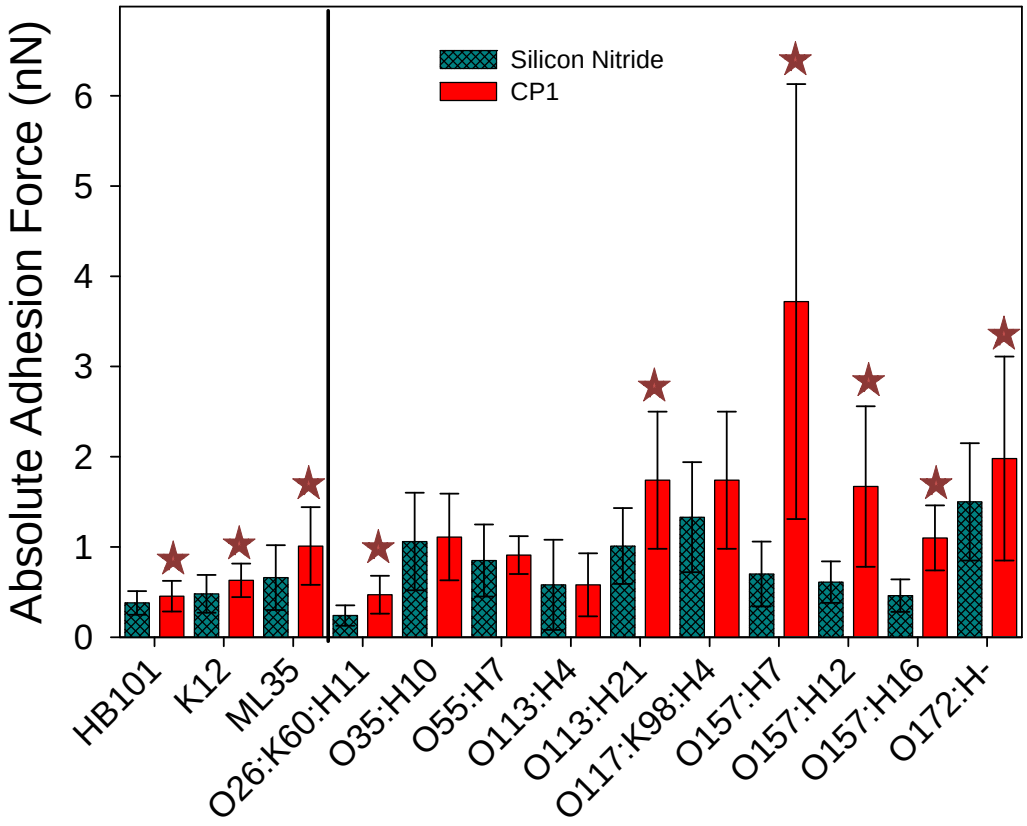

Figure 4.28 AFM was used to measure F_{adh} between *E. coli* and silicon nitride probe, or the silicon nitride probe that was pre-functionalized with CP1. Each bar represents absolute adhesion forces measured from 50 force cycles per bacterial strain. Stars represent significant difference between adhesion force of bacteria with silicon nitride and adhesion force of bacteria with CP1-tip ($P<0.05$). Bars to the right of solid black line represent *E. coli* strains expressing O-antigen.

4.4.6 F_{adh} *O-antigen Strains Comparison to Control Strains*

Eight of the O-antigen strains adhered significantly better to CP1 than compared to the averaged adhesion force of the control strains; HB101, K12, and ML35. All of the O157 strains adhered significantly better to CP1 than the K12 strains. This differs from

probing with silicon nitride, where none of the strains differed significantly. Only strains O26:K60:H11 and O113:H4 did not differ significantly from the control (Figure 4.29).

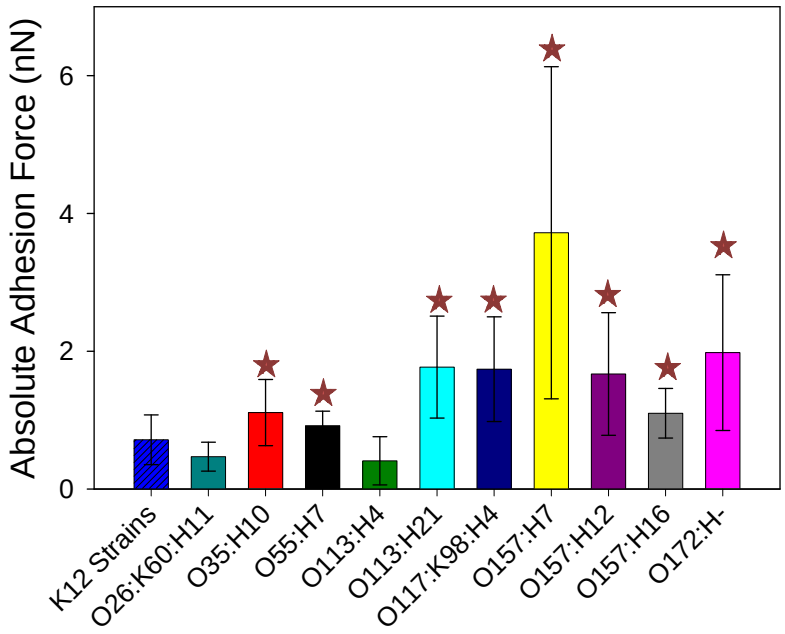

Figure 4.29 AFM Retraction Force Analyses of CP1 Modified Probe. Stars represent statistical difference between K12 strains and O-antigen containing strains ($P<0.05$).

4.4.7 Bacterial Retention and Viability on Cecropin P1 Surfaces

The effectiveness of an adsorbed peptide on bacterial inactivation was quantified by comparing bacterial viability when interacting with CP1 physically adsorbed to silicon nitride, or with CP1-cys covalently bound to gold. Since the control surfaces are different (bare silicon nitride vs. bare gold), the bacterial inactivation to a peptide-bound surface was always compared to that same surface, but containing no peptide.

E. coli attached more to the CP1-cys on gold than to bare gold for 9 of the 13 strains studied (Figure 4.30 A). The attachment of the three control strains was generally lowest. Gold has a relatively high antimicrobial activity (Figure 4.30 B; green bars), but

in 4 of the 13 strains studied (O113:H4, O157:H7, O157:H12, and O35:H10), we still saw a significantly significant increase in the percentage of dead bacteria on CP1-cys gold than on peptide adsorbed to gold (Figure 4.30 B; blue bars). Strains O113:H4 and O35:H10 were most susceptible to the effects of peptide, as four times as many bacteria were dead on the peptide-coated gold surface than on bare gold. None of the control bacterial strains (lacking O-antigen) showed differences in their viability on gold vs. CP1-cys coated gold, although all showed differences in attachment of bacteria per area.

On silicon nitride, to which the peptide adsorbed non-specifically, 6 of the 13 strains attached more to the CP1-coated surface than to uncoated silicon nitride (Figure 4.31 A). For O157 strains, we observed 25-65% increases in *E. coli* adhesion to CP1 compared to on silicon nitride, with the largest increase observed for strain O157:H21. However, in contrast to the results seen on gold for the covalently bound CP1, all 13 strains had significantly reduced viability on the CP1 silicon nitride, compared to uncoated silicon nitride (Figure 4.31 B). For all but one strain, >50% of bacteria were killed when attached to the CP1 coated silicon nitride. Bare silicon nitride caused low to moderate killing of attached bacteria.

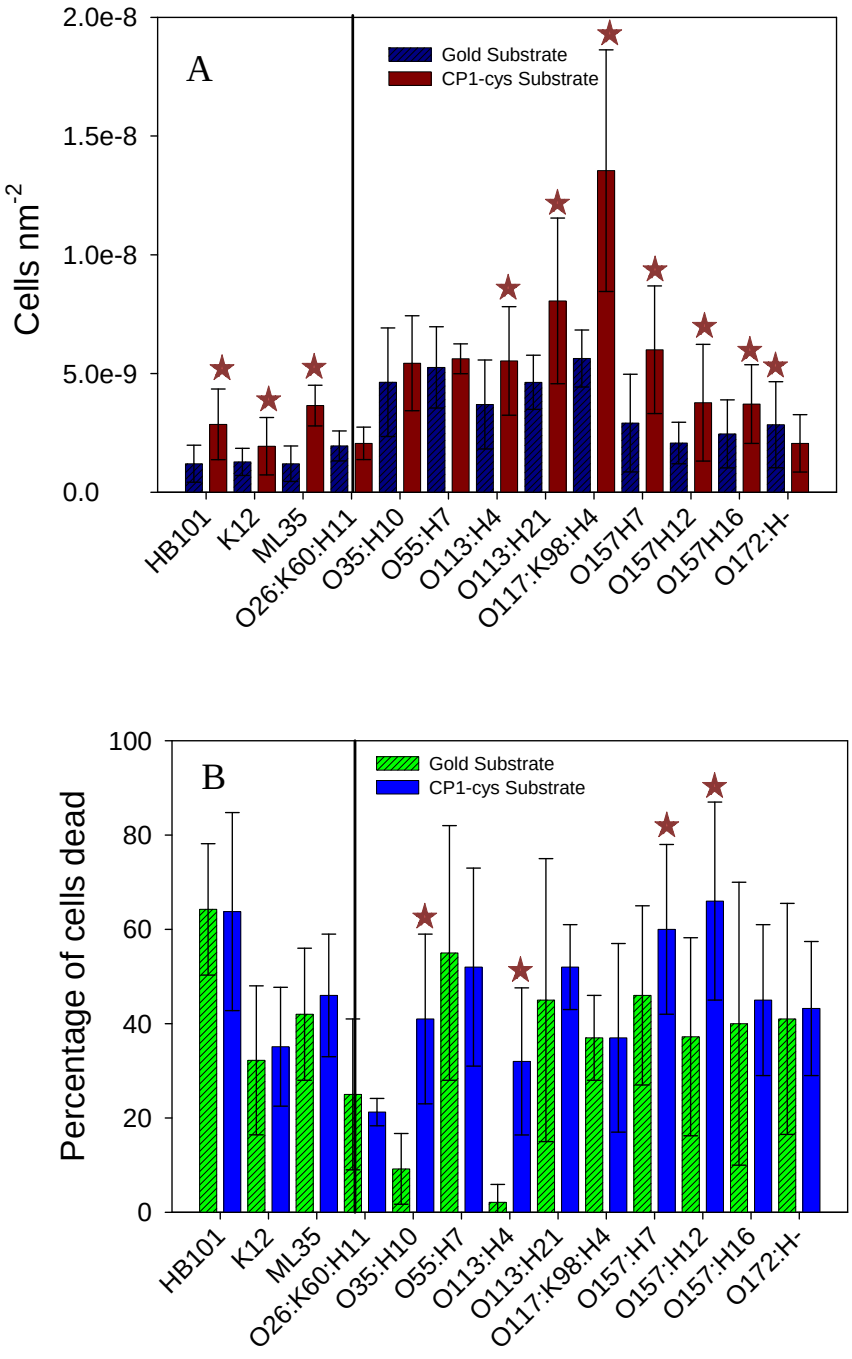

Figure 4.30 Comparing A) whole-cell binding and B) percentage of non-viable attached cells for *E. coli* interacting with gold, or gold that already had CP1-cys adsorbed. After a 20 min rinse with PBS, crystals were removed from the QCM-D, and bacteria were stained with Syto 9 and propidium iodide to quantify bacterial retention and viability. Stars represent significant differences between bacteria interacting with CP1-cys versus bacteria interacting with bare gold ($P<0.05$). Bars to the right of solid black line represent strains expressing the O-antigen.

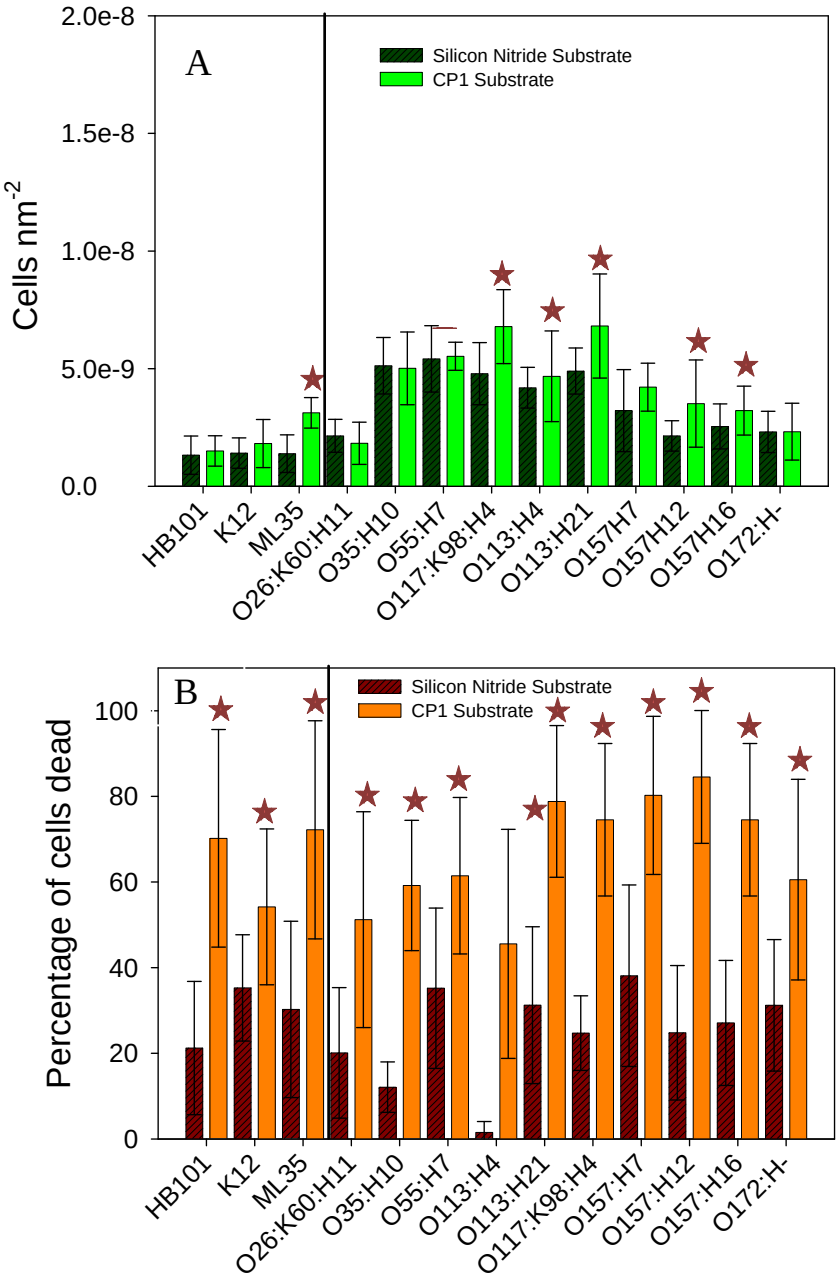

Figure 4.31 Comparing A) whole-cell binding and B) percentage of non-viable attached cells for *E. coli* interacting with silicon nitride, or silicon nitride that already had CP1 adsorbed. After a 20 min rinse with PBS, crystals were removed from the QCM-D, and bacteria were stained with Syto 9 and propidium iodide to quantify bacterial retention and viability. Stars represent significant differences between bacteria interacting with CP1 versus bacteria interacting with bare silicon nitride ($P<0.05$). Bars to the right of solid black line represent strains expressing the O-antigen.

4.4.8 Correlation between LPS Length and Cellular Viability on CP1-cys

Using the steric modeling, a comparison could be made based on LPS length and bacterial viability. LPS length of O-antigen expressing strains were correlated using a Gaussian fit to bacterial viability, which was determined using the dual-staining technique (R^2=0.86; Figure 4.32). A different pattern was observed for control strains that do not express the O-antigen and were not included in the model. Bacteria were most susceptible to CP1-cys with LPS lengths of 29 nm. By subtracting the averaged LPS length of control strains that do not express the O-antigen, which is equal to 3.5 nm, the optimal O-antigen length for CP1-cys to inhibit bacterial viability is 25.5 nm. The correlation was independent of O-antigen composition. Once the O-antigen reaches >54 nm, the effect of CP1-cys would be negligible.

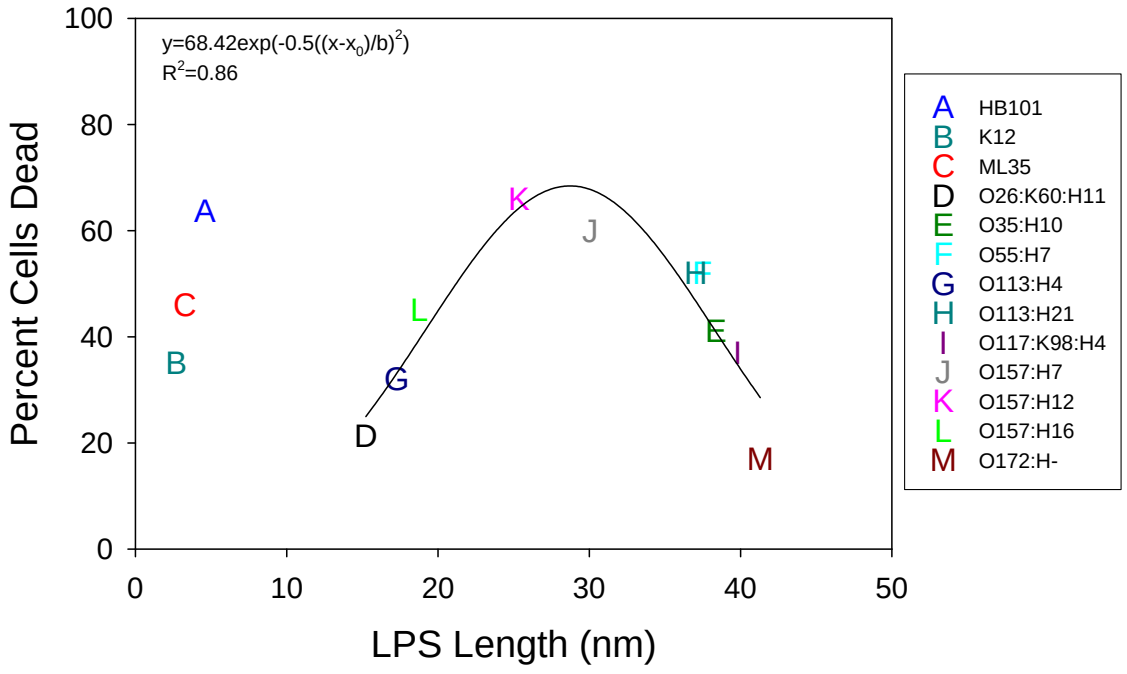

Figure 4.32 Correlating *E. coli* LPS length to *E. coli* viability as monitored with fluorescence microscopy using syto 9 and propidium iodide. O-antigen expressing bacteria were analyzed using a Gaussian fit of whole cell viability versus equilibrium length.

4.4.9 Interfacial Free Energy

Interfacial free energy calculations for the 13 strains with bare gold, CP1-cys gold, silicon nitride, and CP1 silicon nitride and indicated that the nonspecific interactions measured by this test did not correlate well with AFM retraction forces. The interfacial free energy calculations measured for each condition. Strains O26:K60:H11, O55:H7, O113:H4, and O157:H16 are predicted to adhere better to CP1 coated silicon nitride and CP1-cys coated gold versus bare surfaces. Strains K12, ML35, O113:H4, O157:H7, and O157:H12 preferentially bound to CP1-cys gold and O35:H10, O117:K98:H4, and O172:H- showed stronger adhesion to CP1 silicon nitride. Only strain HB101 is predicted to bind stronger to both bare surfaces (Figure 4.33).

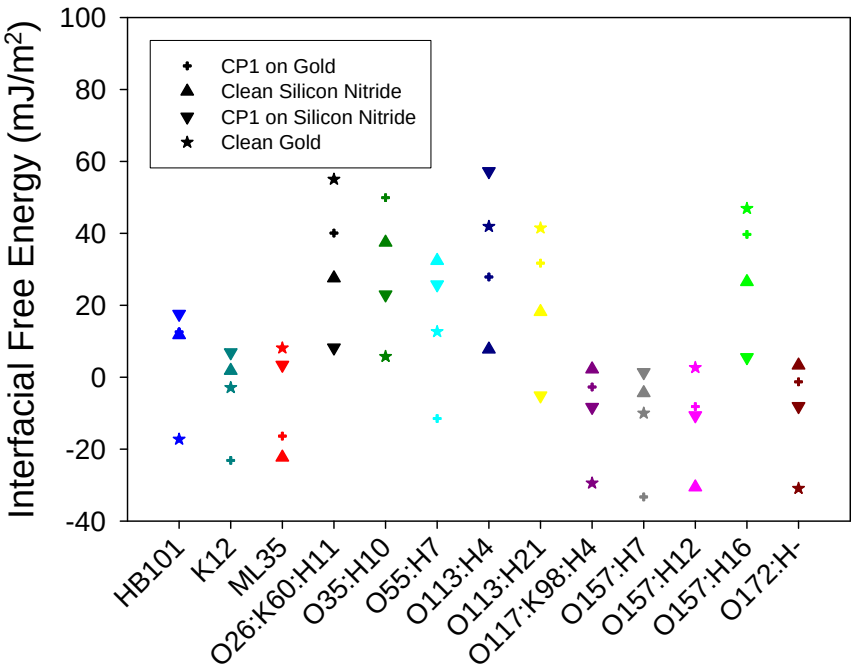

Figure 4.33 Interfacial Free Energy Calculations of 13 *E. coli* Strains on Silicon Nitride and Gold Substrates

The IFE calculation results do not correspond well with retraction force curve results (Figures 4.34 & 4.35). The linear regression value for bare silicon nitride is R^2=0.11 and R^2=0.25 for CP1 silicon nitride. The trends were opposite as might have been expected, which indicate that non-specific interactions for which IFE calculates do not predict the specific interactions between CP1 and *E. coli*[216]. White and Wimley studied the free energies that can be transferred from the water phase from the 20 amino acids and found that the amino acids interfacial free energies can be altered by unfolding events[274]. With regards to the 31 amino acid chain CP1, by interacting with gold and silicon nitride that differ in terms of hydrophobicity (App H), we can therefore expect differing SFE calculations depending on the surface of deposition.

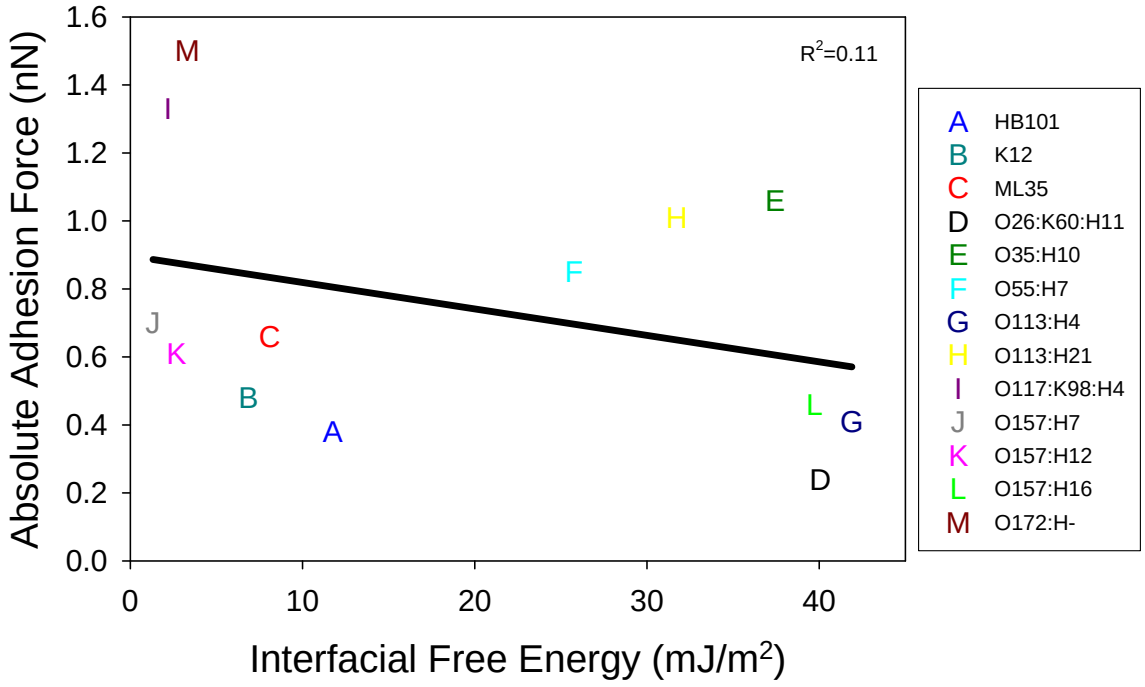

Figure 4.34 Interfacial Free Energy Calculations Compared to Retraction Forces Measured with Silicon Nitride Probes

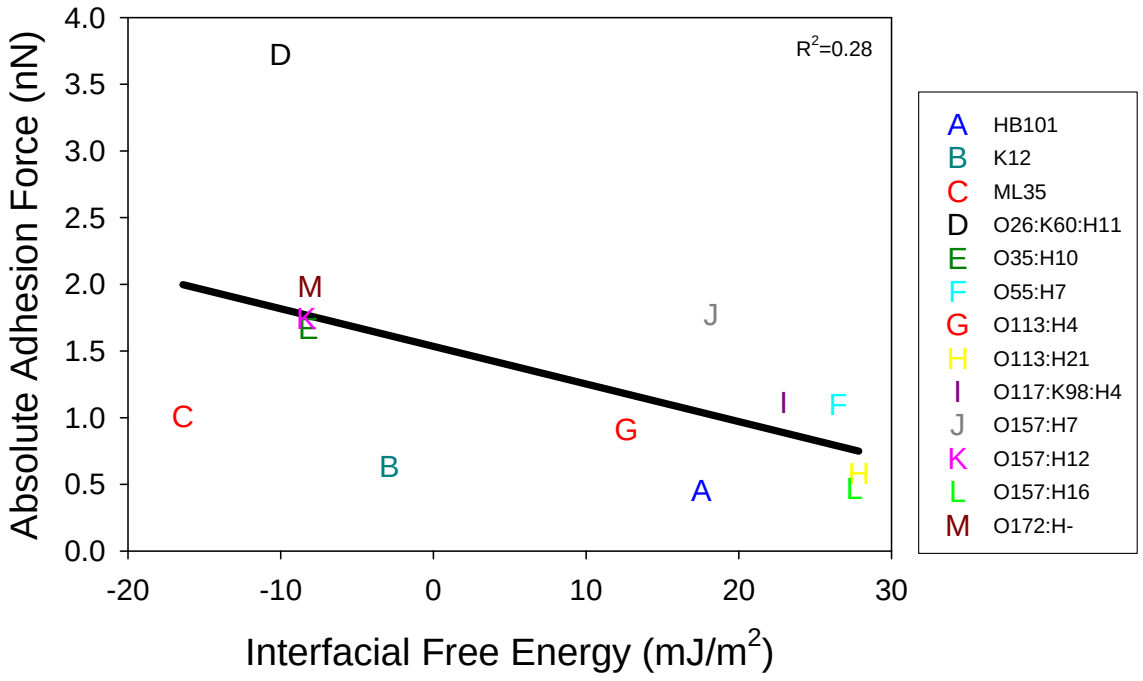

Figure 4.35 Interfacial Free Energy Calculations Compared to Retraction Forces Measured with CP1 Modified Probes

4.4.10 Zeta Potential

Control strains were the most negatively charged at <-40 mV (Figure 4.36). There is no clear trend of zeta potentials versus LPS length for control strains. However, when considering the relation of *E. coli* LPS length to zeta potential, we found a positive linear correlation (Figure 4.37; R^2=0.81). *E. coli* O113:H4, O157:H16, and O26:K60:H11, which had the shortest LPS length, were comparable in terms of their zeta potentials. *E. coli* with equilibrium polymer lengths ≥30 nm were the only strains with zeta potentials >-15 mV (Figure 4.37). Strain O35:H10 was the only strains with LPS length >30 that had zeta potentials <-15 mV. Zeta potential was independent of O-antigen or core oligosaccharide composition.

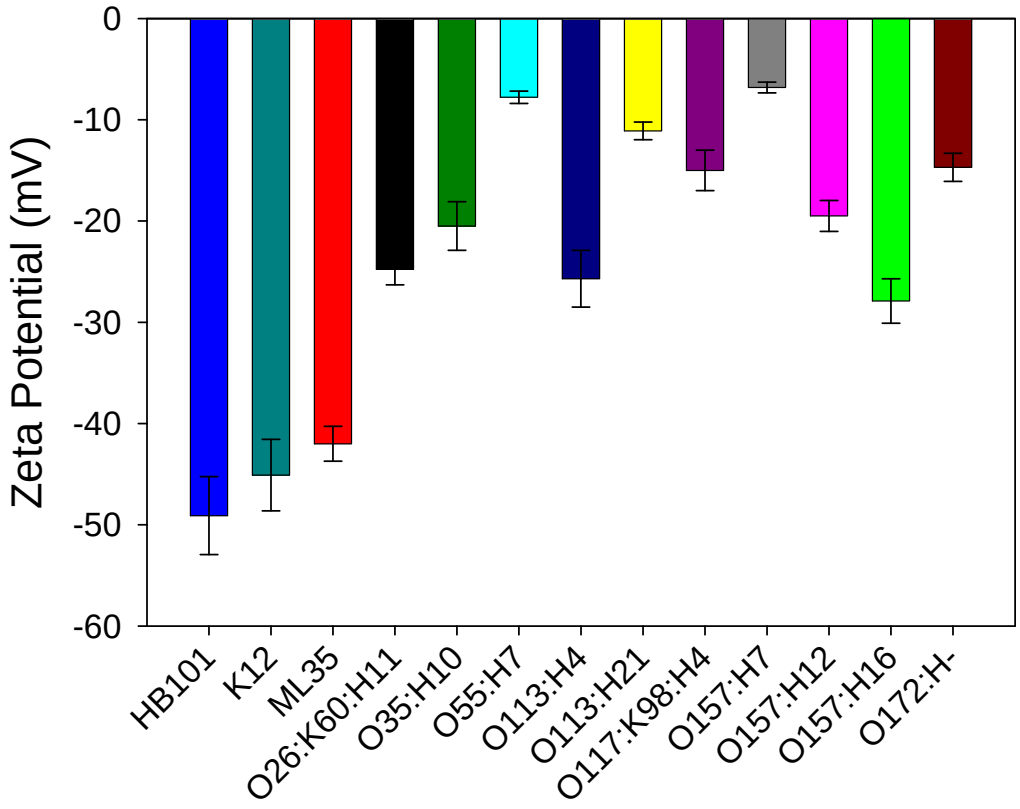

Figure 4.36 Zeta Potentials for the 13 *E. coli* Strains Measured in Water

The zeta potential results are consistent with the IFE calculations in that the retraction force curve analysis did not correlate well in a linear regression; R^2=0.31 with bare silicon nitride and R^2=0.41 for CP1 silicon nitride (Figure 4.38 & 4.39). The greatest outlier was O157:H7, however, omitting this bacterium causes no appreciable difference in linear regression. Grouping all strains together, we found a positive linear correlation between LPS length and zeta potential (R^2=0.81). Zeta potential was not directly related to the nature of the O-antigen, and varied, for example, among strains of the O113 or O157 group.

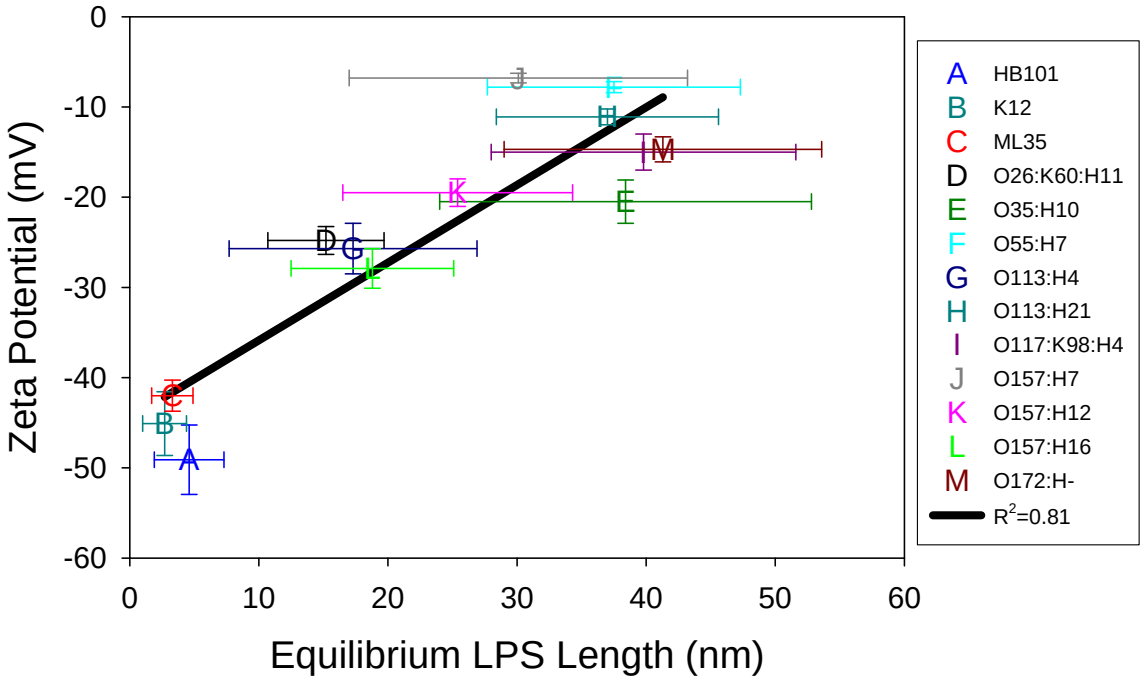

Figure 4.37 Zeta Potentials Correlated with Equilibrium LPS Length

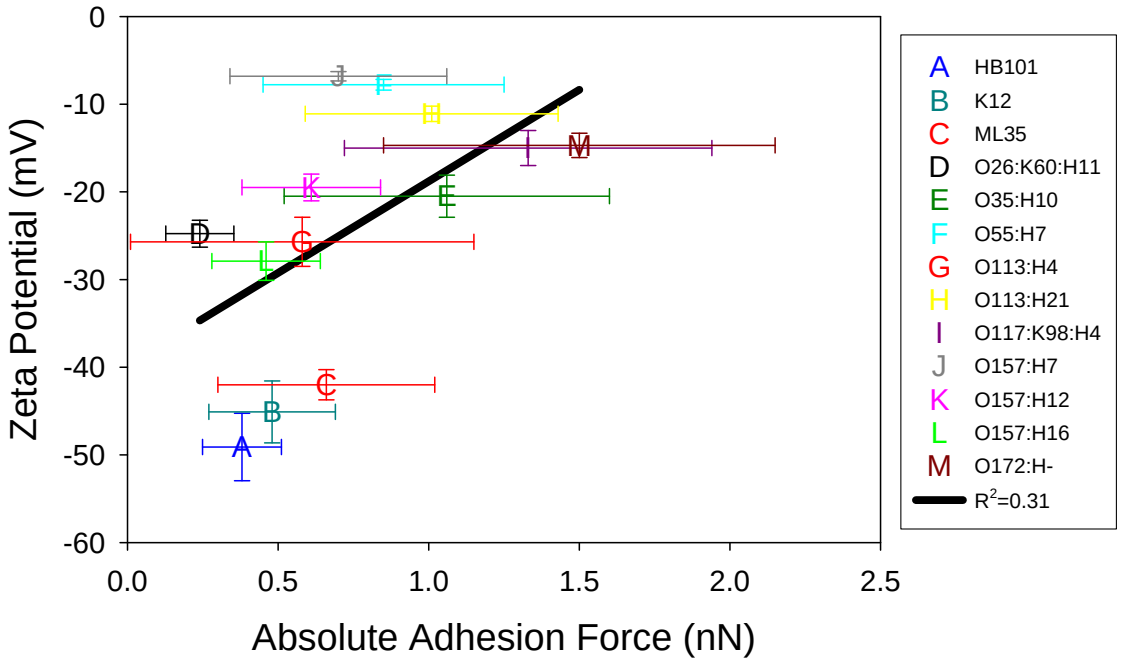

Figure 4.38 Zeta Potentials for the 13 *E. coli* Strains Correlated with Retraction Forces Measured with Silicon Nitride Probes

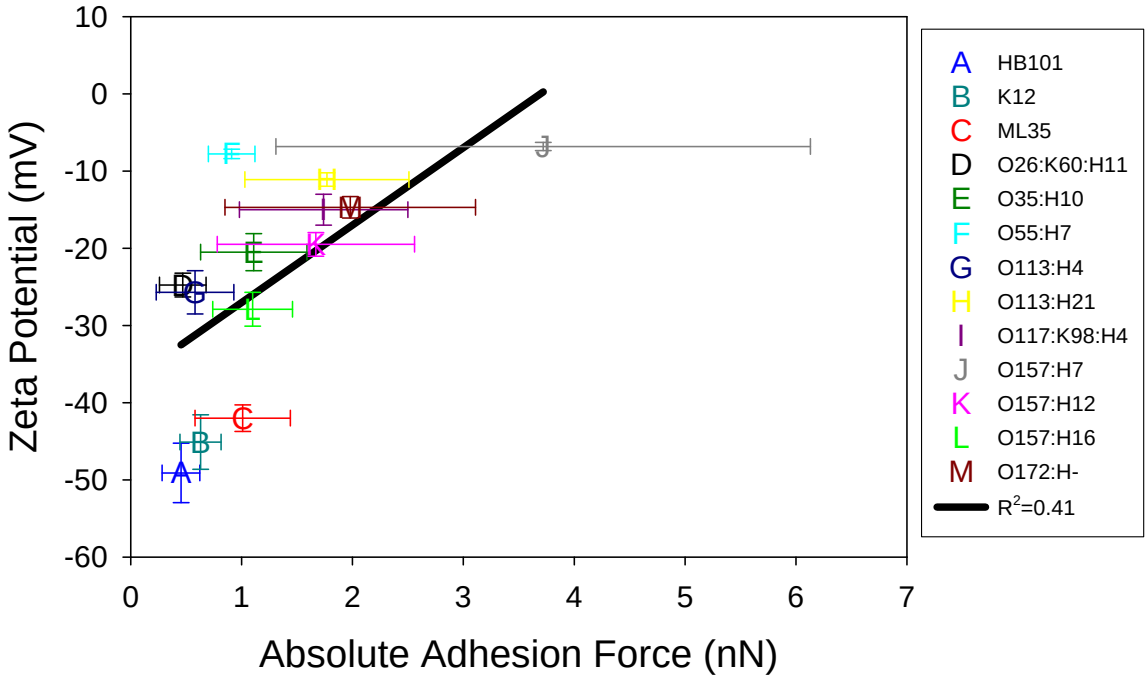

Figure 4.39 Zeta Potentials for the 13 *E. coli* Strains Compared to Retraction Forces Measured with CP1 Modified Probes

The electrostatic potentials of peptide solutions were measured to understand the role charge plays in peptide interaction with *E. coli*. CP1 and CP1-cys solutions had zeta potentials of 17.6 ± 3.2 mV and 18.2 ± 2.7 mV.

5: Discussion

5.1: Studying Protein Adsorption with QCM-D and AFM

When changing the liquid media from PBS to FBS, viscosity and density changes contributed to shifts in the frequency and dissipation. The magnitude of the viscosity change can be calculated via dissipation monitoring[167, 168]. A rinsing procedure of PBS is therefore necessary to remove loosely deposited FBS and to change the viscosity of the bulk liquid back to that of PBS. A discrepancy between thicknesses obtained from QCM-D and AFM was seen for the protein-free system. Since the underlying quartz crystal is not perfectly smooth, AFM section analysis resulted in a nonzero thickness, even though only PBS was introduced to the chamber.

The variability in the data was greater for AFM measurements than QCM-D modeling, which is mainly due to the small region of the quartz that could be sampled in a single AFM image. The number of molecules that can be sampled in the solution and flow system of the QCM-D is much greater, and therefore the resulting thickness calculations show less variability.

Since researchers use both air and liquid measurements for AFM thickness calculations, we also compared the air thickness measurements with those from the QCM-D. In air, the thickness measurements did not agree with the AFM liquid or QCM-D results. The topography of the samples was noticeably different, which we attribute to crystallization of the PBS and aggregation of the protein following drying[275]. The

crystalline features on the 0% FBS crystal were not found in the cases with FBS deposition and were clearly FBS deposits.

Although researchers are interested in both techniques, this is the first study to demonstrate that QCM-D and AFM thickness measurements yield the same result for the case of determining protein layer thicknesses. We also demonstrated that the Voigt viscoelastic model is appropriate to calculate the thickness of adsorbed protein layers. The advantages of using QCM-D are that it represents a faster way to obtain reliable thickness measurements, highly concentrated solutions can be studied, and it does not suffer from artifacts due to the drying process sometimes used for AFM imaging. Although not our focus, QCM-D can also be very useful for determination of kinetic properties of protein adsorption. Advantages of the AFM are that very dilute solutions and single molecules can be observed. These two techniques can provide powerful and complementary information on protein and biomolecule adsorption.

5.2: Enhancing Adsorption of CP1-cys to Gold

The adhesion of CP1 used to adsorb to silicon nitride was the same 31 amino chain peptide found in nature. To enhance adsorption to gold, a thiol-gold bond was enabled by inserting an N-terminal cysteine group[276-278]. There are, however, other means for the peptide to adsorb to gold, which include the many cationic regions on the peptide, amine groups[279-281], and lysines[282]. For these reasons, we experimented with numerous additives such as Tris(2-carboxyethyl)phosphine (TCEP)[283-285] and trifluorethanol (TFE)[286-289], adjusting the pH to neutralize the cationic regions and concentration to alter peptide orientation and enhance surface density.

At neutral pH, CP1-cys binding affinity to gold was enhanced by 55% versus CP1 to gold or silicon nitride. While our results demonstrated that the cysteine residure at the C-terminal was effective, Uzarksi *et al.* discovered that the reducing agent TCEP can double the amount of peptide adsorbing to gold quartz crystal[256]. Our findings suggest that CP1-cys adsorbs ~50% better to gold quartz crystals in the presence of TCEP versus the case of TFE or no additive, based on film thickness calculations. Scenarios where the pH was raised to 9.2 resulted in minor decreases in peptide adsorption, which indicates the charged lysine residues had a minor role in peptide adsorption at neutral pH.

TCEP operates by cleaving disulfide bonds and is safer to use than other similar agents such as DTT and β-mercaptoethanol[283]. In addition, TCEP is thiol-free, which makes it more advantageous to use over DTT. Since TCEP does not adsorb through a mechanism as strong as a gold-thiol bond, it is conceivable that CP1-cys would be able to compete effectively in an environment containing a mixture of the two agents. Additionally, TCEP is a reducing agent, and therefore enhances peptide hybridization[290]. This may have further enhanced peptide orientation that assisted greater amounts of peptide to adsorb to gold and could impact the peptide's ability to adhere to bacteria[291, 292]. Uzarksi *et al*. found regardless of additives, CP1-cys layed flat along a gold substrate. However, with the addition of TCEP, the density of the CP1-cys adhering to the gold was doubled when compared to experiments without chemical additives[256]. Other product information regarding the enhancements of TCEP to peptides and proteins can be found from Uptima, Inc[283].

TFE is a strong hydrogen donor and the concentrations used in the current study were far greater than that of TCEP[293]. Kypr *et al*. suggest using aqueous concentrations

as high as 60-80% TFE to mimic the physiological conditions of crystalline DNA[294]. TFE reduces hydrophobic-hydrophobic interactions, which can enhance the alpha helical form of the peptide[295, 296]. However, despite potential enhancements in peptide orientation, our results show that preventing disulfide bonding does not have significant impact on CP1-cys adsorption.

5.3: Bacterial Adhesion + Properties of LPS

5.3.1 Steric Modeling of Control Strains

While the LPS lengths of the control strains should be approximately the same, differences in adhesion with silicon nitride were observed. These differences may have been due to length differences and the presence of other biomacromolecules on the surfaces. Normally, the O-antigen masks underlying proteins in the outer membrane. However, since the control strains lack the O-antigen, F_{adh} that we observed may also have been related to the lipid A and other biomacromolecules. For strains HB101, K12, and ML35, the calculated LPS length is due to the combination of the core polysaccharide and lipid A.

Steric modeling resulted in a calculated LPS length that is consistent with the findings of Lee *et al*. and Pangburn. Lee *et al*. estimated the lipid A region to be ~2.3 nm [297], with the length due to fatty acids of C12, C14, C16, and C18 [298]. The length of a single O-antigen unit was estimated to be ~1.0 to 1.3 nm [76, 299]. The combination of the lipid A plus inner, and outer cores was 4.4 nm for *E. coli* and *Salmonella typhimurium* [299]. Our control strains had LPS lengths estimated close to these values.

We sometimes calculated shorter LPS lengths with our steric model than might be expected from the literature for control strains. Although our prior work has shown that

steric repulsion dominates bacterial AFM approach curves, electrostatic interactions can also influence LPS conformation[232, 272]. Lower ionic strength solutions correlate to increased steric repulsion[300]. For example, an ionic strength increase from 0.01 M to 0.1 M reduced bacterial polymer length 4-fold due to coiling of bacterial surface molecules [232]. At the ionic strengths used in the present study, the reported LPS length values may also reflect the coiling of biopolymers on the bacterial surface. However, the same ionic strength was used for all experiments, so this coiling effect would have been constant for all strains.

Since the adhesion forces were not the same for the three control strains, we looked for other factors (besides LPS) that would have caused different adhesion forces. ML35 produces the enzyme β-galactosidase, which acts as a phenotype marker[301]. ML35 releases larger quantities of β-galactosidase following membrane penetration[301]. The presence of β-galactosidase may have enhanced adhesion with the silicon nitride probe, although this would need to be confirmed with other experiments.

5.3.2 Steric Modeling of O-antigen Expressing Strains (O157 & O113)

Bacteria are classified in terms of repeating chains of their O-antigen, capsular composition, and flagella antigens[65], but the number of repeating O-antigen units is not part of the serotype classification and may vary greatly within a population of bacteria. *E. coli* equilibrium LPS lengths were O113:H21>O157:H7>O157:H12>O157:H16>O113:H4 for strains that have O-antigens identical to at least one other strain. The O157 strains did not significantly differ from one another in terms of average adhesion forces with silicon nitride. *E. coli* O113:H21 was significantly more adhesive to silicon nitride than all other strains ($P<0.05$).

The O-antigen is a highly variable structure that enables *E. coli* attachment to a host cell or biomaterial using specific ligand-receptor bonding. For instance, *E. coli* O113 and O157 can adhere well to the intestinal tract and fresh produce[64].

Our results suggest differing sections of the LPS mediated adhesion to silicon nitride for control and O-antigen expressing strains. With the exception of O113:H21, F_{adh} was the same for control and O-antigen expressing strains. However, F_{adh} was independent of core length for control strains, while an increasing number of O-antigen units present caused F_{adh} to increase. Underlying proteins and lipids may have adhered to the silicon nitride probe in the case of the control strains[302]. Even the shortest calculated O-antigen of 13 nm for O113:H4 (calculated by subtracting LPS length of O113:H4 with averaged LPS length of control strains) may have blocked the effects of underlying proteins and lipids. LPS binding may have been governed by the number of O-antigen units interacting with the silicon nitride. The O-antigen of O113:H4 may be too short to adhere as well to silicon nitride as O113:H21. Murray *et al* found 16 to 35 units of the O-antigen expressed by *Salmonella enterica* to be most efficient for macrophage cells to adhere to and uptake bacteria[76]. This study found a similar trend in that ~15-35 units of the O-antigen on average was most efficient for *E. coli* adhesion to silicon nitride. However, based on force cycle analysis, longer O-antigens extending >60 nm had the strongest F_{adh}.

E. coli O113 is an enterohaemorrhagic strain (EHEC) due to expression of Shiga-like toxins[303]. Adhesion to host cells in the intestinal tract is a precondition to symptoms of dysentery[96, 304]. Whether LPS length, which correlates well to F_{adh} in the present study, can predict *E. coli* virulence could be the basis for further study.

5.3.3 Steric Modeling of Remaining Strains

Strains O35:H10, O117:K98:H4, and O172:H- adhered significantly better to silicon nitride than the control strains. Strain O55:H7 was comparable to the control strains and O26:K60:H11 was significantly less adhesive. Strains O172:H- and O117:K98:H4 are enterohaemorrhagic *E. coli* (EHEC), while O55:H7 and O26:K60:H11 are EHEC and Enteropathogenic *E. coli* (EPEC). Intimins, which are outer membrane proteins of *E. coli*, determine whether strains are EPEC or EHEC strains[90]. For instance, α intimin is associated with EPEC and intimins ε and γ are associated with EHEC. The β intimin is found in strains that are both EHEC and EPEC, such as the O26 serotype[89]. The AFM probe did not adhere to the intimins because intimins specifically target receptors of epithelial cells[305].

The estimated O-antigen lengths for strains O26:K60:H11, O35:H10, O117:K98:H4, O55:H7, and O172:H- are 15 nm, 38 nm, 40 nm, 37 nm, and 41 nm, respectively. The adhesion forces did not correlate well to O-antigen lengths in this group. *E. coli* O26:K60:H11, having the shortest LPS, had the weakest adhesion forces, while O55:H7 was comparable to the control strains in terms of attraction force, but the LPS length was significantly longer ($P<0.05$). Surface free energy calculation may be more appropriate for correlating *E. coli* adhesion to abiotic surfaces than LPS composition because non-specific forces govern adhesion of LPS to silicon nitride[178].

The literature to this point has focused namely on the genetic traits necessary for creating the O-antigen, while spending little time investigating the purpose of the O-antigen. Russo *et al*. found that deleting the O4 antigen from *E. coli* CP9.137 and CP922 has a minor role in the level of virulence in serum[306]. In contradiction, Merino *et al.*

found that the O-antigen O34 was necessary for *Aeromonas hydrophila* to adhere to the chicken gut[307]. At temperatures below 20°C, the *bacteria* expressed the O-antigen, while at 37°C the bacteria no longer expressed the O-antigen and hence could no longer colonize the chicken gut. *Salmonella enterica*, which is a major food contaminant, was also found to require the O-antigen to express virulence in eggs[308].

5.3.4 Comparing O-antigen Composition to F_{adh}

The profile of exponentially increasing adhesion forces to longer LPS indicates that more sugars of the O-antigen chain were binding to the silicon nitride. Comparing adhesion profiles (Figure 4.28 & Table 4.5), O113 appears to operate more efficiently with fewer O-antigen units than O157. The O157 O-antigen is comprised of the sugars rhamnose, fucose, glucose, and galactose, while each chain unit for O113 contains four galactose sugars and one glucose (App E). Galactose is a necessary carbohydrate for binding to proteins such as galectins[309]. Glucose has also been found to metabolically enhance bacterial adhesion. *Staphylococcus epidermidis* grown in the presence of glucose has been found to adhere strongly to plastic, while strains grown in TSB neglecting glucose were unable to attach[310]. However, the effects of glucose on binding to biomolecules in the O-antigen have no been investigated. The sugars Fucose[311] and rhamnose[312] are necessary for mediating O-antigen adhesion to biomolecules. From our force analysis, galactose may also be necessary for strong adhesion to silicon nitride probes, while glucose is also necessary for adhesion. The combination of the 4 sugars, however, appears to not be as efficient for binding to silicon nitride as O-antigen comprised of 80% galactose based sugars.

The complexities regarding the number of O-antigen units make identifying the mechanism for these differences is a daunting task. For example, *E. coli* O35:H10 contains multiple αLRha sugar groups, while O117:K98:H4 contains one unit in the O-antigen. The αLRha sugar could be responsible for the greater adhesion ability to silicon nitride, however, O26:K60:H11, which also contains the αLRha sugar was statistically less adhesive than the control strains, and with strains O35:H10 and O26:K60:H11 ($P<0.05$).

5.3.5 Effect of Core Type on F_{adh}

The core oligosaccharide serves as bridge between the highly variable O-antigen and lipid A. There are only 5 core groups for *E. coli*; K12, R1, R2, R3, and R4. The O-antigen is not conserved to particular core oligosaccharides. For instance, O113:H4 has the R3 core and O113:H21 R1 core. *E. coli* O117 serotype has been reported to have the K12 core oligosaccharide and the R1 core[1]. Similarly O157:H7 has an R3 core, while O157:H12 and O157:H16 have the R2 core. The R2 and K12 cores share backbones, with differences found in the terminal side chains[313]. Bacterial cores serve as intermediaries between O-antigen and lipid A and whether the core is actively involved in bacterial adhesion is unknown.

The core oligosaccharide had little influence over core length or attraction force. For example, the R3 core incorporates O113:H4 and O157:H7. Strains O157:H12 and O157:H16 had R2 cores and the core lengths were nearly identical. Strain O113:21 had the R1 core, which behaved very differently from O113:H4 in terms of adhesion force. The R1 core dominates the O113 serotype, which signifies an adaptive advantage for the R1 core type over R3 in O113[1]. Because adhesion forces were so different between

O113:H4 and O113:H21 it appears the core group of the LPS has a pivotal role for selecting which materials the bacterium can adhere to.

5.4: Peptide-*E. coli* Interactions

5.4.1 Non-specific and Covalent Bonding of Cecropin P1 to Silicon Nitride and Gold

For CP1 adsorbing to silicon nitride, the dissipation reached a maximum of 6.0 x 10^{-7} and a final value of 5.0 x 10^{-7}, which was a sixth of what we observed with CP1-cys adsorbing to gold. While the quantity of adsorbed mass could explain discrepancies between dissipation values, the frequency change response was only twice as much for CP1-cys. Thus in addition to changes in the amount of adsorbed mass, the way that the peptide adsorbed to gold or silicon nitride apparently were through different orientations of the peptide on the surface.

When CP1 was introduced to the gold quartz crystal, peptide immediately adsorbed, as could be seen by the rapid drop in frequency change. However, the change in dissipation was slower to respond. This indicates that initially peptide adsorbed in a rigid fashion, possibly in a conformation parallel to the gold surface. As more CP1 was added, the frequency change began to drop more slowly, indicating that the rate of adsorption decreased. However, dissipation continued to increase to a maximum dissipation of 6 x 10^{-7}. We considered that this might be due to the formation of multilayers, since CP1 that formed multilayers would be more viscous than a peptide monolayer. At higher peptide concentrations than used in this study, alpha-helical peptides can form multilayers[314]. However, formation of multilayers would result in significant drops in frequency due to the added mass, which we did not observe.

Therefore discrepancies in dissipation response of CP1 on gold and silicon nitride were due to peptide standing more vertically on gold than silicon nitride.

We think that CP1 may adsorb differently on gold and silicon nitride, even though both types of binding are non-specific. The local properties of each substrata may be responsible for binding with different orientations. Differences in peptide orientation and adsorption to polystyrene and silica have been observed to be dependent on local surface hydrophobicity[315]. Increases in dissipation changes, such as what we observed for CP1 on gold, indicate changes in peptide orientation to a slightly more upright position[316]. This may have occurred as CP1 already adsorbed prevented additional mass of CP1 to orientate and adsorb in a parallel orientation to the gold. When PBS was rinsed over the crystal surface, the loosely deposited peptide was removed and the remaining CP1 was parallel to the gold crystal, which is consistent with the dissipation change dropping by ~2.0 x 10^{-7} during the rinse phase.

The PBS rinse did not remove as much CP1 on silicon nitride compared to CP1 on gold, which would be consistent with a more firmly attached rigid peptide layer, possibly due to strong hydrogen bonding with silanol groups. CP1 may bind without specific orientation using hydrogen bonds to silanol groups on silica[317, 318], which coats the silicon nitride when oxidized. In addition, hydrophobic regions of peptides can align with hydrophobic residues on silica[315]. Our water contact angle of silicon nitride of 54° supports the presumption that the hydrophobic side of the peptide was facing the substratum.

CP1-cys adsorbed ~55% more to gold than CP1 adsorbed to either silicon nitride or gold based on areal mass calculations. It also appears that the peptide conformation

changed, depending on the surface that CP1 or CP1-cys was adsorbing to. Our dissipation data reveals a significantly more rigid peptide film for CP1 on silicon nitride, compared with CP1-cys on gold. The maximum dissipation change achieved for CP1-cys adsorbing to gold was between ~3.0 x 10^{-6} and ~2.8 x 10^{-6}, depending on the harmonic, and the frequency and dissipation changes data mirrored each other.

CP1-cys on gold may have been in a more upright orientation, as peptide that retained on the surface had a dissipation of 2.8 x 10^{-6}. Peptide standing upright and attached to a substrata in with a single covalent bond will be more viscous than peptide laying parallel to a surface and attached to the substrate in multiple points. While standing more upright than CP1, CP1-cys may still not have been in a perfectly ordered film. Previous work showed that addition of the reducing agent tris(2-carboxyethyl)phosphine (TCEP) helped CP1-cys form a more ordered peptide film on gold[256]. The use of reducing agents was not tested in the present study.

5.4.2 Binding Between E. coli *and Antimicrobial Peptides (AMPs)*

By enhancing the understanding of the mechanism by which AMPs interact with bacterial LPS, more potent AMPs can be designed. CP1 is a model antimicrobial peptide that has demonstrated strong binding to pathogenic *E. coli*, such as O157:H7[143]. Our goals were to characterize which features of bacterial LPS enhance selectivity and antimicrobial activity of CP1, and to determine if bound CP1 maintains antimicrobial properties.

While the antimicrobial activity of CP1 in solution has been documented[319, 320], the ability of a bound peptide to inactivate bacteria has not been proven. Our results show that peptide physisorbed to silicon nitride was antimicrobial against pathogenic *E.*

coli, but had only moderate activity against *E. coli* when CP1-cys was covalently bound to gold. The bond between CP1-cys and gold apparently decreased the mobility of the peptide, and therefore CP1-cys had less ability to penetrate the bacterial membrane.

While interactions of antimicrobial peptides with bacterial phospholipids have been well studied[125, 286, 288, 321], there have been few studies of AMP interactions with the O-antigen region of the LPS, even though peptides must pass through the O-antigen before interacting with the underlying phospholipids[302, 322].

In our work, non-specific forces such as hydrophobic interactions and hydrogen bonding appeared to govern the initial adhesion of CP1 to the O-antigen region of the *E. coli* LPS. Electrostatic interactions played a lesser role for interaction with the *E. coli* O-antigen. The chemical structure of the O-antigen was not dominant, since F_{adh} and the number of bacteria that attached to a CP1-coated substrate varied significantly among *E. coli* strains with identical O-antigens, and a trend could not be seen with regard to the type of sugar in the LPS O-antigen and either adhesion forces or attachment. In a previous study that did not involve antimicrobial peptides, showed that the chemical nature of the O-antigen did not control adhesion forces with clean silicon nitride[273].

Hydrogen bonding could explain the nonspecific interactions that we observed between O-antigen and peptide. While we could not directly measure hydrogen binding between the O-antigen and peptide, Jucker *et al.* found hydrogen bonding is an important function of the O-antigen that initiates adhesion to biomolecules and minerals[302]. Additionally, hydrophobic helical hexadecapeptides will bind to self-assembled monolayers terminated with carboxyl groups[323], which may also be a mechanism for peptide binding with the O-antigen. *E. coli* expressing the O-antigen have good

correlations between F_{adh} of silicon nitride and O-antigen length, which was associated with increased hydrogen bonding[273]. While we could not measure F_{adh} with CP1 and correlate with LPS length per force cycle due to limitations of the steric model, we observed stronger F_{adh} with CP1 with the overall LPS length of the bacterium (Figure 4.27).

In addition to hydrogen bonding, hydrophobic interactions may have also played a large part in the interaction force between peptide and O-antigen. In our AFM experiments, the orientation of CP1 on the tip was partially controlled by hydrophobic interactions[315]. The water contact angles for silicon nitride and gold were 54° ± 2 and 63° ± 1, respectively. If the hydrophobic section of the peptide was facing the silicon nitride substrate, then the O-antigen was seeing the hydrophilic portion of the peptide. Control strains and bacteria with shorter O-antigens would have had their hydrophobic lipid A exposed, which may have hindered both whole cell binding and reduced adhesion with the exposed hydrophilic regions of peptide, since previous studies showed that hydrophobicity controlled adhesion to minerals[324] and aggregation of LPS is driven by hydrophobic forces[325]. We observed that F_{adh} with CP1 increased exponentially as O-antigen length increased, possibly due to peptide interacting with the more hydrophilic O-antigen[326].

The N-terminal region of CP1 is highly charged and may be attracted to the O-antigen, which can be neutral or negatively charged under physiological conditions[327]. From zeta potentials of peptide in PBS, we know under experimental conditions the peptide retained a cationic charge. However, electrostatic interactions do not appear to dominate the binding forces or attachment between the bacterial strains and CP1, since

trends observed between bacterial zeta potentials and either attachment of bacteria to a CP1 surface, or adhesion forces between bacteria and the CP1 were opposite than would be expected (Figures 4.37-39). Whole cell binding data followed a similar trend between F_{adh} with CP1 and LPS length. Bacterial retention was greater to cys-CP1 compared to CP1 and peptide laden substrata all had greater or equal numbers of bacteria than for substrata not coated with peptides. We even observed greater whole-cell binding of control strains with peptide, despite hydrophobic interactions being unfavorable. However, electrostatic interactions with the negatively charged phospholipids may have been significant enough to enhance bacterial retention.

5.4.3 Nature of O-antigen on Influencing Bacterial Binding with Cecropin P1

F_{adh} between *E. coli* and the CP1 coated AFM tip did not show any systematic trend in terms of O-antigen composition. Instead, O-antigen length appears to be a significantly more important factor based on correlations of F_{adh} and LPS length. For example, F_{adh} was significantly different among strains expressing the O157 strains and O113 O-antigens ($P<0.05$). Even when comparing bacteria with different O-antigens, there was a strong correlation between LPS length and F_{adh}.

Bacterial attachment studies also showed that *E. coli* expressing longer LPS were better retained to the quartz crystals. O-antigen compositions were poor predictors of whether *E. coli* would preferentially bind to peptide. For example, of O113 strains, only *E. coli* O113:H21 preferentially bound to CP1. Whether it be CP1 or CP1-cys, *E. coli* O157:H7 bound to peptide > than O157:H12, which was > than O157:H16. This also correlates to the calculated LPS length, where O157:H7 is estimated to have LPS of 30 nm, O157:H12 is estimated to be 25 nm, and O157:H16 is estimated to be 19 nm.

These findings suggest nonspecific interactions are occurring such as hydrogen bonding between the O-antigen and CP1. A study by Jucker *et al.* also found that no correlation between isolated O-antigen composition and binding to minerals such as SiO_2 exists[328]. Hydrogen bonding has been found to play an important role for the O-antigen and no study has explored binding between AMPs and O-antigens. The results of the current study demonstrate that non-specific hydrophobic/electrostatic interactions governed binding between peptide and O-antigen.

5.4.4 Relation between Bacterial Viability and Method of Peptide Adsorption

All 13 strains were susceptible to killing when exposed to physisorbed CP1 on silicon nitride, whereas only four strains lost viability when exposed to CP1-cys on gold. One model of how antimicrobial peptides inactivate bacteria suggests that the peptide molecule needs to orient itself such that the hydrophobic end is towards the lipids and the hydrophilic section is closer to the phospholipids[140]. According to this "carpet model", the bacterial membrane eventually disintegrates due to alterations in the membrane curvature[141]. This model may explain why bound CP1-cys could not kill the bacteria as well as the physisorbed CP1, since the thiol bond prevented the peptide from freely changing orientation. However, another model suggests that peptides can be taken up by bacteria from a perpendicular orientation to the bacterial membrane, which is called the barrel stave model[329]. By forming pores in the bacterial membrane, this would make it easier for the peptide to lyse bacteria, even in the presence of the thiol bond.

5.4.5 Interfacial Free Energy; Modeling E. coli *Binding with Peptide*

Fattal and Ben-Shaul developed a model for calculating interfacial free energy between lipids and proteins that may be applicable to the current study[330]; however, the

current study focuses namely on polysaccharide-peptide interactions and neglects the effects of the lipid A. Indeed, multiple studies have explored peptide-lipid interactions and have found favorable interactions to exist[331-334], however, none have explored whole cells interacting with peptides. Lipid-peptide interactions are favorable, but none have incorporated the O-antigen or core polysaccharide to study whether the peptide-bacterial interaction is favorable. It is possible that several different mechanisms are necessary for peptides to interact favorably with the complexities of the bacterial LPS such as electrostatic interactions, hydrophobic interactions, and ligand-receptor bonding. Our results suggest that the O-antigen requires hydorgen bonding with the bacterial LPS, and then the peptide may pass through the lipid-A region and interact with the hydrophobic domains to disrupt the cellular membrane.

5.4.6 Relation between LPS Length and Electronegativity

Our zeta potential results are consistent with the findings from the literature in which *E. coli* O157:H7 has zeta potentials ranging from -4.0 to -19.7 mV[335, 336]. Zeta potentials among similar serotypes vary widely, as is evident among the O157:H7 serotype. The range of zeta potentials calculated in the present study are consistent for *E. coli*[337, 338]. However, *E. coli* zeta potentials did not correlate as expected since more negatively charged *E. coli* had lower F_{adh} whole cell binding to peptide.

Zeta potential is partially determined by the negatively charged phospholipids. The lipid region of the LPS was considered to have a conserved length among all strains since differences in chain lengths from C_{10} to C_{16} are in the range of Angstroms. LPS length is highly dependent on the numbers of O-antigen repeating units[76] and since these

units are neutrally charged or slightly negatively charged , they did not contribute greatly to observed zeta potentials[327].

When all bacterial zeta potentials are correlated to LPS length, an inverse relation was found. This was unexpected since electrostatic interactions are considered very important for AMPs to target bacteria[339, 340]. Indeed, control strains had the lowest zeta potential <-40 mV, while O-antigen expressing strains had zeta potentials >-30 mV. Further, zeta potentials of peptide solution were found to be 18 mV, which favor interaction with the more negatively charged *E. coli*. The correlation of LPS length versus zeta potential demonstrates that the O-antigen region may be shielding the electrostatic double-layer from being detected by the zeta potential analyzer (Figure 4.37). *E. coli* O157:H7 had a particularly long LPS and may have masked some of the negatively charged phospholipids, whereas the control strains that did not express O-antigen were found to have the lowest Zeta potential.

The zeta potentials for control strains were significantly greater than that of all other strains. There are few differences between strains. *E. coli* ML35 produces β-galactosidase from the *lac* operon[341] and the 1171 amino acids[342] give this molecule an isoelectric point (PI) at pH 4.2[343]. At pH 7.2-7.4, which zeta potentials were measured at, β-galactosidase will have a net negative charge and may have contributed to zeta potentials being significantly lower than other strains.

Truncated LPS have been reported to be associated with more electronegative cells. Razatos *et al.* found *E. coli* D21 to have a zeta potential of -29 mV, while zeta potentials for *E. coli* D2e19, D21f1, D21f2, which had truncated LPS, had zeta potentials >-40 mV[344, 345]. According to Walker *et al.*, the O-antigen may block underlying lipids

and phospholipids from being detected[346]. Walker *et al.* found the O-antigen expressing strain had a zeta potential >-35 mV, while *E. coli* only expressing the core polysaccharide had zeta potential of <-60 mV. In the present study, we quantified the LPS length of 13 *E. coli* strains and found a strong correlation between longer O-antigens and less electronegativity.

While charge is clearly important for AMPs to lyse bacteria based on proposed carpet model and cationic charge of peptides, the initial interaction between pathogenic *E. coli* and peptides may be not be driven by electrostatic forces. Our AFM and whole cell binding results demonstrate strongest attraction of peptide with O-antigen expressing bacteria, which were least electronegative. Although *E. coli* with truncated LPS were most electronegative, F_{adh} with peptide was lower compared to O-antigen strains, and this observation was more evident with whole cell binding to CP1-cys. The O-antigen length appears to dictate the quantity of hydrogen bonds with peptide, extent of hydrophobic interaction, and limits the electrostatic interactions with peptide.

6: Conclusions

This study was comprised of 3 phases that included:

1. Studying the LPS and O-antigen for 10 *E. coli* strains and comparing features such as LPS length and force data with 3 control strains that lack the O-antigen. AFM approach curves were a measurement of steric hindrance of the bacteria, which were useful for calculating surface properties of *E. coli* such as LPS polymer length. In addition, AFM pull-off forces enabled us to measure which O-antigens adhered better to silicon nitride and we could measure the flexibility of the O-antigen. Zeta potentials and IFE calculations further enhanced our understanding of the surface features of the *E. coli*.

2. Measuring the adsorption and retention of CP1 and CP1-cys to silicon nitride and gold substrates, respectively, to determine peptide density, film thickness, and orientation on the substrates. We accomplished CP1 and CP1-cys deposition analysis namely with the QCM-D Voigt Viscoelastic Modeling.

3. Measuring the binding forces and quantifying whole cell binding of 13 *E. coli* strains to determine what features, such as SFE, charge, LPS length, and O-antigen composition, are important to promote *E. coli* adhesion to AMPs. By coating the AFM silicon nitride probe with CP1, we measured binding forces between CP1 and the 13 *E. coli* strains.

Summary of Main Results

With the steric hindrance data we found that the LPS length is pivotal for bacterial adhesion to occur with organic materials such as peptides and inorganic materials such as gold and silicon nitride. O-antigen lengths >30 nm are optimal for promoting adhesion to

silicon nitride and CP1 silicon nitride. Although the control strains adhered better to CP1 than to bare silicon nitride, the differences in adhesion force were small and we associate this preference to electrostatic, hydrophobic interactions, and hydrogen bonding with the O-antigen region of the LPS. Indeed, the LPS was calculated to be ~3-5 nm for the control strains and was useful for estimating the lengths of the O-antigens among the remaining *E. coli*. In 10 of the 13 strains, including all of the O157 serotypes, adhesion to CP1 was significantly greater than compared to bare silicon nitride, which correlated well with LPS length.

Zeta potentials and IFE calculations did not correlate well with AFM adhesion measurements, which may suggest that specific interactions were being measured with the AFM. Hydrophobic/electrostatic interactions cannot alone explain bacterial adhesion to peptide or metallic substrates. We found evidence that O-antigen partially blocked the electrostatic double layer from being detected in the zeta potential measurements.

QCM-D Voigt Viscoelastic Modeling and AFM section analysis correlated well based on thickness calculations for the FBS deposition experiment. Whether for characterizing protein or peptide films, the QCM-D modeling is superior compared to AFM because of the real-time analysis, no sample perturbation during the experimental phase, and availability of numerous substrates versus the limited available with AFM probes (usually silica or silicon nitride).

In the peptide adsorption studies, the QCM-D modeling showed that TCEP enhances CP1-cys adhesion by ~50% to gold on the basis of areal mass calculations. Increasing the pH to 9.2 moderately decreased peptide adsorption and TFE had no significant impact on peptide adsorption or orientation.

Although the results of this study demonstrate the potential of CP1 as a part of biosensor, our findings also reveal the mechanisms by which AMPs lyse bacteria. Two distinct models have been developed to explain how peptides lyse bacteria called the 'barrel stave model' and 'carpet model', and both models neglect important details of cellular destruction. This is the first study to quantitatively measure both *E. coli* LPS length and bacterial electronegativity. Our findings show bacteria with longer LPS (pathogenic *E. coli* strains) being less electronegative, which would seem unfavorable for interaction with AMPs that are cationic. Because of this unexpected relation, we concluded that hydrophobic interactions are dominant during the initial interaction between CP1 and *E. coli*. While this does not necessarily mean the 'barrel stave model' fully describes cellular lyses, we are able to gain insight on how the peptide bypasses the O-antigen, which both models have neglected. Our findings will be useful in designing new peptides to lyse bacteria, which have been largely unsuccessful, partially because studies have only concentrated on peptide interaction with the cellular inner membrane.

This study was initially aimed at describing peptide interactions with *E. coli* based on their O-antigen compositions. While O-antigen composition did not appear to dictate binding or deactivation of *E. coli* in contact with peptide, we made significant progress in understanding several key LPS qualities that do promote interaction with peptide. The literature has very limited information regarding bacterial interactions with AMPs, and studying functionality of covalently immobilized peptide is a novel area of study. We plan on expanding on the number of bacteria and peptides used to further investigate whether we can detect specific interactions between LPS and AMPs.

7: Future Work

The LPS is a complex and highly variable component of the bacterium. If a more automated procedure for analyzing force curves can be devised, force mapping of the bacterial surface for hundreds of bacteria could yield significantly more information about the LPS length and binding forces. Density calculations of the LPS can be measured in solutions of lower ionic strength such overlapping of the LPS molecules is prevented.

CP1 adhesion to the AFM probe may be enhanced by using a gold coated tip or using NHS to assist in CP1 adsorption[347]. However, when modifying the methods for CP1 adsorption, it should be cautioned that chromium, commonly used as an under-layer for gold, can escape and affect bacterial viability[348]. Additionally, ensuring that bacteria are not exposed to NHS immobilized on the AFM probe will be essential since the chemical is used in binding *E. coli* to glass.

Furthermore, obtaining more isolates from differing sources could better our understanding of the natural variability of *E. coli* within a serotype. CP1 was selected for further study because of the results obtained from Mello and Soares[143]. However, the numbers of peptides that exist and can be engineered are limitless. Few studies have considered using peptides as biosensors and it may be beneficial to explore peptides that are known to destroy foreign invaders such as defensin[349, 350], melittin[351], aurein[352], maximin[353], and other cecropins[354]. Once comparative studies are conducted, we might be better positioned to cater a biosensor for detection of a particular serotype and further understand the role the O-antigen has in bacterial adhesion.

8: References

1. **Amor, K., Heinrichs, D. E., Frirdich, E., Ziebell, K., Johnson, R. P. & Whitfield, C. Distribution of core oligosaccharide types in lipopolysaccharides from *Escherichia coli*. Infect. Immun. 68, 1116-1124 (2000).**
2. **Yount, N. Y., Bayer, A. S., Xiong, Y. Q. & Yeaman, M. R. Advances in antimicrobial peptide immunobiology. Biopolymers 84, 435-458 (2006).**
3. **Gudehus, G. Gleichgewichts-, Umlagerungs- und Transportphänomene bei Peloiden. (2006).**
4. **Arcidiacono, S., Pivarnik, P., Mello, C. M. & Senecal, A. Cy5 labeled antimicrobial peptides for enhanced detection of *Escherichia coli* O157:H7. Biosens. and Bioelectron. 23, 1721 (2008).**
5. **Tam, J. P., Lu, Y.-A., Yang, J.-L. & Chiu, K.-W. An Unusual Structural Motif of Antimicrobial Peptides Containing End-to-End Macrocycle and Cystine-Knot Disulfides. Proc. Nat. Acad. Sci. U. S. A. 96, 8913-8918 (1999).**
6. **Cho-Chung, Y. S. Role of Cyclic AMP Receptor Proteins in Growth, Differentiation, and Suppression of Malignancy: New Approaches to Therapy. Anticancer Res. 50, 7093-7100 (1990).**
7. **Wachinger, M., Kleinschmidt, A., Winder, D., von Pechmann, N., Ludvigsen, A., Neumann, M. *et al.* Antimicrobial peptides melittin and cecropin inhibit replication of human immunodeficiency virus 1 by suppressing viral gene expression. J. Gen. Virol. 79, 731-740 (1998).**
8. **Hancock, R. E. W. & Lehrer, R. Cationic peptides: a new source of antibiotics. Trends Biotechnol. 16, 82 (1998).**
9. **Costerton, J. W., Stewart, P. S. & Greenberg, E. P. Bacterial biofilms: A common cause of persistent infections. Sci. 284, 1318-1322 (1999).**
10. **Brown, M. R. W., Allison, D. G. & Gilbert, P. Resistance of bacterial biofilms to antibiotics a growth-rate related effect? J. Antimicrob. Chemother. 22, 777-780 (1988).**
11. **Stewart, P. S. Theoretical aspects of antibiotic diffusion into microbial biofilms. Antimicrob. Agents Chemother. 40, 2517-2522 (1996).**
12. **Okeke, I. N., Laxminarayan, R., Bhutta, Z. A., Duse, A. G., Jenkins, P., O'Brien, T. F. *et al.* Antimicrobial resistance in developing countries. Part I: recent trends and current status. Lancet Infectious Dis. 5, 481-493 (2005).**
13. **Okeke, I. N., Klugman, K. P., Bhutta, Z. A., Duse, A. G., Jenkins, P., O'Brien, T. F. *et al.* Antimicrobial resistance in developing countries. Part II: strategies for containment. Lancet Infectious Dis. 5, 568-580 (2005).**
14. **Herida, M., Sednaoui, P. & Goulet, V. Gonorrhoea surveillance system in France: 1986-2000. Sexually Trans. Dis. 31, 209-214 (2004).**
15. **Davies, J. & Wright, G. D. Bacterial resistance to aminoglycoside antibiotics. Trends Microbiol. 5, 234 (1997).**

16. **Russell, A. D., Tattawasart, U., Maillard, J. Y. & Furr, J. R. Possible link between bacterial resistance and use of antibiotics and biocides. Antimicrob. Agents Chemother. 42, 2151-2151 (1998).**
17. **Walsh, C. T., Fisher, S. L., Park, I. S., Prahalad, M. & Wu, Z. Bacterial resistance to vancomycin: five genes and one missing hydrogen bond tell the story. Chem. Biol. 3, 21 (1996).**
18. **Andersson, D. I. & Levin, B. R. The biological cost of antibiotic resistance. Curr. Opin. Microbiol. 2, 489 (1999).**
19. **Levy, S. B. The challenge of antibiotic resistance. Sci. Am. 278, 46-53 (1998).**
20. **Boman, H. G. Peptide antibiotics and their role in innate immunity. Annu. Rev. Immunol. 13, 61-92 (1995).**
21. **Ganz, T., Selsted, M. E., Szklarek, D., Harwig, S. S. L., Daher, K., Bainton, D. F. *et al.* Defensins - natural peptide antibiotics of human-neutrophils. J. Clin. Inves. 76, 1427-1435 (1985).**
22. **Hultmark, D., Engstrom, A., Bennich, H., Kapur, R. & Boman, H. G. Insect immunity - isolation and structure of cecropin-D and 4 minor antibacterial components from cecropia pupae. Eur. J. Biochem. 127, 207-217 (1982).**
23. **Lee, J. Y., Boman, A., Sun, C. X., Andersson, M., Jornvall, H., Mutt, V. *et al.* Antibacterial peptides from pig intestine: Isolation of a mammalian cecropin. Proc. Nat. Acad. Sci. U. S. A. 86, 9159-9162 (1989).**
24. **Agawa, Y., Lee, S., Ono, S., Aoyagi, H., Ohno, M., Taniguchi, T. *et al.* Interaction with phospholipid bilayers, ion channel formation, and antimicrobial activity of basic amphipathic alpha-helical model peptides of various chain lengths. J. Biol. Chem. 266, 20218-20222 (1991).**
25. **Shin, S. Y., Lee, S. H., Yang, S. T., Park, E. J., Lee, D. G., Lee, M. K. *et al.* Antibacterial, antitumor and hemolytic activities of alpha-helical antibiotic peptide, P18 and its analogs. J. Pept. Res. 58, 504-514 (2001).**
26. **Reddy, K. V. R., Yedery, R. D. & Aranha, C. Antimicrobial peptides: premises and promises. Int. J. Antimicrob. Agents 24, 536-547 (2004).**
27. **Buchman, G. W., Banerjee, S. & Hansen, J. N. Structure, expression, and evolution of a gene encoding the precursor of nisin, a small protein antibiotic. J. Biol. Chem. 263, 16260-16266 (1988).**
28. **Jaquette, C. B. & Beuchat, L. R. Combined effects of pH, nisin, and temperature on growth and survival of psychrotrophic Bacillus cereus. J. Food Prot. 61, 563-570 (1998).**
29. **Beuchat, L. R., Clavero, M. R. S. & Jaquette, C. B. Effects of nisin and temperature on survival, growth, and enterotoxin production characteristics of psychrotrophic Bacillus cereus in beef gravy. Appl. Environ. Microbiol. 63, 1953-1958 (1997).**
30. **Dathe, M. & Wieprecht, T. Structural features of helical antimicrobial peptides: their potential to modulate activity on model membranes and biological cells. BBA 1462, 71 (1999).**
31. **Guo, L., Lim, K. B., Poduje, C. M., Daniel, M., Gunn, J. S., Hackett, M. *et al.* Lipid A acylation and bacterial resistance against vertebrate antimicrobial peptides. Cell 95, 189 (1998).**

32. Ganz, T. Defensins: antimicrobial peptides of vertebrates. C. R. Biol. 327, 539 (2004).

33. Peschel, A. How do bacteria resist human antimicrobial peptides? Trends Microbiol. 10, 179 (2002).

34. Ivnitski, D., Abdel-Hamid, I., Atanasov, P. & Wilkins, E. Biosensors for detection of pathogenic bacteria. Biosens. Bioelectron. 14, 599-624 (1999).

35. Ziegler, C. & Gopel, W. Biosensor development. Curr. Opin. Chem. Biol. 2, 585-591 (1998).

36. Rangel, J. M., Sparling, P. H., Crowe, C., Griffin, P. M. & Swerdlow, D. L. Epidemiology of *Escherichia coli* O157: H7 outbreaks, United States, 1982-2002. Emerg. Infectious Dis. 11, 603-609 (2005).

37. Mead, P. S. & Griffin, P. M. *Escherichia coli* O157:H7. The Lancet 352, 1207 (1998).

38. Uhlich, G. A., Sinclair, J. R., Warren, N. G., Chmielecki, W. A. & Fratamico, P. Characterization of shiga toxin-producing *Escherichia coli* isolates associated with two multistate food-borne outbreaks that occurred in 2006. Appl. Environ. Microbiol. 74, 1268-1272 (2008).

39. CDC. Escherichia coli O157:H7 Infections Associated with Eating a Nationally Distributed Commercial Brand of Frozen Ground Beef Patties and Burgers -- Colorado, 1997. MMWR 46, 777-778 (1997).

40. Proctor, M. E., Kurzynski, T., Koschmann, C., Archer, J. R. & Davis, J. P. Four Strains of Escherichia coli O157:H7 Isolated from Patients during an Outbreak of Disease Associated with Ground Beef: Importance of Evaluating Multiple Colonies from an Outbreak-Associated Product. J. Clin. Microbiol. 40, 1530-1533 (2002).

41. Ciftcioglu, G., Arun, O. O., Vural, A., Aydin, A. & Aksu, H. Survival of *Escherichia coli* O157:H7 in minced meat and hamburger patties. J. Food Agriculture Environm. 6, 24-27 (2008).

42. Strachan, N. J. C., Dunn, G. M., Locking, M. E., Reid, T. M. S. & Ogden, I. D. *Escherichia coli* O157: Burger bug or environmental pathogen? Int. J. Food Microbiol. 112, 129 (2006).

43. Blot, S. I., Depuydt, P., Annemans, L., Benoit, D., Hoste, E., de Waele, J. J. *et al.* Clinical and economic outcomes in critically ill patients with nosocomial catheter-related bloodstream infections. Clin. Infectious Dis. 41, 1591-1598 (2005).

44. Giesbrecht, P., Kersten, T., Maidhof, H. & Wecke, J. *Staphylococcal* Cell Wall: Morphogenesis and Fatal Variations in the Presence of Penicillin. Microbiol. Mol. Biol. Rev. 62, 1371-1414 (1998).

45. Morales, M., Mendez-Alvarez, S., Martin-Lopez, J. V., Marrero, C. & Freytes, C. Biofilm: the microbial "bunker" for intravascular catheter-related infection. Supportive Care Cancer 12, 701-707 (2004).

46. Vuong, C., Gerke, C., Somerville, G. A., Fischer, E. R. & Otto, M. Quorum-sensing control of biofilm factors in *Staphylococcus epidermidis*. J. Infectious Dis. 188, 706-718 (2003).

47. Grubisic, A. & Suljagic, V. Prevention of intravascular catheter-related infections. Bone Marrow Transplantation 39, S260-S261 (2007).

48. **O'Toole, G., Kaplan, H. B. & Kolter, R. Biofilm formation as microbial development. Annu. Rev. Microbiol. 54, 49-79 (2000).**

49. **Boyd, A. & Chakrabarty, A. M. Role of alginate lyase in cell detachment of *Pseudomonas aeruginosa*. Appl. Environ. Microbiol. 60, 2355-2359 (1994).**

50. **Costerton, J. W., Cheng, K. J., Geesey, G. G., Ladd, T. I., Nickel, J. C., Dasgupta, M. *et al.* Bacterial biofilms in nature and disease. Annu. Rev. Microbiol. 41, 435-464 (1987).**

51. **Bettelheim, K. A., Breadon, A., Faiers, M. C., O'Farrell, S. M. & Shooter, R. A. The origin of O serotypes of *Escherichia coli* in babies after normal delivery. J. Hygiene 72, 67-70 (1974).**

52. **Hutchison, M. L., Walters, L. D., Avery, S. M., Munro, F. & Moore, A. Analyses of livestock production, waste storage, and pathogen levels and prevalences in farm manures. Appl. Environ. Microbiol. 71, 1231-1236 (2005).**

53. **Ackers, M.-L., Mahon, B. E., Leahy, E., Goode, B., Damrow, T., Hayes, P. S. *et al.* An outbreak of *Escherichia coli* O157:H7 infections associated with leaf lettuce consumption. J. Infectious Dis. 177, 1588-1593 (1998).**

54. **Jiang, X. P., Morgan, J. & Doyle, M. P. Fate of *Escherichia coli* O157: H7 in manure-amended soil. Appl. Environ. Microbiol. 68, 2605-2609 (2002).**

55. **Chapman, P. A., Cornell, J. & Green, C. Infection with verocytotoxin-producing *Escherichia coli* O157 during a visit to an inner city open farm. Epidemiol. Infection 125, 531-536 (2000).**

56. **Armstrong, G. L., Hollingsworth, J. & Morris, J. G., Jr. Emerging foodborne pathogens: *Escherichia coli* O157:H7 as a model of entry of a new pathogen into the food supply of the developed world. Epidemiol. Rev. 18, 29-51 (1996).**

57. **Griffin, P. M. & Tauxe, R. V. The epidemiology of infections caused by *Escherichia coli* O157 H7, other enterohemorrhagic *Escherichia coli*, and the associated hemolytic uremic syndrome. Epidemiol. Rev. 13, 60-98 (1991).**

58. **Dean-Nystrom, E. A., Bosworth, B. T., Cray, W. C., Jr. & Moon, H. W. Pathogenicity of *Escherichia coli* O157:H7 in the intestines of neonatal calves. Infect. Immun. 65, 1842-1848 (1997).**

59. **Nataro, J. P. & Kaper, J. B. Diarrheagenic *Escherichia coli*. Clin. Microbiol. Rev. 11, 142-201 (1998).**

60. **Parma, A. E., Sanz, M. E., Blanco, J. E., Blanco, J., Vinas, M. R., Blanco, M. *et al.* Virulence genotypes and serotypes of verotoxigenic *Escherichia coli* isolated from cattle and foods in Argentina - Importance in public health. Eur. J. Epidemiol. 16, 757-762 (2000).**

61. **Bell, B. P., Goldoft, M., Griffin, P. M., Davis, M. A., Gordon, D. C., Tarr, P. I. *et al.* A multistate outbreak of *Escherichia coli* O157:H7-associated bloody diarrhea and hemolytic uremic syndrome from hamburgers. The Washington experience. JAMA 272, 1349-1353 (1994).**

62. **Besser, R. E., Lett, S. M., Weber, J. T., Doyle, M. P., Barrett, T. J., Wells, J. G. *et al.* An outbreak of diarrhea and hemolytic uremic syndrome from *Escherichia coli* O157:H7 in fresh-pressed apple cider. JAMA 269, 2217-2220 (1993).**

63. **Maki, D. G. Don't eat the spinach -- controlling foodborne infectious disease. N. Engl. J. Med. 355, 1952-1955 (2006).**

64. **Manges, A. R., Johnson, J. R., Foxman, B., O'Bryan, T. T., Fullerton, K. E. & Riley, L. W. Widespread distribution of urinary tract infections caused by a multidrug-resistant *Escherichia coli* clonal group. N. Engl. J. Med. 345, 1007-1013 (2001).**

65. **Hitchcock, P. J., Leive, L., Makela, P. H., Rietschel, E. T., Strittmatter, W. & Morrison, D. C. Lipopolysaccharide nomenclature--past, present, and future. J. Bacteriol. 166, 699-705 (1986).**

66. **Goldman, R. C. & Hunt, F. Mechanism of O-Antigen distribution in lipopolysaccharide. J. Bacteriol. 172, 5352-5359 (1990).**

67. **Caroff, M. & Karibian, D. Structure of bacterial lipopolysaccharides. Carbohydr. Res. 338, 2431-2447 (2003).**

68. **Velasco, J., Moll, H., Knirel, Y. A., Sinnwell, V., Moriyon, I. & Zahringer, U. Structural studies on the lipopolysaccharide from a rough strain of Ochrobactrum anthropi containing a 2,3-diamino-2,3-dideoxy--glucose disaccharide lipid A backbone. Carbohydr. Res. 306, 283 (1998).**

69. **Knirel, Y. A., Moll, H. & Zahringer, U. Structural study of a highly O-acetylated core of Legionella pneumophila serogroup 1 lipopolysaccharide. Carbohydr. Res. 293, 223 (1996).**

70. **Raetz, C. R. H. & Whitfield, C. Lipopolysaccharide endotoxins. Annu. Rev. Biol. 71, 635-700 (2002).**

71. **Mariani-Kurkdjian, P. & Bingen, E. *Escherichia coli* O157: H7, an emerging pathogen. Presse Medicale 28, 2067-2074 (1999).**

72. **Gavin, P. J., Peterson, L. R., Pasquariello, A. C., Blackburn, J., Hamming, M. G., Kuo, K. J. *et al.* Evaluation of performance and potential clinical impact of ProSpecT Shiga toxin *Escherichia coli* microplate assay for detection of Shiga toxin-producing *E. coli* in stool samples. J. Clin. Microbiol. 42, 1652-1656 (2004).**

73. **Young, K., Silver, L. L., Bramhill, D., Cameron, P., Eveland, S. S., Raetz, C. R. H. *et al.* The envA permeability/cell division gene of *Escherichia coli* encodes the second enzyme of lipid A biosynthesis. J. Biol. Chem. 270, 30384-30391 (1995).**

74. **Stenutz, W. a. W. (Stockholm, 2008).**

75. **Franco, A. V., Liu, D. & Reeves, P. R. The Wzz (Cld) Protein in *Escherichia coli*: amino acid sequence variation determines O-antigen chain length specificity. J. Bacteriol. 180, 2670-2675 (1998).**

76. **Murray, G. L., Attridge, S. R. & Morona, R. Altering the length of the lipopolysaccharide O-antigen has an impact on the Interaction of *Salmonella enterica* and *Serovar typhimurium* with macrophages and complement. J. Bacteriol. 188, 2735-2739 (2006).**

77. **Whitfield, C. Biosynthesis of lipopolysaccharide O antigens. Trends Microbiol. 3, 178 (1995).**

78. **Abu-Lail, N. I. & Camesano, T. A. Role of lipopolysaccharides in the adhesion, retention, and transport of *Escherichia coli* JM109. Environ. Sci. Technol. 37, 2173-2183 (2003).**

79. **Tomme, P., Creagh, A. L., Kilburn, D. G. & Haynes, C. A. Interaction of polysaccharides with the N-terminal cellulose-binding domain of Cellulomonas fimi CenC.1. Binding specificity and calorimetric analysis. Biochem. 35, 13885-13894 (1996).**

80. **Gutsmann, T., Schromm, A. B. & Brandenburg, K. The physicochemistry of endotoxins in relation to bioactivity. Int. J. Med. Microbiol. 297, 341 (2007).**

81. **Stenutz, R. (2005).**

82. **Chan, M. K., Gong, W. M., Rajagopalan, P. T. R., Hao, B., Tsai, C. M. & Pei, D. H. Crystal structure of the *Escherichia coli* peptide deformylase. Biochem. 36, 13904-13909 (1997).**

83. **Orskov, I., Orskov, F., Jann, B. & Jann, K. Serology, chemistry, and genetics of O and K antigens of *Escherichia coli*. Microbiol. Mol. Biol. Rev. 41, 667-710 (1977).**

84. **Levine, M. M. *Escherichia coli* that cause diarrhea - Enterotoxigenic, Enteropathogenic, Enteroinvasive, Enterohemorrhagic, and Enteroadherent. J. Infectious Dis. 155, 377-389 (1987).**

85. **Karmali, M. A. Infection vy verocytotoxin-producing *Escherichia coli*. Clin. Microbiol. Rev. 2, 15-38 (1989).**

86. **Griffin, P. M. & Tauxe, R. V. The epidemiology of infections caused by *Escherichia coli* O157 H7, other enterohemorrhagic *Escherichia coli*, and the associated hemolytic uremic syndrome. Epidemiol. Rev. 13, 60-98 (1991).**

87. **Pruimboom-Brees, I. M., Morgan, T. W., Ackermann, M. R., Nystrom, E. D., Samuel, J. E., Cornick, N. A. *et al.* Cattle lack vascular receptors for *Escherichia coli* O157: H7 Shiga toxins. Proc. Nat. Acad. Sci. U. S. A. 97, 10325-10329 (2000).**

88. **Gill, D. M. Bacterial toxins - A table of lethal amounts. Microbiol. Rev. 46, 86-94 (1982).**

89. **Caprioli, A., Morabito, S., Brugere, H. & Oswald, E. Enterohaemorrhagic *Escherichia coli*: emerging issues on virulence and modes of transmission. Veterinary Res. 36, 289-311 (2005).**

90. **Oswald, E., Schmidt, H., Morabito, S., Karch, H., Marches, O. & Caprioli, A. Typing of intimin genes in human and animal Enterohemorrhagic and Enteropathogenic *Escherichia coli*: Characterization of a new intimin variant. Infect. Immun. 68, 64-71 (2000).**

91. **Adu-Bobie, J., Frankel, G., Bain, C., Goncalves, A. G., Trabulsi, L. R., Douce, G. *et al.* Detection of Intimins alpha, beta, gamma, and delta, four intimin derivatives expressed by attaching and effacing microbial pathogens. J. Clin. Microbiol. 36, 662-668 (1998).**

92. **Gyles, C. L. Shiga toxin-producing *Escherichia coli*: An overview. J. Anim Sci. 85, E45-62 (2007).**

93. **Paton, A. W. & Paton, J. C. Detection and characterization of shiga toxigenic *Escherichia coli* by using multiplex PCR assays for stx1, stx2, eaeA, enterohemorrhagic *E. coli* hlyA, rfbO111, and rfbO157. J. Clin. Microbiol. 36, 598-602 (1998).**

94. **Bastian, S. N., Carle, I. & Grimont, F. Comparison of 14 PCR systems for the detection and subtyping of stx genes in Shiga-toxin-producing *Escherichia coli*. Res. Microbiol. 149, 457 (1998).**

95. **Wieler, L. H., Vieler, E., Erpenstein, C., Schlapp, T., Steinruck, H., Bauerfeind, R. *et al.* Shiga toxin-producing *Escherichia coli* strains from bovines: association of adhesion with carriage of eae and other genes. J. Clin. Microbiol. 34, 2980-2984 (1996).**

96. **Yu, J. & Kaper, J. B. Cloning and characterization of the eae gene of enterohaemorrhagic *Escherichia coli* O157:H7. Mol. Microbiol. 6, 411-417 (1992).**

97. **Frankel, G., Phillips, A. D., Rosenshine, I., Dougan, G., Kaper, J. B. & Knutton, S. Enteropathogenic and enterohaemorrhagic *Escherichia coli*: more subversive elements. Mol. Microbiol. 30, 911-921 (1998).**

98. **Boerlin, P., McEwen, S. A., Boerlin-Petzold, F., Wilson, J. B., Johnson, R. P. & Gyles, C. L. Associations between virulence factors of shiga toxin-producing *Escherichia coli* and disease in humans. J. Clin. Microbiol. 37, 497-503 (1999).**

99. **Werber, D., Fruth, A., Buchholz, U., Prager, R., Kramer, M. H., Ammon, A. *et al.* Strong association between shiga toxin-producing *Escherichia coli* O157 and virulence genes stx(2) and eae as possible explanation for predominance of serogroup O157 in patients with haemolytic uraemic syndrome. Eur. J. Clin. Microbiol. Infectious Dis. 22, 726-730 (2003).**

100. **Konowalchuk, J., Dickie, N., Stavric, S. & Speirs, J. I. Properties of an Escherichia coli cytotoxin. Infect. Immun. 20, 575-577 (1978).**

101. **Robinson, C. M., Sinclair, J. F., Smith, M. J. & O'Brien, A. D. Shiga toxin of enterohemorrhagic *Escherichia coli* type O157: H7 promotes intestinal colonization. Proc. Nat. Acad. Sci. U. S. A. 103, 9667-9672 (2006).**

102. **Johannessen, G. S., Froseth, R. B., Solemdal, L., Jarp, J., Wasteson, Y. & M. Rorvik, L. Influence of bovine manure as fertilizer on the bacteriological quality of organic Iceberg lettuce. J. Appl. Micro. 96, 787-794 (2004).**

103. **Orden, J. A., Ruiz-Santa-Quiteria, J. A., Cid, D., García, S., Sanz, R. & de la Fuente, R. Verotoxin-producing *Escherichia coli* (VTEC) and eae-positive non-VTEC in 1-30-days-old diarrhoeic dairy calves. Veterinary Microbiol. 63, 239 (1998).**

104. **Stenutz, R., Weintraub, A. & Widmalm, G. The structures of *Escherichia coli* O-polysaccharide antigens. Fems. Microbiol. Rev. 30, 382-403 (2006).**

105. **Robins-Browne, R. M. The rise and rise of enteropathogenic *Escherichia coli*. Samj. South African Med. J. 97, 1182-1186 (2007).**

106. **Robins-Browne, R. M., Bordun, A. M., Tauschek, M., Bennett-Wood, V. R., Russell, J., Oppedisano, F. *et al. Escherichia coli* and community-acquired gastroenteritis, Melbourne, Australia. Emerg. Infectious Dis. 10, 1797-1805 (2004).**

107. **Robins-Browne, R. M. & Hartland, E. L. *Escherichia coli* as a cause of diarrhea. J. Gastroenterology Hepatology 17, 467-475 (2002).**

108. **Jiang, Z.-D., Lowe, B., Verenkar, M. P., Ashley, D., Steffen, R., Tornieporth, N. *et al.* Prevalence of nnteric pathogens among international travelers with**

diarrhea acquired in Kenya (Mombasa), India (Goa), or Jamaica (Montego Bay). J. Infectious Dis. 185, 497 (2002).

109. Nataro, J. P., Steiner, T. & Guerrant, R. L. Enteroaggregative *Escherichia coli*. Emerg. Infectious Dis. 4, 251-261 (1998).

110. Scaletsky, I. C. A., Fabbricotti, S. H., Carvalho, R. L. B., Nunes, C. R., Maranhao, H. S., Morais, M. B. *et al.* Diffusely adherent *Escherichia coli* as a cause of acute diarrhea in young children in northeast Brazil: a case-control study. J. Clin. Microbiol. 40, 645-648 (2002).

111. Beinke, C., Laarmann, S., Wachter, C., Karch, H., Greune, L. & Schmidt, M. A. Diffusely adhering *Escherichia coli* strains induce attaching and effacing phenotypes and secrete homologs of esp proteins. Infect. Immun. 66, 528-539 (1998).

112. Brogden, K. A., Ackermann, M., McCray, P. B. & Tack, B. F. Antimicrobial peptides in animals and their role in host defences. Int. J. Antimicrob. Agents 22, 465-478 (2003).

113. Wang, G. (2008).

114. Izadpanah, A. & Gallo, R. L. Antimicrobial peptides. J. Am. Acad. Dermatology 52, 381-392 (2005).

115. Zasloff, M. Antimicrobial peptides of multicellular organisms. Nature 415, 389-395 (2002).

116. Chen, L. H., Li, Y. H., Li, J. X., Xu, X. Q., Lai, R. & Zou, Q. M. An antimicrobial peptide with antimicrobial activity against Helicobacter pylori. Peptides 28, 1527-1531 (2007).

117. Kulagina, N. V., Shaffer, K. M., Anderson, G. P., Ligler, F. S. & Taitt, C. R. Antimicrobial peptide-based array for *Escherichia coli* and *Salmonella* screening. Analytica Chimica Acta 575, 9-15 (2006).

118. Lad, M. D., Birembaut, F., Clifton, L. A., Frazier, R. A., Webster, J. R. P. & Green, R. J. Antimicrobial peptide-lipid binding interactions and binding selectivity. Biophys. J. 92, 3575-3586 (2007).

119. Rossetto, G., Bergese, P., Colombi, P., Depero, L. E., Giuliani, A., Nicoletto, S. F. *et al.* Atomic force microscopy evaluation of the effects of a novel antimicrobial multimeric peptide on *Pseudomonas aeruginosa*. Nanomed. Nanotech. Biol. Med. 3, 198-207 (2007).

120. Alessandro Tossi, L. S. A. G. Amphipathic.

121. Yeaman, M. R. & Yount, N. Y. Mechanisms of antimicrobial peptide action and resistance. Pharmacol. Rev. 55, 27-55 (2003).

122. Thomas, P. J. & Law, J. H. Biosynthesis of Cyclopropane Compounds. IX. Structural and stereochemical requirements for the cyclopropane synthetase substrate. J. Biol. Chem. 241, 5013-5018 (1966).

123. Baev, D., Rivetta, A., Vylkova, S., Sun, J. N., Zeng, G.-F., Slayman, C. L. *et al.* The TRK1 potassium transporter Is the critical effector for killing of *Candida albicans* by the cationic protein, Histatin 5. J. Biol. Chem. 279, 55060-55072 (2004).

124. Scott, M. G., Yan, H. & Hancock, R. E. W. Biological properties of structurally related alpha -helical cationic antimicrobial peptides. Infect. Immun. 67, 2005-2009 (1999).

125. Matsuzaki, K., Yoneyama, S., Fujii, N., Miyajima, K., Yamada, K., Kirino, Y. *et al.* Membrane permeabilization mechanisms of a cyclic antimicrobial peptide, Tachyplesin I, and its linear analog. Biochem. 36, 9799-9806 (1997).

126. Peschel, A., Jack, R. W., Otto, M., Collins, L. V., Staubitz, P., Nicholson, G. *et al.* *Staphylococcus aureus* resistance to human defensins and evasion of neutrophil killing via the novel virulence factor MprF is based on modification of membrane lipids with L-Lysine. J. Exp. Med. 193, 1067-1076 (2001).

127. Nizet, V. Antimicrobial peptide resistance mechanisms of human bacterial pathogens. Curr. Issues Mol. Biol. 8, 11-26 (2006).

128. Guo, L., Lim, K. B., Poduje, C. M., Daniel, M., Gunn, J. S., Hackett, M. *et al.* Lipid A acylation and bacterial resistance against vertebrate antimicrobial peptides. Cell 95, 189-198 (1998).

129. Jin, T., Bokarewa, M., Foster, T., Mitchell, J., Higgins, J. & Tarkowski, A. *Staphylococcus aureus* resists human defensins by production of staphylokinase, a novel bacterial evasion mechanism. J. Immun. 172, 1169-1176 (2004).

130. Levy, S. B. Active efflux, a common mechanism for biocide and antibiotic resistance. J. Appl. Micro. 92, 65S-71S (2002).

131. Zgurskaya, H. I. Molecular analysis of efflux pump-based antibiotic resistance. Int. J. Med. Microbiol. 292, 95-105 (2002).

132. Dorschner, R. A., Pestonjamasp, V. K., Tamakuwala, S., Ohtake, T., Rudisill, J., Nizet, V. *et al.* Cutaneous injury induces the release of cathelicidin anti-microbial peptides active against group A *Streptococcus*. J. Inves. Dermatology 117, 91-97 (2001).

133. Birchler, T., Seibl, R., Buchner, K., Loeliger, S., Seger, R., Hossle, J. P. *et al.* Human Toll-like receptor 2 mediates induction of the antimicrobial peptide human beta-defensin 2 in response to bacterial lipoprotein. Eur. J. Immun. 31, 3131-3137 (2001).

134. Wang, X. R., Zhang, Z., Louboutin, J. P., Moser, C., Weiner, D. J. & Wilson, J. M. Airway epithelia regulate expression of human beta-defensin 2 through toll-like receptor 2. Faseb. J. 17, 1727-+ (2003).

135. Taggart, C. C., Greene, C. M., Smith, S. G., Levine, R. L., McCray, P. B., Jr., O'Neill, S. *et al.* Inactivation of human {beta}-Defensins 2 and 3 by elastolytic cathepsins. J. Immunol. 171, 931-937 (2003).

136. Lande, R., Gregorio, J., Facchinetti, V., Chatterjee, B., Wang, Y. H., Homey, B. *et al.* Plasmacytoid dendritic cells sense self-DNA coupled with antimicrobial peptide. Nature 449, 564-U6 (2007).

137. Paulsen, F., Pufe, T., Conradi, L., Varoga, D., Tsokos, M., Papendieck, J. *et al.* Antimicrobial peptides are expressed and produced in healthy and inflamed human synovial membranes. J. Pathol. 198, 369-377 (2002).

138. Tew, G. N., Clements, D., Tang, H. Z., Arnt, L. & Scott, R. W. Antimicrobial activity of an abiotic host defense peptide mimic. Biochimica Et Biophysica Acta-Biomembranes 1758, 1387-1392 (2006).

139. Rosenfeld, Y. & Shai, Y. Lipopolysaccharide (Endotoxin)-host defense antibacterial peptides interactions: Role in bacterial resistance and

prevention of sepsis. Biochimica Et Biophysica Acta-Biomembranes 1758, 1513-1522 (2006).

140. Shai, Y. Mode of action of membrane active antimicrobial peptides. Biopolymers 66, 236-248 (2002).

141. Shai, Y. Mechanism of the binding, insertion and destabilization of phospholipid bilayer membranes by [alpha]-helical antimicrobial and cell non-selective membrane-lytic peptides. Biochimica et Biophysica Acta (BBA) - Biomembranes 1462, 55 (1999).

142. Gregory, K. & Mello, C. M. Immobilization of *Escherichia coli* cells by use of the antimicrobial peptide cecropin P1. Appl. Environ. Microbiol. 71, 1130-1134 (2005).

143. Mello, C. M. & Soares, J. (eds.) Membrane selectivity of antimicrobial peptides (ACS, San Francisco, 2007).

144. Binnig, G., Quate, C. F. & Gerber, C. Atomic force microscope. Phys. Rev. Lett. 56, 930-933 (1986).

145. Tersoff, J. & Hamann, D. R. Theory of the scanning tunneling microscope. Phys. Rev. B 31, 805-813 (1985).

146. Tersoff, J. & Hamann, D. R. Theory and application for the scanning tunneling microscope. Phys. Rev. B 50, 1998-2001 (1983).

147. Akamine, S., Kuwano, H. & Yamada, H. Scanning near-field optical microscope using an atomic force microscope cantilever with integrated photodiode. Appl. Phys. Lett. 68, 579-581 (1996).

148. Villarrubia, J. S., Ward, J. & Scire, F. The topografiner: An instrument for measuring surface microtopography. Rev. Sci. Instrum. 43, 214-218 (1999).

149. M. J. Allen, E. M. B., and R. Balhorn. AFM analysis of DNA-protamine complexes bound to mica. Nucleic Acids Research 25, 2221-2226 (1997).

150. N. H. Thomson, S. K., B. Smith, H. G. Hansma, and P. K. Hansma. Reversible Binding of DNA to Mica for AFM Imaging. Langmuir 12, 5905-5908 (1996).

151. Claudio Rivetti, M. G., and Carlos Bustamante. Wrapping of DNA around the E. coli RNA polymerase open promoter complex. The EMBO Journal 18, 4464-4475 (1999).

152. Hansma, H. G. & Hoh, J. H. Biomolecular imaging with the atomic force microscope. Annu. Rev. Biol. 23, 115-140 (1994).

153. Rambourg, A. & Leblond, C. P. Electron microscope observations on the carbohydrate rich cell coat present at the surface of cells in the rat. J. Cell Biol. 32, 27-53 (1967).

154. Palade, G. E. A study of fixation for electron microscopy. J. Exp. Med. 95, 285-298 (1952).

155. Hansma, H. G., Kasuya, K. & Oroudjev, E. Atomic force microscopy imaging and pulling of nucleic acids. Curr. Opin. Struct. Biol. 14, 380-385 (2004).

156. Hansma, P. K., Cleveland, J. P., Radmacher, M., Walters, D. A., Hillner, P. E., Bezanilla, M. *et al.* Tapping mode atomic force microscopy in liquids. Appl. Phys. Lett. 64, 1738 (1994).

157. Garcia, R. & Perez, R. Dynamic atomic force microscopy methods. Surf. Sci. Rep. 47, 197 (2002).

158. Sader, J. E., Larson, I., Mulvaney, P. & White, L. R. Method for the calibration of atomic force microscope cantilevers. Rev. Sci. Instrum. 66, 3789 (1995).

159. Burnham, N. A., Chen, X., Hodges, C. S., Matei, G. A., Thoreson, E. J., Roberts, C. J. *et al.* Comparison of calibration methods for atomic-force microscopy cantilevers. Nanotechnol. 14, 1-6 (2003).

160. Liu, Y. T., Black, M. A., Caron, L. & Camesano, T. A. Role of cranberry juice on molecular-scale surface characteristics and adhesion behavior of *Escherichia coli*. Biotechnol. Bioeng. 93, 297-305 (2006).

161. Atabek, A. & Camesano, T. A. Atomic force microscopy study of the effect of lipopolysaccharides and extracellular polymers on adhesion of *Pseudomonas aeruginosa*. J. Bacteriol. 189, 8503-8509 (2007).

162. Voinova, M. V., Jonson, M. & Kasemo, B. Missing mass' effect in biosensor's QCM applications. Biosens. Bioelectron. 17, 835 (2002).

163. Sauerbrey, G. Verwendung non schwingquarzen zur waegung duenner schichten und zur mikrowaegung. Z. Phys., 206-222 (1959).

164. Ekholm, P., Blomberg, E., Claesson, P., Auflem, I. H., Sjoblom, J. & Kornfeldt, A. A quartz crystal microbalance study of the adsorption of asphaltenes and resins onto a hydrophilic surface. J. Colloid Interface Sci. 247, 342-350 (2002).

165. Rodahl, M., Hook, F., Krozer, A., Brzezinski, P. & Kasemo, B. Quartz crystal microbalance setup for frequency and Q-factor measurements in gaseous and liquid environments. Rev. Sci. Instrum. 66, 3924 (1995).

166. Cooper, M. A. & Singleton, V. T. A survey of the 2001 to 2005 quartz crystal microbalance biosensor literature: applications of acoustic physics to the analysis of biomolecular interactions. J. Mol. Recognit. 20, 154-184 (2007).

167. Kanazawa, K. K. & Gordon, J. G. The oscillation frequency of a quartz resonator in contact with a liquid. Analytica Chimica Acta 175, 99-105 (1985).

168. Rechendorff, K., Hovgaard, M. B., Foss, M. & Besenbacher, F. Influence of surface roughness on quartz crystal microbalance measurements in liquids. J. Appl. Phys. 101 (2007).

169. Voinova, M. V., Rodahl, M., Jonson, M. & Kasemo, B. Viscoelastic acoustic response of layered polymer films at fluid-solid interfaces: Continuum mechanics approach. Physica. Scripta. 59, 391-396 (1999).

170. Dutta, A. K., Nayak, A. & Belfort, G. Viscoelastic properties of adsorbed and cross-linked polypeptide and protein layers at a solid-liquid interface. J. Colloid Interface Sci. 324, 55 (2008).

171. Park, E. J., Draper, D. D. & Flynn, N. T. Adsorption and thermoresponsive behavior of poly(N-isopropylacrylamide-co-N,N'-cystaminebisacrylamide) thin films on gold. Langmuir 23, 7083-7089 (2007).

172. Liu, Y., Mu, L., Liu, B. H. & Kong, J. L. Controlled switchable surface. Chemistry-A European Journal 11, 2622-2631 (2005).

173. Hurlebaus, S. & Gaul, L. Smart structure dynamics. Mech. Syst. Signal Proc. 20, 255-281 (2006).
174. Hook, F., Rodahl, M., Keller, C., Glasmastar, K., Fredriksson, C., Dahlqvist, P. *et al.* The dissipative QCM-D technique interfacial phenomena and sensor applications for proteins, biomembranes, living cells and polymers. EFTF Joint Meeting EFTF, 966-972 (1999).
175. Hedin, J., Lofroth, J. E. & Nyden, M. Adsorption behavior and cross-linking of EHEC and HM-EHEC at hydrophilic and hydrophobic modified surfaces monitored by SPR and QCM-D. Langmuir 23, 6148-6155 (2007).
176. Wu, K., Wu, B., Wang, P., Hou, Y., Zhang, G. Z. & Zhu, D. M. Adsorption isotherms and dissipation of adsorbed Poly(N-isopropylacrylamide) in its swelling and collapsed states. J. Phys. Chem. B 111, 8723-8727 (2007).
177. Wu, B., Wu, K., Wang, P. & Zhu, D. M. Adsorption kinetics and adsorption isotherm of poly(N-isopropylacrylamide) on gold surfaces studied using QCM-D. J. Phys. Chem. C 111, 1131-1135 (2007).
178. Liu, Y., Strauss, J. & Camesano, T. A. Thermodynamic investigation of *Staphylococcus epidermidis* interactions with protein-coated substrata. Langmuir 23, 7134-7142 (2007).
179. Hemmersam, A. G., Foss, M., Chevallier, J. & Besenbacher, F. Adsorption of fibrinogen on tantalum oxide, titanium oxide and gold studied by the QCM-D technique. Colloids Surf., B 43, 208-215 (2005).
180. Gopel, W. & Heiduschka, P. Interface analysis in biosensor design. Biosens. Bioelectron. 10, 853-883 (1995).
181. Okahata, Y., Matsunobu, Y., Ijiro, K., Mukae, M., Murakami, A. & Makino, K. Hybridization of nucleic-acids immobilized on a quartz crystal microbalance. J. Am. Chem. Soc. 114, 8299-8300 (1992).
182. Lazerges, M., Perrot, H., Rabehagasoa, N., Antoine, E. & Compere, C. 45- and 70-base DNA supramolecular polymerizations on quartz crystal microbalance biosensor. Chem. Commun., 6020-6022 (2005).
183. Carmon, K. S., Baltus, R. E. & Luck, L. A. A biosensor for estrogenic substances using the quartz crystal microbalance. Anal. Biochem. 345, 277-283 (2005).
184. Webster, N. J. G., Green, S., Rui Jin, J. & Chambon, P. The hormone-binding domains of the estrogen and glucocorticoid receptors contain an inducible transcription activation function. Cell 54, 199 (1988).
185. Eberlein, W. R., Bongiovanni, A. M. & Franis, C. M. Urinary oestriol and placental function. Br. Med. J. 2, 194-195 (1965).
186. Andersson, A. S., Glasmastar, K., Sutherland, D., Lidberg, U. & Kasemo, B. Cell adhesion on supported lipid bilayers. J. Biomed. Mat. Res. Part A 64A, 622-629 (2003).
187. Ishihara, K., Iwasaki, Y., Ebihara, S., Shindo, Y. & Nakabayashi, N. Photoinduced graft polymerization of 2-methacryloyloxyethyl phosphorylcholine on polyethylene membrane surface for obtaining blood cell adhesion resistance. Colloids Surf., B 18, 325-335 (2000).
188. Iwasaki, Y., Sawada, S., Nakabayashi, N., Khang, G., Lee, H. B. & Ishihara, K. The effect of the chemical structure of the phospholipid polymer on

fibronectin adsorption and fibroblast adhesion on the gradient phospholipid surface. Biomaterials 20, 2185-2191 (1999).

189. Hasegawa, T., Iwasaki, Y. & Ishihara, K. Preparation and performance of protein-adsorption-resistant asymmetric porous membrane composed of polysulfone/phospholipid polymer blend. Biomaterials 22, 243-251 (2001).

190. Iwasaki, Y., Ishihara, K., Nakabayashi, N., Khang, G., Jeon, J. H., Lee, J. W. *et al.* Platelet adhesion on the gradient surfaces grafted with phospholipid polymer. J. Biomaterials Sci.-Polym. Ed. 9, 801-816 (1998).

191. Marx, K. A., Zhou, T. A., Montrone, A., Schulze, H. & Braunhut, S. J. A quartz crystal microbalance cell biosensor: detection of microtubule alterations in living cells at nM nocodazole concentrations. Biosens. Bioelectron. 16, 773-782 (2001).

192. Wang, Y. C. & Burke, D. J. Checkpoint genes required to delay cell-division in response to nocodazole respond to impaired kinetochore function in the yeast *Saccharomyces cerevisiae*. Mol. Cell. Biol. 15, 6838-6844 (1995).

193. Ghadimi, B. M., Sackett, D. L., Difilippantonio, M. J., Schrock, E., Neumann, T., Jauho, A. *et al.* Centrosome amplification and instability occurs exclusively in aneuploid, but not in diploid colorectal cancer cell lines, and correlates with numerical chromosomal aberrations. Genes Chromo. Cancer 27, 183-190 (2000).

194. Tighe, A., Johnson, V. L., Albertella, M. & Taylor, S. S. Aneuploid colon cancer cells have a robust spindle checkpoint. Embo Reports 2, 609-614 (2001).

195. Marx, K. A., Zhou, T., Montrone, A., McIntosh, D. & Braunhut, S. J. Quartz crystal microbalance biosensor study of endothelial cells and their extracellular matrix following cell removal: Evidence for transient cellular stress and viscoelastic changes during detachment and the elastic behavior of the pure matrix. Anal. Biochem. 343, 23-34 (2005).

196. Le, D., He, F.-j., Jiang, T. J., Nie, L. & Yao, S. A goat-anti-human IgG modified piezoimmunosensor for *Staphylococcus aureus* detection. J. Microbiol. Methods 23, 229 (1995).

197. Bao, L., Deng, L., Nie, L., Yao, S. & Wei, W. Determination of microorganisms with a quartz crystal microbalance sensor. Analytica chimica acta 319, 97 (1996).

198. Hobson, N. S., Tothill, I. & Turner, A. P. F. Microbial detection. Biosens. and Bioelectron. 11, 455 (1996).

199. Lin, H. C. & Tsai, W. C. Piezoelectric crystal immunosensor for the detection of *staphylococcal* enterotoxin B. Biosens. and Bioelectron. 18, 1479-1483 (2003).

200. Spangler, B. D. & Tyler, B. J. Capture agents for a quartz crystal microbalance-continuous flow biosensor: functionalized self-assembled monolayers on gold. Analytica Chimica Acta 399, 51-62 (1999).

201. Otto, K., Elwing, H. & Hermansson, M. Effect of ionic strength on initial interactions of Escherichia coli with surfaces, studied on-line by a novel quartz crystal microbalance technique. J. Bacteriol. 181, 5210-5218 (1999).

202. **Reipa, V., Almeida, J. & Cole, K. D. Long-term monitoring of biofilm growth and disinfection using a quartz crystal microbalance and reflectance measurements. J. Microbiol. Methods 66, 449-459 (2006).**

203. **Cooper, M. A., Dultsev, F. N., Minson, T., Ostanin, V. P., Abell, C. & Klenerman, D. Direct and sensitive detection of a human virus by rupture event scanning. Nat. Biotechnol. 19, 833-837 (2001).**

204. **Dultsev, F. N., Ostanin, V. P. & Klenerman, D. "Hearing" bond breakage. Measurement of bond rupture forces using a quartz crystal microbalance. Langmuir 16, 5036-5040 (2000).**

205. **Edvardsson, M., Rodahl, M., Kasemo, B. & Hook, F. A dual-frequency QCM-D setup operating at elevated oscillation amplitudes. Anal. Chem. 77, 4918-4926 (2005).**

206. **Ulman, A. Formation and structure of self-assembled monolayers. Chem. Rev. 96, 1533-1554 (1996).**

207. **Liao, S., Shnidman, Y. & Ulman, A. Adsorption kinetics of rigid 4-Mercaptobiphenyls on gold. J. Am. Chem. Soc. 122, 3688-3694 (2000).**

208. **Briand, E., Gu, C., Boujday, S., Salmain, M., Herry, J. M. & Pradier, C. M. Functionalisation of gold surfaces with thiolate SAMs: Topography/bioactivity relationship - A combined FT-RAIRS, AFM and QCM investigation. Surf. Sci. 601, 3850-3855 (2007).**

209. **Iwata, F., Saruta, K. & Sasaki, A. In situ atomic force microscopy combined with a quartz-crystal microbalance study of Ag electrodeposition on Pt thin film. Appl. Phys. A: Mat. Sci. Proc. 66, 463-466 (1998).**

210. **Hayden, O. & Dickert, F. L. Selective microorganism detection with cell surface imprinted polymers. Adv. Mater. 13, 1480-+ (2001).**

211. **Hayden, O., Bindeus, R. & Dickert, F. L. Combining atomic force microscope and quartz crystal microbalance studies for cell detection. Meas. Sci. Technol. 14, 1876-1881 (2003).**

212. **deKerchove, A. J. & Elimelech, M. Structural Growth and Viscoelastic Properties of Adsorbed Alginate Layers in Monovalent and Divalent Salts. Macromolecules 39, 6558-6564 (2006).**

213. **Sutherland, I. W. Microbial polysaccharides from Gram-negative bacteria. Int. Dairy J. 11, 663 (2001).**

214. **Korstgens, V., Flemming, H. C., Wingender, J. & Borchard, W. Influence of calcium ions on the mechanical properties of a model biofilm of mucoid Pseudomonas aeruginosa. Water Sci. Technol. 43, 49-57 (2001).**

215. **Hook, F., Kasemo, B., Nylander, T., Fant, C., Sott, K. & Elwing, H. Variations in Coupled Water, Viscoelastic Properties, and Film Thickness of a Mefp-1 Protein Film during Adsorption and Cross-Linking: A Quartz Crystal Microbalance with Dissipation Monitoring, Ellipsometry, and Surface Plasmon Resonance Study. Analytical Chemistry 73, 5796-5804 (2001).**

216. **Absolom, D. R., Lamberti, F. V., Policova, Z., Zingg, W., Vanoss, C. J. & Neumann, A. W. Surface thermodynamics of bacterial adhesion. Appl. Environ. Microbiol. 46, 90-97 (1983).**

217. Neumann, A. W., Good, R. J., Hope, C. J. & Sejpal, M. An equation-of-state approach to determine surface tensions of low-energy solids from contact angles. Colloid Interface Sci. 49, 291-304 (1974).

218. Neumann, A. W., Absolom, D. R., Francis, D. W. & Vanoss, C. J. Conversion tables of contact angles to surface tensions. Sep. Purif. Methods 9, 69-163 (1980).

219. Busscher, H. J., Weerkamp, A. H., Vandermei, H. C., Vanpelt, A. W. J., Dejong, H. P. & Arends, J. Measurement of the surface free-energy of bacterial-cell surfaces and its relevance for adhesion. Appl. Environ. Microbiol. 48, 980-983 (1984).

220. Gallardo-Moreno, A. M., Gonzalez-Martin, M. L., Bruque, J. M. & Perez-Giraldo, C. Changes on the physico-chemical surface properties and adhesion behaviour of *Enterococcus faecalis* by the addition of serum or urine to the growth medium. PCCP 6, 1512-1517 (2004).

221. Gallardo-Moreno, A. M., Gonzalez-Martin, M. L., Perez-Giraldo, C., Bruque, J. M. & Gomez-Garcia, A. C. Serum as a factor influencing adhesion of *Enterococcus faecalis* to glass and silicone. Appl. Environ. Microbiol. 68, 5784-5787 (2002).

222. Simoes, M., Simoes, L. C., Cleto, S., Pereira, M. O. & Vieira, M. J. The effects of a biocide and a surfactant on the detachment of *Pseudomonas fluorescens* from glass surfaces. Int. J. Food Microbiol. 121, 335 (2008).

223. Postollec, F., Busscher, H. J., Kooten, T. G. v., Mei, H. C. v. d. & Norde, W. Path-dependency of the interaction between coaggregating and between non-coaggregating oral bacterial pairs--a thermodynamic approach. Colloids Surf., B 37, 53 (2004).

224. Alvarez, O., Brodwick, M., Latorre, R., McLaughlin, A., McLaughlin, S. & Szabo, G. Large divalent-cations and electrostatic potentials adjacent to membranes - Experimental results with hexamethonium. Biophys. J. 44, 333-342 (1983).

225. McLaughlin, S. The electrostatic properties of membranes. Annu. Rev. Biophys. Biophys. Chem. 18, 113-136 (1989).

226. Kinraide, T. B. Use of a Gouy-Chapman-Stern model for membrane-surface electrical potential to interpret some features of mineral rhizotoxicity. Plant Physiol. 106, 1583-1592 (1994).

227. Horn, R. G. & Israelachvili, J. N. Direct measurement of structural forces between two surfaces in a nonpolar liquid. J. Chem. Phys. 75, 1400 (1981).

228. Derjaguin, B. V., Abrikosova, II & Lifshitz, E. M. Direct measurement of molecular attraction between solids separated by a narrow gap (Reprinted From Quart Rev, Vol 10, Pg 295-329, 1956). Prog. Surf. Sci. 40, 83-117 (1992).

229. Sharma, P. K. & Hanumantha Rao, K. Adhesion of *Paenibacillus polymyxa* on chalcopyrite and pyrite: surface thermodynamics and extended DLVO theory. Colloids Surf., B 29, 21 (2003).

230. Yoon, R.-H. & Mao, L. Application of extended DLVO theory, IV: derivation of flotation rate equation from first principles. J. Colloid Interface Sci. 181, 613 (1996).

231. Tsuneda, S., Jung, J., Hayashi, H., Aikawa, H., Hirata, A. & Sasaki, H. Influence of extracellular polymers on electrokinetic properties of heterotrophic bacterial cells examined by soft particle electrophoresis theory. Colloids Surf., B 29, 181 (2003).

232. Abu-Lail, N. I. & Camesano, T. A. Role of ionic strength on the relationship of biopolymer conformation, DLVO contributions, and steric interactions to bioadhesion of Pseudomonas putida KT2442. Biomacromolecules 4, 1000-1012 (2003).

233. McClaine, J. W. & Ford, R. M. Reversal of flagellar rotation is important in initial attachment of *Escherichia coli* to glass in a dynamic system with high- and low-ionic-strength buffers. Appl. Environ. Microbiol. 68, 1280-1289 (2002).

234. Vanloosdrecht, M. C. M., Lyklema, J., Norde, W. & Zehnder, A. J. B. Bacterial Adhesion - A Physicochemical Approach. Microbial Ecology 17, 1-15 (1989).

235. Hermansson, M. The DLVO theory in microbial adhesion. Colloid Surf., B 14, 105 (1999).

236. Jucker, B. A., Zehnder, A. J. B. & Harms, H. Quantification of Polymer Interactions in Bacterial Adhesion. Environ. Sci. Technol. 32, 2909-2915 (1998).

237. Vanloosdrecht, M. C. M., Norde, W., Lyklema, J. & Zehnder, A. J. B. Hydrophobic And Electrostatic Parameters In Bacterial Adhesion. Aquatic Sci. 52, 103-114 (1990).

238. Hayashi, H., Tsuneda, S., Hirata, A. & Sasaki, H. Soft particle analysis of bacterial cells and its interpretation of cell adhesion behaviors in terms of DLVO theory. Colloids and Surfaces B: Biointerfaces 22, 149 (2001).

239. Ong, Y.-L., Razatos, A., Georgiou, G. & Sharma, M. M. Adhesion Forces between E. coli Bacteria and Biomaterial Surfaces. Langmuir 15, 2719-2725 (1999).

240. Van Loosdrecht, M. C. M., Norde, W. & Zehnder, A. J. B. Physical Chemical Description of Bacterial Adhesion. J Biomater Appl 5, 91-106 (1990).

241. Emerson, R. J. & Camesano, T. A. Nanoscale investigation of pathogenic microbial adhesion to a biomaterial. Appl. Environ. Microbiol. 70, 6012-6022 (2004).

242. Azeredo, J., Visser, J. & Oliveira, R. Exopolymers in bacterial adhesion: interpretation in terms of DLVO and XDLVO theories. Colloids and Surfaces B: Biointerfaces 14, 141 (1999).

243. Meinders, J. M., van der Mei, H. C. & Busscher, H. J. Deposition Efficiency and Reversibility of Bacterial Adhesion under Flow. Journal of Colloid and Interface Science 176, 329 (1995).

244. Poortinga, A. T., Bos, R., Norde, W. & Busscher, H. J. Electric double layer interactions in bacterial adhesion to surfaces. Surface Science Reports 47, 1 (2002).

245. Theil, H. Principles of Econometrics (Wiley; 1st edition, New York, 1971).

246. Schoff, C. K. & Morfesis, A. Zeta potential. Jct Coatingstech 4, 64-64 (2007).

247. Smoluchowski, V. M. v. Drei vortraege ueber diffusion, brownsche molekularbewegun und koagulation von kolloidtielchen. Physik. Zeitschr. 37, 557-570 (1916).
248. Matei, G. A., Thoreson, E. J., Pratt, J. R., Newell, D. B. & Burnham, N. A. Precision and accuracy of thermal calibration of atomic force microscopy cantilevers. Rev. Sci. Instrum. 77, 083703 (2006).
249. Lu, S. Q., Ye, Z. Y., Zhu, C. & Long, M. Quantifying the effects of contact duration, loading rate, and approach velocity on P-selectin-PSGL-1 interactions using AFM. Polymer 47, 2539-2547 (2006).
250. A I Kiprianov, G. G. D. a. F. A. M. The Colour of Dyes and Steric Hindrance in their Molecules. Russ. Chem. Rev. 35, 361 (1966).
251. Alexander, S. Adsorption of chain molecules with a polar head a scaling description. J. Physique 38, 983-987 (1977).
252. Degennes, P. G. Polymers At An Interface - A Simplified View. Advances In Colloid And Interface Science 27, 189-209 (1987).
253. Butt, H. J., Kappl, M., Mueller, H., Raiteri, R., Meyer, W. & Ruhe, J. Steric forces measured with the atomic force microscope at various temperatures. Langmuir 15, 2559-2565 (1999).
254. Yang, W. R., Gooding, J. J. & Hibbert, D. B. Characterisation of gold electrodes modified with self-assembled monolayers of L-cysteine for the adsorptive stripping analysis of copper. Journal Of Electroanalytical Chemistry 516, 10-16 (2001).
255. Dubois, L. H. & Nuzzo, R. G. Synthesis, Structure, and Properties of Model Organic Surfaces. Annual Review of Physical Chemistry 43, 437-463 (1992).
256. Uzarski, J. R., Tannous, A., Morris, J. R. & Mello, C. M. The effects of solution structure on the surface conformation and orientation of a cysteine-terminated antimicrobial peptide cecropin P1. Colloids and Surfaces B: Biointerfaces 67, 157 (2008).
257. Lucklum, R. & Hauptmann, P. The quartz crystal microbalance: mass sensitivity, viscoelasticity and acoustic amplification. Colloids Surf., B 70, 30 (2000).
258. Richter, R. P. & Brisson, A. QCM-D on mica for parallel QCM-D-AFM studies. Langmuir 20, 4609-4613 (2004).
259. Richter, R. P. & Brisson, A. R. Following the formation of supported lipid bilayers on mica: A study combining AFM, QCM-D, and ellipsometry. Biophys. J. 88, 3422-3433 (2005).
260. Richter, R. P., Him, J. L. K., Tessier, B., Tessier, C. & Brisson, A. R. On the kinetics of adsorption and two-dimensional self-assembly of annexin A5 on supported lipid bilayers. Biophysical Journal 89, 3372-3385 (2005).
261. Sedin, D. L. & Rowlen, K. L. Influence of tip size on AFM roughness measurements. Appl. Surf. Sci. 182, 40 (2001).
262. Browne, M. M., Lubarsky, G. V., Davidson, M. R. & Bradley, R. H. Protein adsorption onto polystyrene surfaces studied by XPS and AFM. Surf. Sci. 553, 155 (2004).

263. Muller, B., Riedel, M., Michel, R., De Paul, S. M., Hofer, R., Heger, D. *et al.* Impact of nanometer-scale roughness on contact-angle hysteresis and globulin adsorption. J. Vac. Sci. Technol., B 19, 1715 (2001).
264. Bottone, E. J. Yersinia enterocolitica: the charisma continues. Clin. Microbiol. Rev. 10, 257-276 (1997).
265. Royston, J. P. Some techniques for assessing multivarate normality based on the Shapiro- Wilk W. Appl. Stat. 32, 121-133 (1983).
266. Shapiro, S. S., Wilk, M. B. & Chen, H. J. A comparative study of various tests for normality. J. Am. Stat. Assoc. 63, 1343-1372 (1968).
267. D'Agostino, R. B., Belanger, A. & D'Agostino, R. B., Jr. A suggestion for using powerful and informative tests of normality. Am. Stat. 44, 316-321 (1990).
268. Auerbach, I. D., Sorensen, C., Hansma, H. G. & Holden, P. A. Physical morphology and surface properties of unsaturated *Pseudomonas putida* biofilms. J. Bacteriol. 182, 3809-3815 (2000).
269. van der Aa, B. C. & Dufrêne, Y. F. In situ characterization of bacterial extracellular polymeric substances by AFM. Colloids Surf., B 23, 173 (2002).
270. Dufrêne, Y. F. Application of atomic force microscopy to microbial surfaces: from reconstituted cell surface layers to living cells. Micron. 32, 153 (2001).
271. Xiao, X. & Qian, L. Investigation of humidity-dependent capillary force. Langmuir 16, 8153-8158 (2000).
272. Camesano, T. A. & Logan, B. E. Probing bacterial electrosteric interactions using atomic force microscopy. Environ. Sci. Technol. 34, 3354-3362 (2000).
273. Strauss, J., Burnham, N. A. & Camesano, T. A. Probing role of LPS O-antigen on *E. coli* adhesion using atomic force microscopy. Journal of Molecular Recognition (Submitted for publication).
274. White, S. H. & Wimley, W. C. Hydrophobic interactions of peptides with membrane interfaces. BBA 1376, 339 (1998).
275. Strauss, J. A., Liu, Y., Milkani, E., McGimpsey, W. G. & Camesano, T. A. Retention and Viability of Staphlyococcus epidermidis on Protein-Coated Self-Assembled Monolayers. ACS symposium series 984 (2008).
276. Johansson, Å. & Stafström, S. Interactions between molecular wires and a gold surface. Chem. Phys. Lett. 322, 301 (2000).
277. Levy, R., Thanh, N. T. K., Doty, R. C., Hussain, I., Nichols, R. J., Schiffrin, D. J. *et al.* Rational and combinatorial design of peptide capping Ligands for gold nanoparticles. J. Am. Chem. Soc. 126, 10076-10084 (2004).
278. Hager, G. & Brolo, A. G. Adsorption/desorption behaviour of cysteine and cystine in neutral and basic media: electrochemical evidence for differing thiol and disulfide adsorption to a Au(1 1 1) single crystal electrode. J. Electroanal. Chem. 550-551, 291 (2003).
279. Quek, S. Y., Venkataraman, L., Choi, H. J., Louie, S. G., Hybertsen, M. S. & Neaton, J. B. Amine-gold linked single-molecule circuits: experiment and theory. Nano Lett. 7, 3477-3482 (2007).
280. Westcott, S. L., Oldenburg, S. J., Lee, T. R. & Halas, N. J. Construction of simple gold nanoparticle aggregates with controlled plasmon-plasmon interactions. Chem. Phys. Lett. 300, 651 (1999).

281. Emrick*, T. & Fréchet, J. M. J. Self-assembly of dendritic structures. Current Opinion in Colloid & Interface Science 4, 15 (1999).
282. Roddick-Lanzilotta, A. D. & McQuillan, A. J. An in situ infrared spectroscopic investigation of lysine peptide and polylysine adsorption to TiO2 from aqueous solutions. J. Colloid Interface Sci. 217, 194 (1999).
283. Uptima. (Mongiucon Cedex, 2008).
284. Burns, J. A., Butler, J. C., Moran, J. & Whitesides, G. M. Selective reduction of disulfides by Tris(2-Carboxyethyl)Phosphine. J. Org. Chem. 56, 2648-2650 (1991).
285. Kizek, R., Vacek, J., Trnková, L. & Jelen, F. Cyclic voltammetric study of the redox system of glutathione using the disulfide bond reductant tris(2-carboxyethyl)phosphine. Bioelectrochemistry 63, 19 (2004).
286. Ludtke, S. J., He, K., Heller, W. T., Harroun, T. A., Yang, L. & Huang, H. W. Membrane pores induced by magainin. Biochem. 35, 13723-13728 (1996).
287. Chatterjee, C. & Gerig, J. T. Interactions of trifluroethanol with the Trp-cage peptide. Biopolymers 87, 115-123 (2007).
288. Gazit, E., Miller, I. R., Biggin, P. C., Sansom, M. S. P. & Shai, Y. Structure and orientation of the mammalian antibacterial peptide cecropin P1 within phospholipid membranes. J. Mol. Biol. 258, 860 (1996).
289. Luo, P. & Baldwin, R. L. Mechanism of helix induction by trifluoroethanol: A framework for extrapolating the helix-forming properties of peptides from trifluoroethanol/water mixtures back to water. Biochem. 36, 8413-8421 (1997).
290. Hwang, S., Kim, E. & Kwak, J. Electrochemical detection of DNA hybridization using biometallization. Anal. Chem. 77, 579-584 (2005).
291. Bechinger, B., Zasloff, M. & Opella, S. J. Structure and orientation of the antibiotic peptide magainin in membranes by solid-state nuclear magnetic resonance spectroscopy. Protein Sci. 2, 2077-2084 (1993).
292. Chia, C. S. B., Torres, J., Cooper, M. A., Arkin, I. T. & Bowie, J. H. The orientation of the antibiotic peptide maculatin 1.1 in DMPG and DMPC lipid bilayers. Support for a pore-forming mechanism. FEBS Letters 512, 47 (2002).
293. Noronha, M., Lima, J. C., Lamosa, P., Santos, H., Maycock, C., Ventura, R. *et al.* Intramolecular fluorescence quenching of tyrosine by the peptide α-carbonyl group revisited. J. Phys. Chem. A 108, 2155-2166 (2004).
294. Kypr, J., Chladkova, J., Zimulova, M. & Vorlickova, M. Aqueous trifluorethanol solutions simulate the environment of DNA in the crystalline state. Nucleic Acids Res. 27, 3466-3473 (1999).
295. Ulrich, H. E. H. Generalized-ensemble simulations of the human parathyroid hormone fragment PTH(1-34). J. Chem. Phys. 120, 417-422 (2004).
296. Marx, U. C., Adermann, K., Bayer, P., Forssmann, W.-G. & Rösch, P. Solution structures of human parathyroid hormone fragments hPTH(1-34) and hPTH(1-39) and bovine parathyroid hormone fragment bPTH(1-37). Biochem. Biophys. Res. Commun. 267, 213 (2000).
297. Lee, A. G. Lipid-protein interactions in biological membranes: a structural perspective. BBA 1612, 1 (2003).

298. Rietschel, E. T., Kirikae, T., Schade, F. U., Mamat, U., Schmidt, G., Loppnow, H. *et al.* Bacterial endotoxin: molecular relationships of structure to activity and function. FASEB J. 8, 217-225 (1994).

299. Kastowsky, M., Gutberlet, T. & Bradaczek, H. Molecular modelling of the three-dimensional structure and conformational flexibility of bacterial lipopolysaccharide. J. Bacteriol. 174, 4798-4806 (1992).

300. Johnson, C. P., Fujimoto, I., Rutishauser, U. & Leckband, D. E. Direct evidence that neural cell adhesion molecule (NCAM) polysialylation increases intermembrane repulsion and abrogates adhesion. J. Biol. Chem. 280, 137-145 (2005).

301. Guven, K., Yolcu, M., Gul-Guven, R., Erdogan, S. & De Pomerai, D. The effects of organic pesticides on inner membrane permeability in *Escherichia coli* ML35. Cell Biol. Toxicol. 21, 73-81 (2005).

302. Jucker, B. A., Harms, H., Hug, S. J. & Zehnder, A. J. B. Adsorption of bacterial surface polysaccharides on mineral oxides is mediated by hydrogen bonds. Colloids Surf., B 9, 331-343 (1997).

303. Paton, A. W., Woodrow, M. C., Doyle, R. M., Lanser, J. A. & Paton, J. C. Molecular characterization of a shiga toxigenic *Escherichia coli* O113: H21 strain lacking eae responsible for a cluster of cases of hemolytic-uremic syndrome. J. Clin. Microbiol. 37, 3357-3361 (1999).

304. Phillips, A. D., Navabpour, S., Hicks, S., Dougan, G., Wallis, T. & Frankel, G. Enterohaemorrhagic *Escherichia coli* O157:H7 target Peyer's patches in humans and cause attaching/effacing lesions in both human and bovine intestine. Gut 47, 377-381 (2000).

305. Agin, T. S. & Wolf, M. K. Identification of a family of intimins common to *Escherichia coli* causing attaching-effacing lesions in rabbits, humans, and swine. Infect. Immun. 65, 320-326 (1997).

306. Russo, T. A., Sharma, G., Brown, C. R. & Campagnari, A. A. Loss of the O4 antigen moiety from the lipopolysaccharide of an extraintestinal isolate of *Escherichia coli* has only minor effects on serum sensitivity and virulence in vivo. Infect. Immun. 63, 1263-1269 (1995).

307. Merino, S., Rubires, X., Aguillar, A., Guillot, J. F. & Tomás, J. M. The role of the O-antigen lipopolysaccharide on the colonizationin vivoof the germfree chicken gut byAeromonas hydrophilaserogroup O:34. Microb. Pathogenesis 20, 325 (1996).

308. Guard-Petter, J., Keller, L. H., Rahman, M. M., Carlson, R. W. & Silvers, S. A novel relationship between O-antigen variation, matrix formation, and invasiveness of *Salmonella enteritidis*. Epidemiol. Infection 117, 219-231 (1996).

309. Colin Hughes, R. Galectins as modulators of cell adhesion. Biochimie 83, 667 (2001).

310. Mack, D., Siemssen, N. & Laufs, R. Parallel induction by glucose of adherence and a polysaccharide antigen specific for plastic-adherent *Staphylococcus epidermidis*: evidence for functional relation to intercellular adhesion. Infect. Immun. 60, 2048-2057 (1992).

311. Lasky, L. A. Selectin-carbohydrate interactions and the initiation of the inflammatory response. Annu. Rev. Biochem. 64, 113-140 (1995).

312. Kolenbrander, P. E., Ganeshkumar, N., Cassels, F. J. & Hughes, C. V. Coaggregation: specific adherence among human oral plaque bacteria. FASEB J. 7, 406-413 (1993).

313. Heinrichs, D. E., Monteiro, M. A., Perry, M. B. & Whitfield, C. The assembly system for the lipopolysaccharide R2 core-type of *Escherichia coli* Is a hybrid of those found in *Escherichia coli* K-12 and *Salmonella enterica*. Structure and function of the R2 WaaK and WaaL homologs. J. Biol. Chem. 273, 8849-8859 (1998).

314. Miura, Y., Xu, G.-C., Kimura, S., Kobayashi, S., Iwamoto, M., Imanishi, Y. *et al.* Multilayer formation of oriented helical peptides glued by hydrogen bonding. Thin Solid Films 393, 59 (2001).

315. Phillips, D. C., York, R. L., Mermut, O., McCrea, K. R., Ward, R. S. & Somorjai, G. A. Side chain, chain length, and sequence effects on amphiphilic peptide adsorption at hydrophobic and hydrophilic surfaces studied by sum-frequency generation vibrational spectroscopy and quartz crystal microbalance. J. Phys. Chem. C 111, 255-261 (2007).

316. Hook, F. & Rudh, M. Quartz crystal microbalances (QCM) in biomacromolecular recognition. Mol. Bio. (2005).

317. Griotm, O. & Kitchener, J. A. Role of Surface Silanol Groups in the Flocculation of Silica Suspensions by Polyacrylamide. RSC (1964).

318. Zhuravlev, L. T. Concentration of hydroxyl-groups on the surface of amorphous silicas. Langmuir 3, 316-318 (1987).

319. Boman, H. G., Agerberth, B. & Boman, A. Mechanisms of action on *Escherichia coli* of cecropin-P1 and Pr-39, 2 antibacterial peptides from pig intestine. Infect. Immun. 61, 2978-2984 (1993).

320. Ziv Oren, Y. S. Mode of action of linear amphipathic &agr;-helical antimicrobial peptides. Peptide Science 47, 451-463 (1998).

321. Mecke, A., Lee, D. K., Ramamoorthy, A., Orr, B. G. & Holl, M. M. B. Membrane thinning due to antimicrobial peptide binding: An atomic force microscopy study of MSI-78 in lipid bilayers. Biophys. J. 89, 4043-4050 (2005).

322. Makin, S. A. & Beveridge, T. J. The influence of A-band and B-band lipopolysaccharide on the surface characteristics and adhesion of *Pseudomonas aeruginosa* to surfaces. Microbiology-Uk 142, 299-307 (1996).

323. Miura, Y., Kimura, S., Imanishi, Y. & Umemura, J. Oriented Helical Peptide Layer on the Carboxylate-Terminated Alkanethiol Immobilized on a Gold Surface. Langmuir 15, 1155-1160 (1999).

324. Stenstrom, T. A. Bacterial hydrophobicity, an overall parameter for the measurement of adhesion potential to soil particles. Appl. Environ. Microbiol. 55, 142-147 (1989).

325. Parikh, S. J. & Chorover, J. Infrared spectroscopy studies of cation effects on lipopolysaccharides in aqueous solution. Colloids And Surfaces B-Biointerfaces 55, 241-250 (2007).

326. Soares, T. A., Straatsma, T. P. & Lins, R. D. Influence of the B-band O-antigen chain in the structure and electrostatics of the lipopolysaccharide membrane of Pseudomonas aeruginosa. Journal Of The Brazilian Chemical Society 19, 312-320 (2008).

327. Paton, A. W. & Paton, J. C. Molecular Characterization of the Locus Encoding Biosynthesis of the Lipopolysaccharide O Antigen of Escherichia coli Serotype O113. Infect. Immun. 67, 5930-5937 (1999).

328. Jucker, B. A., Harms, H. & Zehnder, A. J. B. Polymer interactions between five gram-negative bacteria and glass investigated using LPS micelles and vesicles as model systems. Colloids Surf., B 11, 33-45 (1998).

329. Shai, Y. Molecular recognition between membrane-spanning polypeptides. Trends in Biochemical Sciences 20, 460 (1995).

330. Fattal, D. R. & Ben-Shaul, A. A molecular model for lipid-protein interaction in membranes: the role of hydrophobic mismatch. Biophys. J. 65, 1795-1809 (1993).

331. Ambroggio, E. E., Separovic, F., Bowie, J. & Fidelio, G. D. Surface behaviour and peptide-lipid interactions of the antibiotic peptides, Maculatin and Citropin. BBA 1664, 31 (2004).

332. Ladokhin, A. S. & White, S. H. Folding of amphipathic [alpha]-helices on membranes: energetics of helix formation by melittin. J. Mol. Biol. 285, 1363 (1999).

333. Heerklotz, H. & Seelig, J. Detergent-like action of the antibiotic peptide surfactin on lipid membranes. Biophys. J. 81, 1547-1554 (2001).

334. Seelig, J. Thermodynamics of lipid-peptide interactions. BBA 1666, 40 (2004).

335. Li, J. & McLandsborough, L. A. The effects of the surface charge and hydrophobicity of *Escherichia coli* on its adhesion to beef muscle. Int. J. Food Microbiol. 53, 185 (1999).

336. Hassan, A. N. & Frank, J. F. Attachment of *Escherichia coli* O157:H7 grown in tryptic soy broth and nutrient broth to apple and lettuce surfaces as related to cell hydrophobicity, surface charge, and capsule production. Int. J. Food Microbiol. 96, 103 (2004).

337. Busscher, H. J., Dijkstra, R. J. B., Langworthy, D. E., Collias, D. I., Bjorkquist, D. W., Mitchell, M. D. *et al.* Interaction forces between waterborne bacteria and activated carbon particles. J. Colloid Interface Sci. 322, 351 (2008).

338. Soni, K. A., Balasubramanian, A. K., Beskok, A. & Pillai, S. D. Zeta potential of selected bacteria in drinking water when dead, starved, or exposed to minimal and rich culture media. Curr. Microbiol. 56, 93-97 (2008).

339. DeGray, G., Rajasekaran, K., Smith, F., Sanford, J. & Daniell, H. Expression of an Antimicrobial Peptide via the Chloroplast Genome to Control Phytopathogenic Bacteria and Fungi. Plant Physiol. 127, 852-862 (2001).

340. Philippe Bulet, R. S. L. M. Anti-microbial peptides: from invertebrates to vertebrates. Immunological Reviews 198, 169-184 (2004).

341. Rohlfing, S. R. & Crawford, I. P. Purification and characterization of the {beta}-Galactosidase of *Aeromonas formicans*. J. Bacteriol. 91, 1085-1097 (1966).
342. Fowler, A. V., Zabin, I. & with the technical assistance of Karin, P. The Amino Acid Sequence of {beta}-Galactosidase. Isolation and composition of tryptic peptides. J. Biol. Chem. 245, 5032-5041 (1970).
343. Lamb, S. B. & Stuckey, D. C. Enzyme immobilization on colloidal liquid aphrons (CLAs): the influence of system parameters on activity. Enzyme Microb. Technol. 26, 574 (2000).
344. Razatos, A., Ong, Y. L., Sharma, M. M. & Georgiou, G. Evaluating the interaction of bacteria with biomaterials using atomic force microscopy. Journal Of Biomaterials Science-Polymer Edition 9, 1361-1373 (1998).
345. Razatos, A., Ong, Y. L., Sharma, M. M. & Georgiou, G. Molecular determinants of bacterial adhesion monitored by atomic force microscopy. Proceedings Of The National Academy Of Sciences Of The United States Of America 95, 11059-11064 (1998).
346. Walker, S. L., Redman, J. A. & Elimelech, M. Role of cell surface lipopolysaccharides in *Escherichia coli* K12 adhesion and transport. Langmuir 20, 7736-7746 (2004).
347. Horinek, D., Serr, A., Geisler, M., Pirzer, T., Slotta, U., Lud, S. Q. *et al.* Peptide adsorption on a hydrophobic surface results from an interplay of solvation, surface, and intrapeptide forces. Proc. Nat. Acad. Sci. U. S. A. 105, 2842-2847 (2008).
348. Fulladosa, E., J.C. Murat, and I. Villaescusa. Effect of cadmium (II), chromium (VI), and arsenic (V) on long-term viability- and growth-inhibition assays using *Vibrio fischeri* marine bacteria. Arch. Environ. Contam. Toxicol. 49, 299-306 (2005).
349. Wilson, C. L., Ouellette, A. J., Satchell, D. P., Ayabe, T., oacute, pez-Boado, Y. S. *et al.* Regulation of intestinal -defensin activation by the metalloproteinase matrilysin in innate host defense. Science 286, 113-117 (1999).
350. Zhang, L., Yu, W., He, T., Yu, J., Caffrey, R. E., Dalmasso, E. A. *et al.* Contribution of Human alpha -Defensin 1, 2, and 3 to the Anti-HIV-1 Activity of CD8 Antiviral Factor. Science 298, 995-1000 (2002).
351. Dempsey, C. E. The actions of melittin on membranes. BBA 1031, 143 (1990).
352. Ambroggio, E. E., Separovic, F., Bowie, J. H., Fidelio, G. D. & Bagatolli, L. A. Direct visualization of membrane leakage induced by the antibiotic peptides: Maculatin, Citropin, and Aurein. Biophys. J. 89, 1874-1881 (2005).
353. Lai, R., Zheng, Y.-T., Shen, J.-H., Liu, G.-J., Liu, H., Lee, W.-H. *et al.* Antimicrobial peptides from skin secretions of Chinese red belly toad Bombina maxima. Peptides 23, 427 (2002).
354. Lee, J.-Y., Boman, A., Chuanxin, S., Andersson, M., Jornvall, H., Mutt, V. *et al.* Antibacterial peptides from pig intestine: Isolation of a mammalian cecropin. Proc. Nat. Acad. Sci. U. S. A. 86, 9159-9162 (1989).

9: Appendices

Appendix A: Ethanol Calibration Graphs

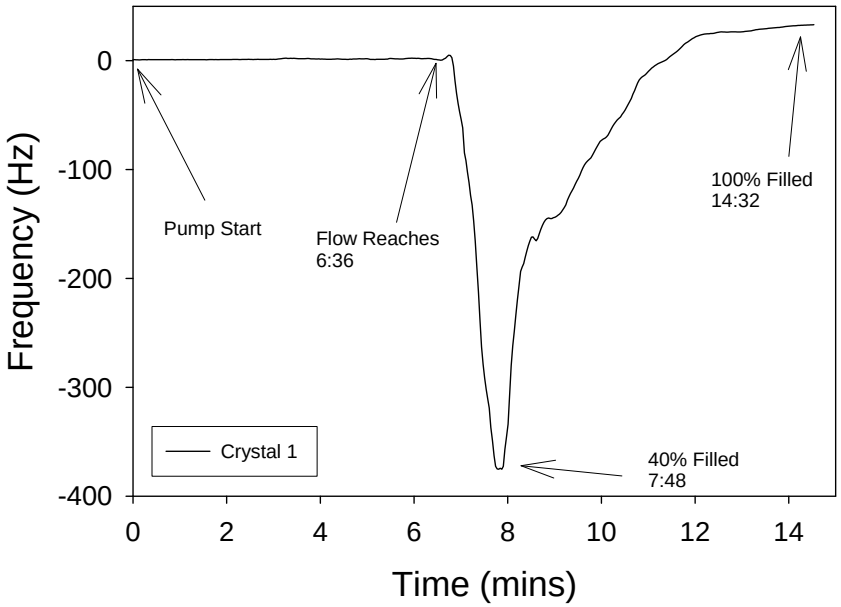

Figure 9.1 50 µl per min ethanol flow rate

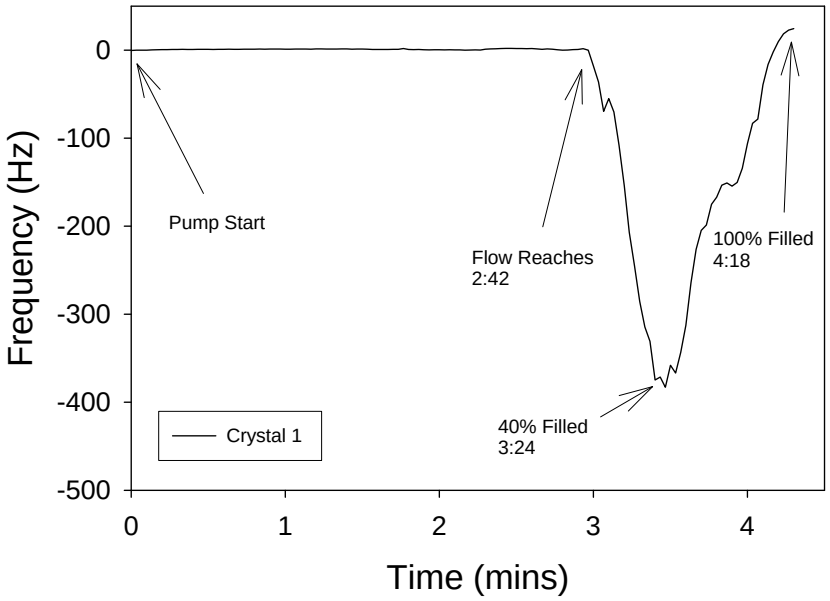

Figure 9.2 100 µl per min ethanol flow rate

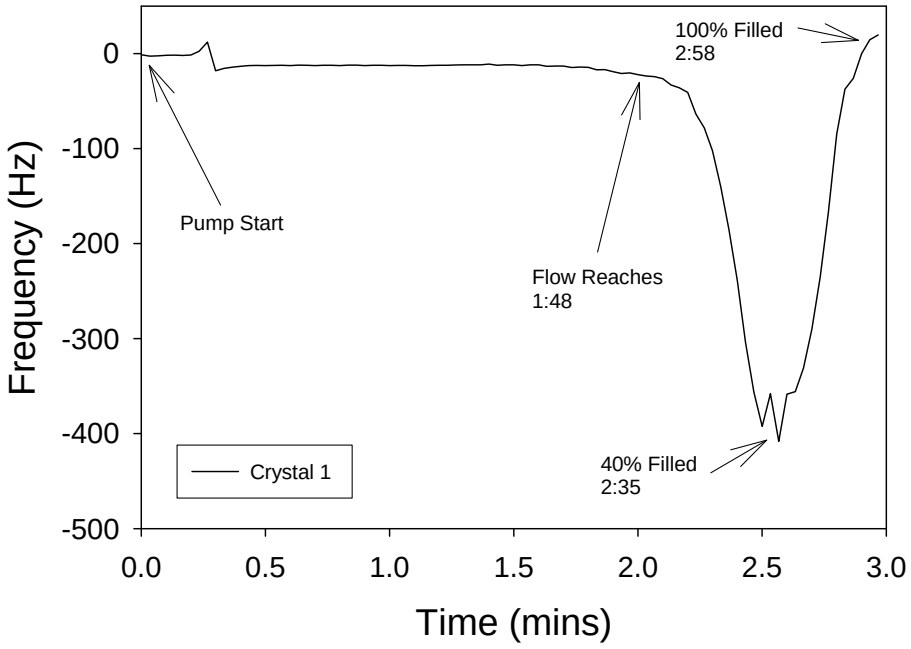

Figure 9.3 150 µl per min ethanol flow rate

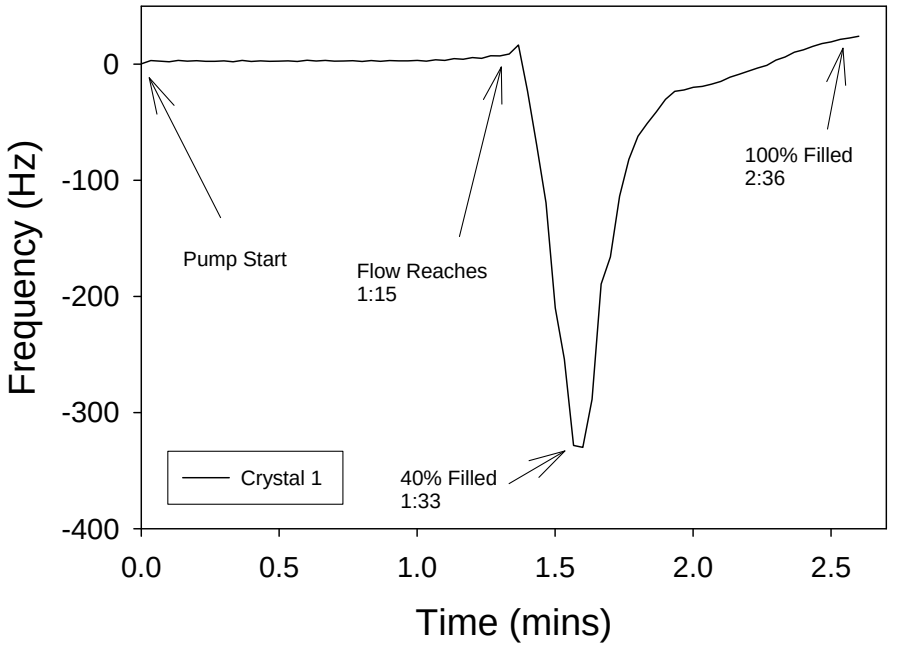

Figure 9.4 200 µl per min ethanol flow rate

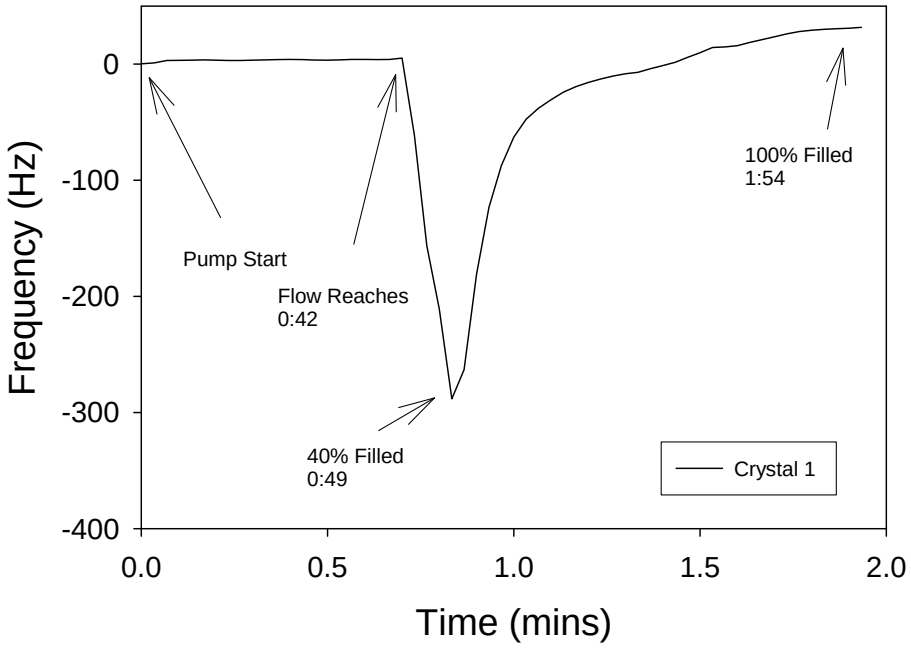

Figure 9.5 400 µl per min ethanol flow rate

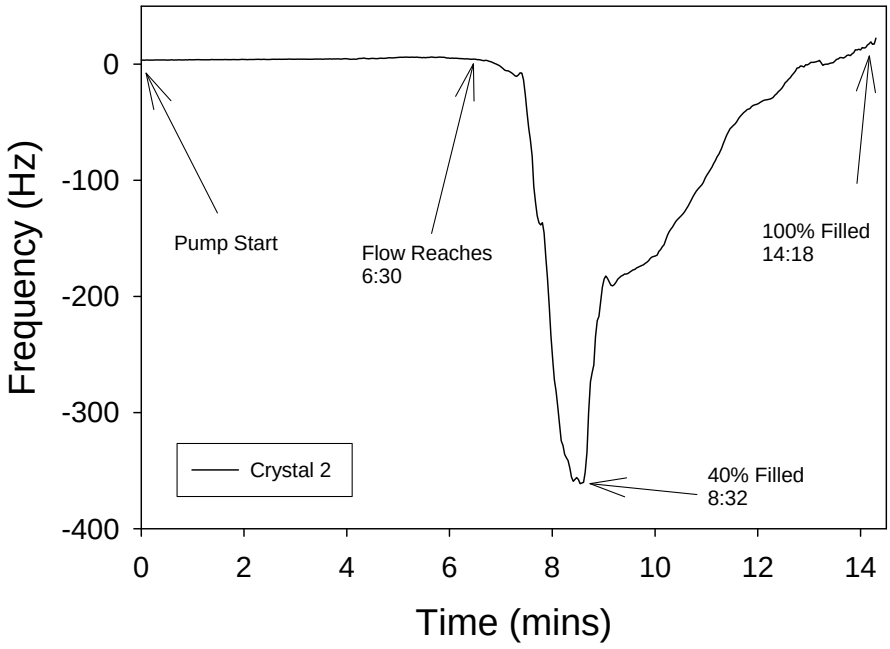

Figure 9.6 50 µl per min ethanol flow rate

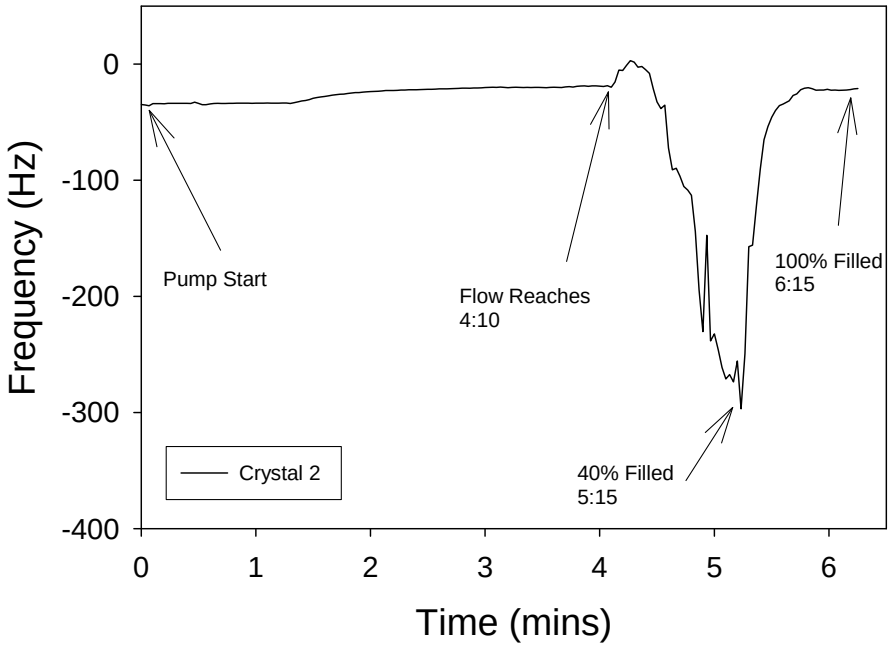

Figure 9.7 100 µl per min ethanol flow rate

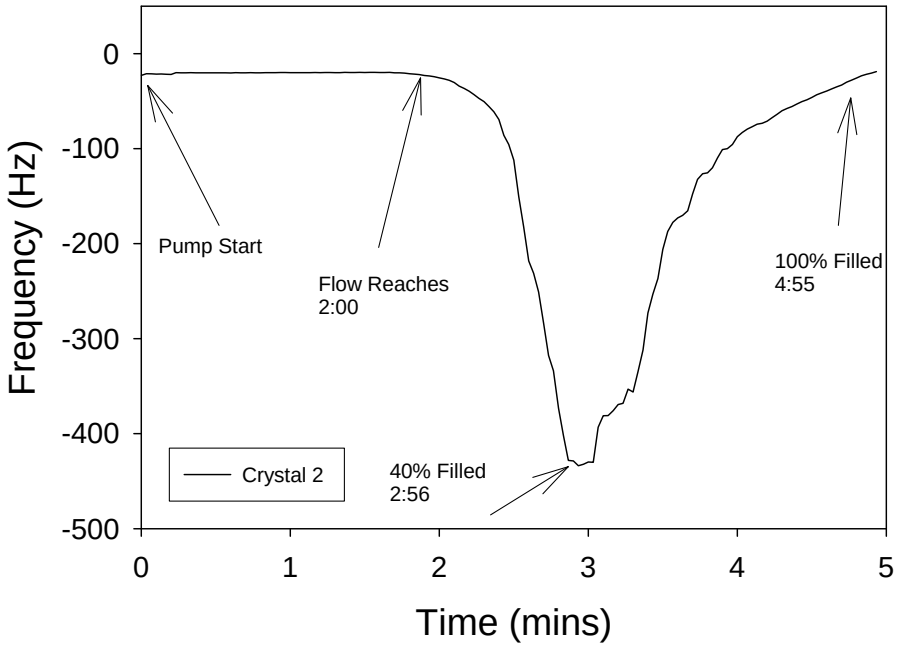

Figure 9.8 150 µl per min ethanol flow rate

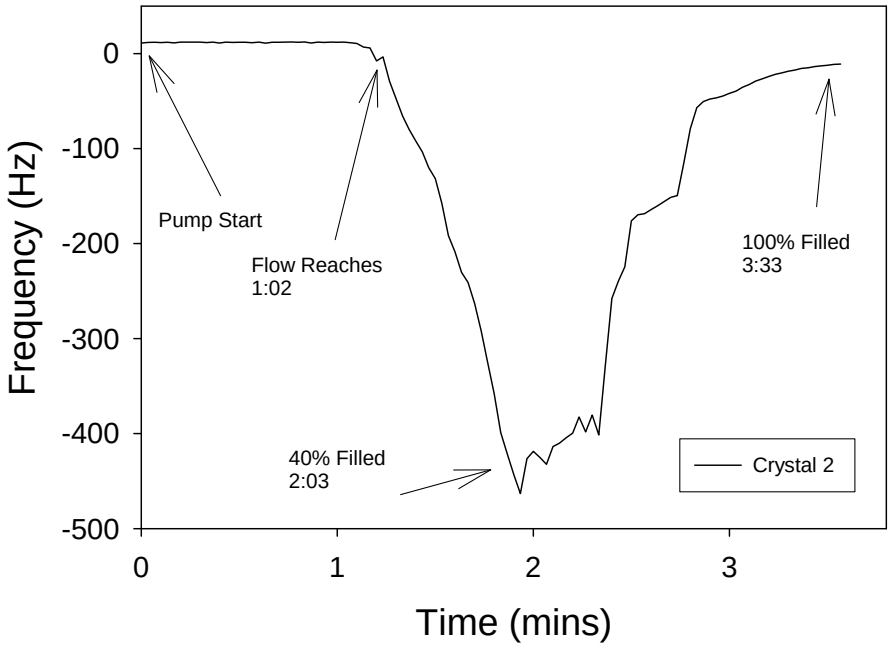

Figure 9.9 200 µl per min ethanol flow rate

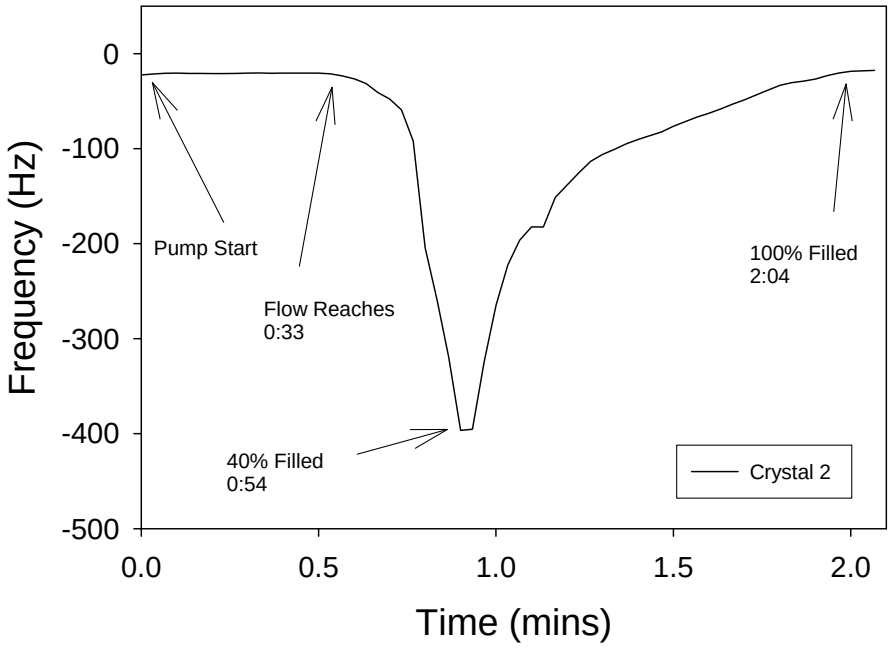

Figure 9.10 400 µl per min ethanol flow rate

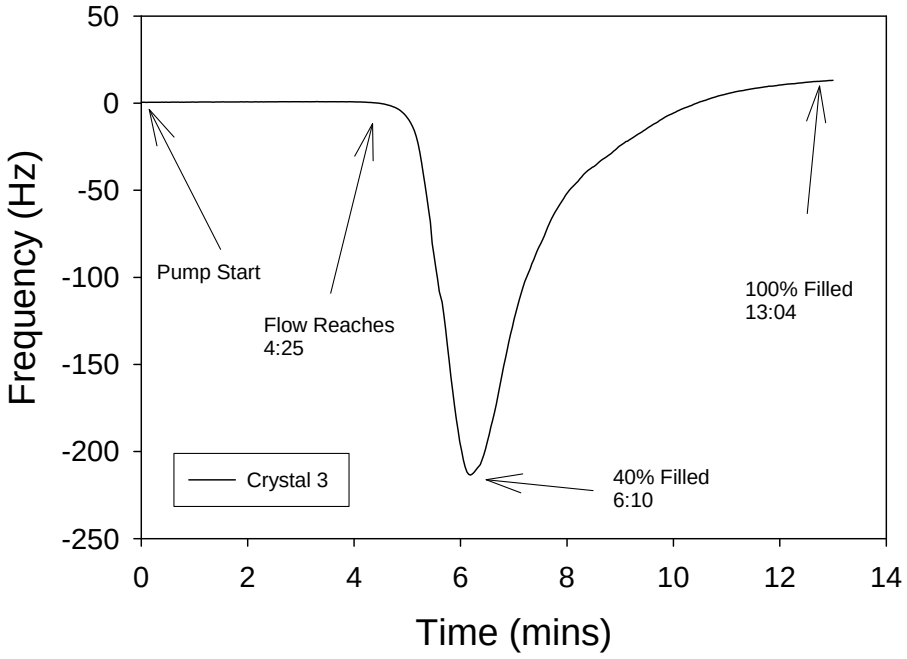

Figure 9.11 50 µl per min ethanol flow rate

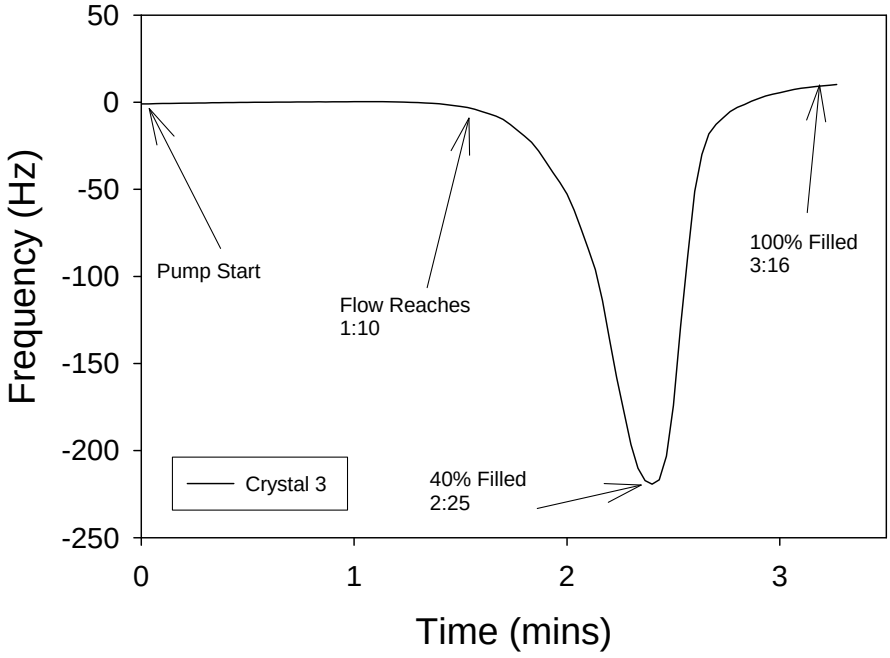

Figure 9.12 100 µl per min ethanol flow rate

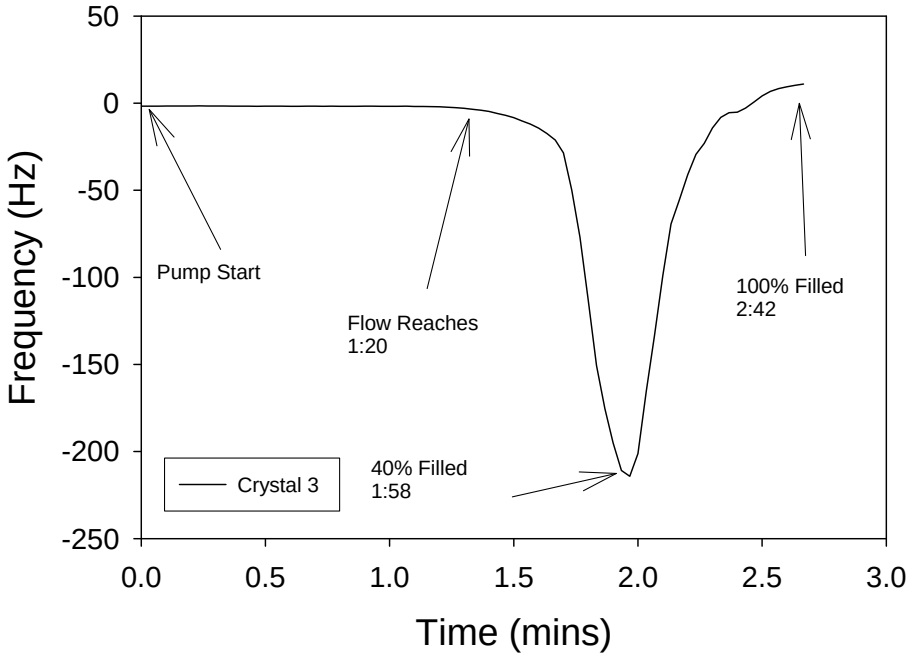

Figure 9.13 150 µl per min ethanol flow rate

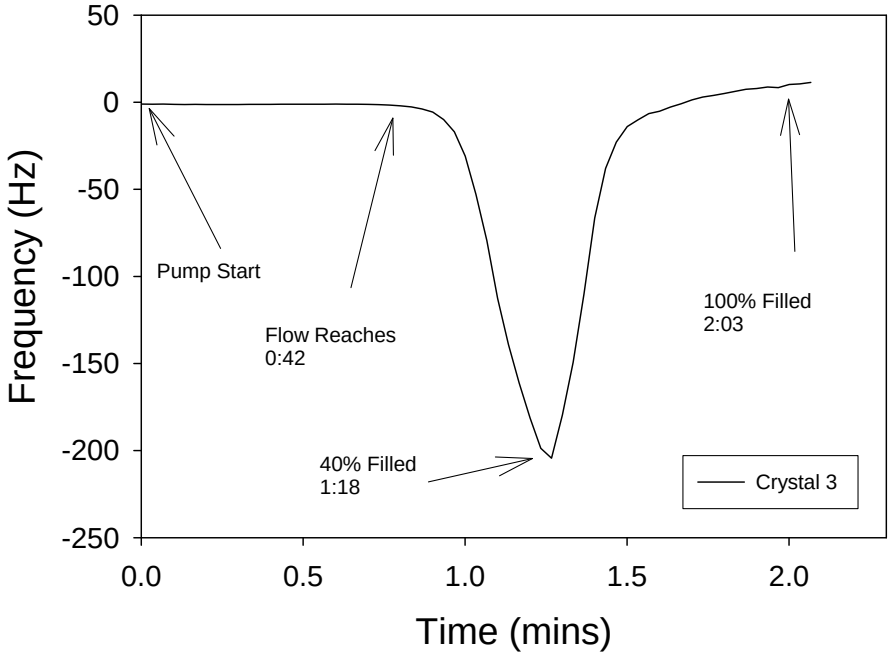

Figure 9.14 200 µl per min ethanol flow rate

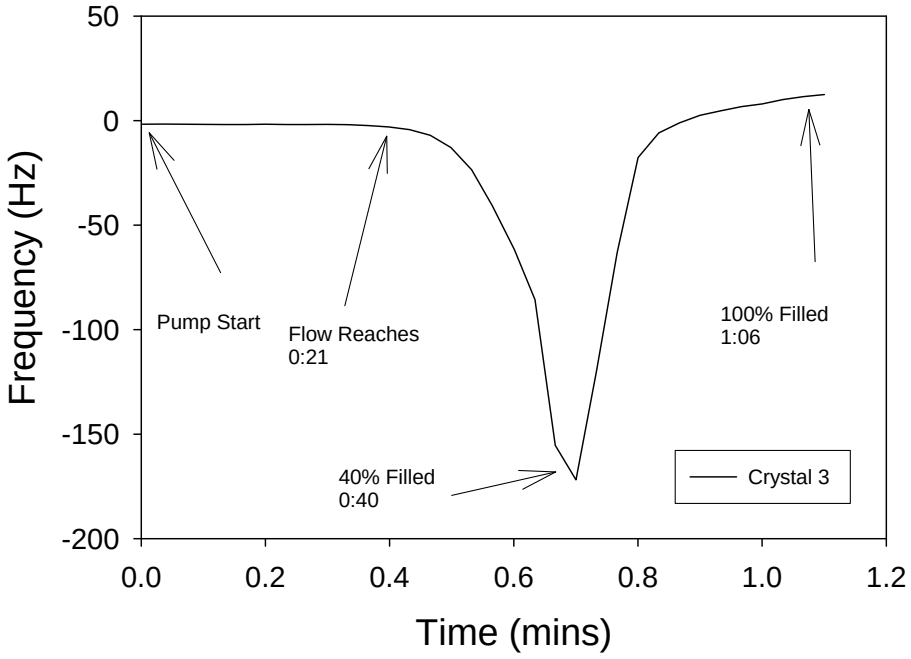

Figure 9.15 400 µl per min ethanol flow rate

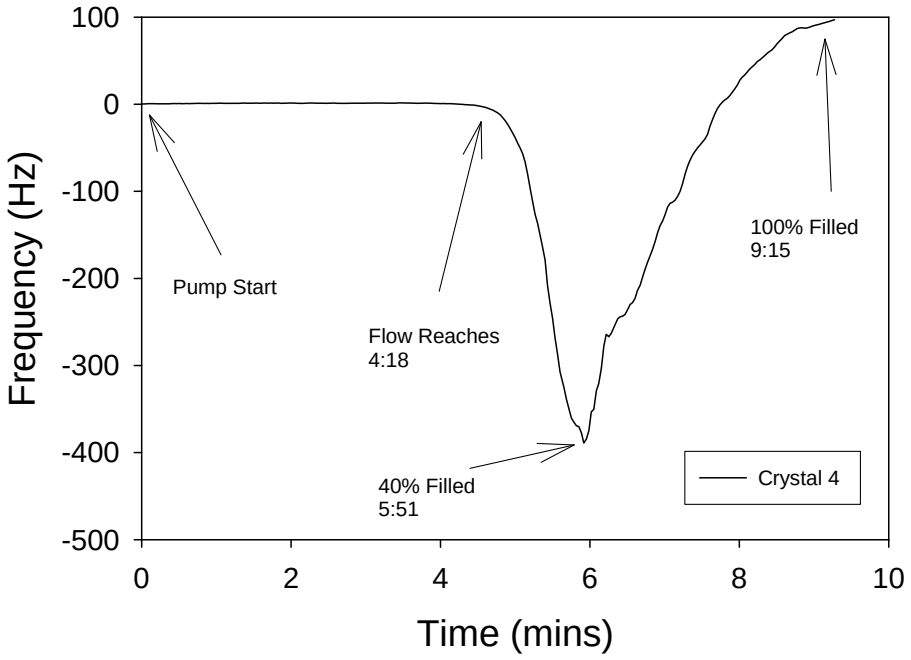

Figure 9.16 50 µl per min ethanol flow rate

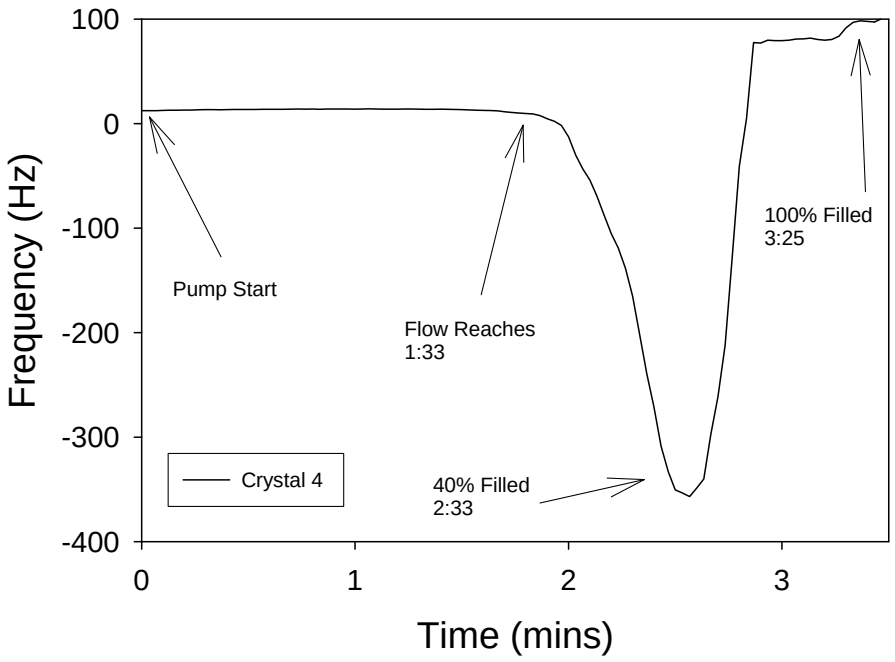

Figure 9.17 100 µl per min ethanol flow rate

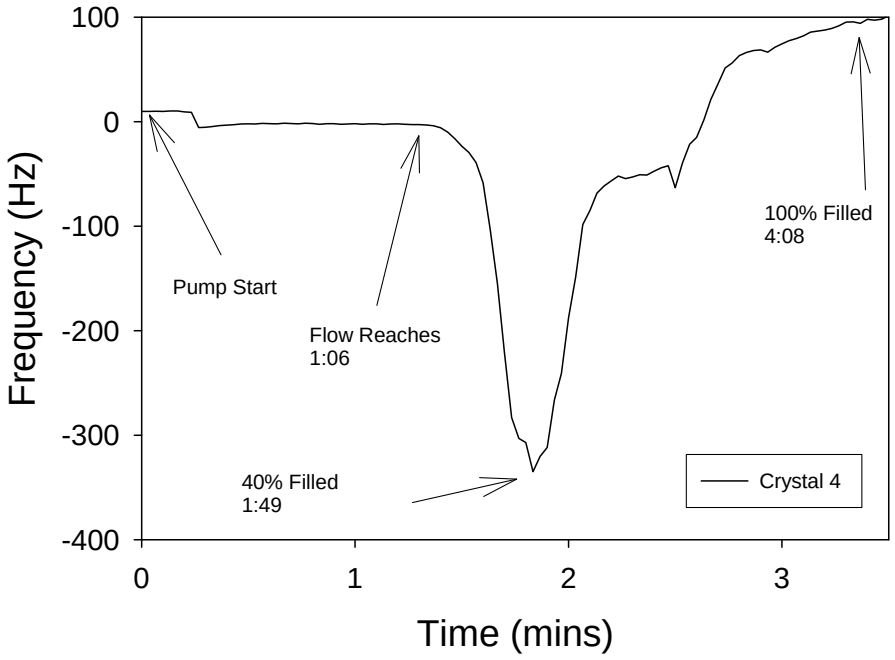

Figure 9.18 150 µl per min ethanol flow rate

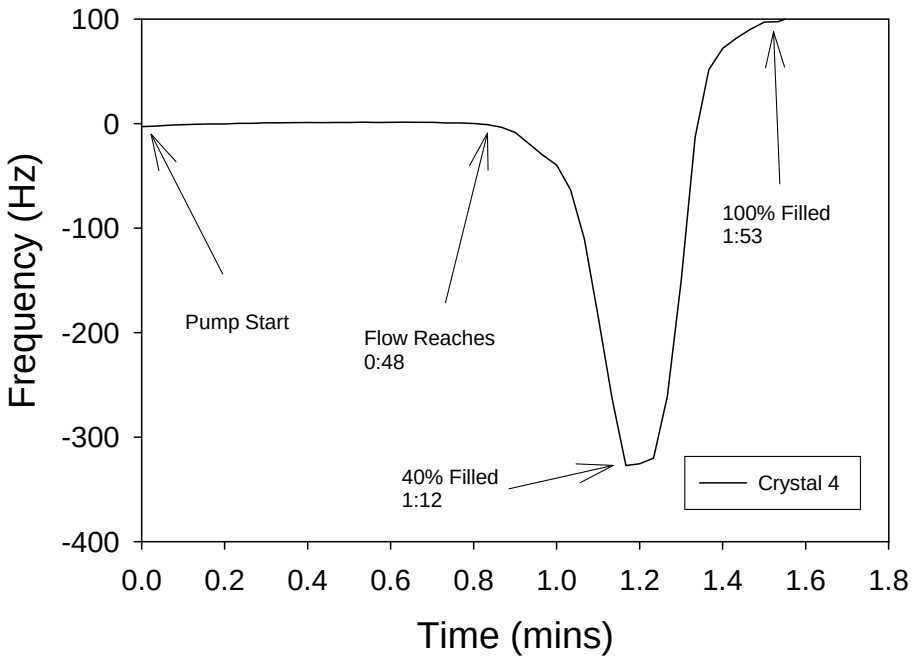

Figure 9.19 200 µl per min ethanol flow rate

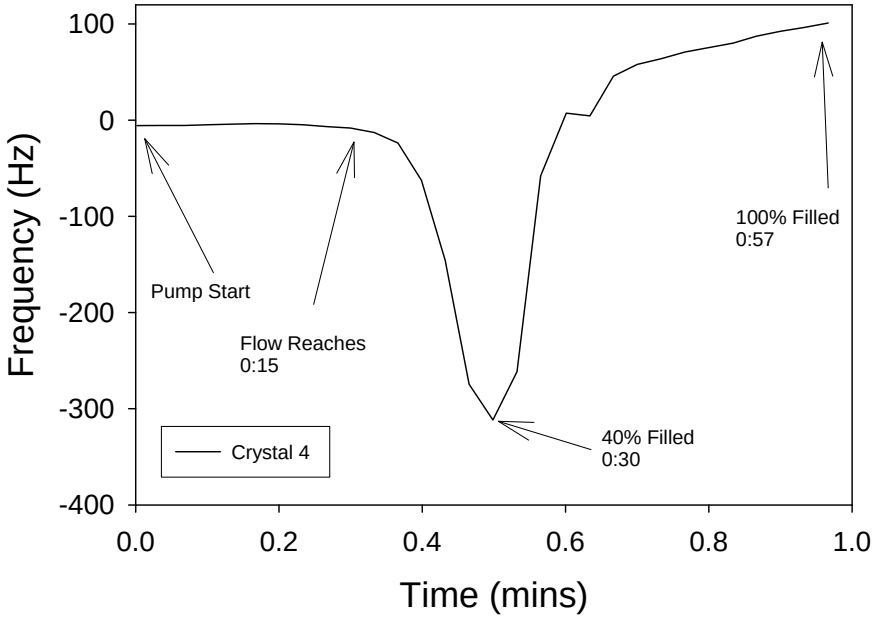

Figure 9.20 400 µl per min ethanol flow rate

Appendix B: FBS Adsorption Graphs

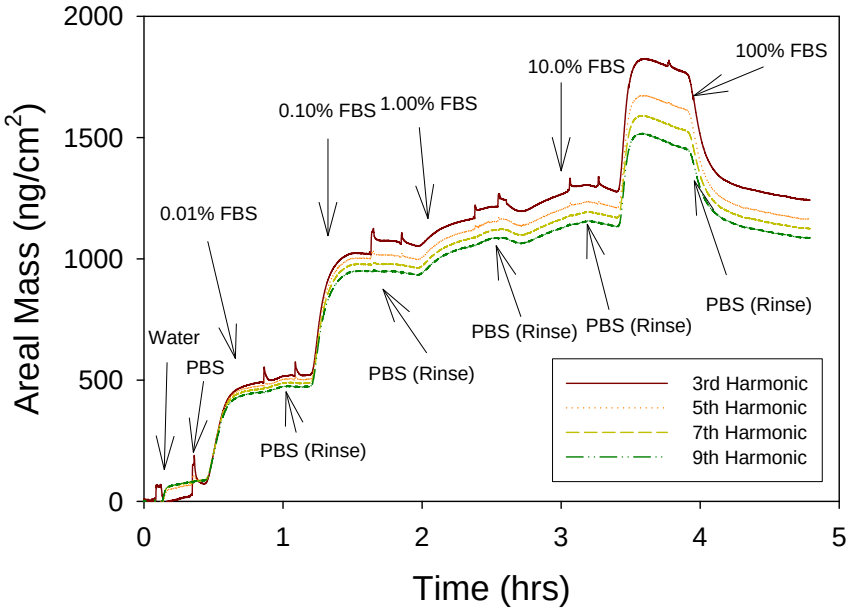

Figure 9.21 Crystal 1 FBS Adsorption

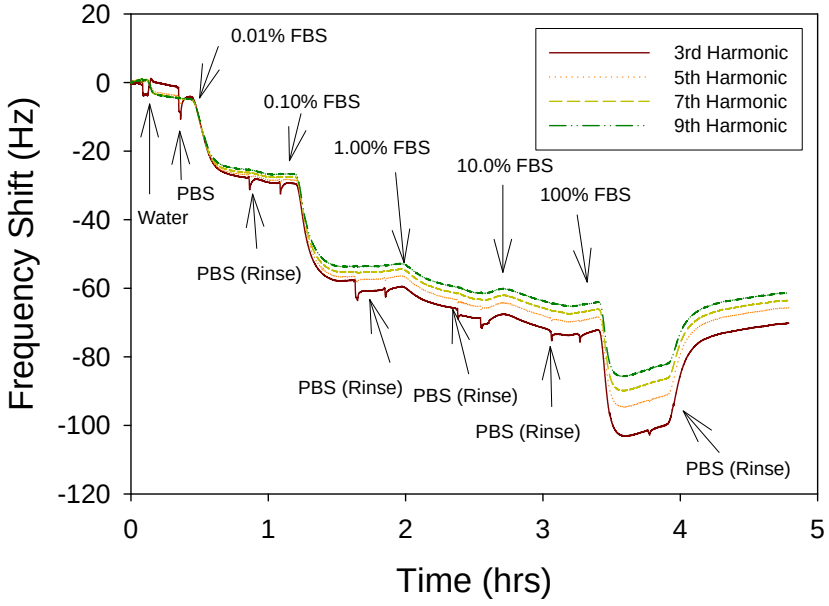

Figure 9.22 Crystal 1 FBS Adsorption

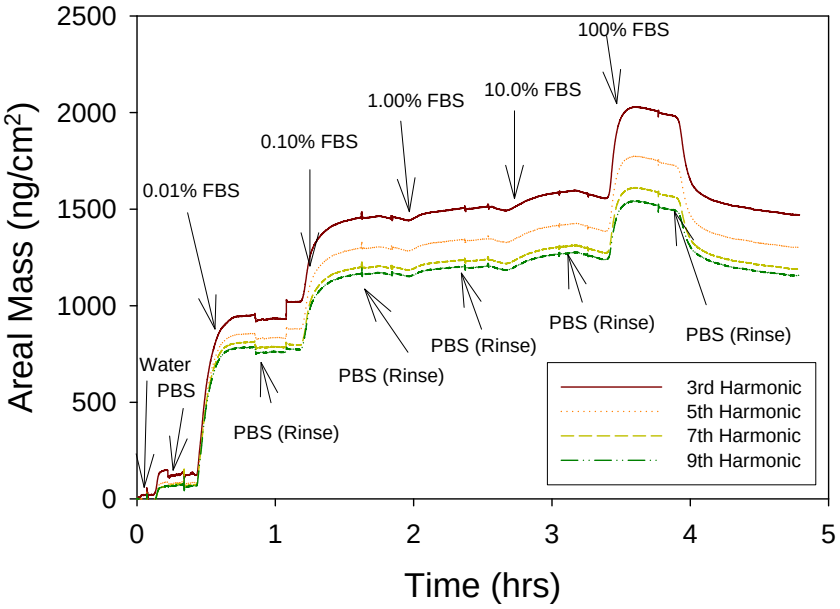

Figure 9.23 Crystal 2 FBS Adsorption

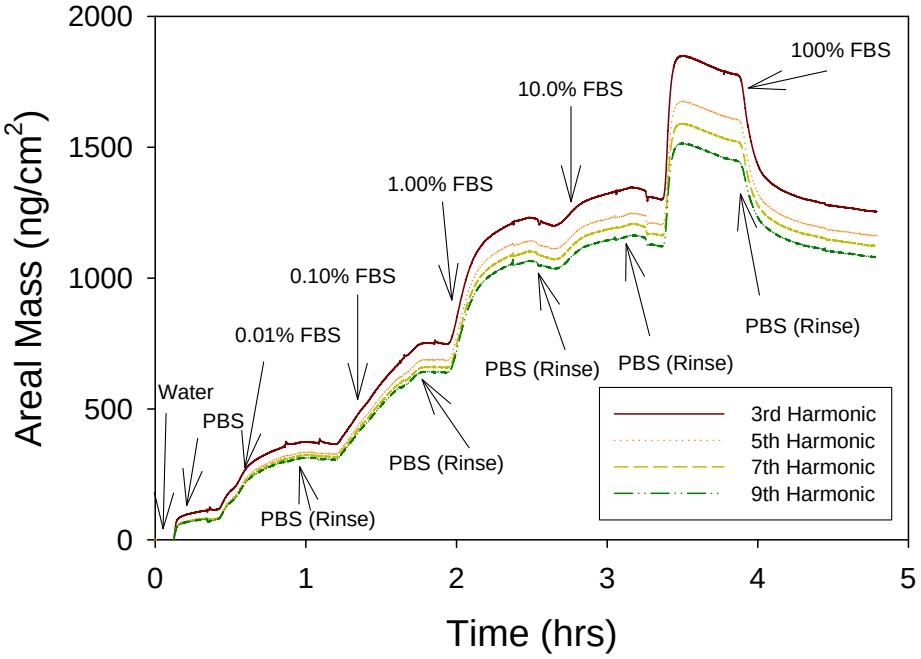

Figure 9.24 Crystal 3 FBS Adsorption

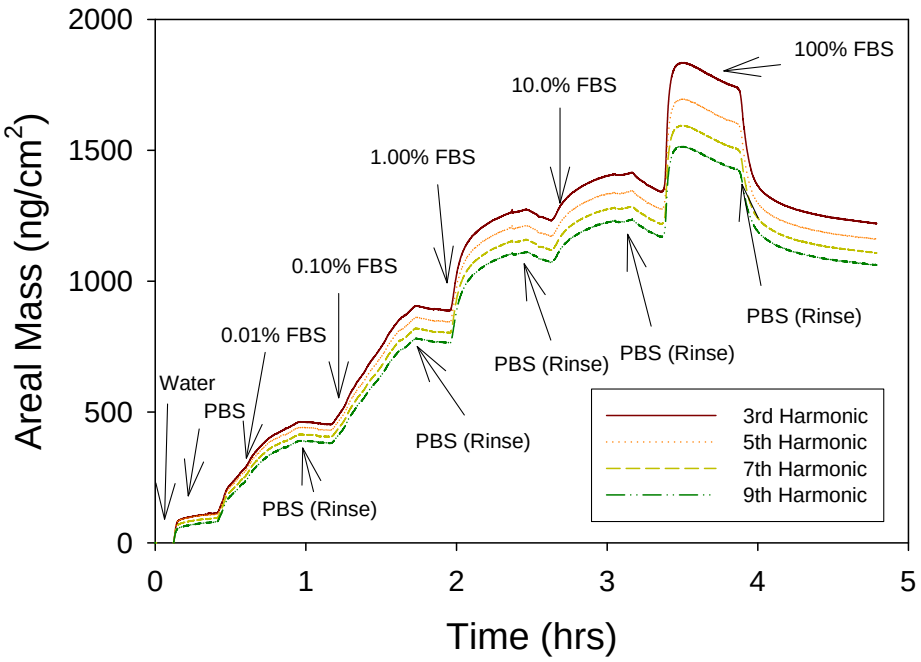

Figure 9.25 Crystal 4 FBS Adsorption

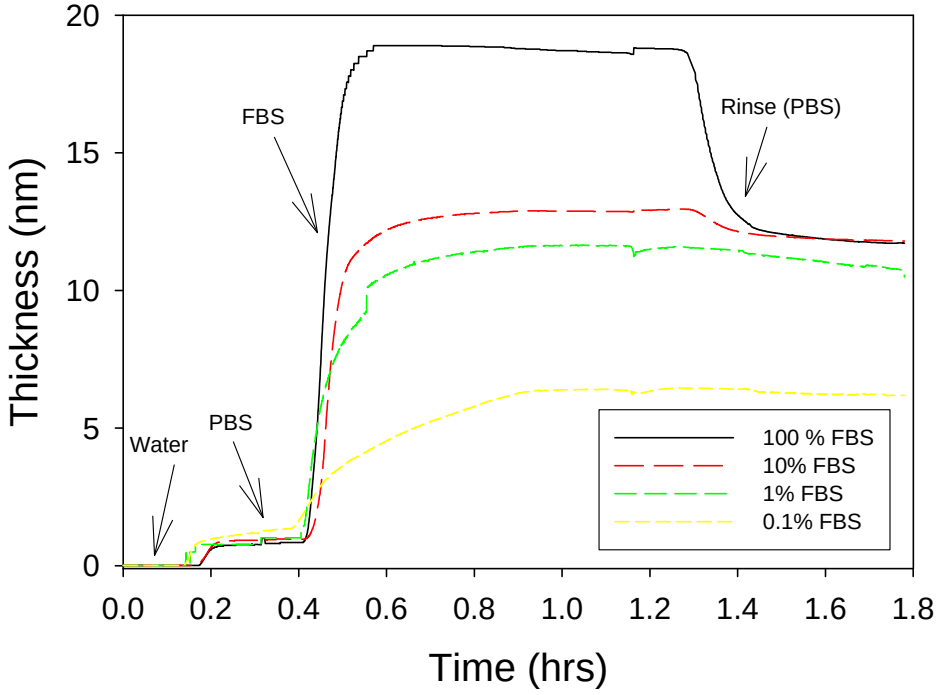

Figure 9.26 Thickness modeling of parallel QCM-D experiments with FBS. Results also analyzed with the AFM.

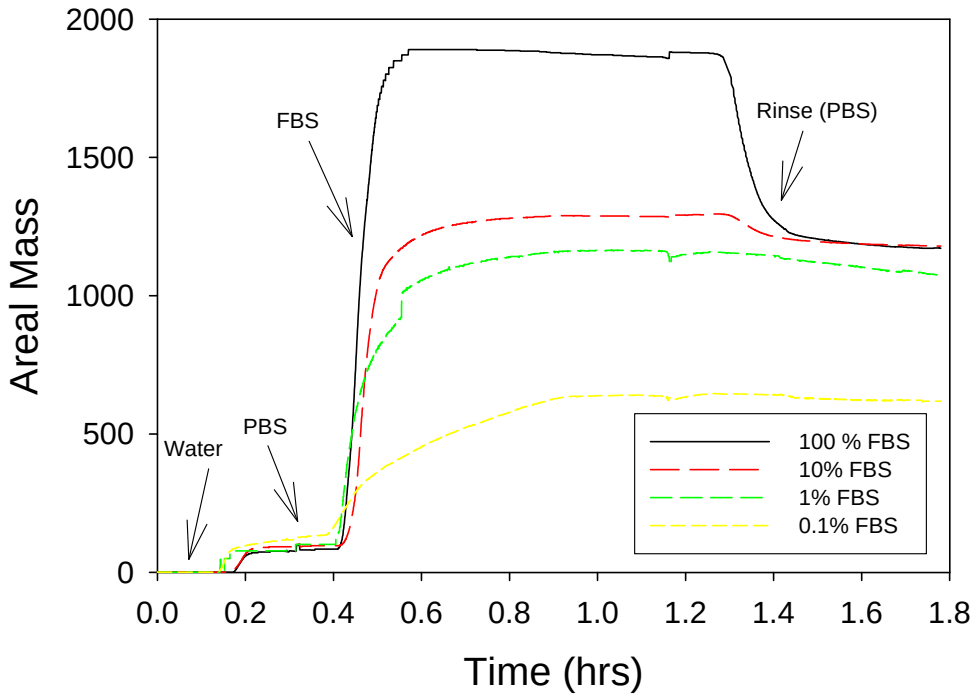

Figure 9.27 Areal mass calculations of parallel QCM-D experiments with FBS

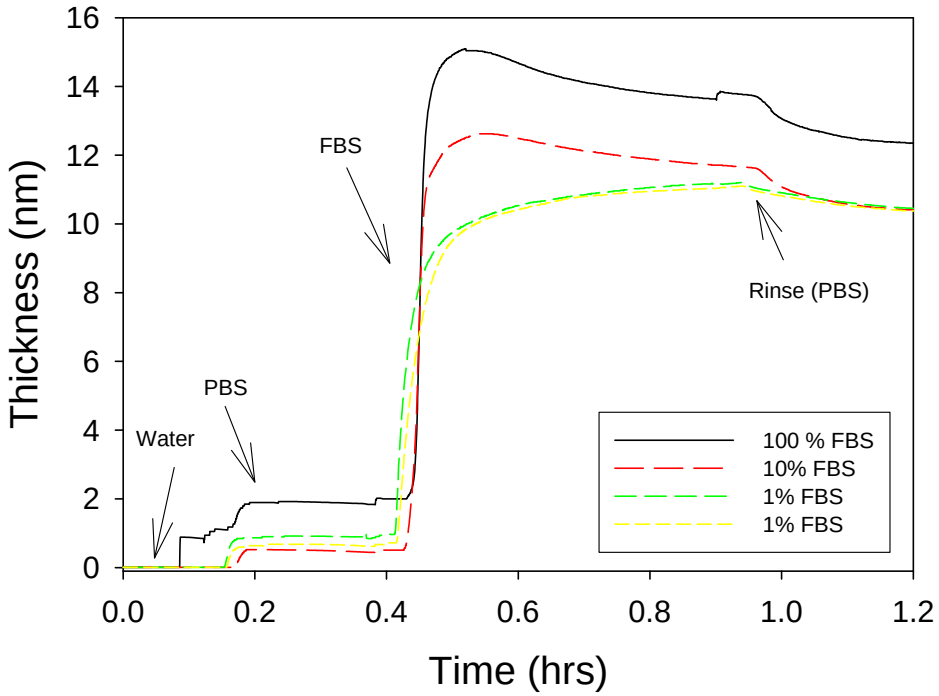

Figure 9.28 FBS thickness modeling with the QCM-D. Results also analyzed with the QCM-D

Appendix C: CP1-cys Adsorption to Gold and CP1 Adsorption to Silicon Nitride

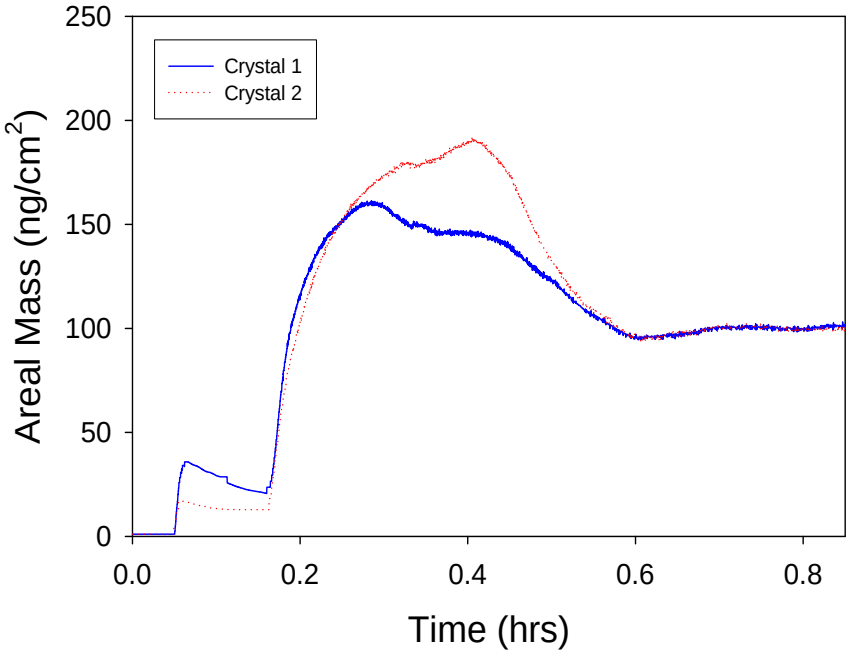

Figure 9.29 Silicon nitride 10 µM Neutral CP1

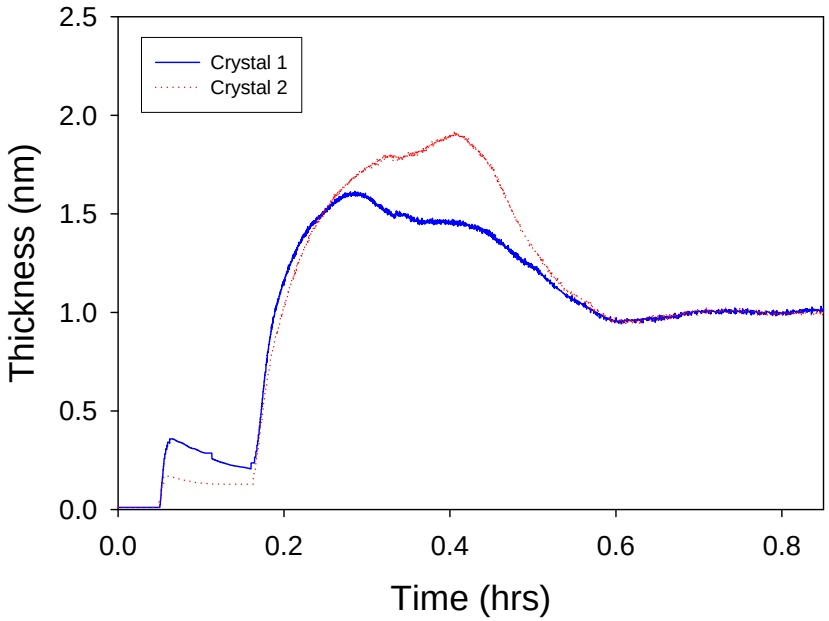

Figure 9.30 Silicon nitride 10 µM Neutral CP1

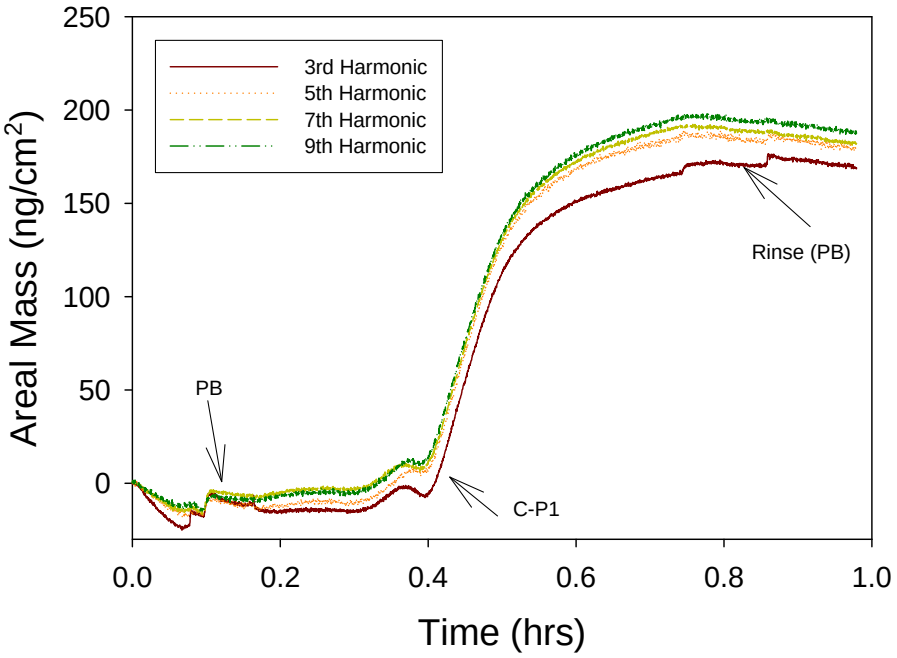

Figure 9.3110 μM Neutral CP1

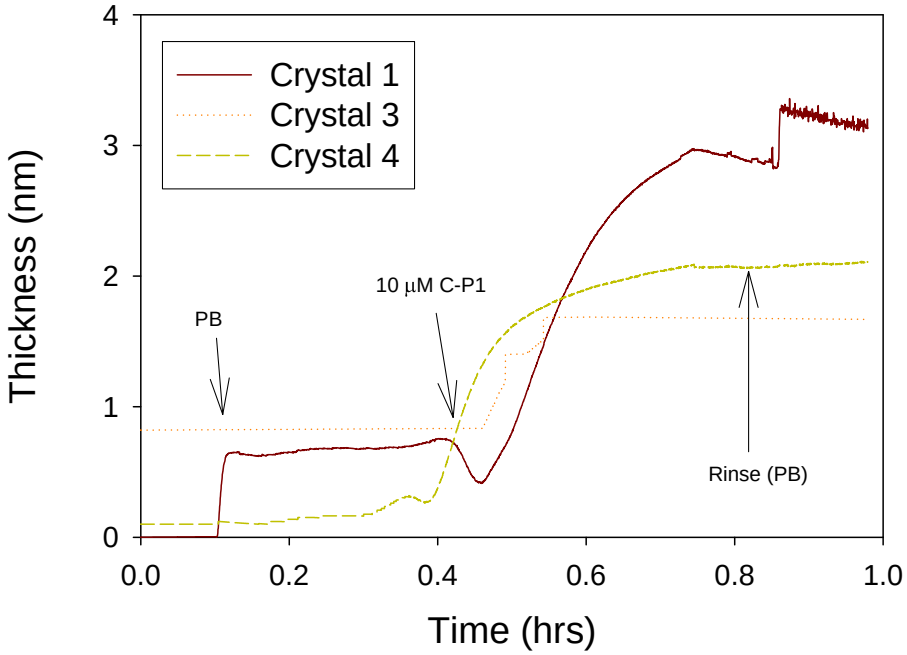

Figure 9.3210 μM Neutral CP1

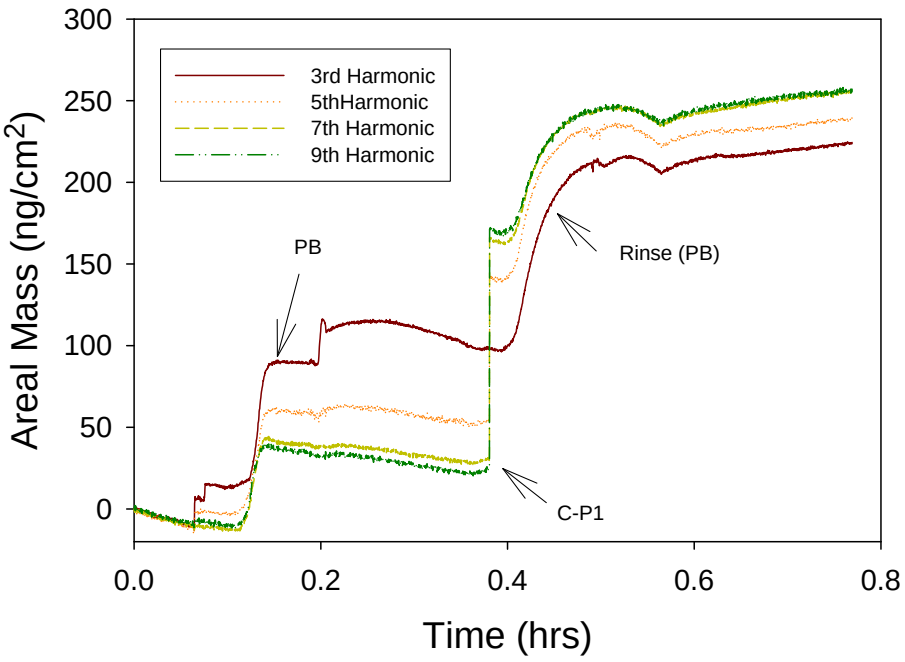

Figure 9.33 10 µM pH 9.2 CP1

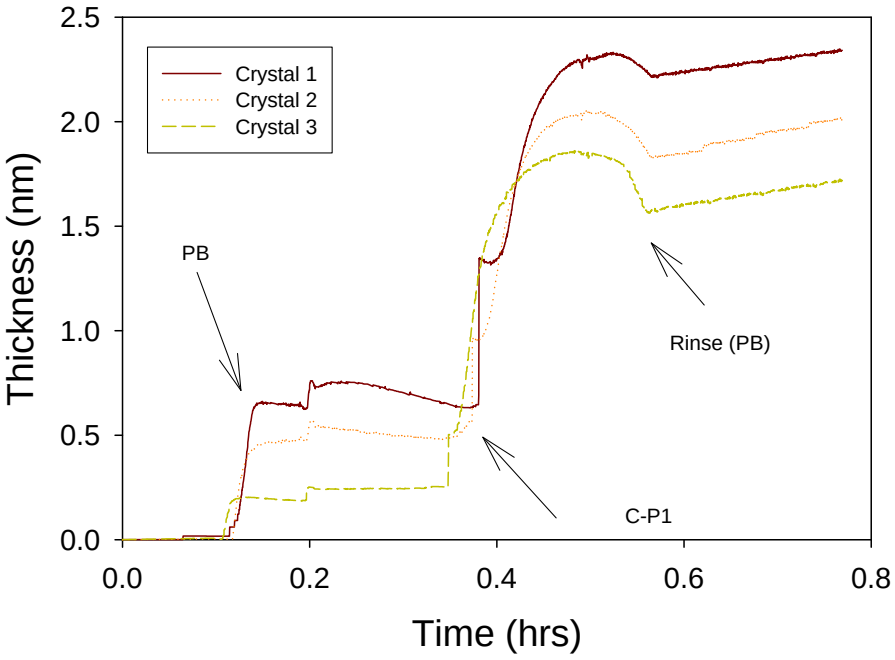

Figure 9.34 10 µM pH 9.2 CP1

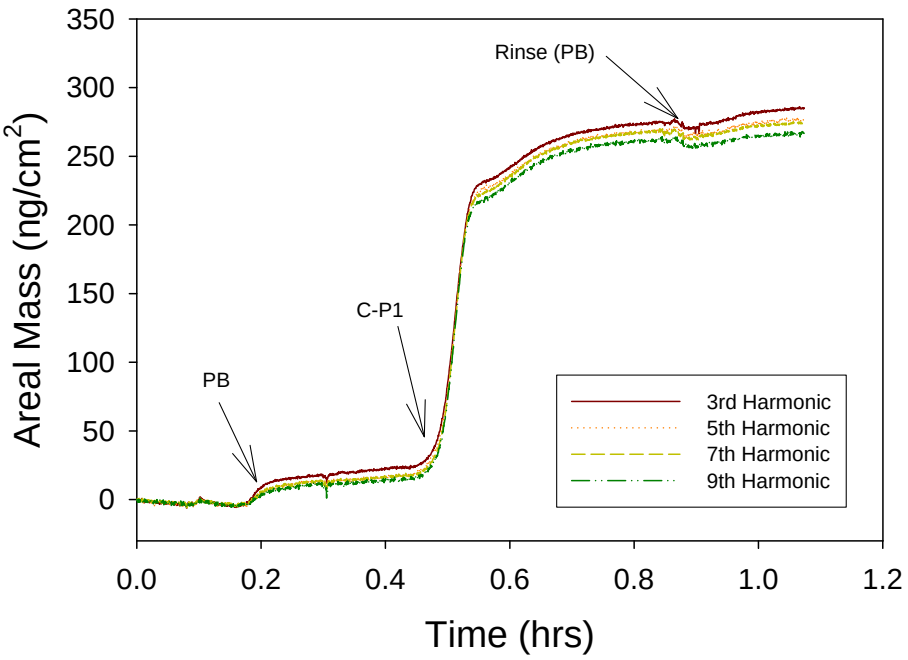

Figure 9.35 29.1 μM neutral CP1

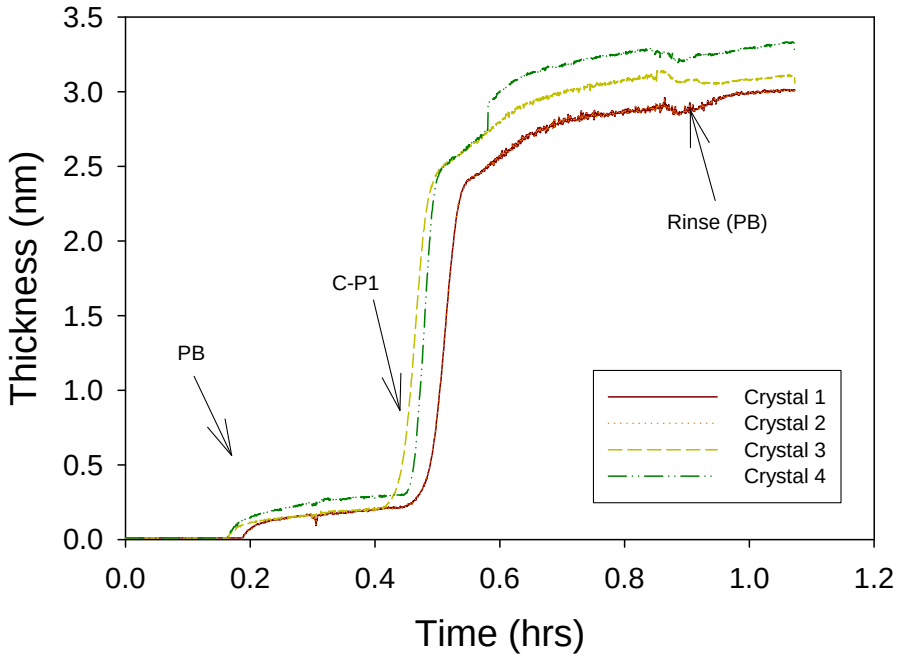

Figure 9.36 29.1 μM neutral CP1

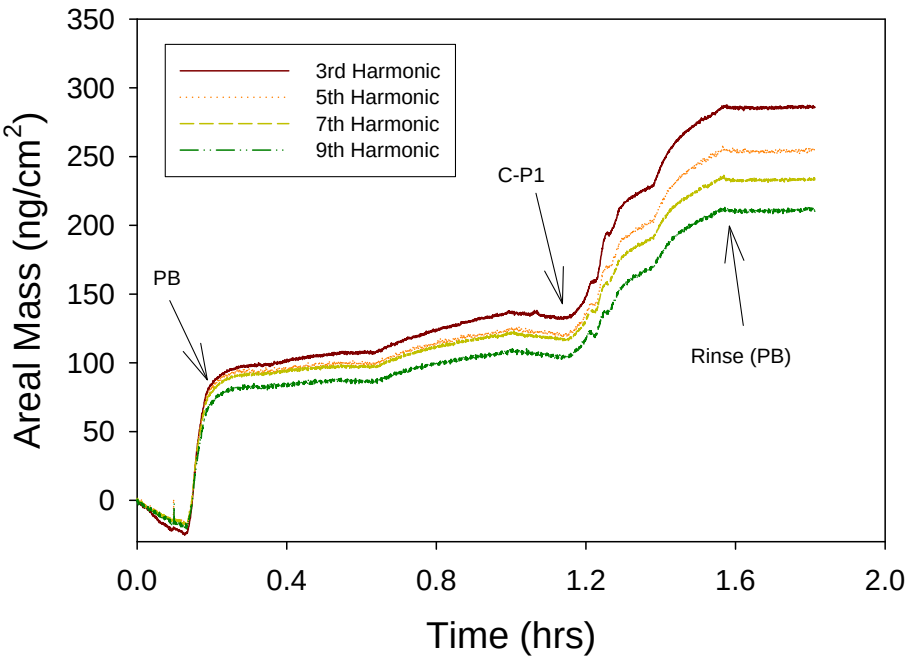

Figure 9.37 29.1 μM pH 9.2 CP1

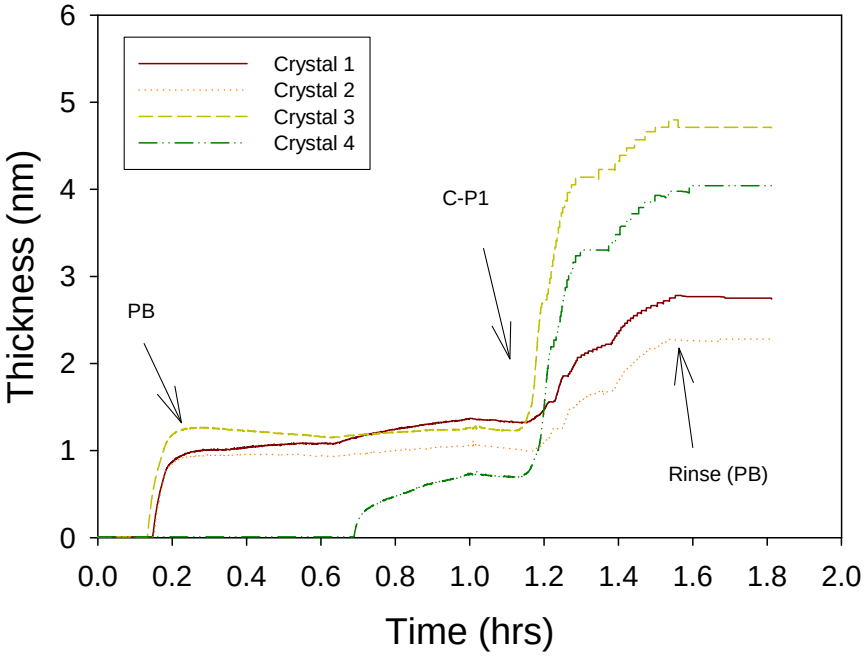

Figure 9.38 29.1 μM pH 9.2 CP1

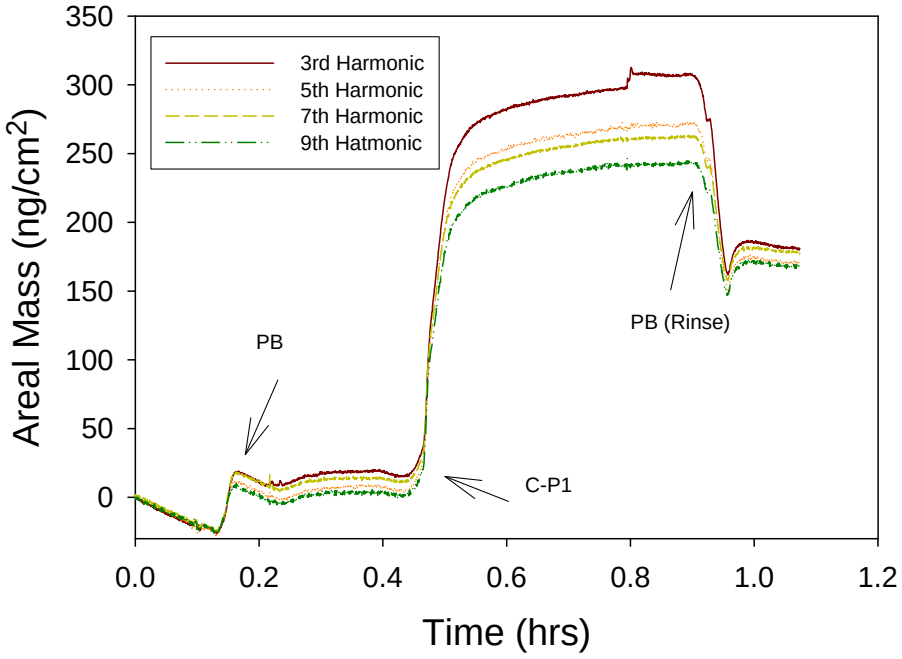

Figure 9.39 TCEP 10 µM neutral CP1

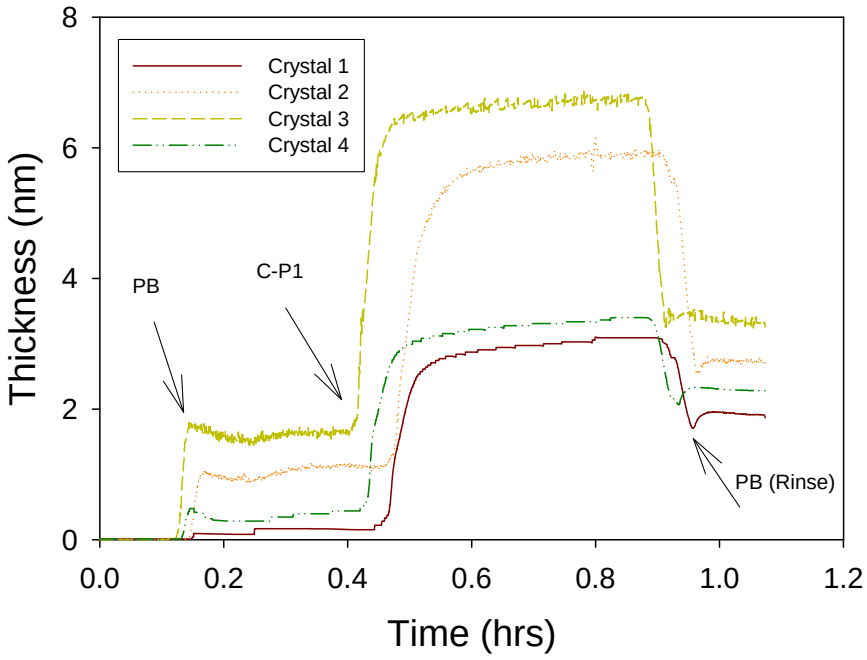

Figure 9.40 TCEP 10 µM neutral CP1

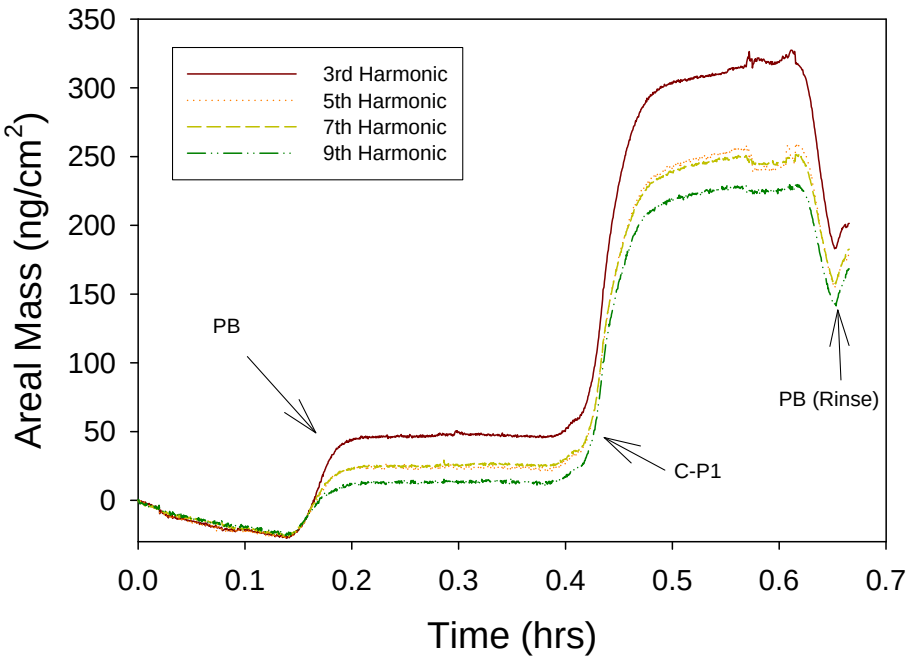

Figure 9.41 TCEP 10 µM pH 9.2 neutral CP1

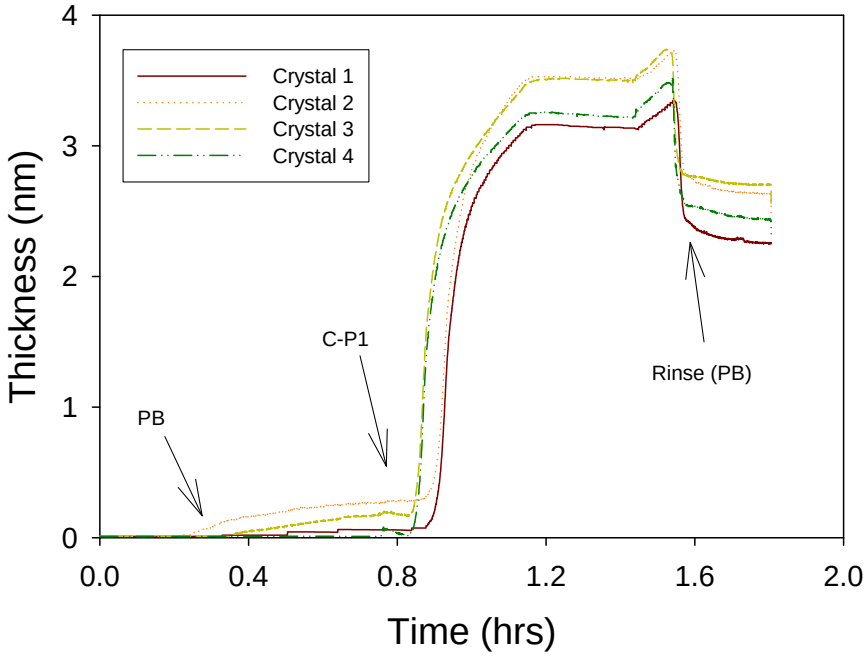

Figure 9.42 TCEP 10 µM pH 9.2 neutral CP1

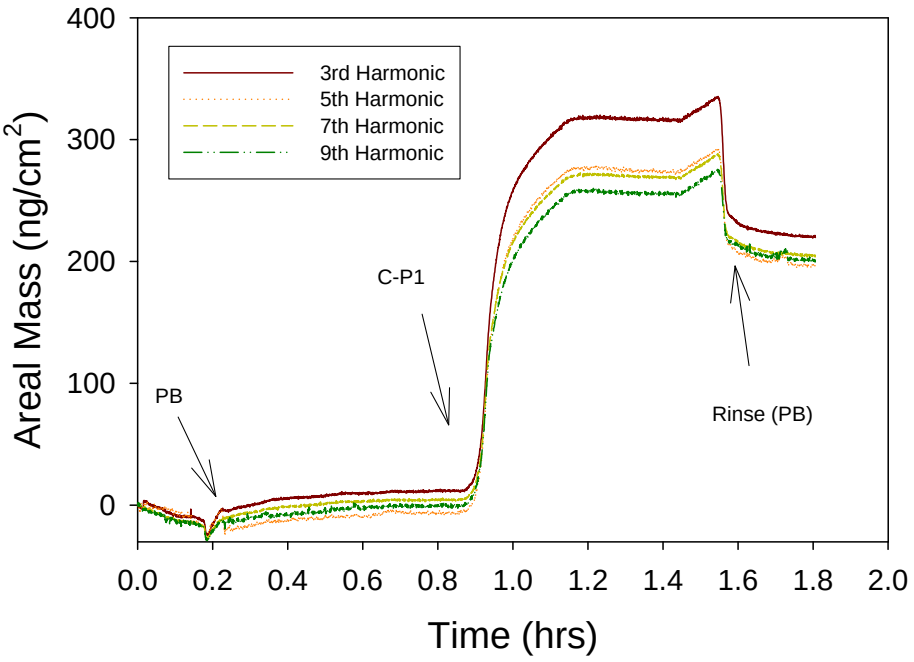

Figure 9.43 TCEP 29.1 µM neutral CP1

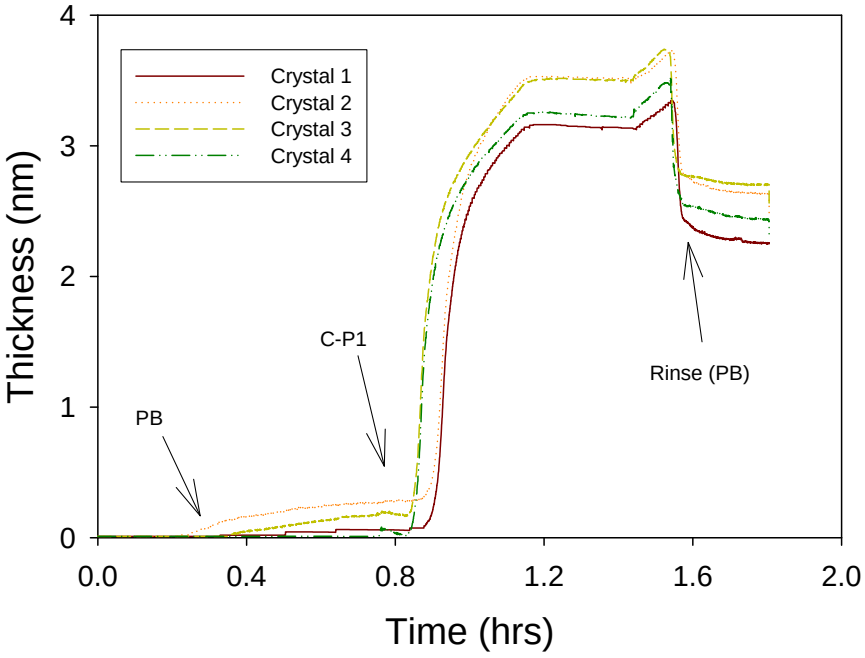

Figure 9.44 TCEP 29.1 µM neutral CP1

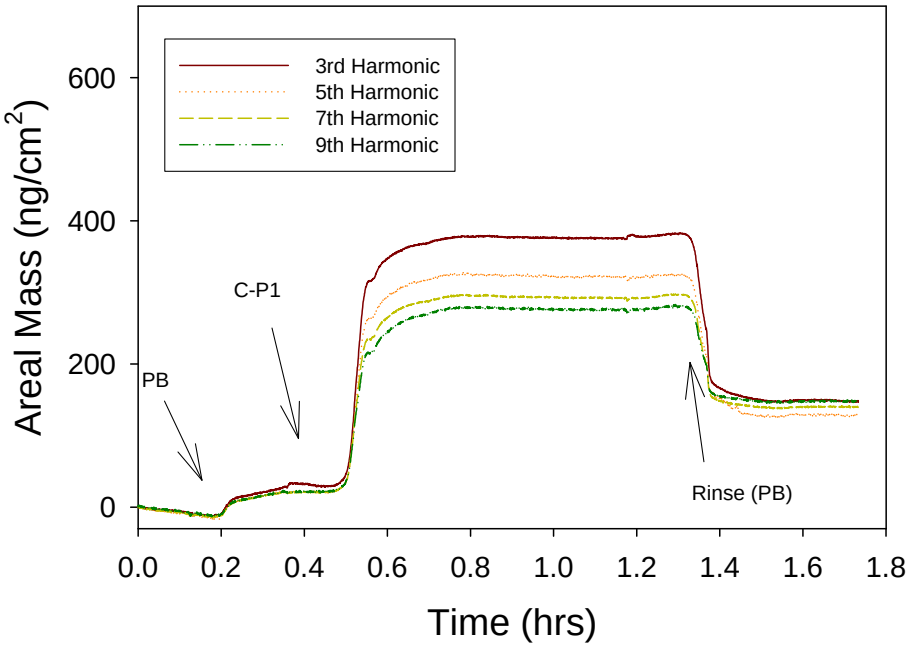

Figure 9.45 TCEP 29.1 µM pH 9.2 CP1

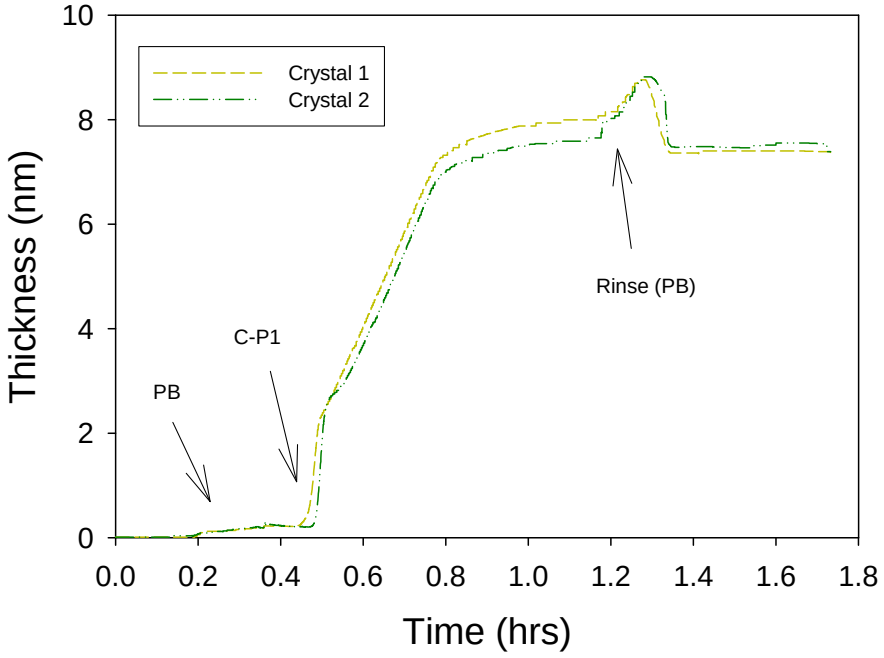

Figure 9.46 TCEP 29.1 µM pH 9.2 CP1

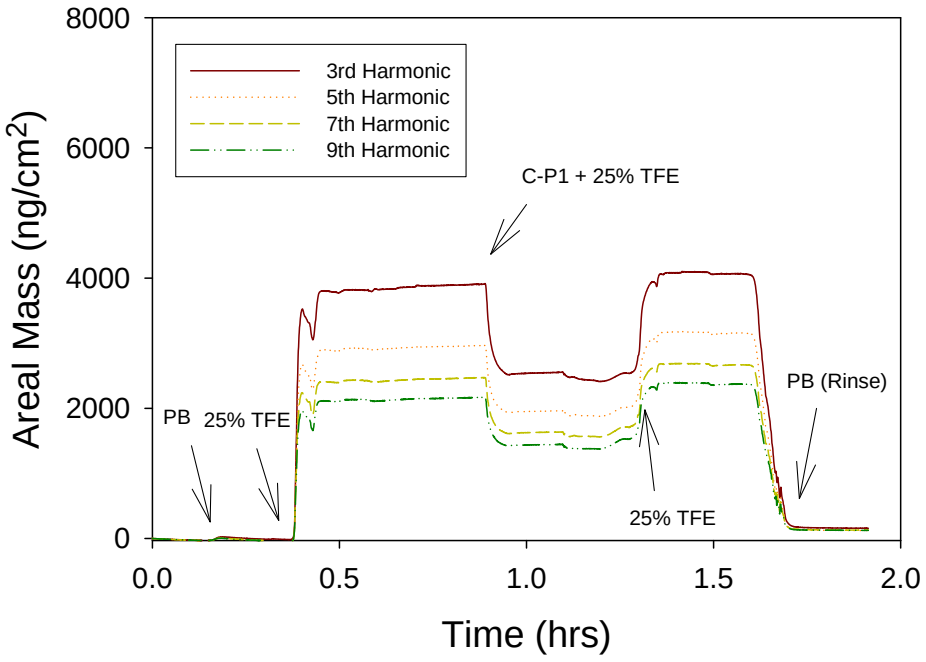

Figure 9.47 TFE 10 µM neutral CP1

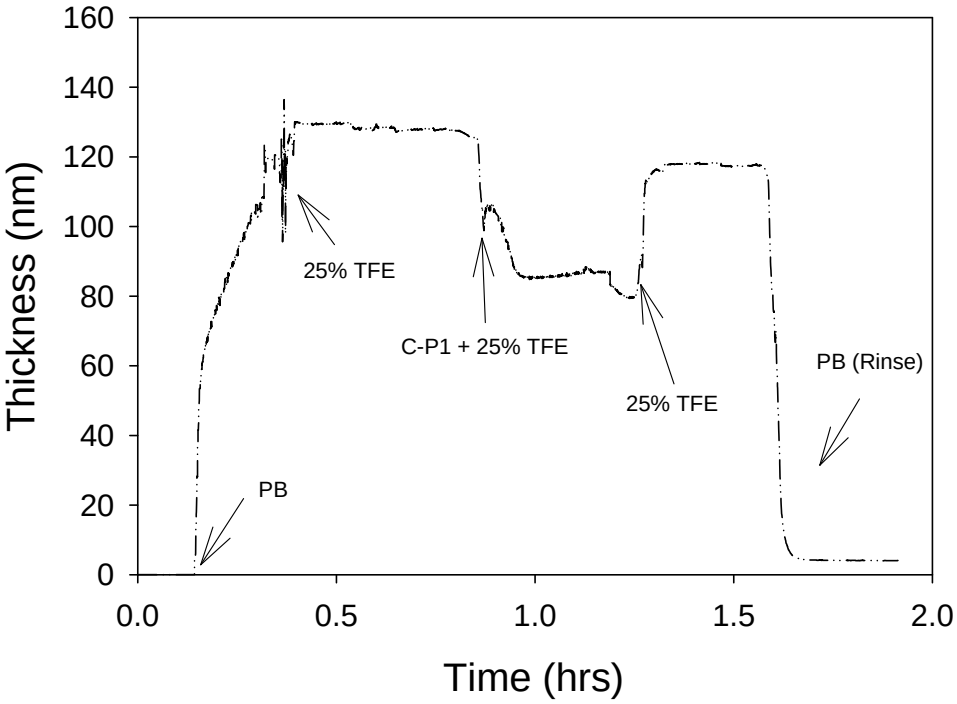

Figure 9.48 TFE 10 µM neutral CP1

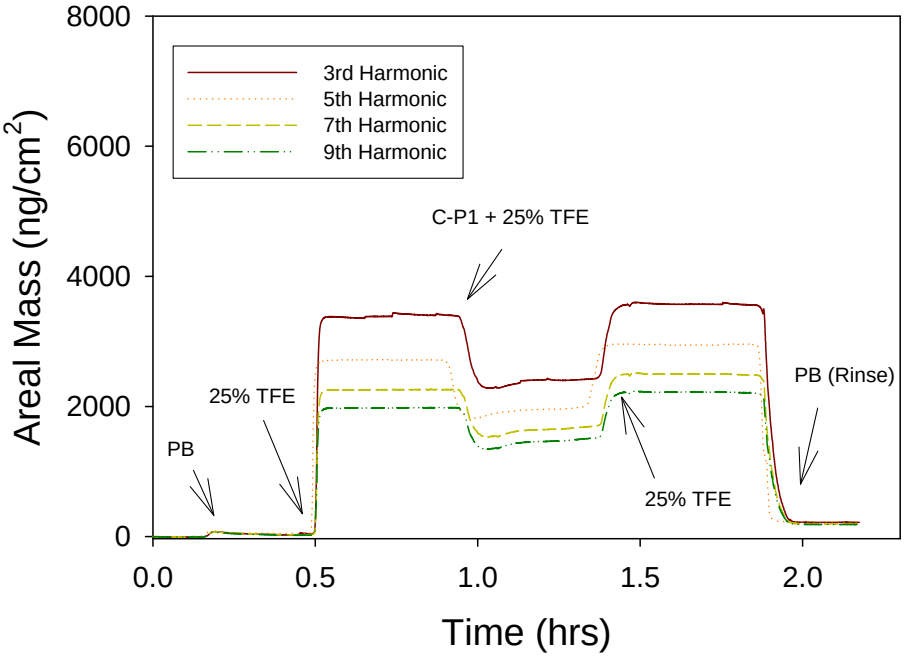

Figure 9.49 TFE 10 µM pH 9.2 CP1

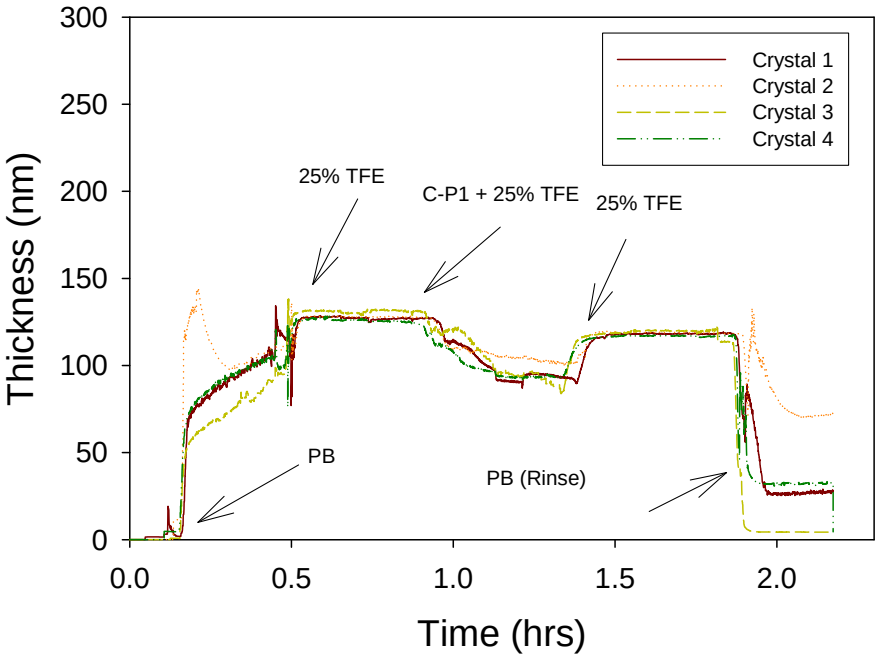

Figure 9.50 TFE 10 µM pH 9.2 CP1

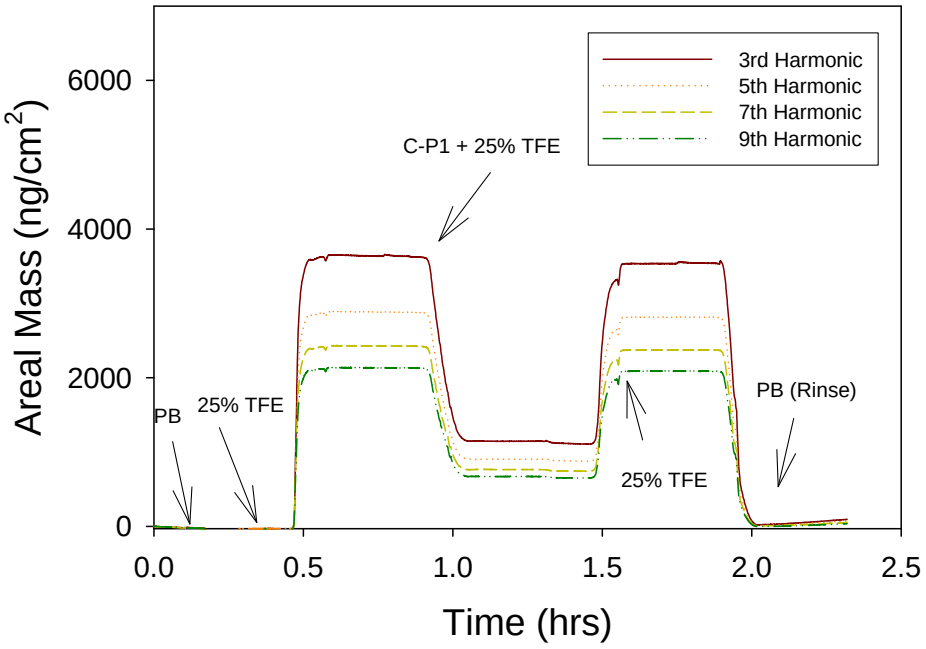

Figure 9.51 TFE 29.1 µM pH neutral CP1

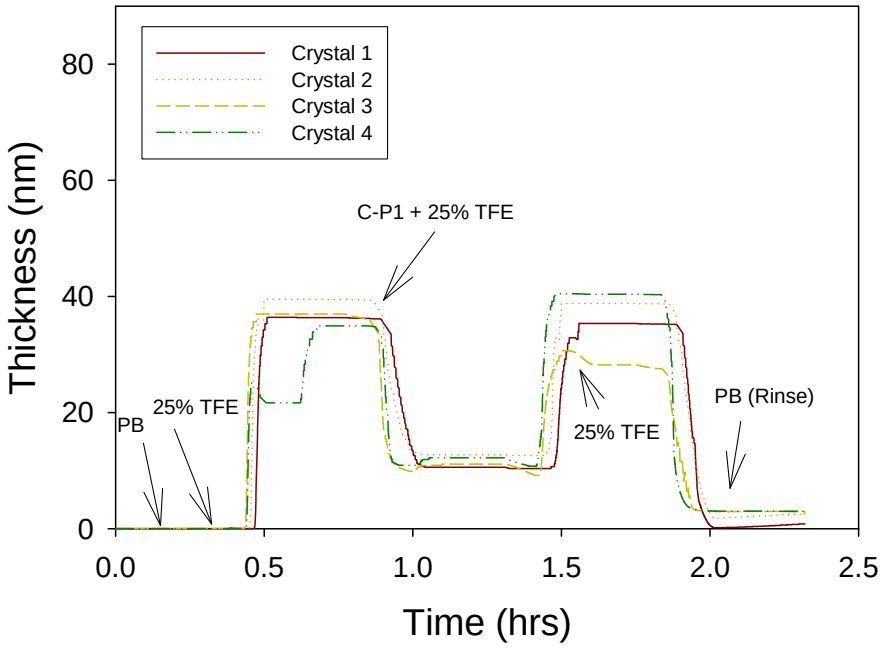

Figure 9.52 TFE 29.1 µM pH neutral CP1

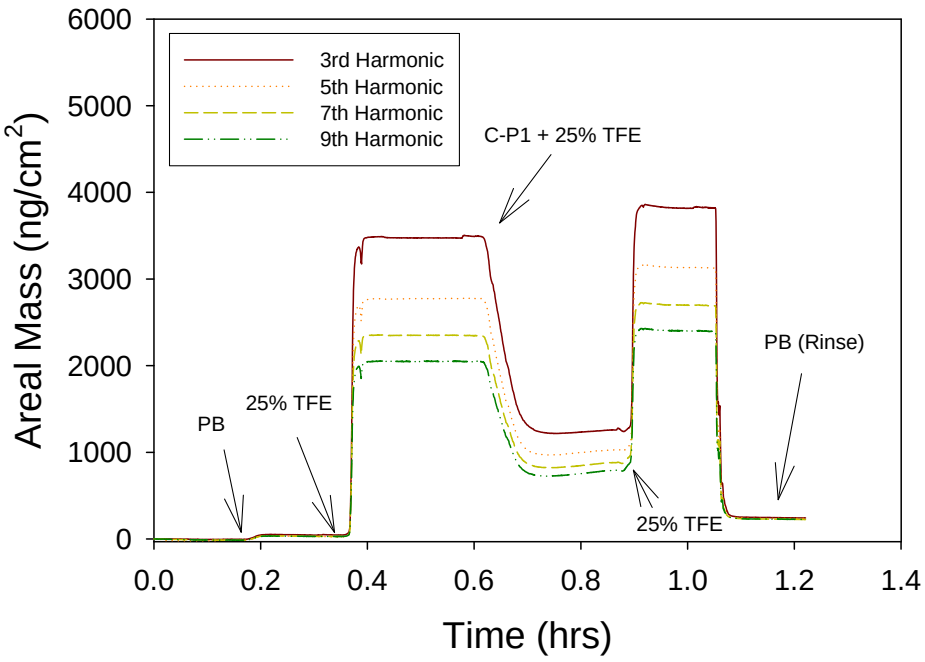

Figure 9.53 TFE 29.1 µM pH pH 9.2 CP1

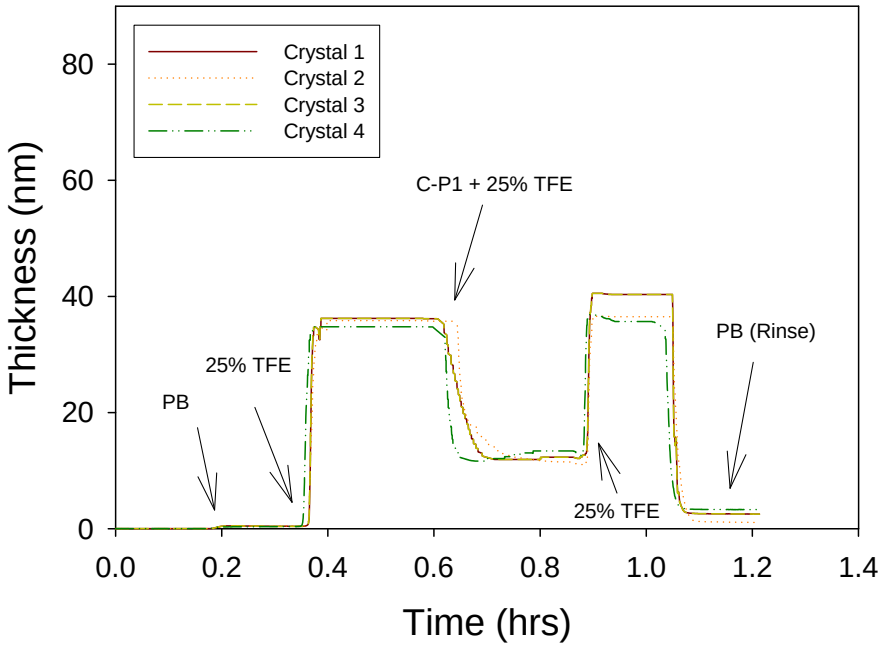

Figure 9.54 TFE 29.1 µM pH pH 9.2 CP1

Appendix D: AFM Whisker Plot of Retraction Data

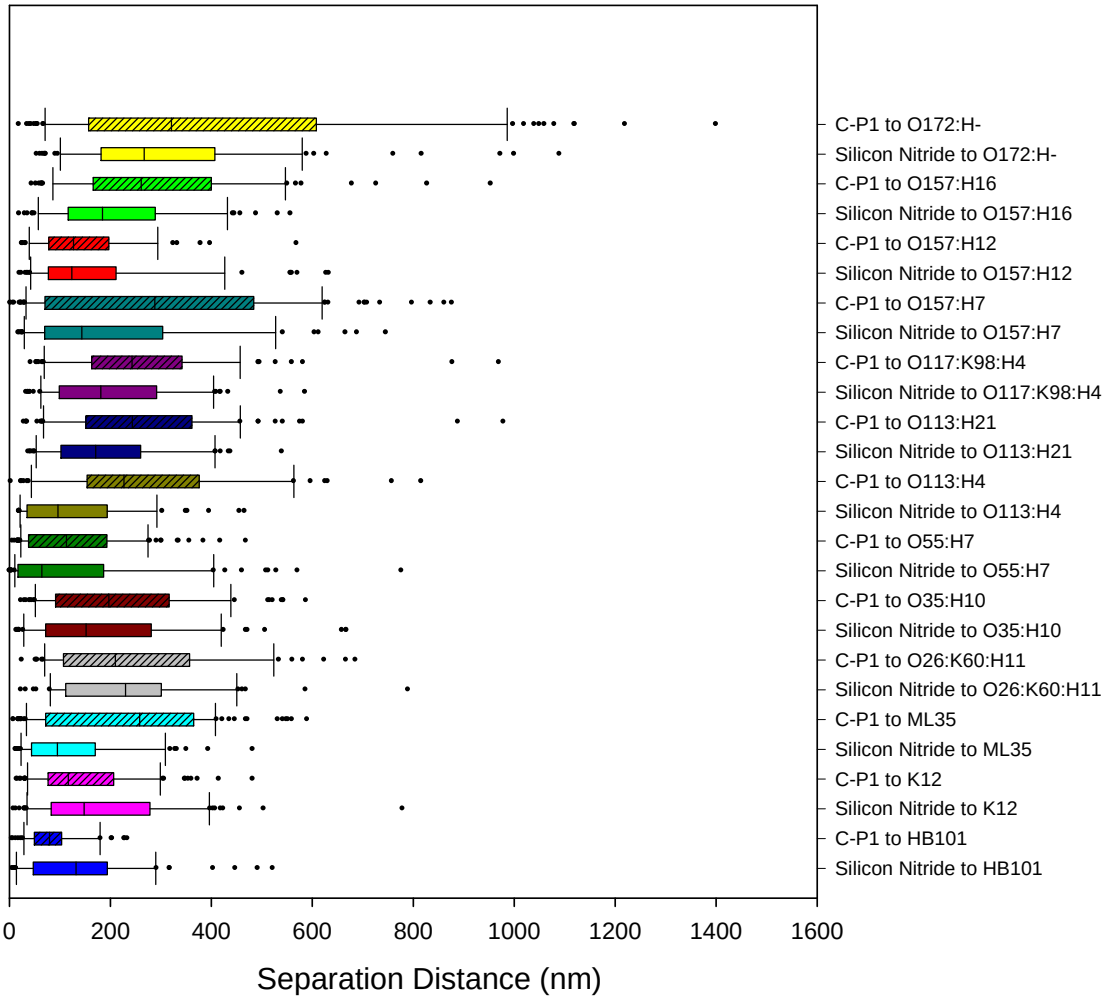

Figure 9.55 Whisker plot of the retraction pull-off distances. Outliers were removed from overall averages

Appendix E: O-antigen and Core Groups for the 13 *E. coli* Strains

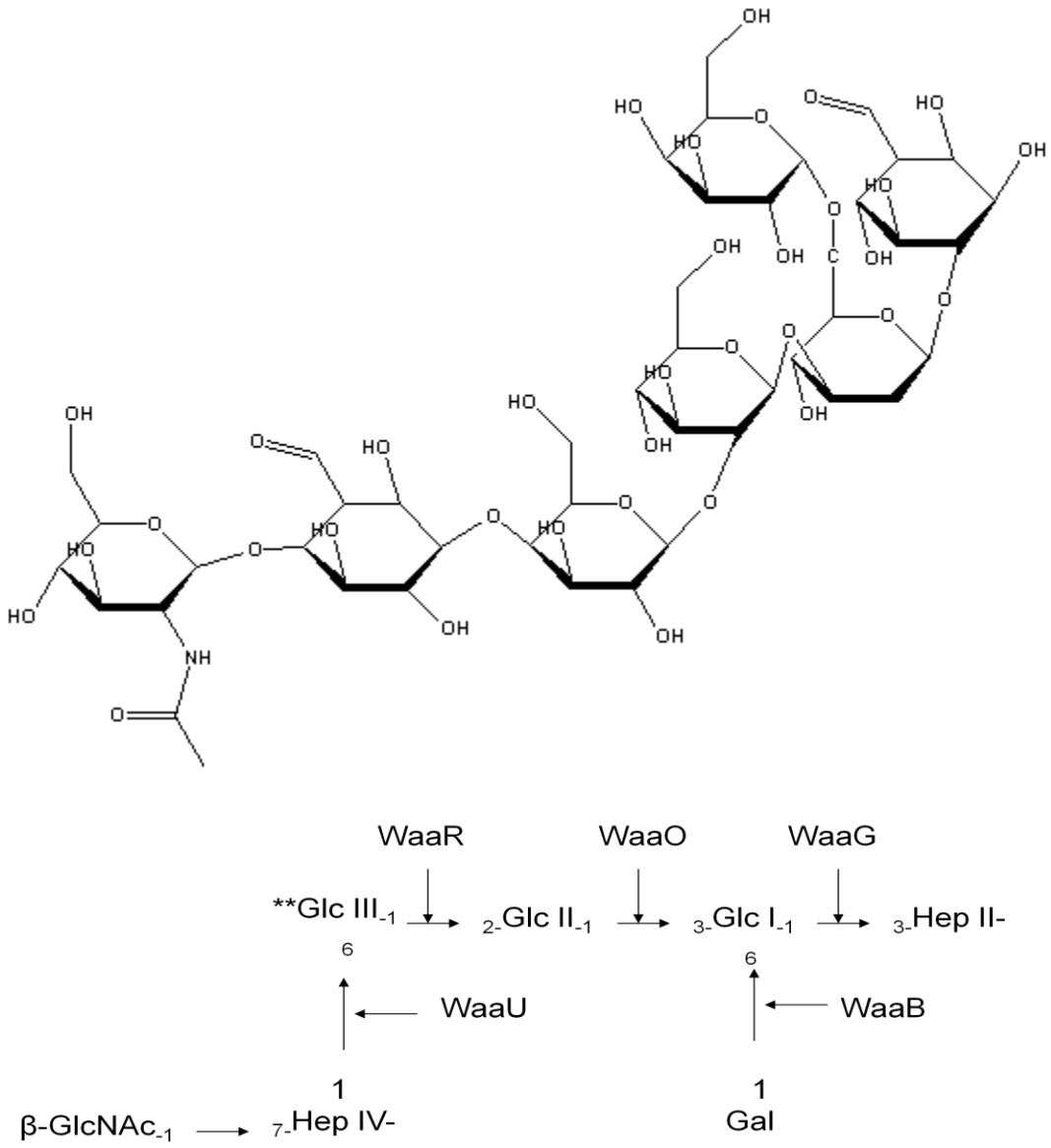

Figure 9.56 O-antigen and core group for the K12 strains

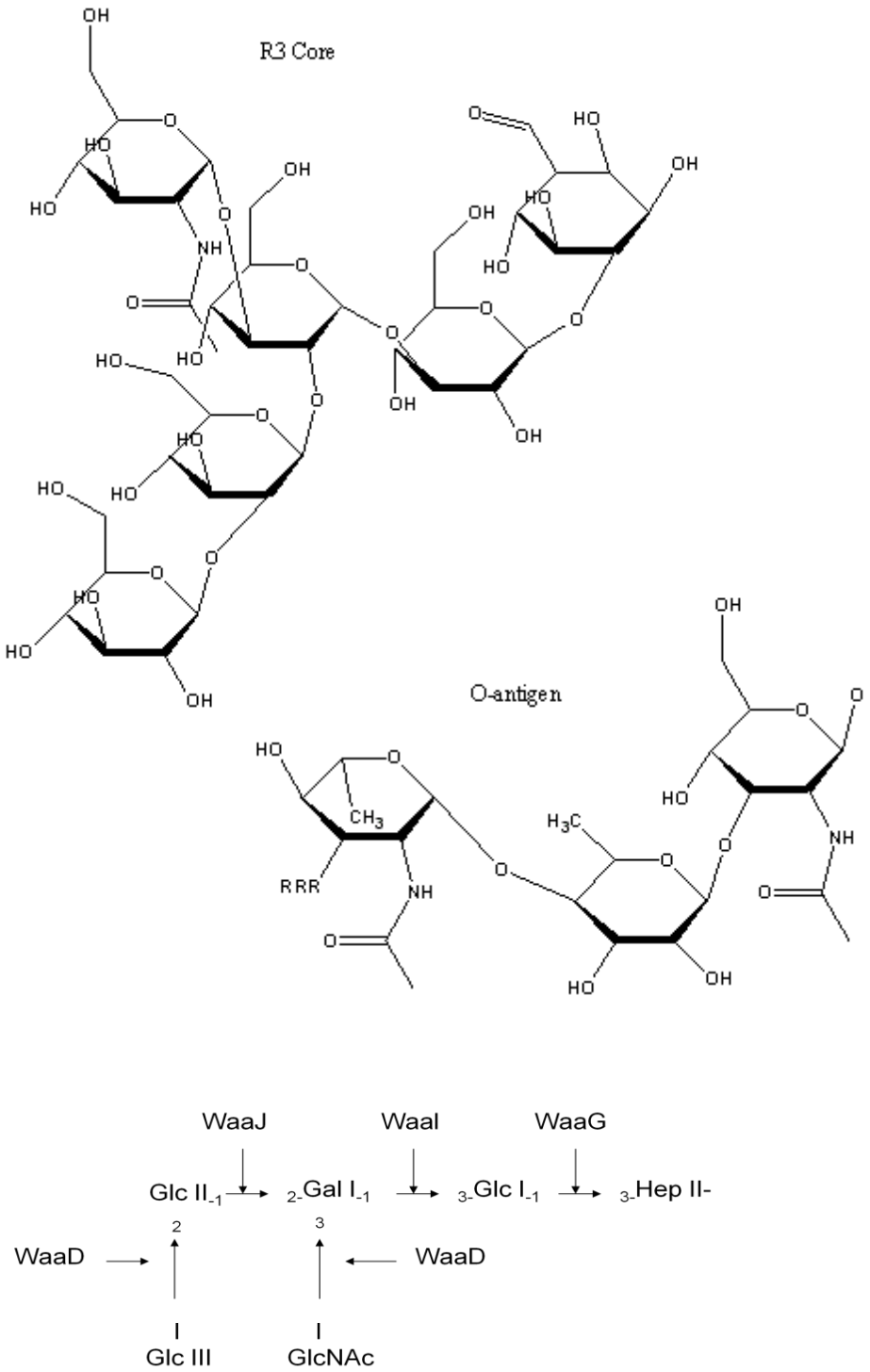

Figure 9.57 O-antigen and core group for O26:K60:H11

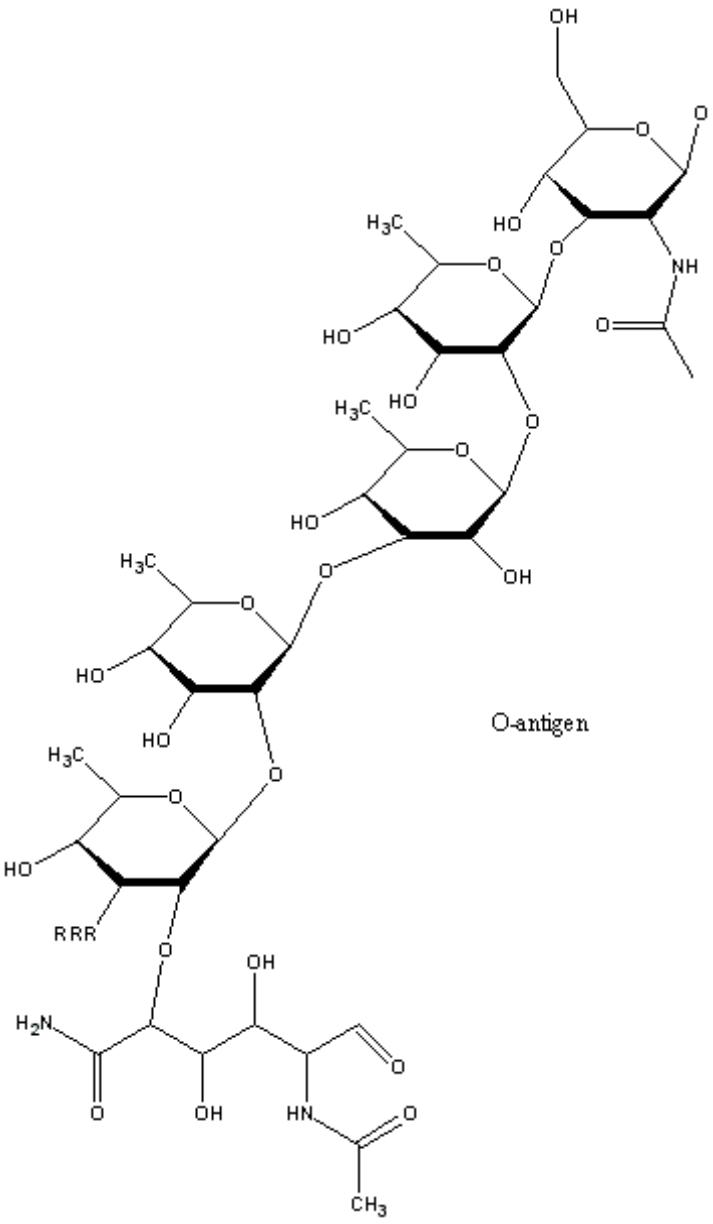

→3)αLRha(1 →2) αLRha(1 →3) αLRha(1 →2) αLRha(1 →3)

|

αDGalNAcA6N(1 →2) βDGlcNAc(1 →

Figure 9.58 O-antigen and for O35:H10

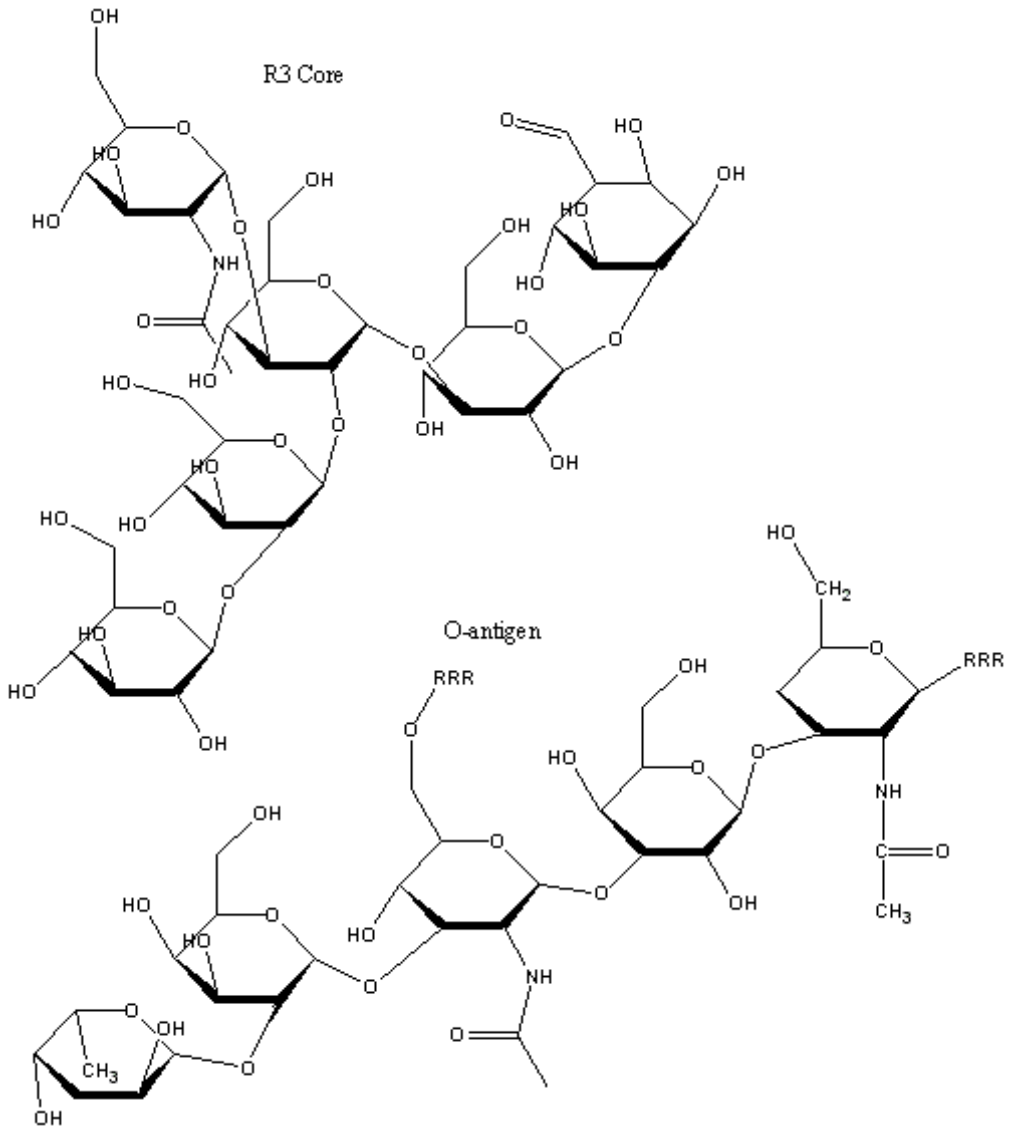

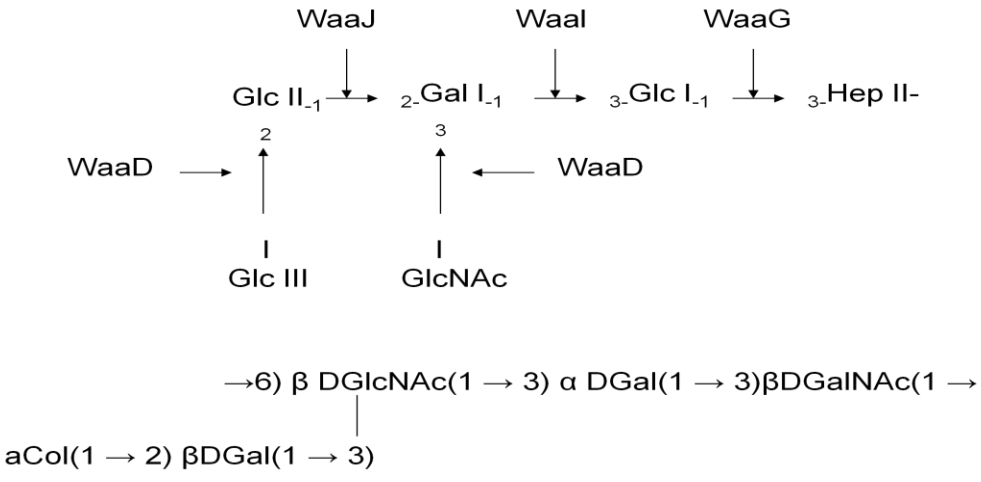

Figure 9.59 O-antigen and core group for O55:H7

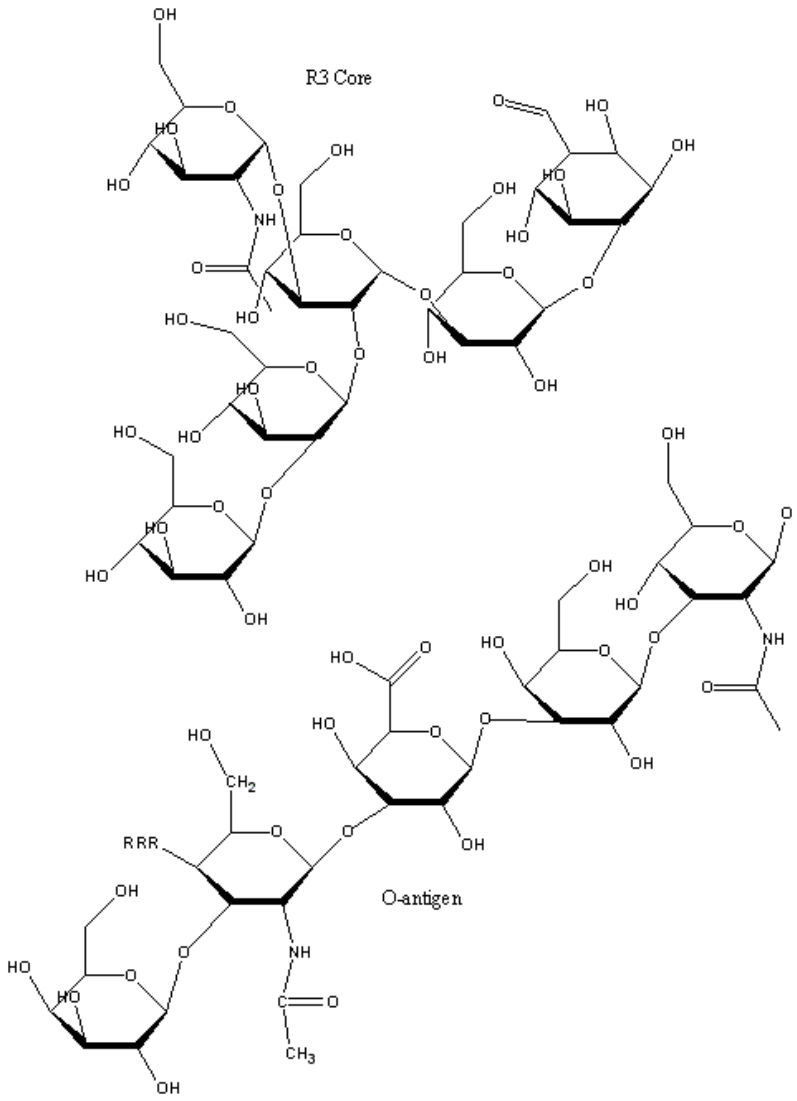

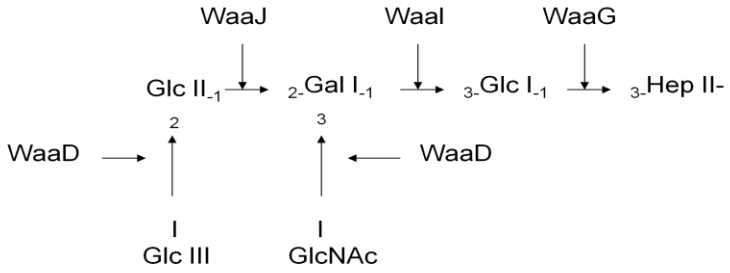

→4) αDGalNAc(1 →4) αDGalA(1 →3) αDGal(1 →3) βDGlcNAc(1 →
|
βDGal(1 →3)

Figure 9.60 O-antigen and core group for O113:H4 and O113:H21

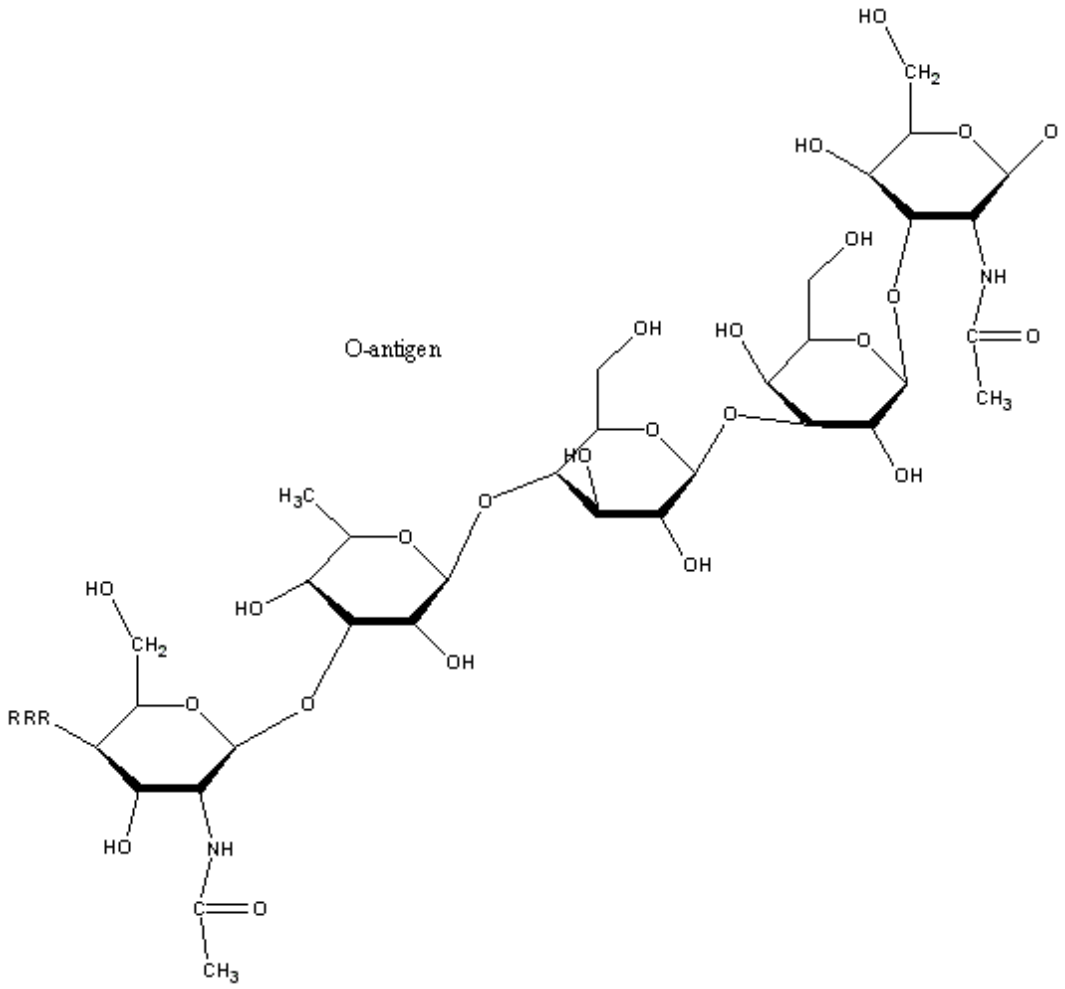

→4) βDGalNAc(1 →3) αLRha(1 →4) α DGlc(1 →4) βDGal(1 →3) αDGalNAc(1 →

Figure 9.61 O-antigen and core groupfor O117:K98:H4

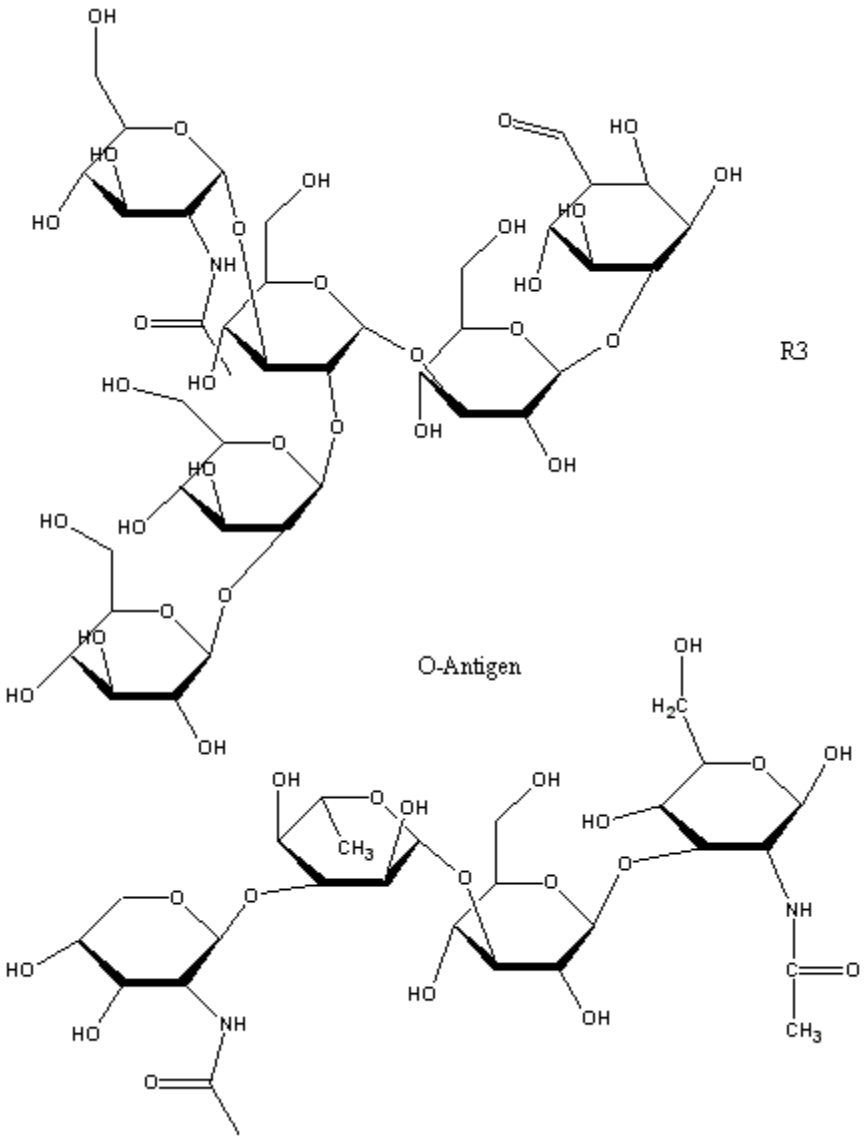

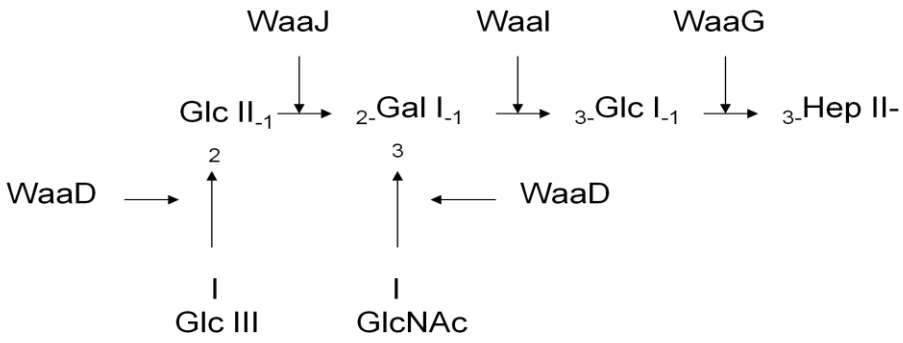

→2) αDRha4NAc(1 →3) αLFuc(1 →4) βDGlc(1 →3) αDGalNAc(1 →

Figure 9.62 O-antigen and core group for O157:H7, O157:H12, and O157:H16

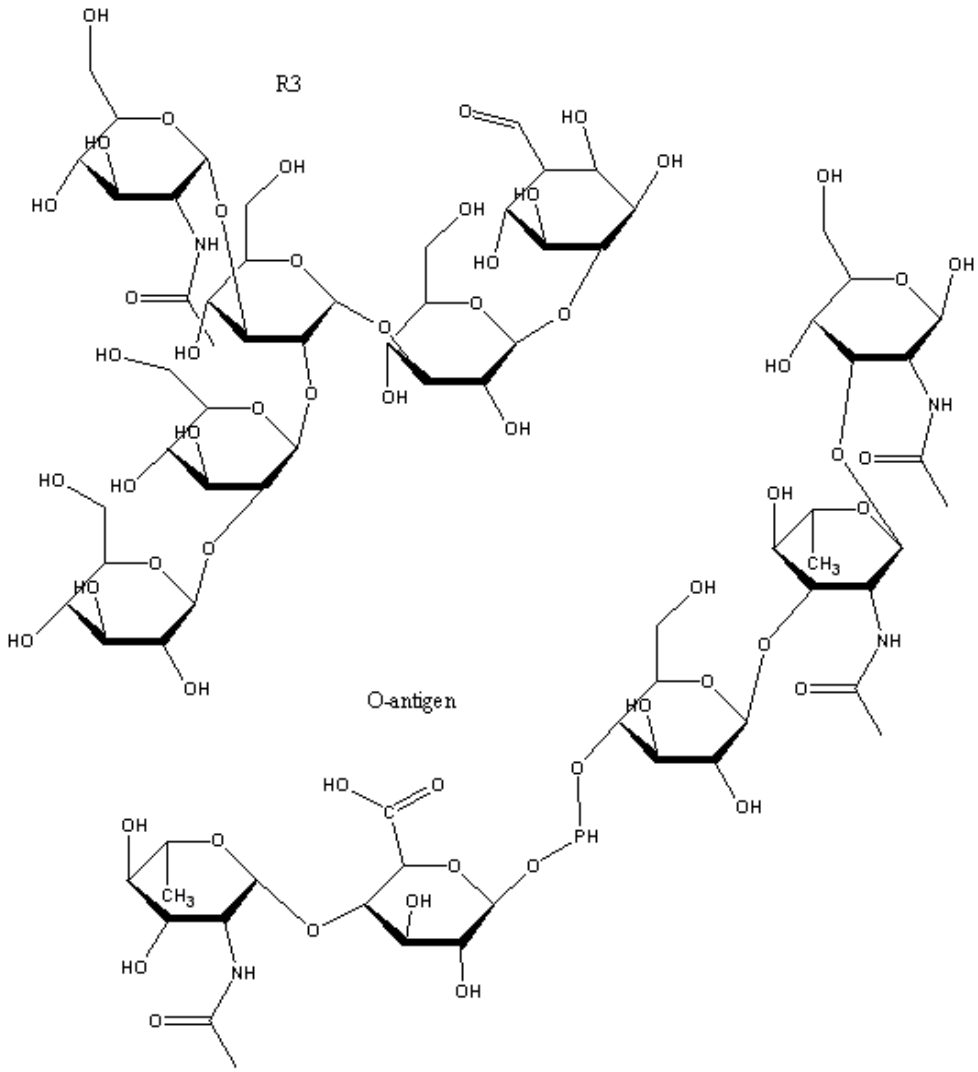

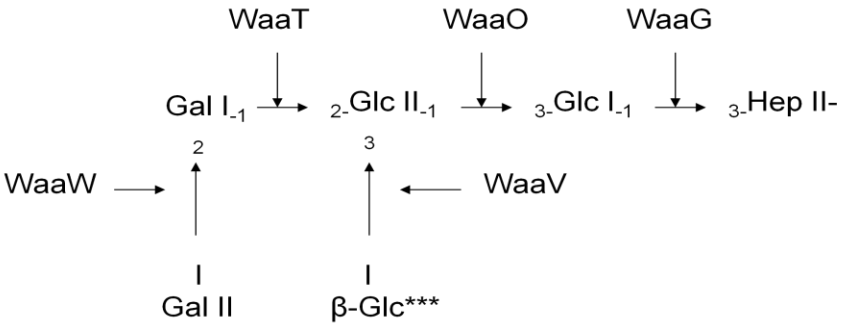

→3) αLFucNAc(1 →4) αDGlc6ac(1 →P → 4) α DGlc(1 →3) α LFucNAc
(1 →3) αDGlcNAc(1 →

Figure 9.63 O-antigen and core group for O172:H-

Appendix F: AFM Retraction Force Data

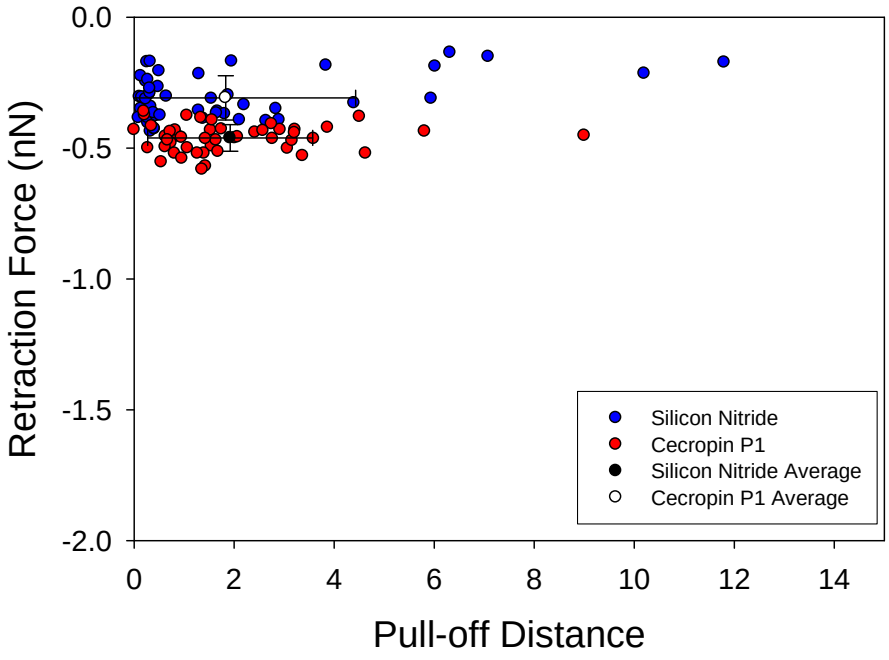

Figure 9.64 Glass slide AFM analysis

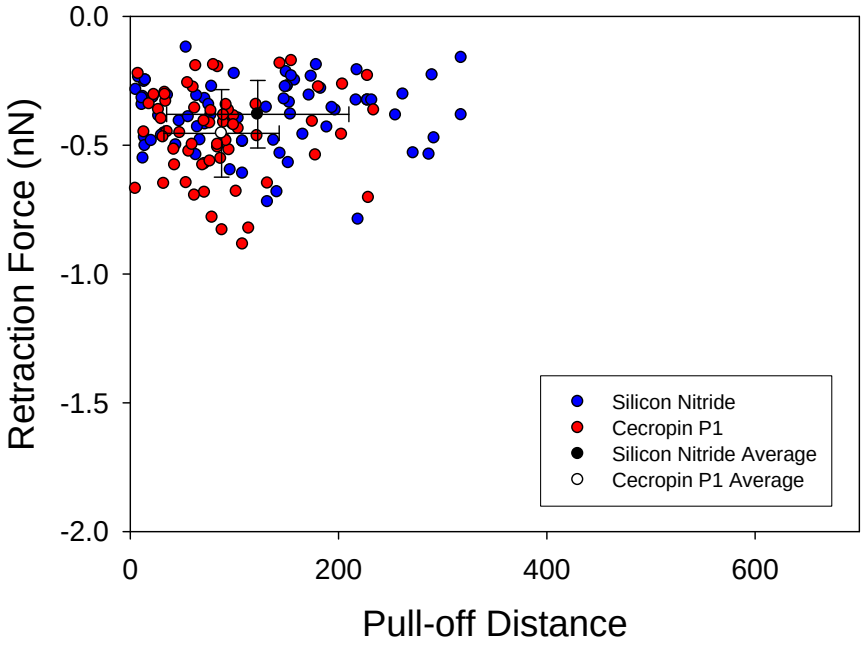

Figure 9.65 HB101 AFM Analysis

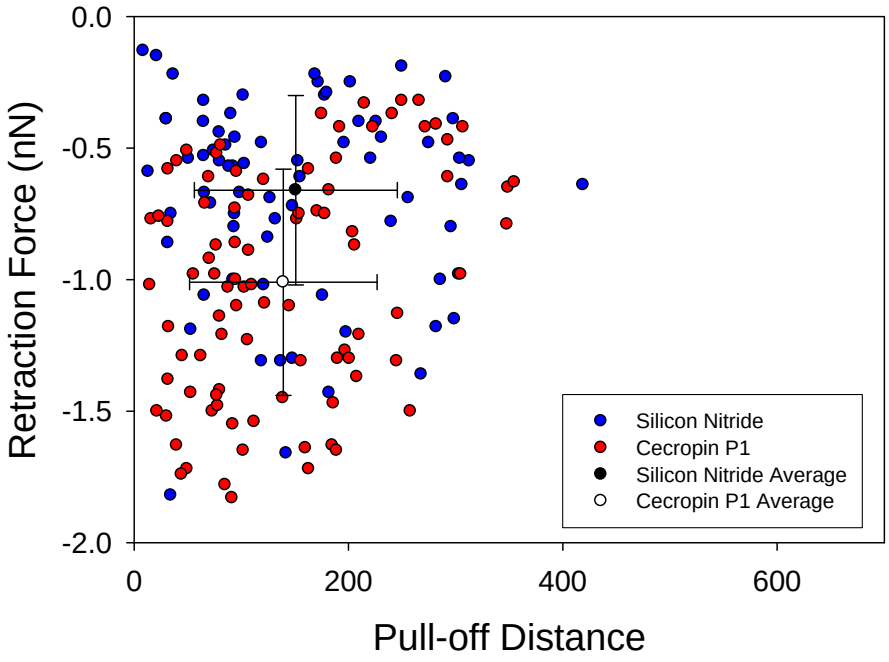

Figure 9.66 K12 AFM Analyses

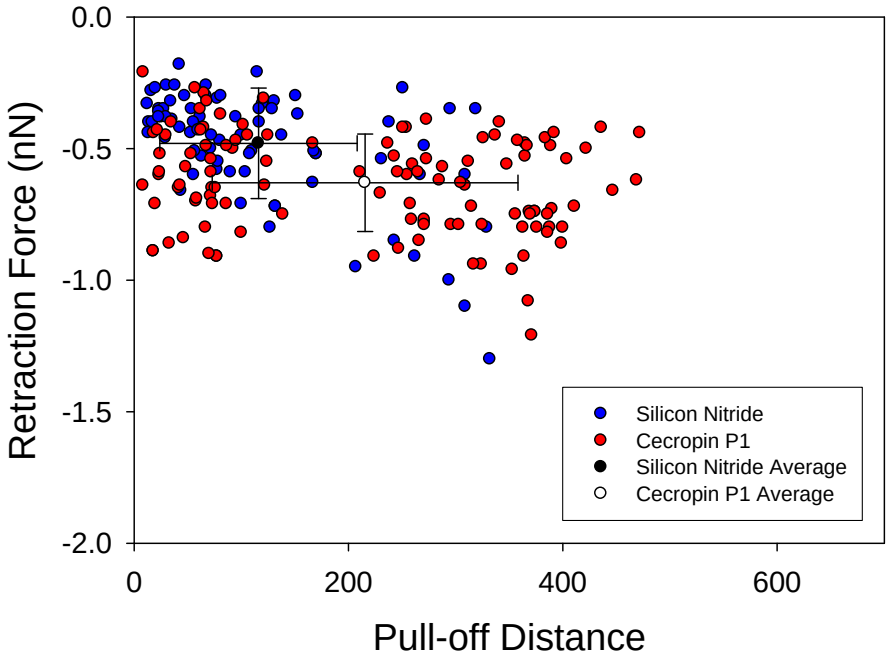

Figure 9.67 ML35 AFM Analyses

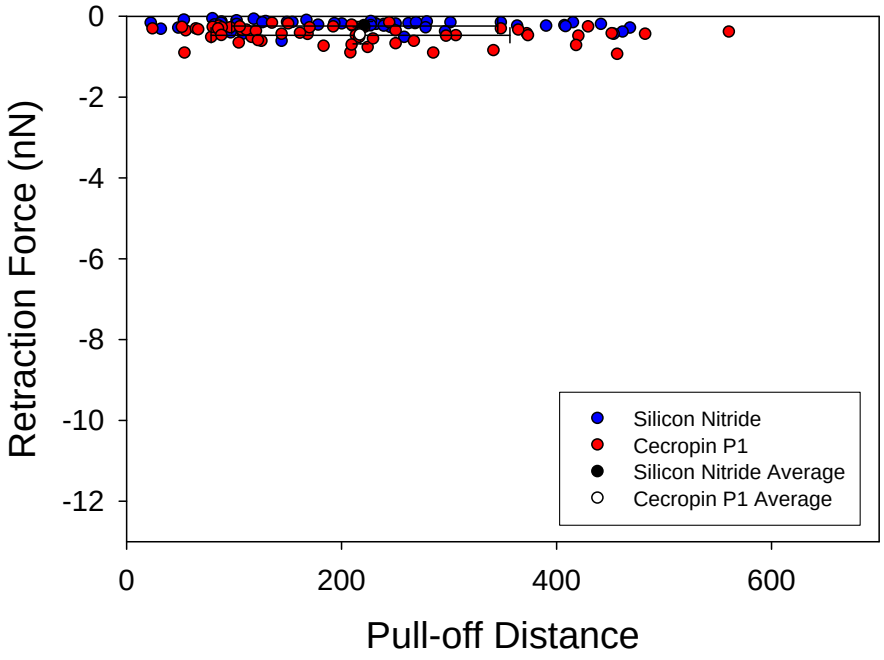

Figure 9.68 O26:K60:H11 AFM Analyses

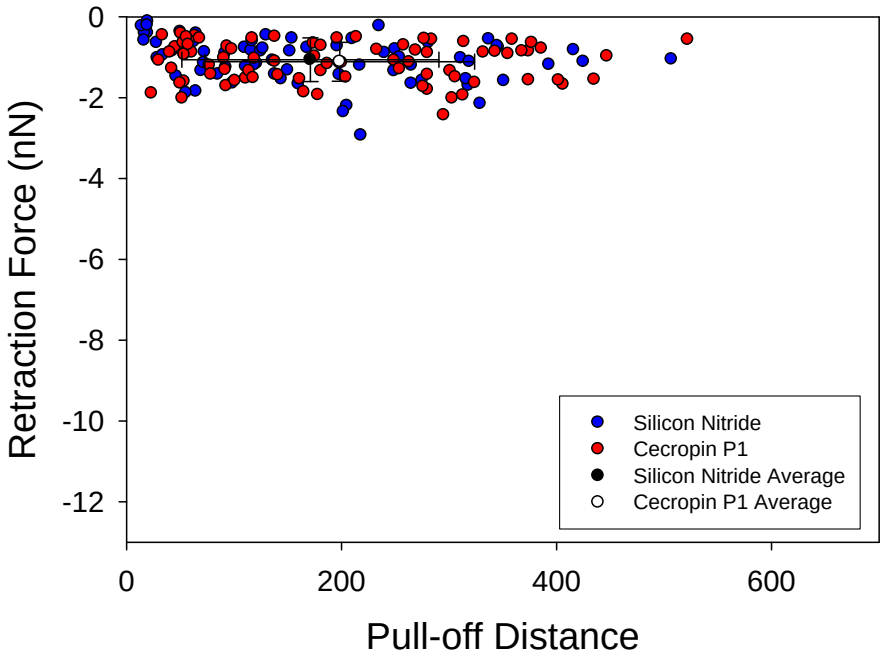

Figure 9.69 O35:H10 AFM Analyses

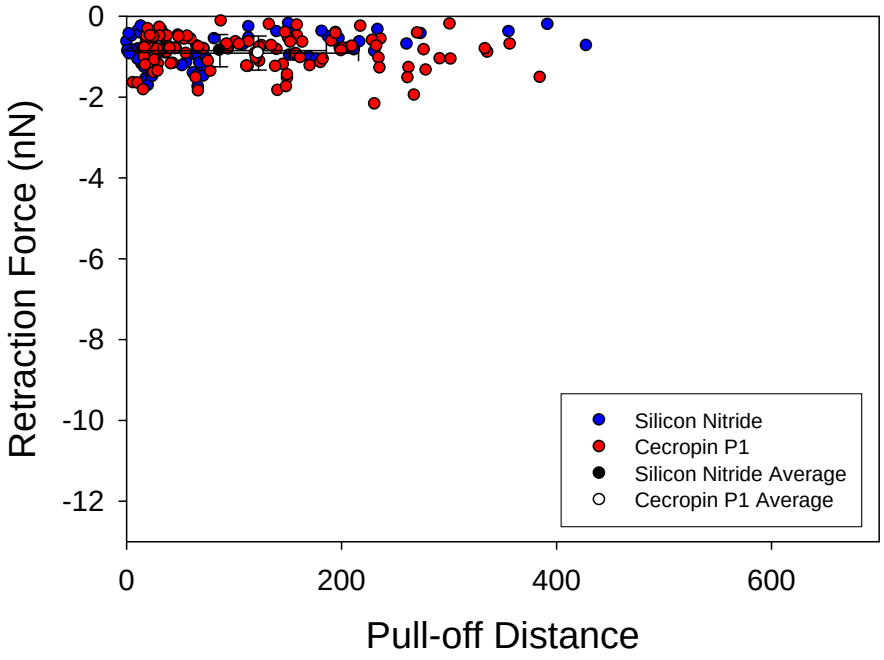

Figure 9.70 O55:H7 AFM Analyses

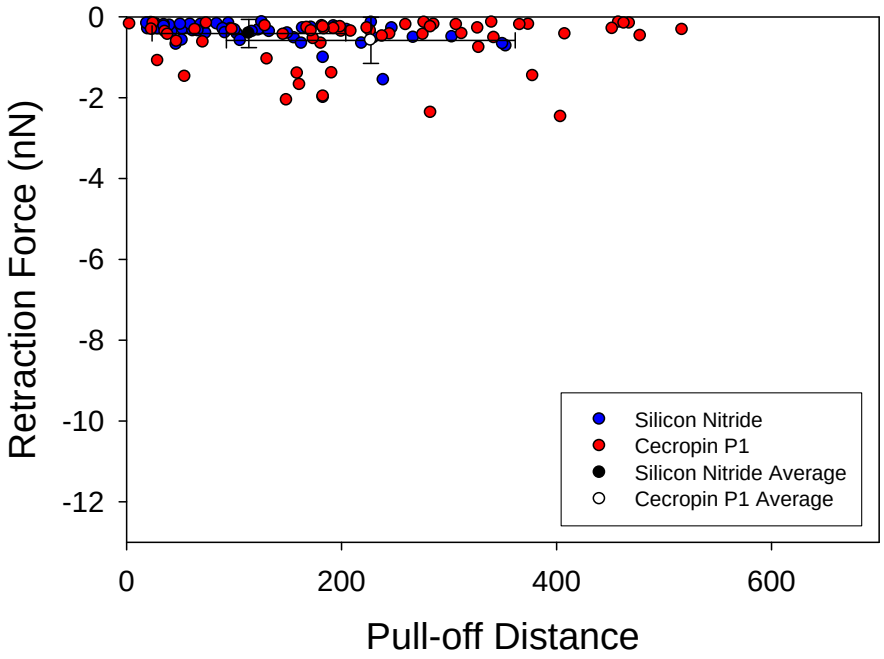

Figure 9.71 O113:H4 AFM Analyses

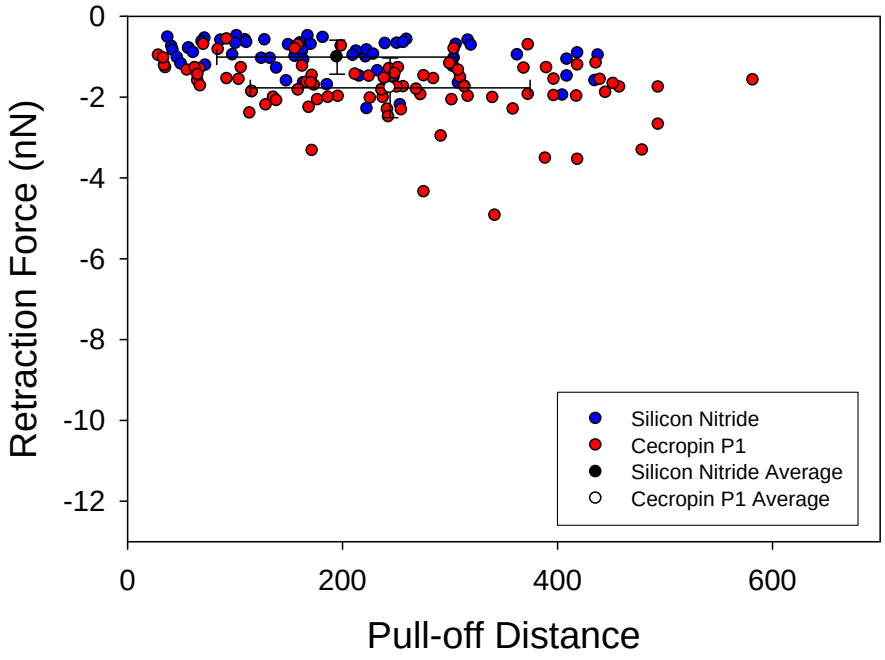

Figure 9.72 O113:H21 AFM Analyses

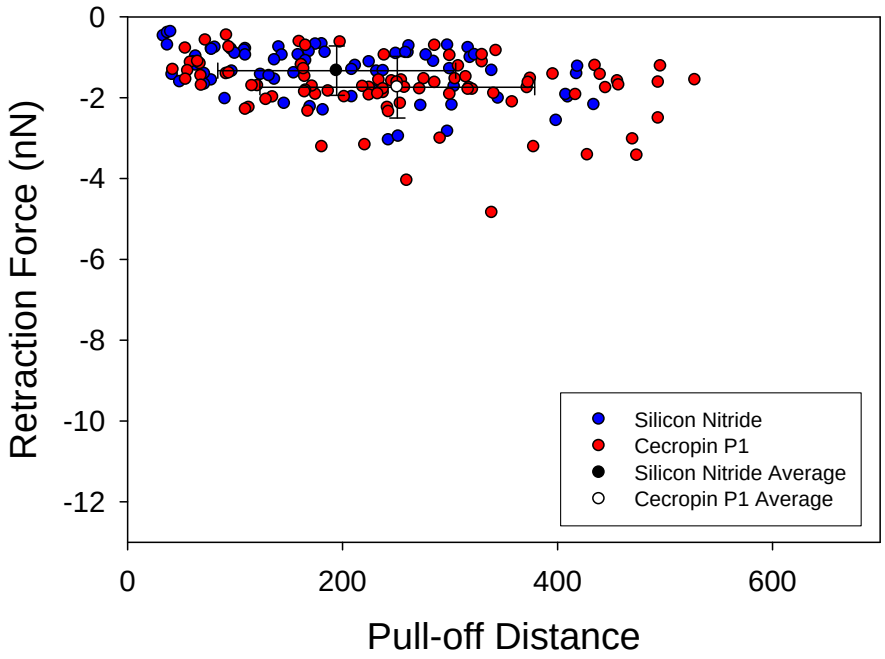

Figure 9.73 O117:K98:H4 AFM Analyses

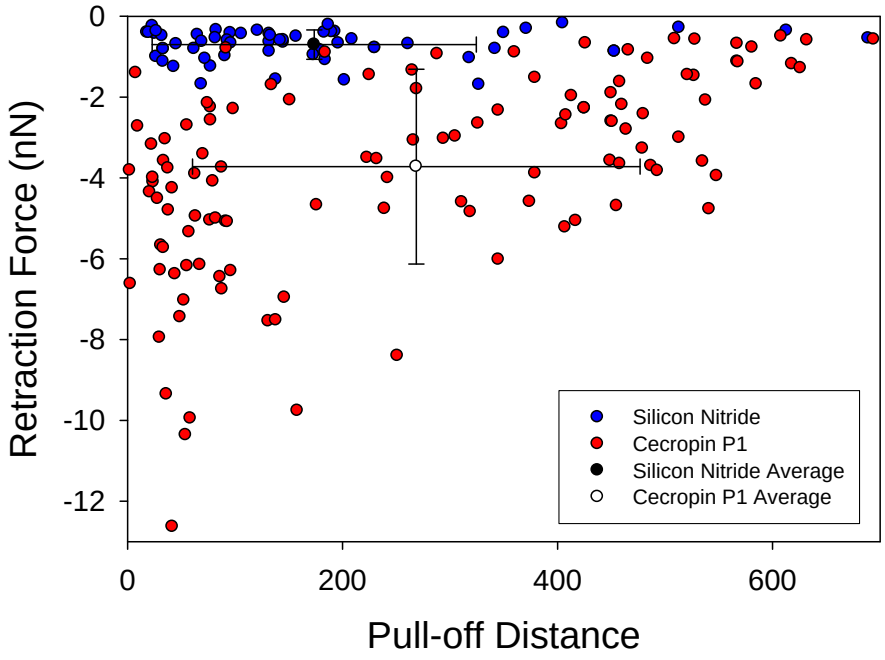

Figure 9.74 O157:H7 AFM Analyses

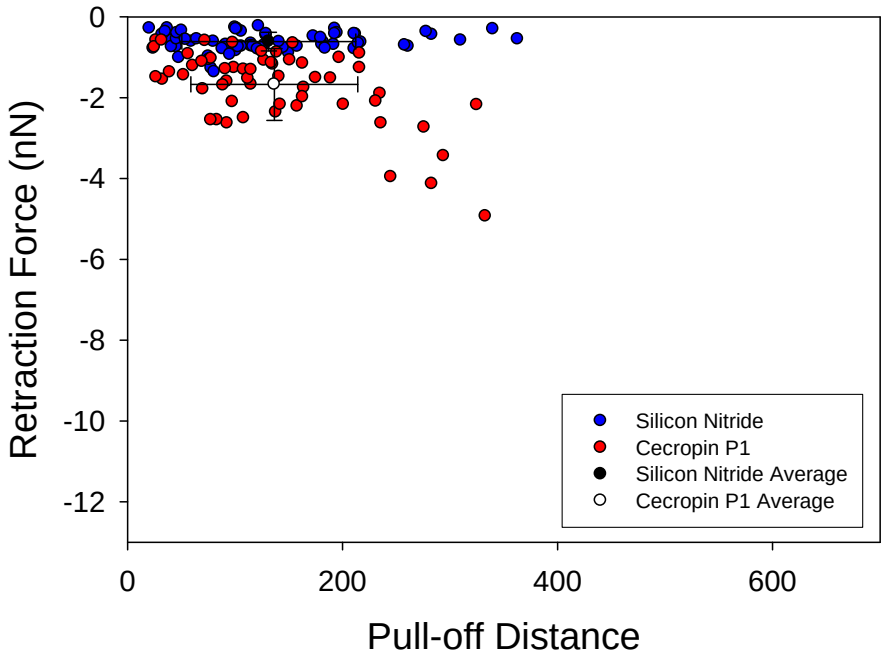

Figure 9.75 O157:H12 AFM Analyses

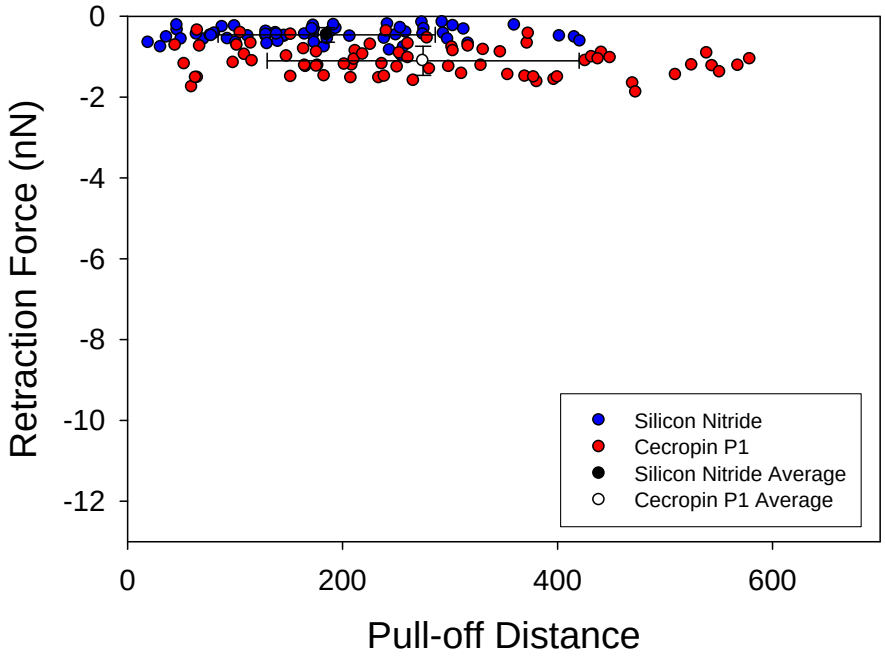

Figure 9.76 O157:H16 AFM Analyses

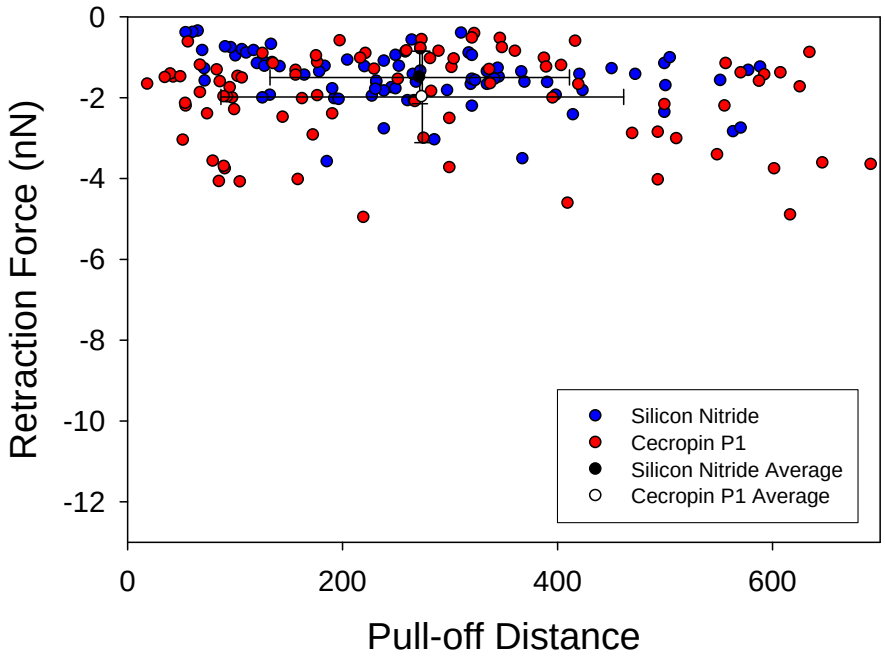

Figure 9.77 O172:H- AFM Analyses

Appendix G: Approach and Retraction Force Plots

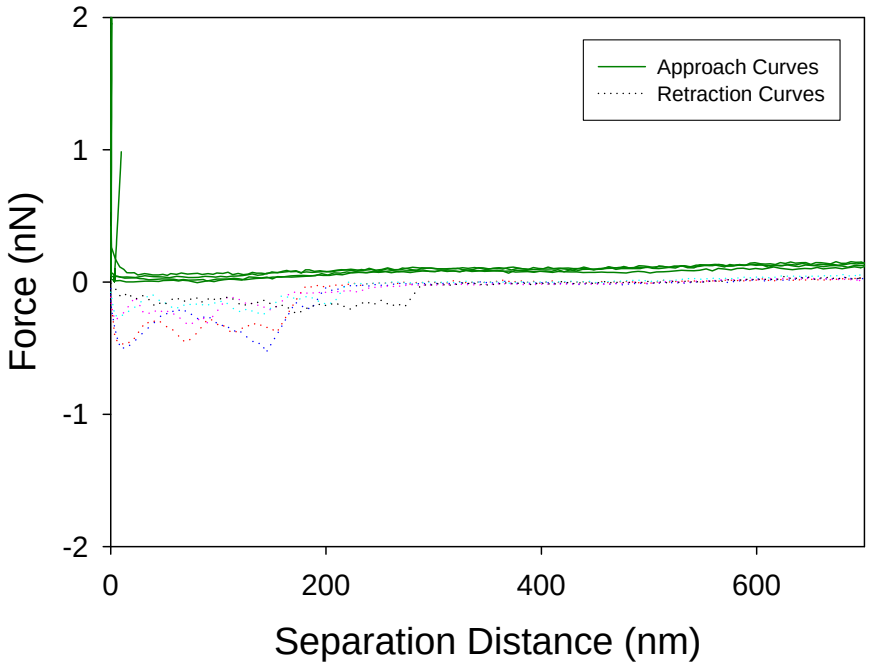

Figure 9.78 5 force plots of HB101 to silicon nitride

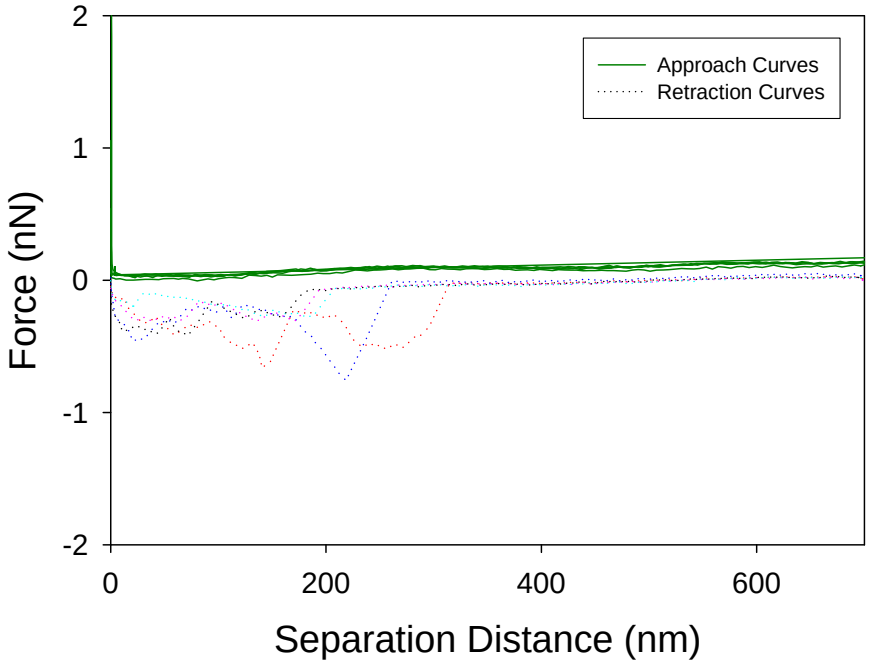

Figure 9.79 5 force plots of HB101 to silicon nitride

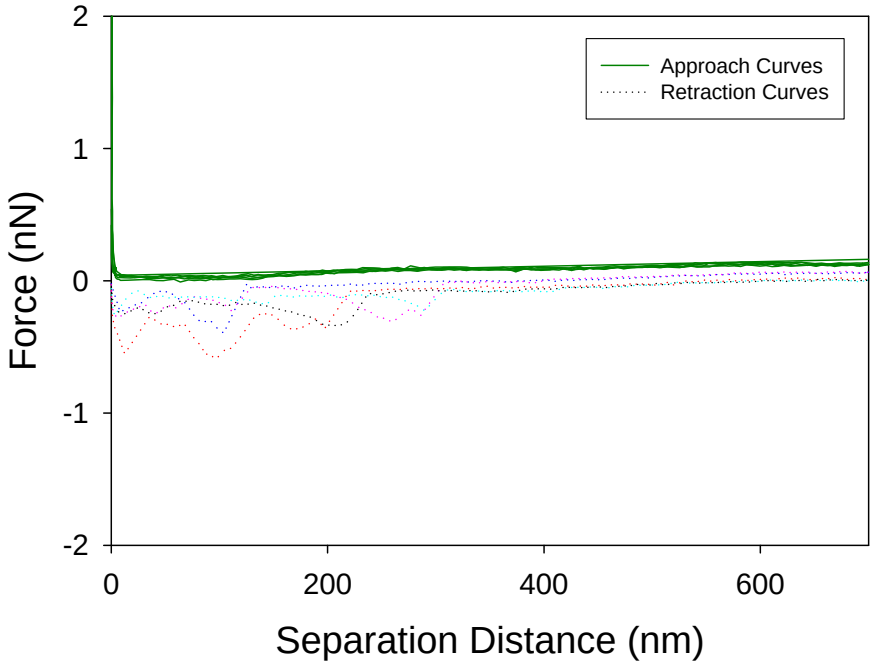

Figure 9.80 5 force plots of HB101 to silicon nitride

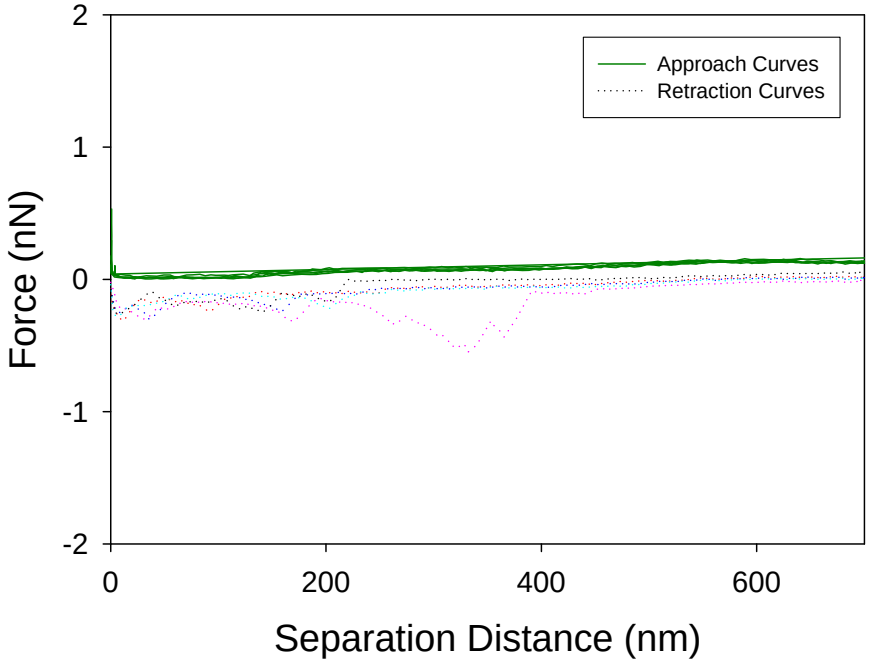

Figure 9.81 5 force plots of HB101 to silicon nitride

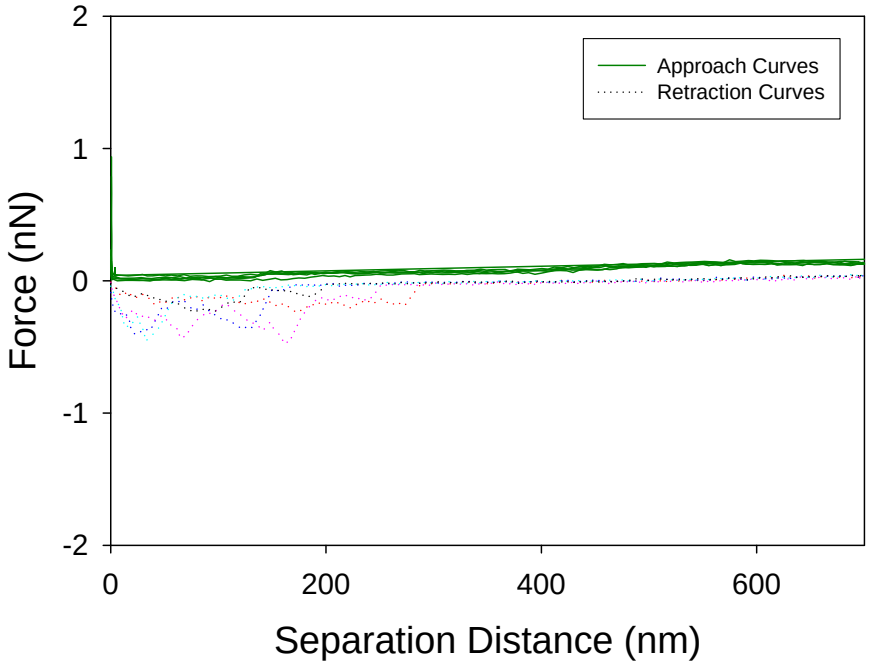

Figure 9.82 5 force plots of HB101 to silicon nitride

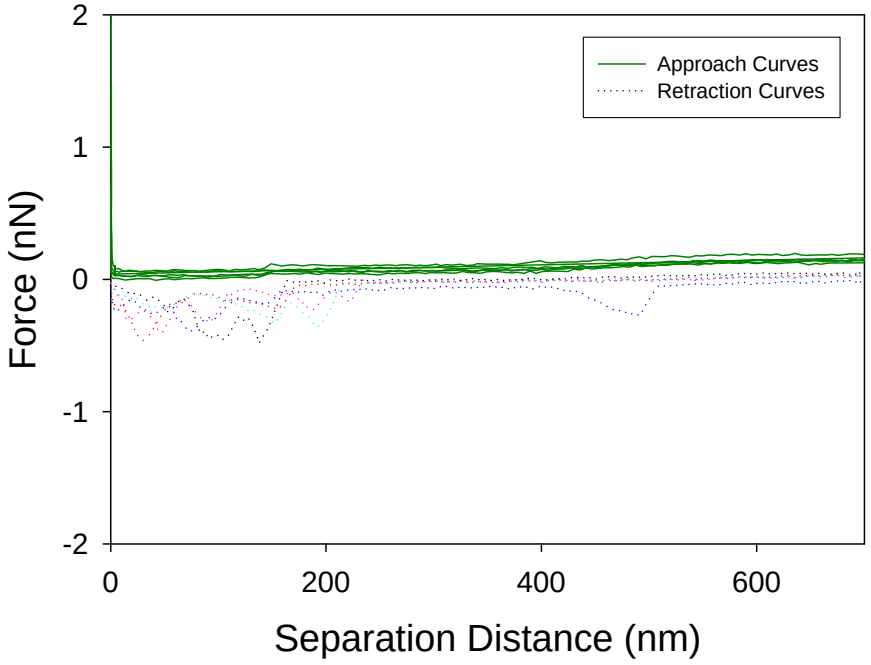

Figure 9.83 5 force plots of HB101 to silicon nitride

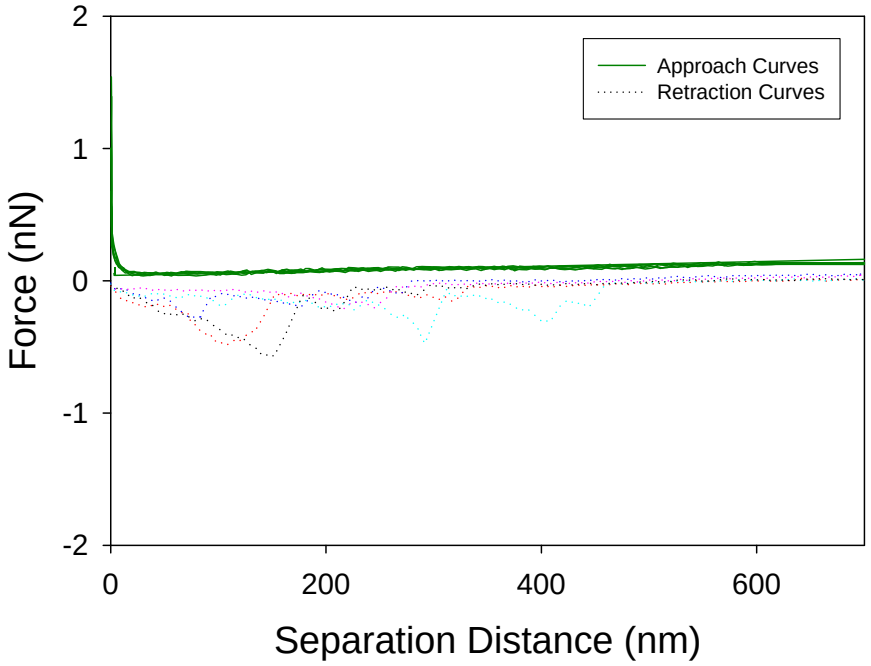

Figure 9.84 5 force plots of HB101 to silicon nitride

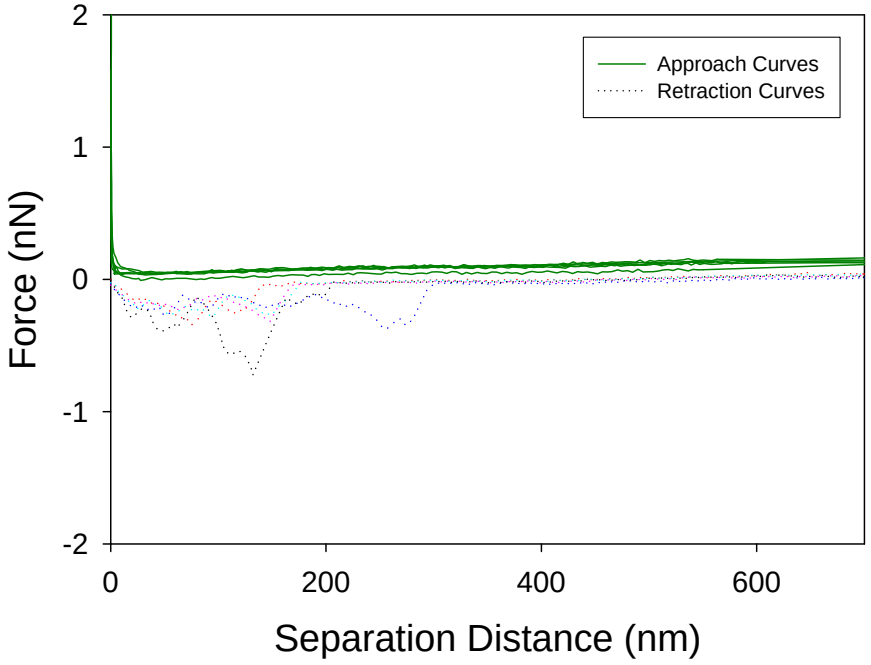

Figure 9.85 5 force plots of HB101 to silicon nitride

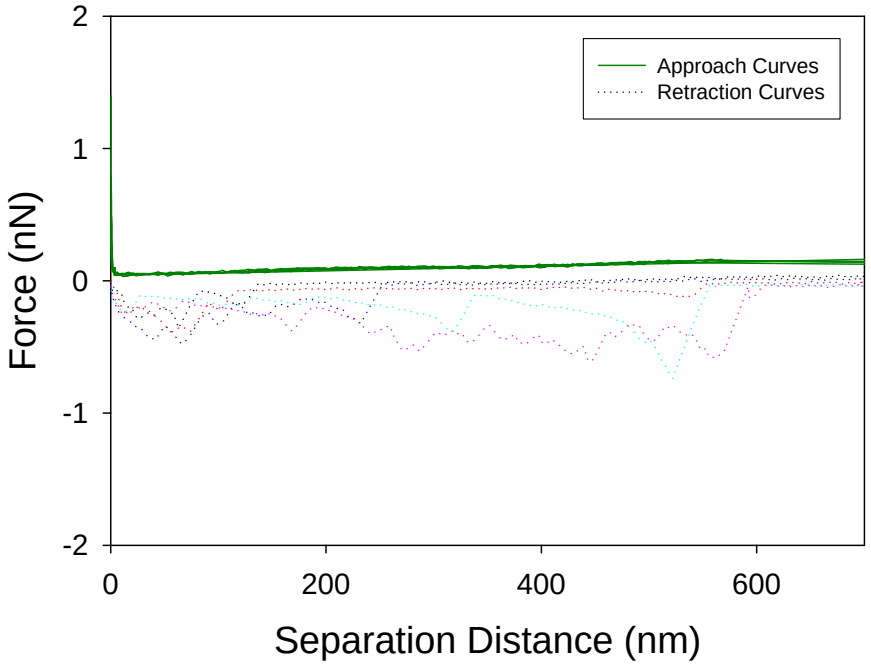

Figure 9.86 5 force plots of HB101 to silicon nitride

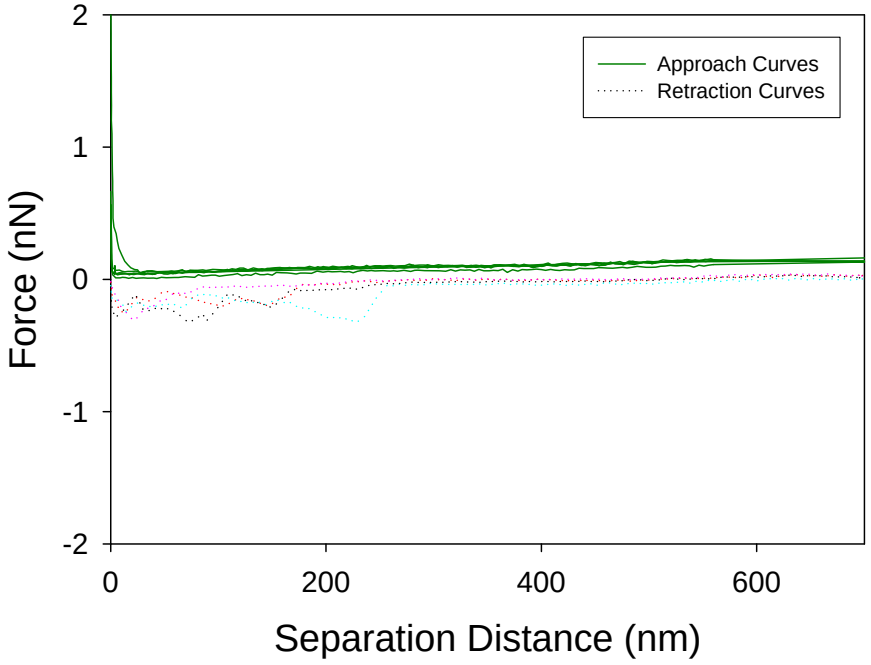

Figure 9.87 5 force plots of HB101 to silicon nitride

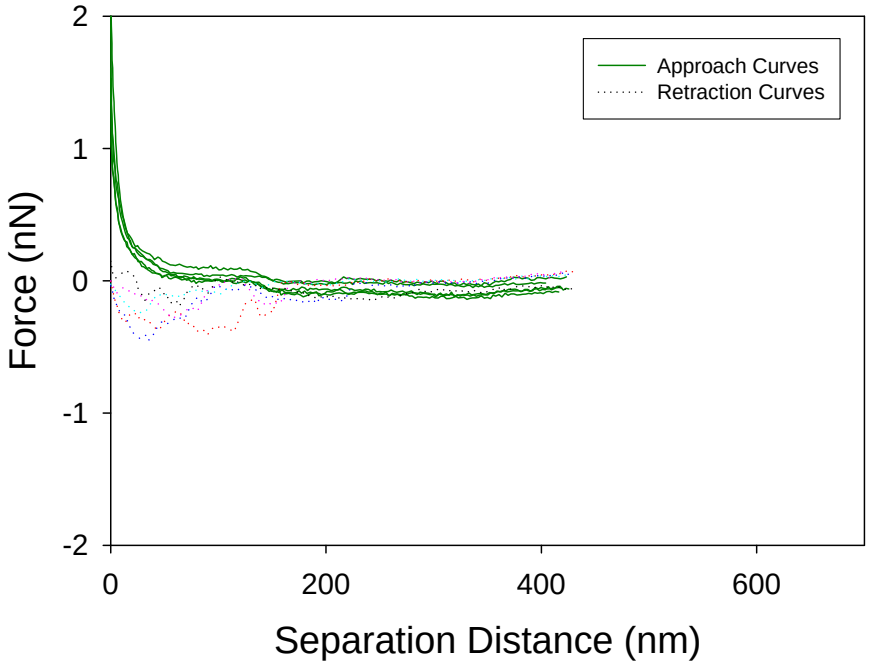

Figure 9.88 5 force plots of HB101 to CP1

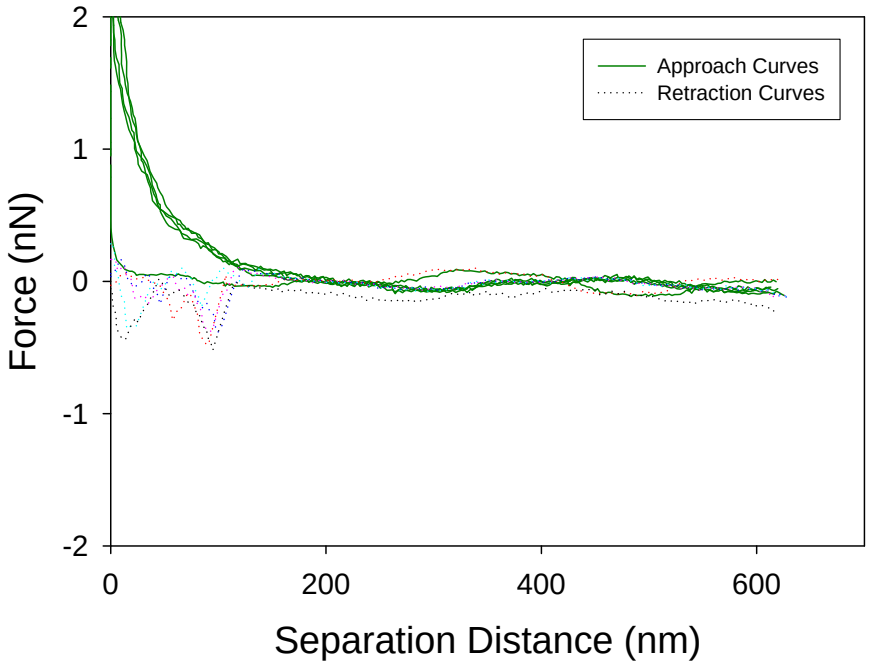

Figure 9.89 5 force plots of HB101 to CP1

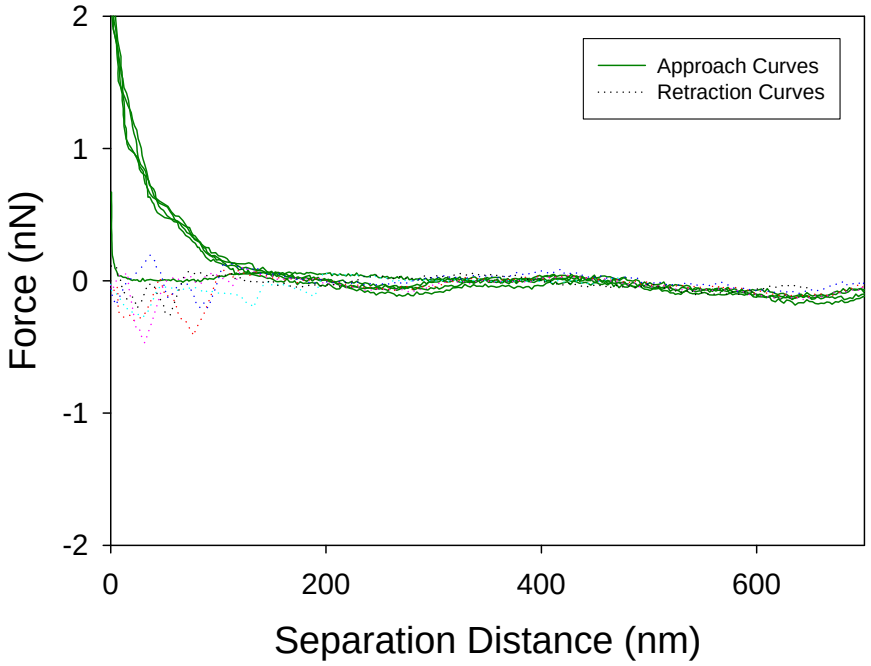

Figure 9.90 5 force plots of HB101 to CP1

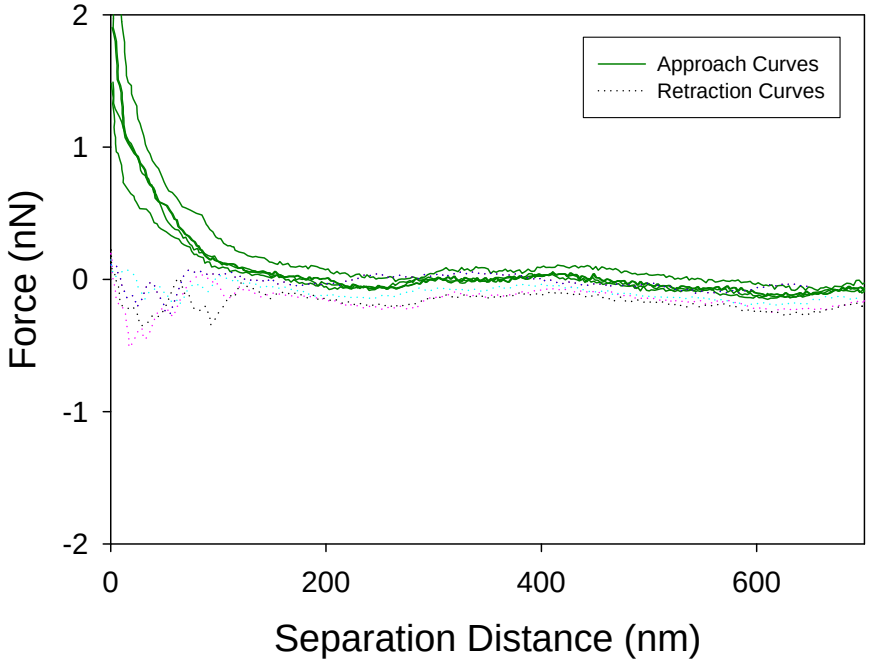

Figure 9.91 5 force plots of HB101 to CP1

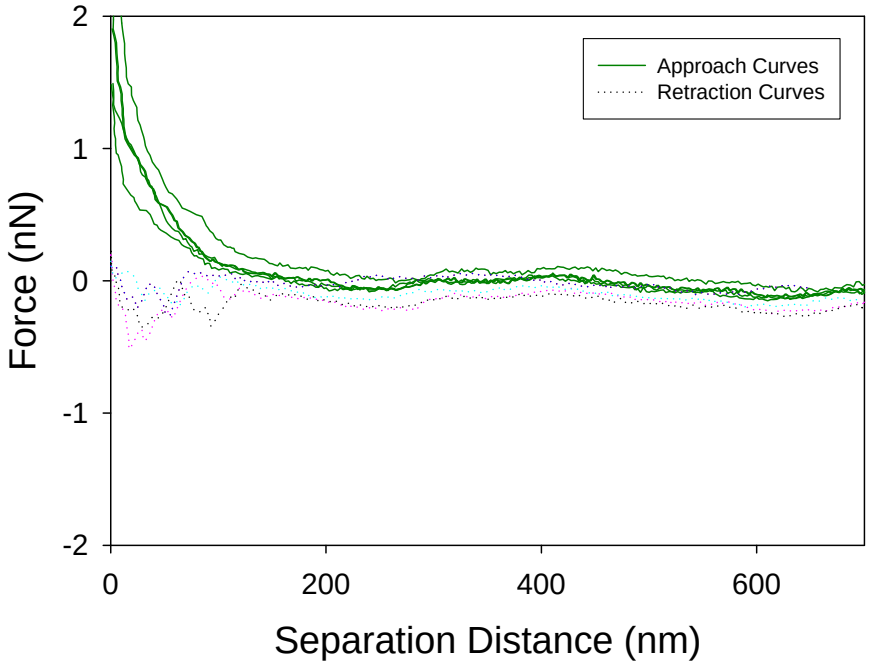

Figure 9.92 5 force plots of HB101 to CP1

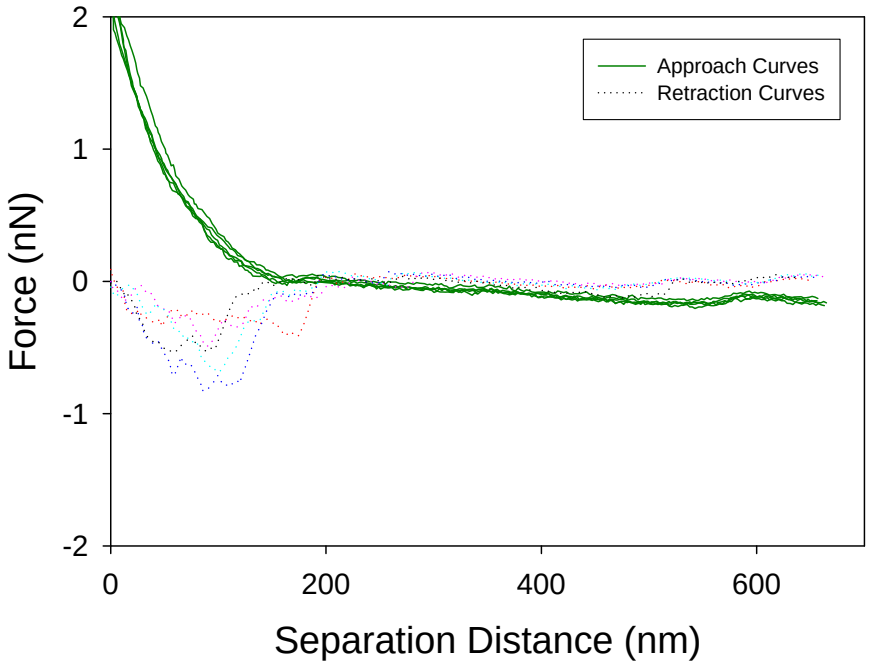

Figure 9.93 5 force plots of HB101 to CP1

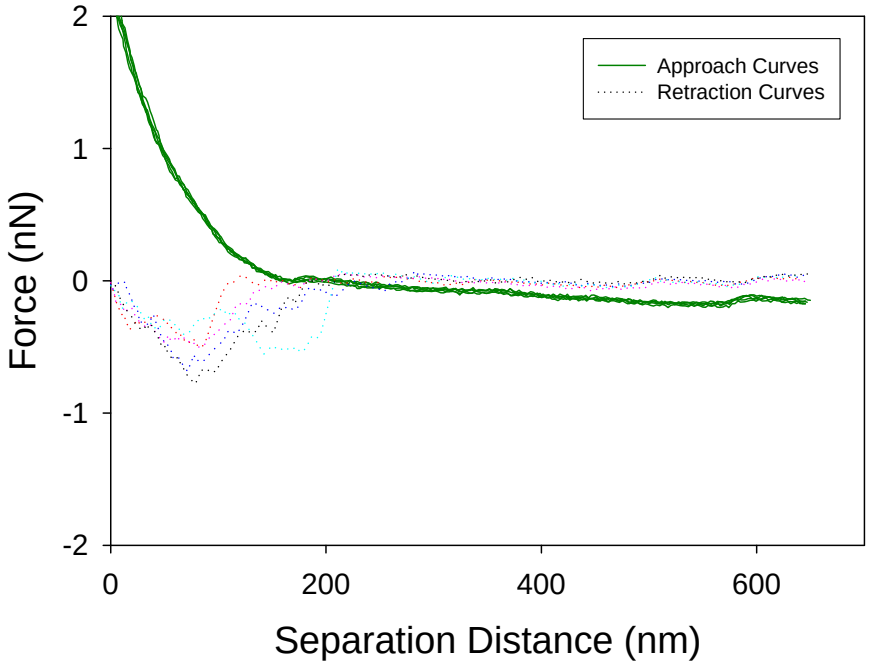

Figure 9.94 5 force plots of HB101 to CP1

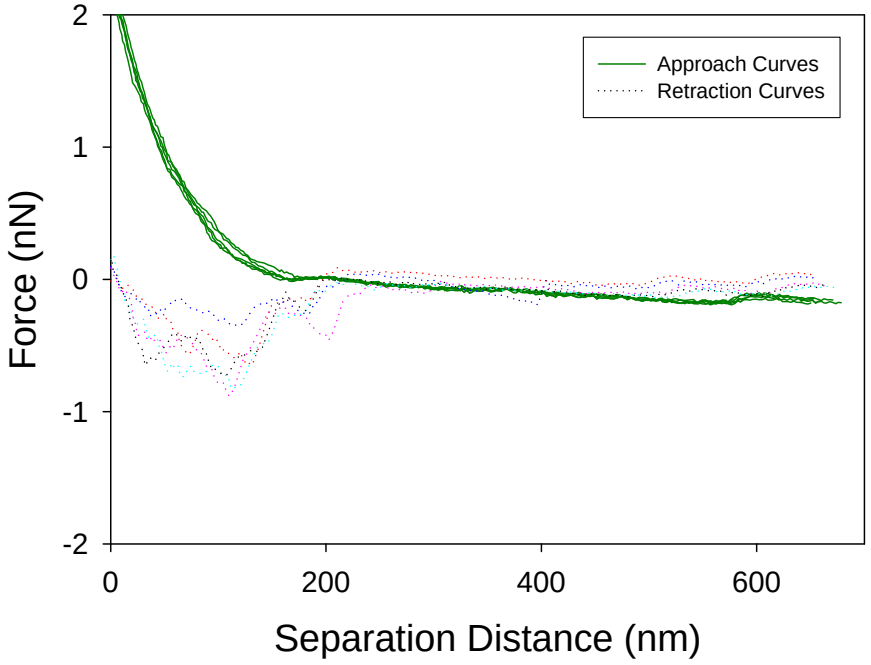

Figure 9.95 5 force plots of HB101 to CP1

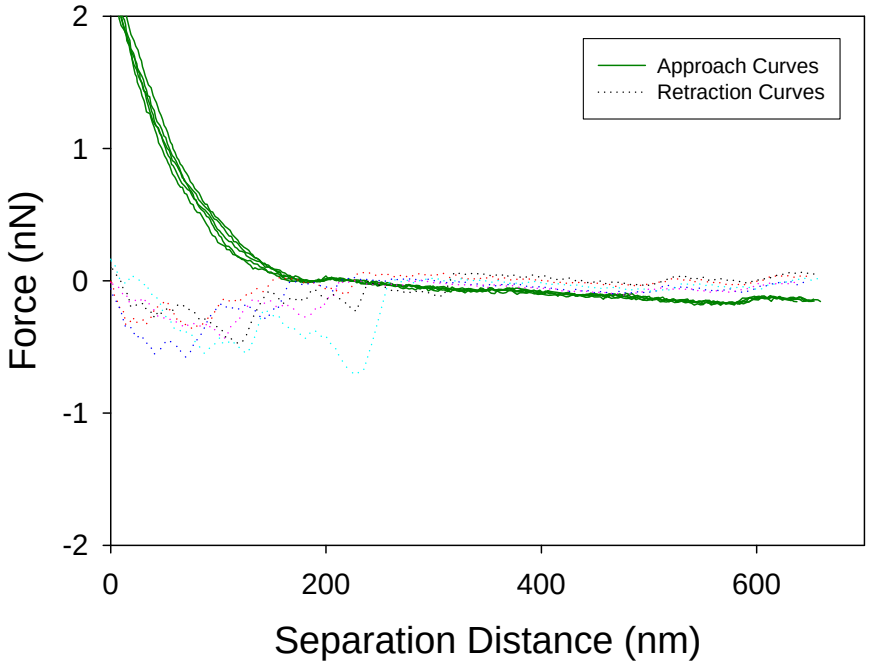

Figure 9.96 5 force plots of HB101 to CP1

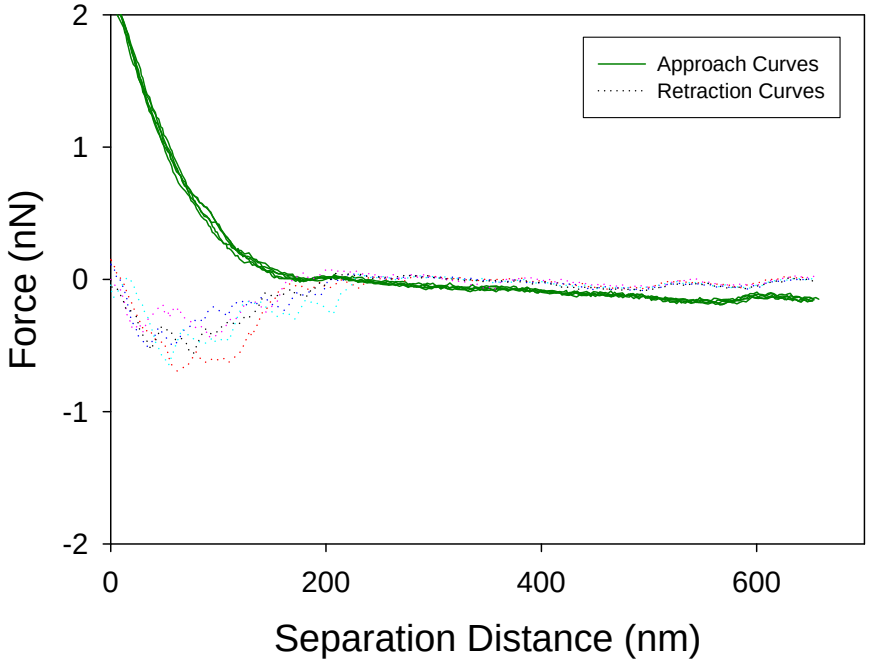

Figure 9.97 5 force plots of HB101 to CP1

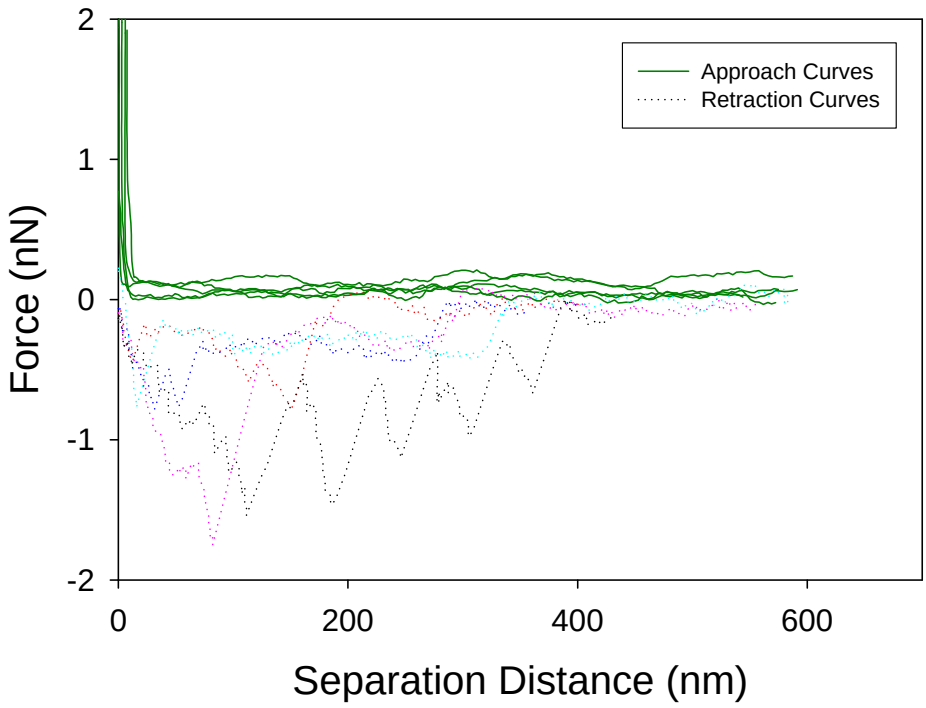

Figure 9.98 5 force plots of K12 to silicon nitride

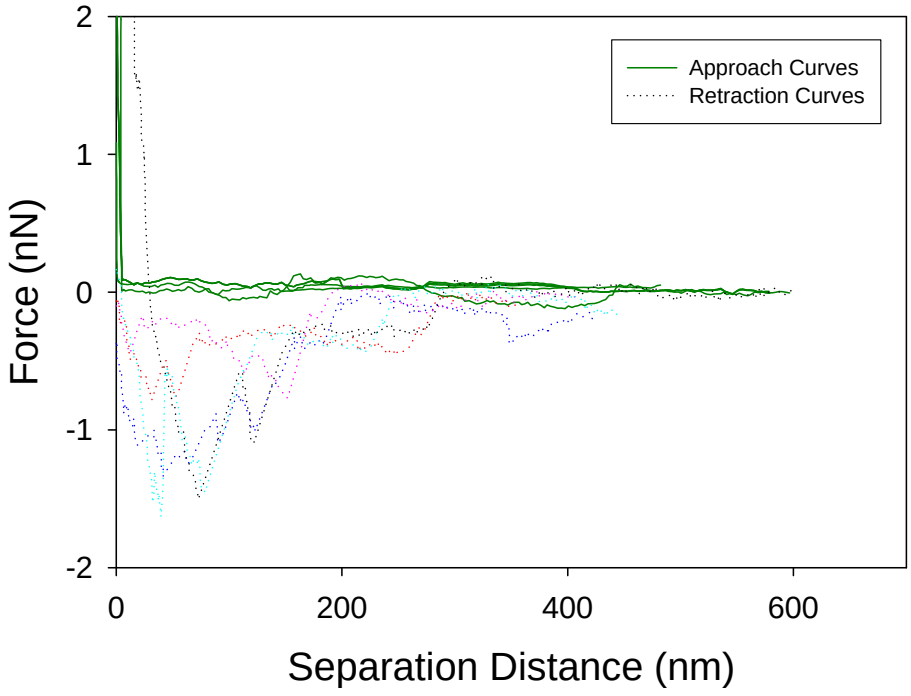

Figure 9.99 5 force plots of K12 to silicon nitride

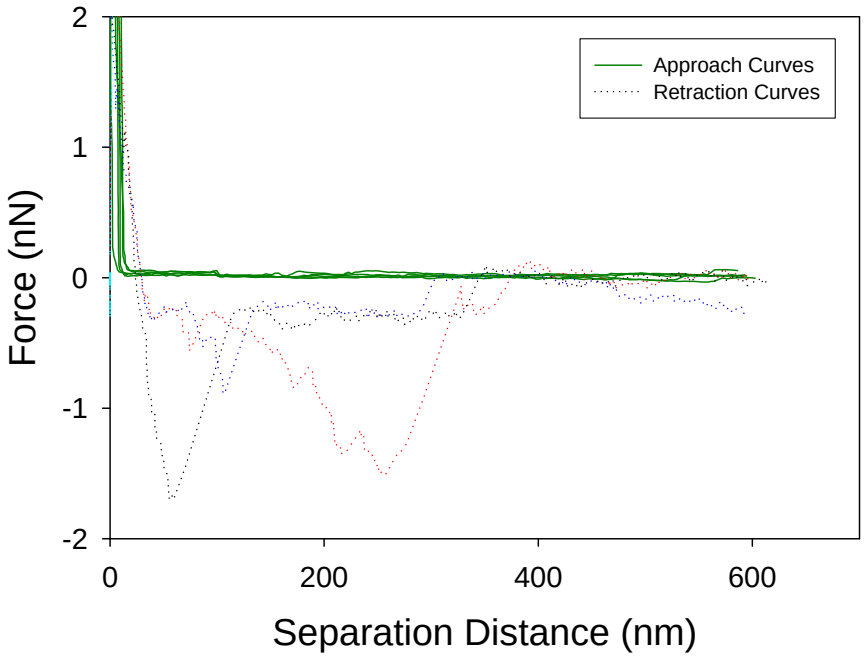

Figure 9.100 5 force plots of K12 to silicon nitride

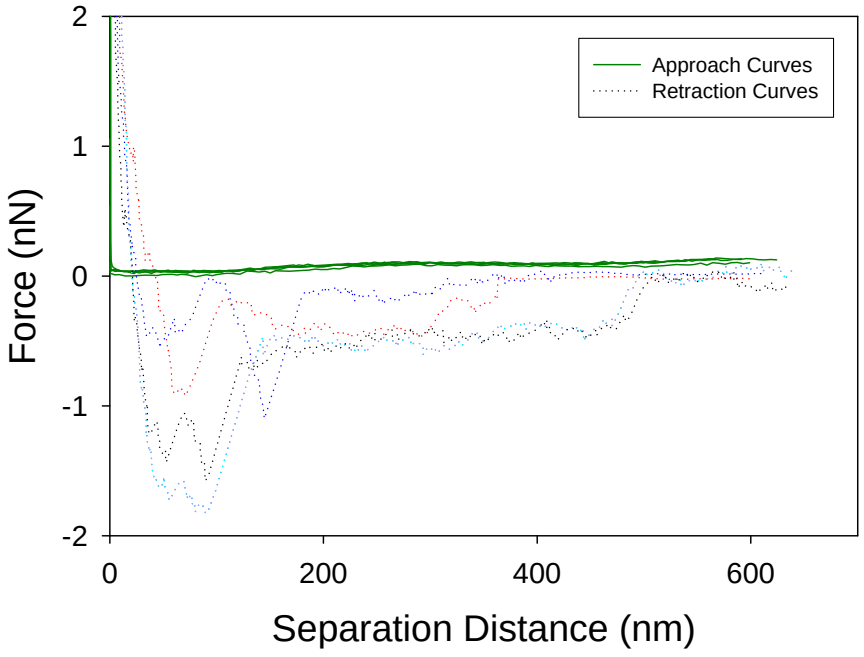

Figure 9.101 5 force plots of K12 to silicon nitride

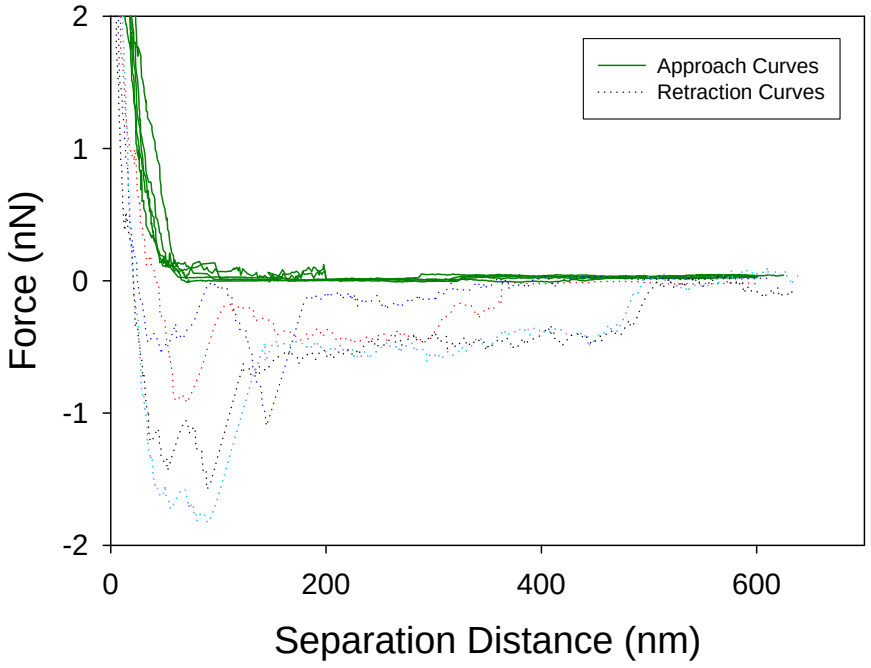

Figure 9.102 5 force plots of K12 to silicon nitride

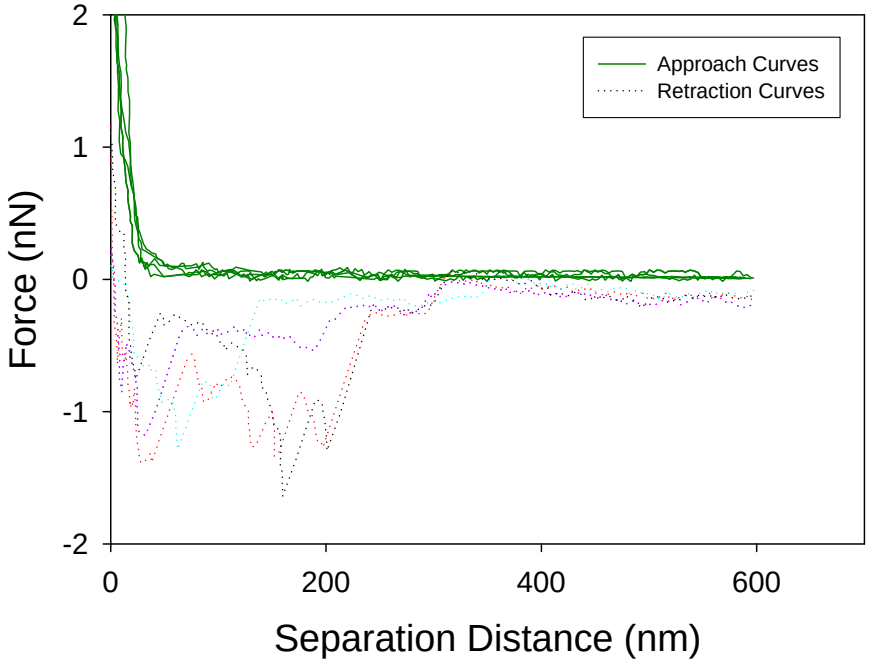

Figure 9.103 5 force plots of K12 to silicon nitride

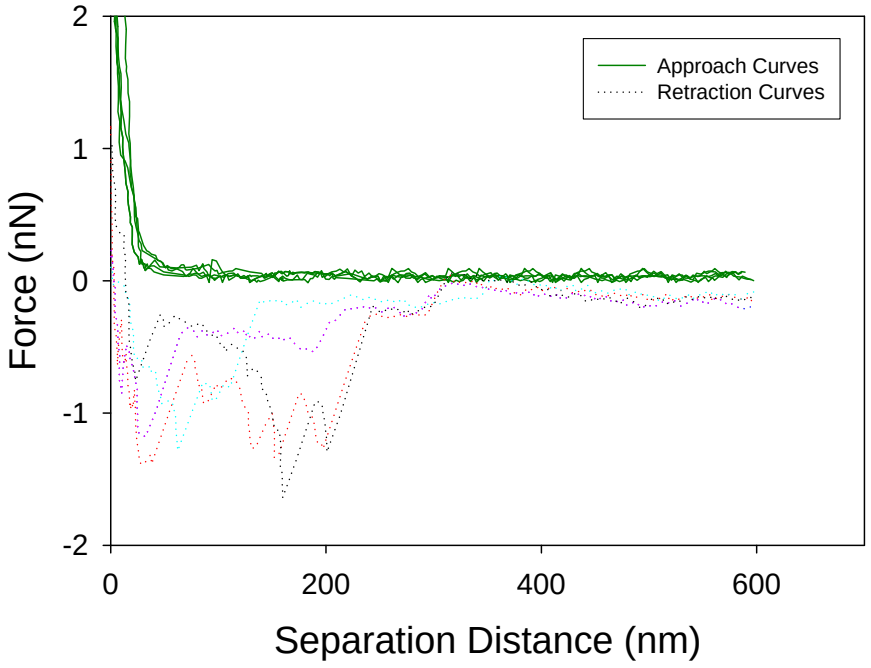

Figure 9.104 5 force plots of K12 to silicon nitride

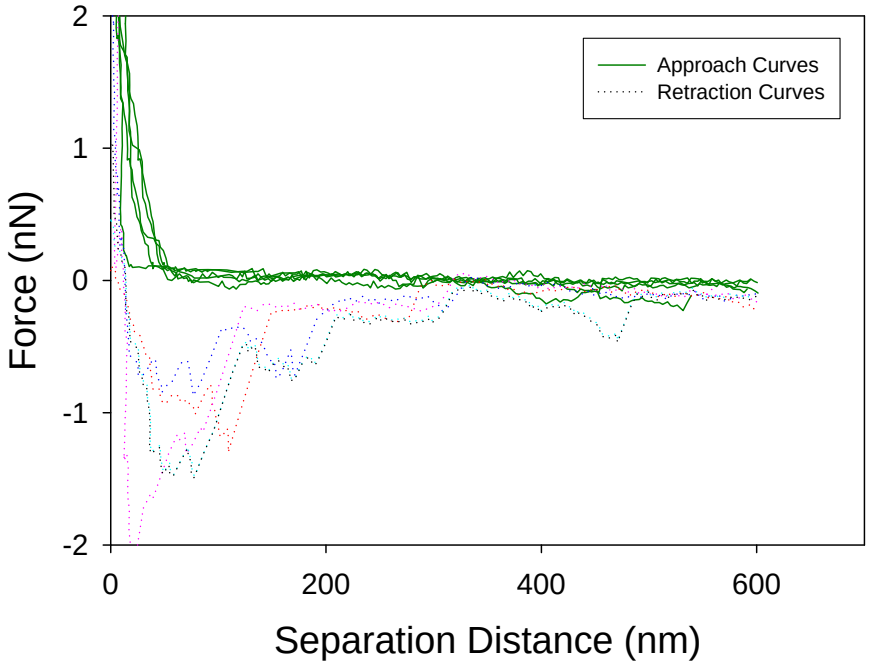

Figure 9.105 5 force plots of K12 to silicon nitride

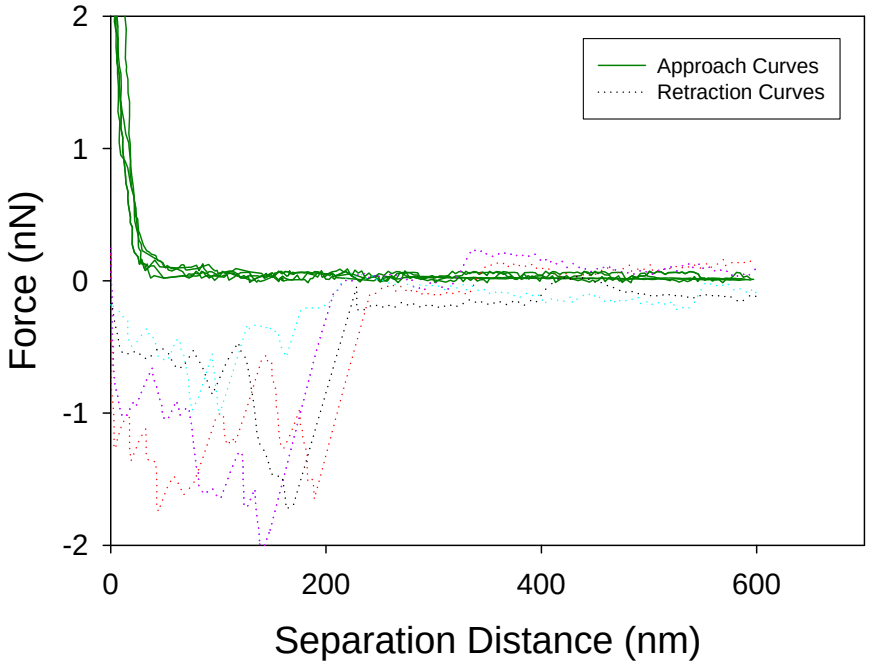

Figure 9.106 5 force plots of K12 to silicon nitride

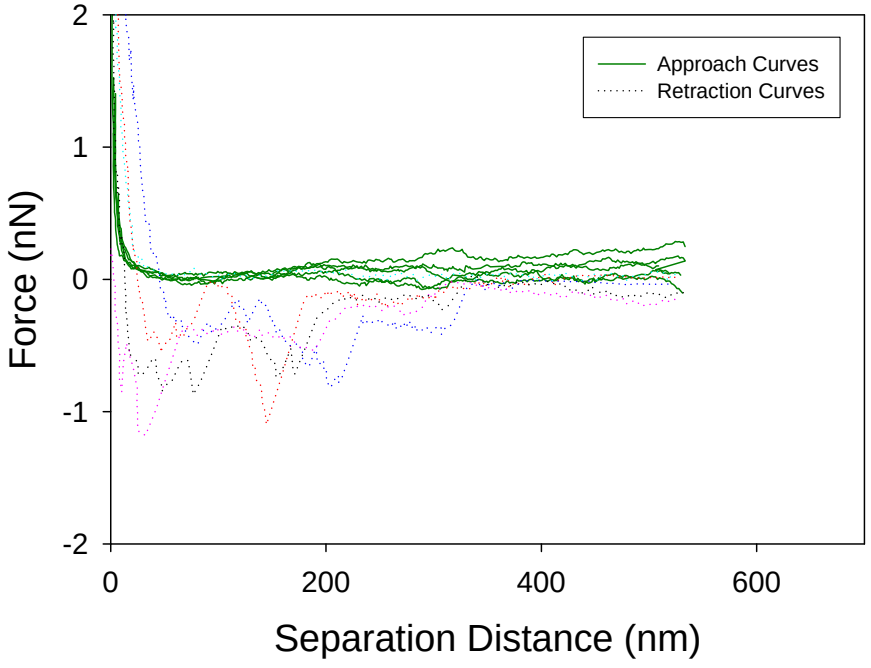

Figure 9.107 5 force plots of K12 to silicon nitride

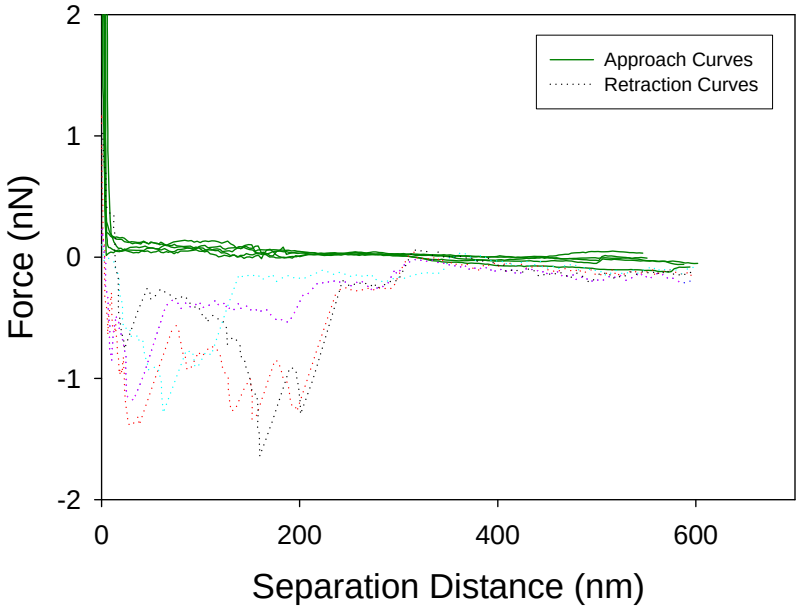

Figure 9.108 5 force plots of K12 to CP1

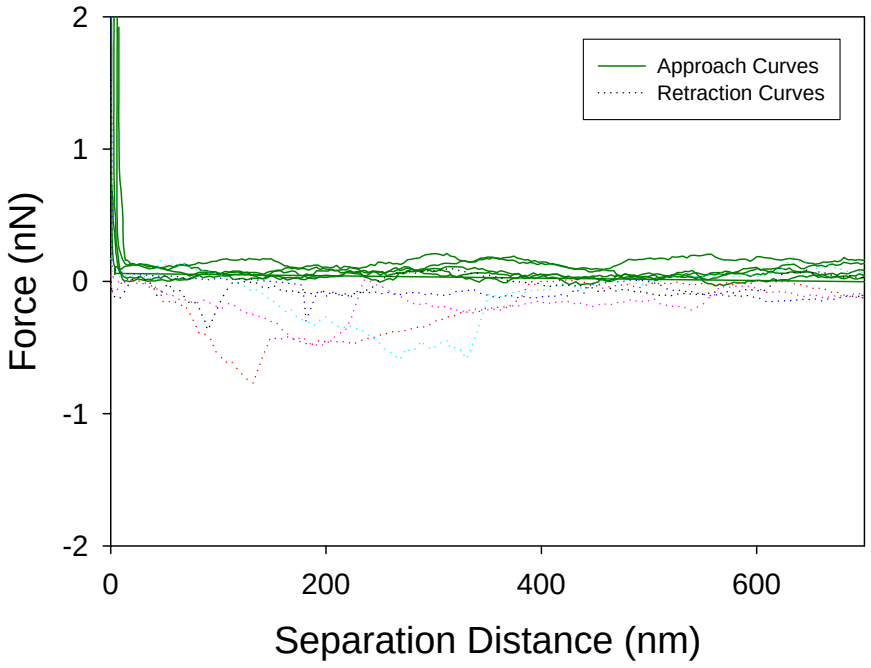

Figure 9.109 5 force plots of K12 to CP1

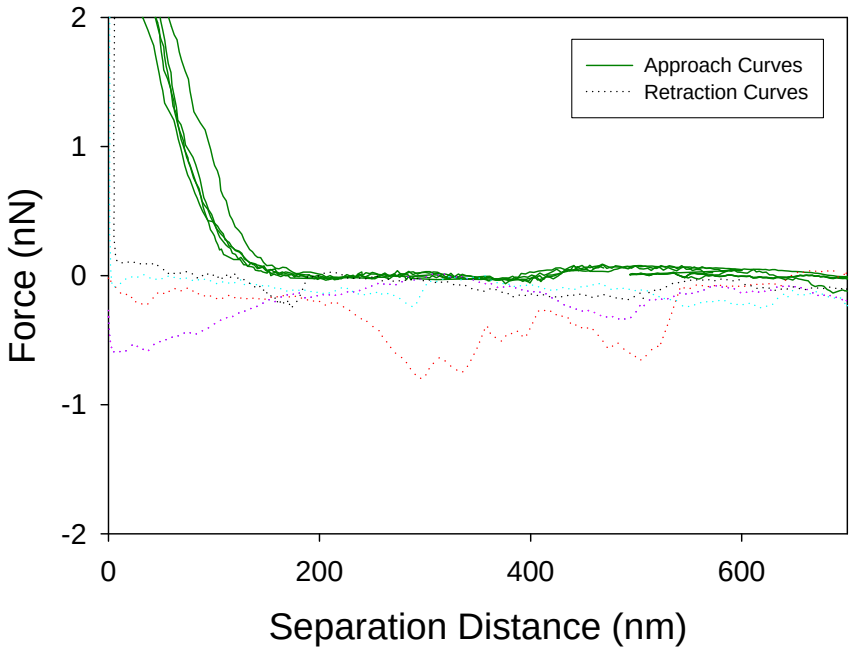

Figure 9.110 5 force plots of K12 to CP1

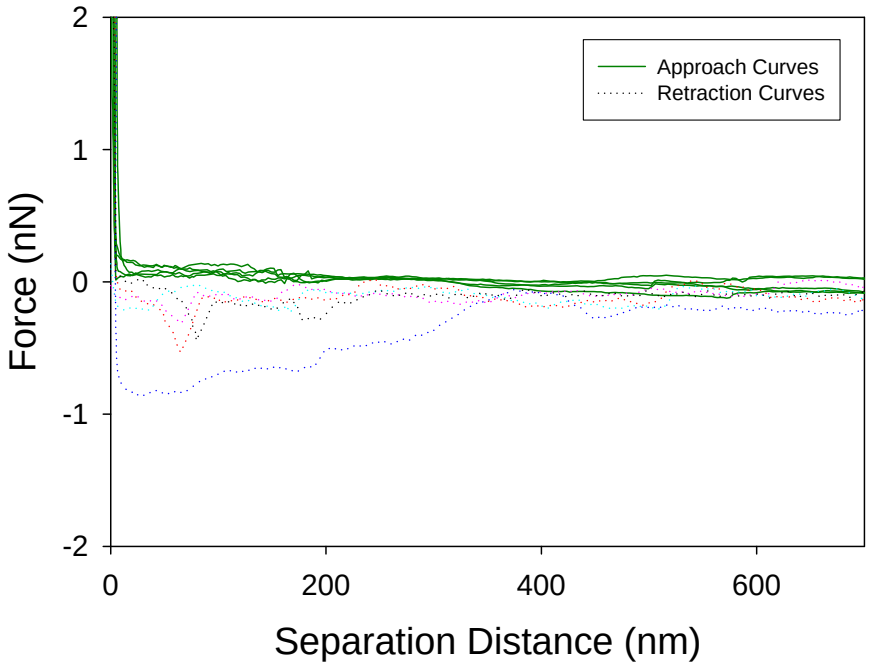

Figure 9.111 5 force plots of K12 to CP1

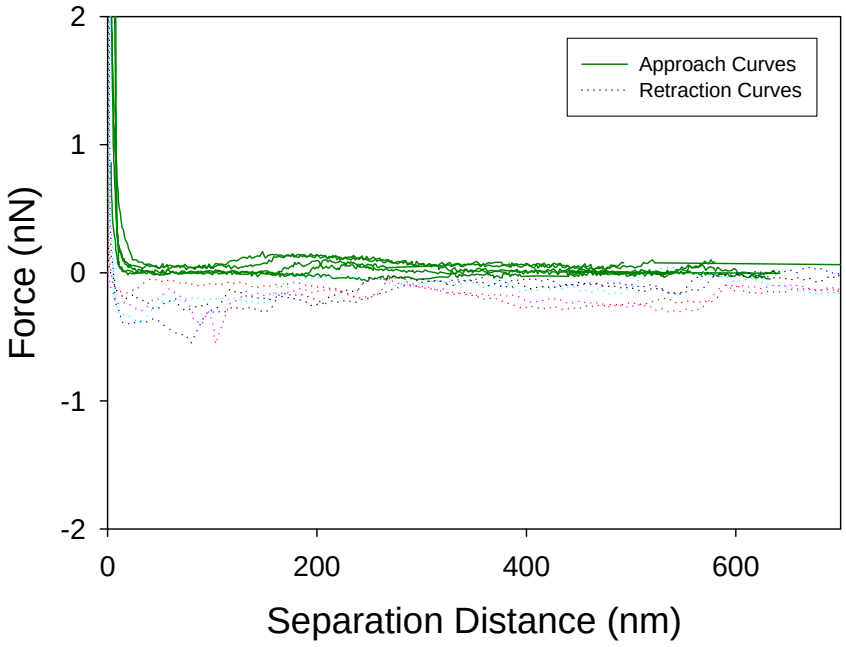

Figure 9.112 5 force plots of K12 to CP1

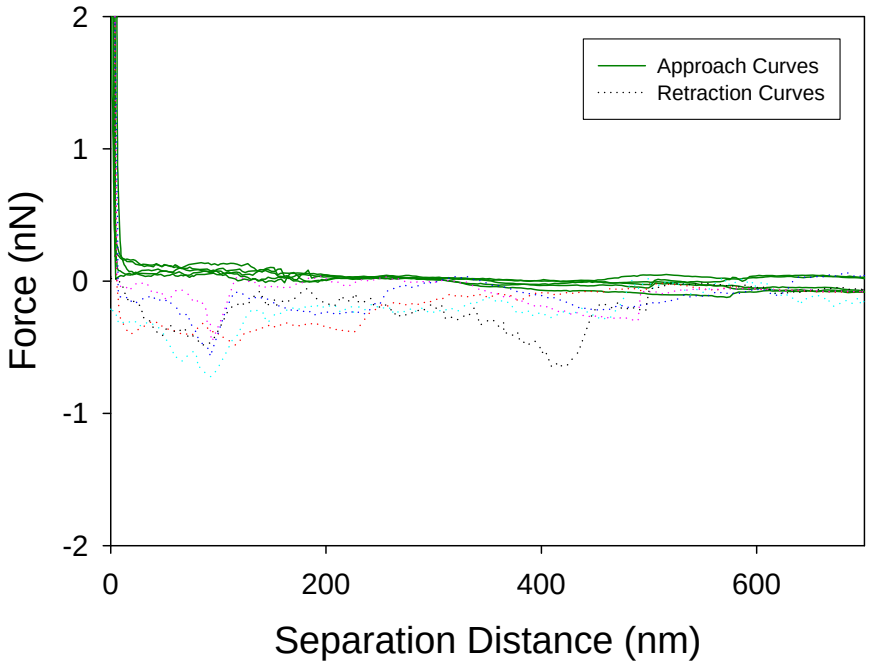

Figure 9.113 5 force plots of K12 to CP1

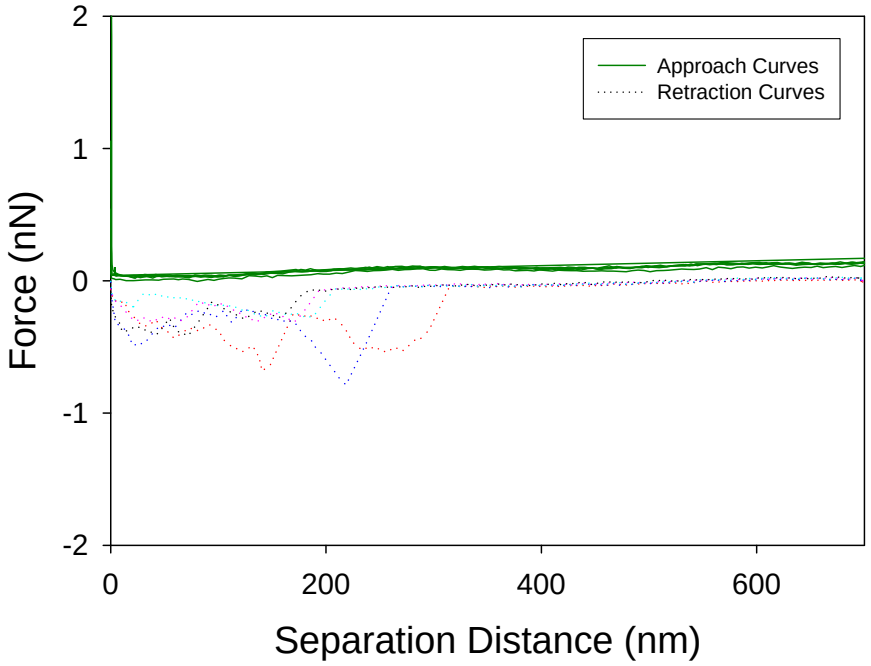

Figure 9.114 5 force plots of K12 to CP1

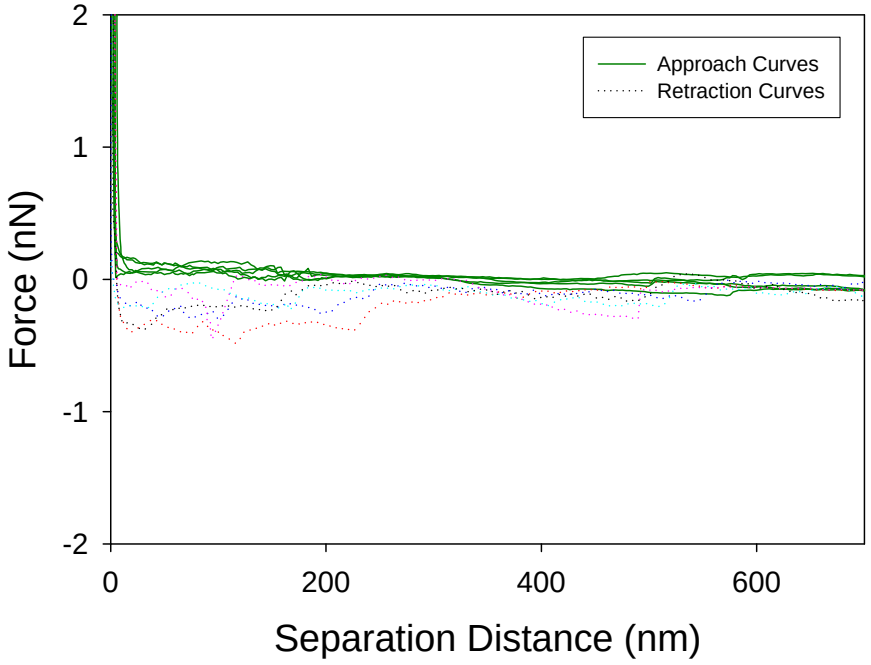

Figure 9.115 5 force plots of K12 to CP1

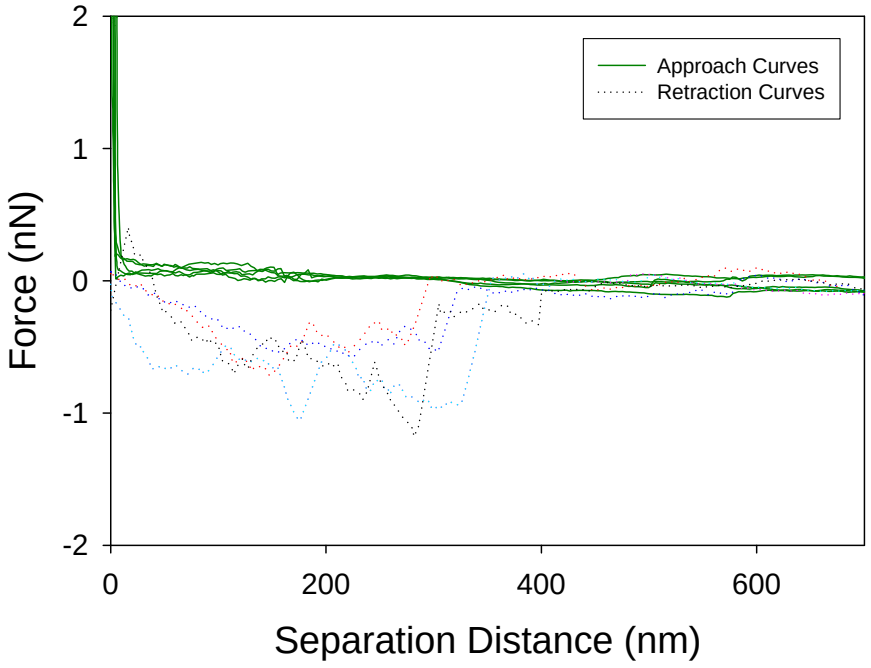

Figure 9.116 5 force plots of K12 to CP1

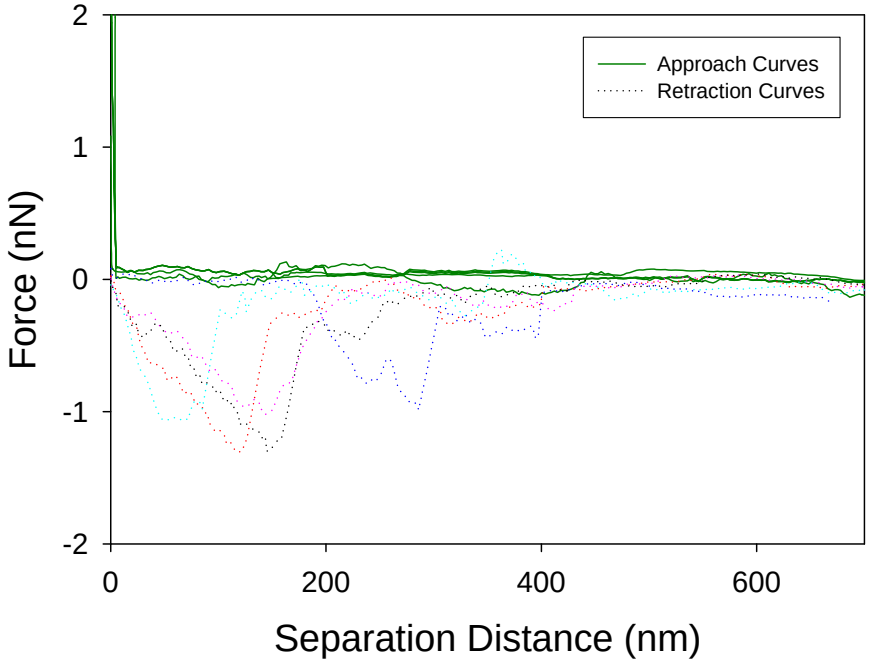

Figure 9.117 5 force plots of K12 to CP1

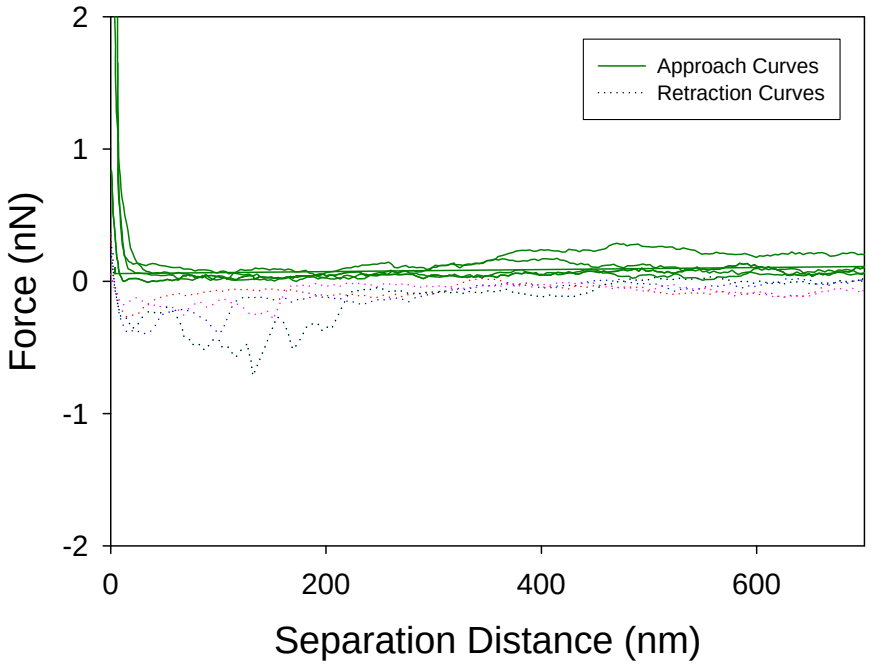

Figure 9.118 5 force plots of ML35 to silicon nitride

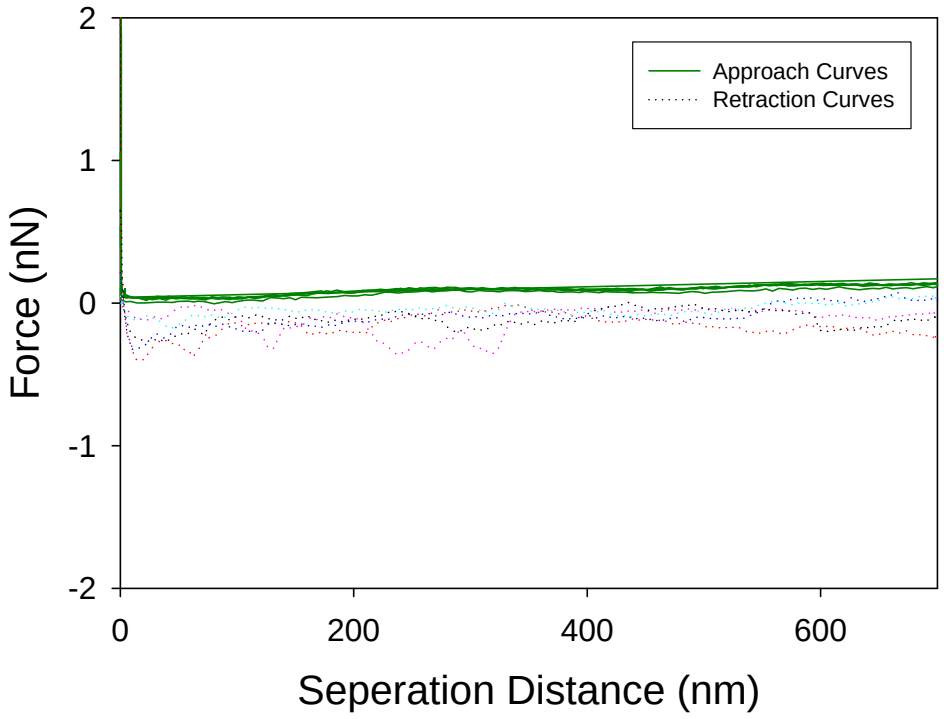

Figure 9.119 5 force plots of ML35 to silicon nitride

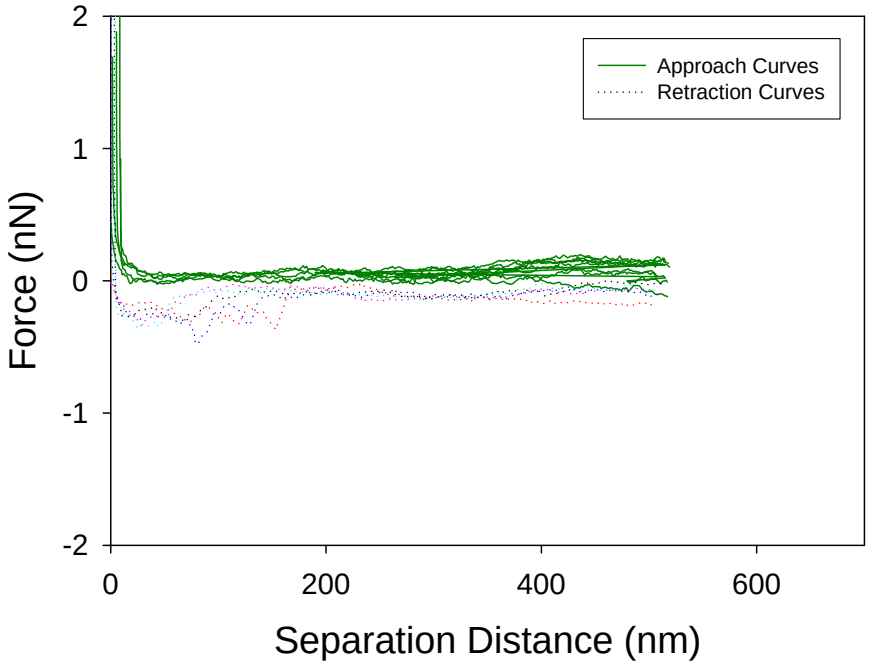

Figure 9.120 5 force plots of ML35 to silicon nitride

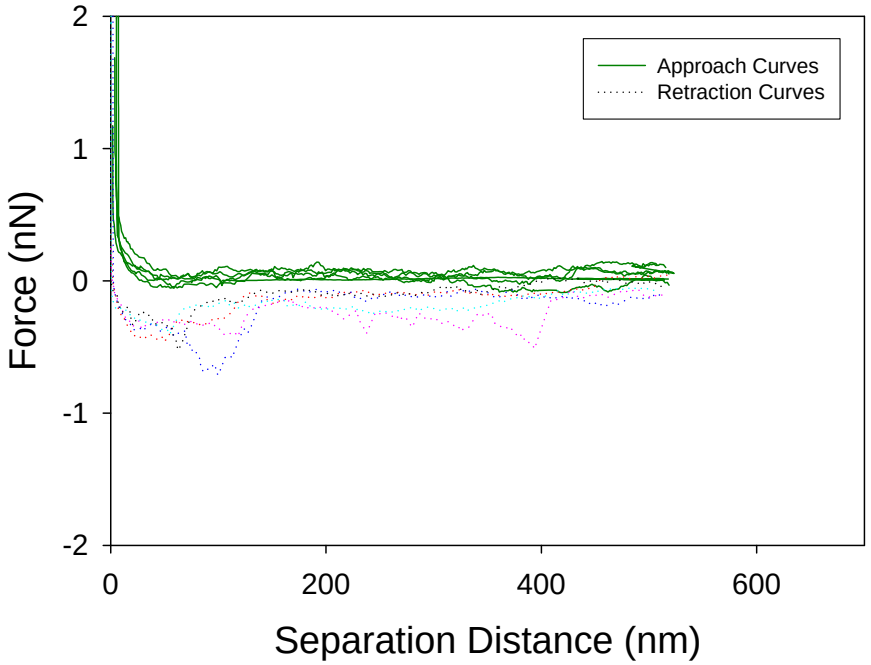

Figure 9.121 5 force plots of ML35 to silicon nitride

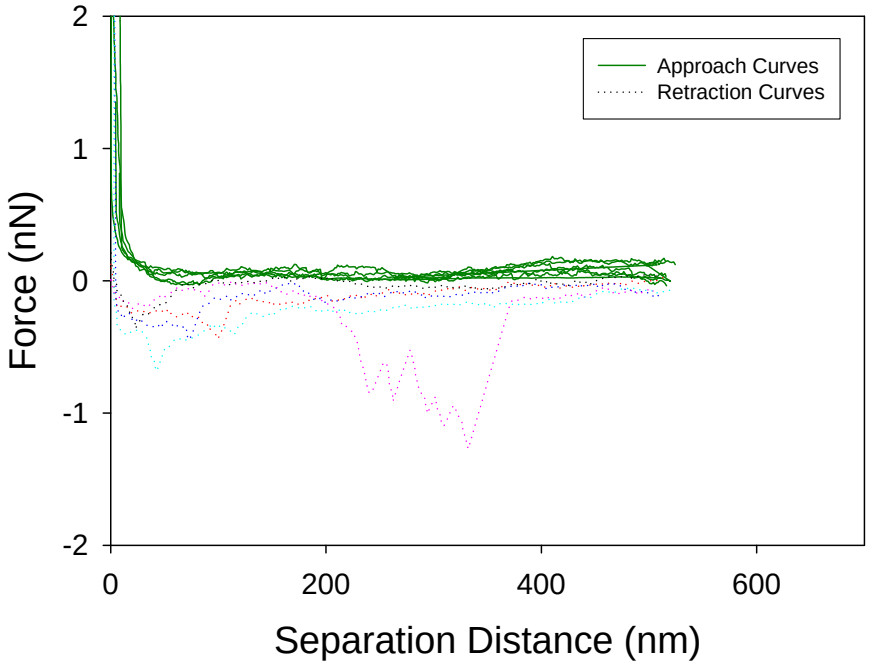

Figure 9.122 5 force plots of ML35 to silicon nitride

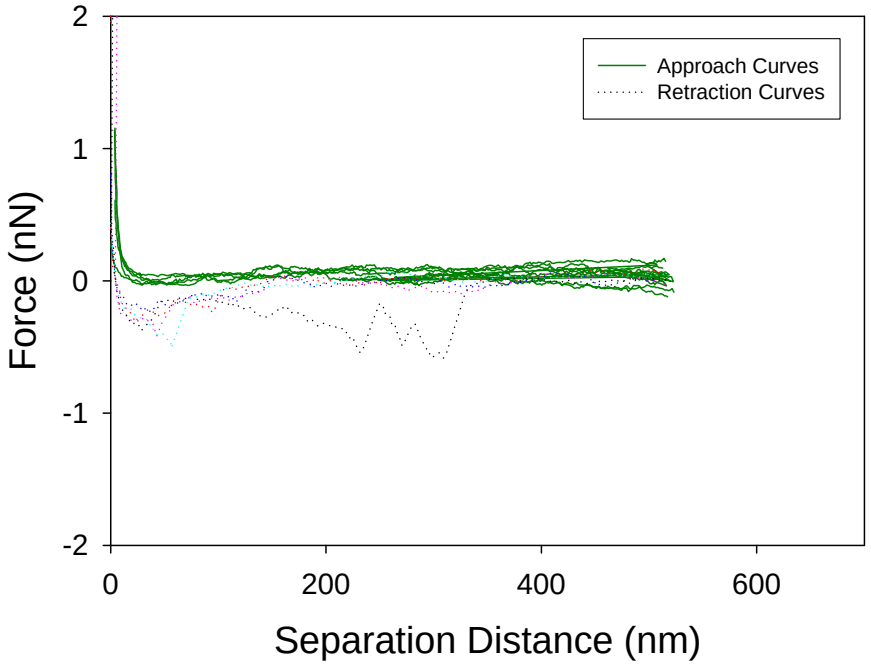

Figure 9.123 5 force plots of ML35 to silicon nitride

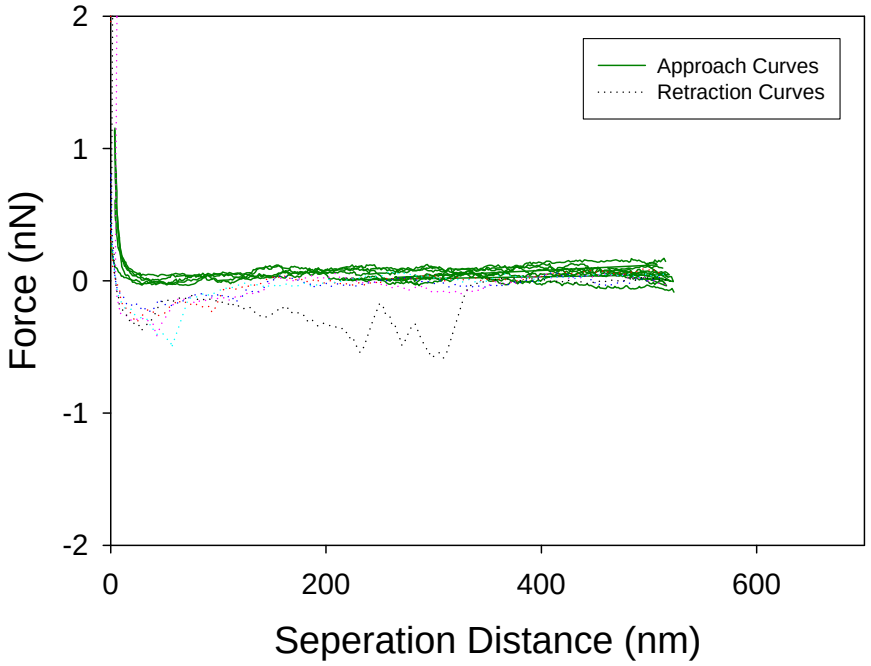

Figure 9.124 5 force plots of ML35 to silicon nitride

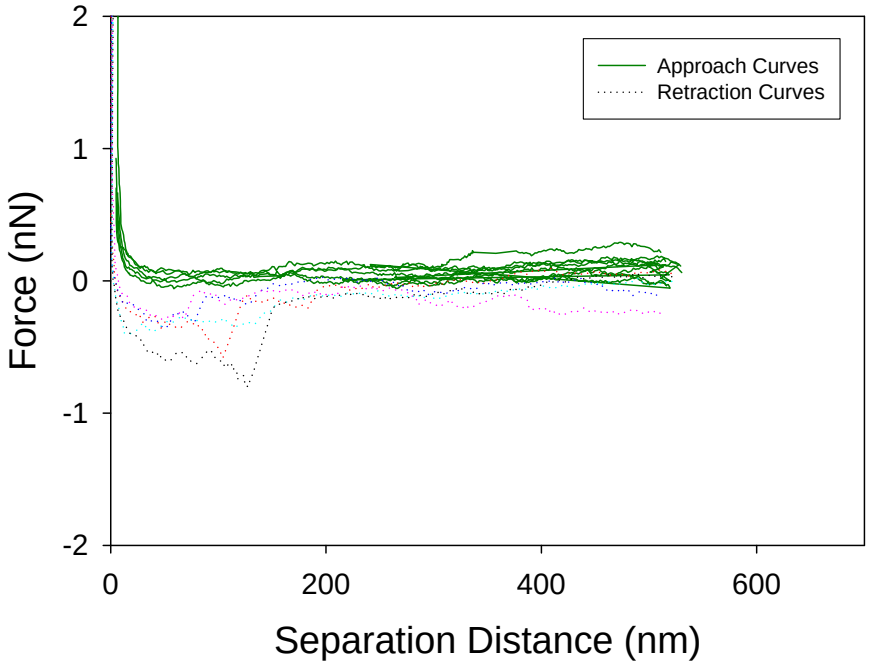

Figure 9.125 5 force plots of ML35 to silicon nitride

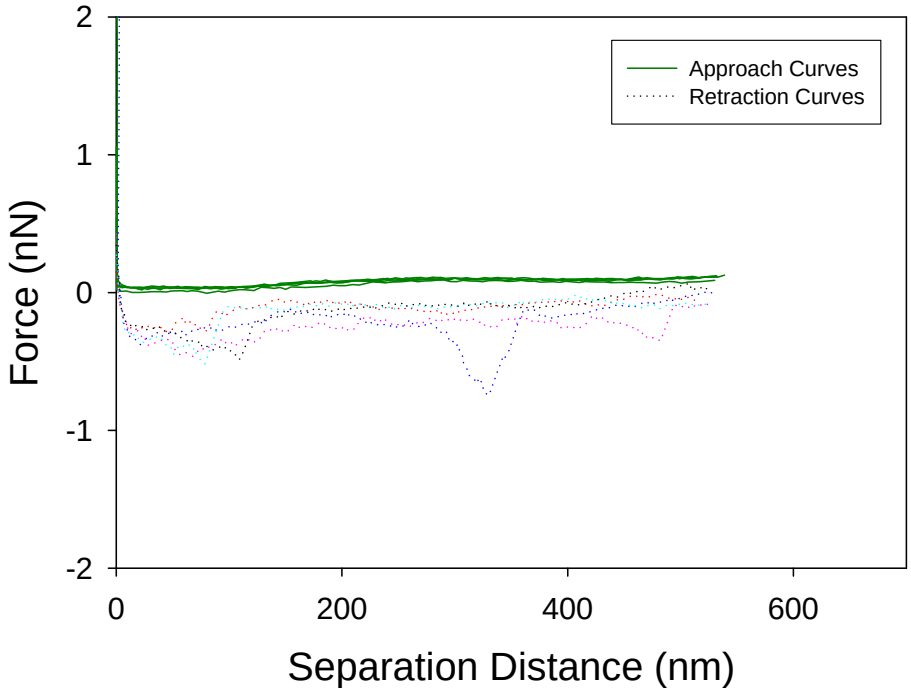

Figure 9.126 5 force plots of ML35 to silicon nitride

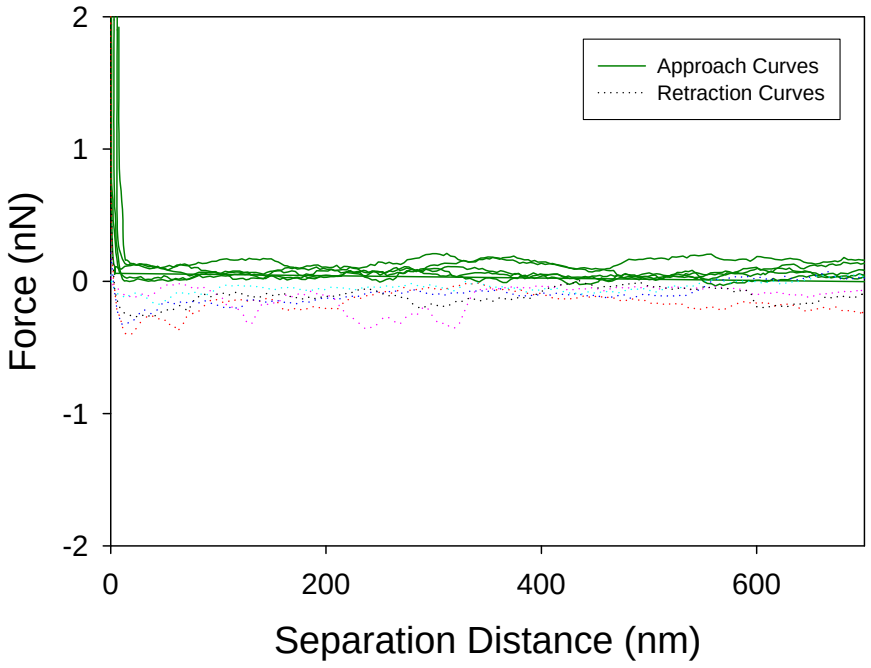

Figure 9.127 5 force plots of ML35 to silicon nitride

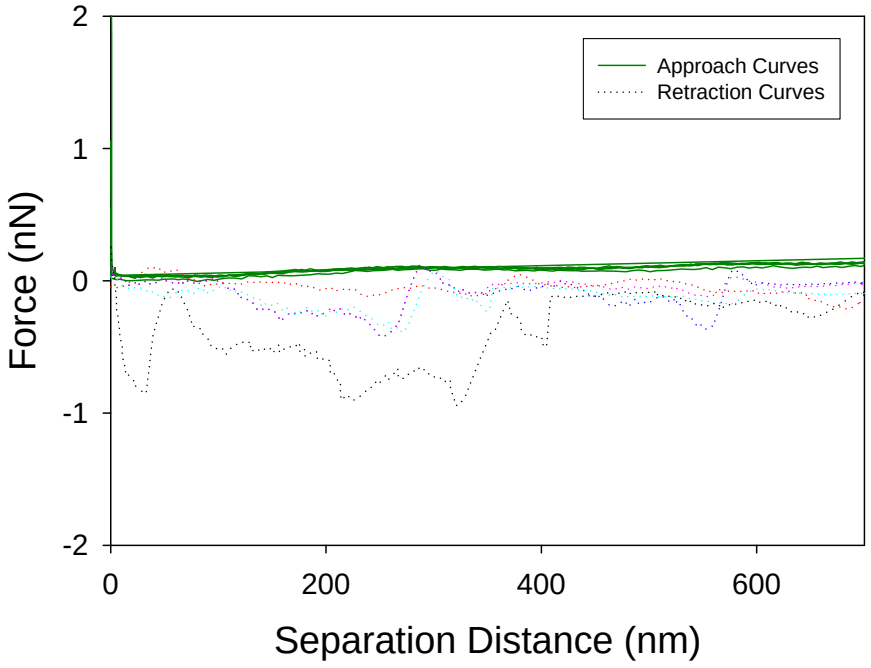

Figure 9.128 5 force plots of ML35 to CP1

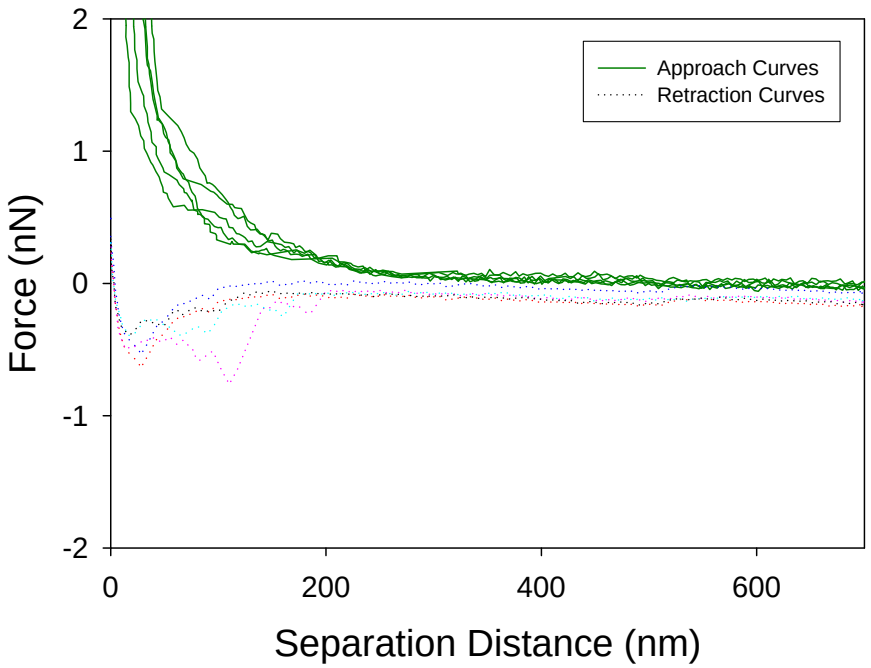

Figure 9.129 5 force plots of ML35 to CP1

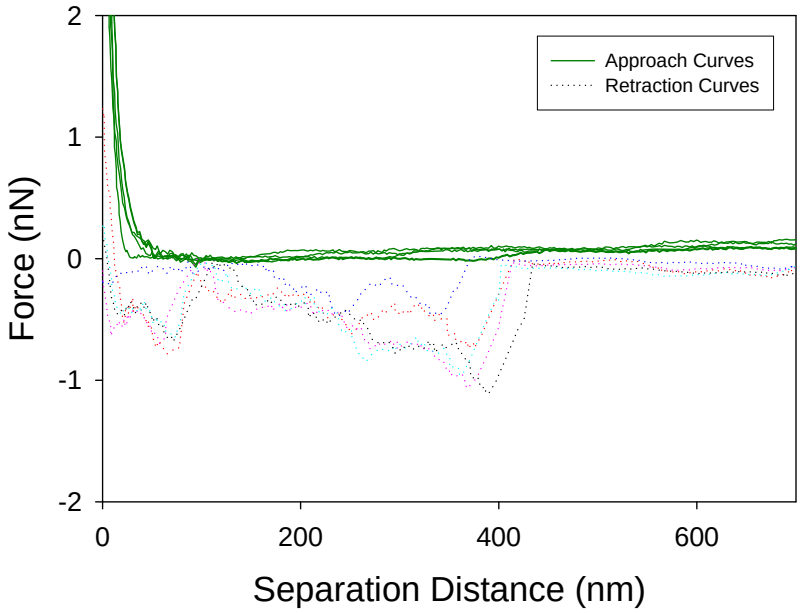

Figure 9.130 5 force plots of ML35 to CP1

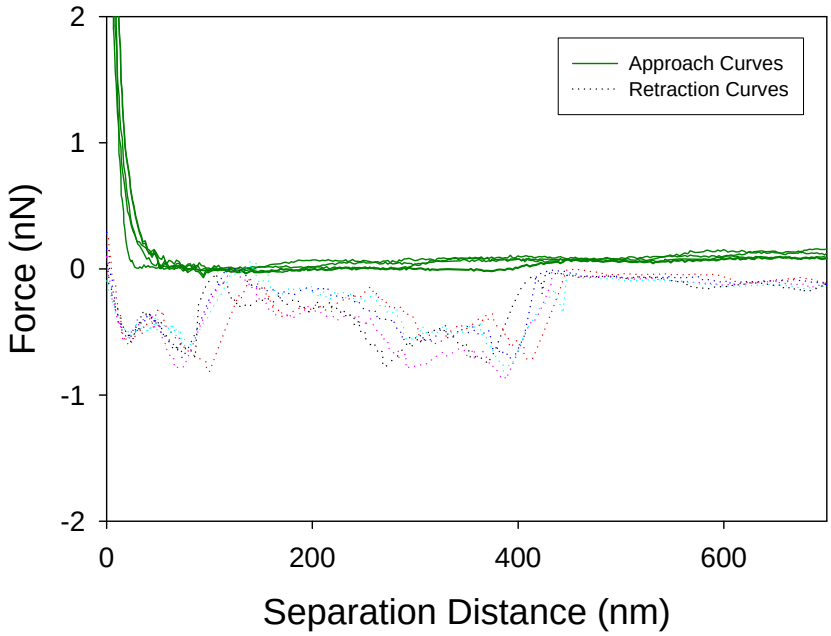

Figure 9.131 5 force plots of ML35 to CP1

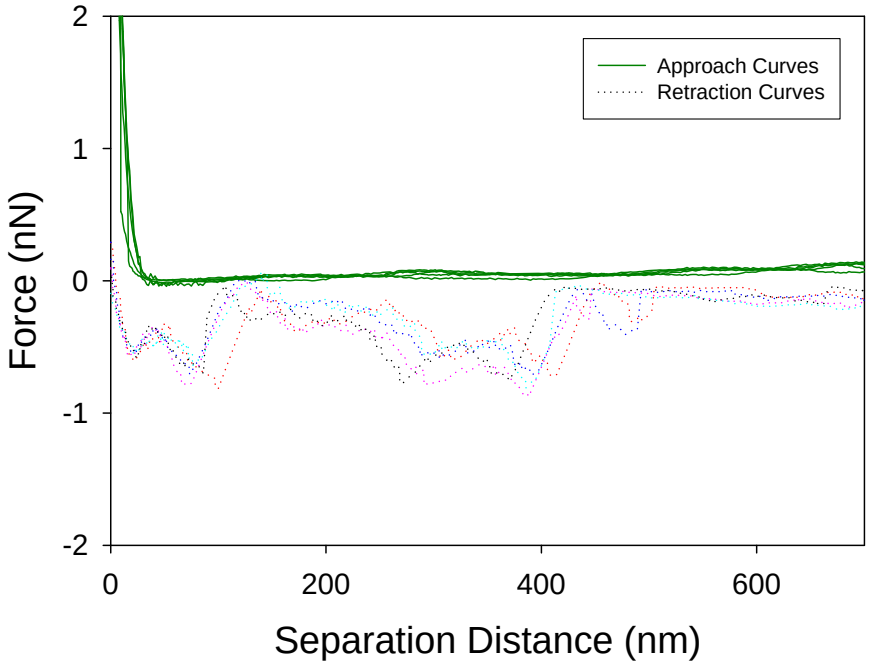

Figure 9.132 5 force plots of ML35 to CP1

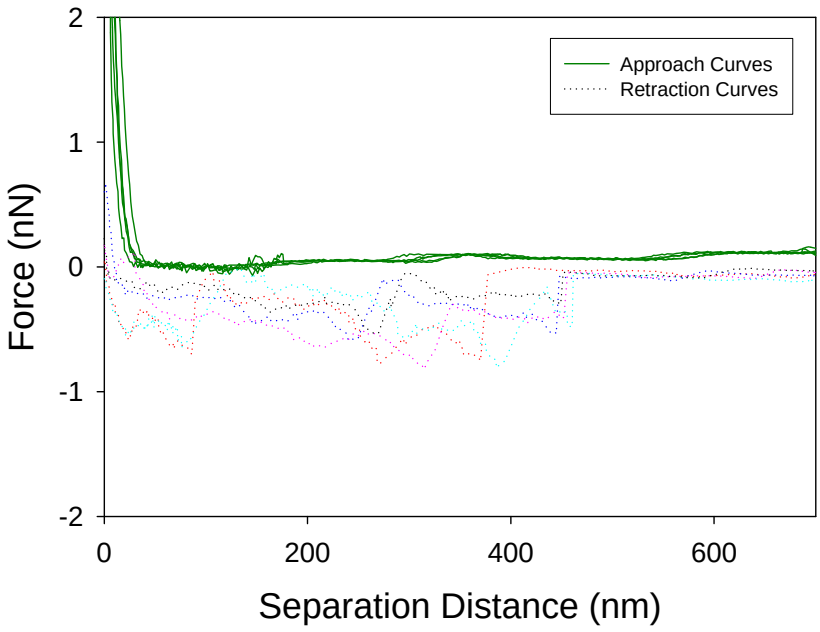

Figure 9.133 5 force plots of ML35 to CP1

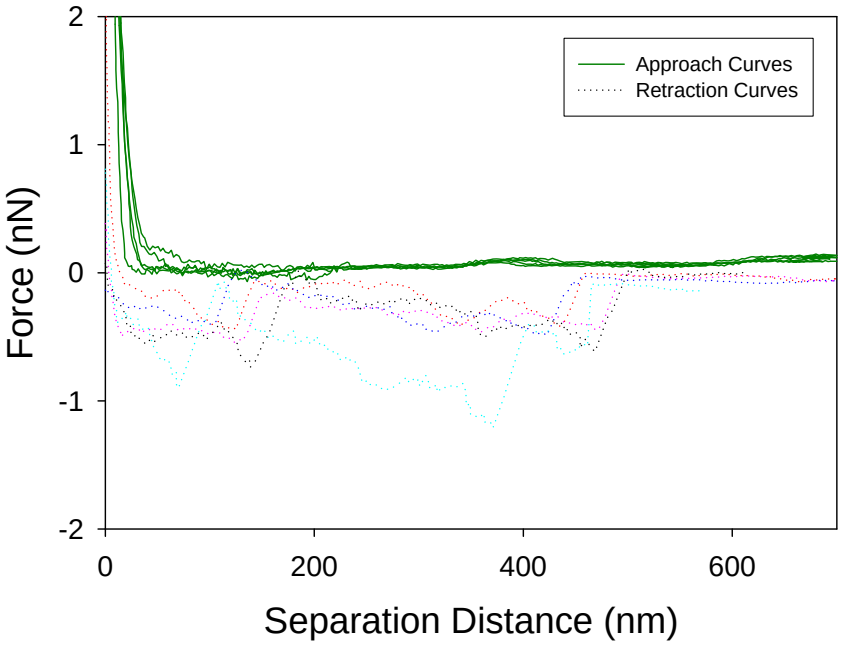

Figure 9.134 5 force plots of ML35 to CP1

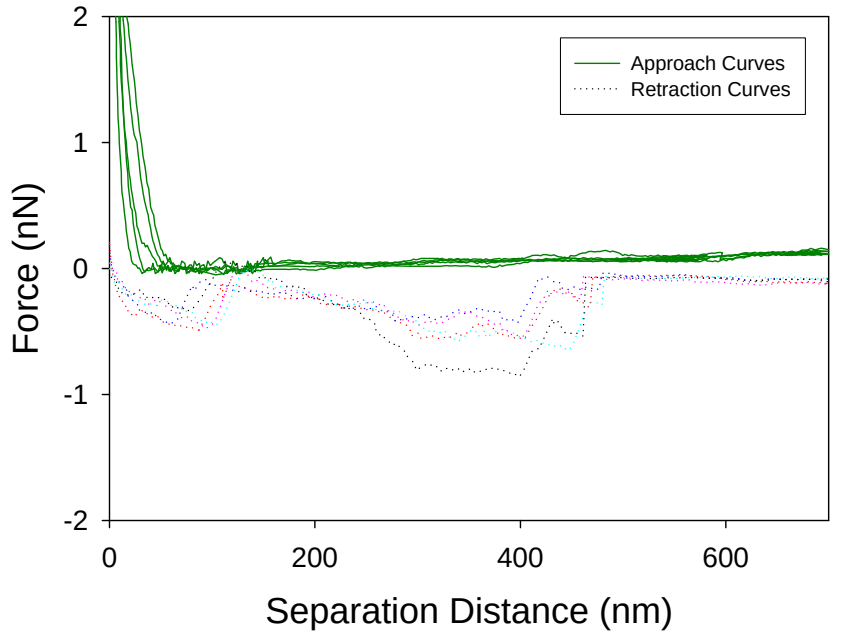

Figure 9.135 5 force plots of ML35 to CP1

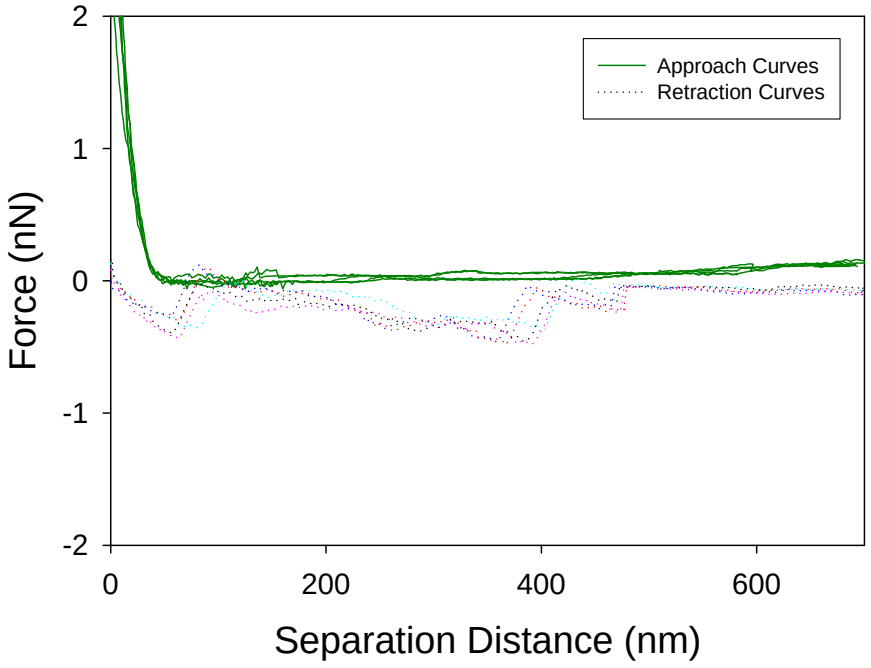

Figure 9.136 5 force plots of ML35 to CP1

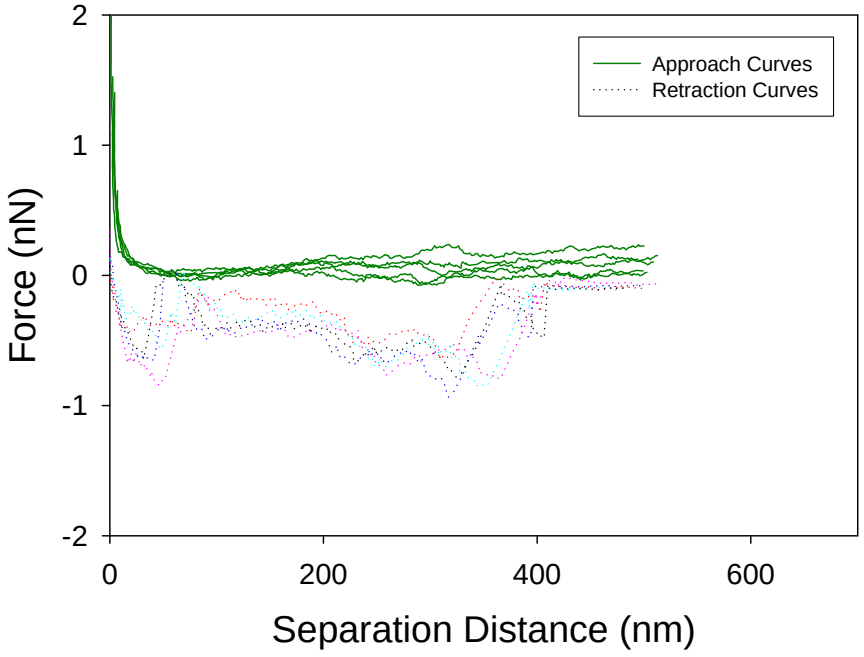

Figure 9.137 5 force plots of ML35 to CP1

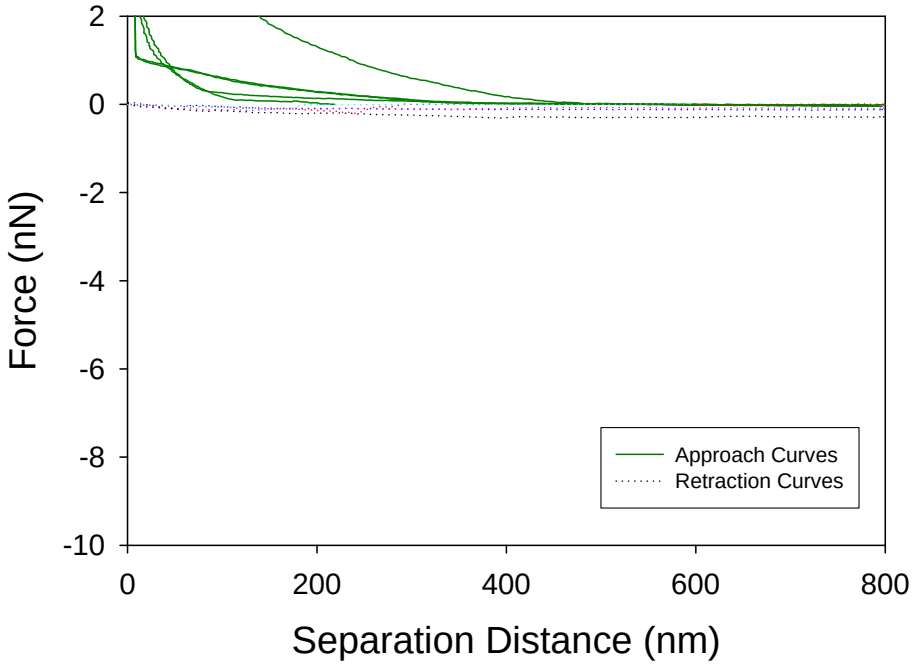

Figure 9.138 5 force plots of O26:K60:H11 to silicon nitride

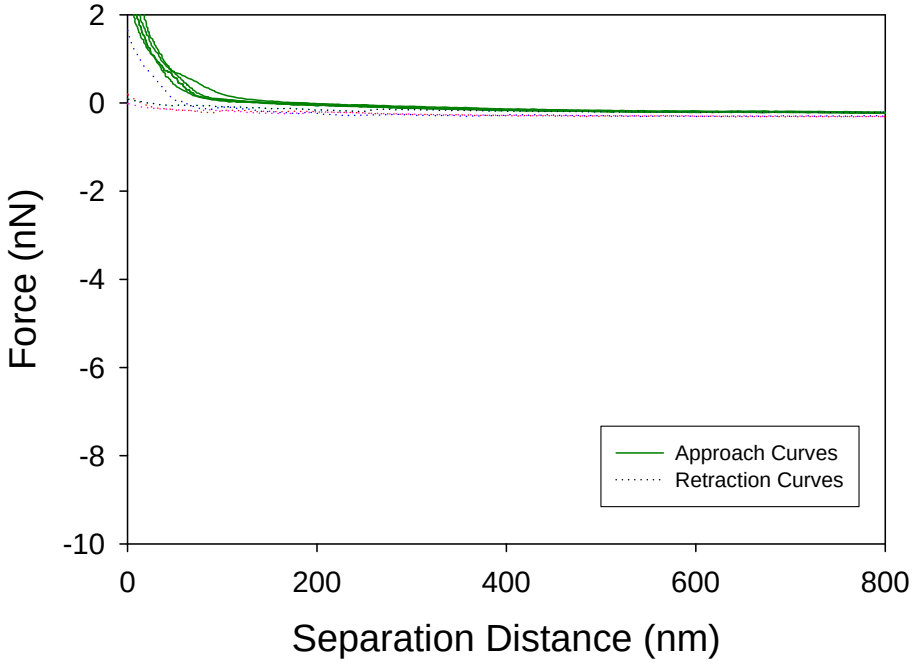

Figure 9.139 5 force plots of O26:K60:H11 to silicon nitride

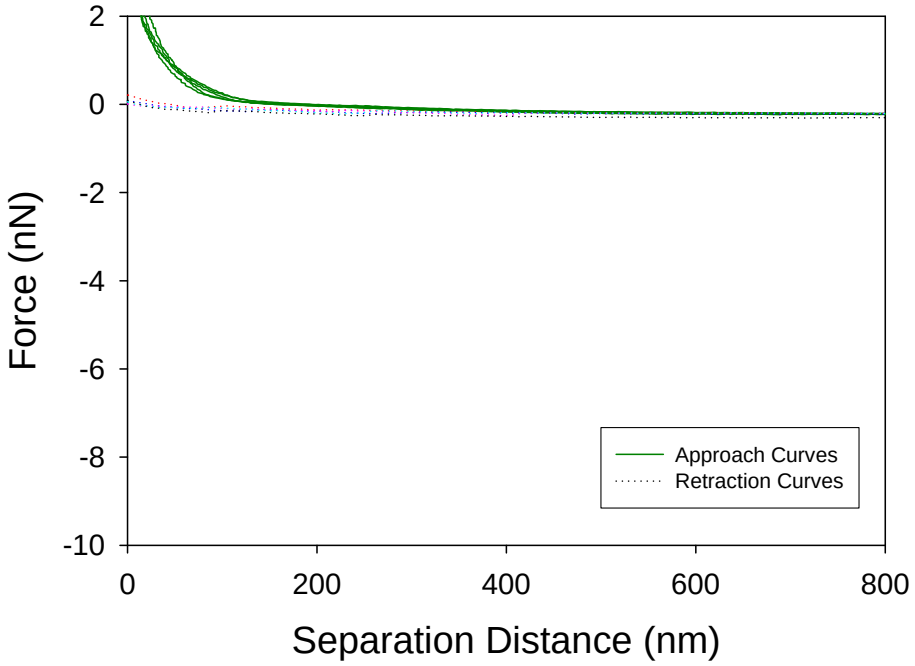

Figure 9.140 5 force plots of O26:K60:H11 to silicon nitride

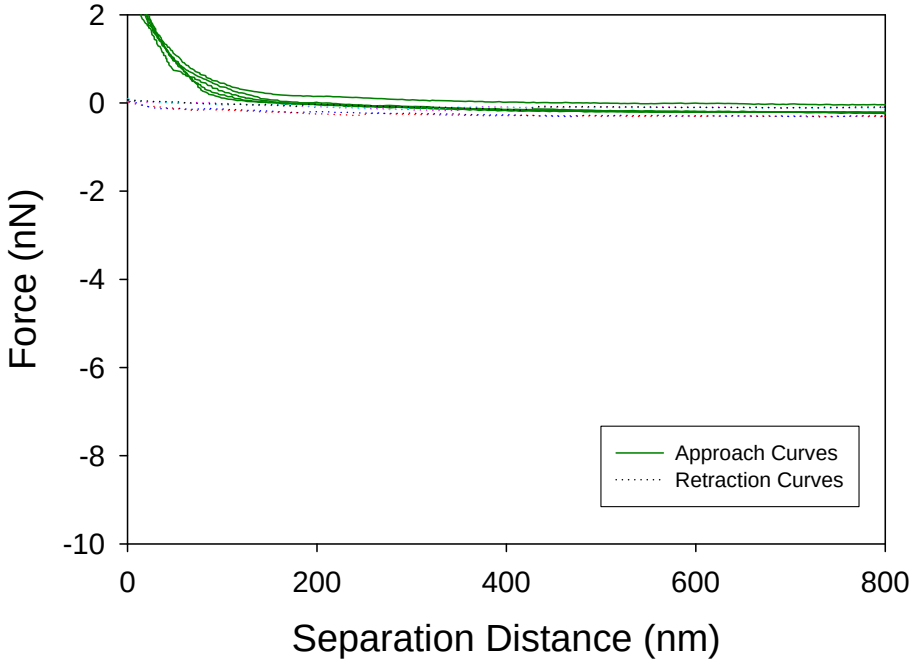

Figure 9.141 5 force plots of O26:K60:H11 to silicon nitride

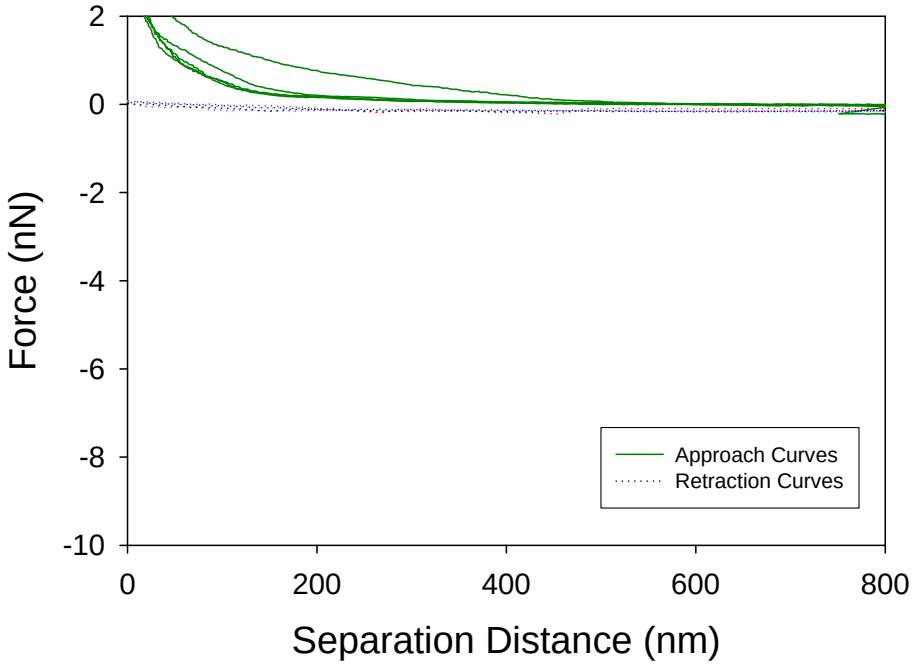

Figure 9.142 5 force plots of O26:K60:H11 to silicon nitride

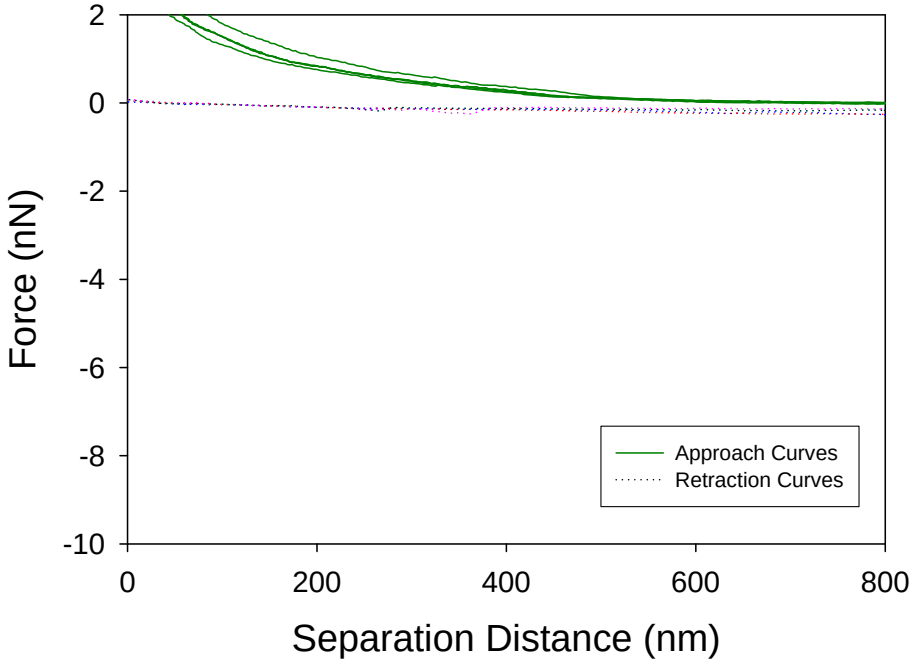

Figure 9.143 5 force plots of O26:K60:H11 to silicon nitride

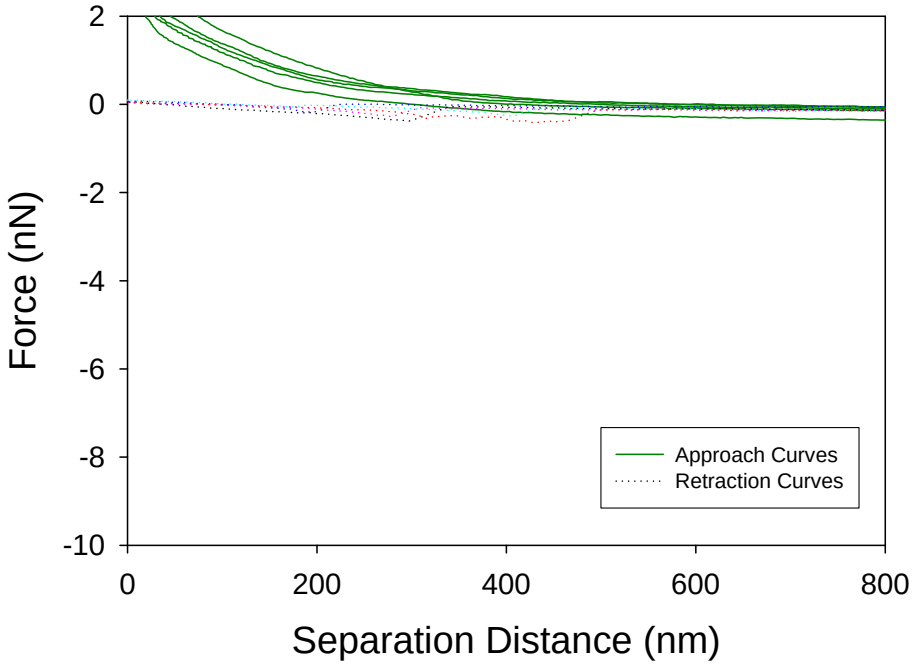

Figure 9.144 5 force plots of O26:K60:H11 to silicon nitride

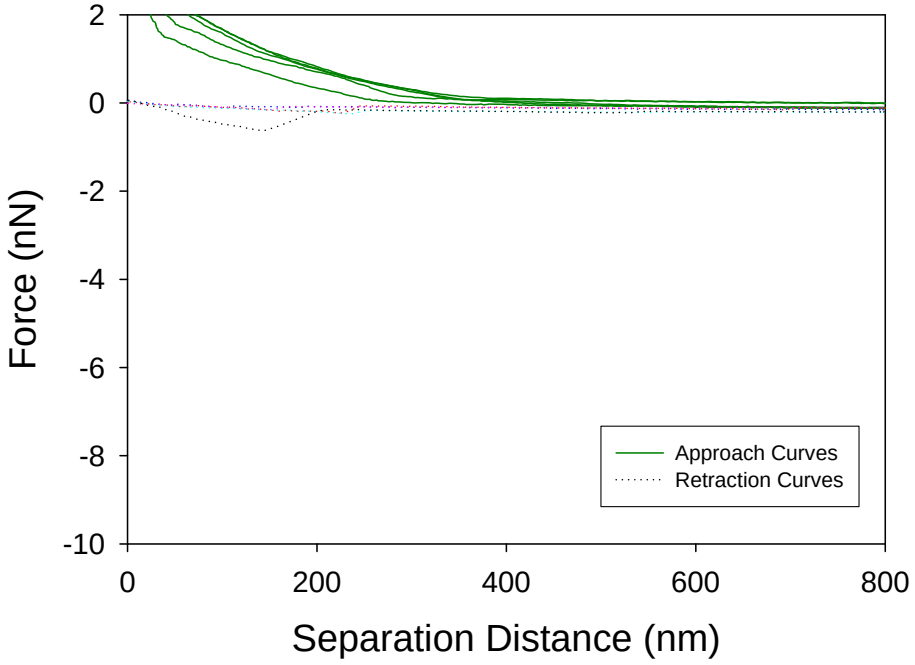

Figure 9.145 5 force plots of O26:K60:H11 to silicon nitride

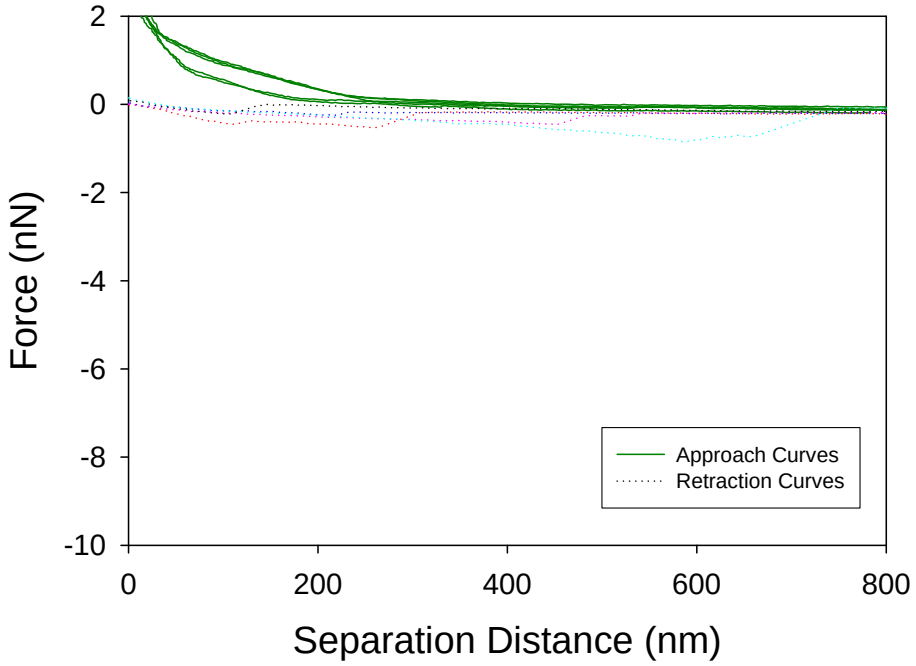

Figure 9.146 5 force plots of O26:K60:H11 to silicon nitride

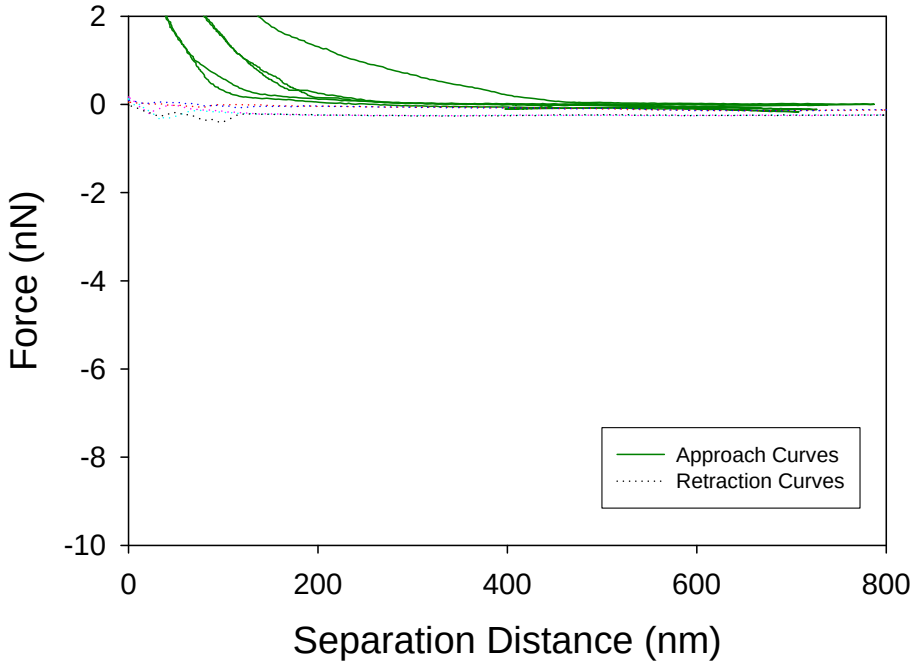

Figure 9.147 5 force plots of O26:K60:H11 to silicon nitride

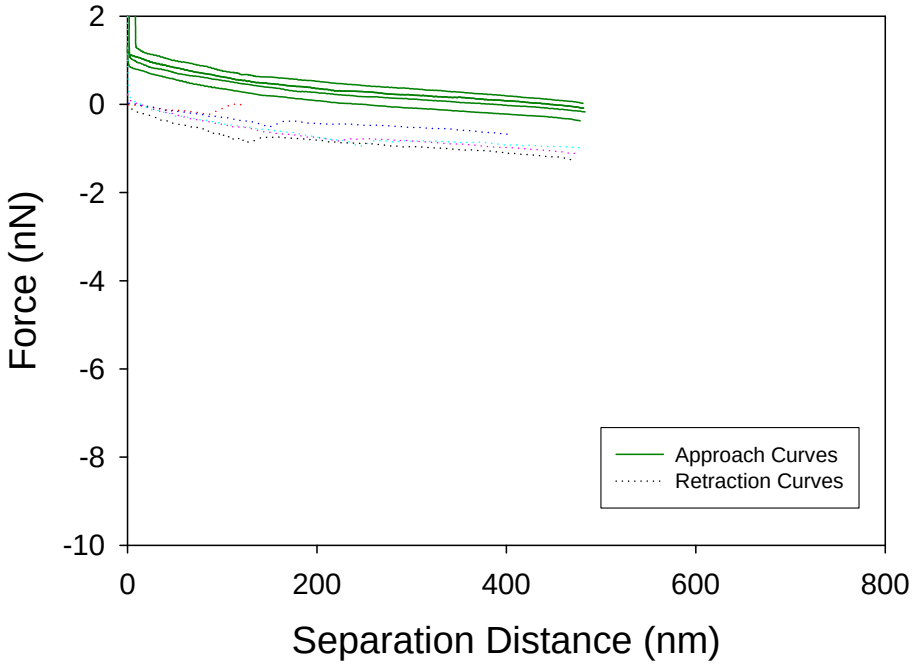

Figure 9.148 5 force plots of O26:K60:H11 to CP1

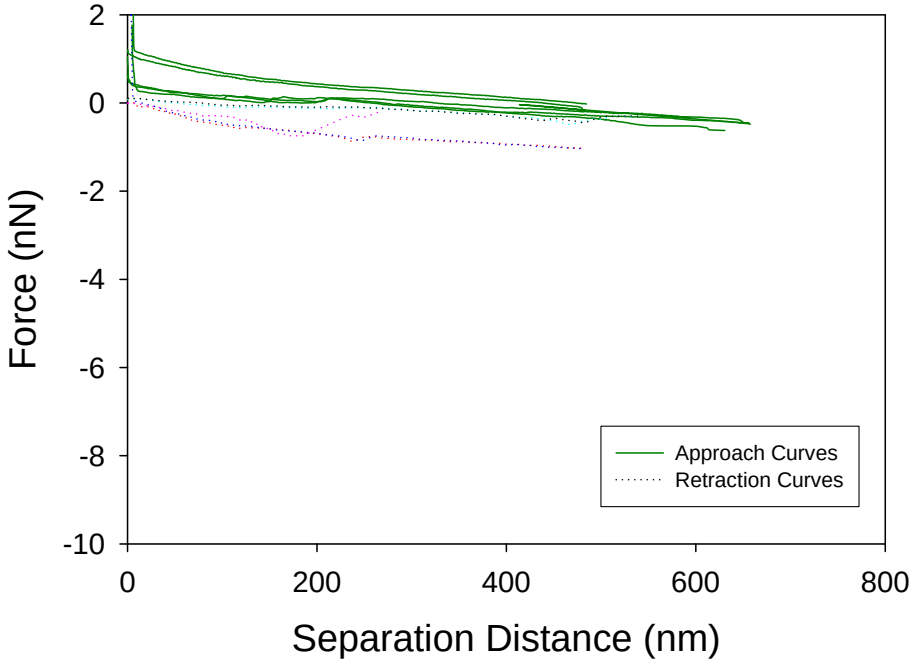

Figure 9.149 5 force plots of O26:K60:H11 to CP1

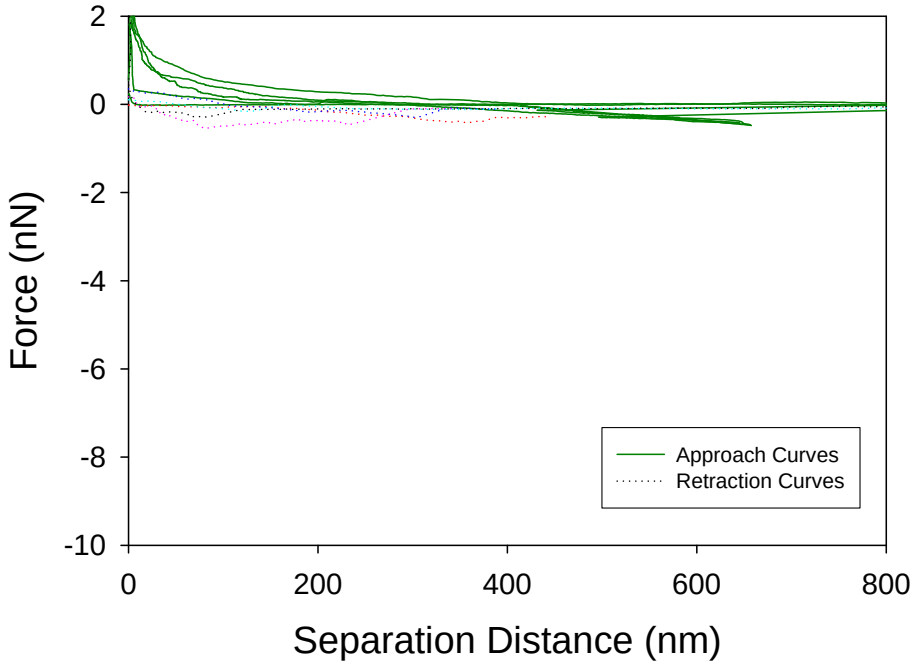

Figure 9.150 5 force plots of O26:K60:H11 to CP1

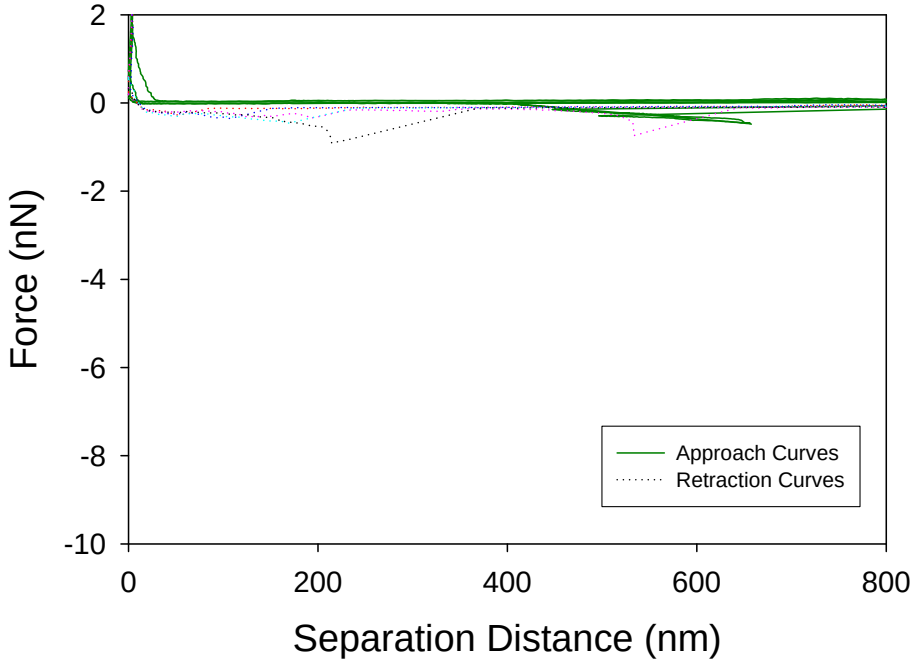

Figure 9.151 5 force plots of O26:K60:H11 to CP1

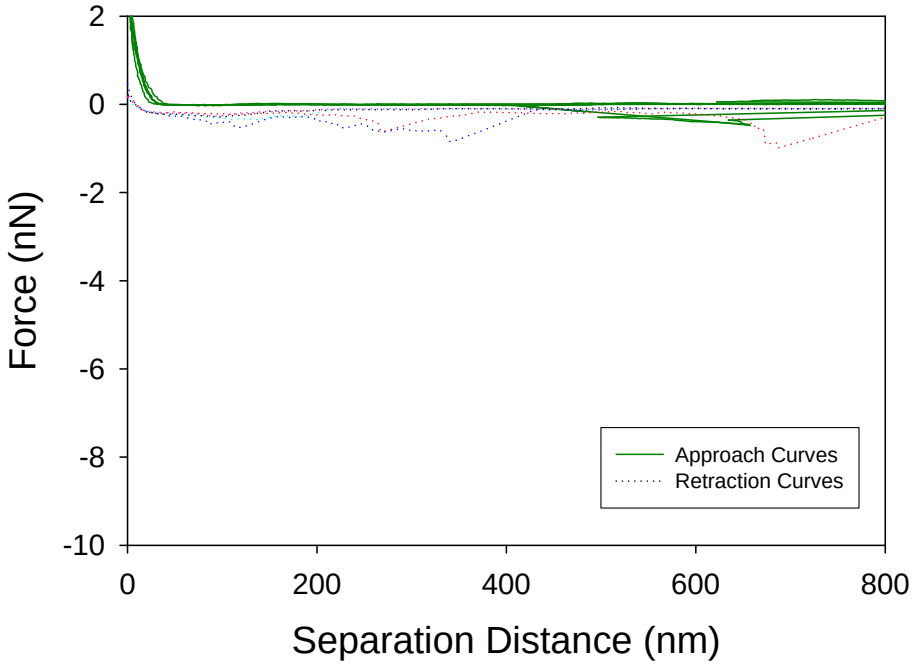

Figure 9.152 5 force plots of O26:K60:H11 to CP1

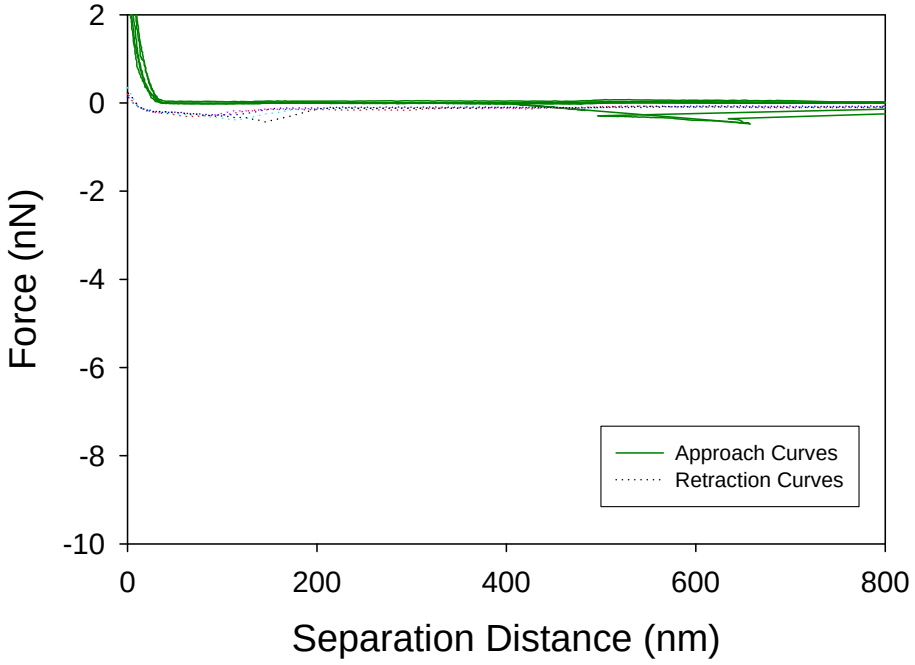

Figure 9.153 5 force plots of O26:K60:H11 to CP1

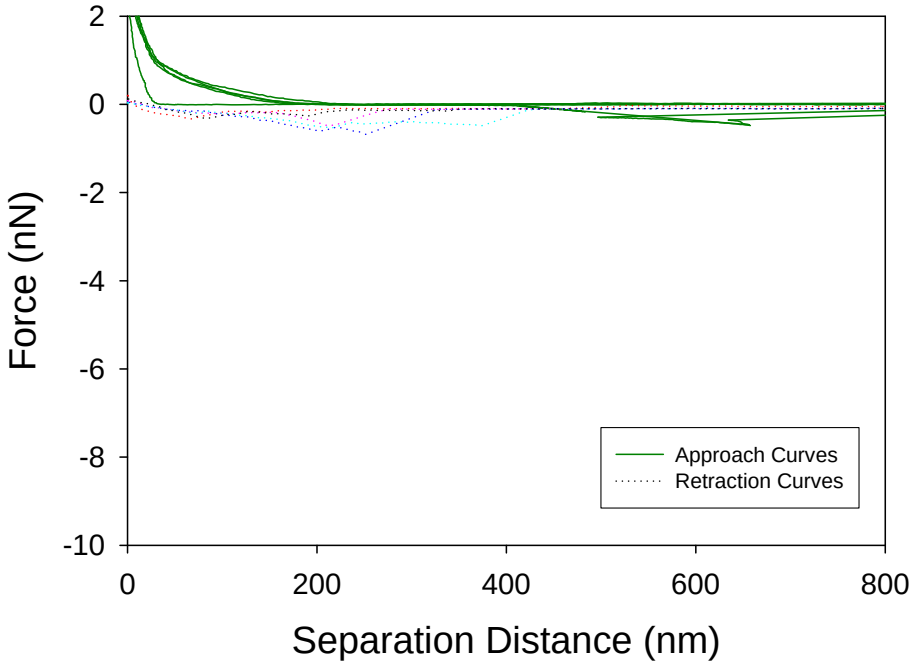

Figure 9.154 5 force plots of O26:K60:H11 to CP1

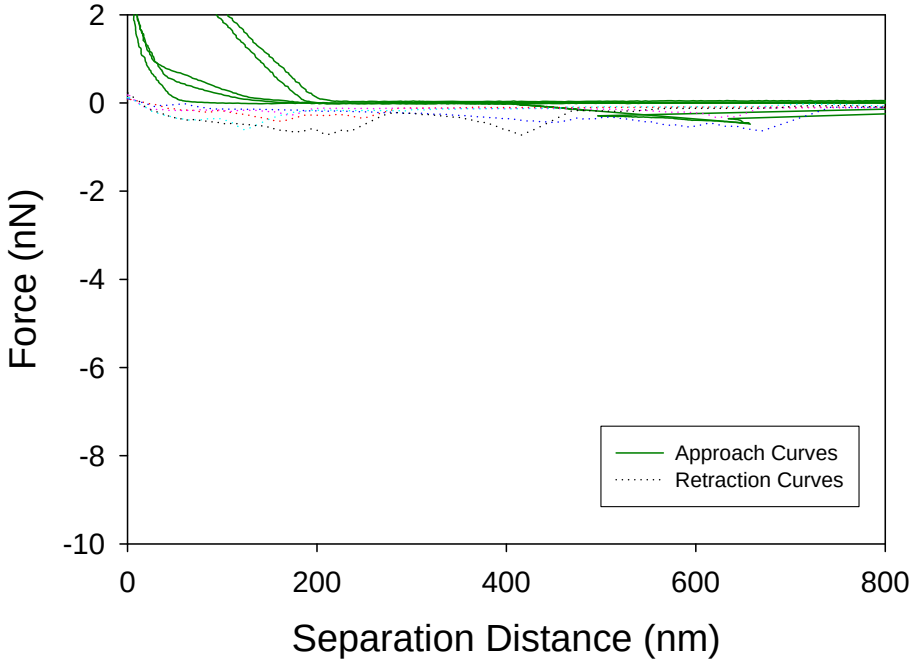

Figure 9.155 5 force plots of O26:K60:H11 to CP1

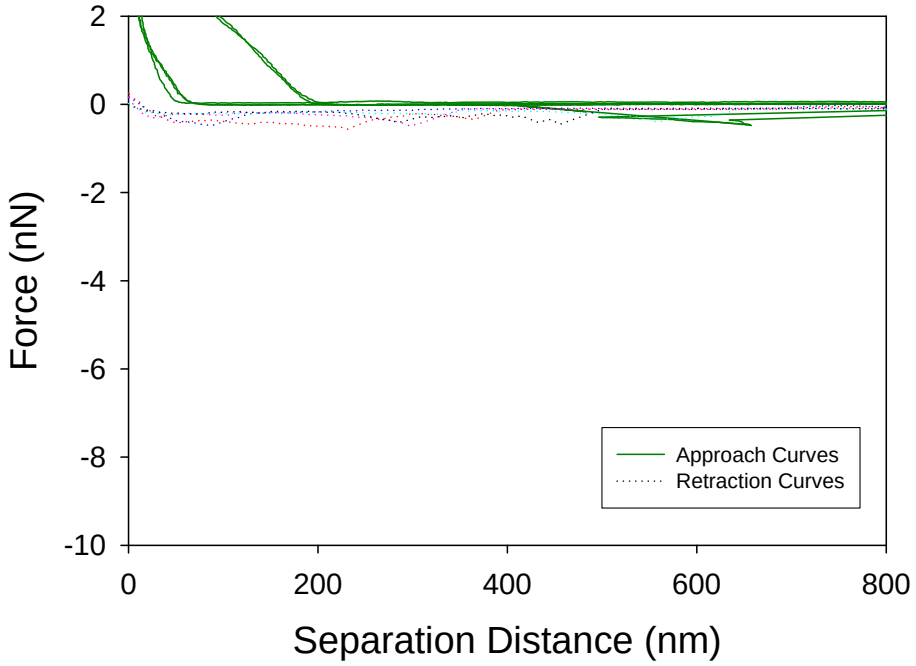

Figure 9.156 5 force plots of O26:K60:H11 to CP1

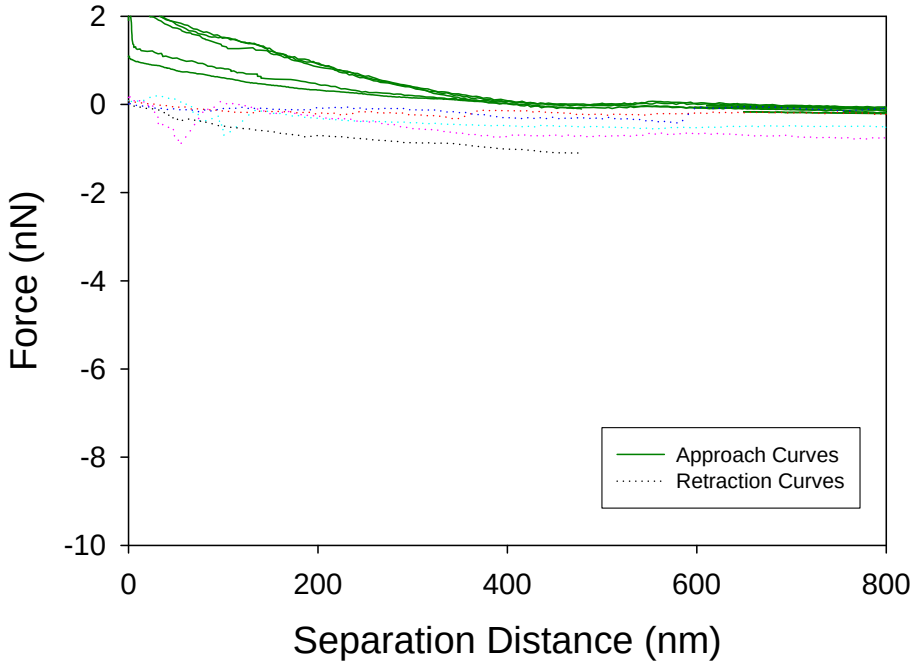

Figure 9.157 5 force plots of O26:K60:H11 to CP1

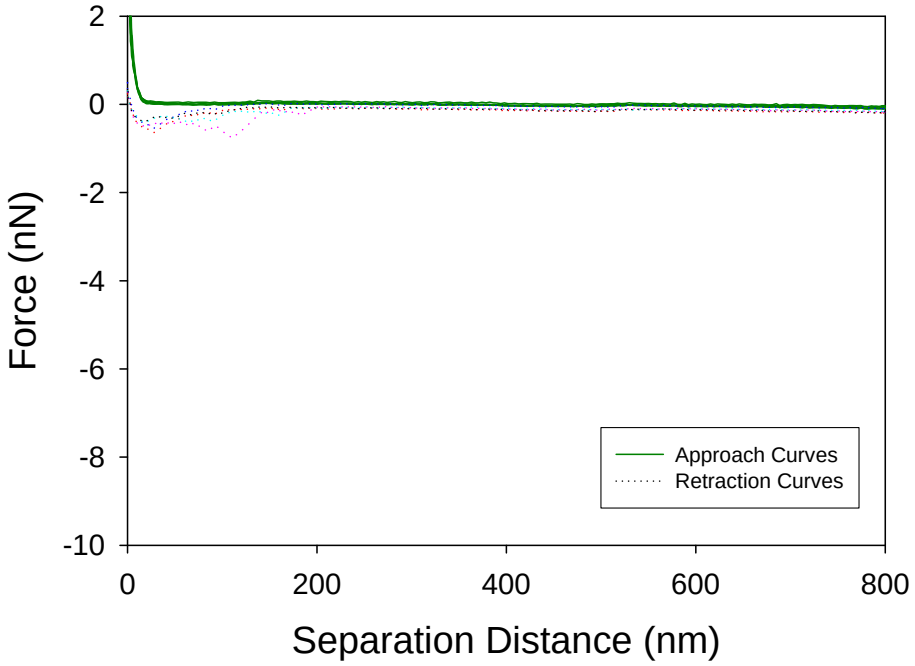

Figure 9.158 5 force plots of O35:H10 to silicon nitride

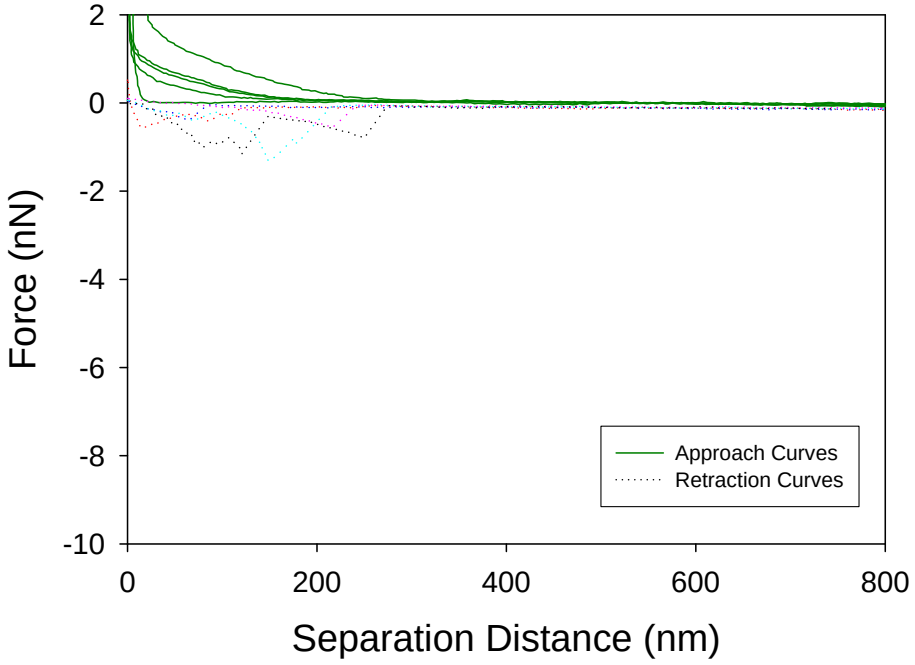

Figure 9.159 5 force plots of O35:H10 to silicon nitride

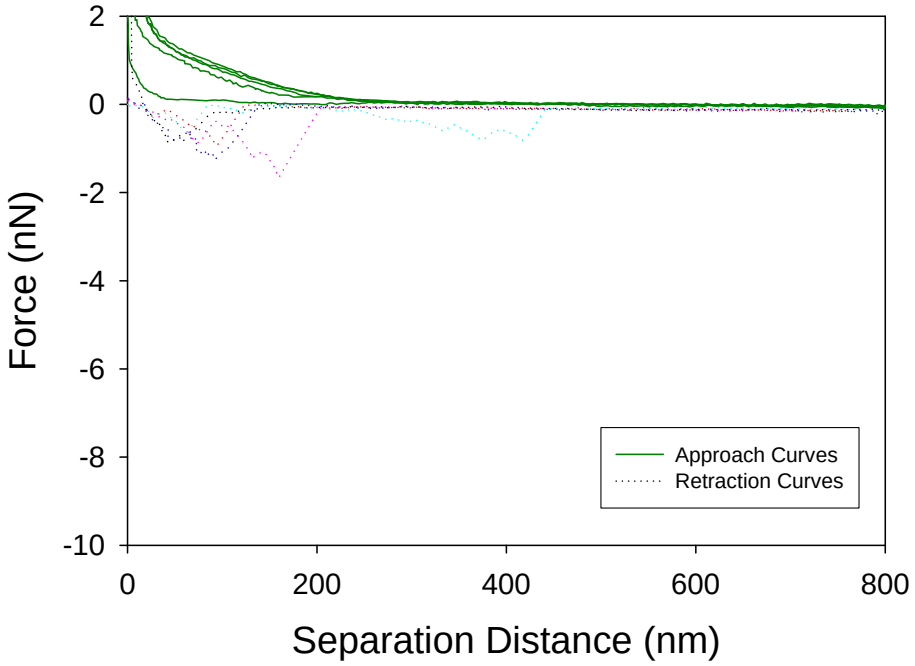

Figure 9.160 5 force plots of O35:H10 to silicon nitride

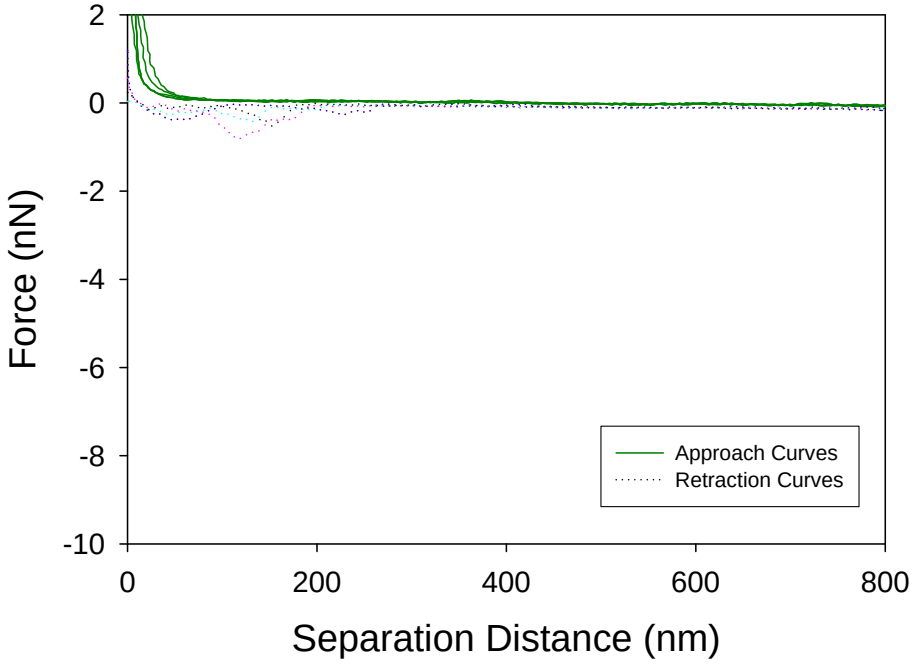

Figure 9.161 5 force plots of O35:H10 to silicon nitride

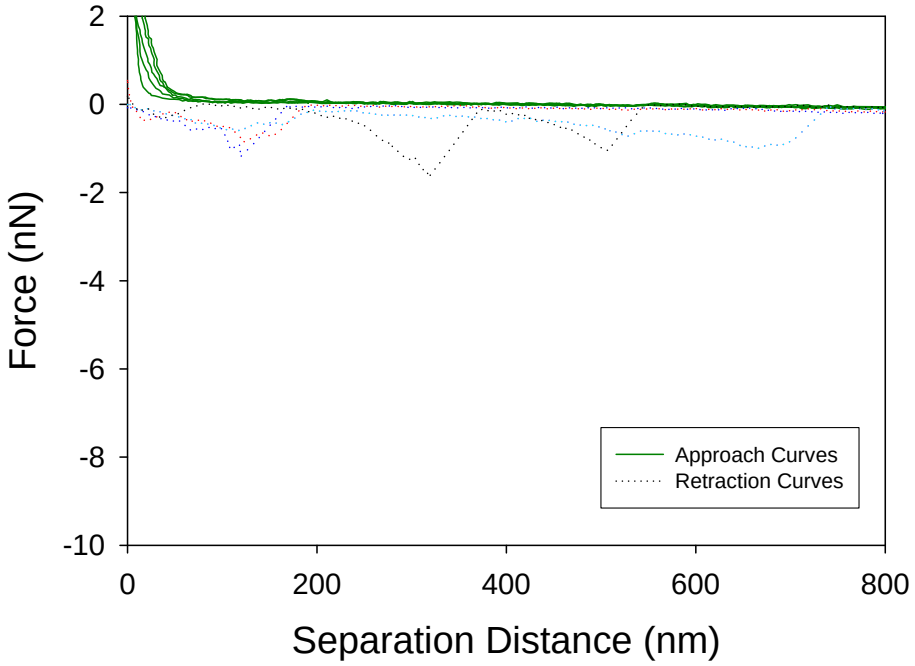

Figure 9.162 5 force plots of O35:H10 to silicon nitride

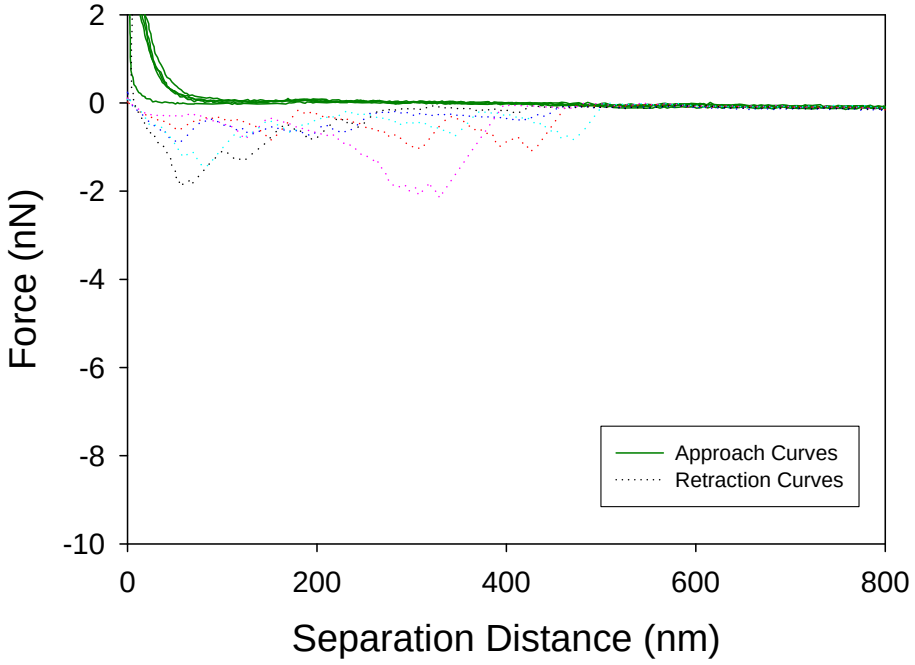

Figure 9.163 5 force plots of O35:H10 to silicon nitride

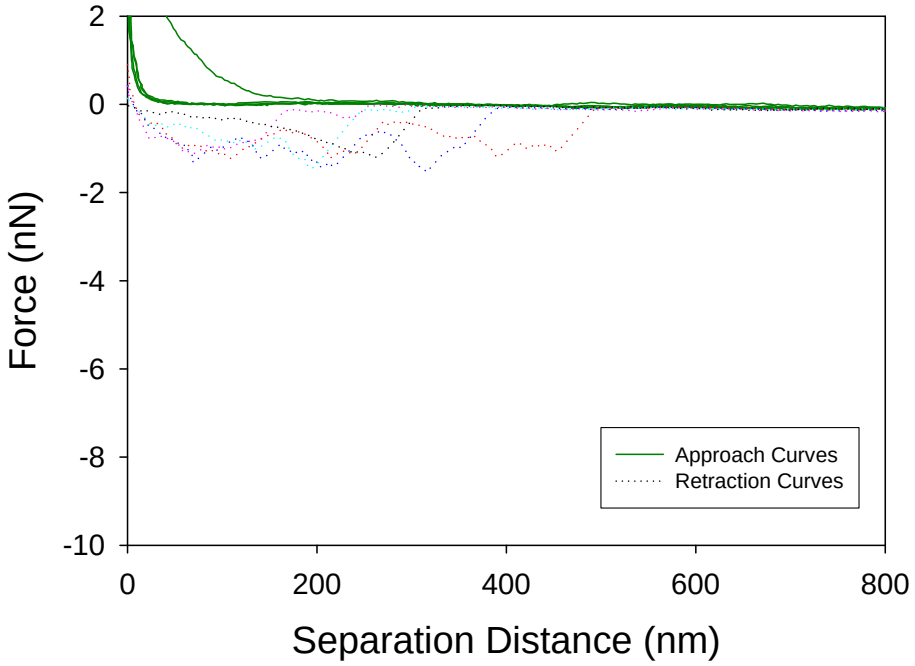

Figure 9.164 5 force plots of O35:H10 to silicon nitride

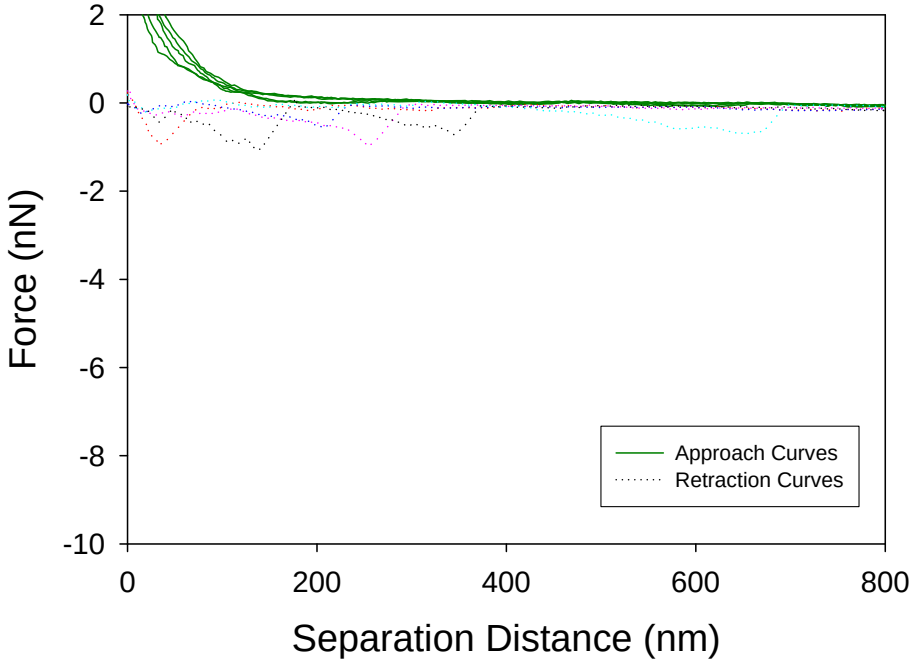

Figure 9.165 5 force plots of O35:H10 to silicon nitride

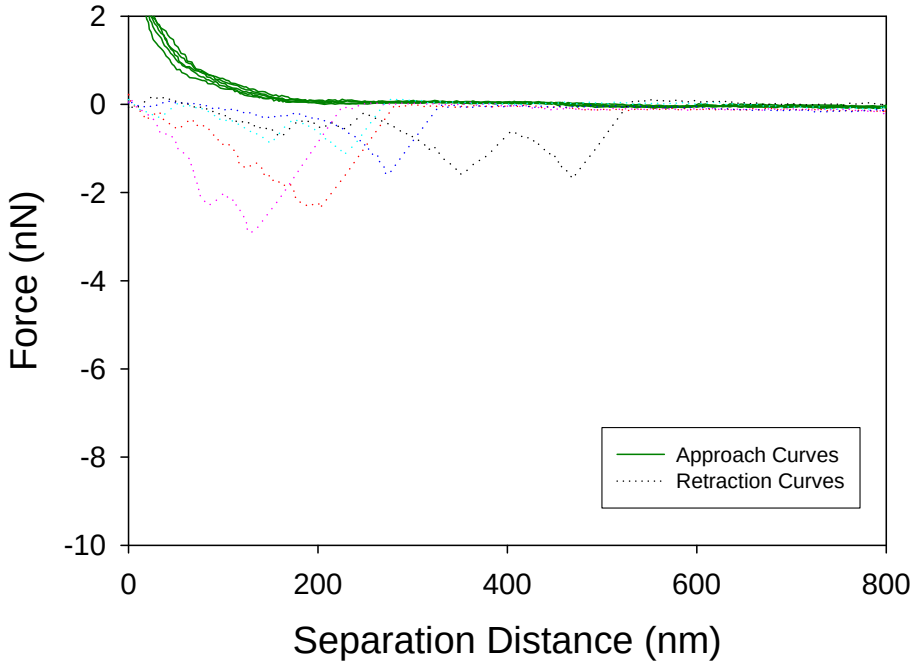

Figure 9.166 5 force plots of O35:H10 to silicon nitride

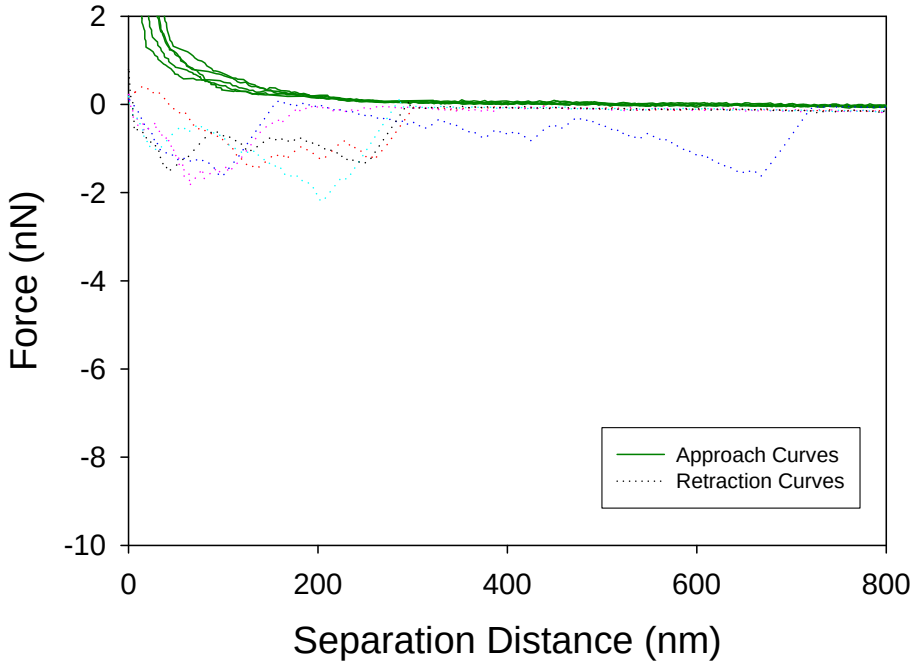

Figure 9.167 5 force plots of O35:H10 to silicon nitride

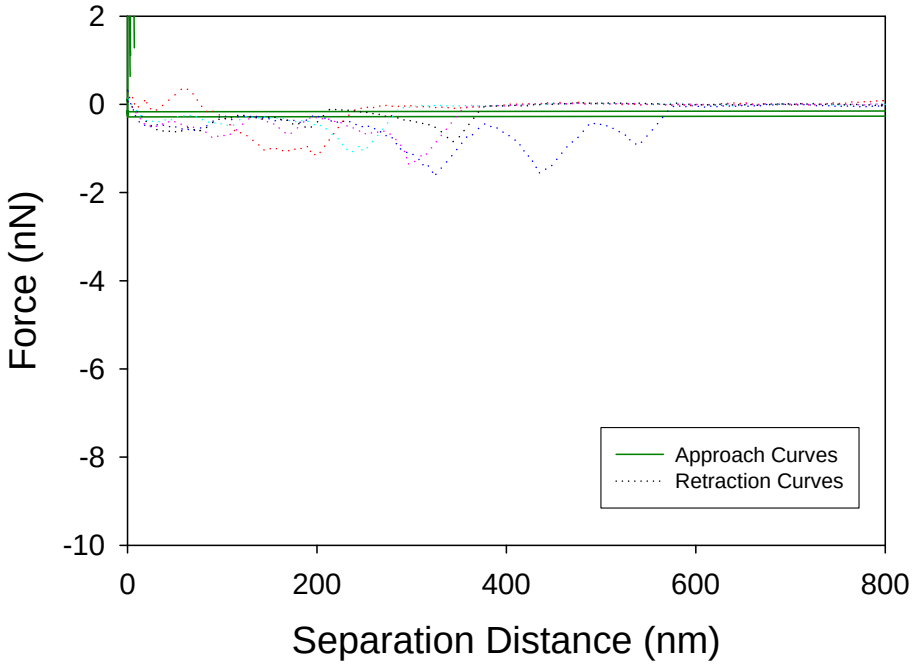

Figure 9.168 5 force plots of O35:H10 to CP1

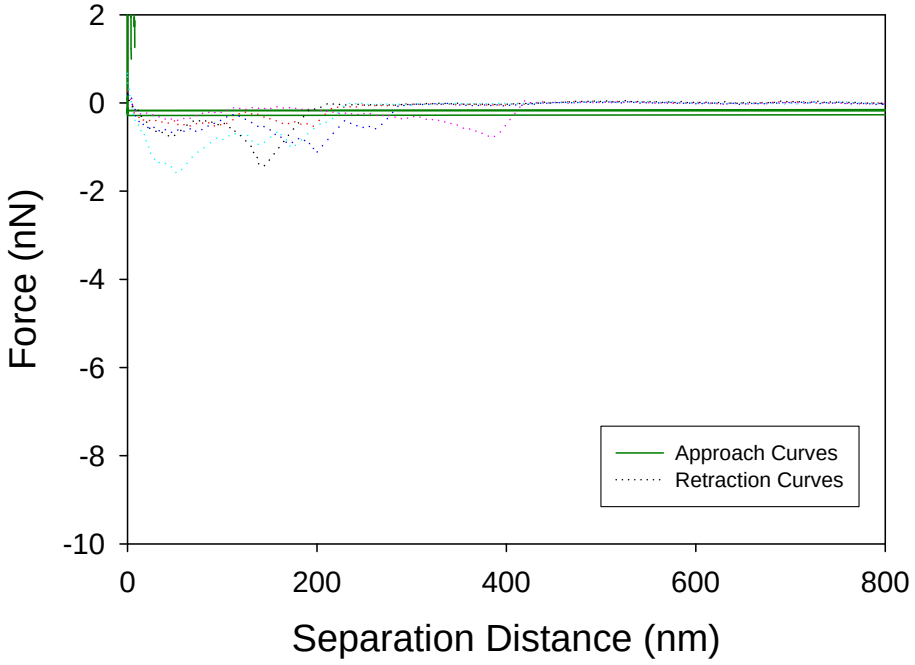

Figure 9.169 5 force plots of O35:H10 to CP1

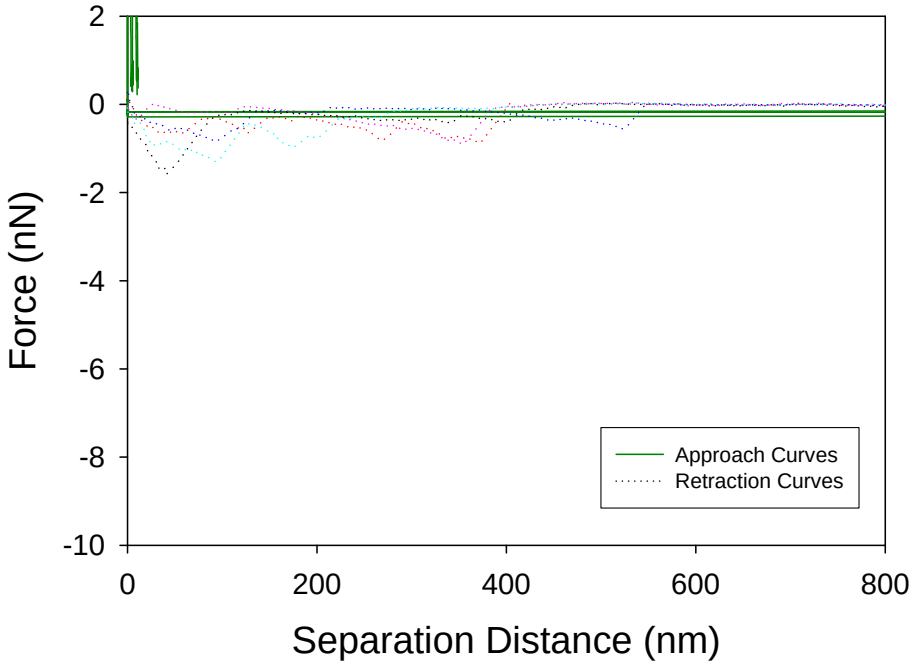

Figure 9.170 5 force plots of O35:H10 to CP1

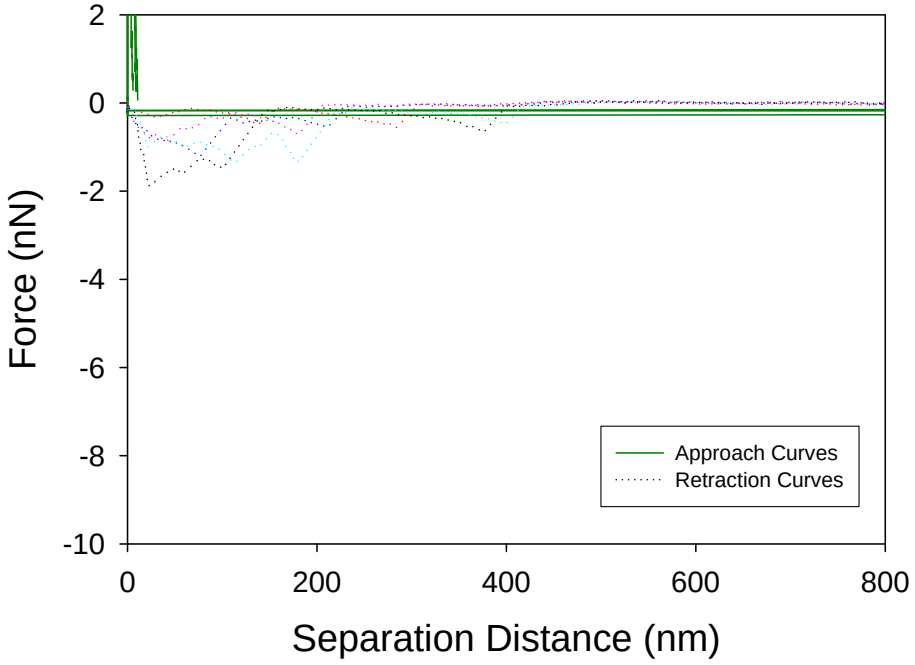

Figure 9.171 5 force plots of O35:H10 to CP1

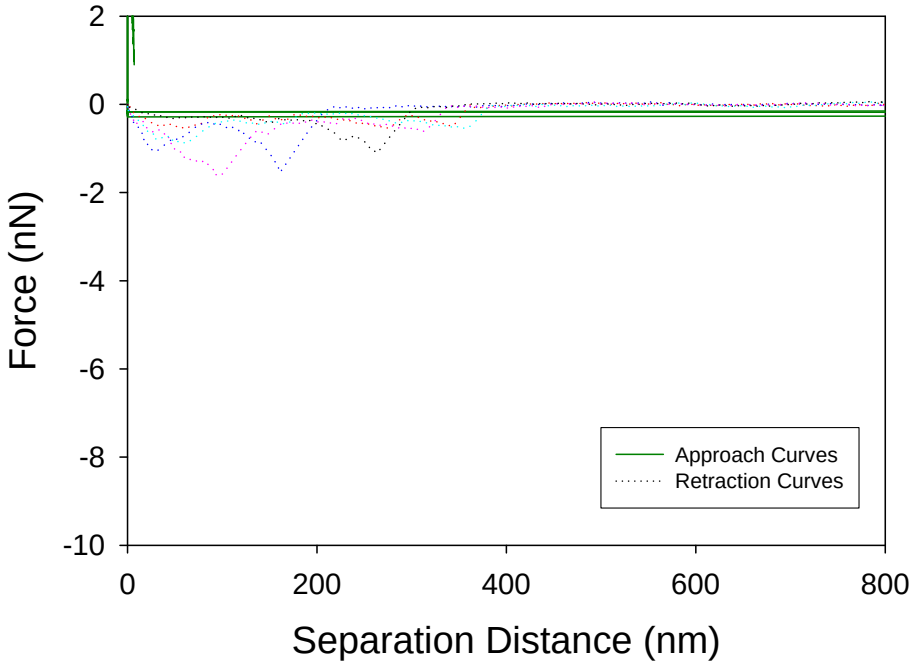

Figure 9.172 5 force plots of O35:H10 to CP1

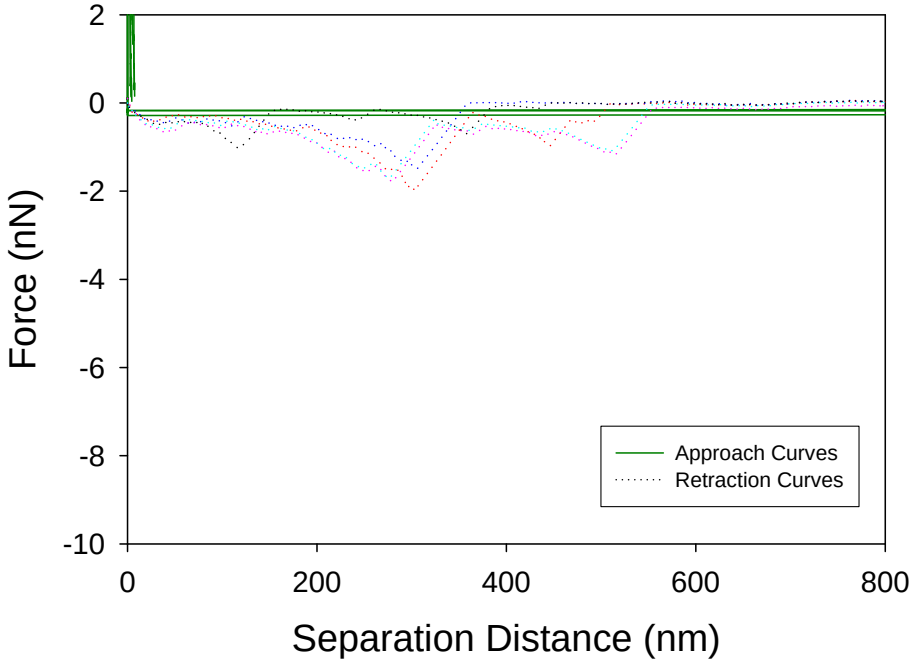

Figure 9.173 5 force plots of O35:H10 to CP1

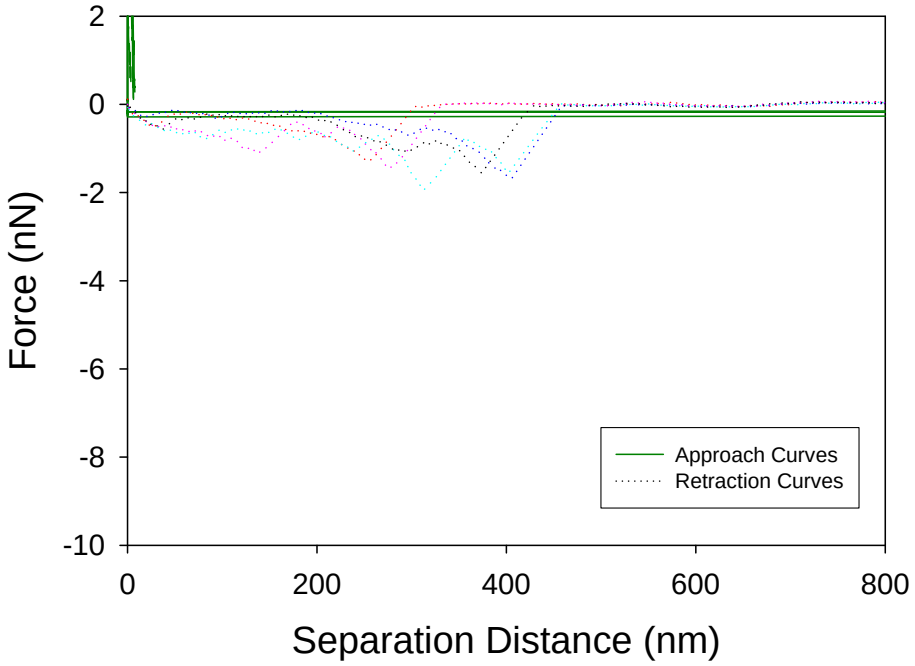

Figure 9.174 5 force plots of O35:H10 to CP1

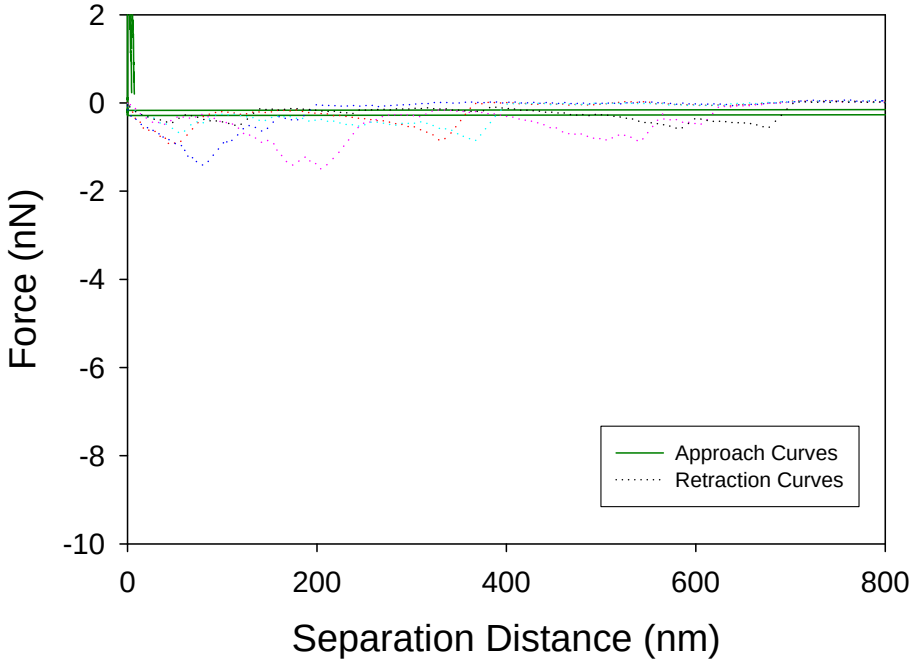

Figure 9.175 5 force plots of O35:H10 to CP1

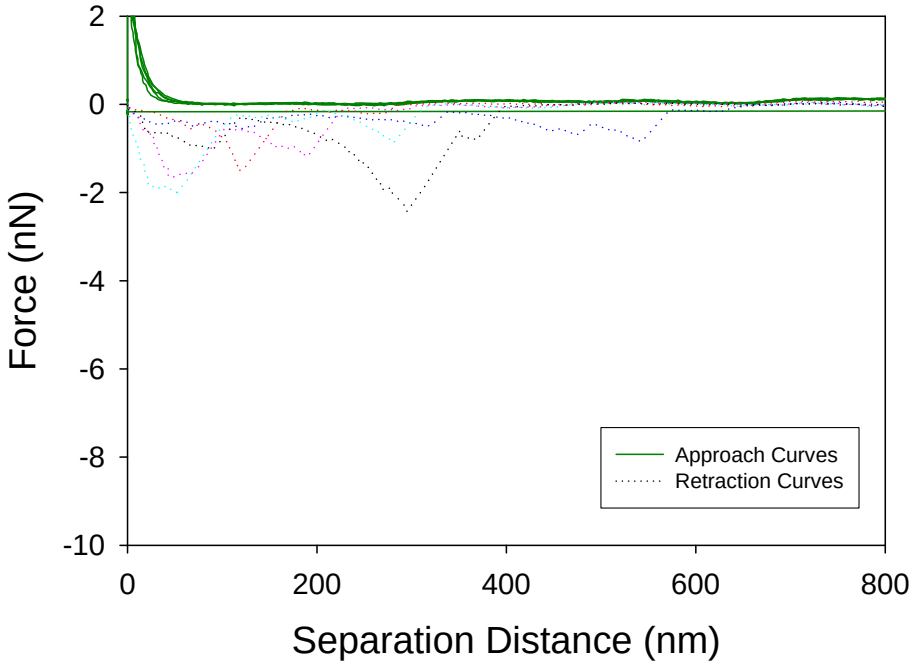

Figure 9.176 5 force plots of O35:H10 to CP1

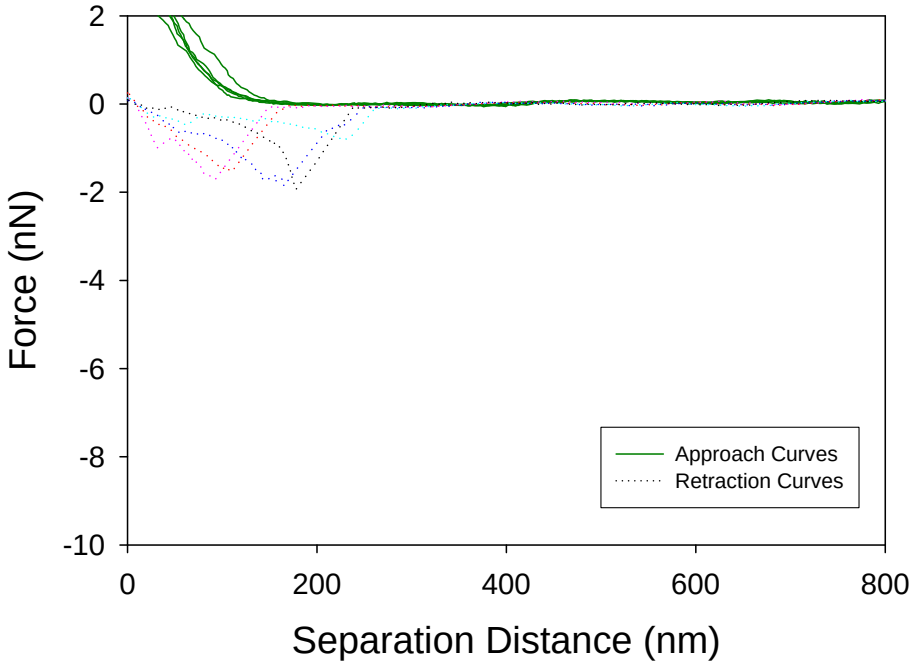

Figure 9.177 5 force plots of O35:H10 to CP1

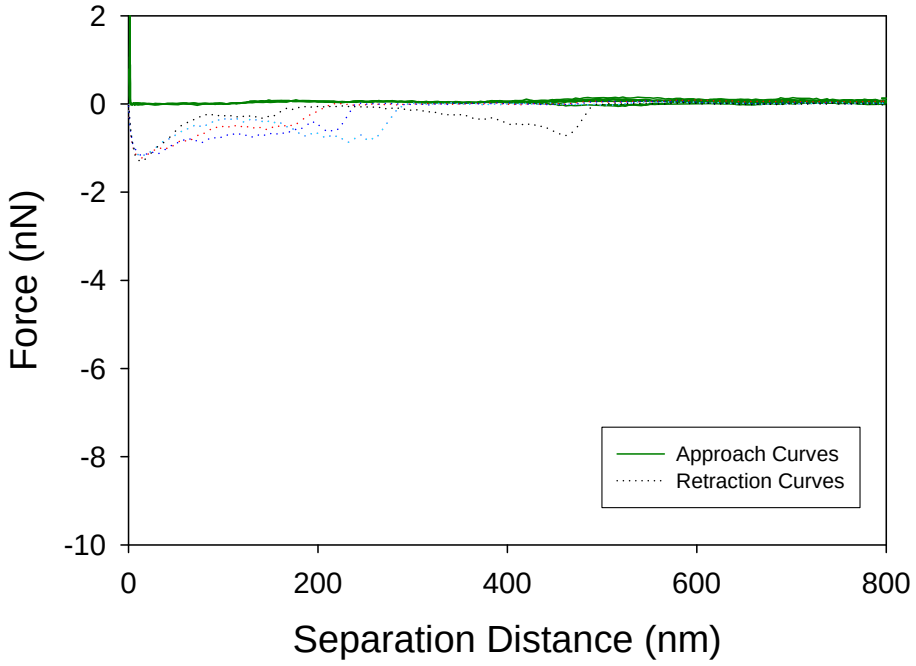

Figure 9.178 5 force plots of O55:H7 to silicon nitride

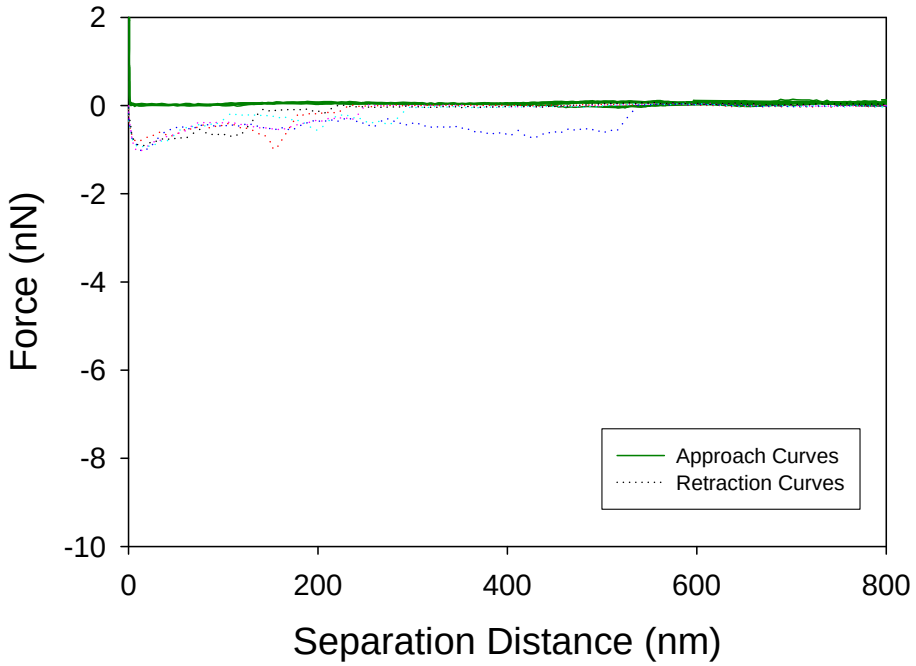

Figure 9.179 5 force plots of O55:H7 to silicon nitride

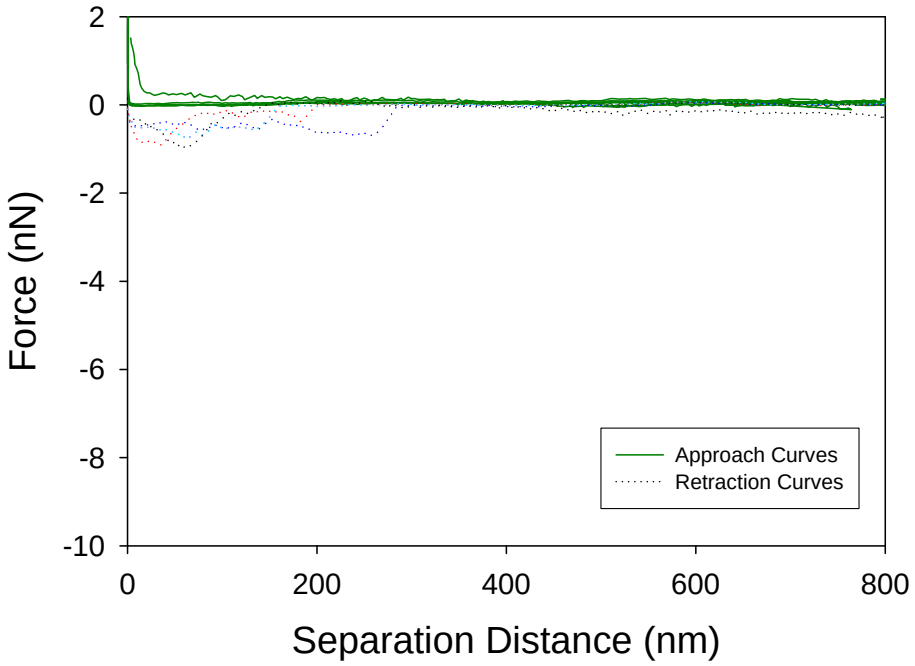

Figure 9.180 5 force plots of O55:H7 to silicon nitride

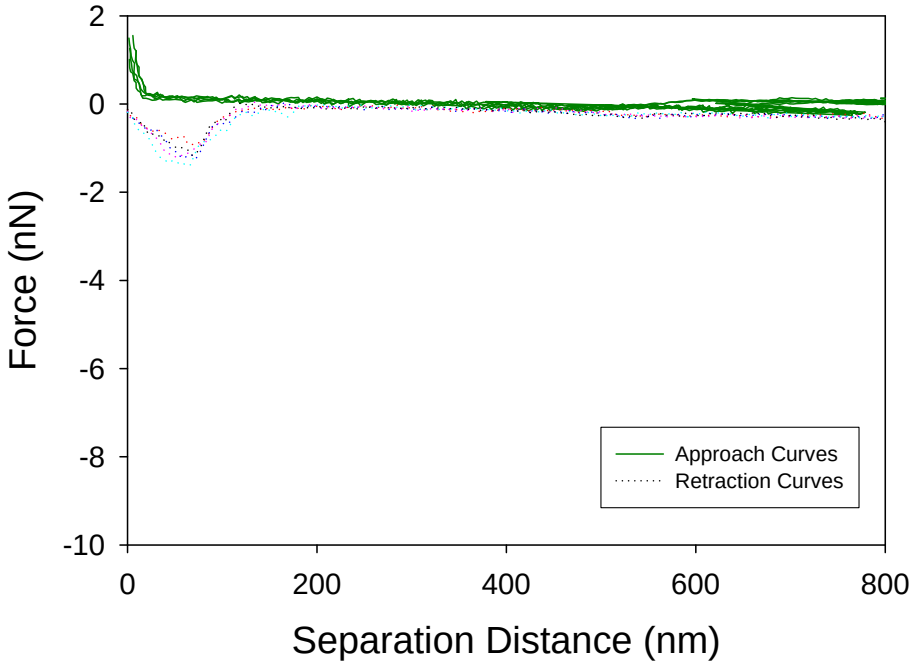

Figure 9.181 5 force plots of O55:H7 to silicon nitride

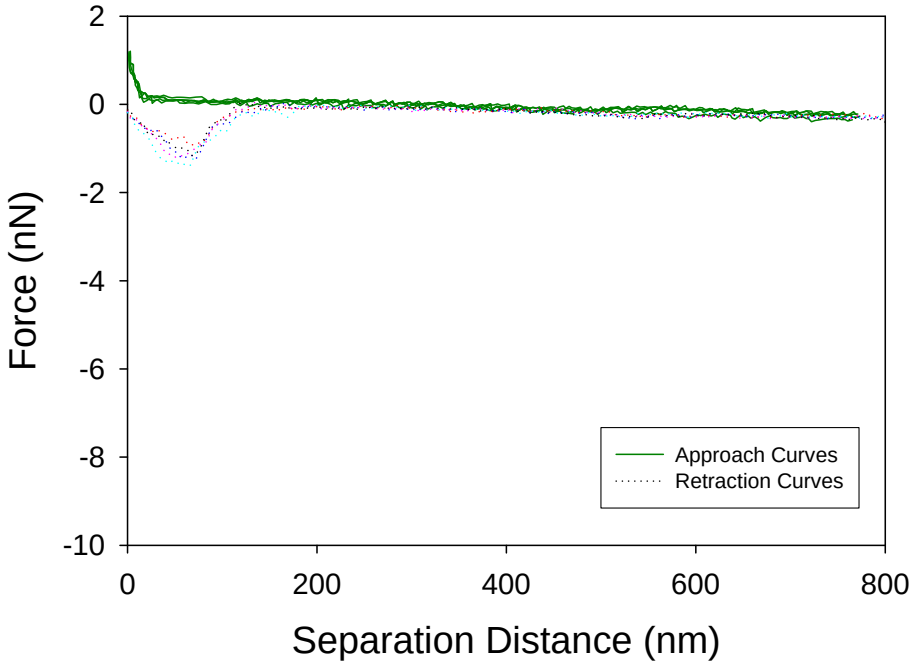

Figure 9.182 5 force plots of O55:H7 to silicon nitride

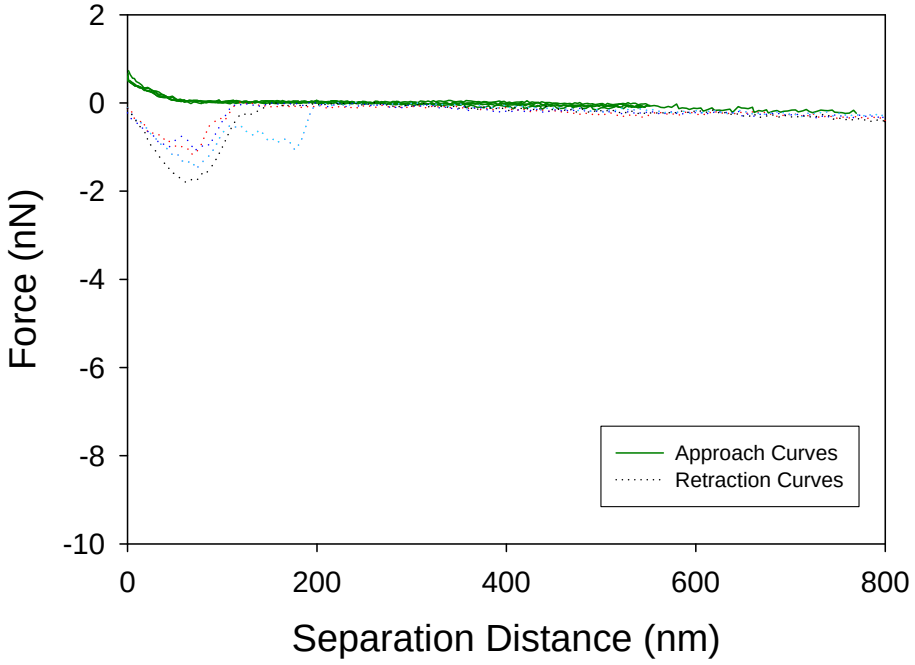

Figure 9.183 5 force plots of O55:H7 to silicon nitride

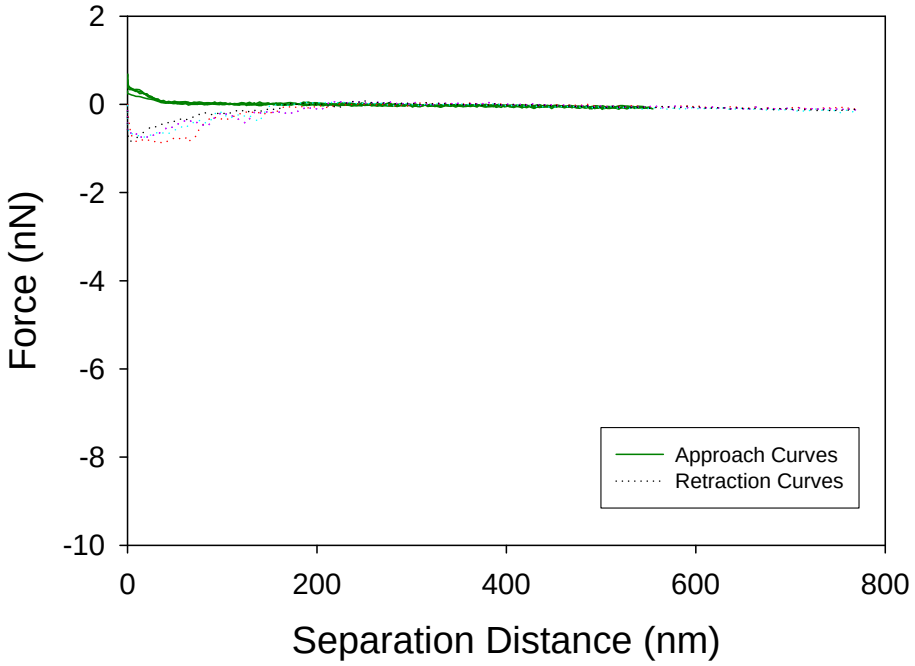

Figure 9.184 5 force plots of O55:H7 to silicon nitride

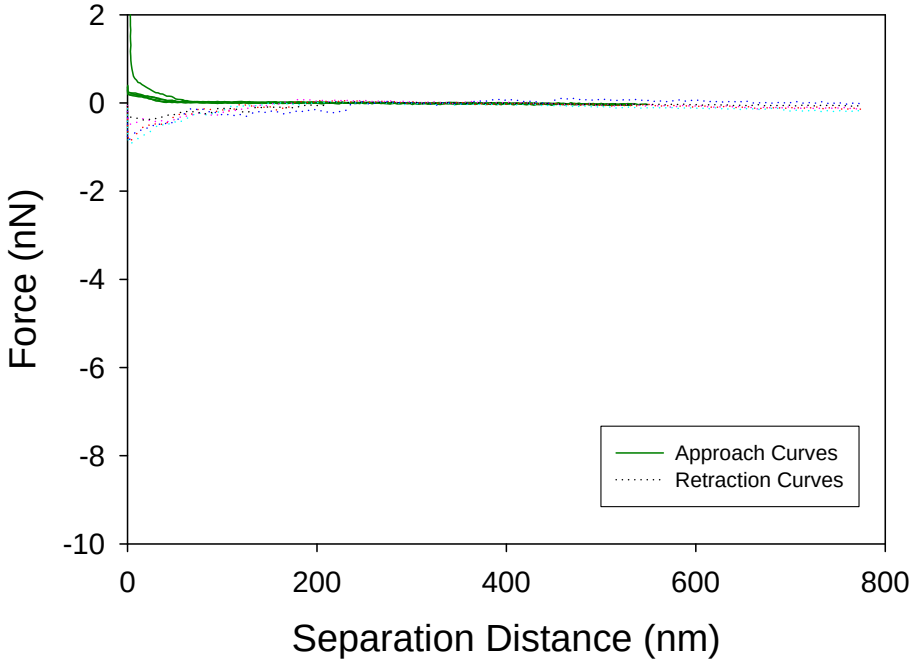

Figure 9.185 5 force plots of O55:H7 to silicon nitride

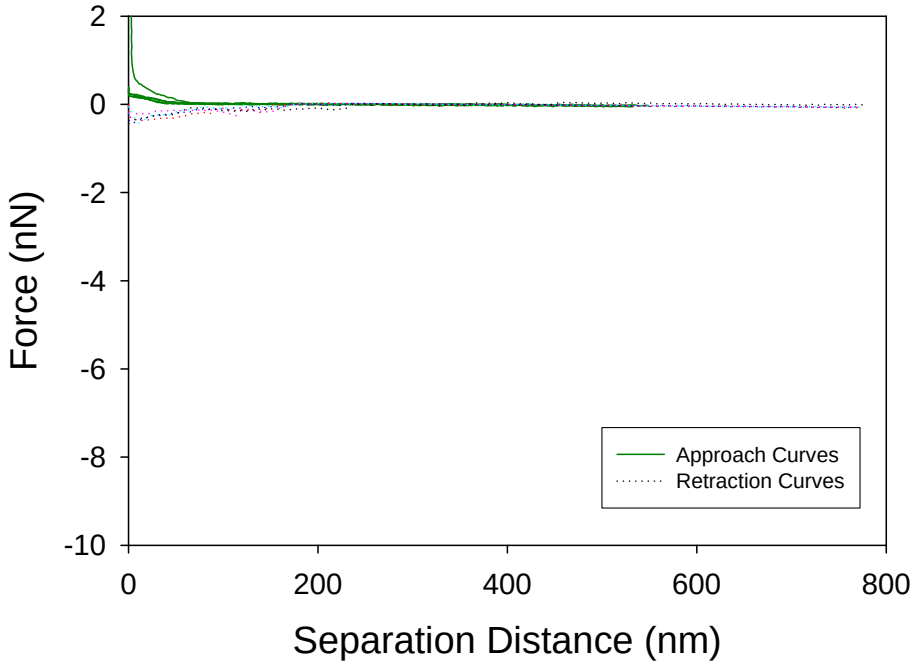

Figure 9.186 5 force plots of O55:H7 to silicon nitride

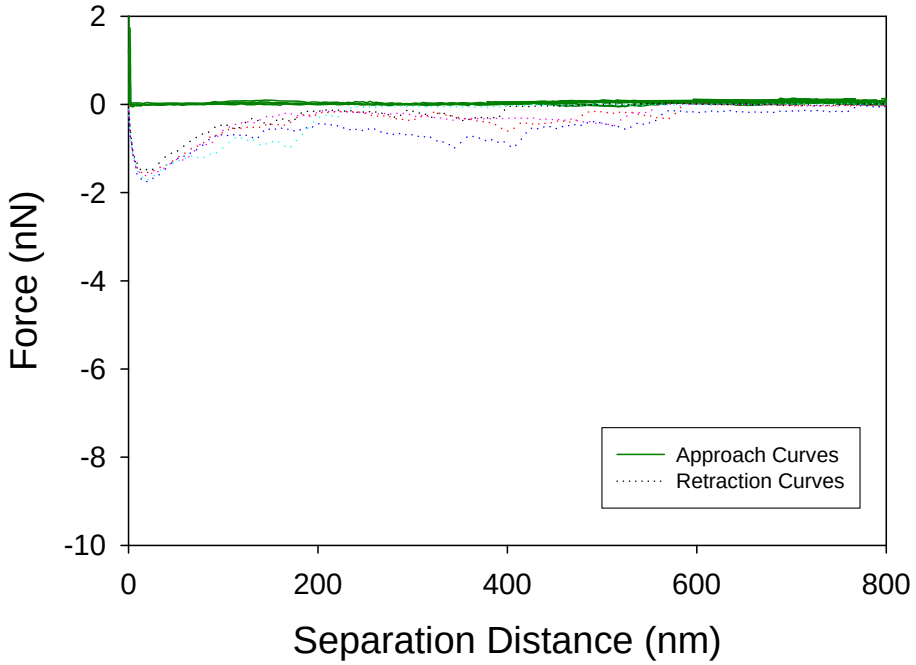

Figure 9.187 5 force plots of O55:H7 to silicon nitride

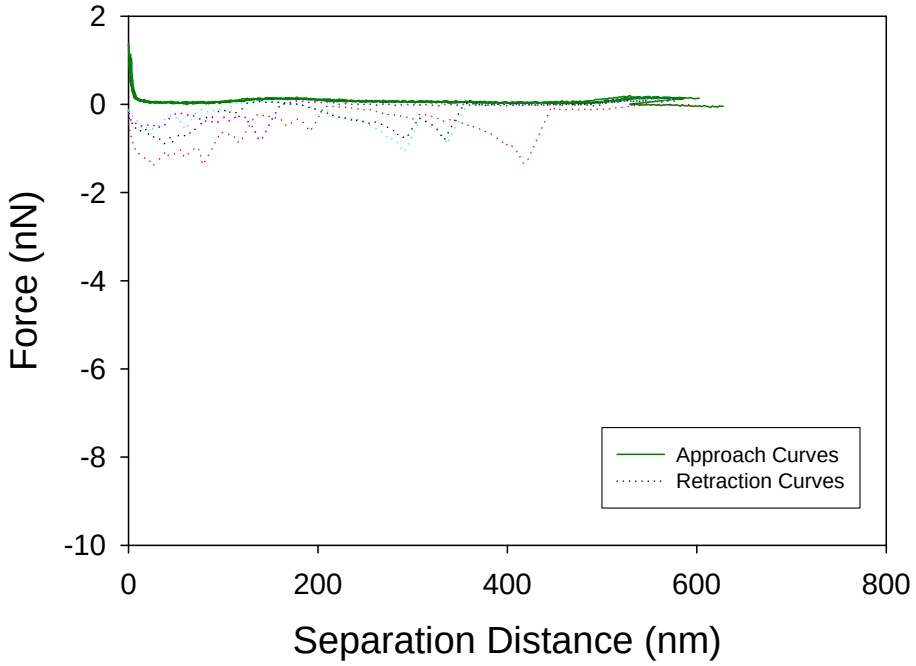

Figure 9.188 5 force plots of O55:H7 to CP1

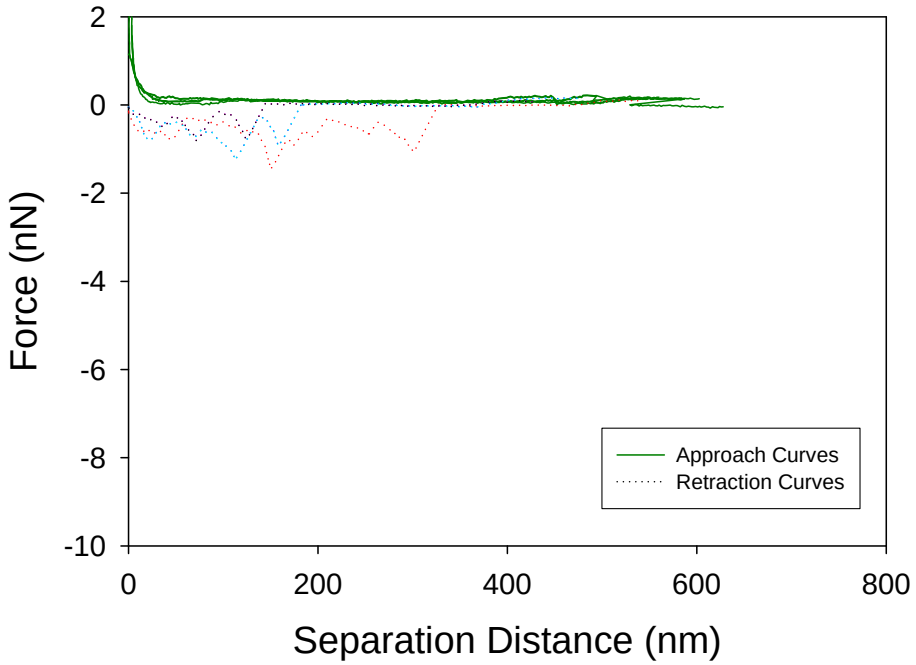

Figure 9.189 5 force plots of O55:H7 to CP1

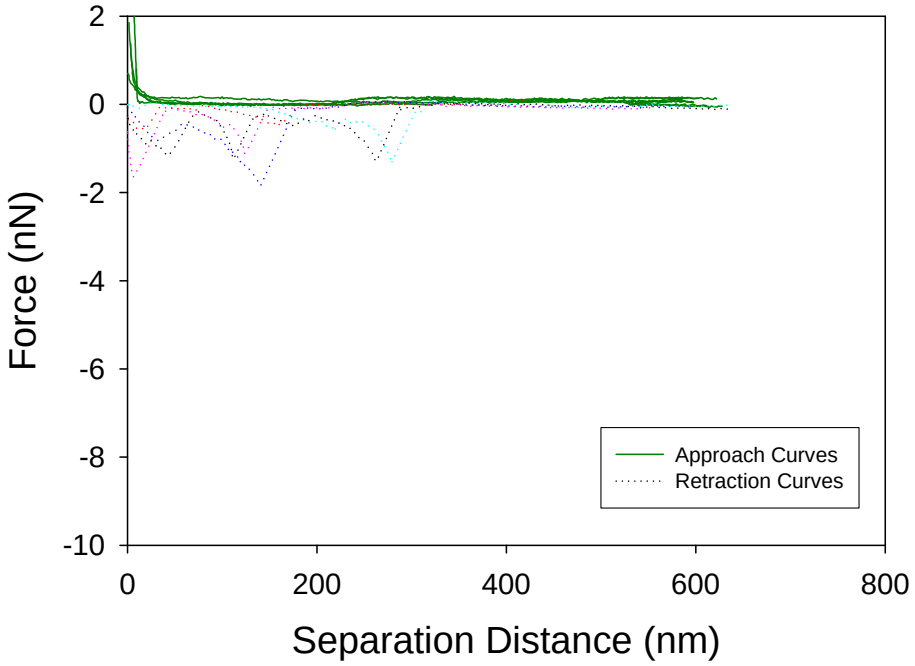

Figure 9.190 5 force plots of O55:H7 to CP1

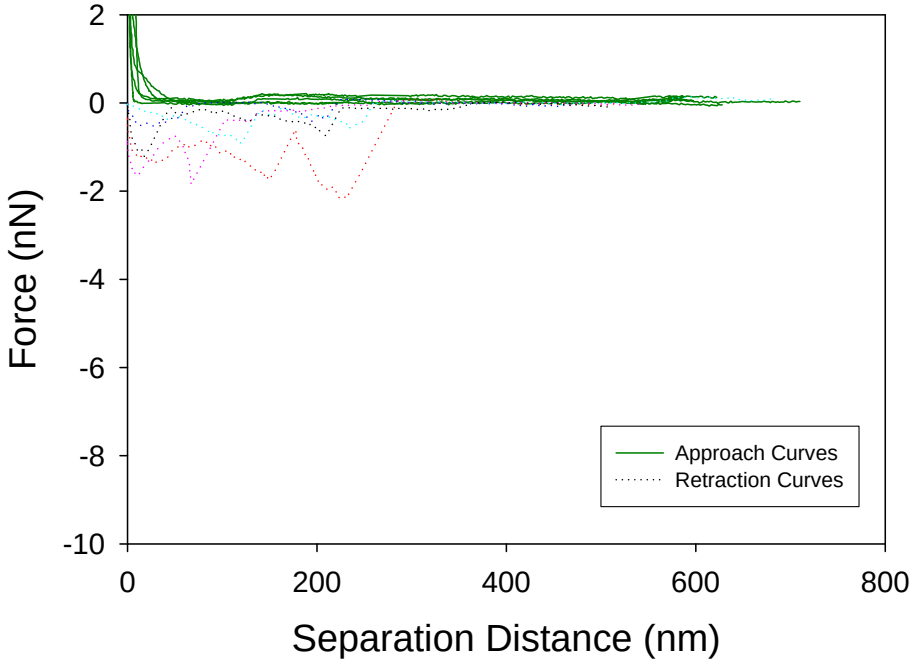

Figure 9.191 5 force plots of O55:H7 to CP1

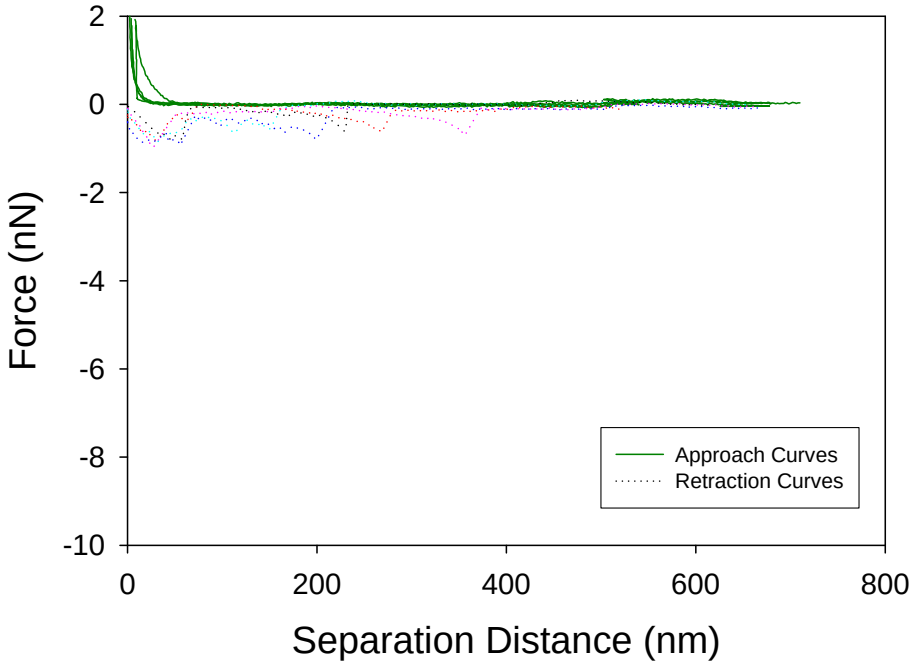

Figure 9.192 5 force plots of O55:H7 to CP1

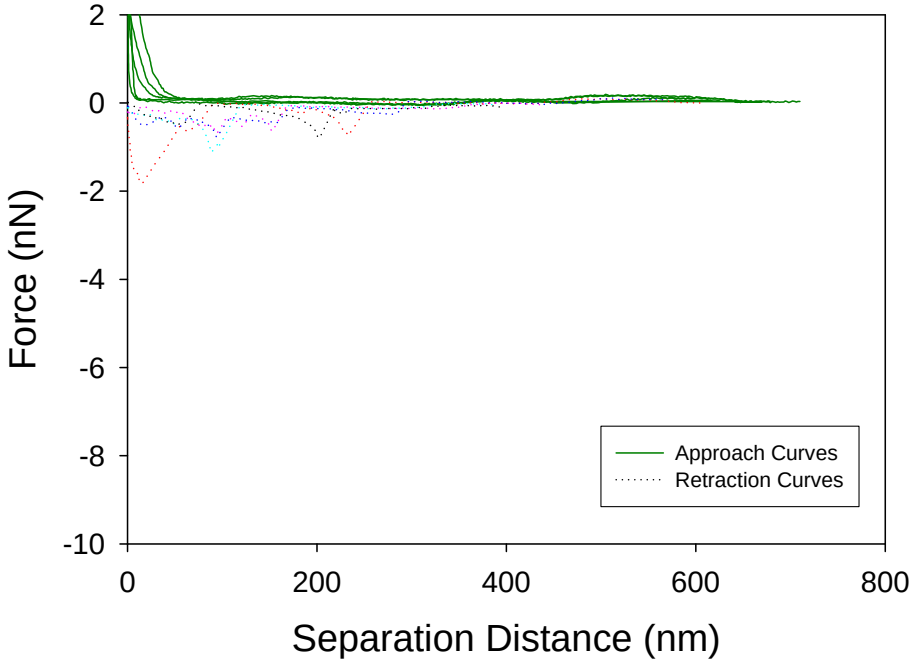

Figure 9.193 5 force plots of O55:H7 to CP1

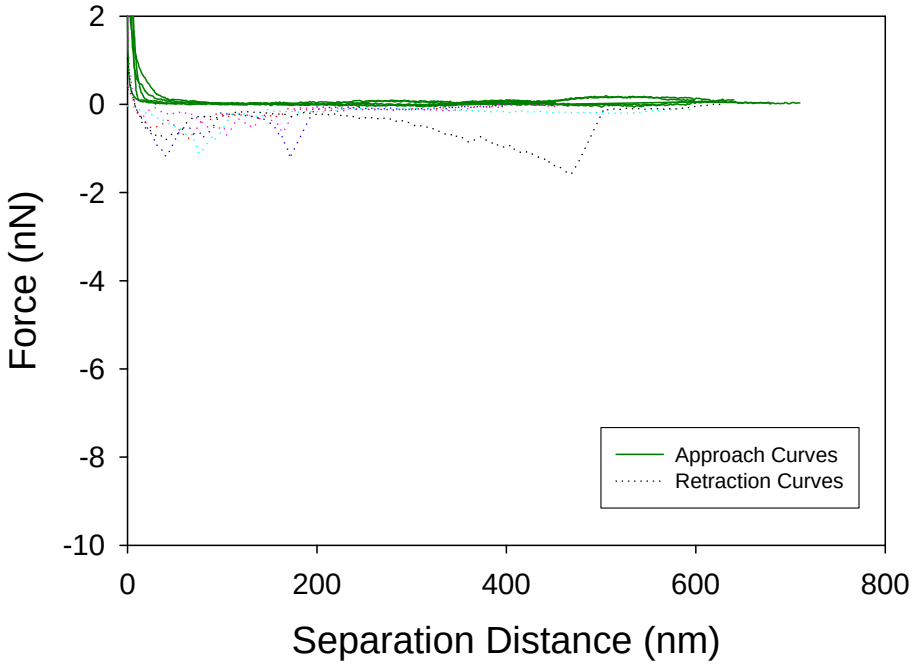

Figure 9.194 5 force plots of O55:H7 to CP1

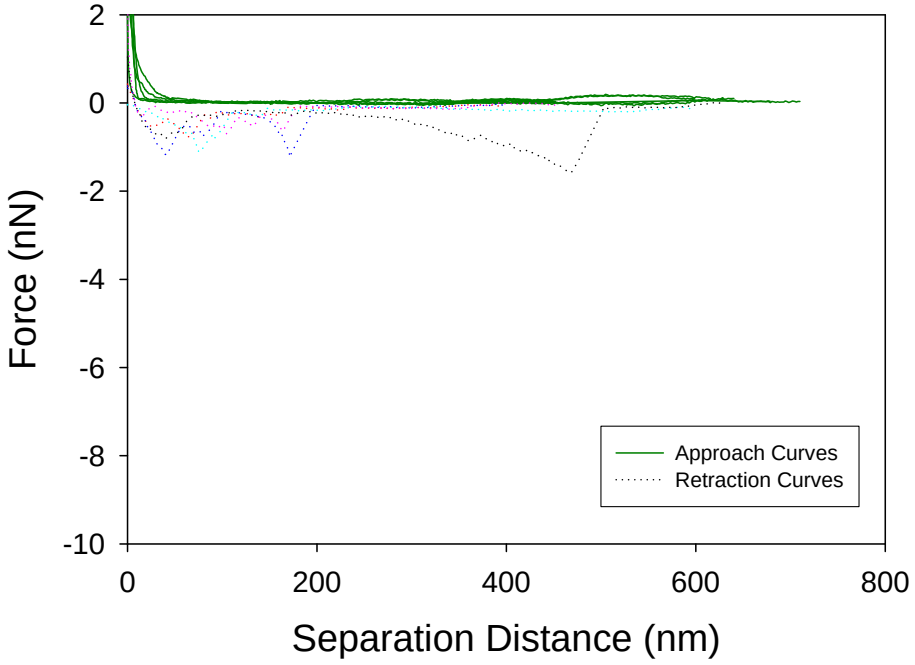

Figure 9.195 5 force plots of O55:H7 to CP1

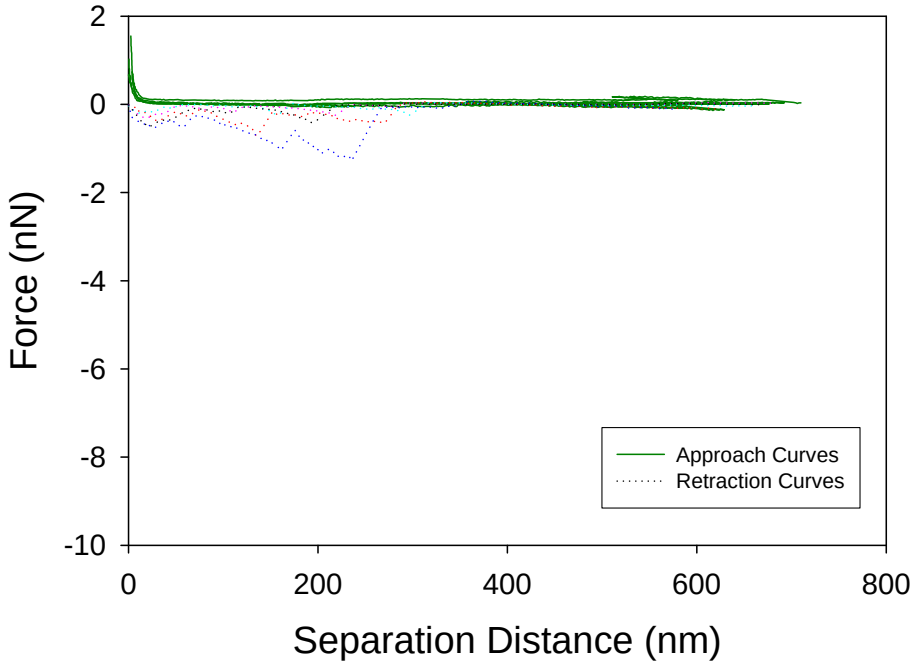

Figure 9.196 5 force plots of O55:H7 to CP1

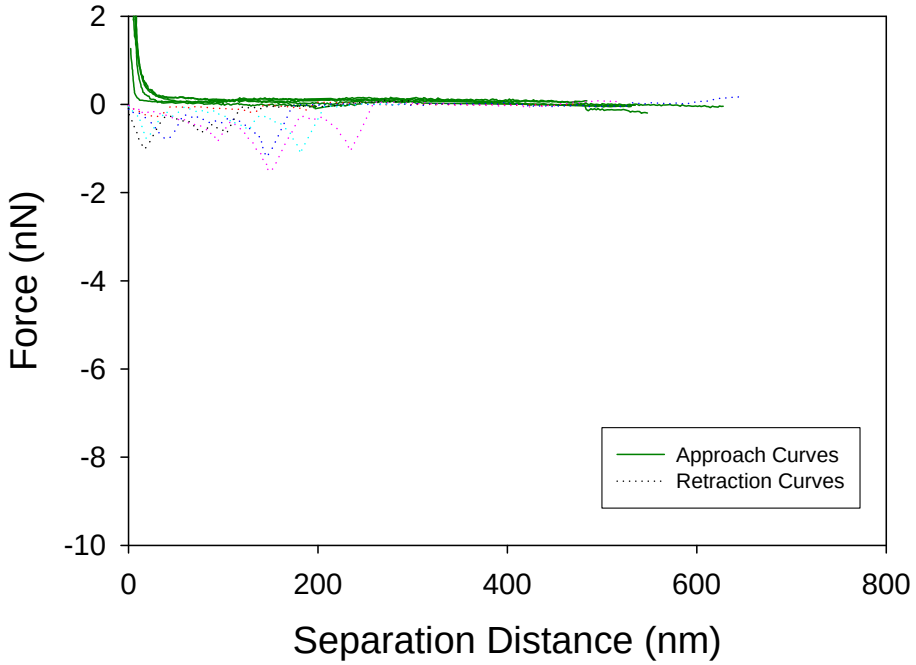

Figure 9.197 5 force plots of O55:H7 to CP1

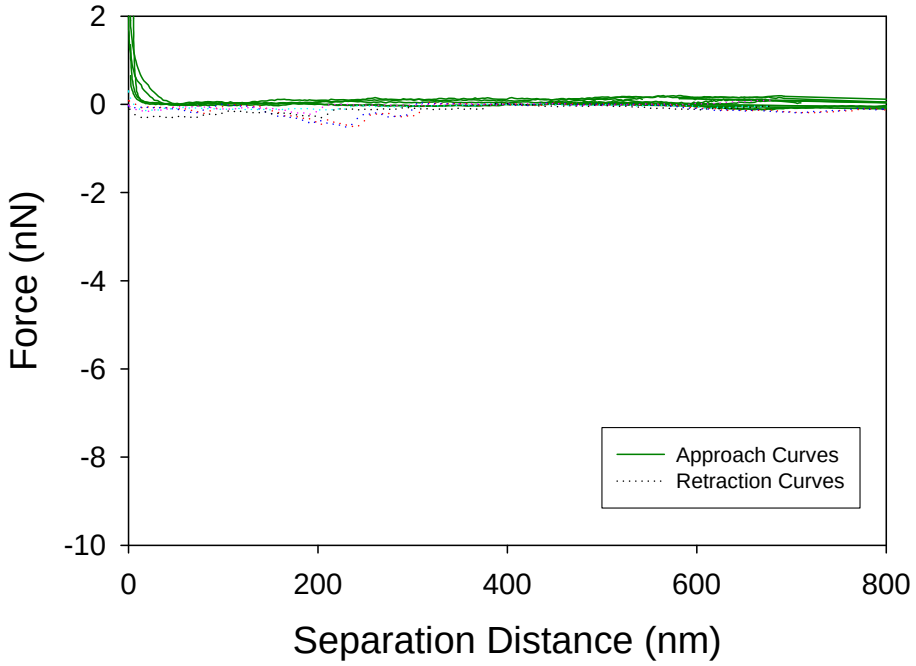

Figure 9.198 5 force plots of O113:H4 to silicon nitride

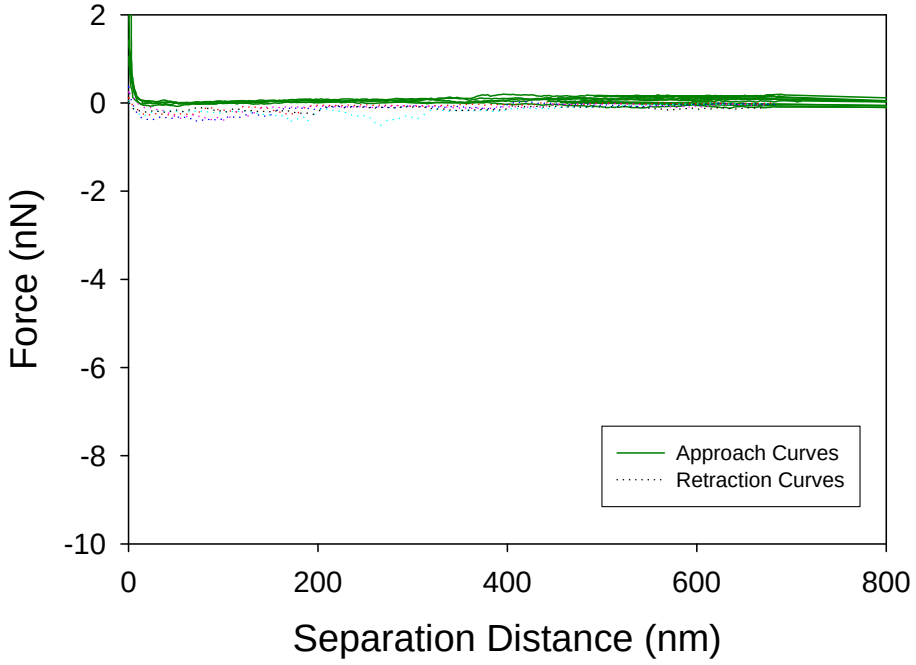

Figure 9.199 5 force plots of O113:H4 to silicon nitride

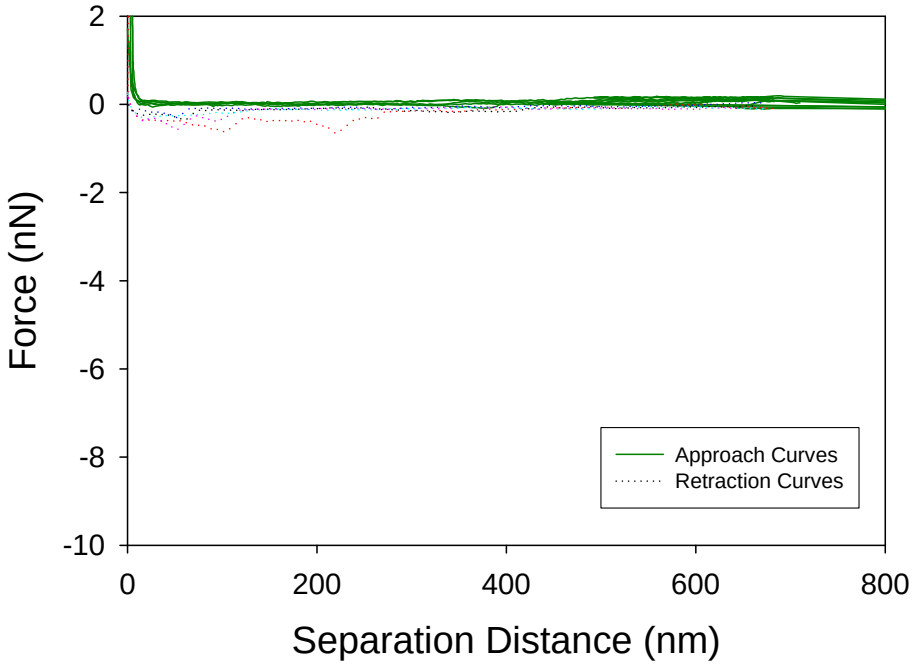

Figure 9.200 5 force plots of O113:H4 to silicon nitride

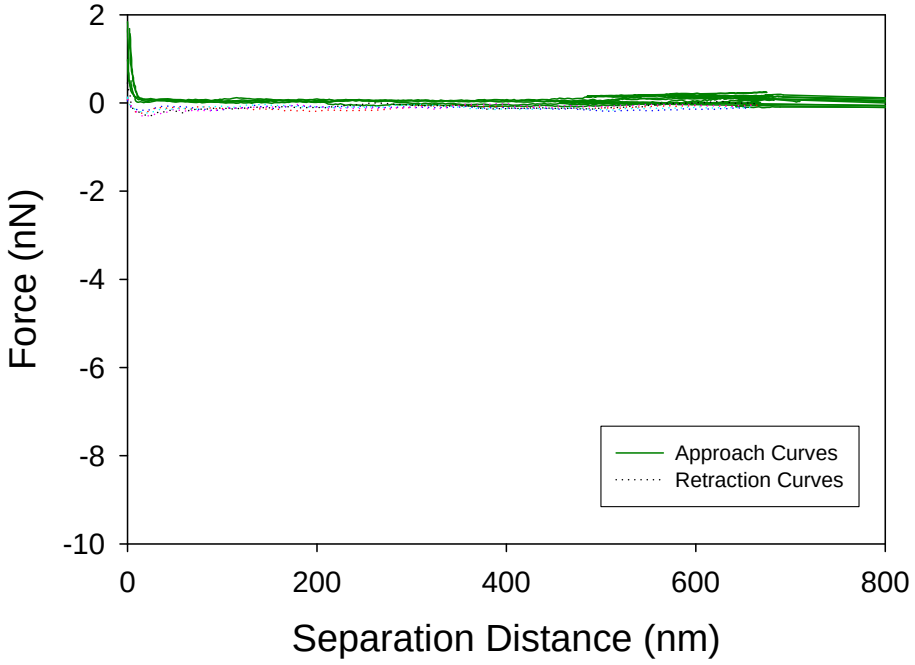

Figure 9.201 5 force plots of O113:H4 to silicon nitride

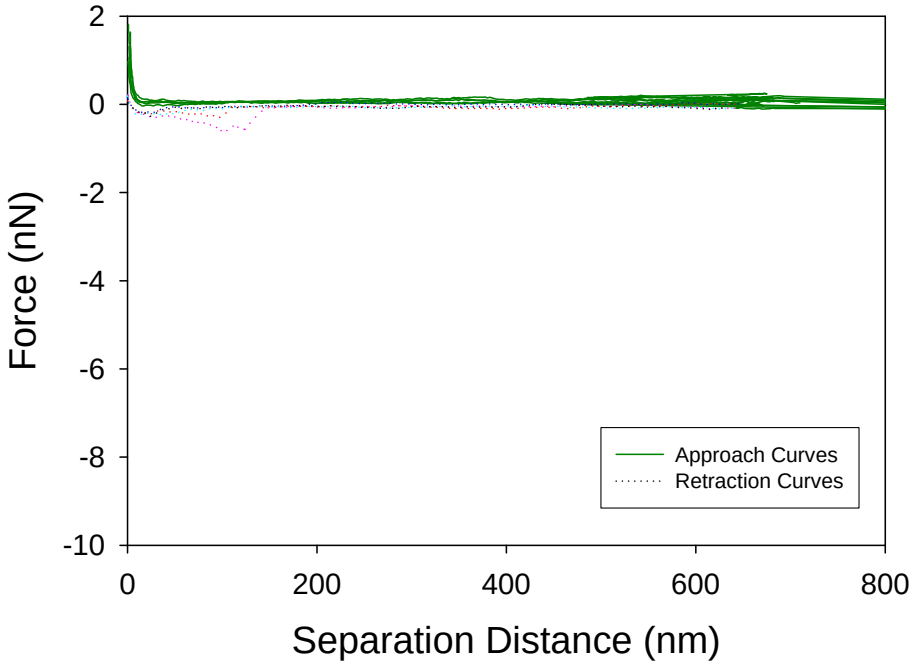

Figure 9.202 5 force plots of O113:H4 to silicon nitride

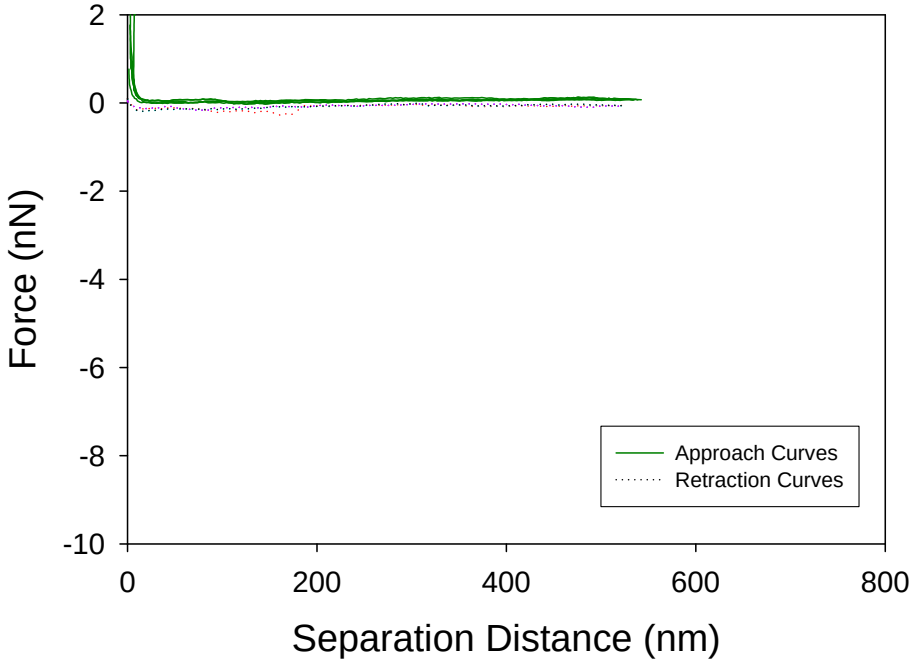

Figure 9.203 5 force plots of O113:H4 to silicon nitride

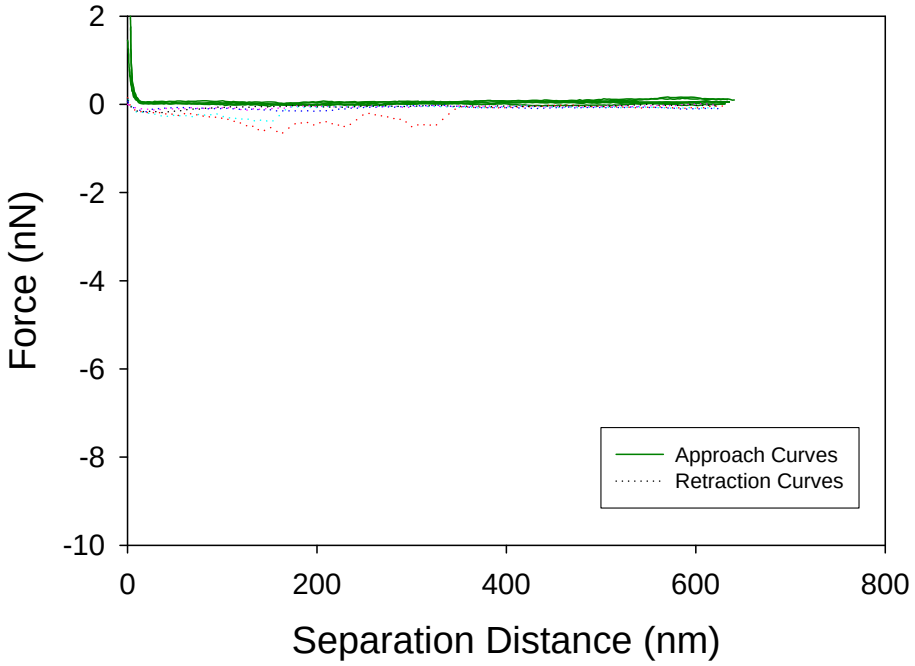

Figure 9.204 5 force plots of O113:H4 to silicon nitride

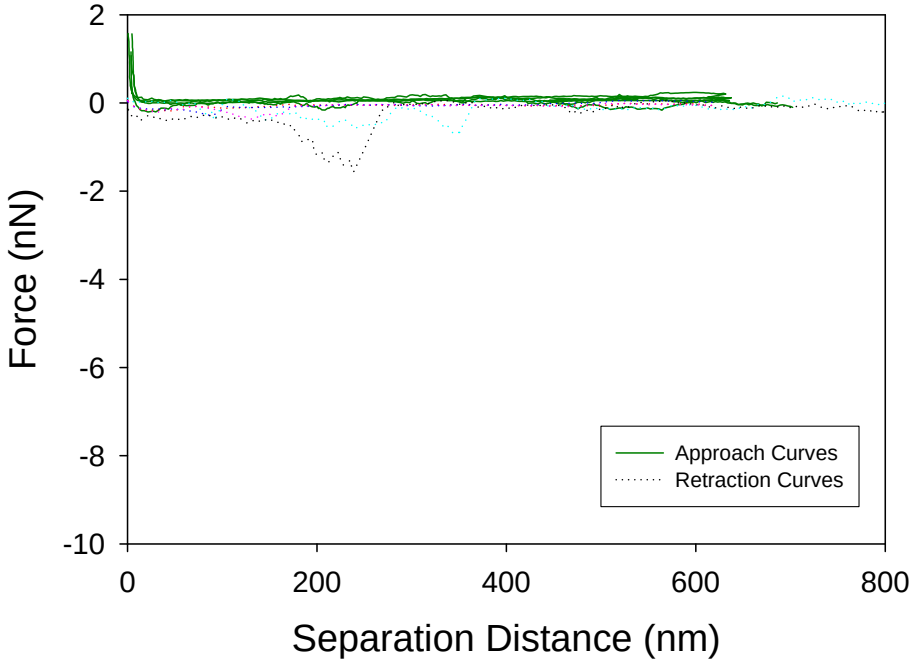

Figure 9.205 5 force plots of O113:H4 to silicon nitride

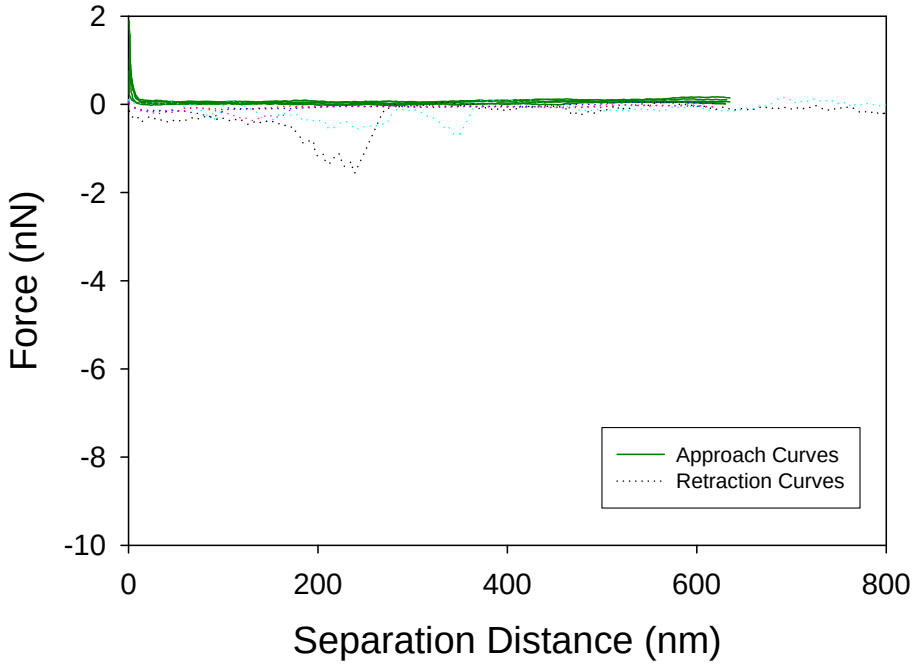

Figure 9.206 5 force plots of O113:H4 to silicon nitride

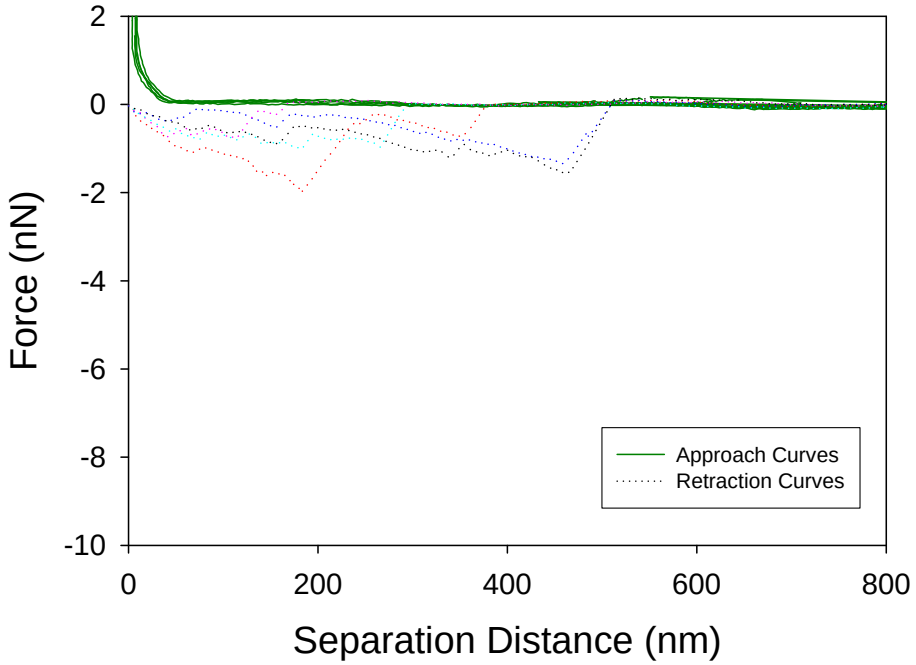

Figure 9.207 5 force plots of O113:H4 to silicon nitride

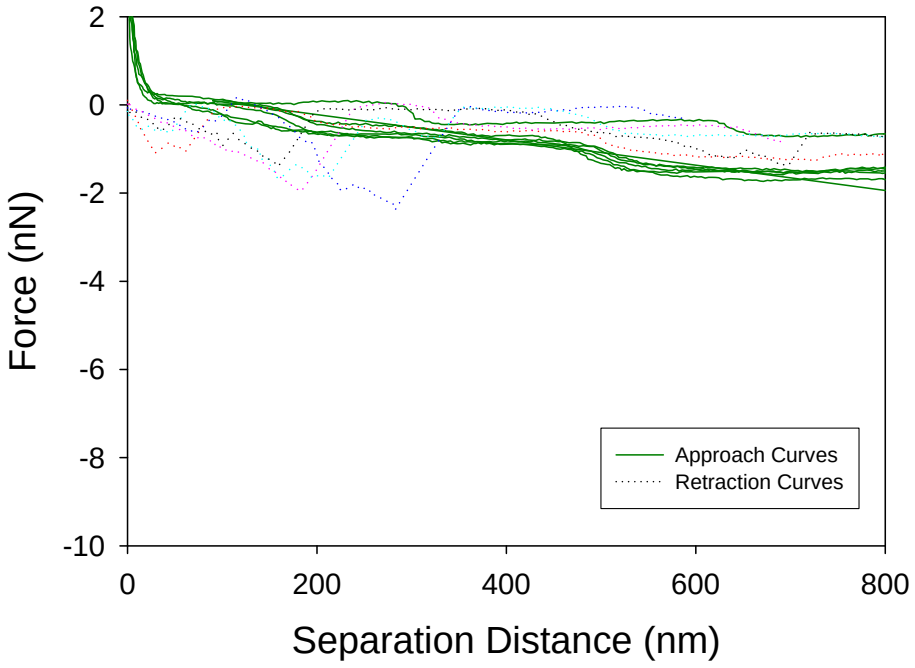

Figure 9.208 5 force plots of O113:H4 to CP1

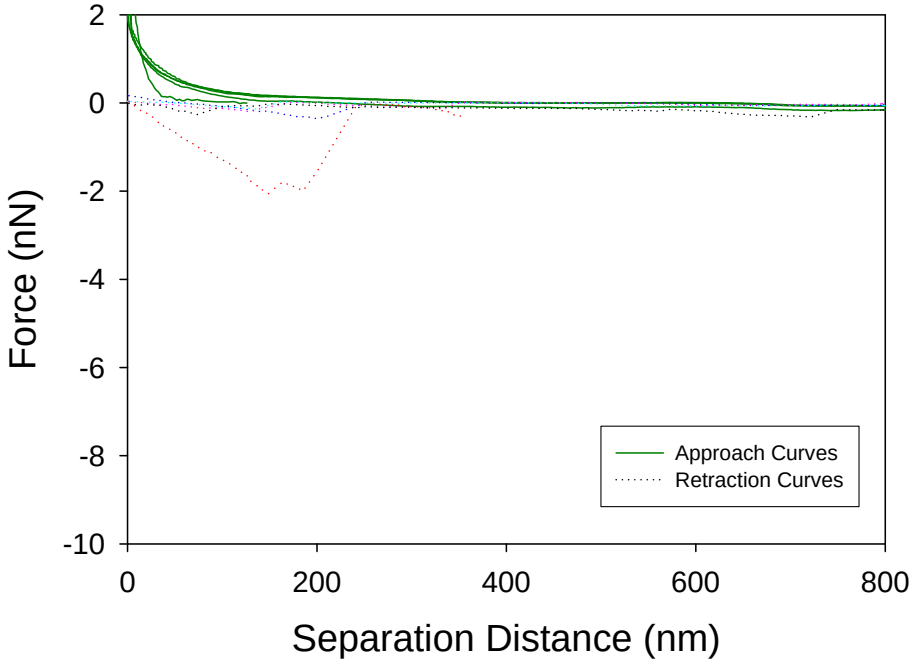

Figure 9.209 5 force plots of O113:H4 to CP1

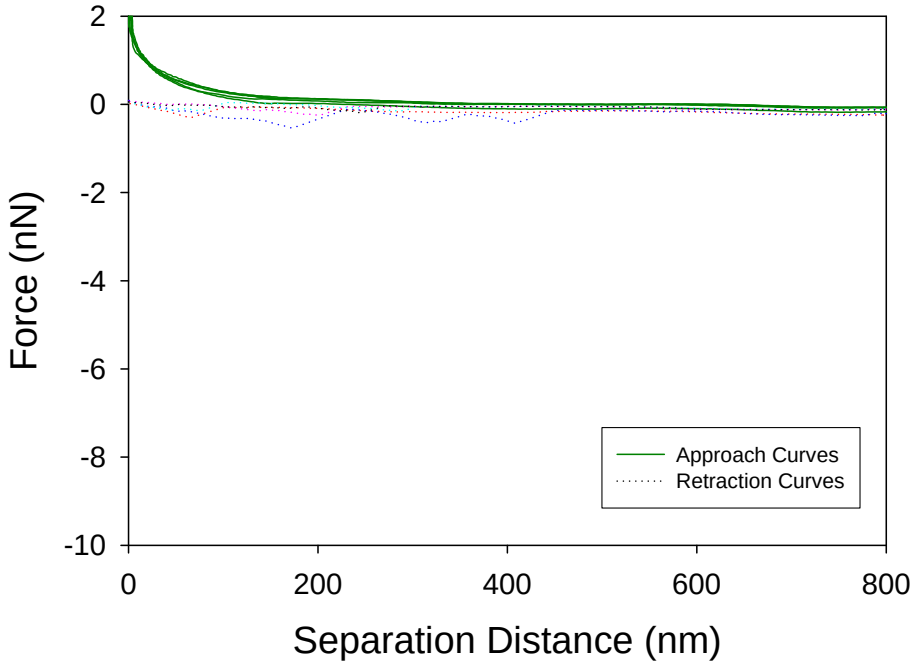

Figure 9.210 5 force plots of O113:H4 to CP1

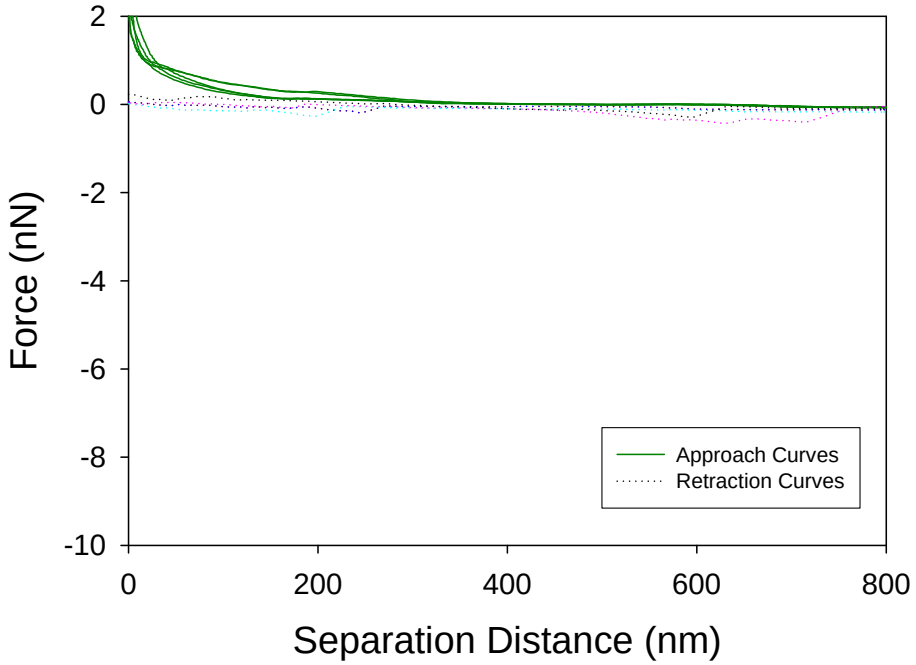

Figure 9.211 5 force plots of O113:H4 to CP1

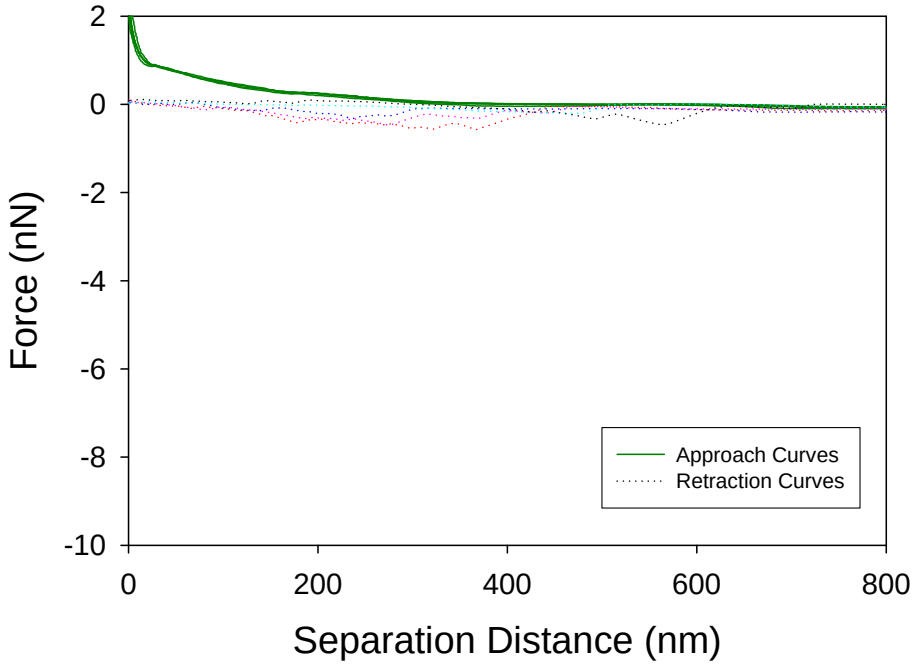

Figure 9.212 5 force plots of O113:H4 to CP1

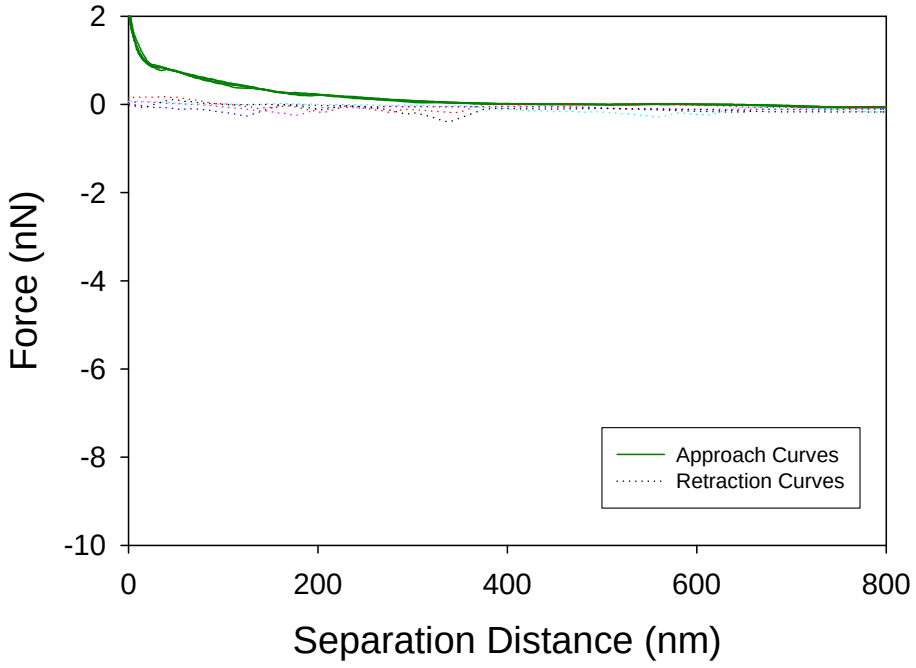

Figure 9.213 5 force plots of O113:H4 to CP1

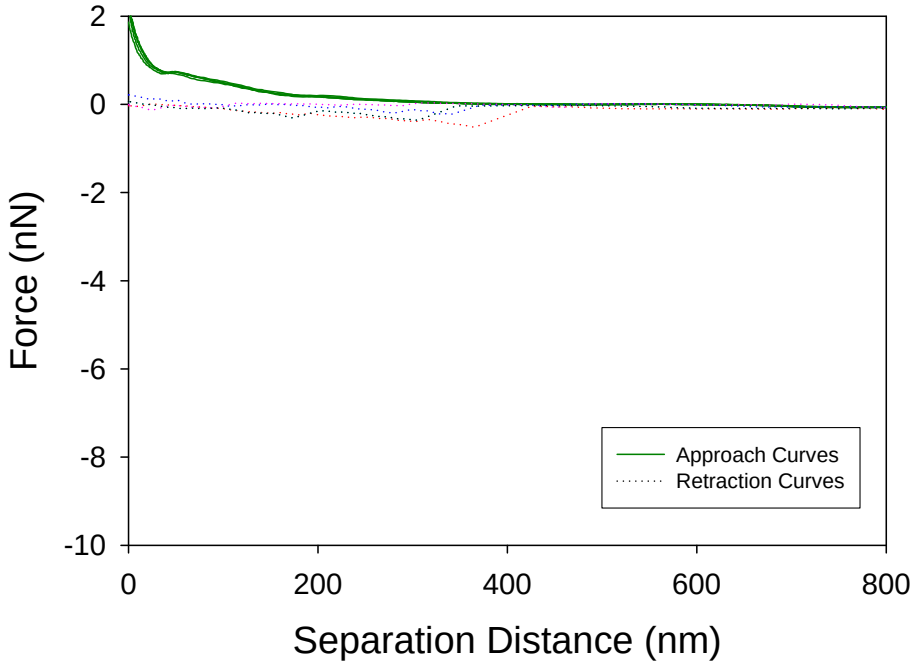

Figure 9.214 5 force plots of O113:H4 to CP1

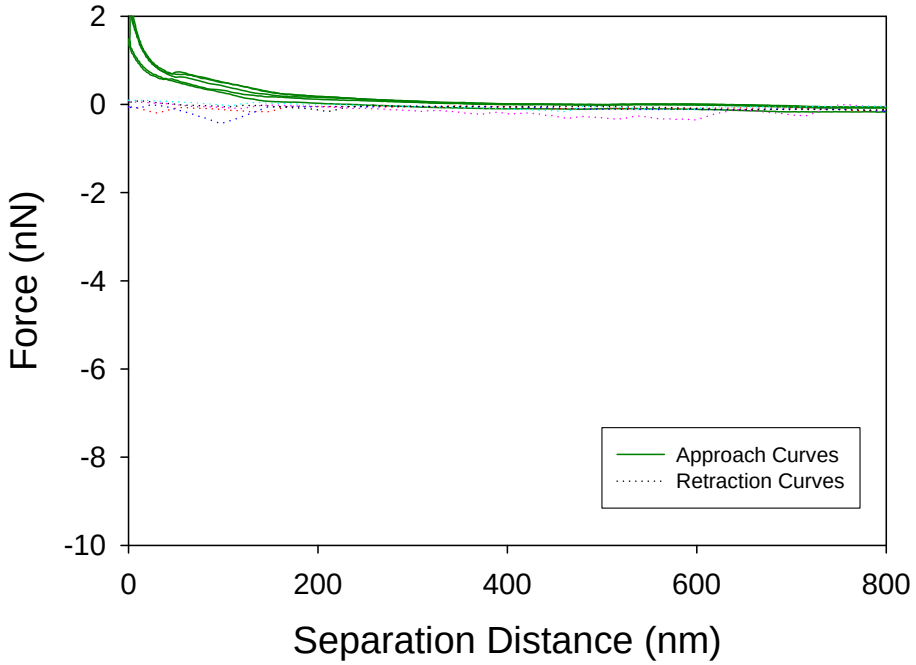

Figure 9.215 5 force plots of O113:H4 to CP1

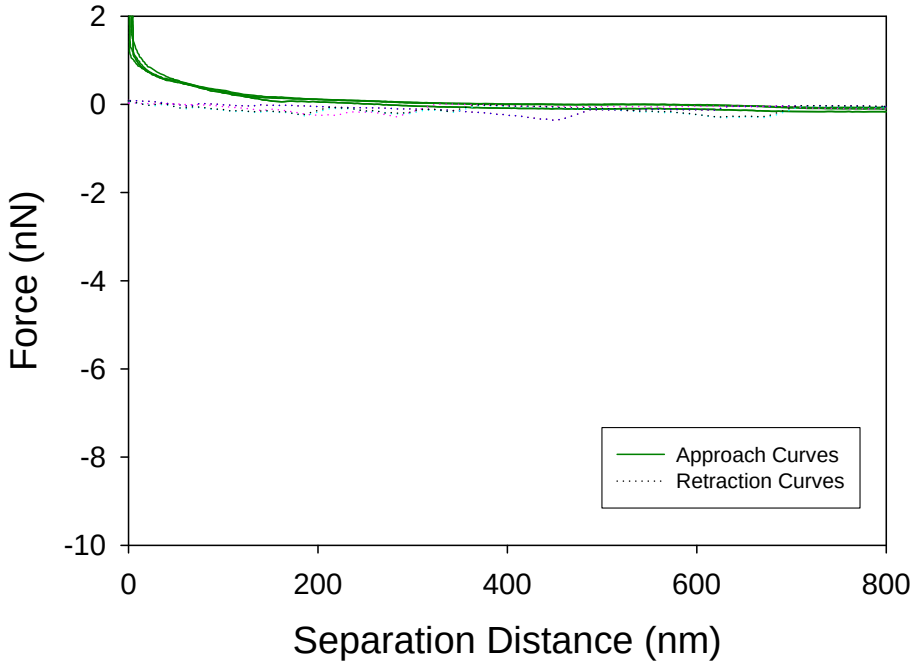

Figure 9.216 5 force plots of O113:H4 to CP1

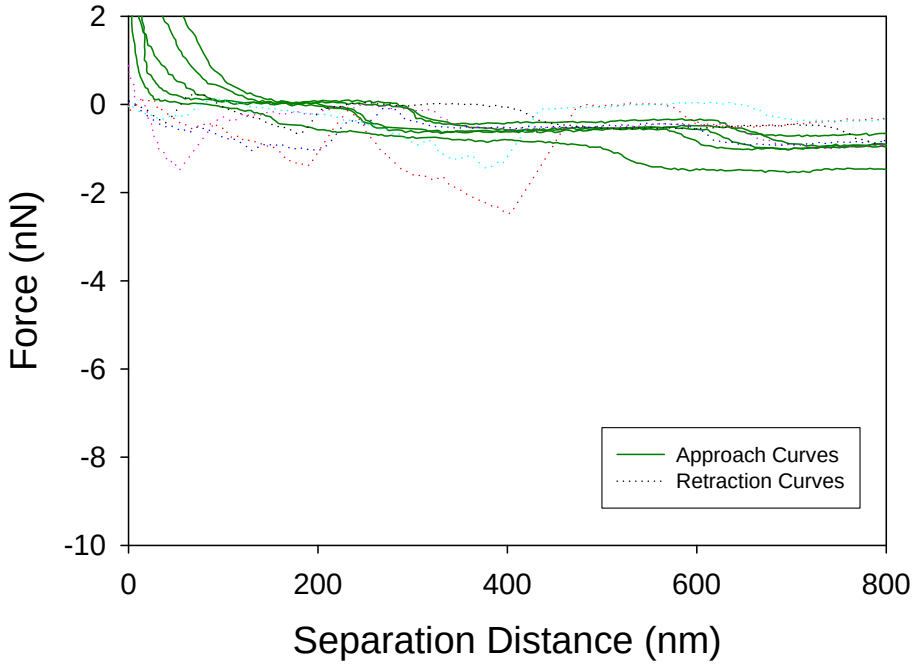

Figure 9.217 5 force plots of O113:H4 to CP1

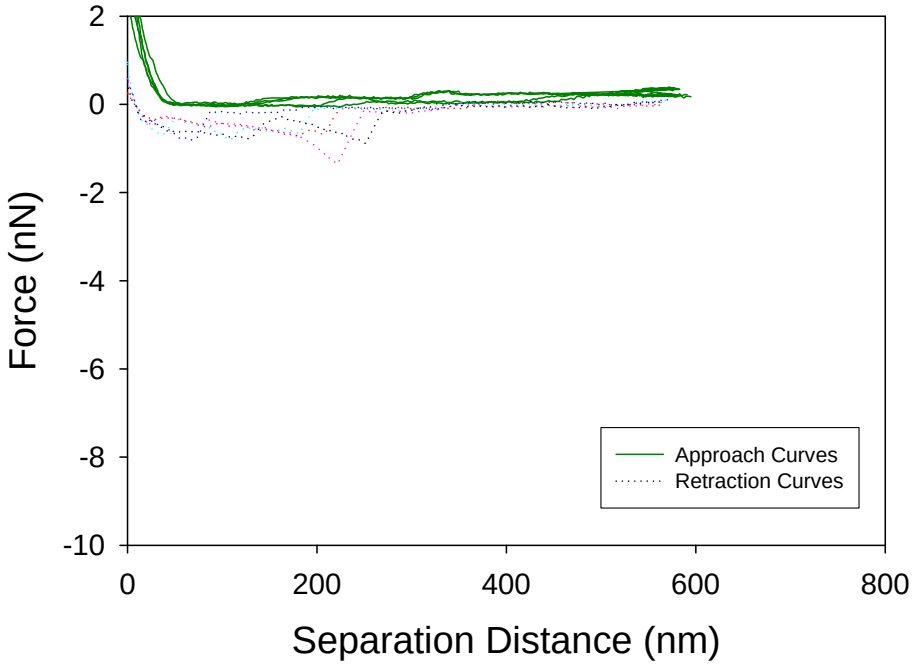

Figure 9.218 5 force plots of O113:H21 to silicon nitride

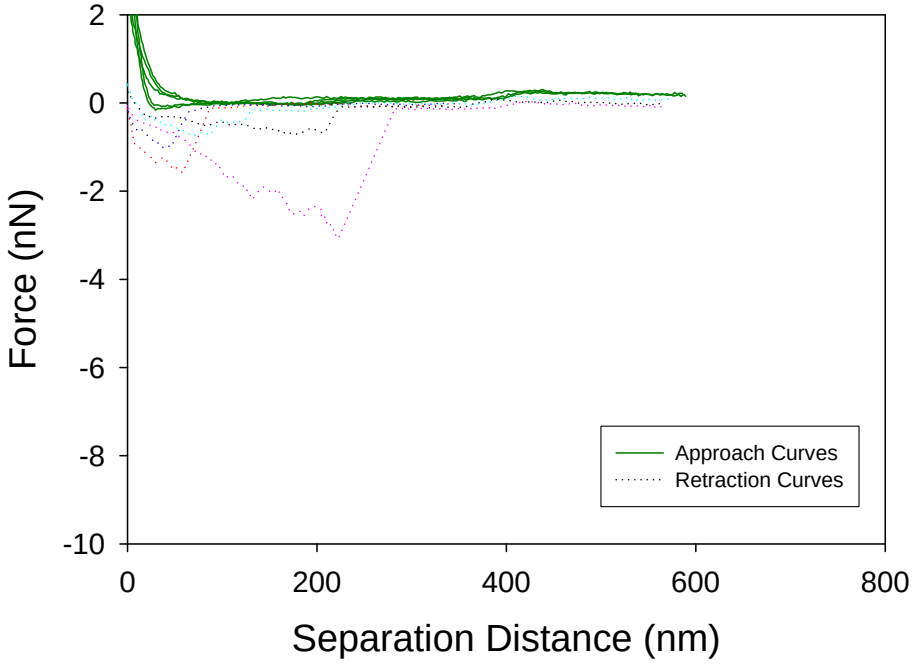

Figure 9.219 5 force plots of O113:H21 to silicon nitride

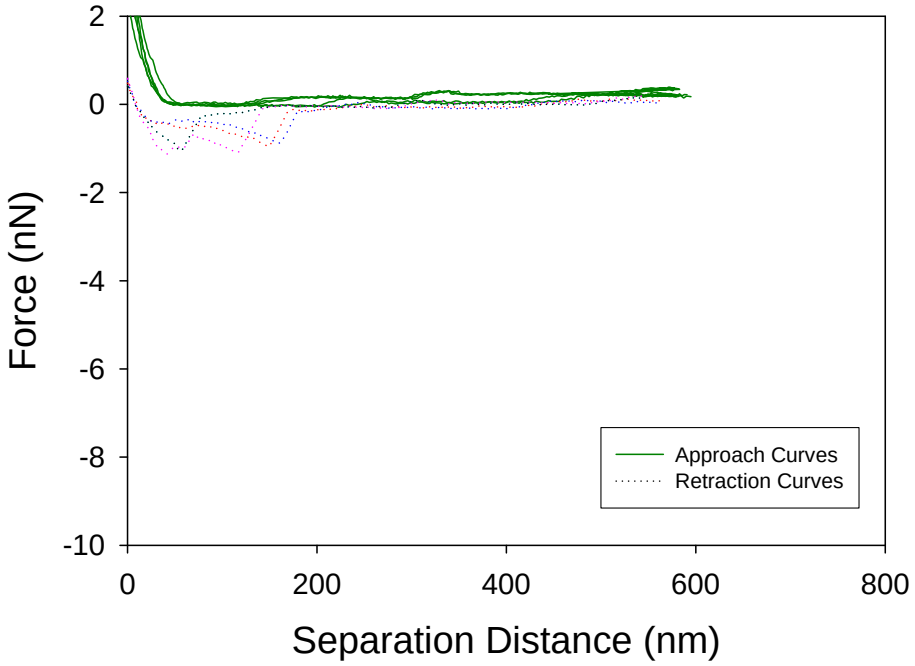

Figure 9.220 5 force plots of O113:H21 to silicon nitride

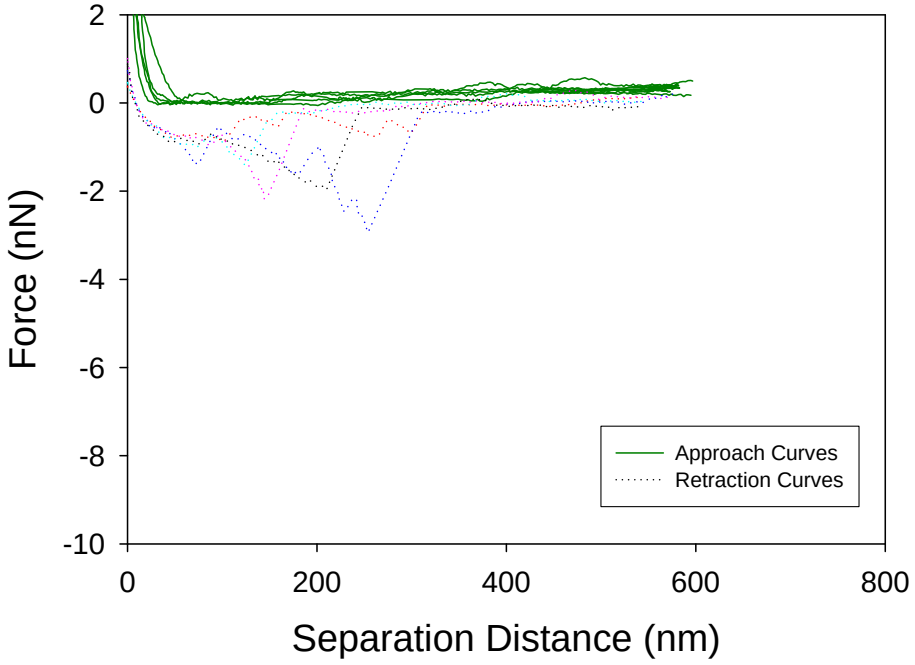

Figure 9.221 5 force plots of O113:H21 to silicon nitride

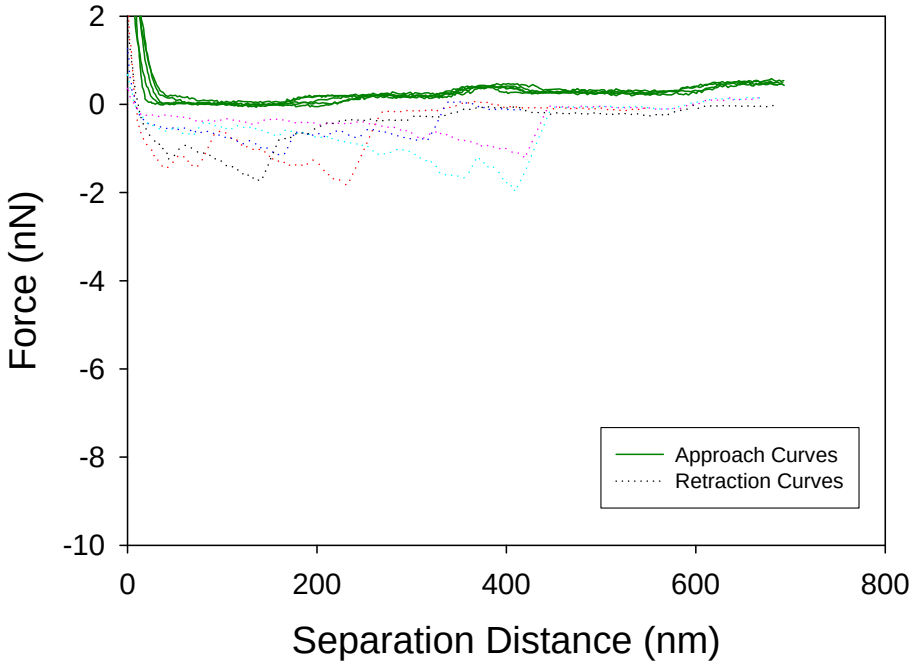

Figure 9.222 5 force plots of O113:H21 to silicon nitride

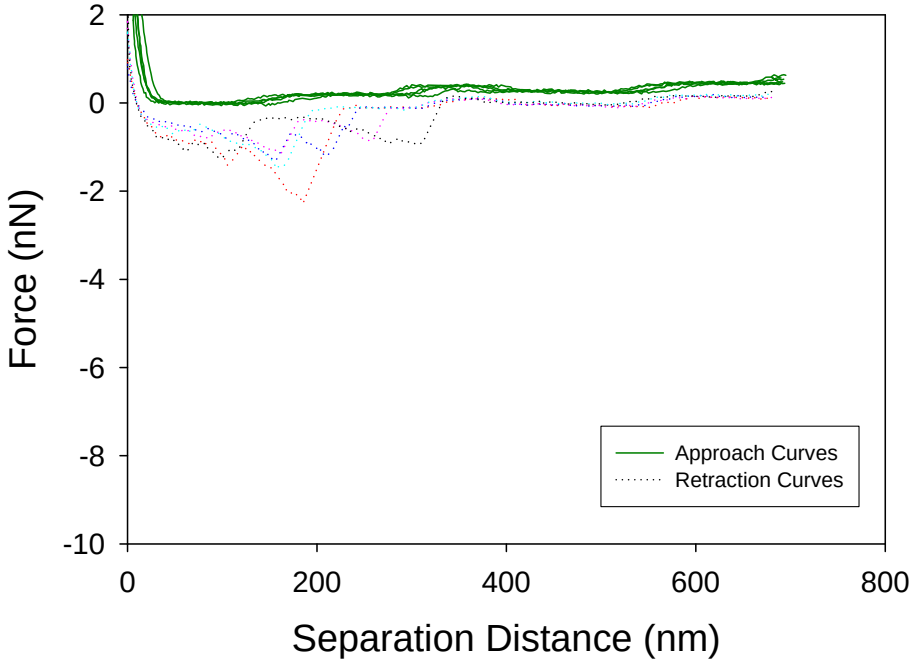

Figure 9.223 5 force plots of O113:H21 to silicon nitride

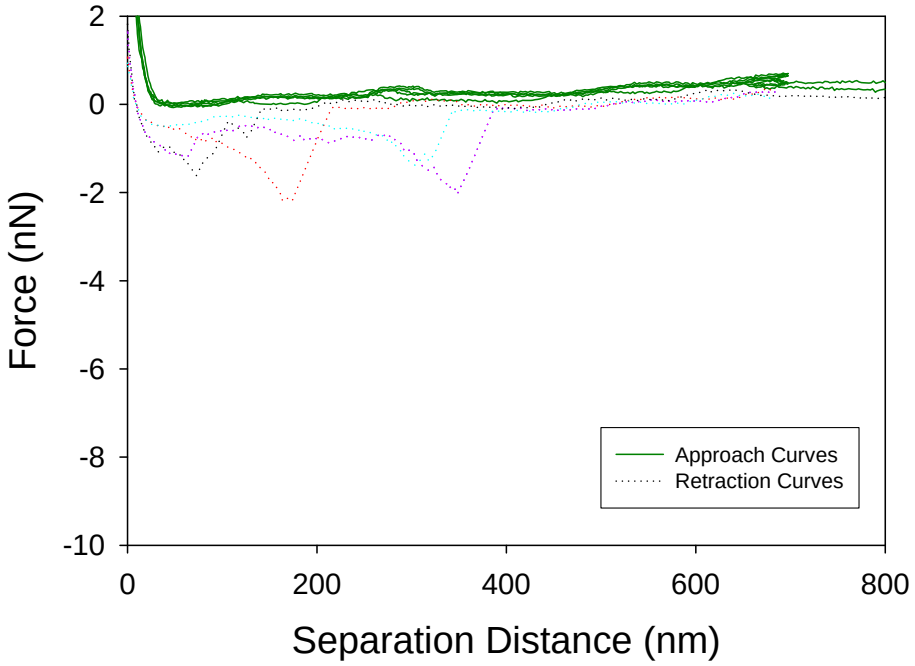

Figure 9.224 5 force plots of O113:H21 to silicon nitride

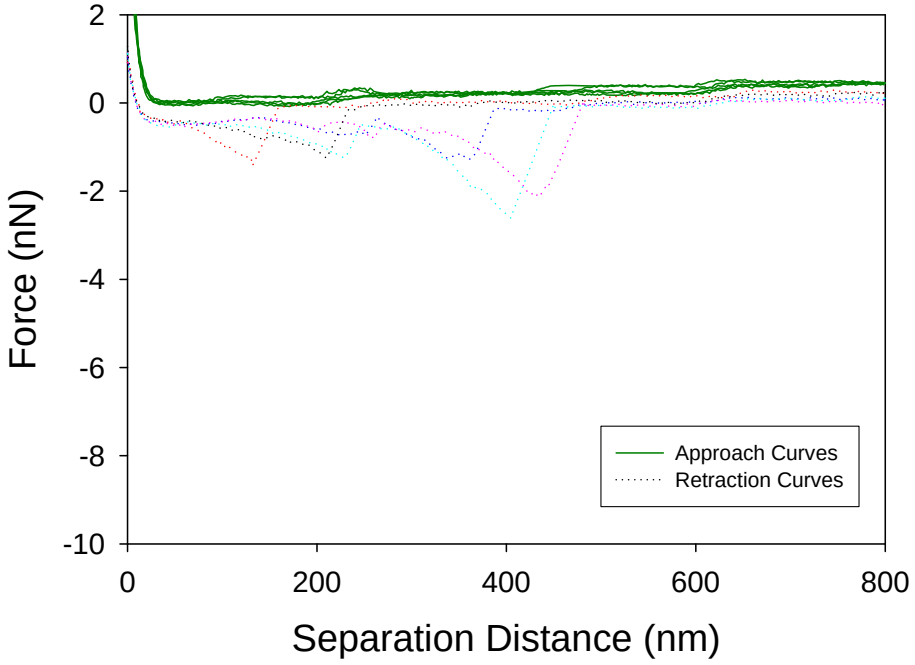

Figure 9.225 5 force plots of O113:H21 to silicon nitride

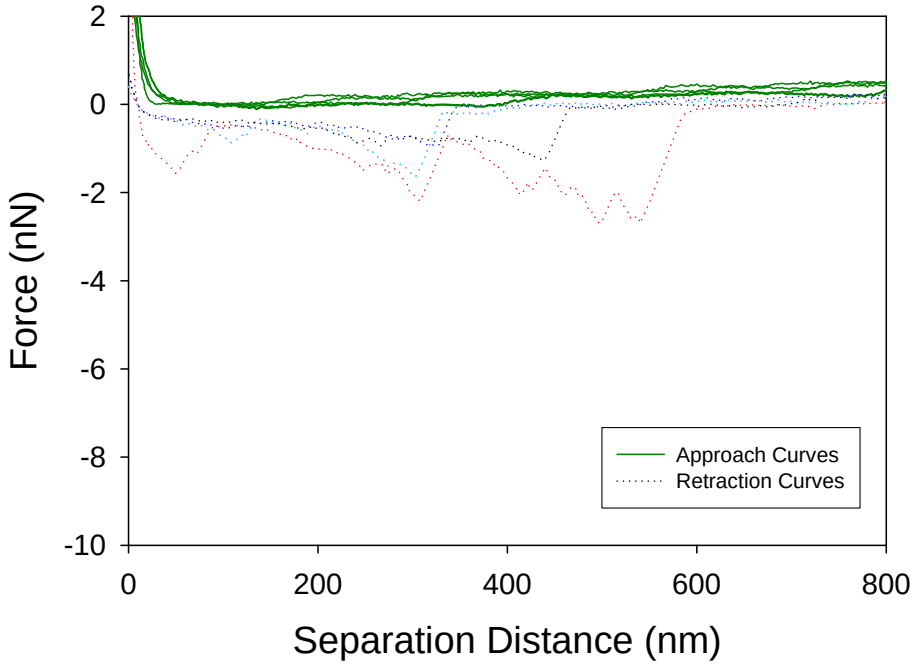

Figure 9.226 5 force plots of O113:H21 to silicon nitride

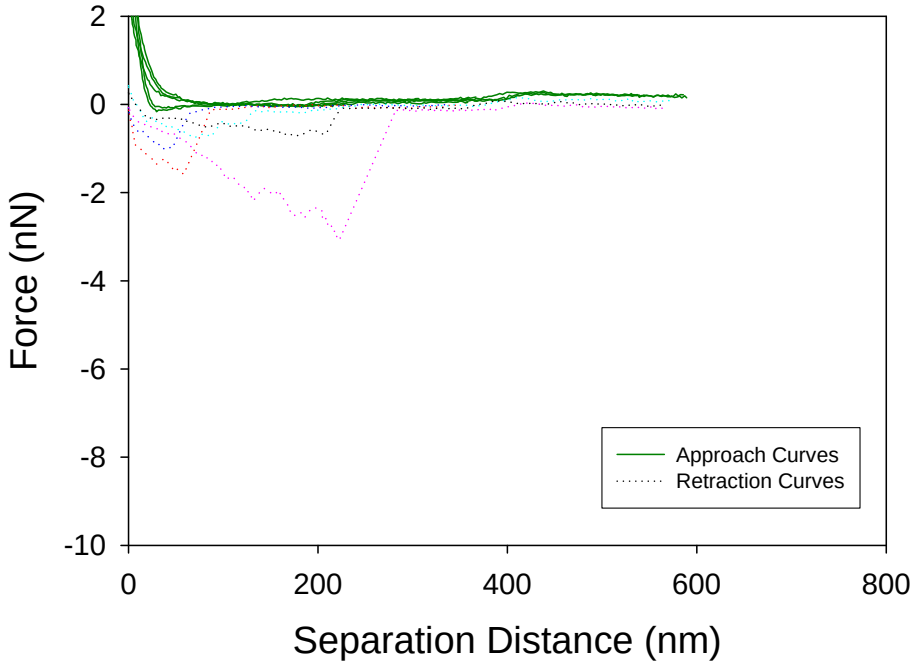

Figure 9.227 5 force plots of O113:H21 to silicon nitride

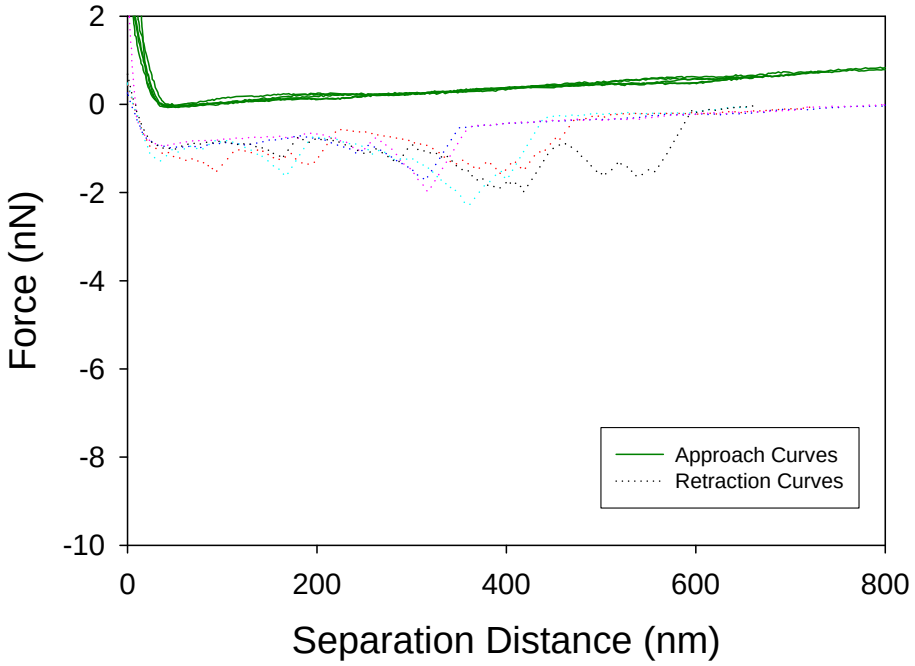

Figure 9.228 5 force plots of O113:H21 to CP1

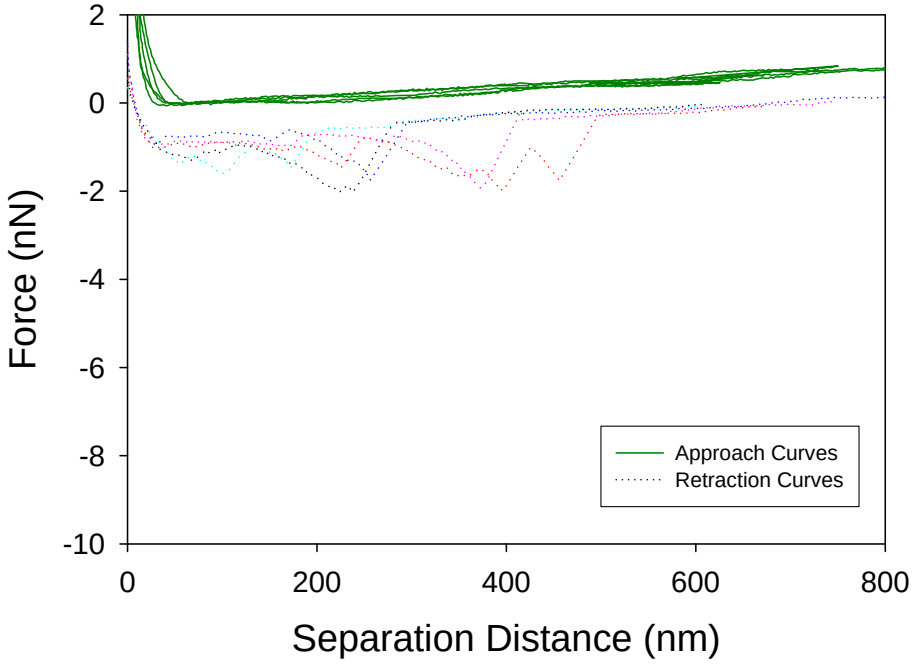

Figure 9.229 5 force plots of O113:H21 to CP1

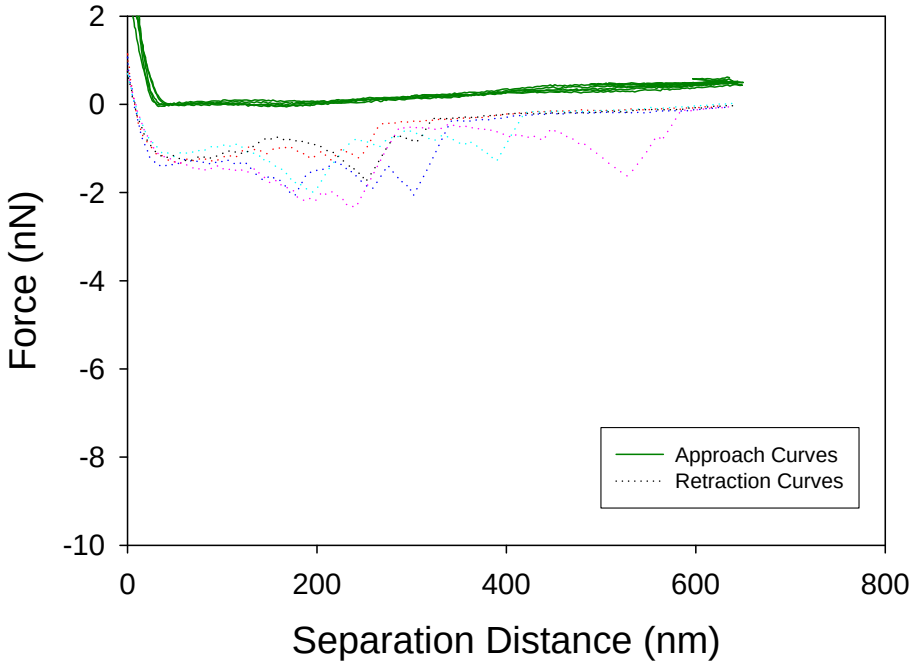

Figure 9.230 5 force plots of O113:H21 to CP1

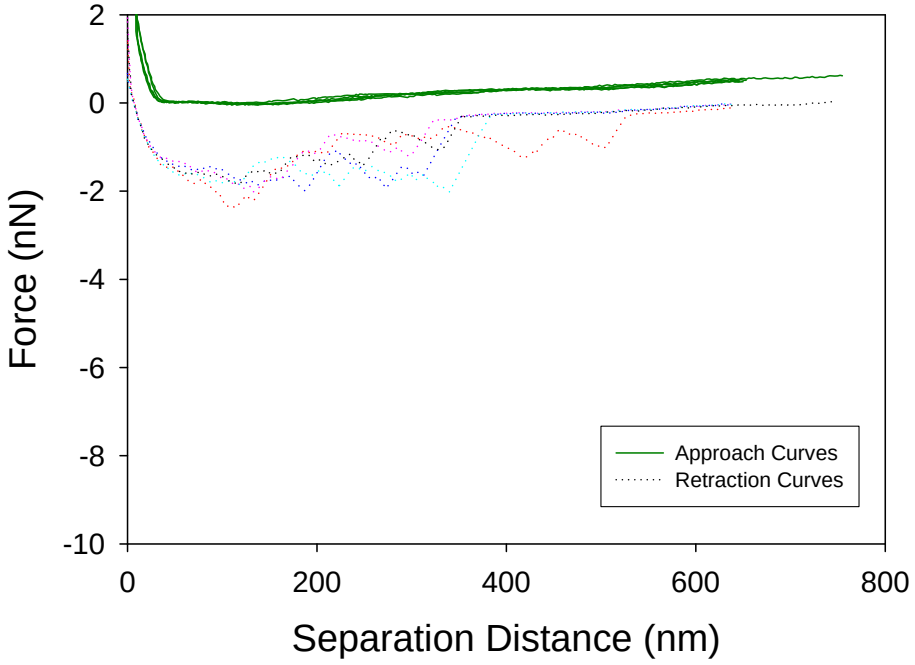

Figure 9.231 5 force plots of O113:H21 to CP1

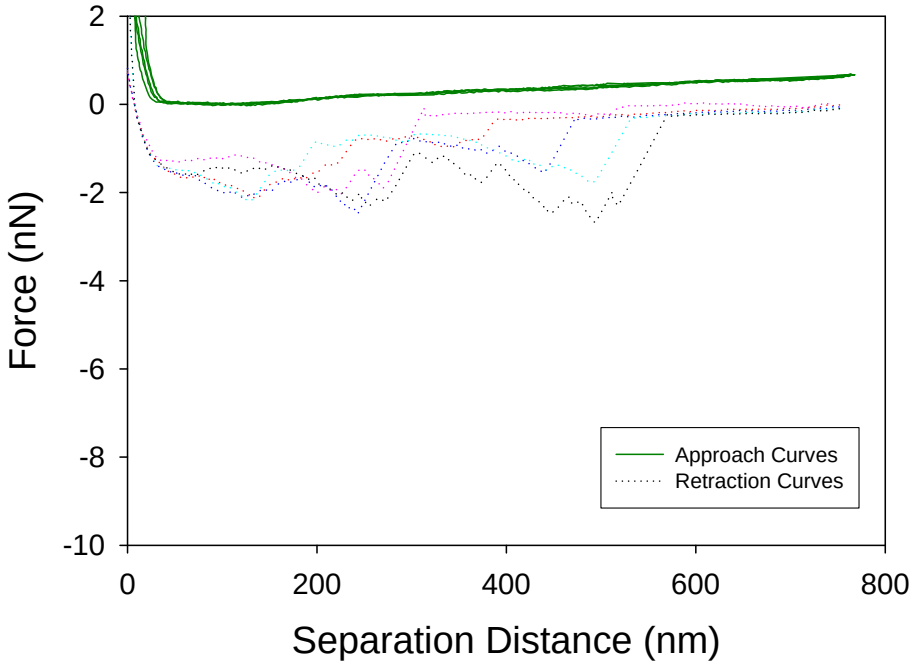

Figure 9.232 5 force plots of O113:H21 to CP1

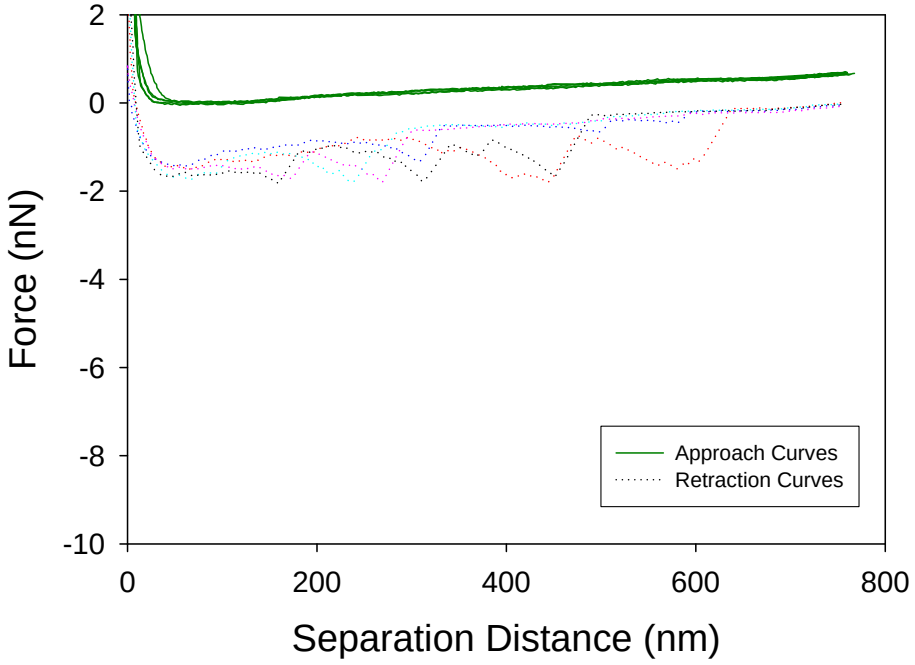

Figure 9.233 5 force plots of O113:H21 to CP1

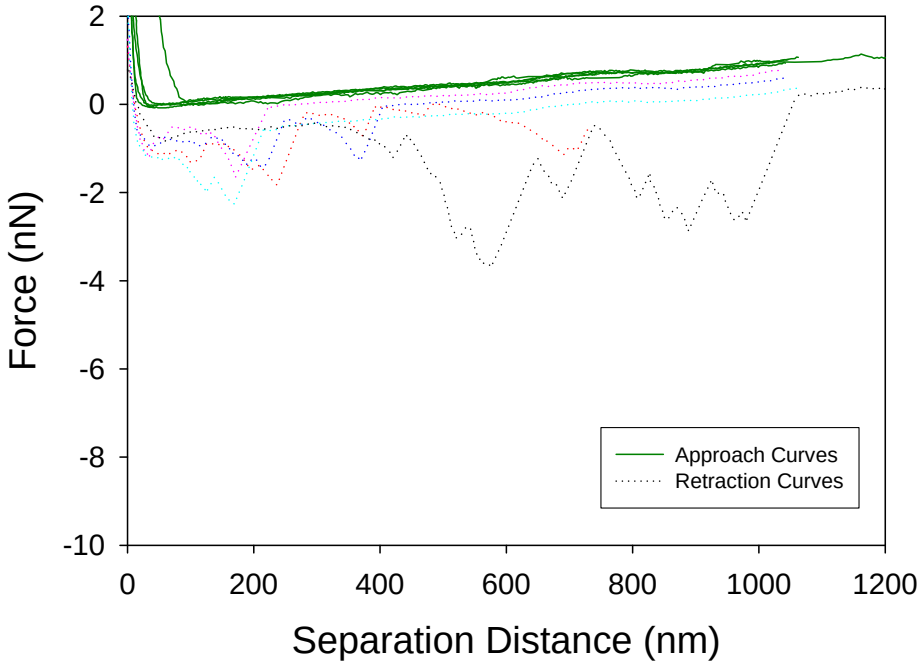

Figure 9.234 5 force plots of O113:H21 to CP1

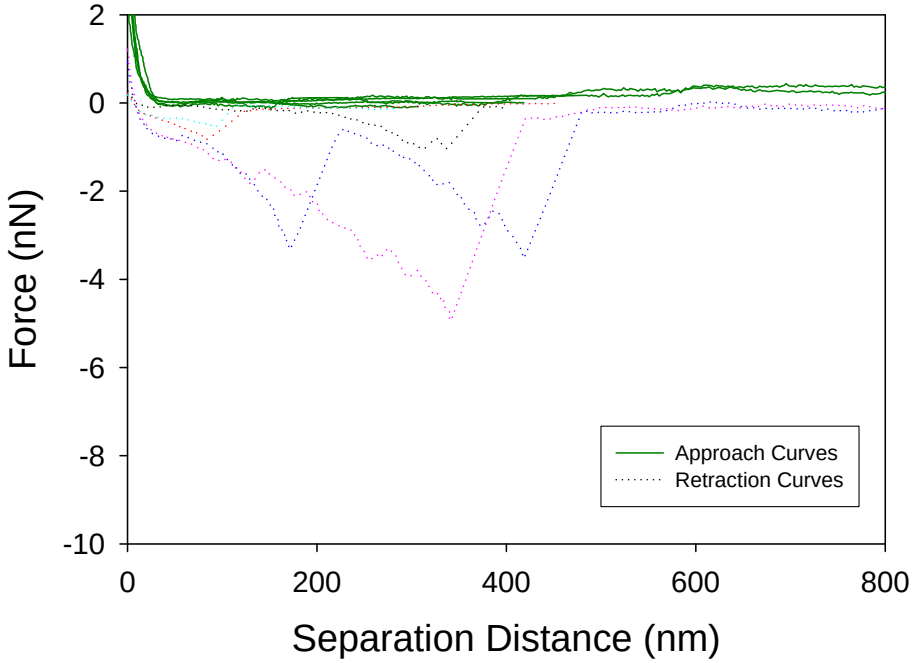

Figure 9.235 5 force plots of O113:H21 to CP1

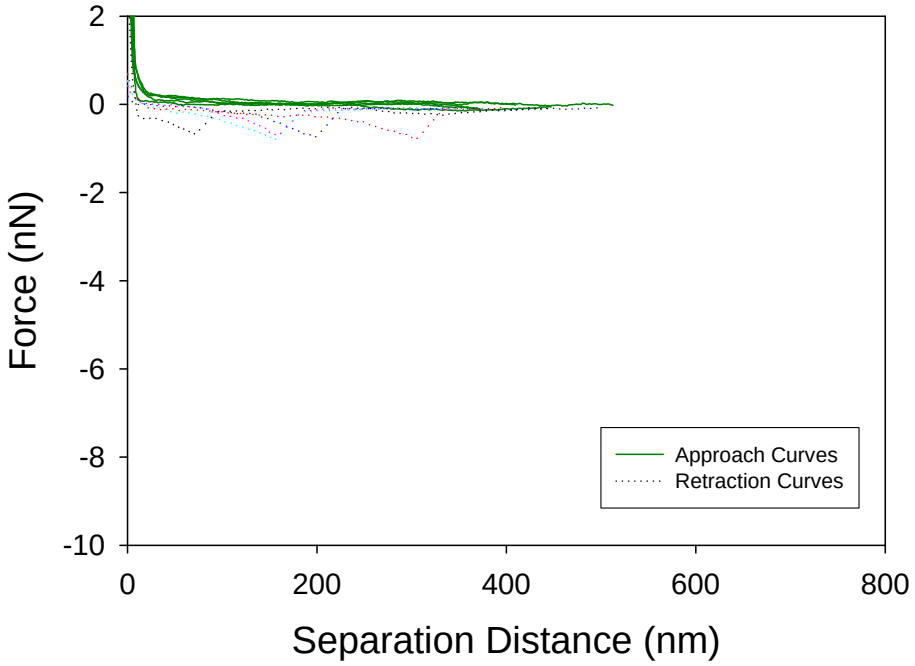

Figure 9.236 5 force plots of O113:H21 to CP1

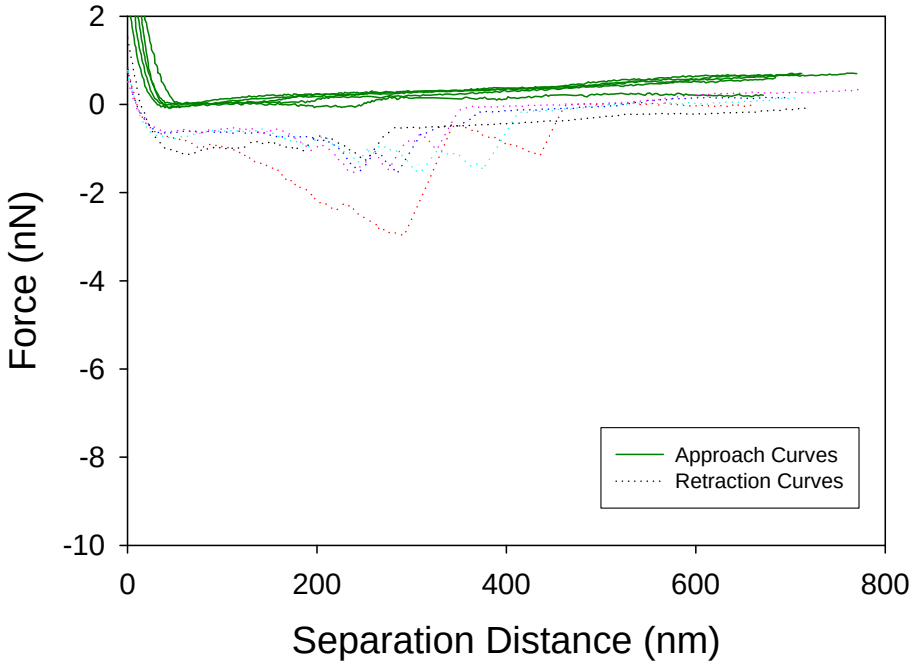

Figure 9.237 5 force plots of O113:H21 to CP1

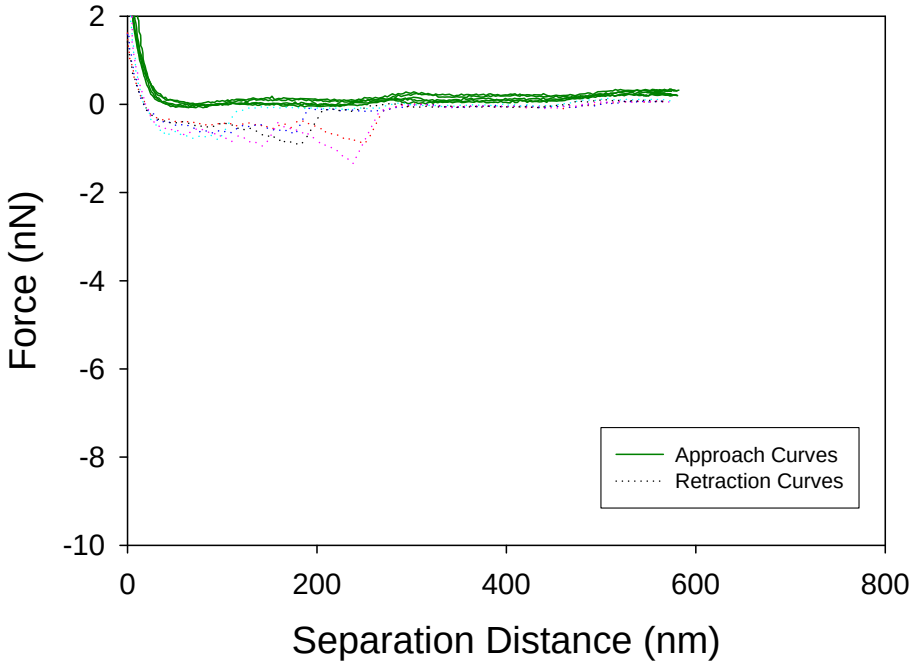

Figure 9.238 5 force plots of O117:K98:H4 to silicon nitride

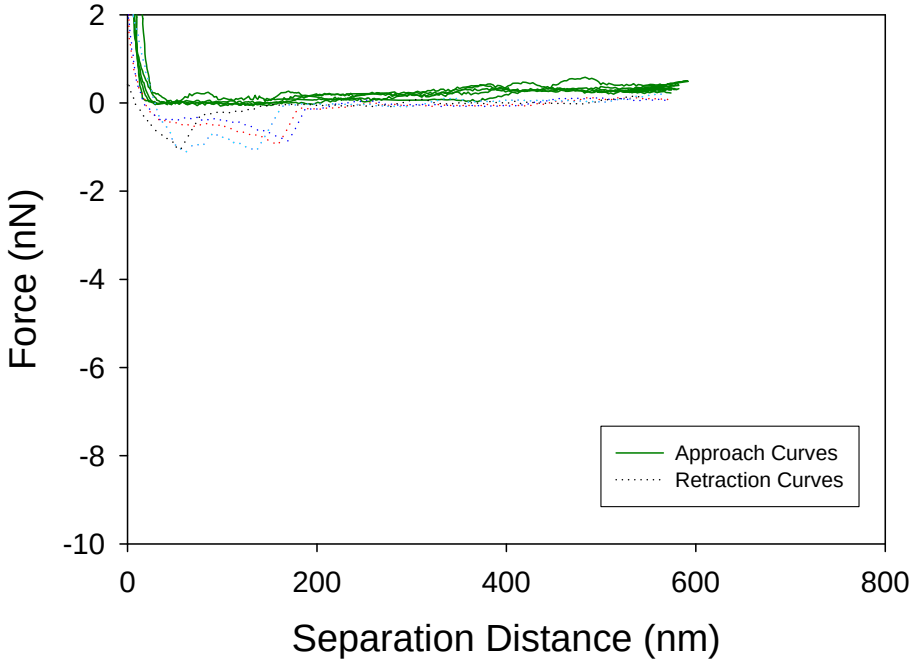

Figure 9.239 5 force plots of O117:K98:H4 to silicon nitride

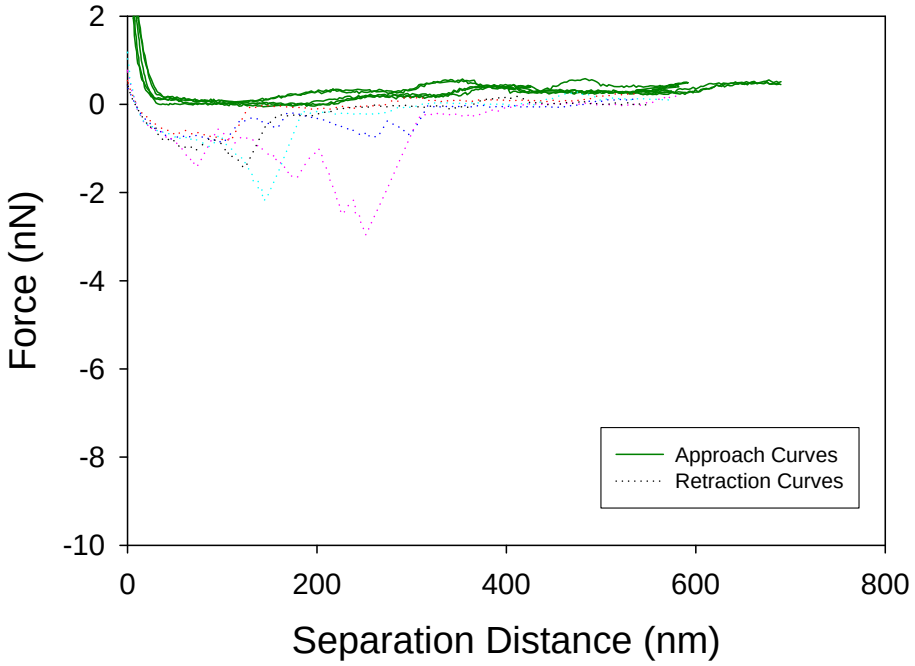

Figure 9.240 5 force plots of O117:K98:H4 to silicon nitride

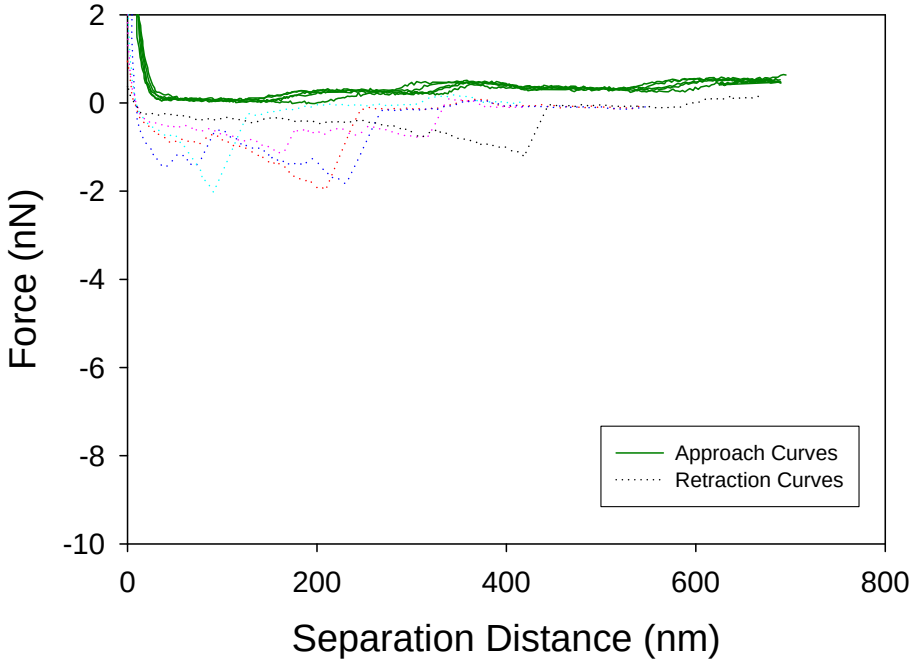

Figure 9.241 5 force plots of O117:K98:H4 to silicon nitride

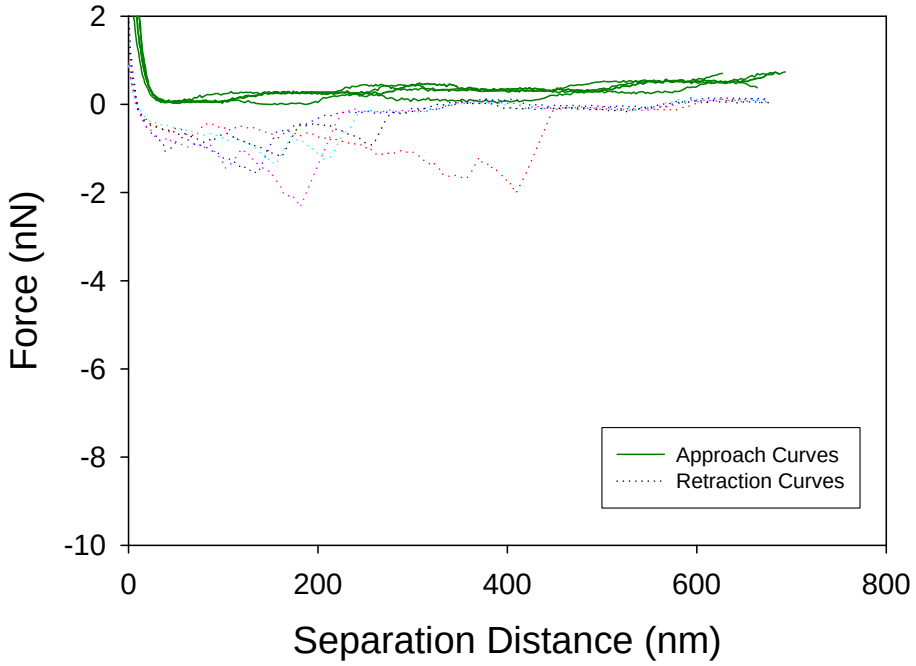

Figure 9.242 5 force plots of O117:K98:H4 to silicon nitride

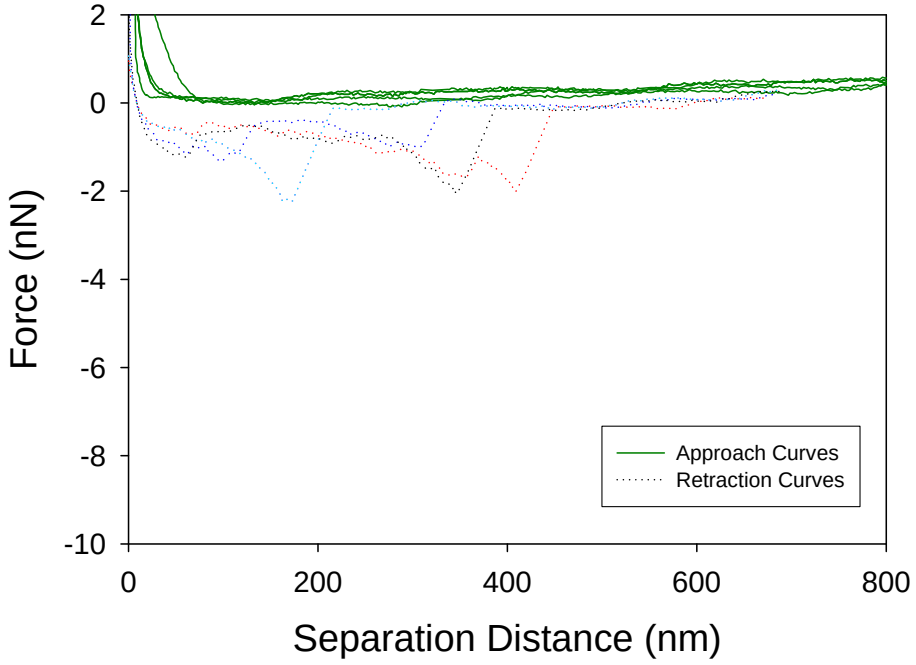

Figure 9.243 5 force plots of O117:K98:H4 to silicon nitride

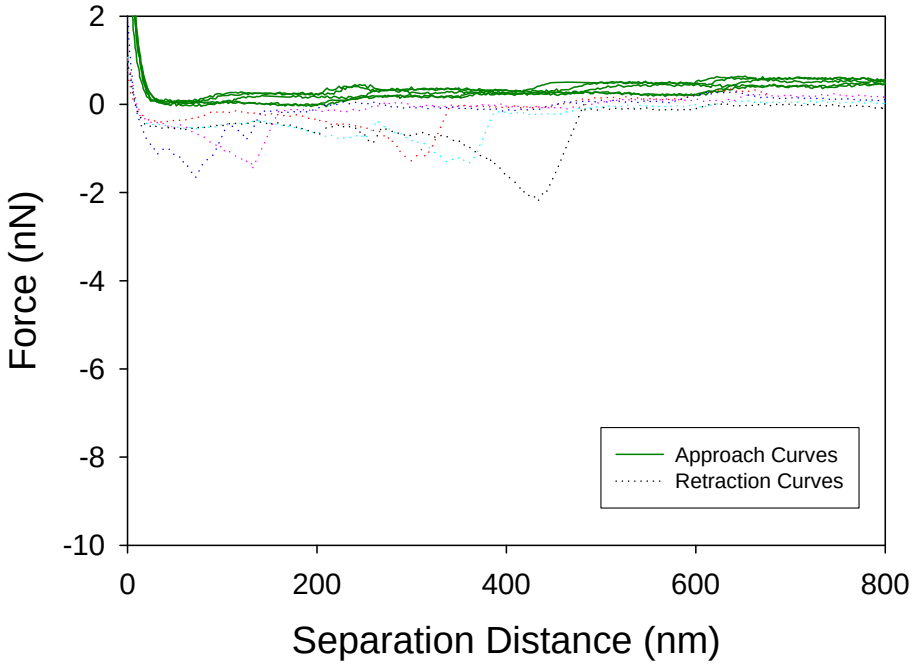

Figure 9.244 5 force plots of O117:K98:H4 to silicon nitride

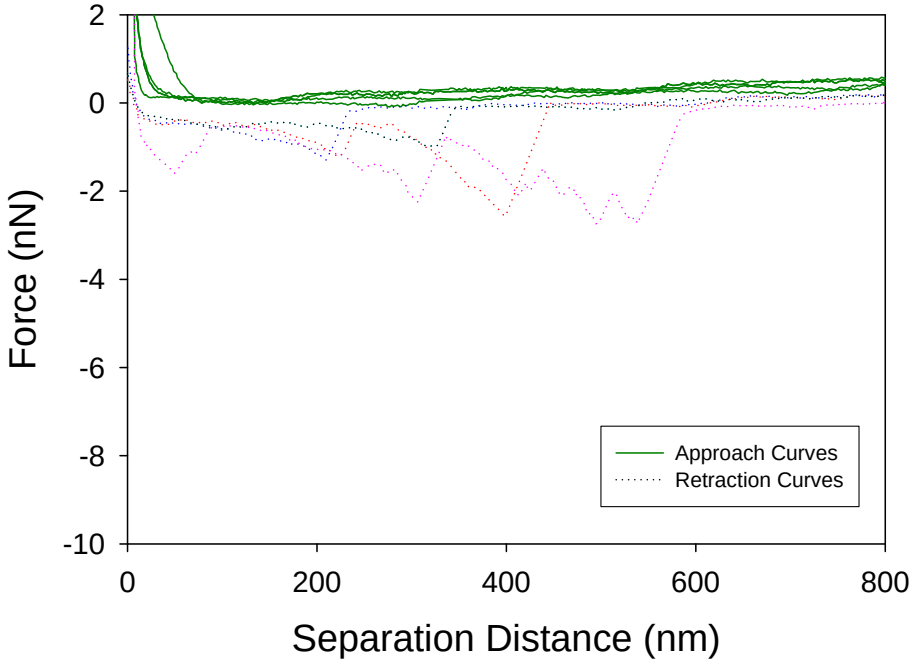

Figure 9.245 5 force plots of O117:K98:H4 to silicon nitride

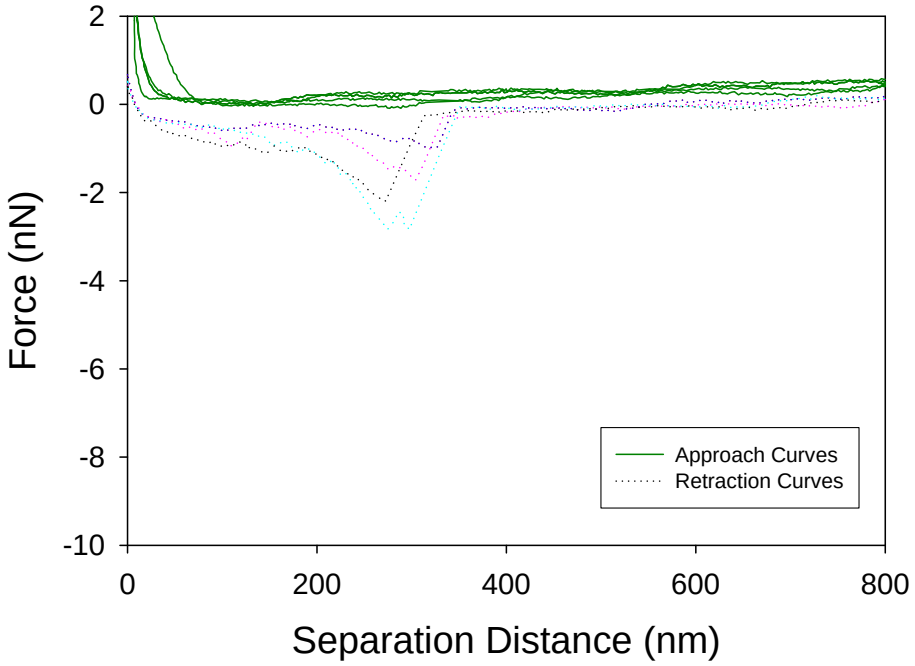

Figure 9.246 5 force plots of O117:K98:H4 to silicon nitride

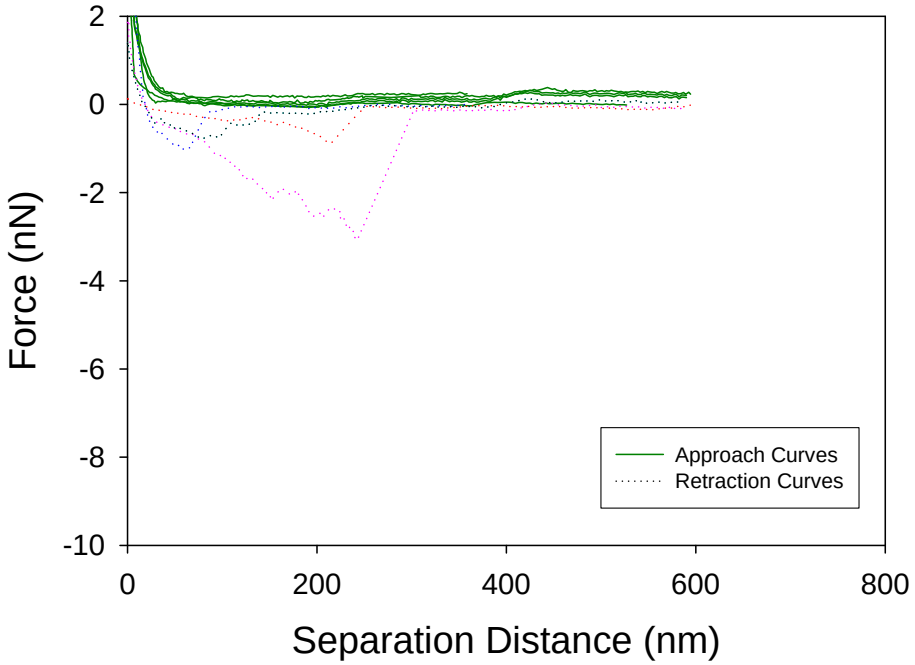

Figure 9.247 5 force plots of O117:K98:H4 to silicon nitride

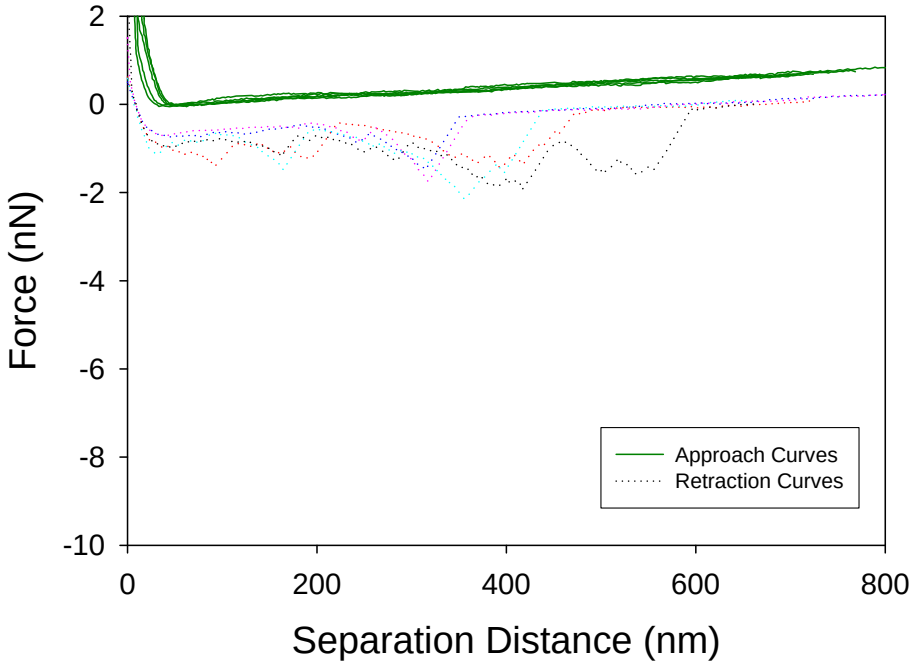

Figure 9.248 5 force plots of O117:K98:H4 to CP1

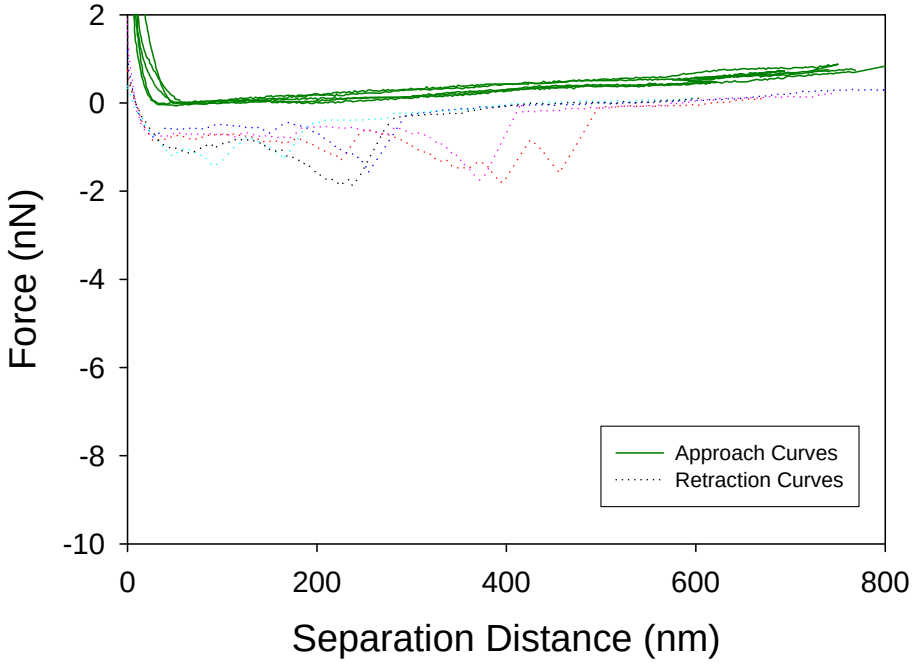

Figure 9.249 5 force plots of O117:K98:H4 to CP1

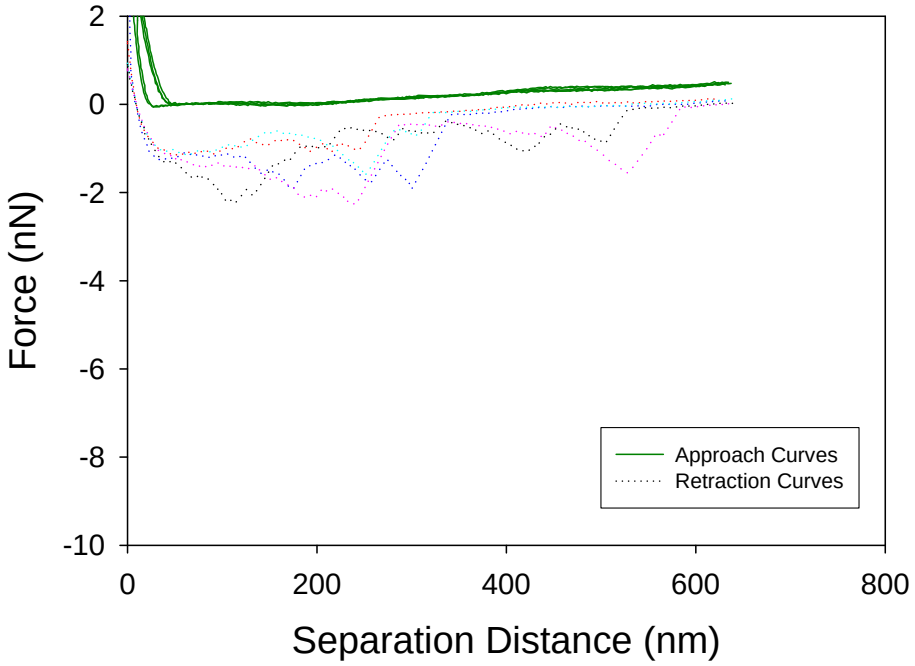

Figure 9.250 5 force plots of O117:K98:H4 to CP1

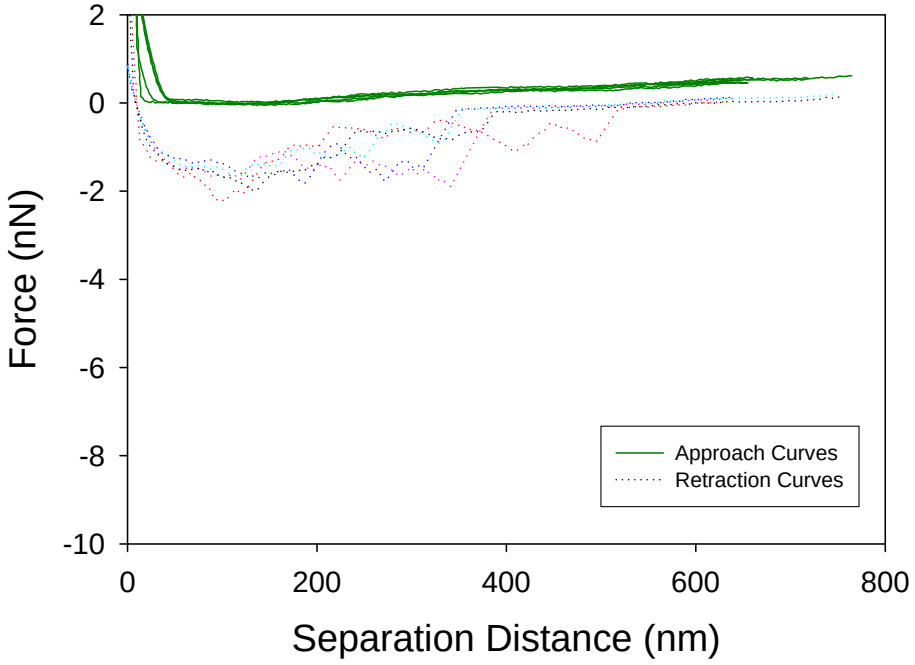

Figure 9.251 5 force plots of O117:K98:H4 to CP1

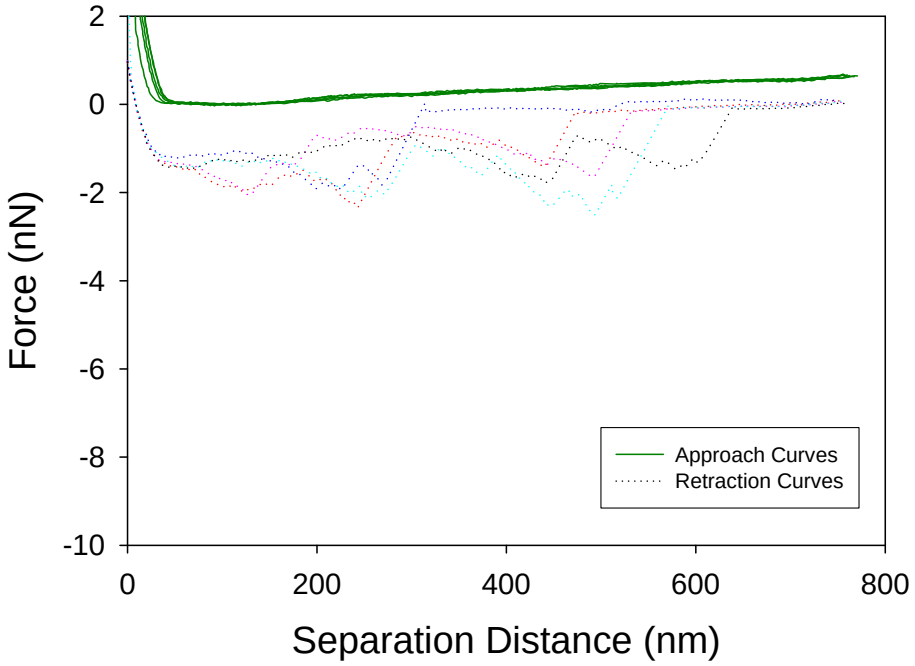

Figure 9.252 5 force plots of O117:K98:H4 to CP1

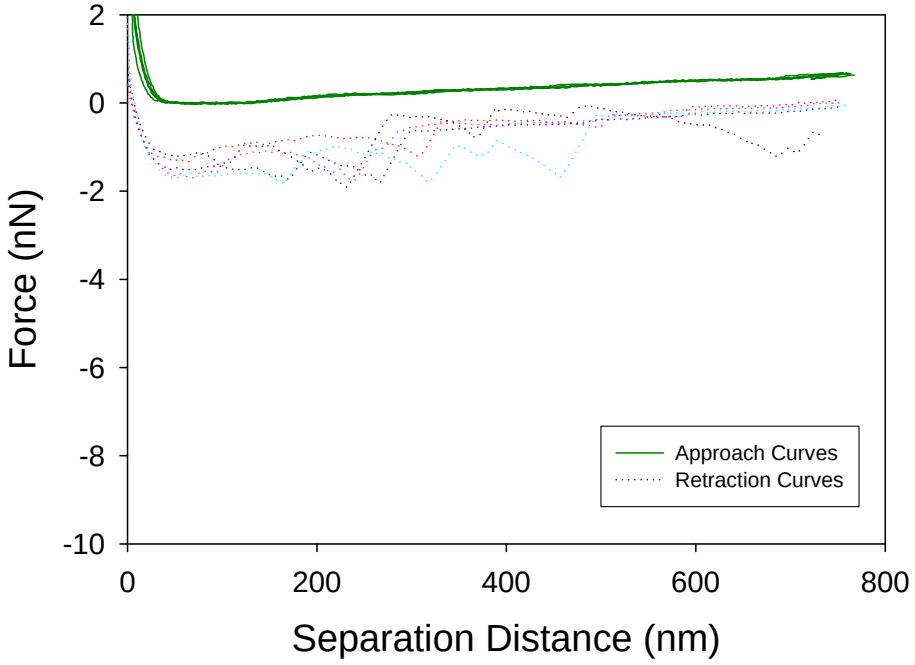

Figure 9.253 5 force plots of O117:K98:H4 to CP1

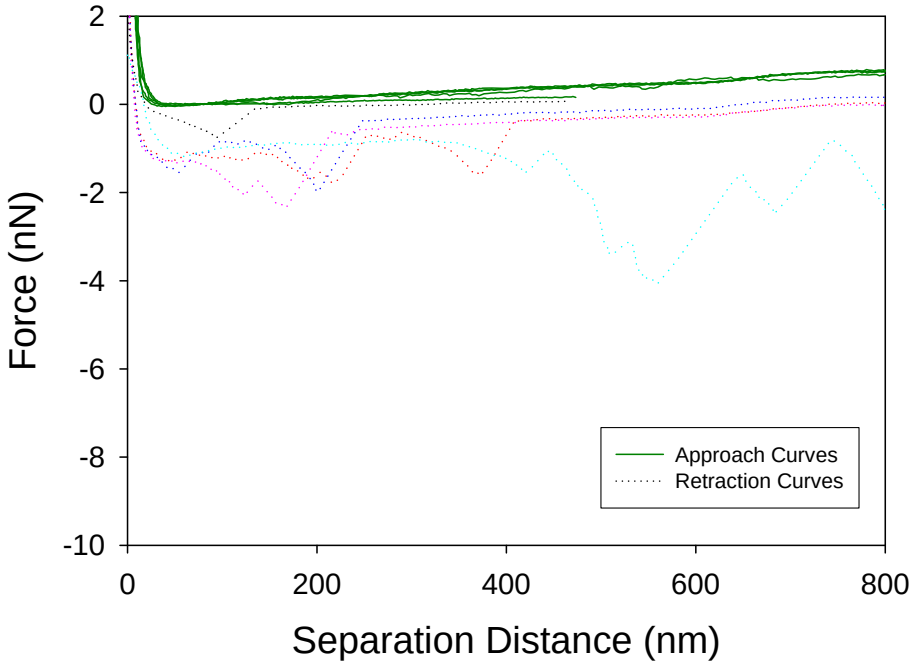

Figure 9.254 5 force plots of O117:K98:H4 to CP1

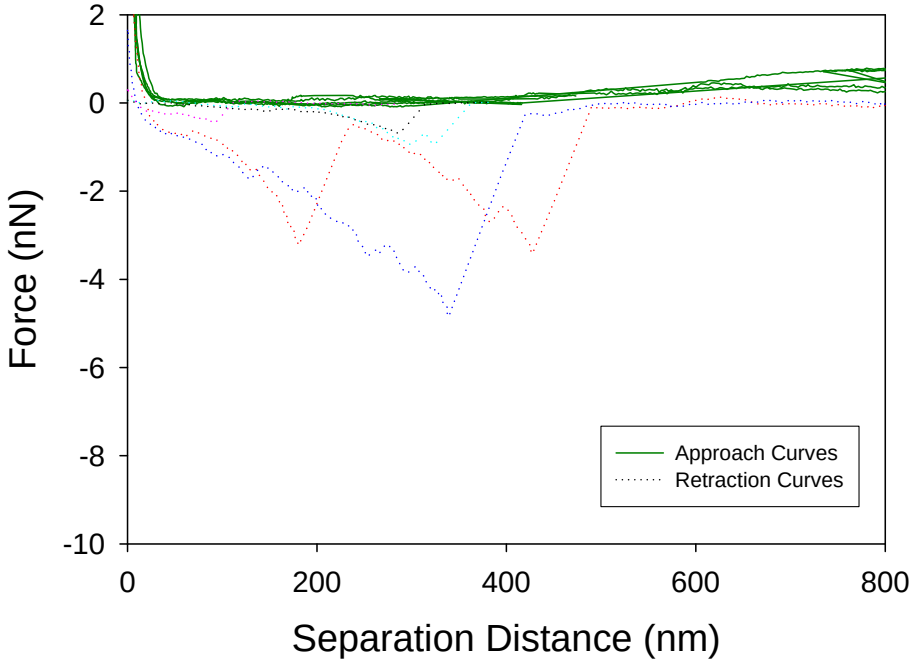

Figure 9.255 5 force plots of O117:K98:H4 to CP1

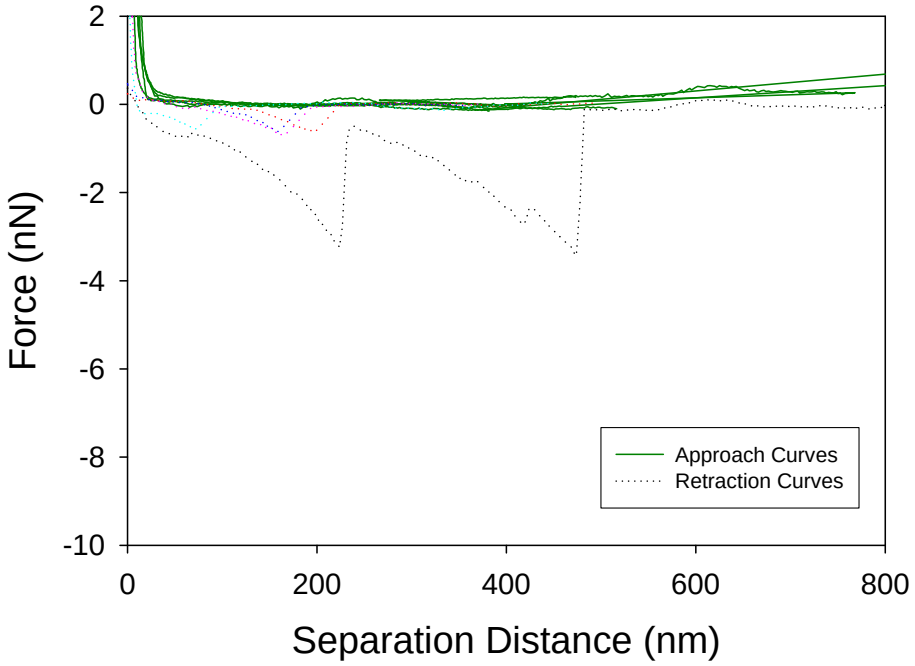

Figure 9.256 5 force plots of O117:K98:H4 to CP1

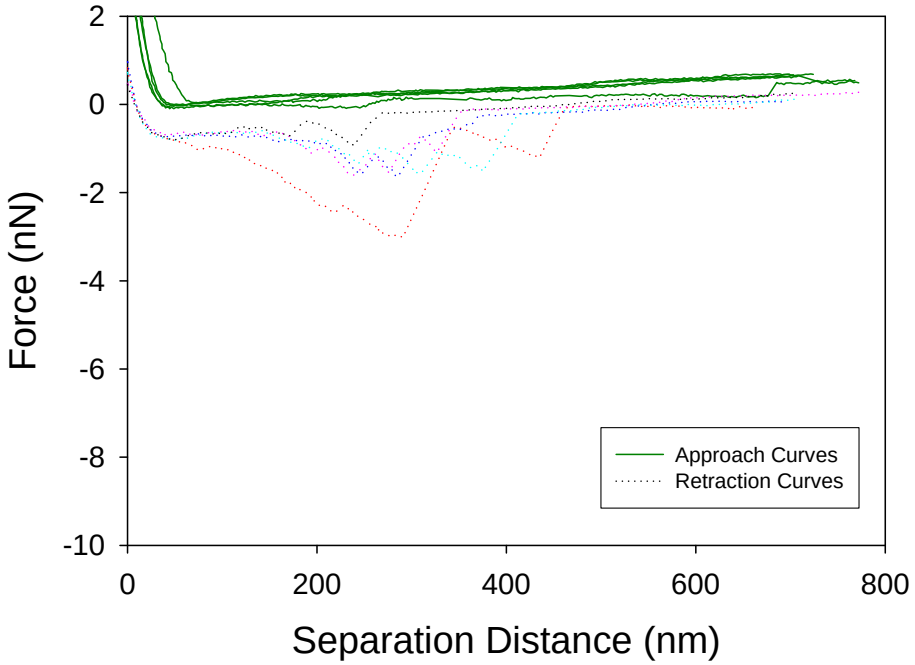

Figure 9.257 5 force plots of O117:K98:H4 to CP1

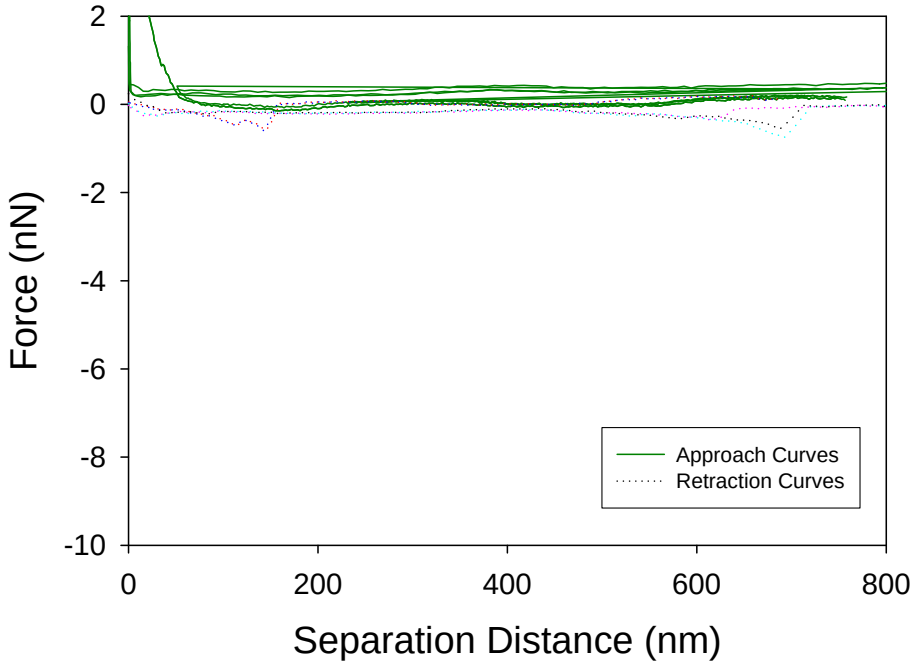

Figure 9.258 5 force plots of O157:H7 to silicon nitride

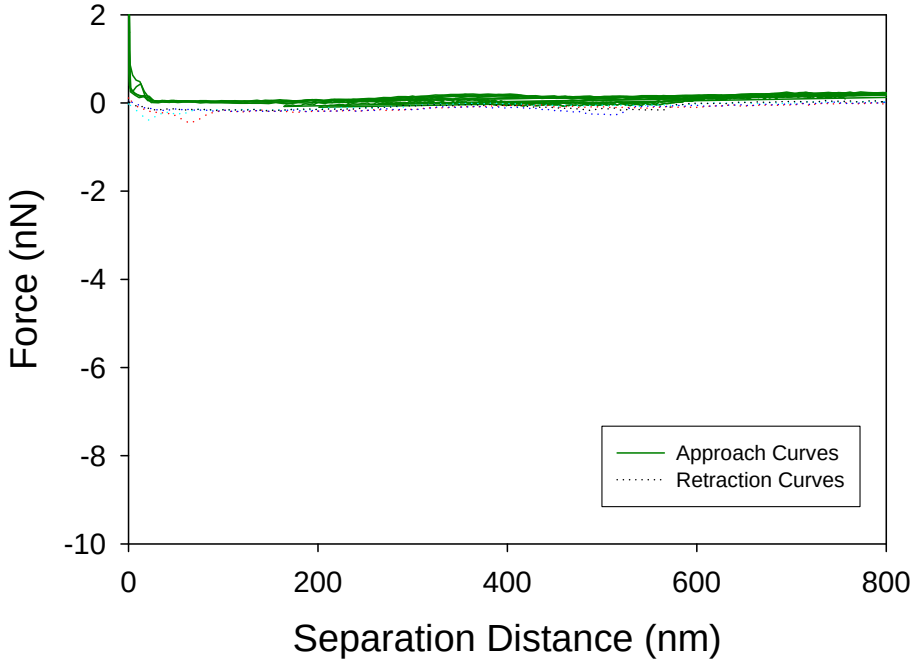

Figure 9.259 5 force plots of O157:H7 to silicon nitride

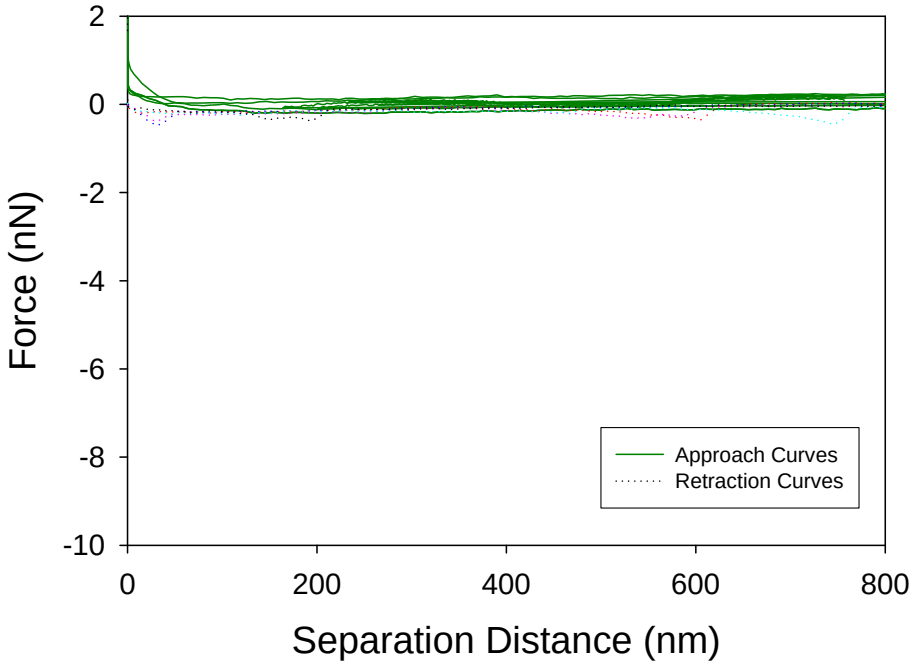

Figure 9.260 5 force plots of O157:H7 to silicon nitride

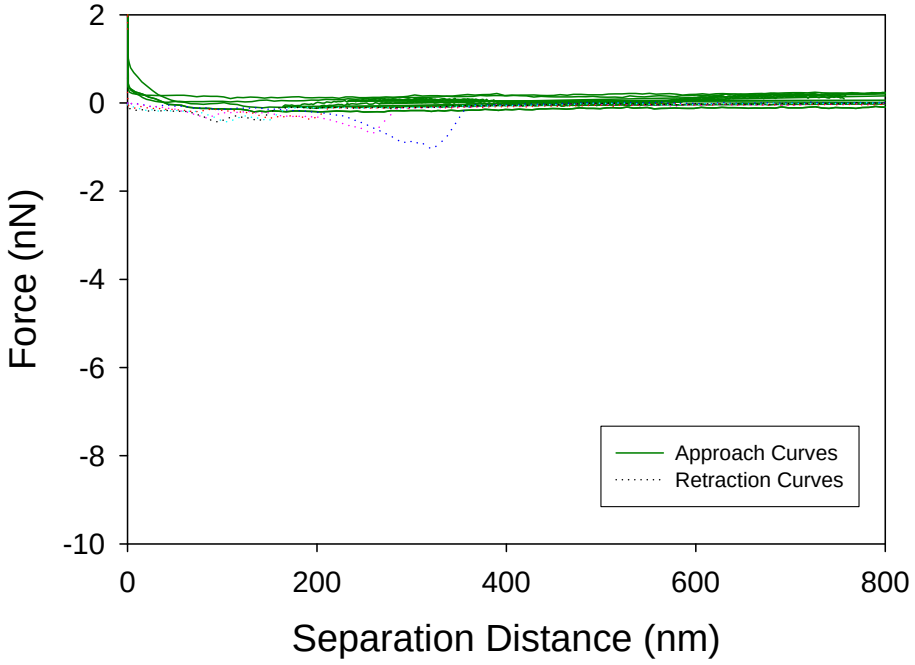

Figure 9.261 5 force plots of O157:H7 to silicon nitride

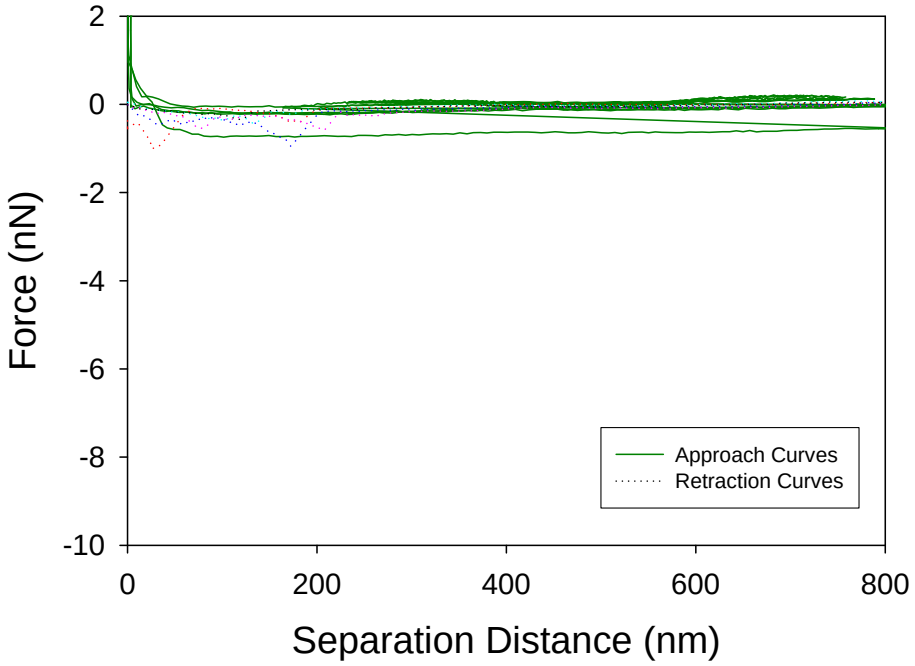

Figure 9.262 5 force plots of O157:H7 to silicon nitride

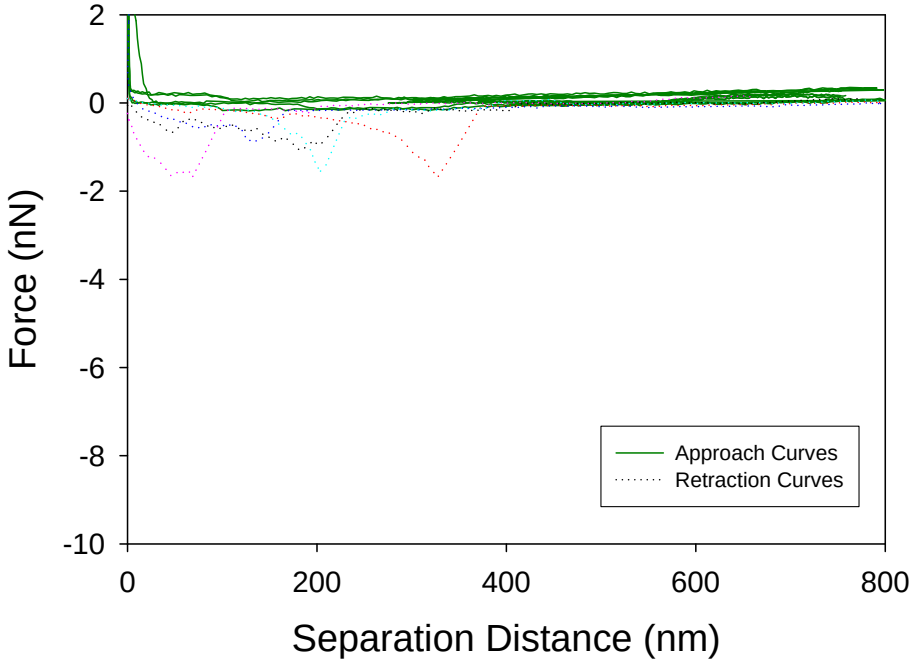

Figure 9.263 5 force plots of O157:H7 to silicon nitride

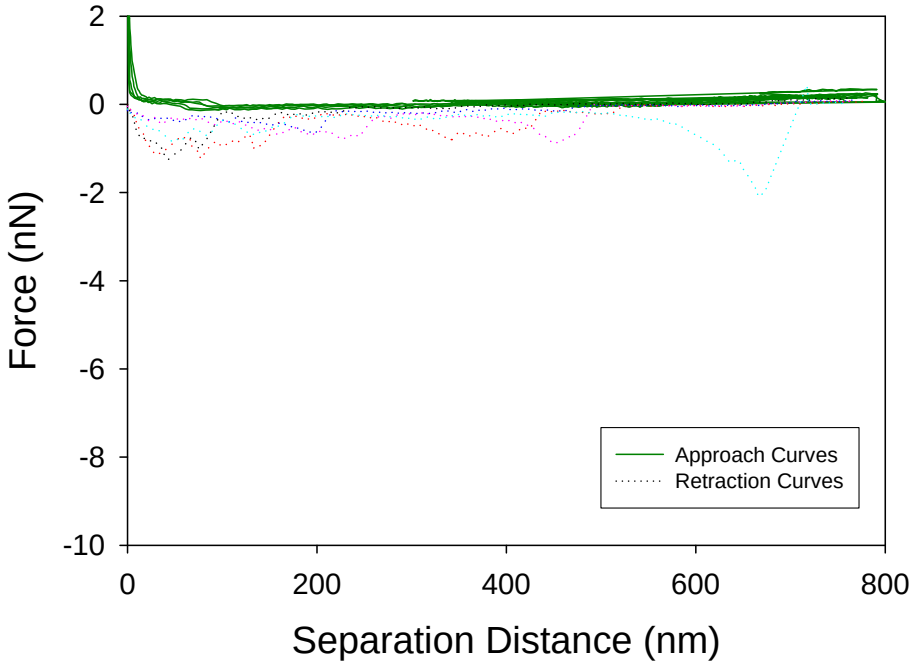

Figure 9.264 5 force plots of O157:H7 to silicon nitride

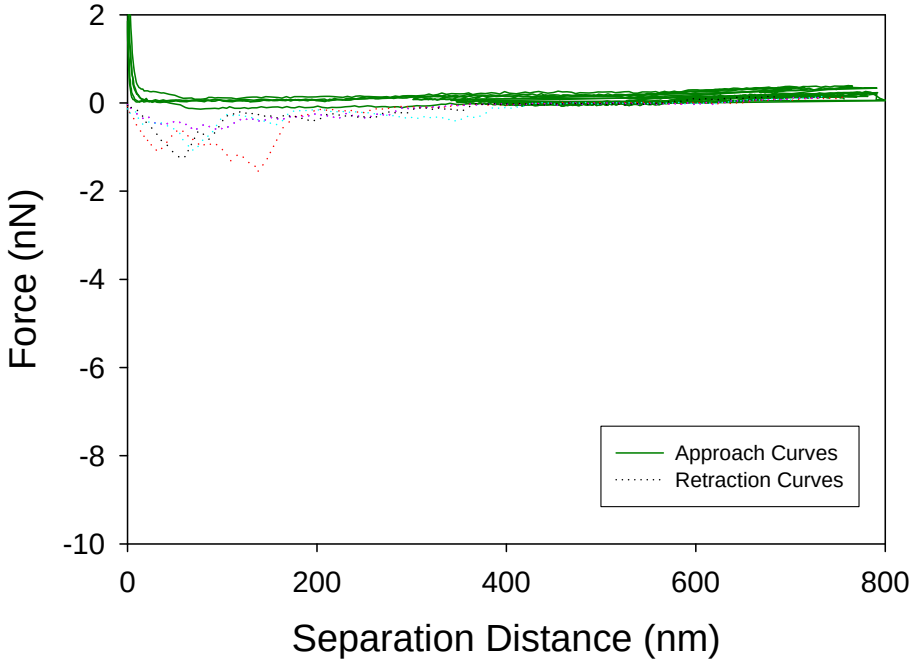

Figure 9.265 5 force plots of O157:H7 to silicon nitride

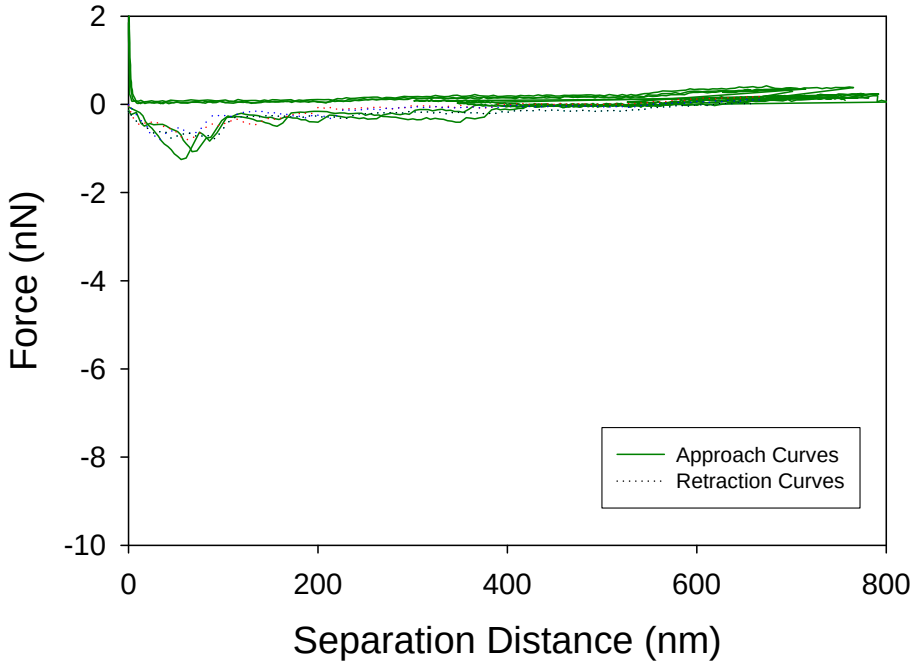

Figure 9.266 5 force plots of O157:H7 to silicon nitride

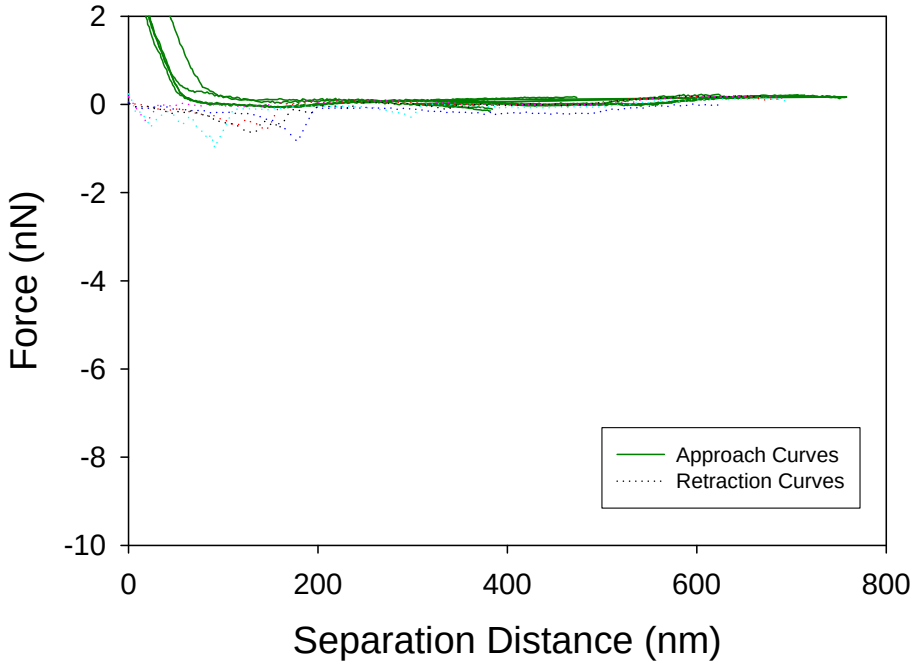

Figure 9.267 5 force plots of O157:H7 to silicon nitride

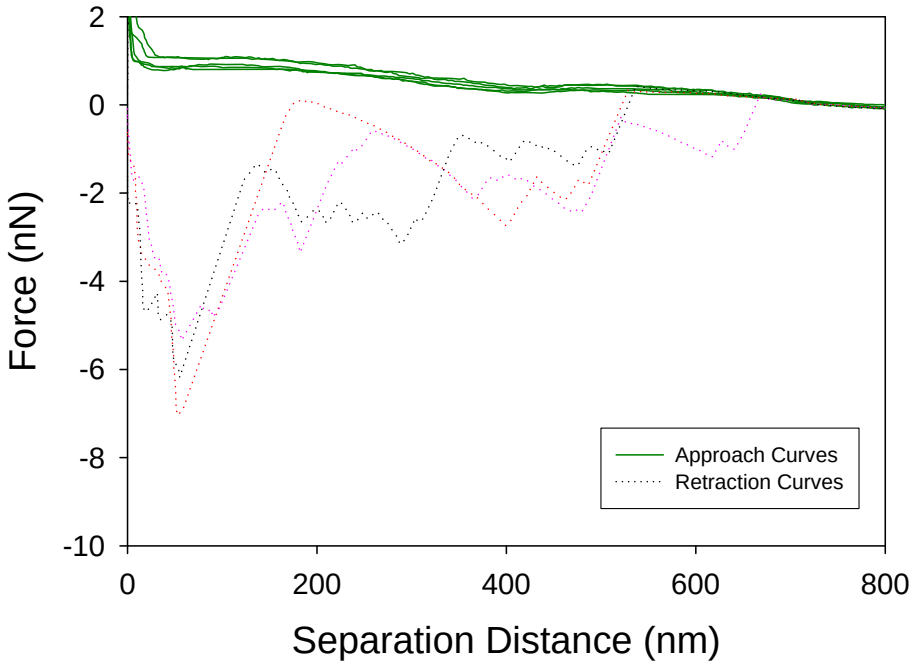

Figure 9.268 5 force plots of O157:H7 to CP1

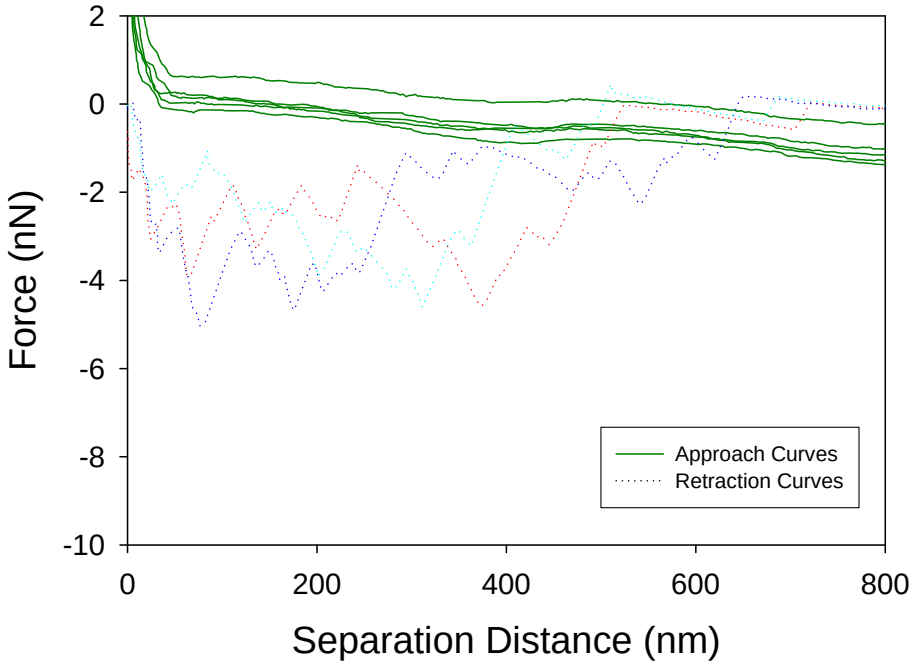

Figure 9.269 5 force plots of O157:H7 to CP1

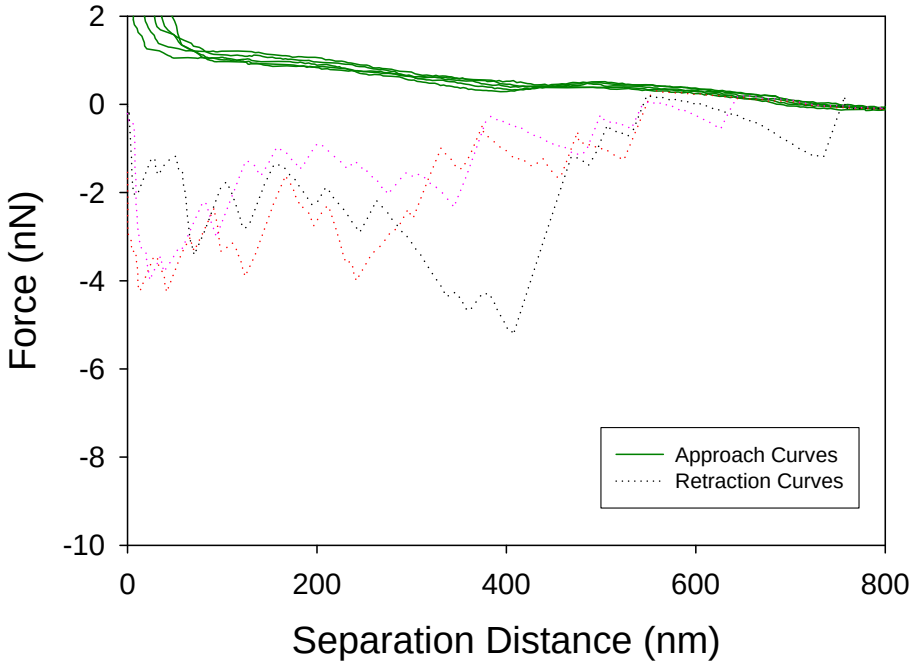

Figure 9.270 5 force plots of O157:H7 to CP1

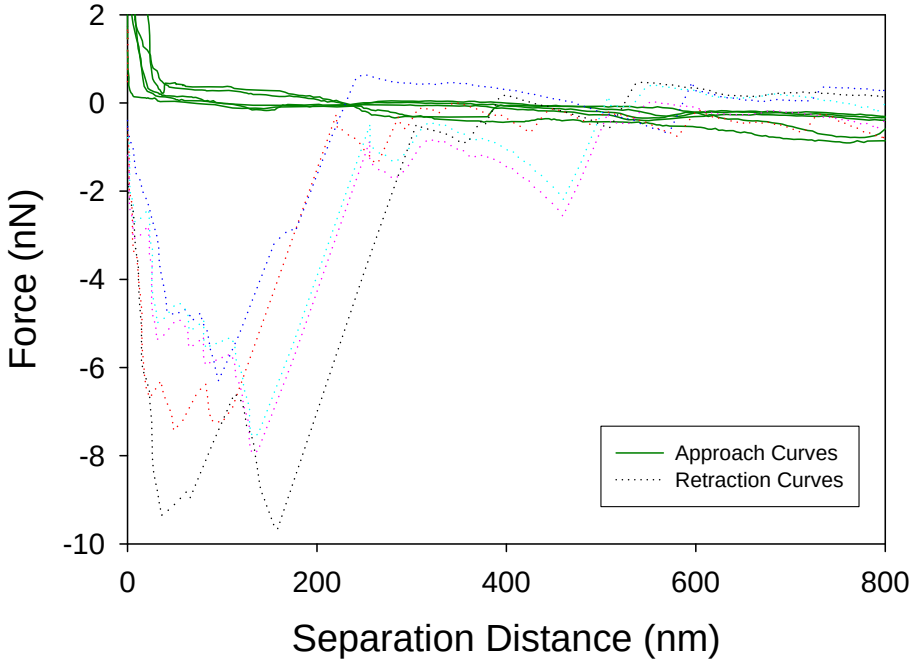

Figure 9.271 5 force plots of O157:H7 to CP1

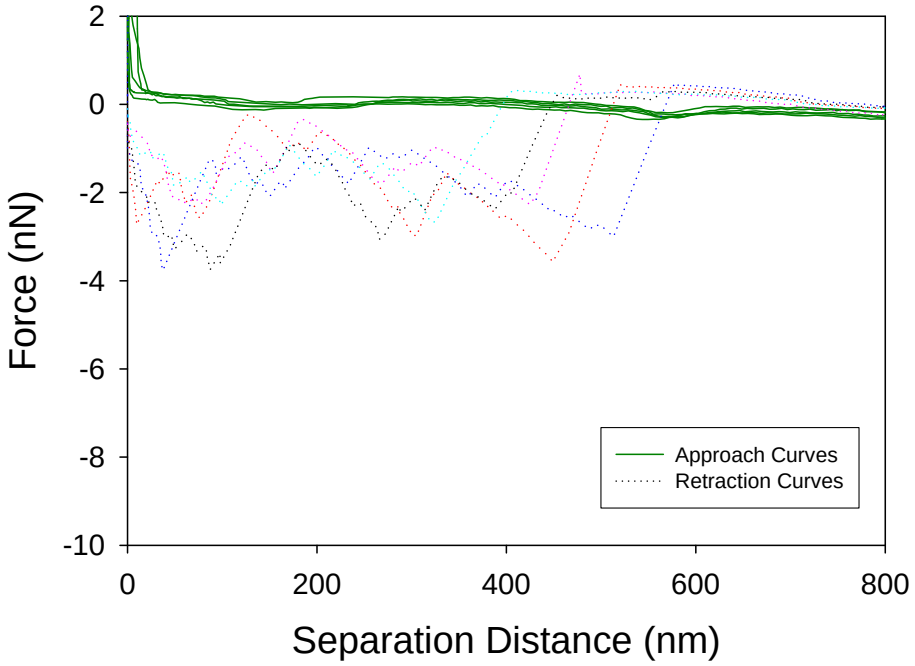

Figure 9.272 5 force plots of O157:H7 to CP1

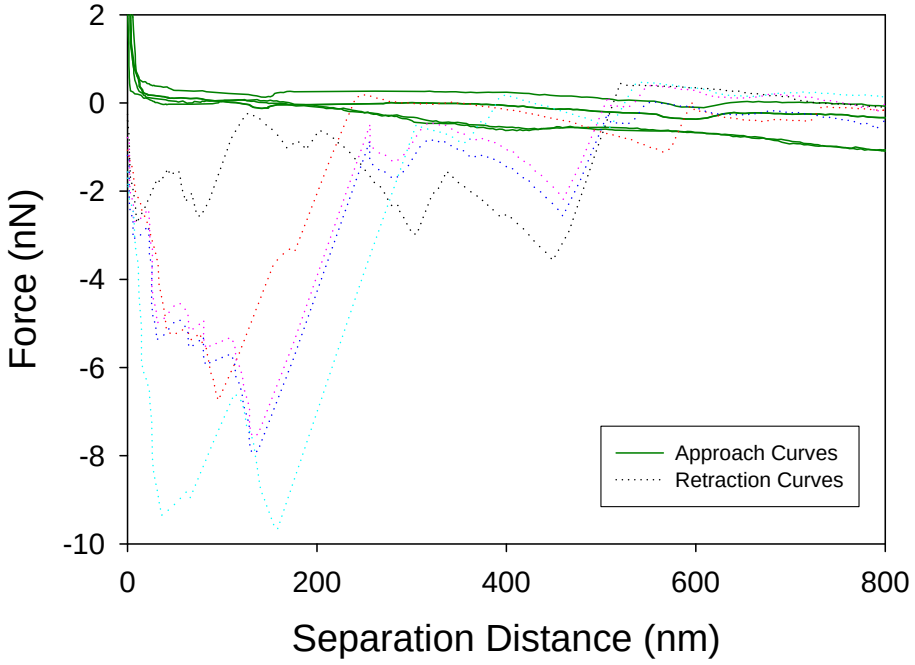

Figure 9.273 5 force plots of O157:H7 to CP1

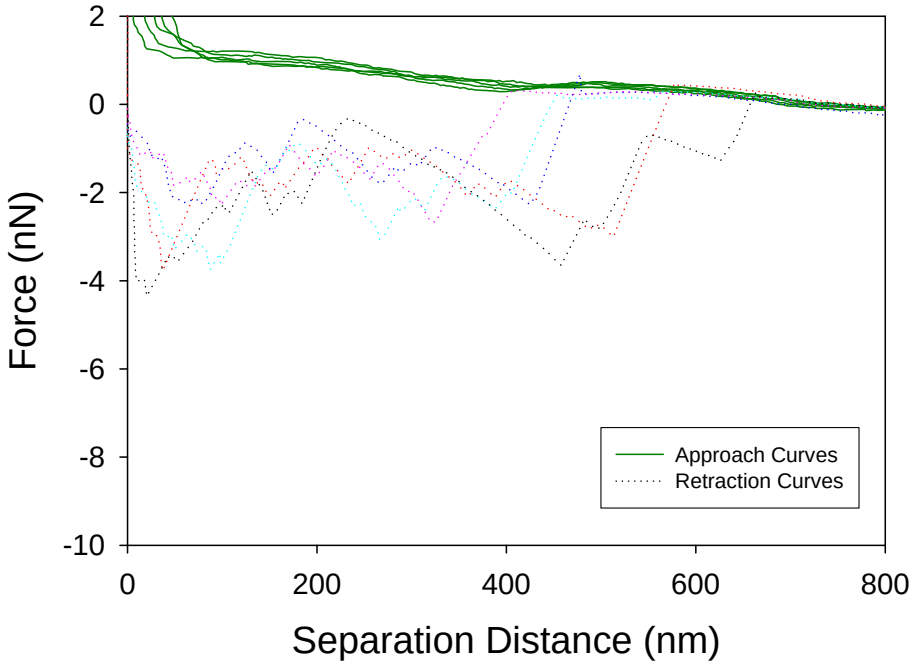

Figure 9.274 5 force plots of O157:H7 to CP1

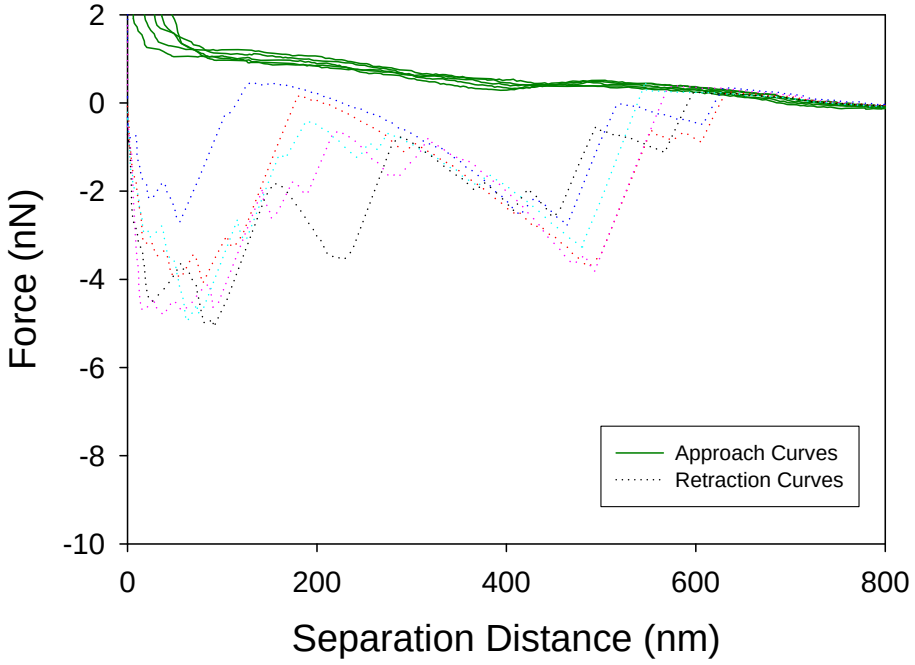

Figure 9.275 5 force plots of O157:H7 to CP1

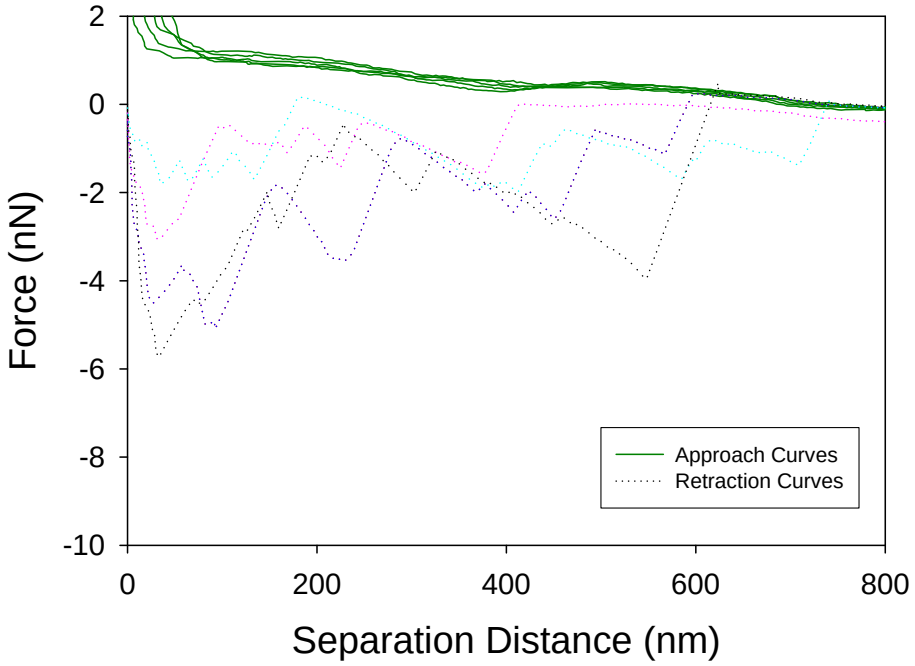

Figure 9.276 5 force plots of O157:H7 to CP1

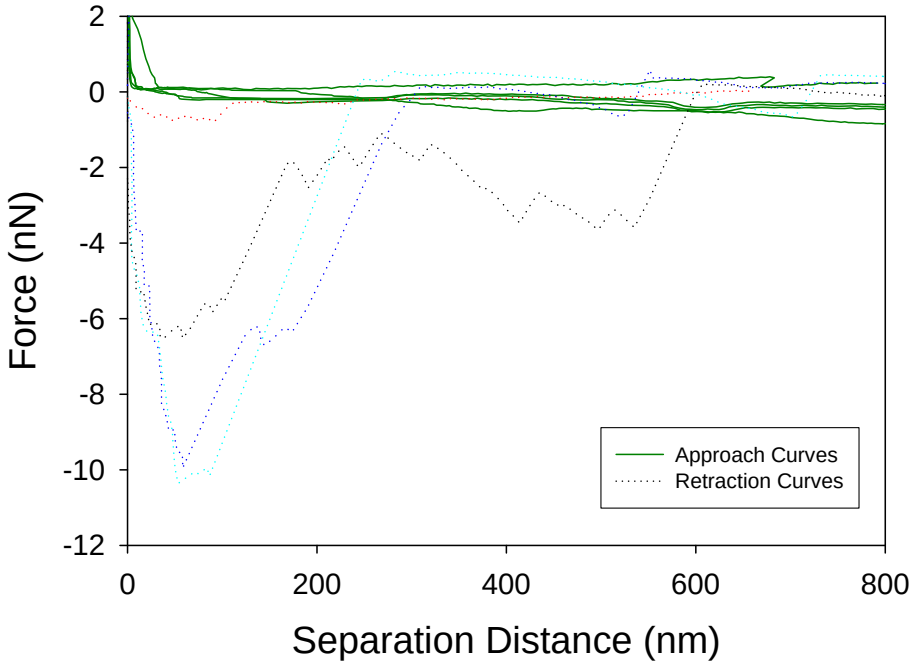

Figure 9.277 5 force plots of O157:H7 to CP1

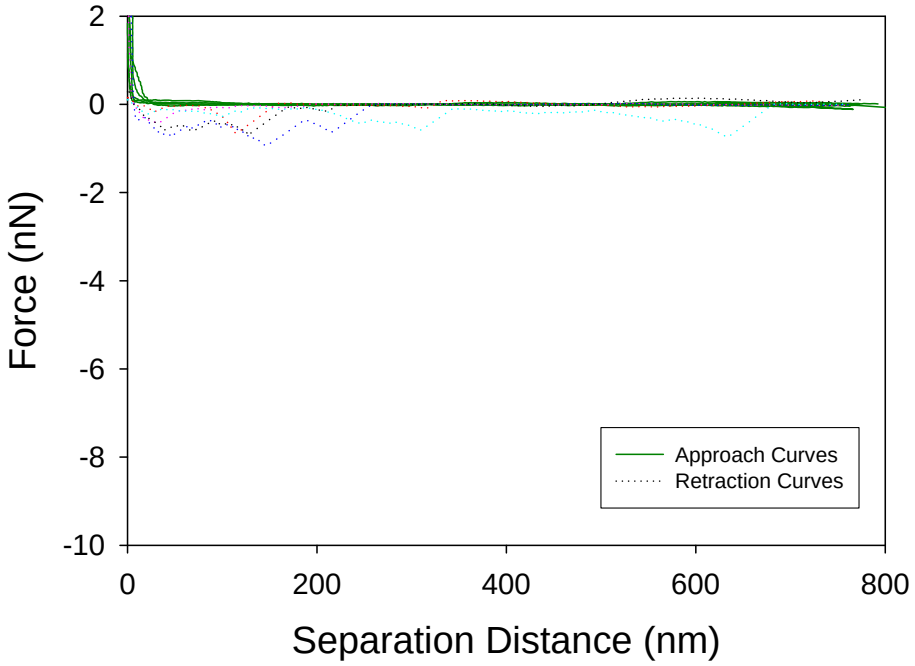

Figure 9.278 5 force plots of O157:H12 to silicon nitride

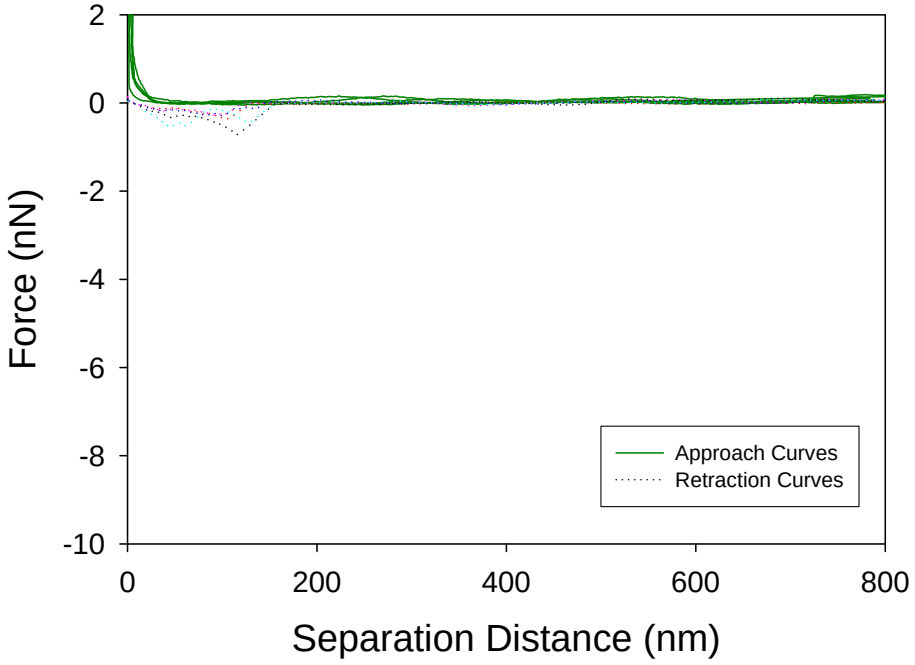

Figure 9.279 5 force plots of O157:H12 to silicon nitride

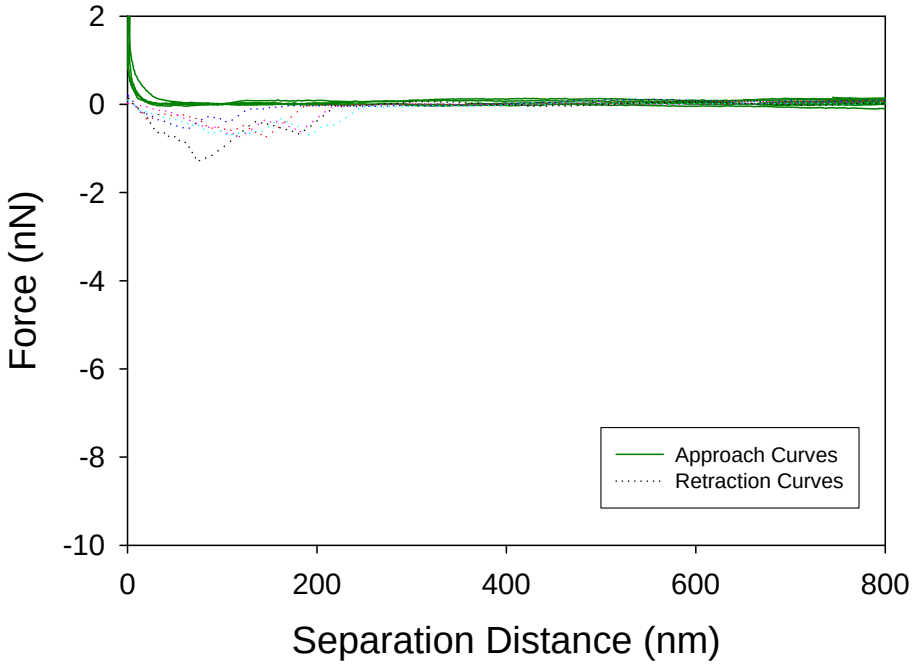

Figure 9.280 5 force plots of O157:H12 to silicon nitride

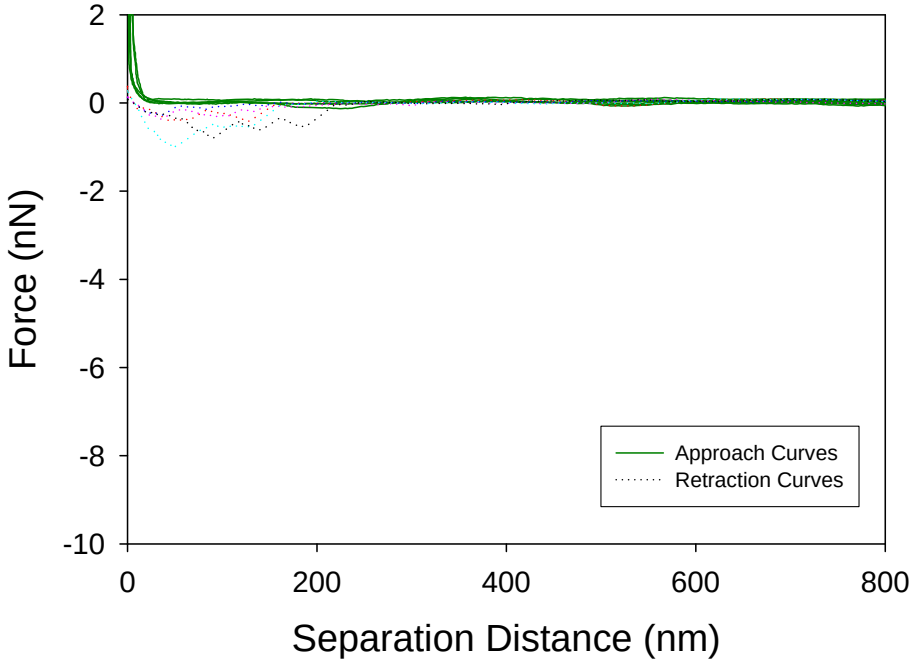

Figure 9.281 5 force plots of O157:H12 to silicon nitride

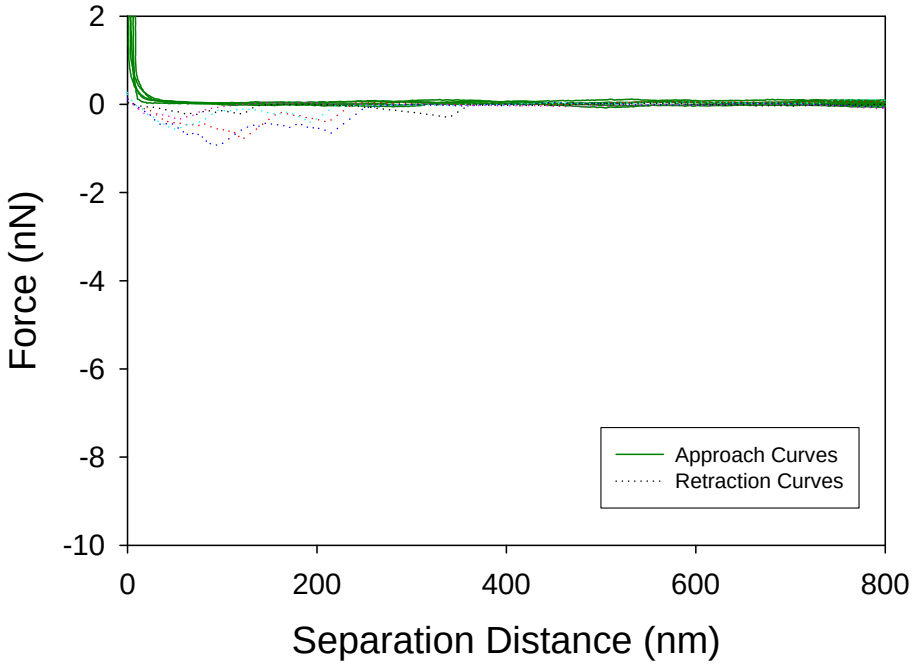

Figure 9.282 5 force plots of O157:H12 to silicon nitride

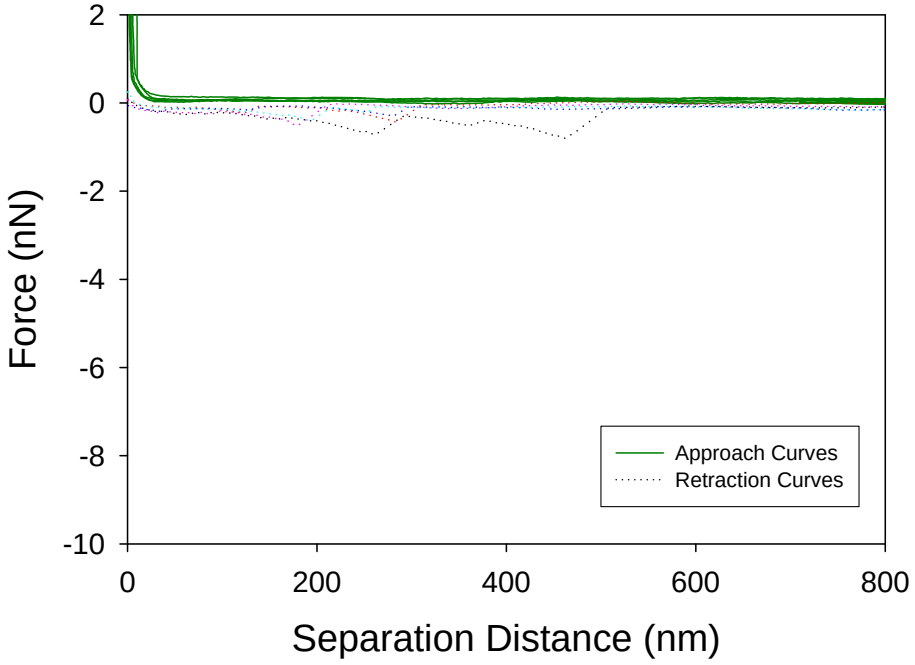

Figure 9.283 5 force plots of O157:H12 to silicon nitride

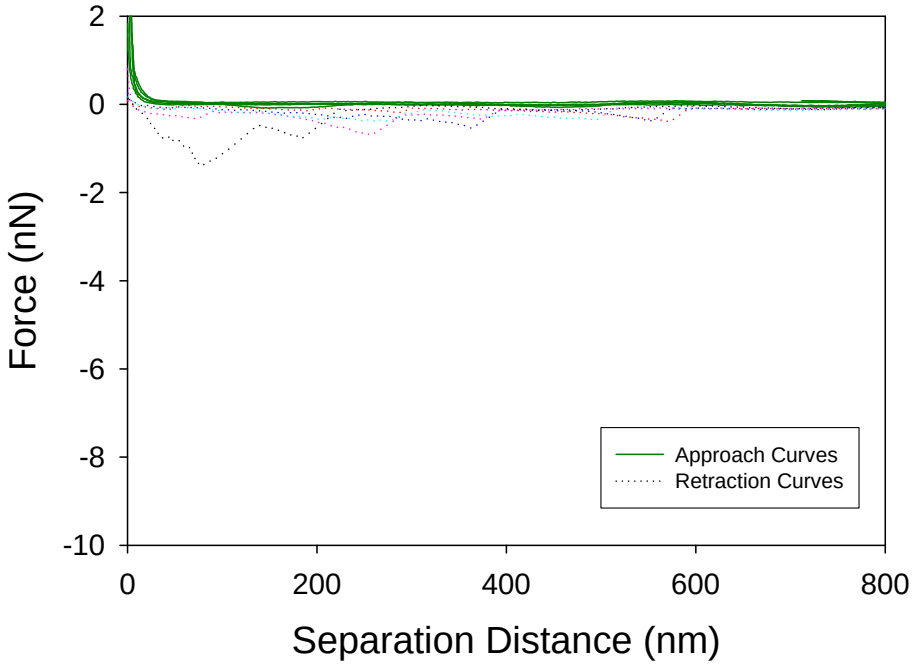

Figure 9.284 5 force plots of O157:H12 to silicon nitride

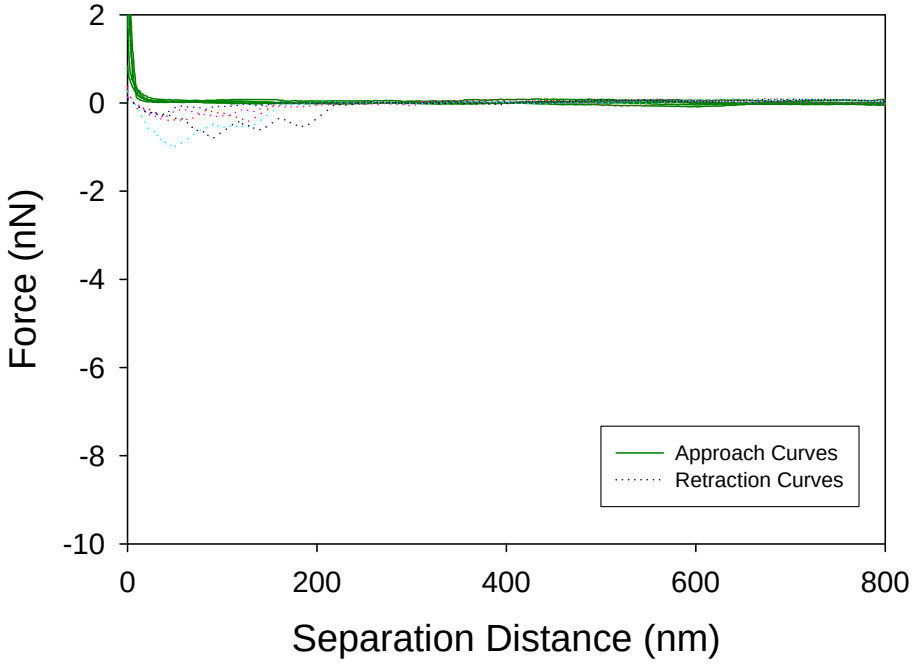

Figure 9.285 5 force plots of O157:H12 to silicon nitride

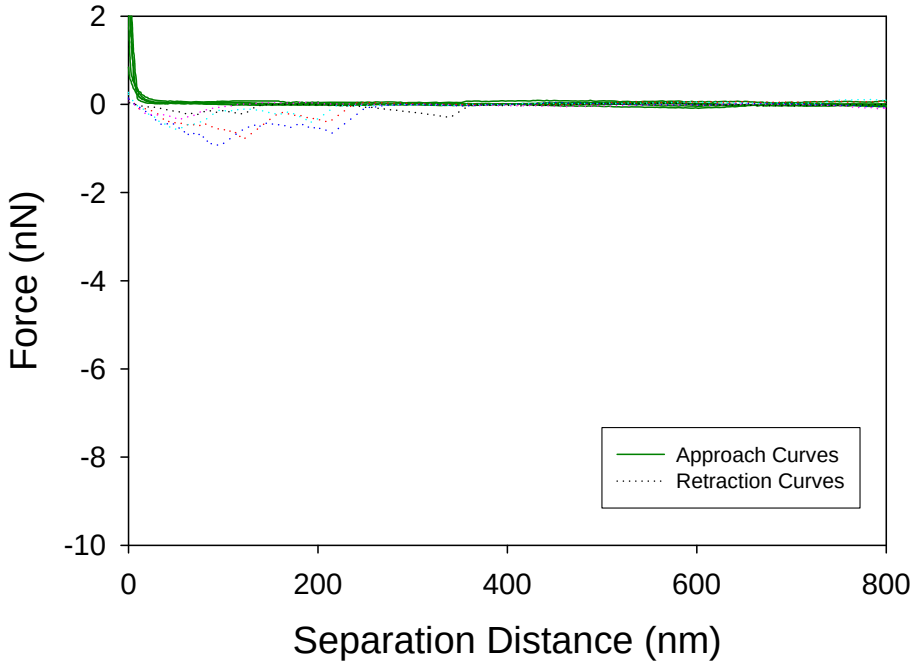

Figure 9.286 5 force plots of O157:H12 to silicon nitride

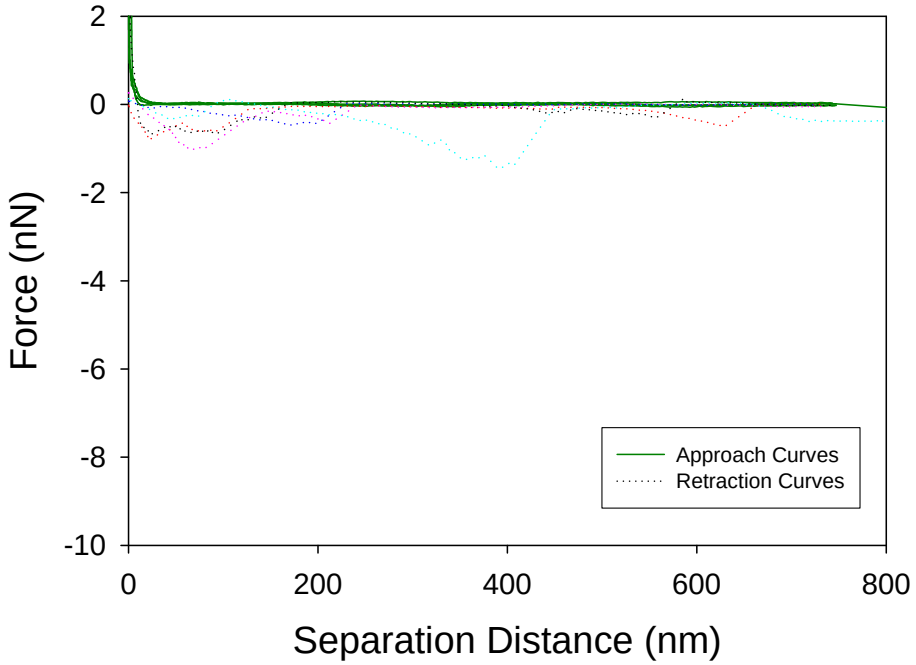

Figure 9.287 5 force plots of O157:H12 to silicon nitride

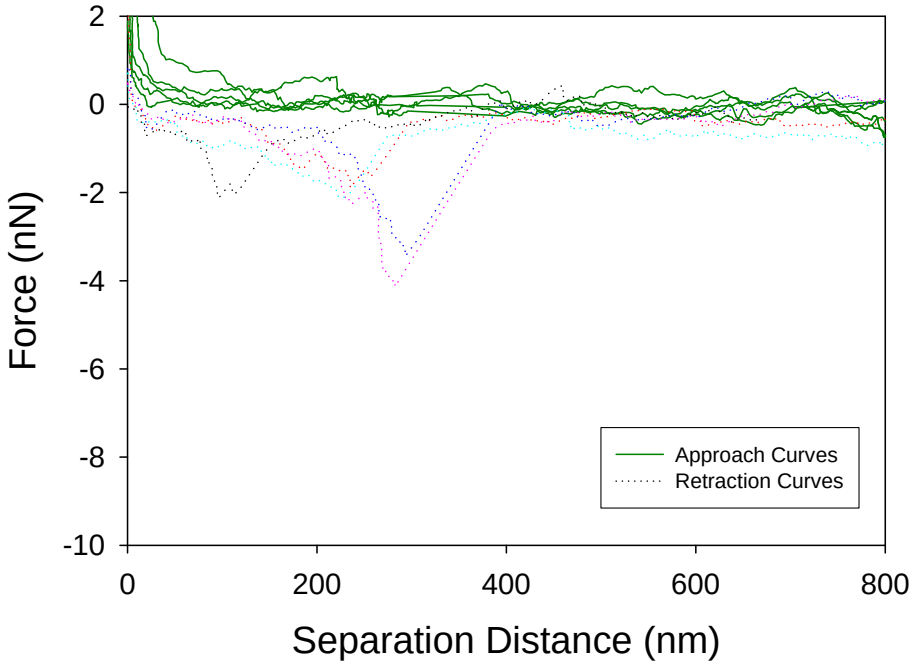

Figure 9.288 5 force plots of O157:H12 to CP1

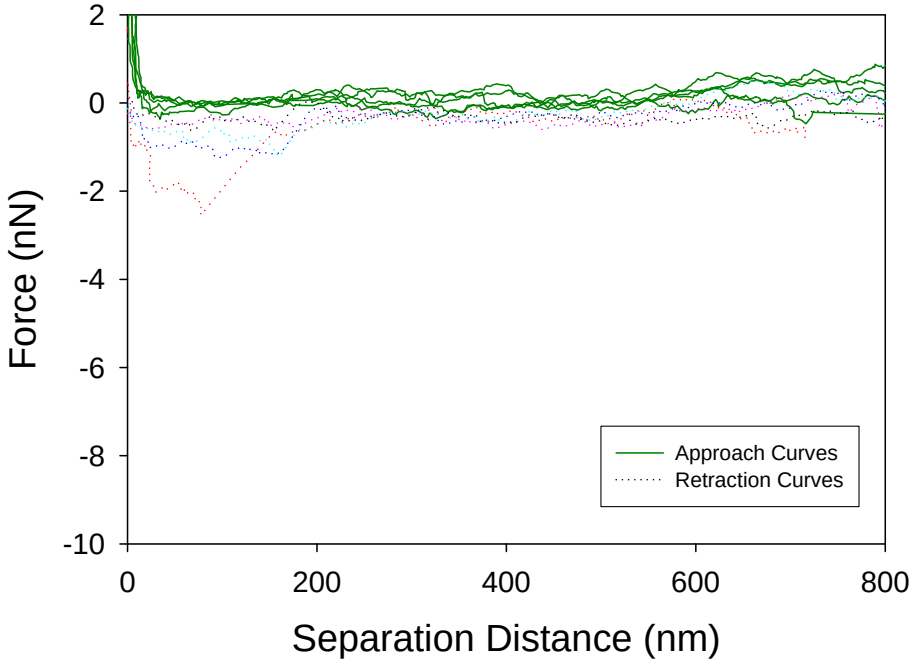

Figure 9.289 5 force plots of O157:H12 to CP1

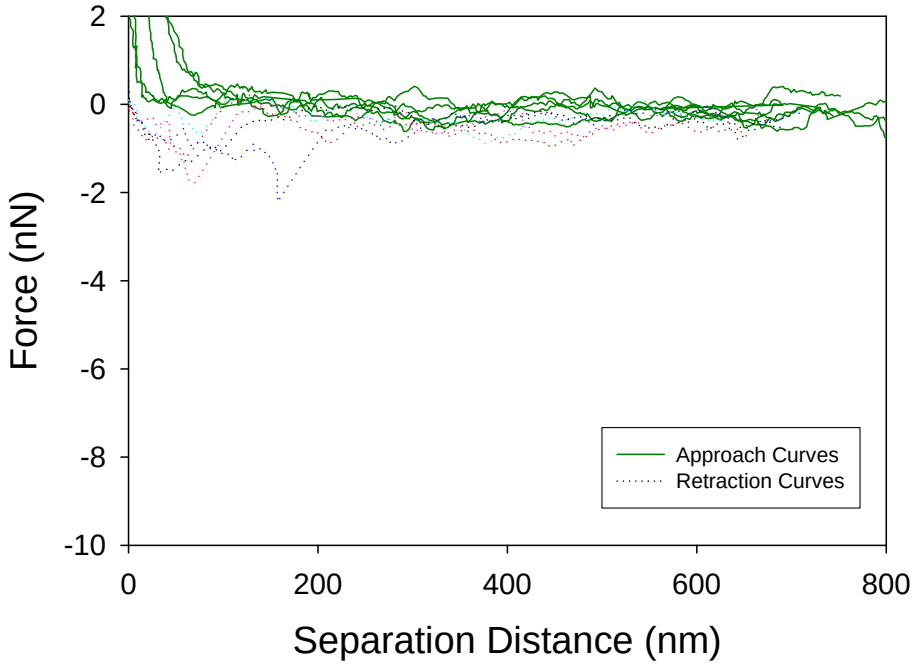

Figure 9.290 5 force plots of O157:H12 to CP1

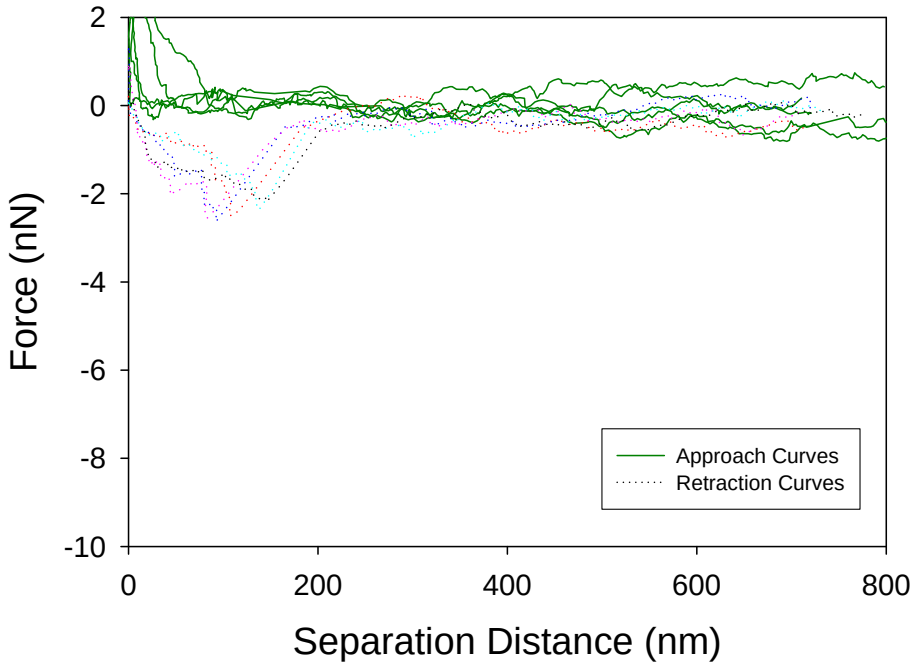

Figure 9.291 5 force plots of O157:H12 to CP1

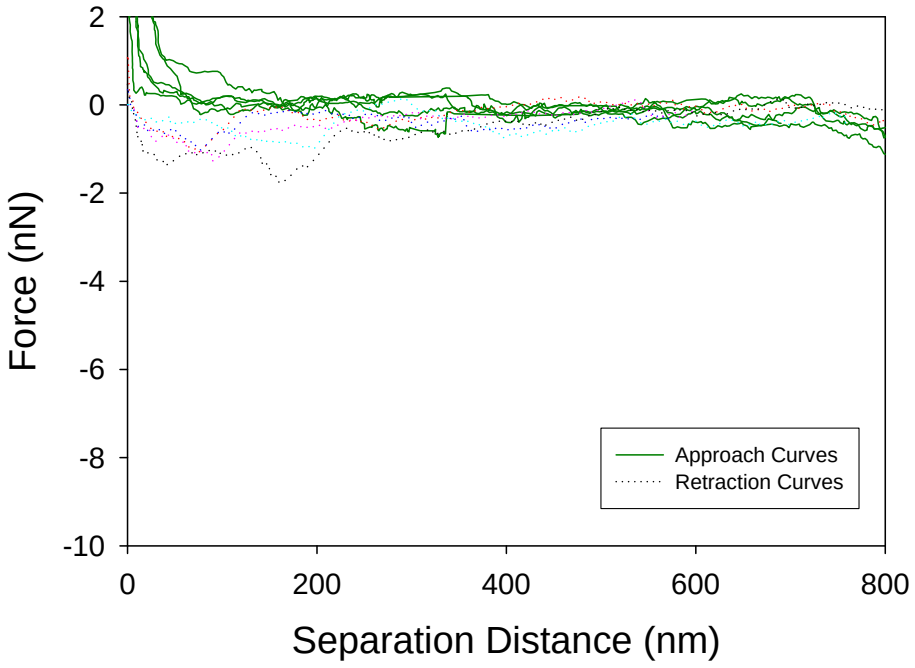

Figure 9.292 5 force plots of O157:H12 to CP1

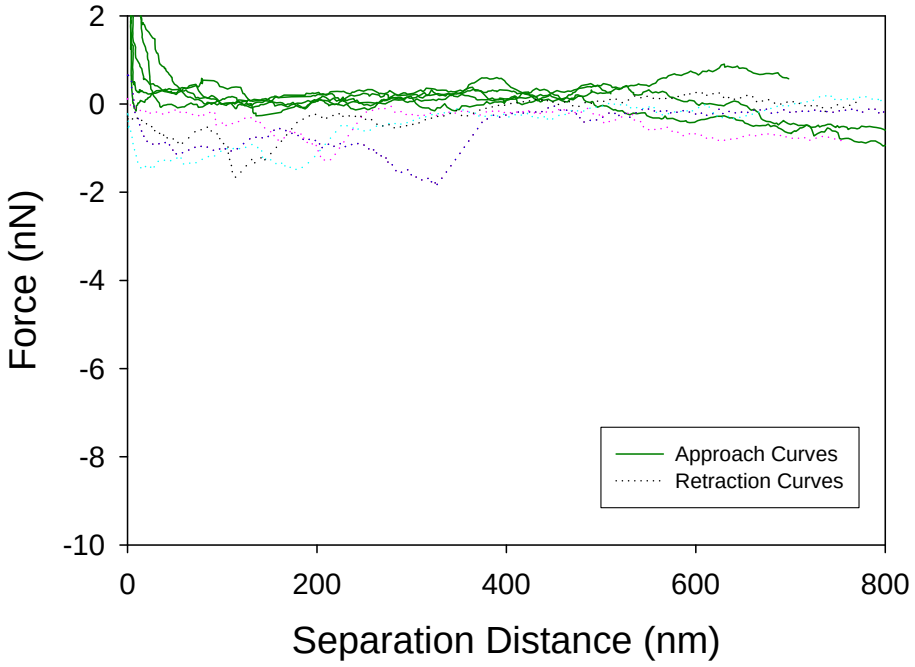

Figure 9.293 5 force plots of O157:H12 to CP1

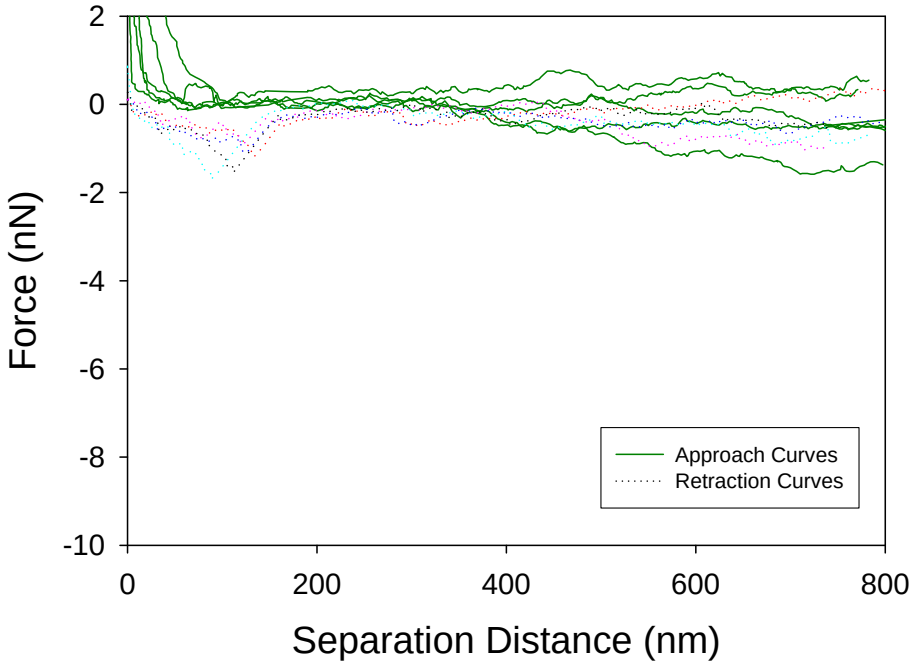

Figure 9.294 5 force plots of O157:H12 to CP1

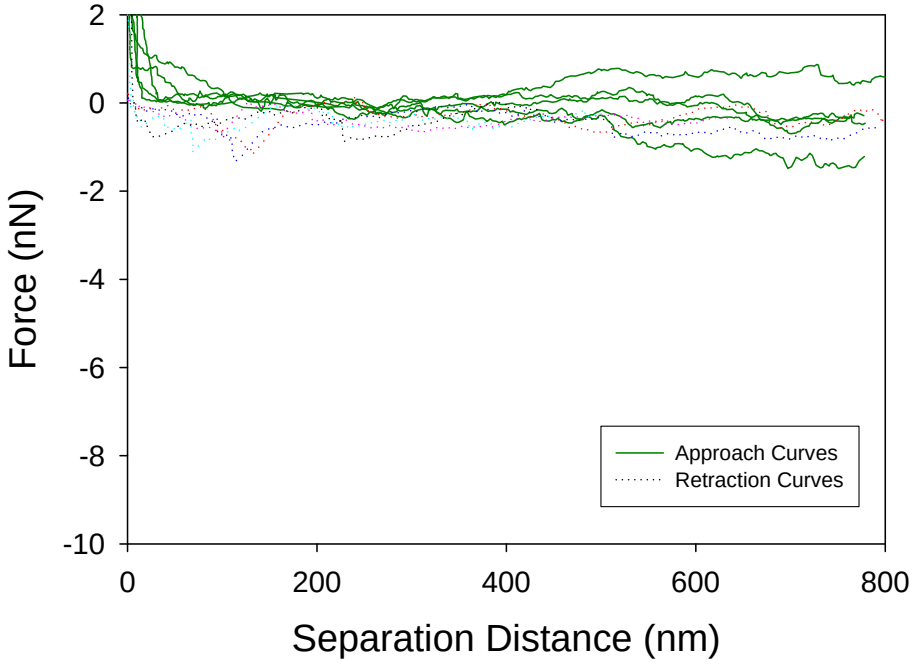

Figure 9.295 5 force plots of O157:H12 to CP1

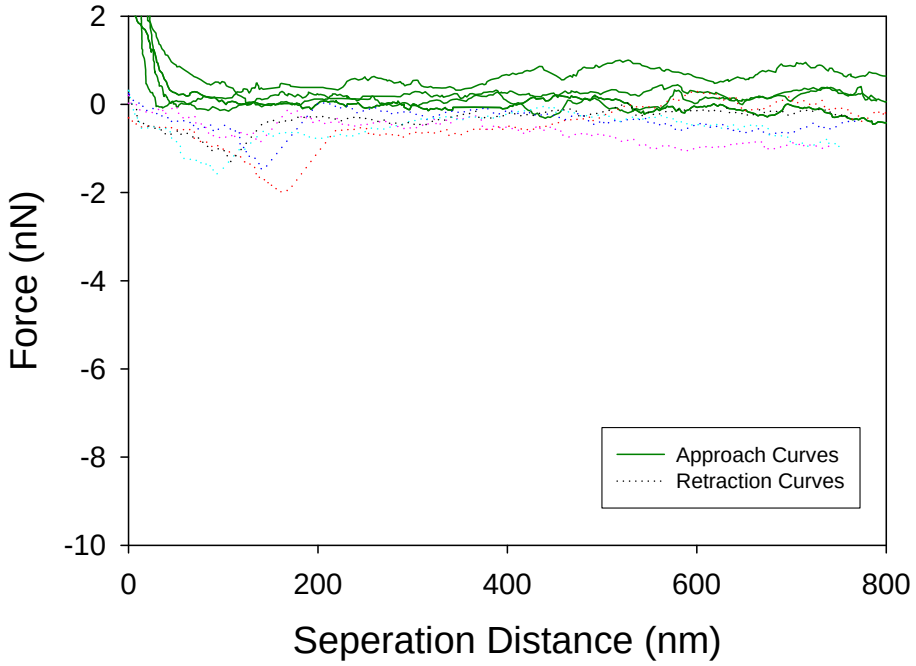

Figure 9.296 5 force plots of O157:H12 to CP1

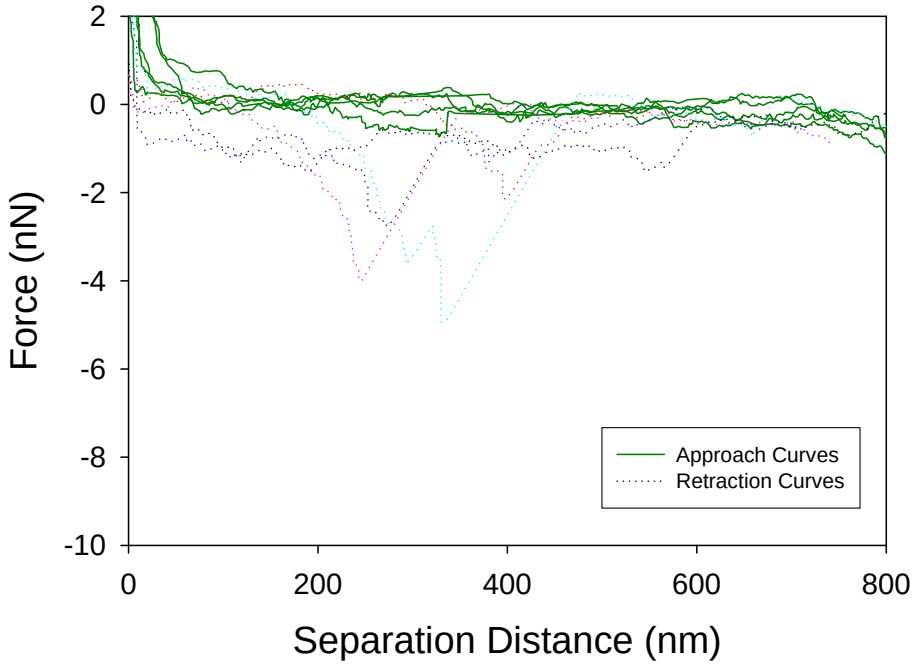

Figure 9.297 5 force plots of O157:H12 to CP1

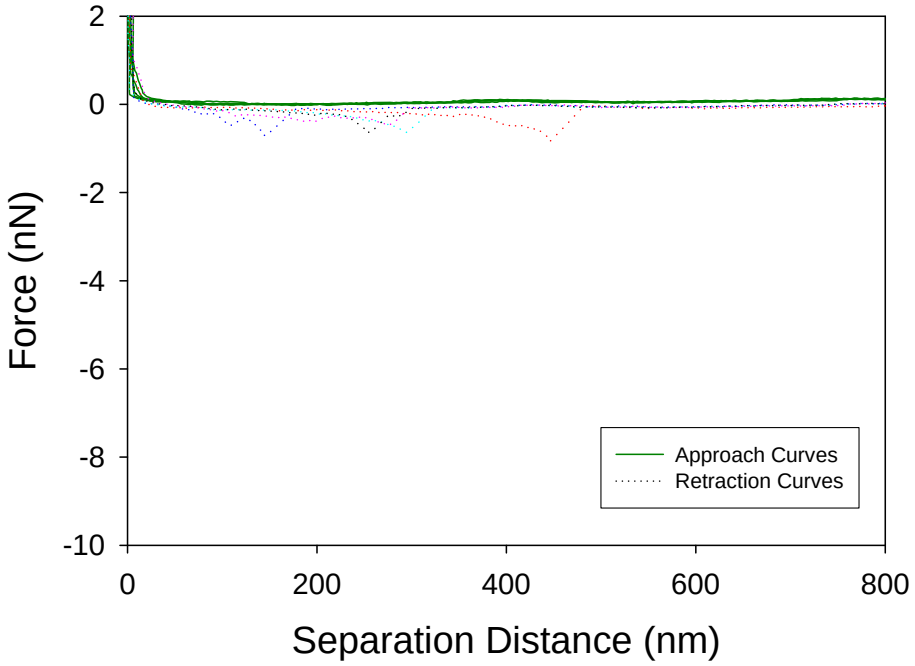

Figure 9.298 5 force plots of O157:H16 to silicon nitride

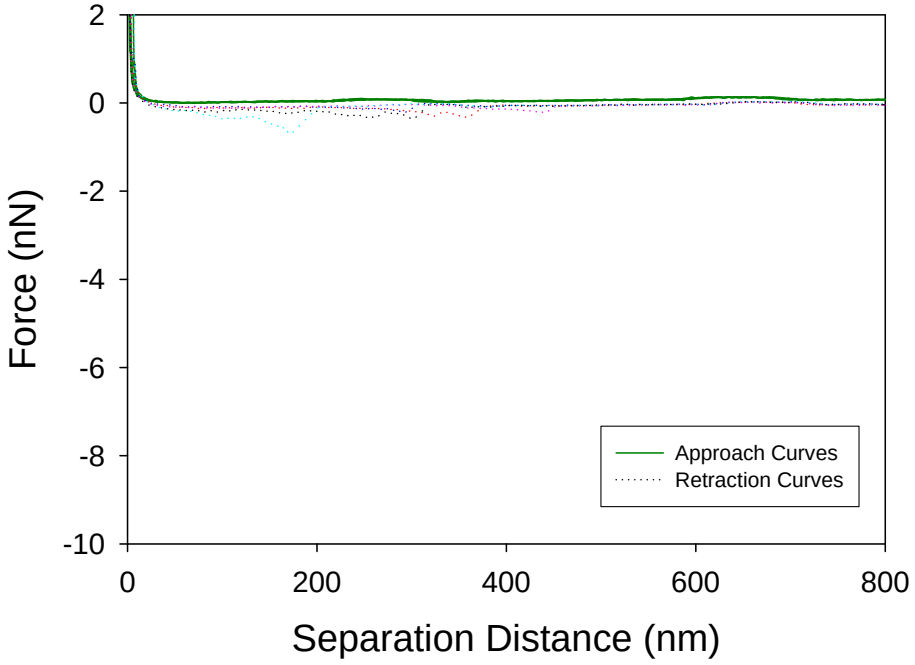

Figure 9.299 5 force plots of O157:H16 to silicon nitride

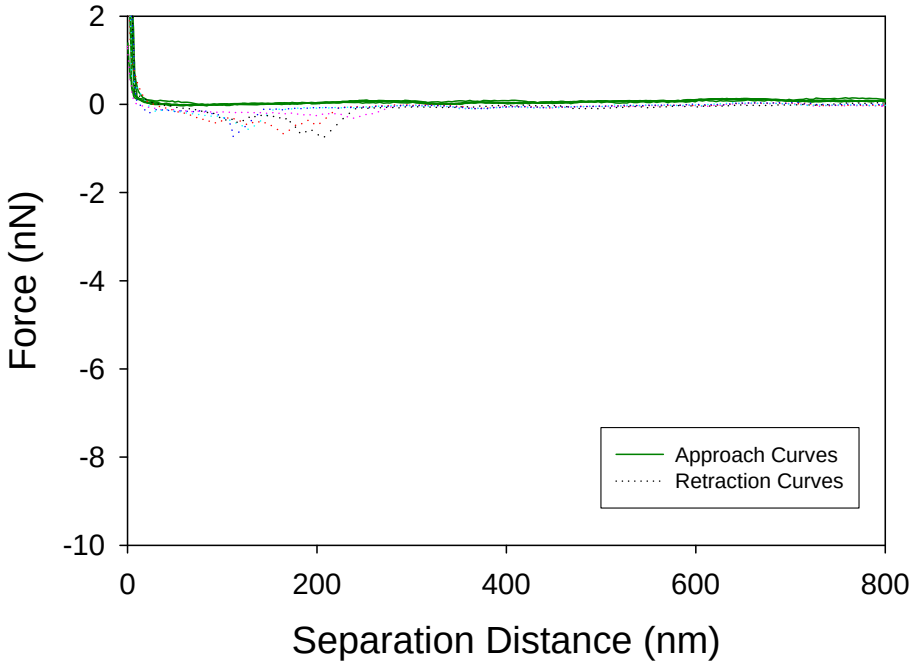

Figure 9.300 5 force plots of O157:H16 to silicon nitride

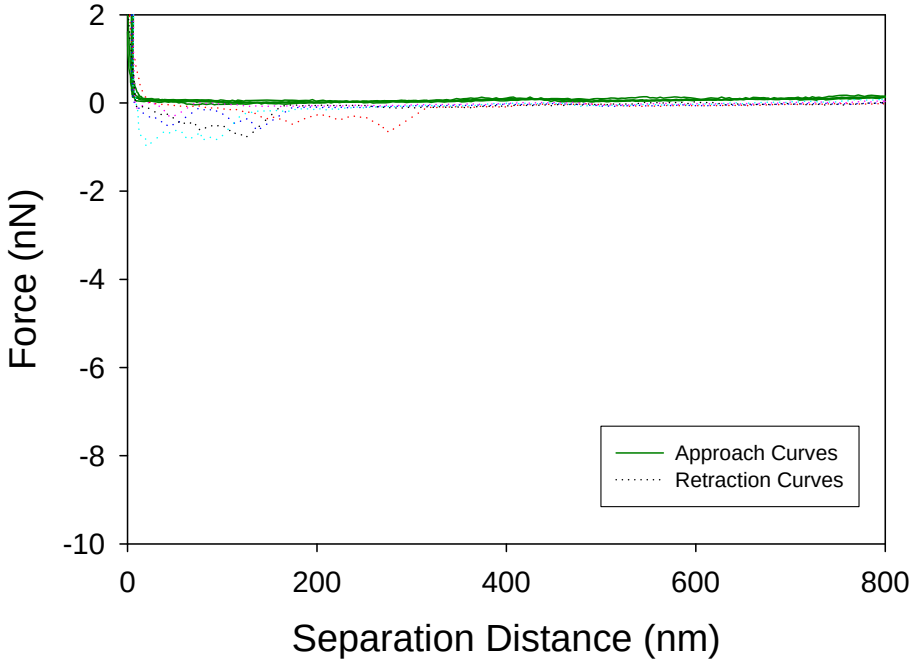

Figure 9.301 5 force plots of O157:H16 to silicon nitride

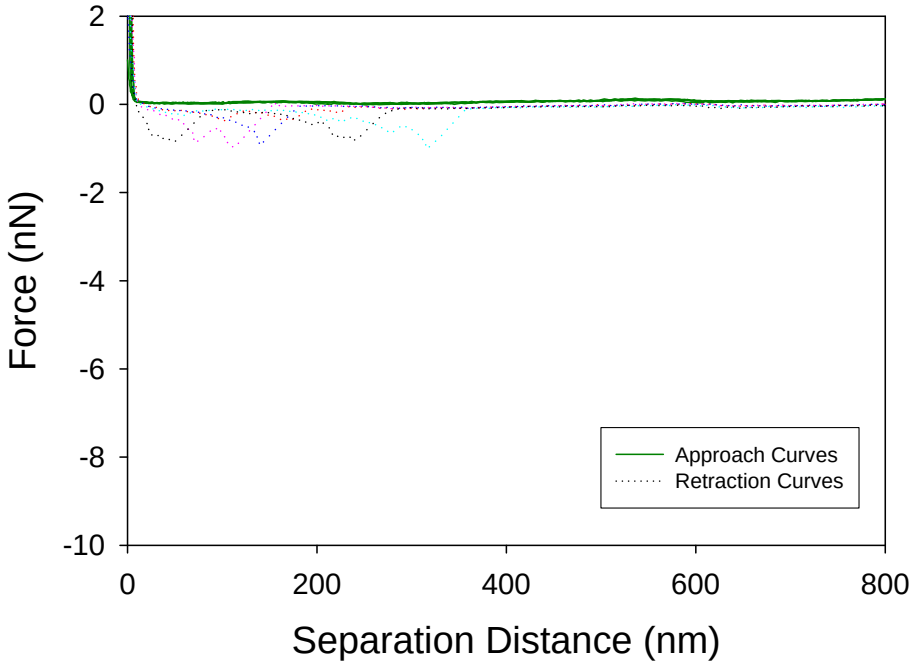

Figure 9.302 5 force plots of O157:H16 to silicon nitride

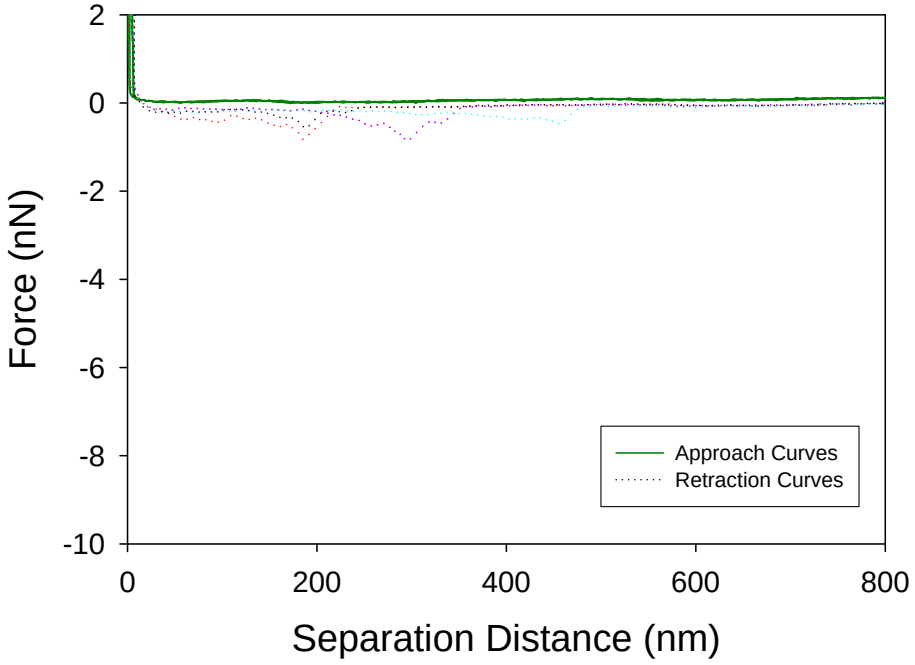

Figure 9.303 5 force plots of O157:H16 to silicon nitride

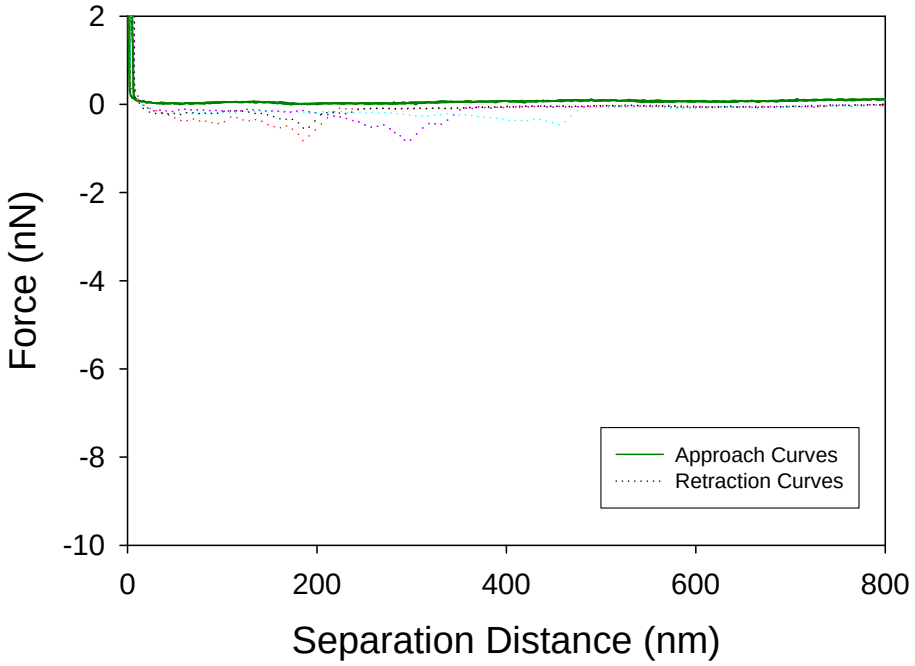

Figure 9.304 5 force plots of O157:H16 to silicon nitride

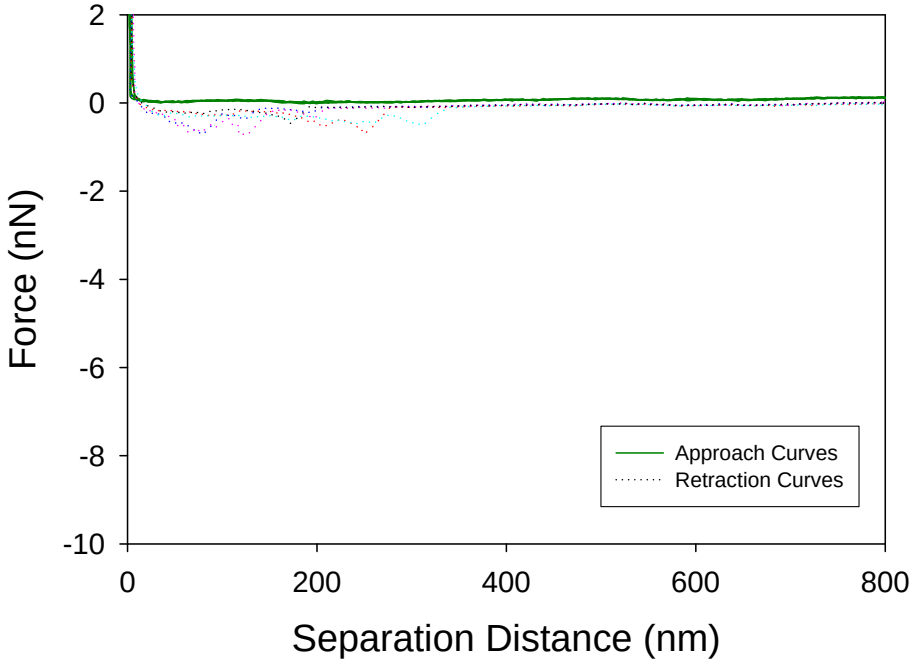

Figure 9.305 5 force plots of O157:H16 to silicon nitride

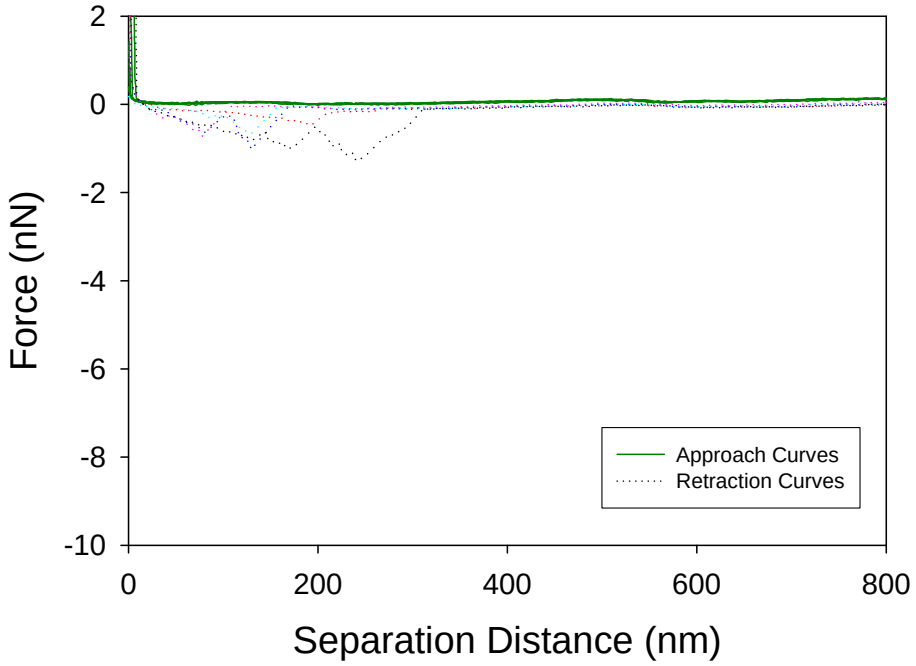

Figure 9.306 5 force plots of O157:H16 to silicon nitride

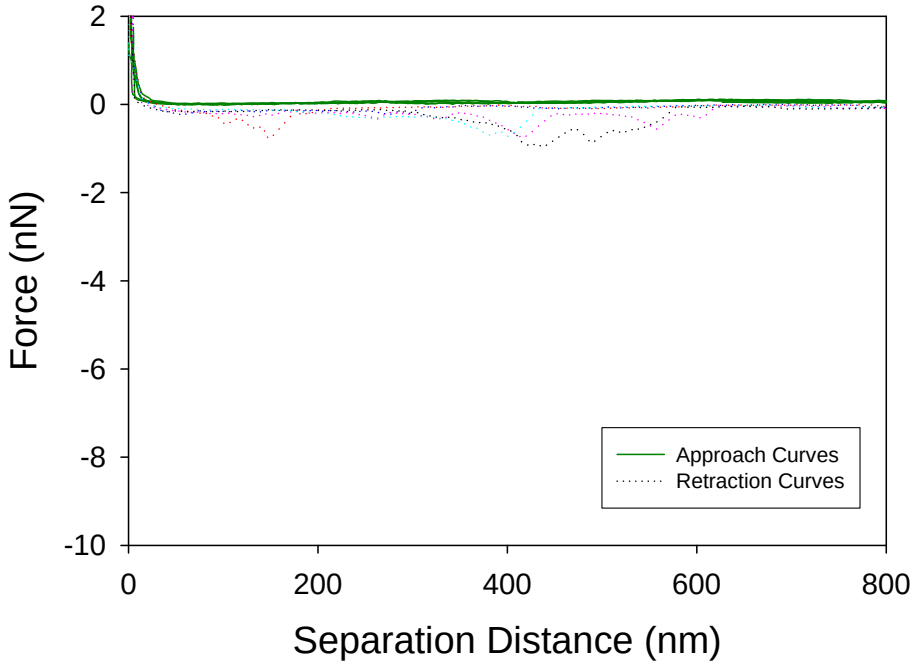

Figure 9.307 5 force plots of O157:H16 to silicon nitride

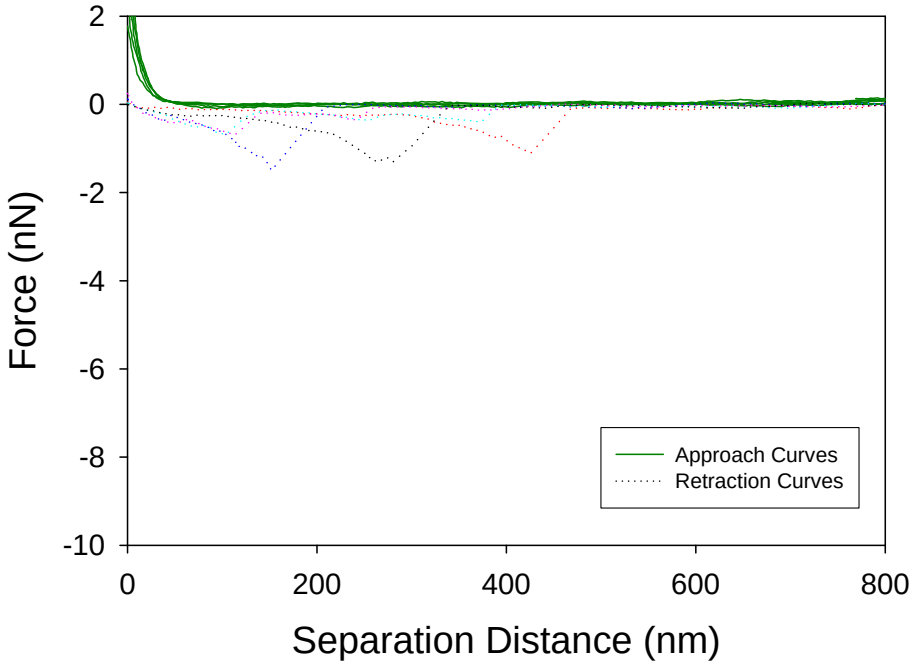

Figure 9.308 5 force plots of O157:H16 to CP1

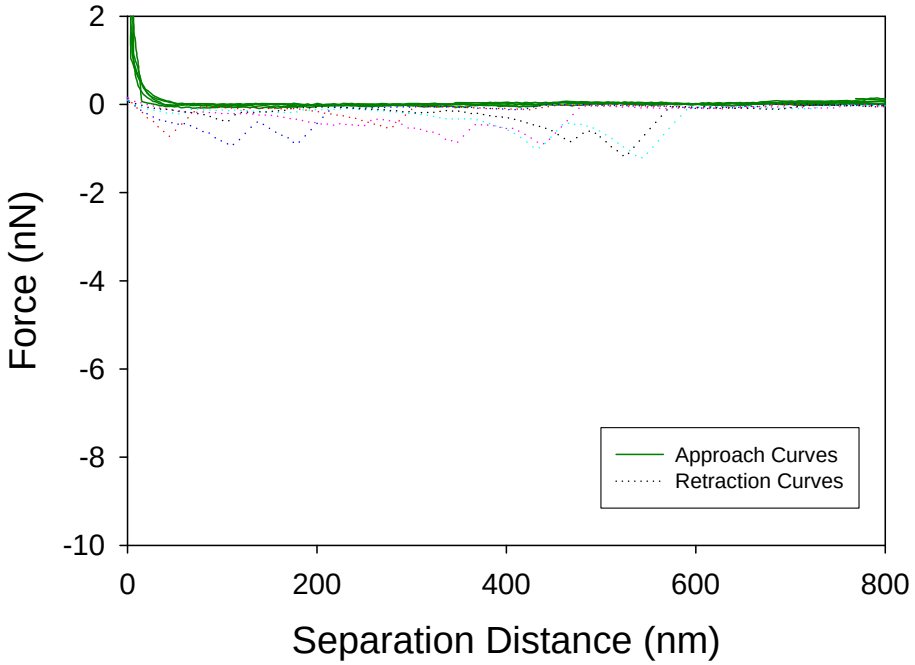

Figure 2.309 5 force plots of O157:H16 to CP1

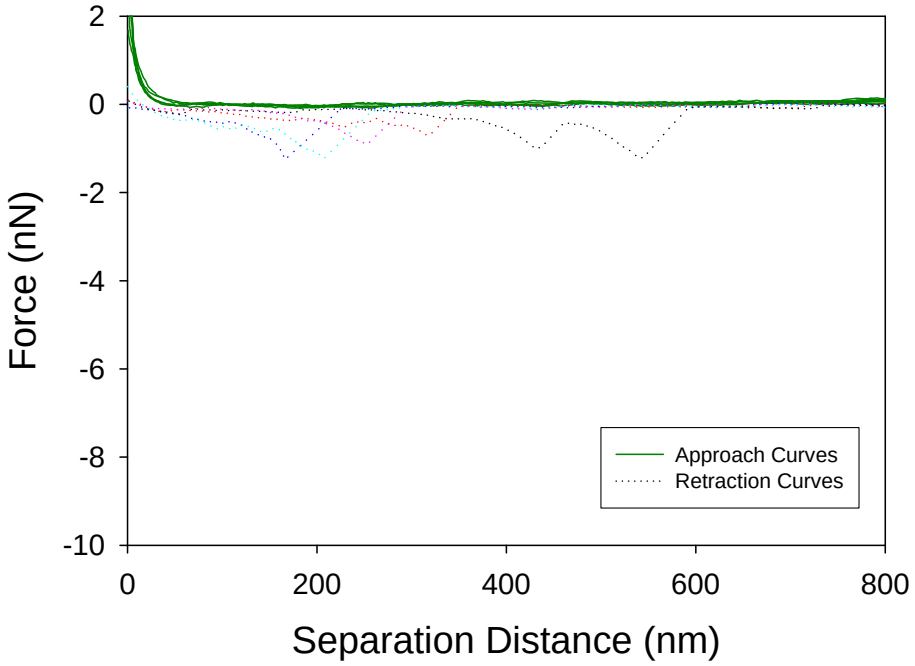

Figure 9.310 5 force plots of O157:H16 to CP1

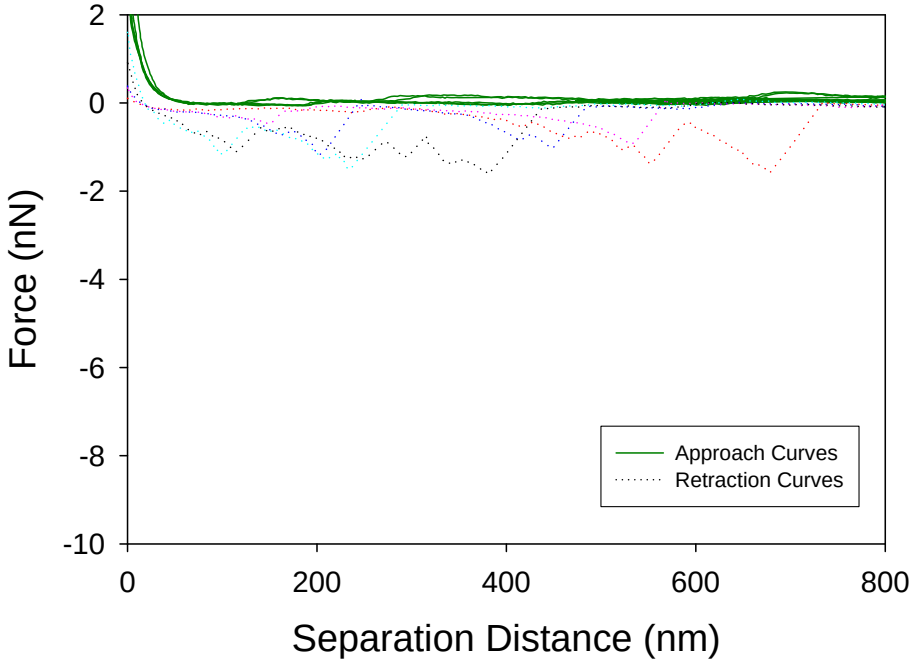

Figure 9.311 5 force plots of O157:H16 to CP1

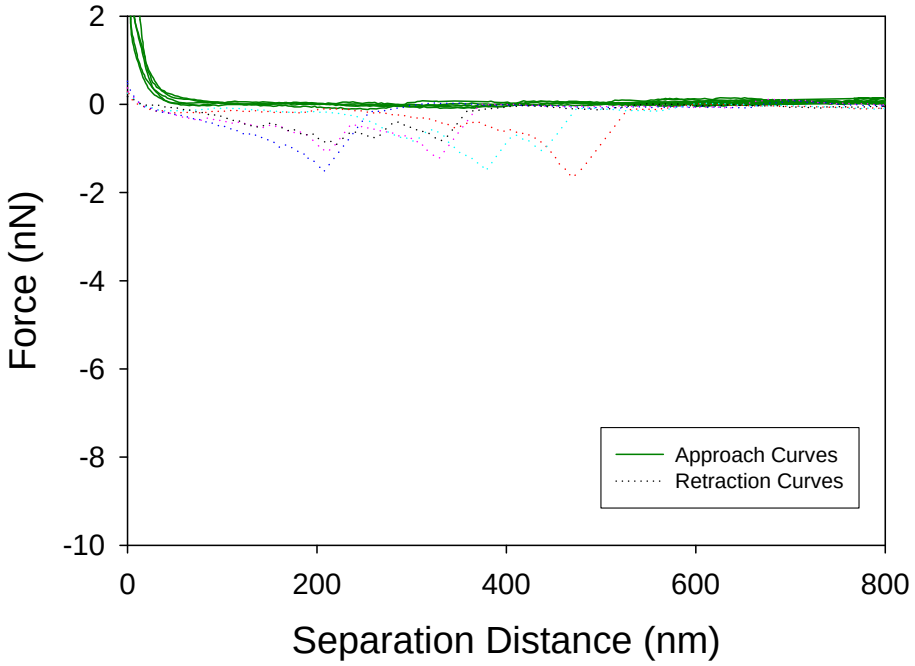

Figure 9.312 5 force plots of O157:H16 to CP1

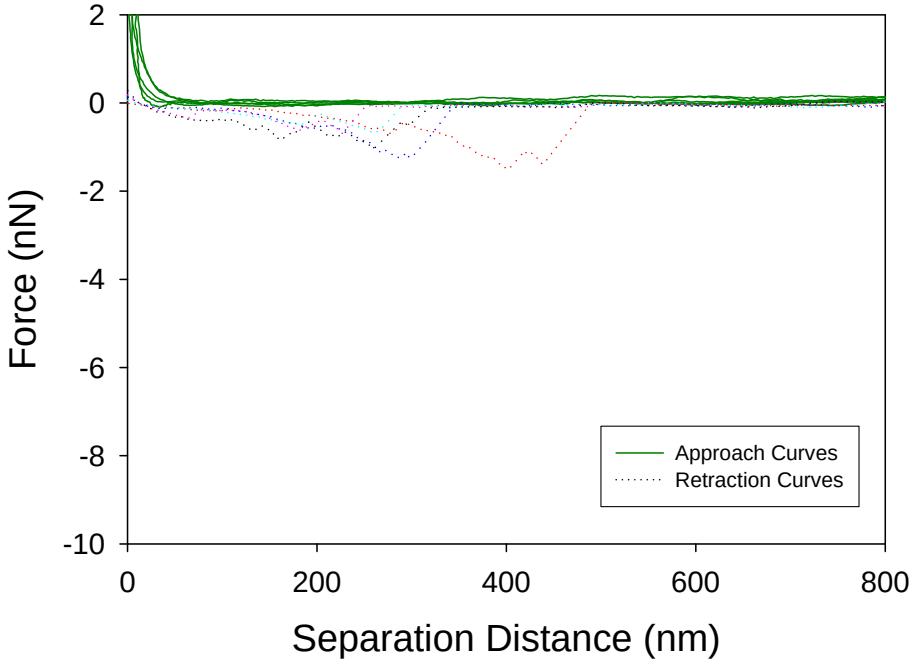

Figure 9.313 5 force plots of O157:H16 to CP1

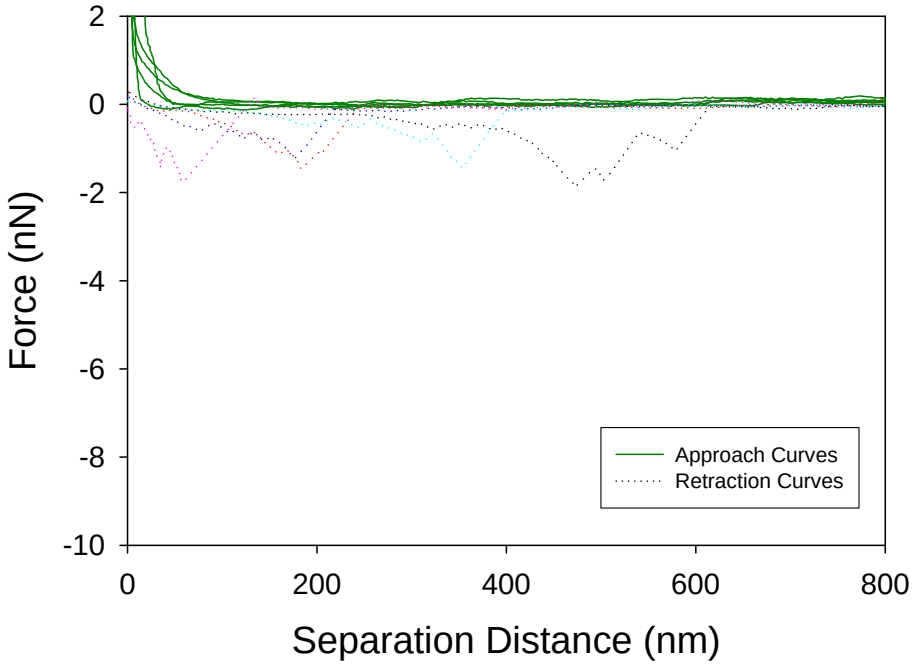

Figure 9.314 5 force plots of O157:H16 to CP1

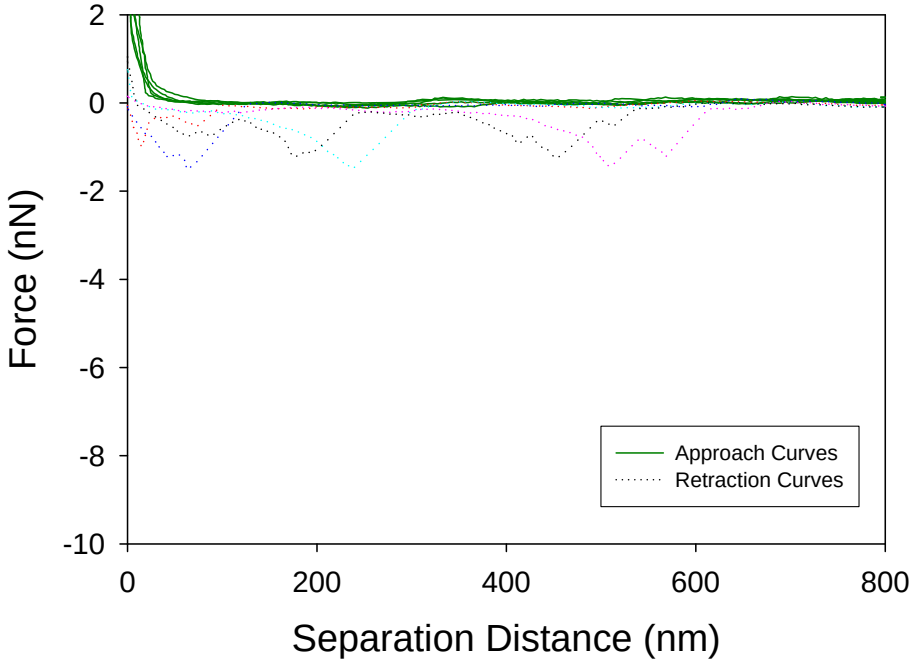

Figure 9.315 5 force plots of O157:H16 to CP1

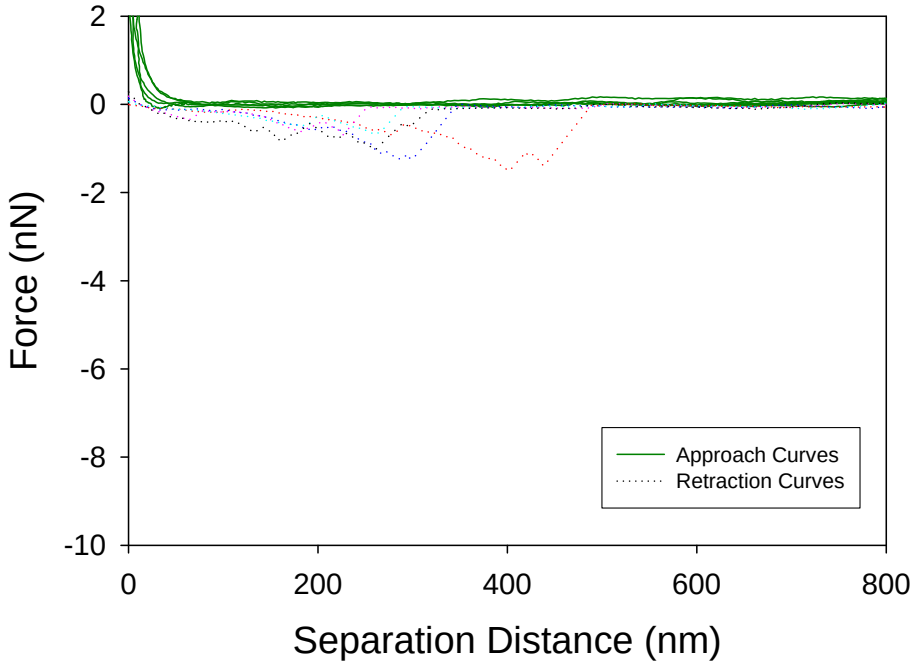

Figure 9.316 5 force plots of O157:H16 to CP1

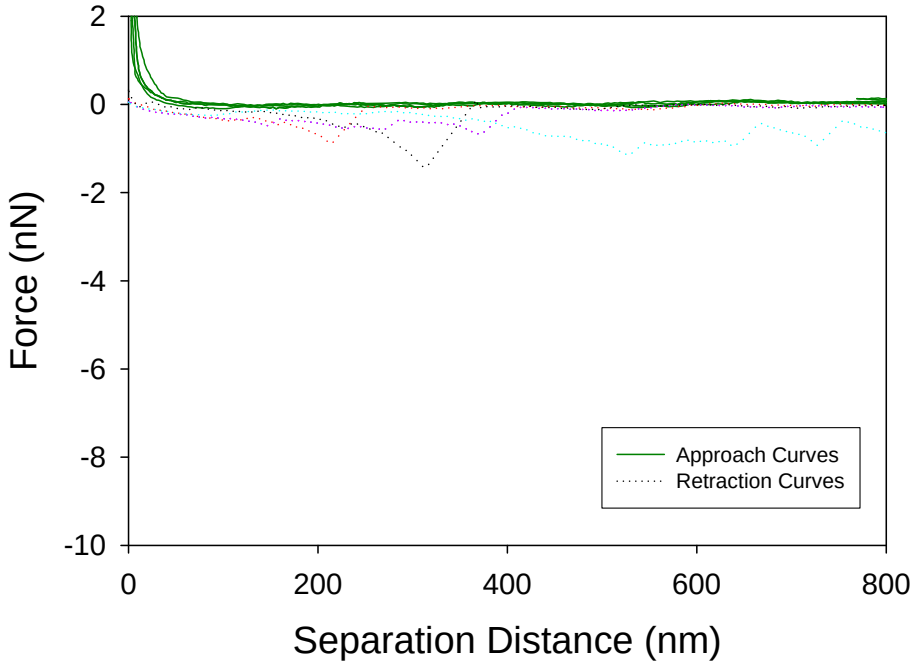

Figure 9.317 5 force plots of O157:H16 to CP1

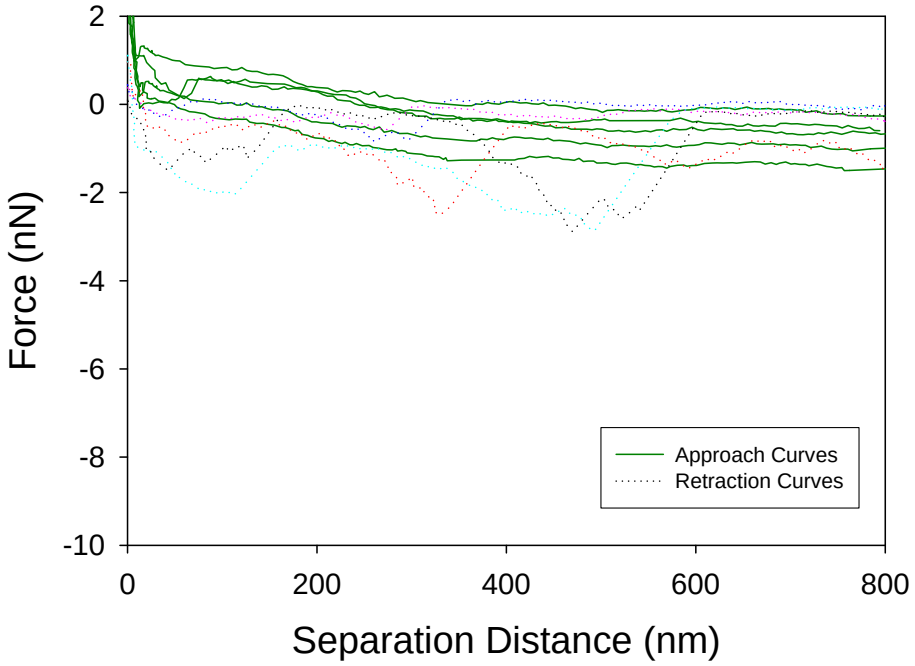

Figure 9.318 5 force plots of O172:H- to silicon nitride

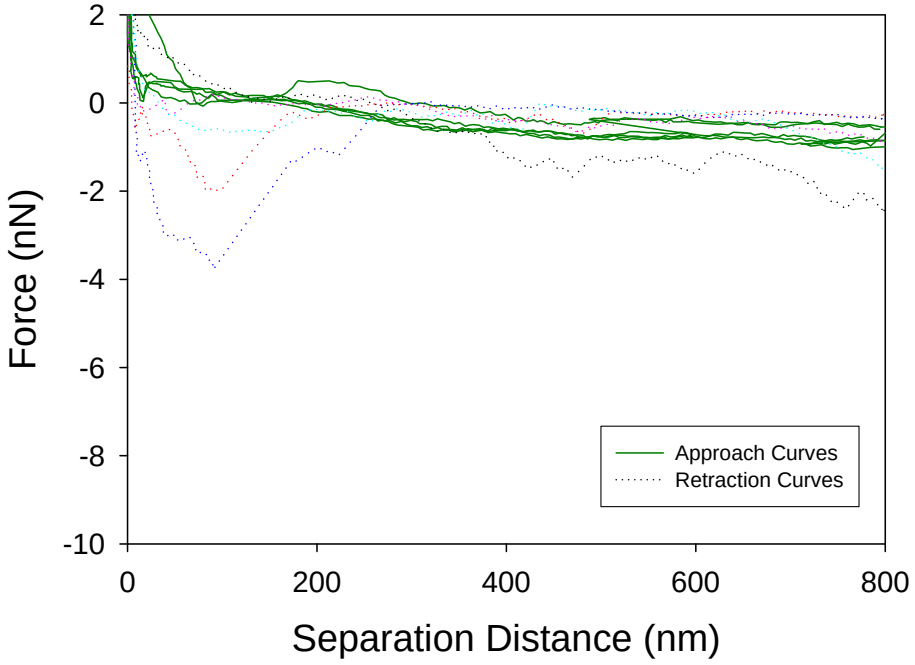

Figure 9.319 5 force plots of O172:H- to silicon nitride

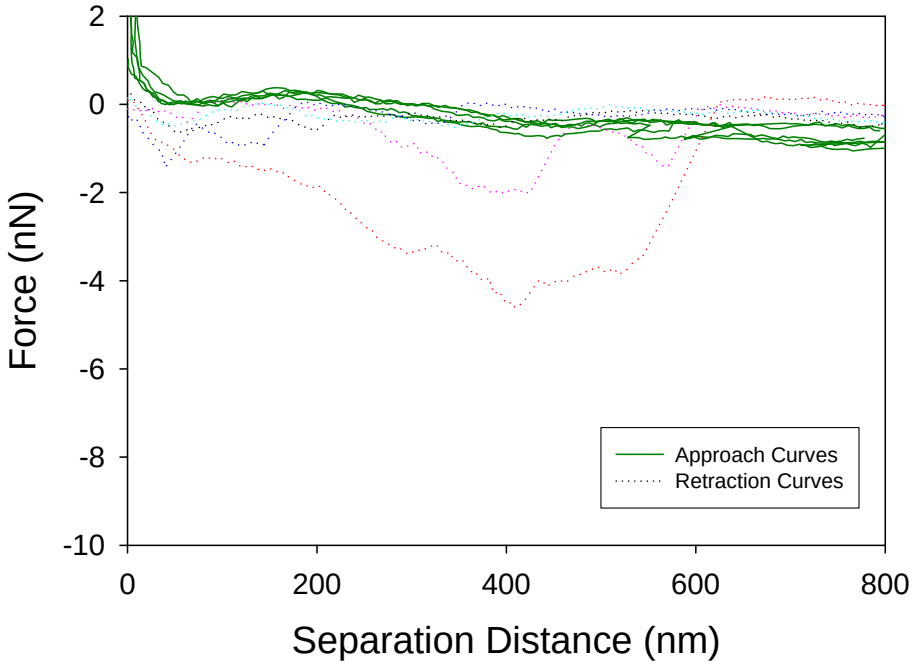

Figure 9.320 5 force plots of O172:H- to silicon nitride

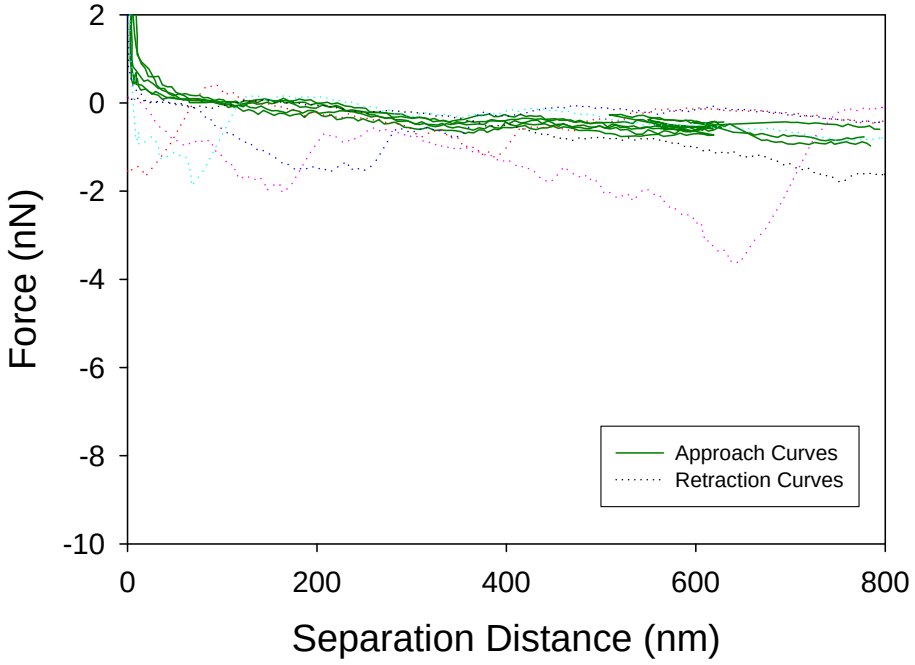

Figure 9.321 5 force plots of O172:H- to silicon nitride

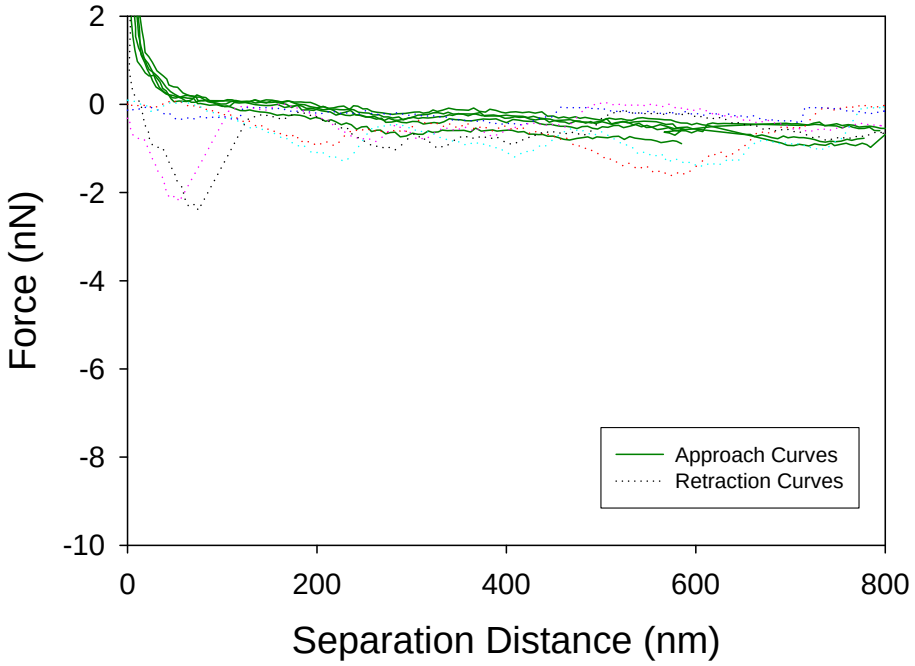

Figure 9.322 5 force plots of O172:H- to silicon nitride

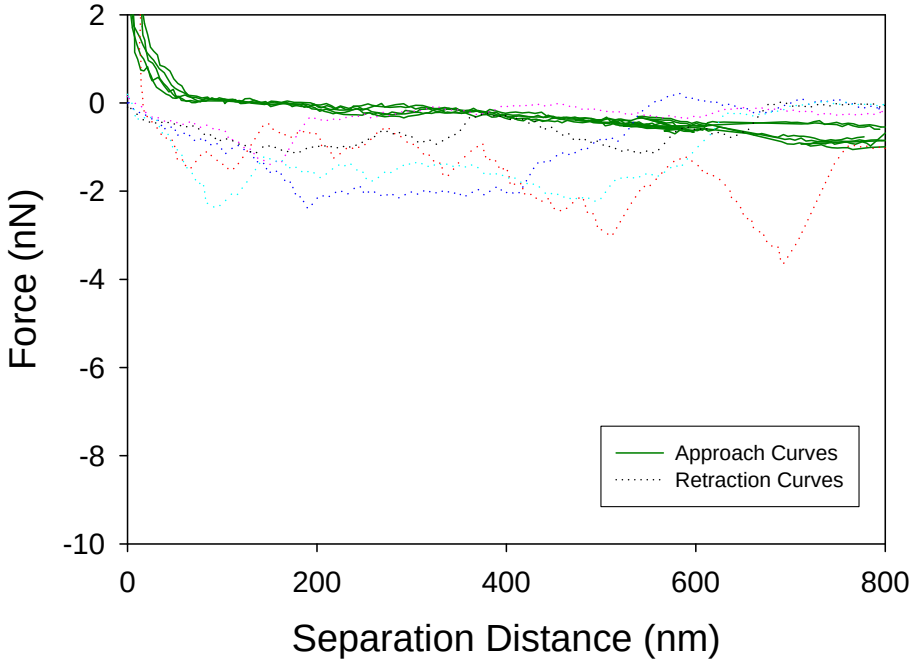

Figure 9.323 5 force plots of O172:H- to silicon nitride

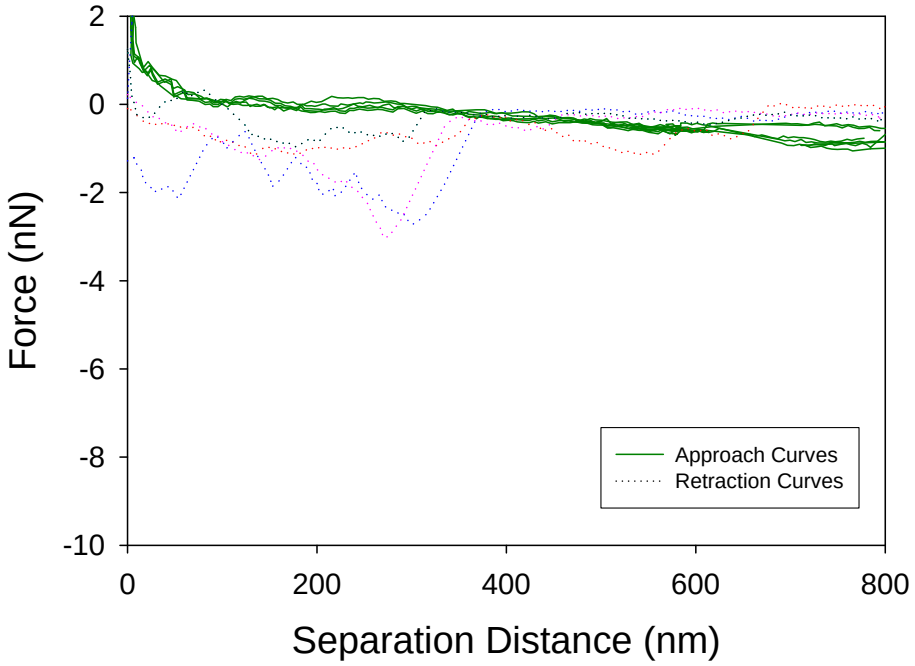

Figure 9.324 5 force plots of O172:H- to silicon nitride

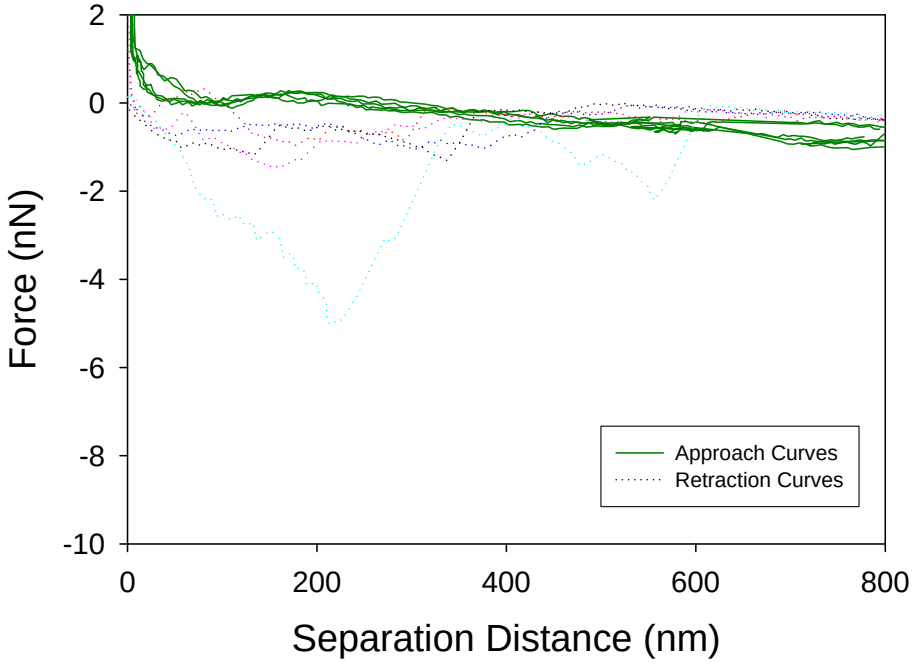

Figure 9.325 5 force plots of O172:H- to silicon nitride

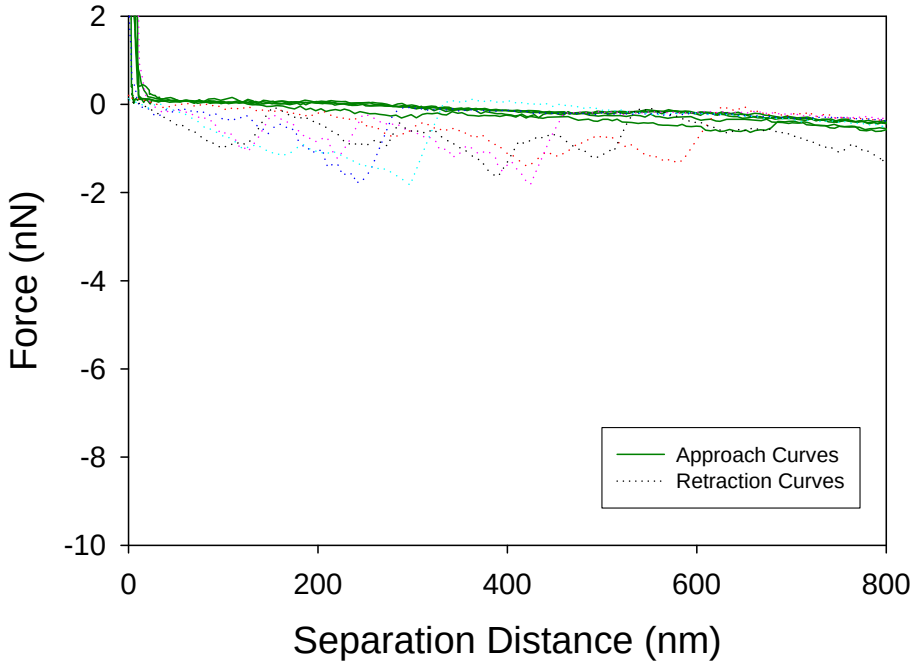

Figure 9.326 5 force plots of O172:H- to silicon nitride

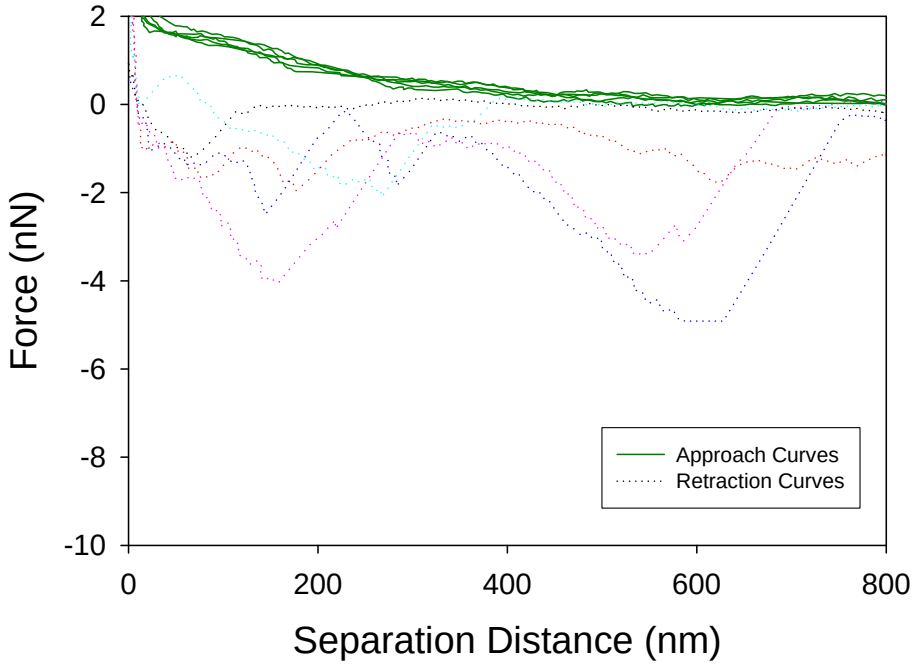

Figure 9.327 5 force plots of O172:H- to silicon nitride

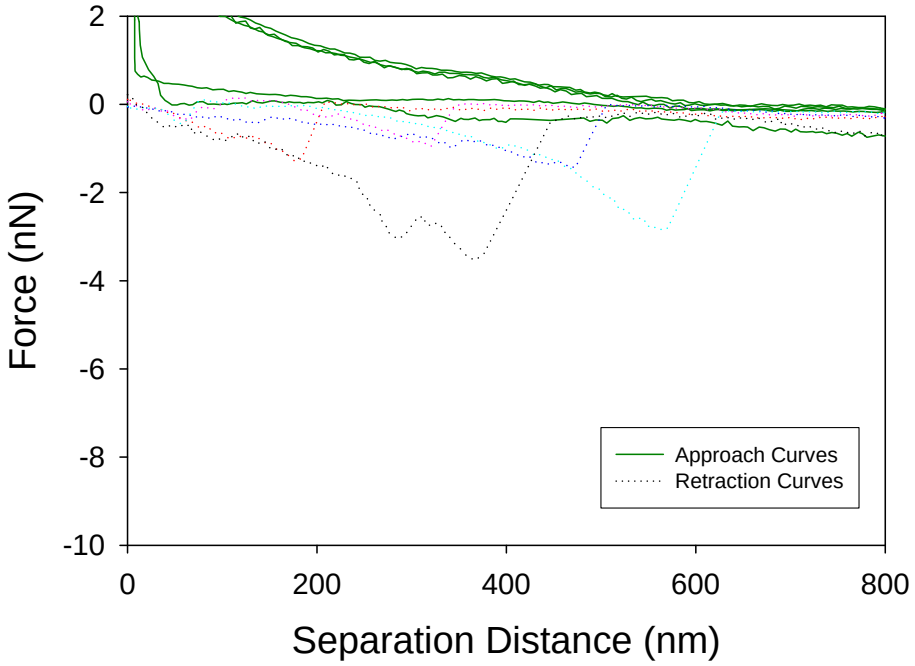

Figure 9.328 5 force plots of O172:H- to CP1

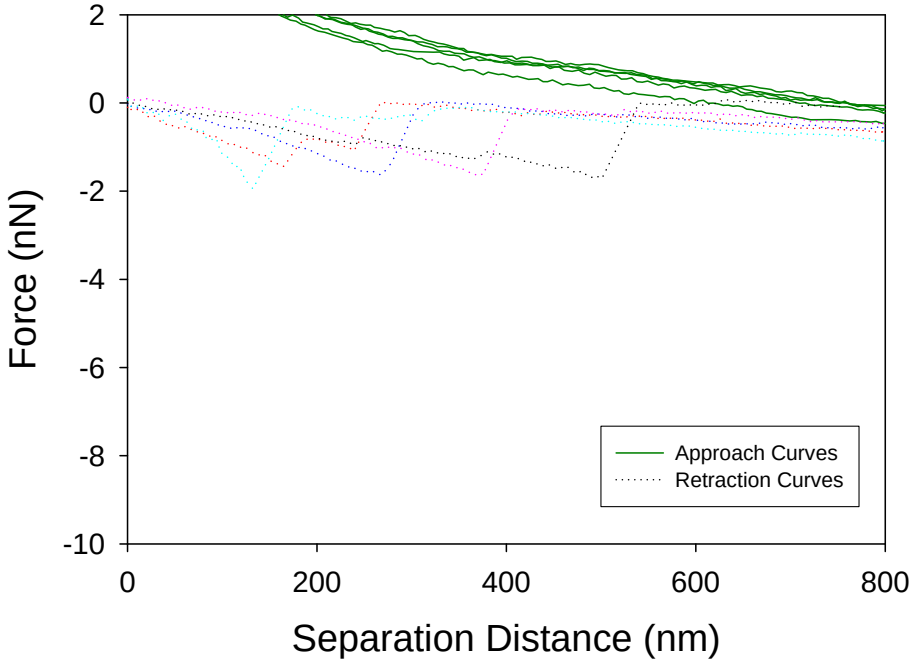

Figure 9.329 5 force plots of O172:H- to CP1

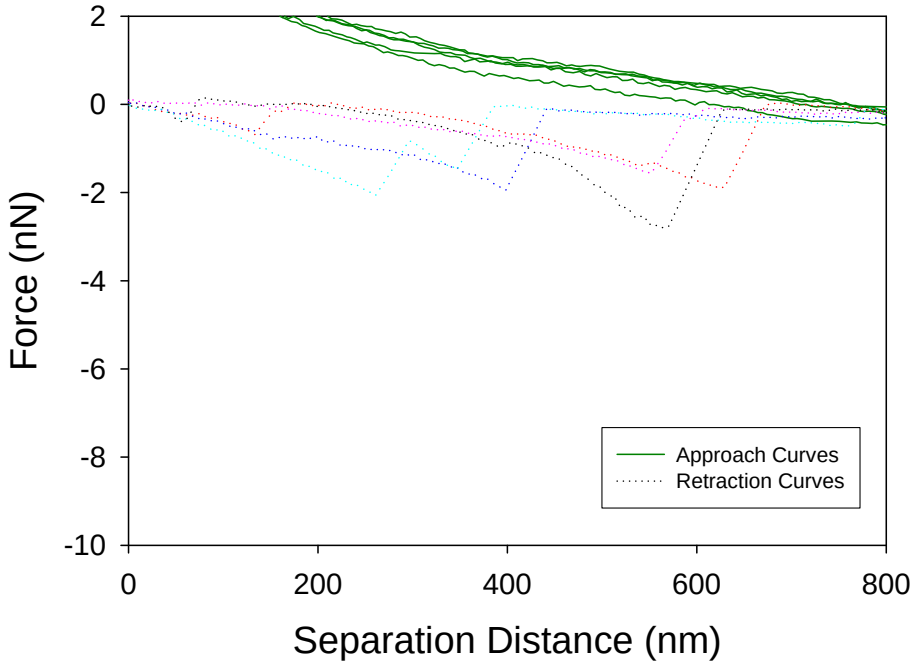

Figure 9.330 5 force plots of O172:H- to CP1

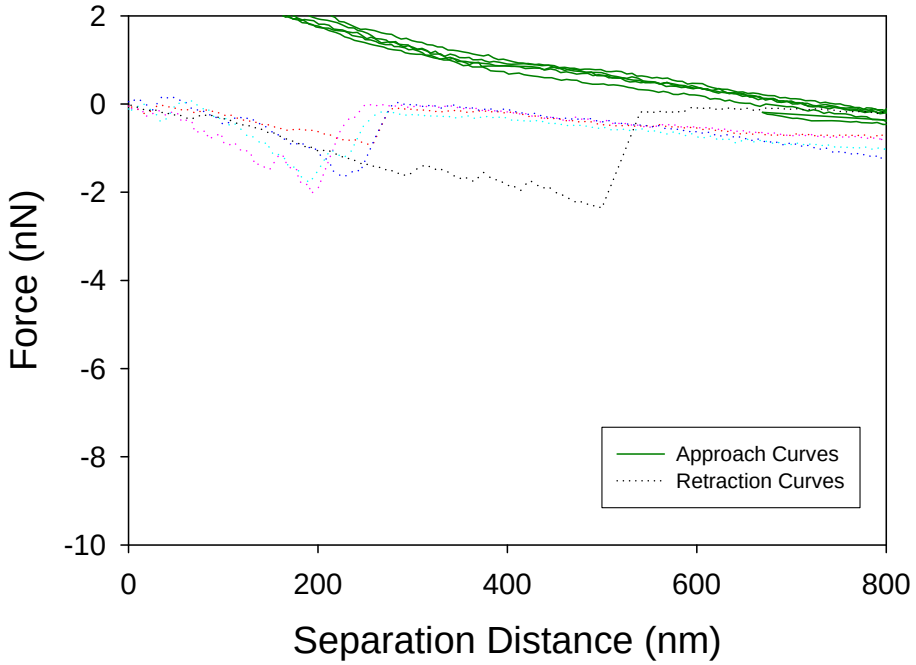

Figure 9.331 5 force plots of O172:H- to CP1

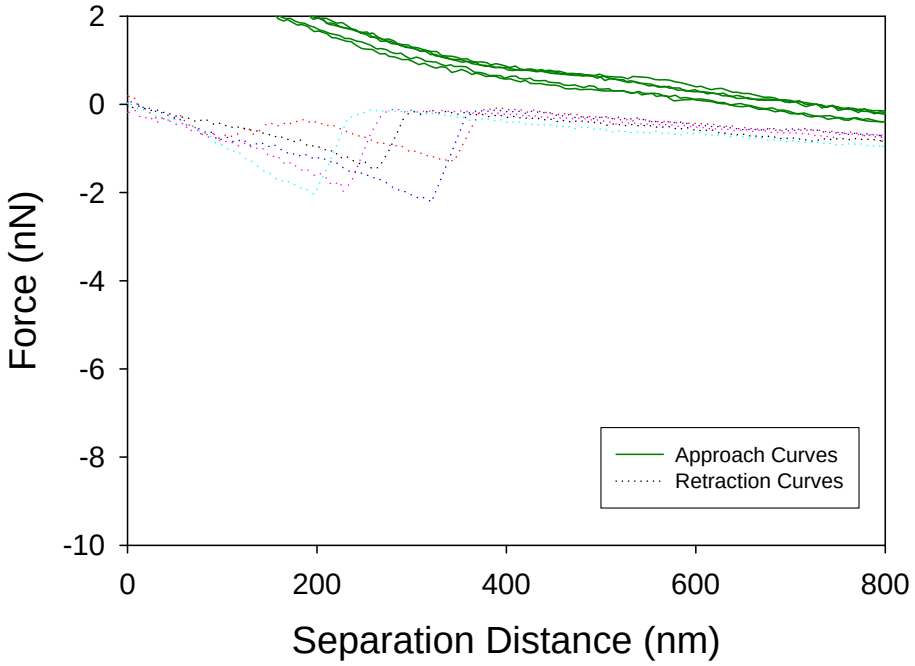

Figure 9.332 5 force plots of O172:H- to CP1

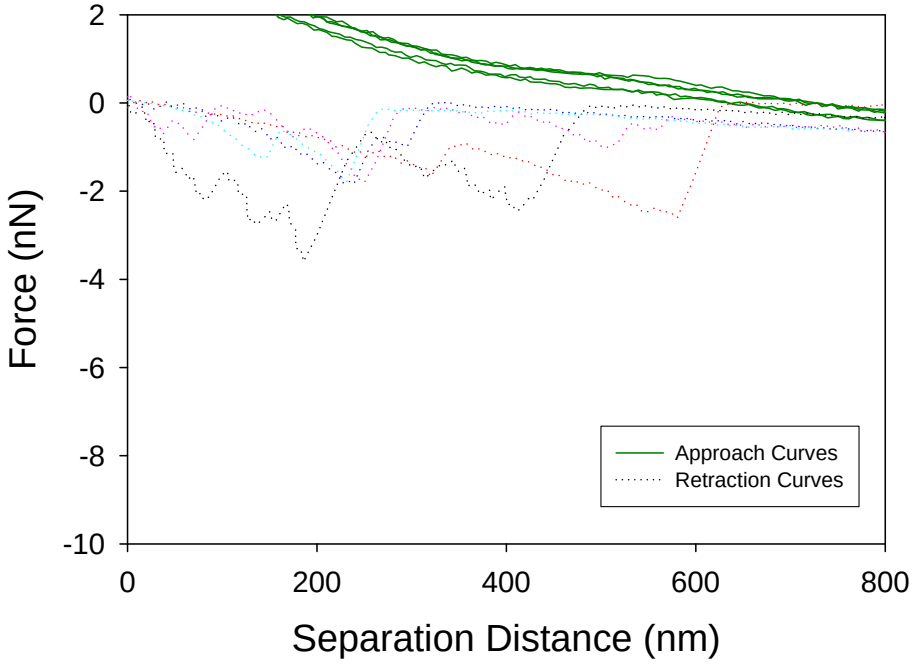

Figure 9.333 5 force plots of O172:H- to CP1

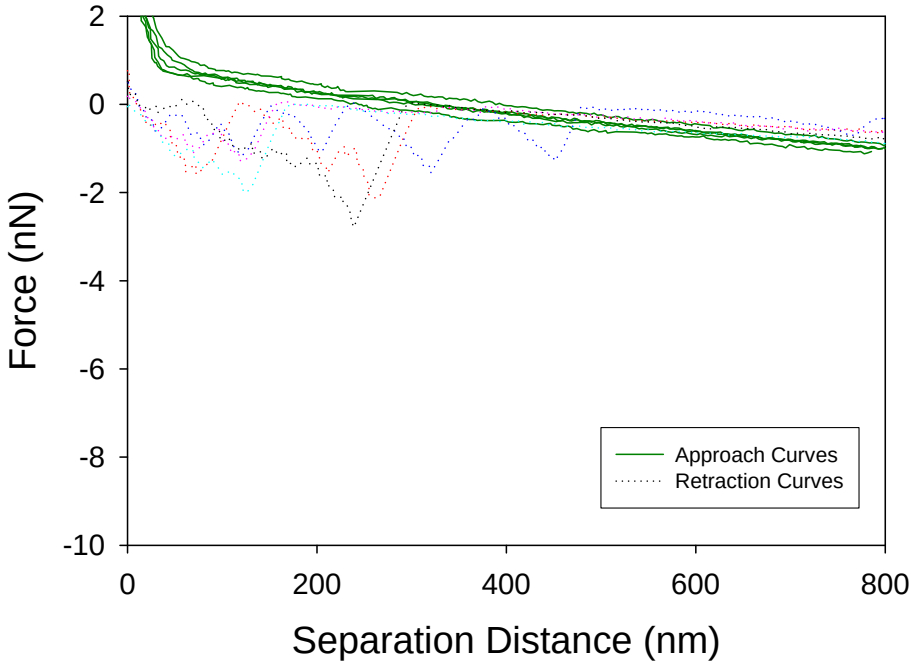

Figure 9.334 5 force plots of O172:H- to CP1

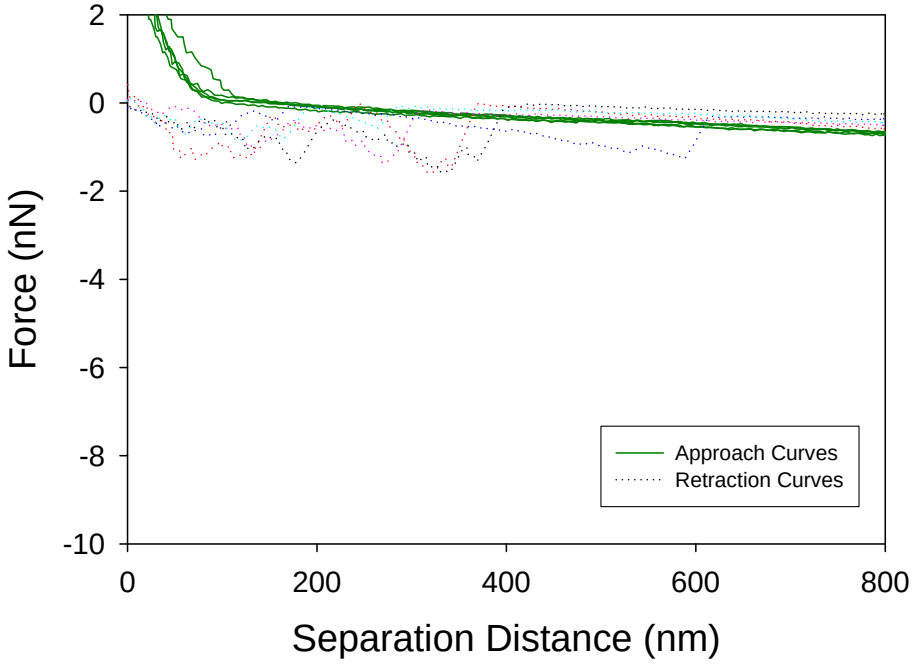

Figure 9.335 5 force plots of O172:H- to CP1

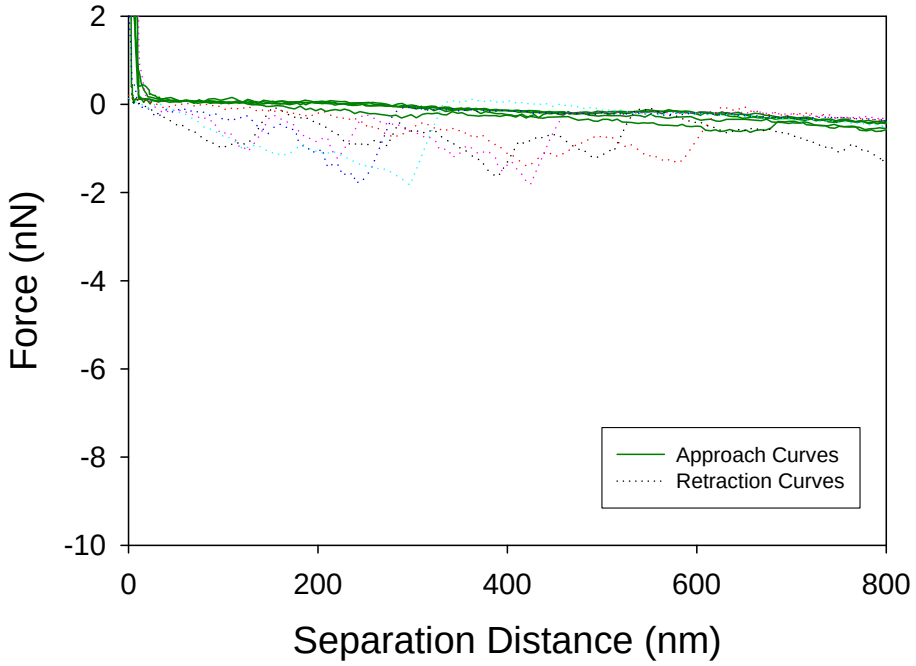

Figure 9.336 5 force plots of O172:H- to CP1

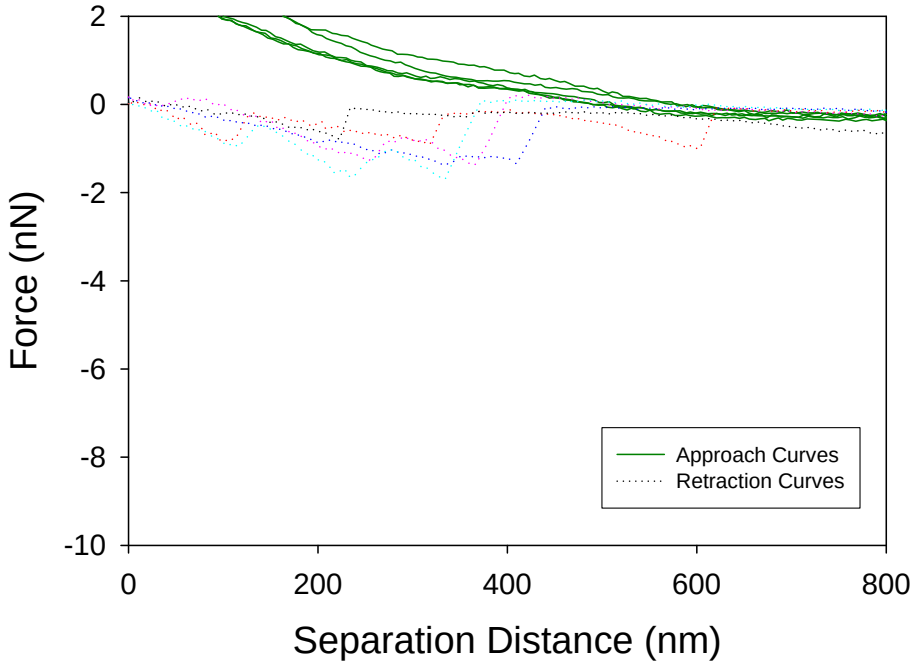

Figure 9.337 5 force plots of O172:H- to CP1

Appendix H: Interfacial Free Energy Calculations

Table 9.1 *E. coli* Contact Angles

Contact angles[1] θ (°), n=9	Bacterium		
	E. coli HB101	*E. coli* K12	*E. coli* ML35
θ^W	63 ± 1	65 ± 2	67 ± 2
θ^D	65 ± 3	60 ± 1	63 ± 1
θ^F	52 ± 2	48 ± 1	50 ± 1
	E. coli O157:H7	*E. coli* O157:H12	*E. coli* O157:H16
θ^W	70 ± 1	70 ± 1	58 ± 2
θ^D	48 ± 1	48 ± 1	80 ± 3
θ^F	41 ± 3	41 ± 3	81 ± 3
	E. coli O55:H7	*E. coli* O113:H4	*E. coli* O35:K:H10
θ^W	70 ± 3	47 ± 2	60 ± 3
θ^D	75 ± 3	66.7 ± 2	72 ± 3
θ^F	77 ± 3	70 ± 2	78 ± 2
	E. coli O113:H21	*E. coli* O117:K98:H4	*E. coli* O26:K60:H11
θ^W	56 ± 2	66 ± 1	54 ± 3
θ^D	75 ± 2	50 ± 1	80 ± 3
θ^F	78 ± 3	37 ± 1	78 ± 2
	E. coli O172:H-		
θ^W	68 ± 1		
θ^D	48 ± 1		
θ^F	41 ± 1		

Table 9.2 SFE Components

Surface energy components[1] (mJ/m^2), n=9	Bacterium		
	E. coli HB101	*E. coli* K12	*E. coli* ML35
γb^{Lw}	20.598	23.843	22.447
γb^{-}	19.228	14.401	13.246
γb^{+}	3.51	3.688	3.924
γb^{AB}	16.43	14.576	14.418
γb^{Total}	37.028	38.42	36.865
	E. coli O157:H7	*E. coli* O157:H12	*E. coli* O157:H16
γb^{Lw}	31.662	29.208	10.596
γb^{-}	6.657	8.159	60.412
γb^{+}	3.498	3.674	0.046
γb^{AB}	9.651	10.949	3.339
γb^{Total}	41.314	40.157	13.935
	E. coli O55:H7	*E. coli* O113:H4	*E. coli* O35:K:H10
γb^{Lw}	14.518	15.853	14.443
γb^{-}	31.672	66.477	52.222
γb^{+}	0.248	0.066	1.857 E-3
γb^{AB}	5.605	4.18	0.623
γb^{Total}	20.122	20.033	15.066
	E. coli O113:H21	*E. coli* O117:K98:H4	*E. coli* O26:K60:H11
γb^{Lw}	13.759	10.417	30.183
γb^{-}	42.059	64.094	8.495
γb^{+}	0.098	0.178	4.508
γb^{AB}	4.053	6.764	12.377
γb^{Total}	17.811	17.181	42.561
	E. coli O172:H-		
γb^{Lw}	31.259		
γb^{-}	8.326		
γb^{+}	3.357		
γb^{AB}	10.573		
γb^{Total}	41.832		

Table 9.3 Gold Contact Angles

Contact angles[1] θ (°), n=9	Substrate	
	Gold	10 µm CP1-cys
θ^W	63 ± 1	39 ± 2
θ^D	65 ± 3	32 ± 3
θ^F	52 ± 2	53 ± 1

Table 9.4 Gold SFE Components

Surface energy components (mJ/m^2), n=9	Substrate	
	Gold	10 µm CP1-cys
γb^{Lw}	28.337	32.125
γb^-	9.783	58.251
γb^+	1.01	8.853 E-3
γb^{AB}	6.287	1.436
γb^{Total}	34.624	33.561

Table 9.5 Silicon Nitride Contact Angles

Contact angles[1] θ (°), n=9	Substrate	
	Silicon Nitride	10 µm CP1
θ^W	54 ± 2	38 ± 2
θ^D	58 ± 1	48 ± 3
θ^F	34 ± 2	27 ± 1

Table 9.6 Silicon Nitride SFE Components

Surface energy components (mJ/m^2), n=9	Substrate	
	Silicon Nitride	10 µm CP1-cys
γb^{Lw}	20.719	27.365
γb^{-}	56.409	35.303
γb^{+}	4.353	4.315
γb^{AB}	31.341	24.684
γb^{Total}	52.06	52.049